Investigation of the deformation rates implied by marine terraces to determine fault slip rates over multiple seismic cycles

BIRKBECK COLLEGE, UNIVERSITY OF LONDON

Investigation of the deformation rates implied by marine terraces to determine fault slip rates over multiple seismic cycles.

Author:

Jennifer Louise Searing Robertson

Supervisor:

Professor Gerald Roberts

Thesis submitted to the

Department of Earth and Planetary Sciences

for the degree of

Doctor of Philosophy

Declaration

Declaration of originality

I, Jennifer Robertson, confirm that the work presented in this thesis is my own. Where information has been derived from other sources, I confirm that this has been indicated in this thesis.

Copyright declaration

Doctoral committee

Professor Gerald Roberts
Department of Earth and Planetary Sciences,
Birkbeck College, University of London.

Funding

This study was part funded by NERC Cosmogenic Isotope Analysis Facility project grants 9186-0418 and 9161-1015 and by NERC Geochronology and Tracers Facility project grant 1734-0517. Fieldwork was funded by the Mike Coward Fund, Geological Society of London; Postgraduate Research Grant, British Society for Geomorphology and the Tim Newling fund, Birkbeck College.

ACKNOWLEDGEMENTS

I am grateful for so many people that have been part of this six-year journey.

My wonderful friends who have always supported me – Rachel, Kelly, Sallie and Charlotte, thank-you for always caring and looking out for me. My Birkbeck crew – those in Room 6.11b who encouraged me to carry on even when I wasn't sure how to, and who made sure that the PhD journey was fun and never lonely – Claudia, Lucy, Ed, Marco, Francesco, and Sam, thank you. Special thanks too to Marco, my fieldwork buddy, for your support during countless trips in the field together. To Steve Hirons, you gave me the research bug and have supported me throughout the entire PhD. To Thanassis Ganas, your generosity with the provision of the DEMs used herein and the time you have kindly given to me during discussions and fieldwork have been instrumental. To Gerald, initially my lecturer, then my supervisor and now friend and colleague – you went above and beyond with your mentorship, for that I will always be grateful; I know I will always be learning from you. Finally, this thesis would not have been possible without the love and support from my family. To my mum – you are my biggest cheerleader, you always believed in me and taught me to persevere no matter what. To my husband Paul – it's not possible to begin to know how to thank you, I am especially grateful for your countless kind words, wise counsel, time, unwavering belief and for keeping me going. You made me see that it was possible and supported me to do something I love for the pure joy of it. Paul, mum, this is as much your achievement as it is mine, without your love and practical and emotional help it simply would not have been possible. To Megan and Harris, let this show you that anything you put your mind to is possible. My darling children, chase your dreams, hold them and never let go. You are both my greatest inspiration and achievement.

This thesis and all of the work it contains is dedicated to my beloved dad, Paul Christopher Searing; always loved, missed and forever driving me forward to never give up.

ABSTRACT

Deformation caused by earthquakes is accommodated along faults over multiple seismic cycles, yet our understanding of fault behaviour is based upon short-term observations over a few thousands of years. This is problematic because some faults have been known to exhibit episodic behaviour, whereby they do not rupture in a time-averaged manner. Thus, it is unclear whether short-term fault observations are representative of fault behaviour over hundreds of thousands of years. This issue confounds our ability to undertake effective seismic hazard assessment, which is vital for population centres and critical facilities located in the vicinity of active faults. Studies on Late-Quaternary palaeoshorelines that are deformed due to upper-plate and subduction-related faulting have been successfully used to interrogate long-term fault behaviour and derive slip and throw rates of faults that are representative of multiple seismic cycles. However, such studies are limited by: (i) a lack of age constraints, (ii) the approach used to correlate undated palaeoshorelines to sea-level highstands and, (iii) the uncertainties associated with sea-level elevations of Late-Quaternary highstands. This thesis employs a new approach to investigate the long-term behaviour of upper-plate extensional faults using deformed palaeoshorelines, it dates wave-cut platforms using ^{36}Cl exposure dating – a method that is yet to be shown to result in reliable age controls for Quaternary wave-cut surfaces, correlates palaeoshorelines to sea-level highstands using the synchronous correlation method and investigates fault-related deformation using half-space elastic modelling. Investigations are focused upon palaeoshorelines in Crete, adjacent to the western Hellenic subduction zone, and within the Gulf of Corinth intracontinental rift. The results presented in this thesis demonstrate that ^{36}Cl exposure dating is an acceptable dating method on Late-Quaternary carbonate wave-cut platforms, and that corals with elevated $\delta^{234}U_i$, usually suggestive of post-depositional diagenesis, can provide reliable palaeoshoreline ages. Synchronous correlation of undated palaeoshorelines to sea-level highstands alongside elastic half-space dislocation modelling allows valuable insight into the dominant tectonic controls of palaeoshoreline deformation. The findings presented herein emphasise that upper-plate extensional faults have the capacity to dominate the deformation observed on coastlines where regional processes were previously thought to dominate and that observations associated with this deformation can provide insights that are essential for seismic hazard assessment for all faults capable of rupture.

CONTENTS

LIST OF FIGURES

LIST OF TABLES

1 CHAPTER 1: INTRODUCTION

1.1 INTRODUCTION TO THE SCIENTIFIC PROBLEM

Earthquakes occur on active normal faults yet our knowledge of how these faults behave over numerous seismic cycles is lacking. In particular, although observations show how single earthquakes cause uplift and subsidence (e.g. Meltzner et al., 2006; Farias et al., 2010; Papanikolaou et al., 2010; Iezzi et al., 2018), and are used to invert for the slip distribution that describes the fault behaviour in that particular earthquake (Barrientos and Ward, 1990; Jonsson et al., 2002; Lavecchia et al., 2016; Cheloni et al., 2017; Brozzetti et al., 2019), we do not know whether faults always rupture with the same slip distribution over multiple seismic cycles (Roberts et al., 1996a; Iezzi et al., 2019). Understanding long-term fault behaviour is further complicated in that evidence suggests some faults do not rupture in a 'time-averaged' manner and instead experience clusters of earthquakes and periods of quiescence. Evidence of episodic earthquake clustering (e.g. Sieh et al., 1989) is apparent on normal faults (Benedetti et al., 2013; Cowie et al., 2017); for example, Benedetti et al. (2013) revealed that in the Italian Apennines, sequences of three to four earthquakes on faults occurred over a 1-2 ka period and were followed by 3-5 ka of relative quiescence. Thus, observations from one seismic cycle cannot be used to forecast future behaviour with certainty (Faure Walker et al., 2010), resulting in uncertainty in seismic hazard assessment and our understanding of this key geological and tectonic process (Stein et al., 2012).

The timescales over which faults are investigated, and the methods employed in such investigations determine the fault-related parameters and knowledge of the parameters that are available to the scientific and seismic hazard modelling community. Understanding the behaviour of active faults predominantly relies on observations and deformation rates (e.g. fault slip/throw rates and hangingwall/footwall uplift rates) obtained throughout the Holocene Epoch, since the Last Glacial Maximum (LGM) ~15 ka (see Roberts and Michetti, 2004, for an explanation of the use of this timing). Such methods include: vertical displacement since the LGM (e.g. Piccardi et al., 1999; Roberts and Michetti, 2004; Panek et al., 2020), dated geomorphic features that are preserved when fault movement perturbs a coastline (e.g. Sieh, 1981; Plafker et al., 1992; Bianca et al., 1999), palaeoseismic trenching (e.g. McCalpin, 1996; Galli et al., 2008), ^{36}Cl fault-scarp dating (e.g. Schlagenhauf et al., 2010;

Cowie et al., 2017) and the historical and instrumental seismicity records (e.g. Tsapanos et al., 2003, 2004; Meletti et al., 2008). The output parameters of such fault investigations include the slip/throw rate, recurrence interval (*Tmean*) and the aperiodicity of the recurrence intervals known as CV ($standard\ deviation\ of\ interearthquake\ time \div Tmean$) (Pace et al., 2006, 2016). These active fault parameters are essential in Probabilistic Seismic Hazard Analysis (PSHA) to estimate the probability of values of ground motion being exceeded in given time periods, from known seismic sources. However, analysis of the most recent ~15 kyrs on a fault is likely to represent just a fraction of the timescale over which a fault has been active. So while such analyses are important, it is unknown to what extent they represent the long-term behaviour of a fault.

Slip rates obtained over different timescales (i.e. present day to 15 ka versus the Quaternary) have been shown to display variations through time (Oskin et al., 2008; Cowgill et al., 2009; Friedrich et al., 2003; Bull et al., 2006; Nicol et al., 2006). These variations have been observed when comparing deformation rates obtained via geodetic studies to those constrained using geological evidence (e.g. Friedrich et al., 2003; Oskin et al., 2008; Cowgill et al., 2009), and from the spatial distribution of individual slip events versus accumulation of displacement over multiple seismic cycles (e.g. Bull et al., 2006) whereby faults host earthquakes that may rupture all or part of a fault (see Iezzi et al., 2019 *and references therein*). In active extensional fault systems where numerous faults accommodate the total regional strain (e.g. Friedrich et al., 2003, Nicol et al., 2006) elastic stress interaction between faults, where rupture on a fault results in stress transfer to adjacent faults (Cowie 1998), has been suggested as one of the processes responsible for temporal slip-rate variability between, for instance, observations over ~10 ka and 300 ka (e.g. Nicol et al., 2006). Elastic stress interaction between faults (referred to as fault interaction, Section 2.2.3) has been shown to occur where the tips of normal faults overlap along strike (e.g. Gupta and Scholz, 2000; Bull et al., 2006) and where faults are closely spaced (~5-15 km) across strike (e.g. Cowie et al., 2017). In this latter setting, fault activity may switch between two across strike faults resulting in periods of earthquake clustering on one fault while the other experiences a period of quiescence before fault activity migrates to the quiescent fault and the originally active fault enters a period of dormancy (e.g. Dolan et al., 2007; Roberts et al., 2009; Cowie et al., 2017; Mildon et al., 2019).

Slip-rate variation through time has the potential to introduce uncertainty about whether a fault is active and capable of producing destructive earthquakes. If a fault is investigated

during a period of quiescence, or has a particularly long recurrence interval that exceeds the historical record and/or low slip rates such that previous ruptures may not be clear in the landscape, then over a Holocene timescale they may be interpreted to be inactive and incapable of producing damaging earthquakes. Similar issues exist when there is a reliance on the relatively short and possibly incomplete historical and instrumental seismicity record as a proxy of future activity on faults. For example, in Greece, instrumental seismicity data has been collected since the late 1800s, and historical records have been reported to go back to before 1000 C.E. but their completeness is strongly debated (Kouskouna and Makropoulus, 2004), though such records differ from country to country. Using data over these relatively short timescales as opposed to data that covers multiple seismic cycles, may be catastrophic, as Stein et al. (2012) elucidate when discussing the destructive 2011 Tohoku, 2008 Wenchuan and 2010 Haiti earthquakes. Further evidence comes from normal faults in the western USA where de Polo and Slemmons (1997) demonstrated that historically recorded seismicity in the Basin and Range Province was inadequate to sample the past 10,000 years of fault activity; these authors showed that when they analysed 17 historic faults, only six had ruptured in historic times (1860 to 2000), but that 16 of the 17 faults had experienced activity since 130 ka.

Knowledge of the long-term (~400 ka) slip/throw rates and recurrence intervals (an indication of the time interval that may occur between earthquakes on the same fault of a similar magnitude) is of use on faults where Holocene data is available and on those where such data has not yet been obtained. The acquisition of long-term fault deformation rates in combination with Holocene data means that the effects of short-term fault clustering on slip/throw rates could be explored within the context of deformation rates over hundreds of ka. This is important because slip/throw rates are an input parameter within PSHA (Pace et al., 2016) and have been shown to contribute to significant uncertainties in the hazard associated with ground motion (Stepp et al., 2001, Faure Walker et al., 2019) if they are in error. Furthermore, knowledge of long-term deformation rates is essential in determining whether a fault is active or not, which is vital for local population centres and in the building and maintenance of critical facilities (nuclear power plants and decommissioning sites) (e.g. Chapman et al., 1994). For instance, the U.S Nuclear Regulatory Commission, the Japan Nuclear Regulation Authorities (NRA), the State of California, and the Western States Seismic Policy (WSSP) (USA) look for evidence of fault movement over the late Quaternary to investigate potentially active faults (Machette, 2000; Stepp et al., 2001;

Chapman et al., 2014); specifically, the Japan NRA and WSSP define an active fault as one with movement within ~130 ka.

What is needed are deformation rates on active faults over numerous seismic cycles. In contrast to fault analysis since the LGM (15 ka), obtaining the same fault parameters over the longer term (10^{4-5} years) is more challenging, but this thesis will show that some important advances can be made. In detail, measurements of long-term slip/throw rates on normal faults (10^{4-5} years) require knowledge of the total vertical offset, the dip and kinematics of the fault, and the time over which the offset has occurred. Such values may be obtained using various methods. Stratigraphic correlation between the footwall and hangingwall of faults can be applied to purely continental settings or where the fault offsets the hangingwall into a marine environment (e.g. Roberts et al., 2002; Bell et al., 2011; de Gelder et al., 2019; Iezzi et al., 2019). In detail, Bell et al. (2009) used seismic reflection data from within the Gulf of Corinth in combination with coastal indicators of uplift (i.e. Holocene notches, late-Quaternary palaeoshorelines) to derive slip rates on the major normal faults in the gulf; while derivation of long-term (~3 Ma) slip rates on faults within the Aterno Valley (central Apennines, Italy) was carried out by Iezzi et al. (2019) using serial geological cross sections across pre-rift strata obtained from detailed geological mapping. Other methods employed to derive deformation rates include studies of the elevations of fault facets (triangular shaped hillslopes located parallel to the range front) formed by normal faulting (e.g. dePolo and Anderson (2000) in the Great Basin and southern Basin and Range (USA)), and the presence of offset markers that allows researchers to directly constrain slip/throw rates where a dated landform (i.e. alluvial surface, palaeoshoreline, pediment surface) has been offset by a fault (Saillard et al., 2011; Burbank and Anderson, 2012; Gutierrez et al., 2020).

This thesis emphasises that coastlines afford excellent opportunities to derive the long-term deformation caused by faulting because evidence of their motion is visible on sets of deformed palaeoshorelines (Fig. 1.1) and their associated marine terraces and wave-cut platforms (e.g. Muhs et al., 1992; Westaway, 1993; Berryman et al., 1993; Armijo et al., 1996; Roberts et al., 2009; Saillard et al., 2009, 2011; Roberts et al., 2013; Binnie et al., 2016; Meschis et al., 2018). A palaeoshoreline is a relict shoreline represented by the intersection between a marine terrace or erosional wave-cut platform and sea cliff (Lajoie, 1986) (Section 2.1.1). Quaternary palaeoshorelines represent markers in the landscape that are produced during sea level highstands associated with interglacial periods (Alexander, 1953) (Section

2.1.2). The palaeoshorelines become uplifted as a result of the interplay between eustatic sea-level change and tectonic uplift (Lajoie, 1986).

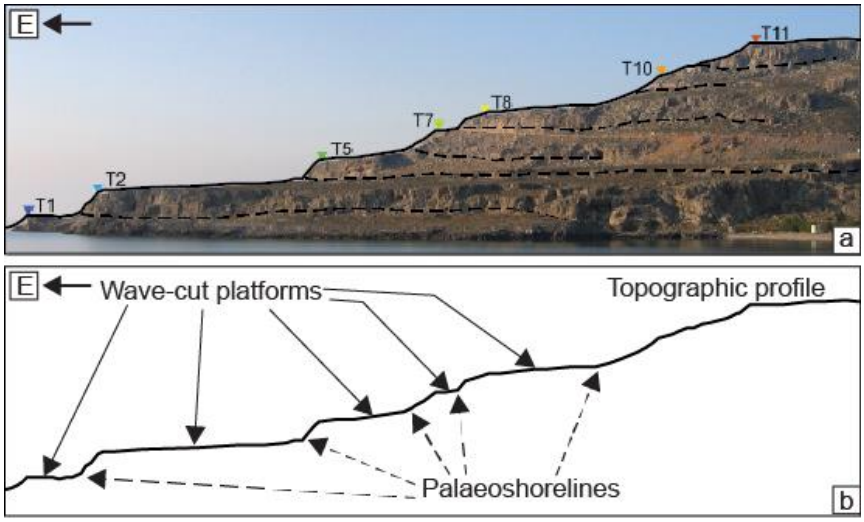

Figure 0.1: (a) Sequence of palaeoshorelines and associated marine terraces from eastern Crete (modified from Strobl et al., 2014), terrace numbers are shown by T1, T2 etc. (b) 2D drawing of (a) detailing the palaeoshorelines and associated wave-cut platforms.

Where faults offset a palaeoshoreline, their deformation rates can be obtained by determining the age of the offset palaeoshorelines in the footwall and hangingwall of the fault (e.g. Saillard et al., 2011). Where determination of both hangingwall and footwall ages are not possible, other successful approaches to derive fault slip/throw rates have been employed. For example, Roberts et al. (2013) constrained the age of a palaeoshoreline located in the hangingwall of the Vibo fault (Calabria, Italy) and used the elevations of other palaeoshorelines in the hangingwall alongside knowledge of past sea-level elevations to assign undated palaeoshorelines to sea-level highstands. They then used observations on the geomorphology of the terraces at the tip of the fault to establish the age of the offset terrace in the footwall and to derive a throw rate since 340 ka. Meschis et al. (2018) employed a similar approach to assign undated palaeoshorelines to highstands on the hangingwall of the Capo D'Orlando fault (Sicily) and calculated fault throw rates using estimated fault uplift to subsidence ratios. Thus, if a fault directly offsets a palaeoshoreline, then the throw/slip rate can be derived directly.

Where the faults are located offshore, but close (<~10 km) to the coastline, the resultant coastal uplift results in sequences of palaeoshorelines which can be used to extrapolate deformation rates (e.g. Armijo et al., 1996, Roberts et al., 2009; Litchfield et al., 2020). This involves constraining the age of one or more palaeoshorelines and correlating undated

palaeoshorelines to sea-level highstands in order to obtain the uplift rates. Palaeoshoreline uplift rates, combined with knowledge of the fault dip and length may be used alongside elastic dislocation modelling (e.g. Armijo et al., 1996; Di Martini et al., 2004) or estimates of fault uplift and subsidence (U:S) ratios (Bianca et al., 1999; Meschis et al., 2018) to derive slip/throw rates. However, these U:S ratios have been shown to vary between 1:2 and 1:7 (Papanikolaou et al., 2010; Stein and Barrientos, 1985; King et al., 1988; Armijo et al., 1996) and may therefore be responsible for introducing significant uncertainty into any inferred slip rate values. Even considering this latter issue, deformed palaeoshorelines provide researchers with an excellent opportunity to derive long-term rates of deformation and recurrence intervals on faults that bound a coastline, especially where there is a lack of, for instance, seismic reflection data to allow correlation between onshore and offshore stratigraphy. For example, in detail, calculating the time averaged long-term recurrence interval of a fault requires knowledge of the average displacement of an earthquake on the fault in question and the throw/slip rate of the fault (Section 2.2.4). In the absence of the throw/slip rate, a datum point – such as a dated palaeoshoreline – may be used to determine absolute vales of uplift over a defined time period and thus infer the recurrence interval (e.g. Cucci and Cinti, 1998; Grant et al., 1999; Cucci and Tertulliani, 2010; Roberts et al., 2013; Meschis et al., 2018), assuming that the elevation of the palaeoshoreline represents only repeated coseismic events.

Deformed palaeoshorelines have been used to provide insight into tectonic deformation along active continental margins (Muhs et al., 1990; Sato and Matsu'ura, 1992; Anderson and Menking, 1994; Saillard et al., 2009; Gallen et al., 2014; Jara-Munoz et al., 2017; Normand et al., 2019; Litchfield et al., 2020) and intra-continental rift zones (e.g. Armijo et al., 1996; De Martini et al., 2004; Roberts et al. 2009; Roberts et al., 2013; Meschis et al., 2018) throughout the world (e.g. Crete, Central Greece, Iran, New Zealand, western USA, Japan, Chile and Italy). However, studies that obtain uplift rates and fault slip/throw rates using deformed palaeoshorelines are not without their issues. These issues relate to age controls, correlating sea-level highstands with undated palaeoshorelines, determining the cause of palaeoshoreline deformation, and a lack of clarity over historic sea-level elevations, as outlined below.

1.2 CHALLENGES ASSOCIATED WITH USING PALAEOSHORELINES TO EXAMINE DEFORMATION

This section introduces some of the issues associated with investigating long-term fault behaviour using deformed palaeoshorelines that will be addressed throughout this thesis.

1.2.1 Determining the age of palaeoshorelines

It has been shown that coastal features (i.e. geomorphology, soil properties and soil/tephra stratigraphy) along sets of deformed palaeoshorelines may be used as relative-age indicators (e.g. Pillans et al., 1994; Berryman et al., 2003; Matsu'ura et al., 2014, 2015). But the degree of confidence associated with these methods is lower than where absolute age controls are used (Muhs, 1990). As such, there is reliance on constraining the age of at least one palaeoshoreline within a sequence in order that undated sea-level highstands can be correlated with palaeoshorelines and uplift rates derived (Burbank and Anderson, 2013). However, the age controls obtained from palaeoshorelines are wholly reliant on the geology (Section 2.1.4). Thus, age controls may be sporadic and dependent on whether the palaeoshoreline hosts datable or correlatable fossils such as corals, molluscs and microfossils (e.g. Cronin, 1981; Pirazzoli et al., 1991; Rockwell et al., 1992; Muhs et al., 1994; Bordoni et al., 1999; Antonioli et al., 2006; Roberts et al., 2009; Papanikolaou et al., 2015) or syn-wave cut platform deposits appropriate for Optically Stimulated Luminescence (OSL) dating (e.g. Barreto et al., 2002; Choi et al., 2009; Gallen et al., 2014; Ott et al., 2019).

One of the most precise and therefore dominantly applied methods of Quaternary fossil dating uses the $^{234}U/^{230}Th$ approach (Section 2.1.4.1); however, there are challenges related to using this method. In $^{234}U/^{230}Th$ dating, the reliability of the carbonates' age is assessed based upon the $\delta^{234}U_i$ (or initial activity ratio of $^{234}U/^{238}U$) matching the present-day oceanic value of ~147‰ (e.g. Stirling and Anderson, 2009; Medina-Elizalde et al., 2013). Applied to corals, the presence of values outside of ~147 ±10‰ is problematic and confusing because some Pleistocene coral ages used as age controls on deformed palaeoshorelines throughout the world have been shown to display elevated $\delta^{234}U_i$ values yet have growth ages in agreement with other coral ages, stratigraphic relationships and the timing of eustatic sea-level highstands (e.g. Poole et al., 1990; Muhs et al., 1994; Bard et al., 1996; Roberts et al., 2009; Houghton, 2010; Roberts et al., 2013).

An alternative method to date palaeoshorelines involves using cosmogenic nuclides on erosive wave-cut platforms (Section 2.1.4.2), such as those within this thesis. Application of cosmogenic nuclide dating is based upon determining the duration of surface exposure to cosmic rays (Dunai, 2010) using measurements of isotopes such as ^{10}Be where there is a

dominant quartz lithology (Saillard et al., 2009, 2011; Lee et al., 2015; Binnie et al., 2016) or ^{36}Cl where a carbonate lithology exists (Stone et al., 1996). These methods are particularly useful where there is a lack of fossils amenable for dating, however, while ^{10}Be has been interpreted to result in successful dating of Late-Quaternary palaeoshorelines, studies using ^{36}Cl have appear to have been less successful, as shown in unpublished theses, owing to erroneously young ages (Wegmann, 2008; Spampinato, 2012; Meschis, 2018) or a broad mix of ages for individual palaeoshorelines that exceed single highstand ages (de Gelder, 2017). Thus, ^{36}Cl exposure dating has not yet been proven to be a reliable method to date Late-Quaternary wave-cut platforms. This may be due to the complexity involved in ^{36}Cl exposure dating because ^{36}Cl can be formed via multiple pathways, requires ancillary geochemical analyses and data analysis is known to be more difficult compared to other exposure dating methods (Cockburn and Summerfield, 2004). Where carbonate wave-cut platforms dominate, application of ^{36}Cl exposure dating has the potential to directly constrain the ages of platforms that may, otherwise, not be datable.

1.2.2 Correlating undated palaeoshorelines to sea-level highstands

It is not always practical or possible to date each palaeoshoreline such that it may be assigned to a sea-level highstand. To combat this, scientists use correlation methods to allocate undated palaeoshorelines to highstands. One such commonly applied method is the sequential method (e.g. Armijo et al., 1996; Saillard et al., 2011; Gallen et al., 2014) which assumes that the preserved palaeoshorelines within a sequence represent all of the past sea-level highstands (Section 2.1.5). This latter point is important, as it has been shown that below uplift rates of ~1 mm/yr (Pirazzoli, 2013), older palaeoshorelines may be overprinted and destroyed by younger sea-level highstands (e.g. Westaway et al., 2000; Roberts et al., 2009; Jara-Munoz and Melnick, 2015; Pedoja et al., 2014, 2018; Normand et al., 2019). Thus, it is possible that sequential correlation may result in the incorrect allocation of undated palaeoshorelines to highstands, which has implications for understanding the temporal history of uplift. The synchronous correlation method developed by Houghton et al. (2003) and applied in Roberts et al. (2009, 2013); Meschis et al. (2018) and Pedoja et al. (2018) combats this issue, making use of the fact that Quaternary sea-level highstands are unevenly spaced in time and thus, with a constant uplift rate, will result in a palaeoshoreline sequence whereby the uneven spacing of the elevations of palaeoshorelines reflects the uneven ages of the Quaternary sea-level highstands.

1.2.3 Multiple uplift mechanisms

Sequences of deformed palaeoshorelines have been shown to exist along the leading-edge of subduction zones and within intra-continental rift zones. In subduction zone settings, the mechanisms of uplift are complex and may include sediment underplating, slip on the subduction interface and, upper-plate reverse, normal or strike-slip faulting located in the forearc (e.g. McNeill et al., 1998; Meltzner et al., 2006; Shaw et al., 2008; Saillard et al., 2011; Mouslopolou et al., 2015a; Mouslopolou et al., 2016; Ott et al., 2019; Litchfield et al., 2020) (Section 2.2.2). Therefore, obtaining long-term fault deformation rates is difficult because it involves making assumptions about the dominant uplift process. For instance, studies may directly associate palaeoshoreline uplift with slip distribution on the subduction interface (e.g. Nalbant et al., 2013; Sato et al., 2016) without considering the effects of upper-plate faulting on observed palaeoshoreline uplift (e.g. Mouslopolou et al., 2016). Furthermore, the presence of closely-spaced faults in both subduction zone and intra-continental rift zone settings means that there is the potential for interaction between faults in the form of stress enhancement (Section 2.2.3), this adds further complexity when attempting to derive long-term deformation rates.

1.2.4 Variation of past sea-level elevations

Knowledge of historic sea-level elevations is vital in order to correlate sea-level highstands with palaeoshorelines (Section 2.1.5). However, owing to differing approaches employed in the construction of Quaternary sea-level curves, it has been shown that different sea-level curves reveal sea-level elevations for past highstands that are not in agreement with one another (Caputo et al., 2007); this observation means that a set of palaeoshorelines may yield varying uplift histories where different sea-level curves are used (de Gelder et al., 2020) and may result in unrecognised uncertainties associated with the fault deformation rates calculated from palaeoshoreline sequences.

1.3 THESIS APPROACH

This thesis uses a new approach to study deformed palaeoshorelines, combining synchronous correlation with $^{234}U/^{230}Th$ coral age dating and ^{36}Cl exposure dating of carbonate wave-cut platforms. This approach, alongside elastic half-space dislocation modelling, allows new insights into the long-term (10^{4-5} years) processes responsible for

palaeoshorelines that are deformed over timescales involving thousands of earthquakes; it also allows determination of fault slip/throw rates and recurrence intervals that are essential for seismic hazard assessment. Specifically, detailed field mapping and interrogation of a 5 m digital elevation model (DEM) is complemented with the application of ^{36}Cl exposure dating on late Quaternary palaeoshorelines. The reliability of new ^{36}Cl exposure ages is determined by cross checking them against existing age controls (obtained from OSL $^{234}U/^{230}Th$ coral ages) and new $^{234}U/^{230}Th$ coral growth ages, and against the results obtained from synchronous correlation modelling. The approach herein, therefore, allows the reliability of both dating methods to be examined with attention paid to the relationship between the locations of the corals, their ages and $\delta^{234}U_i$. Correlation of measured, undated palaeoshoreline elevations with past sea level highstands is carried out using the absolute ages and the synchronous correlation method. Sensitivity testing of the effects of different sea-level curve data to calculating fault-related uplift rates and recurrence intervals is undertaken to ensure that the approach and results presented herein are reliable.

1.4 AIMS AND OBJECTIVES

The aims of this PhD are: (i) establish the reliability of two methods used to investigate deformed palaeoshorelines and their associated wave-cut platforms: cosmogenic ^{36}Cl exposure dating and $^{234}U/^{230}Th$ coral growth ages, (ii) interrogate the sensitivity of uplift calculations and deformation rates to different sea-level curves, (iii) investigate whether synchronous correlation of palaeoshorelines to sea-level highstands outperforms sequential correlation, (iv) apply these methods of dating to deformed palaeoshorelines, correlate palaeoshorelines to eustatic highstands and apply elastic half-space modelling in order to investigate the tectonic processes and faults responsible for uplift in order to, (v) derive deformation rates that are essential to contribute to probabilistic seismic hazard assessment (PSHA) and our understanding of fault deformation over multiple seismic cycles. In this thesis, the use of the term deformation rates relates to that caused by faults and includes palaeoshorelines' uplift rates and fault slip/throw rates. The former can be used to calculate the latter.

The objectives of this thesis are designed to address the problems outlined above, and are as follows:

1) Determine whether ^{36}Cl exposure dating can be used as a method to date late Quaternary wave-cut platforms, detailing the sampling methodology and cross checking new ages against those obtained from other dating methods. If ages are to be interpreted as reliable they should agree with existing ages, produce ages that fit within known eustatic sea-level highstand periods and be able to be explained by uplift modelling. Test whether ^{36}Cl exposure dating can be used to derive age controls interpreted to be reliable on different carbonate lithologies.
2) Alongside the results of objective (1), undertake analyses of a sequence of deformed (uplifted or subsided) palaeoshorelines along southern Crete in order to determine the possible causal faults and the associated long term ($10^{4\text{-}5}$ yr) deformation rates. This is achieved using field mapping, interrogation of a 5 m Digital Elevation Model (DEM), ^{36}Cl exposure dating of wave-cut platforms, uplift modelling using the sea-level curve of Siddall et al. (2003) and elastic half-space modelling.
3) Determine the extent to which the uplift values and deformation rates obtained by matching eustatic sea-level highstands to palaeoshorelines are influenced by the sea-level curve employed. This is achieved using data from a number of different sea level curves to model the measured palaeoshoreline elevation data obtained in objective (2) and through comparison of the results.
4) Determine the formation age of marine terraces at different elevations located on Cape Heraion, eastern Gulf of Corinth, Greece, to explore the cause of the observed uplift. Alongside the results of objective (1) and new and existing $^{234}U/^{230}Th$ coral age dating, detailed mapping is used to establish the relationship between dated and undated surfaces that exist at elevations from 7-62 m. The multiple new age controls are used to derive the summed throw rates of faults throughout the cape. These rates are used in combination with coulomb stress transfer modelling to investigate the dominant tectonic process responsible for uplift.
5) Assess the age reliability of $^{234}U/^{230}Th$ dated corals that grow within coastal margins and restricted marine environments and are used to derive uplift rates of palaeoshorelines. This will be achieved using new coral ages and analysis of all late-Quaternary coral growth age data from within the Gulf of Corinth to carry out a systematic analysis of the initial ratios of $^{234}U/^{238}U$ ($^{234}U/^{238}U_i$) in seawater at the time of coral formation, which is used to determine age reliability.

1.5 STUDY AREAS

Investigations on two palaeoshoreline settings in Greece are used to fulfil the aims and objectives of the thesis, a sequence of uplifted deformed palaeoshorelines located in the forearc of the Western Hellenic Subduction Zone (WHSZ) and an offset marine terrace located in an intracontinental rift zone within the Gulf of Corinth (Fig. 1.2). Both of these locations were selected because wave-cut platforms have been cut into carbonate surfaces on the terraces and they have existing absolute age controls that are important to be able to assess the reliability of ages obtained from ^{36}Cl exposure dating. At both settings, there is ambiguity about whether the uplift is caused by regional subduction-related activity or extensional faulting within the upper plate. These sites, therefore, provide an ideal opportunity to both test the exposure dating method and apply sea-level to palaeoshoreline correlation techniques, spatial analysis of uplift rate change and computational modelling in order to investigate long-term uplift causes and quantify long-term rates of deformation essential for PSHA.

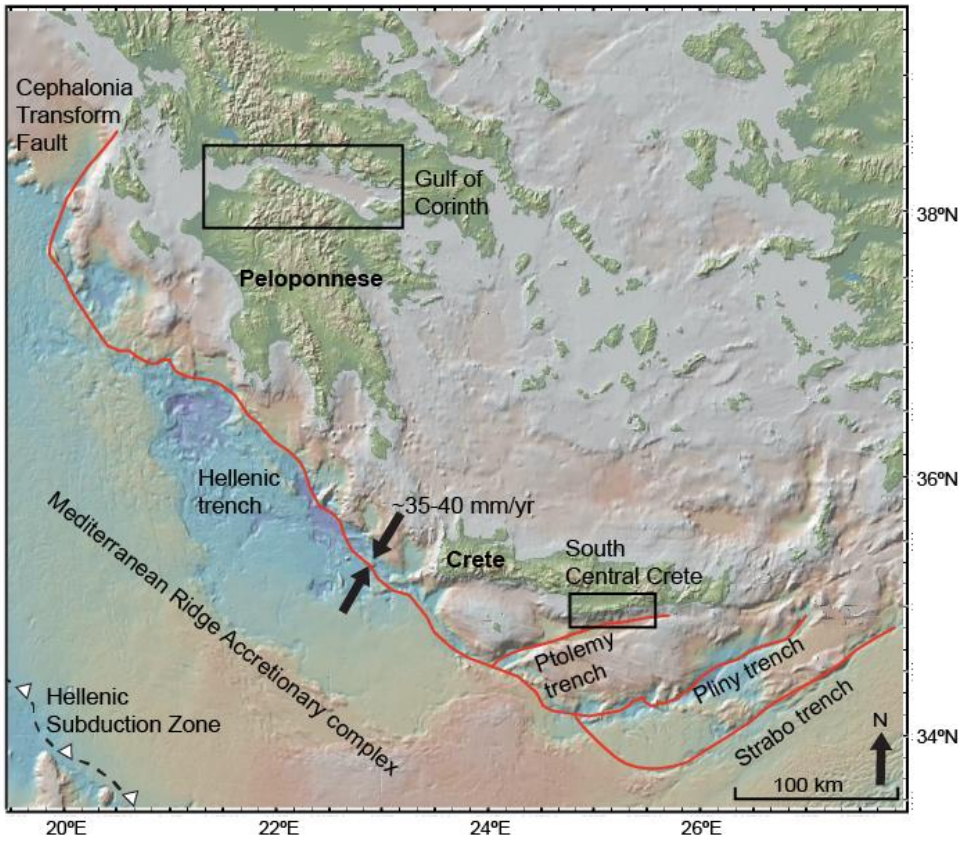

Figure 0.2: Tectonic setting of Greece in relation to the Western Hellenic Subduction Zone. Locations that are the focus of this thesis are shown. GPS data are from Nocquet (2012).

1.6 THESIS STRUCTURE

Chapter one introduces the scientific problem that this thesis aims to address and details the aims and objectives employed. It provides an overview of the issues associated with using deformed palaeoshorelines to quantify tectonic uplift and derive long-term rates of fault deformation.

Chapter two provides an overview of the geological and tectonic background of the study areas and dominant scientific themes related to sequences of palaeoshorelines, specifically their formation, preservation, dating and correlation within the context of eustatic sea-level variation. This chapter also outlines relevant themes related to faulting including fault-related deformation on sequences of palaeoshorelines, elastic fault interaction and seismic hazard.

Chapter three describes the general methods employed in the thesis, in particular identifying the features associated with palaeoshorelines, measuring palaeoshoreline elevations in the field and from a DEM, ^{36}Cl exposure dating and ^{234}U/^{230}Th coral sampling approaches and preparation and calculation of ^{36}Cl exposure ages. It details the application of elastic half-space dislocation modelling using Coulomb 3.4 software.

Chapter four presents an overview of the study area, specific methods and results for the study of a sequence of deformed palaeoshorelines located along the south central coast of Crete (Fig. 1.2). This chapter presents five ^{36}Cl exposure ages from wave-cut platforms that agree with existing OSL age constraints, eustatic sea-level highstand ages and the results of palaeoshoreline modelling using sea-level curve data. The results indicate that ^{36}Cl exposure dating can be used to date limestone wave-cut platforms. The chapter highlights that not all highstands have preserved palaeoshorelines, emphasising the importance of synchronous correlation, and shows that observed spatial uplift rate variations along south central Crete occur as a result of deformation by upper-plate faults in combination with subduction related (regional) activity. This chapter contributes toward objectives (1) and (2). This work is published in Robertson et al. (2019) in *Tectonics*.

Chapter five presents uplift modelling and derivation of recurrence intervals using different sea-level curves. An analysis of the variation between highstand age and relative sea-level elevations from six sea-level curves shows that while the use of different sea-level curves results in small differences between the absolute values of uplift and recurrence intervals,

the overall pattern of uplift identified in Chapter four does not vary significantly. A key finding from this chapter is that the observed variation of deformation rates due to the use of different sea-level curves is highly comparable to the propagated uncertainties when a single sea-level curve is employed. This chapter contributes toward objective (3). This work is under preparation for submission to *Tectonics*.

Chapter six presents an overview of the study area, specific methods and the results of a dual isotope approach to date wave-cut platforms that are at different elevations on Cape Heraion, eastern Gulf of Corinth, Greece (Fig. 1.2). Existing coral growth ages cannot resolve two competing hypotheses of: (i) distributed faulting along a single platform in the tip zone of an active crustal scale fault (Morewood and Roberts, 1997), versus (ii) a sequence of late Quaternary terraces uplifted due to regional forces (Leeder et al., 2003; Leeder et al., 2005). Results from this chapter shows that there is agreement between age determinations of new and existing $^{234}U/^{230}Th$ coral growth ages and ^{36}Cl exposure ages of wave-cut platforms suggestive that Cape Heraion is comprised of a faulted marine terrace that formed during Marine Isotope Stage (MIS) 5e, 125 ka highstand. This chapter provides a further example of the application of ^{36}Cl exposure dating to date palaeoshorelines, this time with differing carbonate lithologies. The age constraints in this chapter and detailed geological mapping are used to show that distributed normal faulting on Cape Heraion results in anomalously high summed throw rates since the Late Quaternary. Comparison of the displacement gradient of this fault to other normal faults and Coulomb stress transfer modelling is used to infer that stress interaction in the overlapping tip zone between two crustal-scale faults is the dominant cause of high throw rates. This chapter contributes toward objectives (1) and (4). This work has been published in *Journal of Structural Geology*.

Chapter seven uses the agreement between the ^{36}Cl exposure dating and $^{234}U/^{230}Th$ coral growth ages in Chapter six to investigate the broader reliability of U-series coral dating to calculate uplift rates of palaeoshorelines. Typically, corals with an elevated $\delta^{234}U_i$ are suggested to have unreliable growth ages. However, ages from within the Gulf of Corinth have elevated $\delta^{234}U_i$, but cluster on known glacio-eustatic highstands, agree with other absolute age constraints and can be explained relative to their stratigraphic position. This chapter presents the results of analysis on new and existing coral growth data from 155 corals dated from within the Gulf of Corinth. The findings of this chapter detail that where late Quaternary corals have grown in a semi-restricted to restricted marine environment, such as along coastal margins or within silled basins, they may have been subjected to growth

conditions that are not reflective of homogenous open oceans and should not be assessed based on the same principles of open ocean corals. This chapter contributes toward objectives (1) and (5). This work is under preparation and intended to be submitted to *Earth and Planetary Science Letters*.

Chapter eight provides a synthesis of the findings from chapters four to seven and discusses the implications of these findings. Specifically, examining the application of ^{36}Cl exposure dating to wave-cut platforms herein, with respect to previous studies. This chapter details the new avenues of research that are possible given the findings presented herein, with specific attention paid to the tectonics of subduction zones and understanding the seismic hazard. This latter point is explored in terms of the seismic potential of faults along the south of Crete and the relationship between slip rates and expected earthquake rates and probabilities.

Chapter nine presents the overall conclusions identified from the research carried out within the thesis.

1.7 AUTHOR STATEMENT

Chapter four: the author of this thesis has completed the collection of field data, interrogation of the DEM, identification of ^{36}Cl sampling locations, sampling and preparation of ^{36}Cl exposure samples, and exposure age determination modelling within in this chapter. The author modified the marine terrace calculator of Roberts et al., 2009, extending it from 410 ka to 900 ka.

Chapter five: the author carried out all modelling and data analysis within this chapter.

Chapter six: the author carried out detailed geological mapping, identification of ^{36}Cl sampling locations, sampling (with the exception of sample 4 that was collected by G. P. Roberts during 2015 field campaign) and preparation of ^{36}Cl exposure samples and coral sampling detailed within this chapter. Compilation of throw data and summed throw analyses and Coulomb stress change modelling was also carried out by the author.

Chapter seven: The author of this thesis carried out systematic analysis of all coral data from within the Gulf of Corinth. Coral samples dated in this chapter were collected by G. P. Roberts during 2015 field campaigns from a location latterly mapped by the author of the thesis. The author of the thesis carried out coral preparation prior to U-series dating.

The results presented in Chapter four are published in: Robertson et al. (2019), *Tectonics.*

The results presented in Chapter five are in preparation for submission to *Tectonics*.

The results presented in Chapter six are published in: Robertson et al. (2020) *Journal of Structural Geology.*

The results presented in Chapter seven are in preparation for submission to *Earth and Planetary Science Letters.*

The author of this thesis has contributed as co-author to the following:

Meschis, M., Scicchitano, G., Roberts, G.P., **Robertson, J**., Barreca, G., Monaco, C., Spampinato, C., Sahy, D., Antonioli, F., Mildon, Z.K. and Scardino, G., 2020. Regional deformation and offshore crustal local faulting as combined processes to explain uplift through time constrained by investigating differentially-uplifted Late Quaternary palaeoshorelines: the foreland Hyblean Plateau, SE Sicily. *Tectonics*, *In press*.

Meschis, M., Roberts, G. P., Mildon, Z. K., **Robertson, J**., Michetti, A. M., & Walker, J. F. (2019). Slip on a mapped normal fault for the 28th December 1908 Messina earthquake (Mw 7.1) in Italy. *Scientific reports*, *9*(1), 1-8.

Meschis, M., Roberts, G. P., **Robertson, J**., & Briant, R. M. (2018). The Relationships Between Regional Quaternary Uplift, Deformation Across Active Normal Faults, and Historical Seismicity in the Upper Plate of Subduction Zones: The Capo D'Orlando Fault, NE Sicily. *Tectonics*, *37*(5), 1231-1255.

Iezzi, F., Mildon, Z., Walker, J. F., Roberts, G., Goodall, H., Wilkinson, M., & **Robertson, J**. (2018). Coseismic throw variation across along-strike bends on active normal faults: Implications for displacement versus length scaling of earthquake ruptures. *Journal of Geophysical Research: Solid Earth*, *123*(11), 9817-9841.

Pedoja, K., Jara-Muñoz, J., De Gelder, G., **Robertson, J**., Meschis, M., Fernández-Blanco, D., ... & Bessin, P. (2018). Neogene-Quaternary slow coastal uplift of Western Europe through the perspective of sequences of strandlines from the Cotentin Peninsula (Normandy, France). *Geomorphology*, *303*, 338-356.

2 CHAPTER 2: LITERATURE AND GEOLOGICAL BACKGROUND

This chapter introduces and explores the key scientific knowledge that underpins the research within this thesis. It begins with describing the formation and preservation of tectonically uplifted palaeoshorelines and eustatic sea-level change throughout the late Quaternary, as this is integral to the study of sequences of palaeoshorelines, and discusses absolute dating and the variation between approaches used to correlate sea-level highstands with palaeoshorelines. The chapter then focuses on faulting, introducing normal faulting and illustrating how fault-related uplift can be investigated using deformed palaeoshorelines before considering fault interaction and seismic hazard. Each of the geological areas discussed throughout the thesis are then introduced.

2.1 FORMATION, PRESERVATION AND INVESTIGATION OF MARINE TERRACES AND PALAEOSHORELINES

2.1.1 Formation of palaeoshorelines and associated features

Palaeoshorelines represent markers in the landscape that are produced during previous sea-level highstands. Pedoja et al. (2011) defined three types of palaeoshorelines: (i) erosional (displaying wave-cut platforms, caves and notches), (ii) depositional (hosting wave-built terraces, beach deposits, beach rocks, beach ridges, tidal flats and other coastal deposits) and, (iii) constructional (represented by algal trottoirs and coral reefs). However, Pedoja et al. (2011) also noted that palaeoshorelines frequently displayed features suggestive of more than one type of palaeoshoreline such that identifying them using individual features is difficult. Furthermore, different types of palaeoshoreline can merge along strike.

The focus of this thesis is within the eastern Mediterranean, where palaeoshorelines that display relatively high uplift, low sedimentation rates and erosive features are prevalent (Pedoja et al., 2011). Therefore, the processes associated with the formation of erosive palaeoshorelines are documented in more detail below. Erosional palaeoshorelines are formed in settings where the dominant processes are mass wasting and wave action (Alexander, 1953; Bradley and Griggs, 1976; Muhs et al., 1994). Features associated with erosional palaeoshorelines include wave-cut platforms and notches (Figs. 2.1, 2.2); a wave-

cut platform is a sub-horizontal erosional unconformity that truncates older strata (Pillans, 1990).

The formation of erosional palaeoshorelines on a rocky shoreline involves the constant attack of waves onto a coastline resulting in the formation of an abrasion notch and wave-cut platform (Pirazzoli, 1986) (Fig. 2.1). In detail, during transgressive sea-level rise in the early highstand (Anderson et al., 1999; Trenhaile, 2000) wave-cut platform formation begins with the development of a notch, continued wave erosion deepens the notch into the cliff and formation of a wave-cut platform occurs (Lajoie, 1986). Over time, undercutting the cliff leads to rock collapse onto the platform below (Burbank and Anderson, 2013); the process of wave erosion continues on the cliff face and its platform, but is enhanced by further abrasion caused by the motion of waves that contain debris from cliff fall (e.g. Bradley and Griggs, 1976; Trenhaile, 2002; Burbank and Anderson, 2013). This cycle of erosion is repeated throughout the duration of the highstand and can result in the formation of wave-cut platforms that are tens of meters wide. Along carbonate coasts, notch formation may also involve biological and chemical processes in addition to the physical process above (Trenhaile, 2015) whereby they form as a result of chemical dissolution and biological abrasion involving rock boring and grazing biota (Pirazzoli, 1986; Rust and Kershaw, 2000). These processes are based upon the dissolution of soluble, and therefore mobile, $CaCO_3$ (calcium carbonate) from the carbonate lithologies that make up the rock surface, however, the processes are complex and the extent to which chemical dissolution occurs is dependent on factors including the lithology of the coastline, temperature and geochemistry of the water (Trenhaile, 2015). In the Mediterranean, with its restricted tidal range (10-20 cm during normal wave conditions, (Bonaduce et al., 2016), fossil marine notches are an established reliable approximation of sea level (Pirazzoli, 1986). However, previous studies have suggested that the elevation of a notch may not directly represent palaeo-sea level and that their reliability as palaeo-sea-level indicators depends on the dominant cause of notch formation, the lithology of the rock being eroded and orientation of bedding (e.g. Kershaw and Guo et al., 2001). The implication of these observations is further discussed in Section 3.1.2.

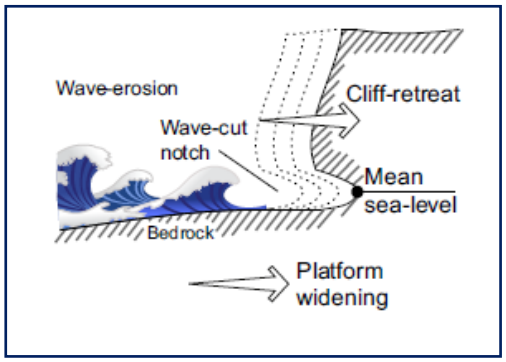

Figure 2.1: Formation of a notch and wave-cut platform over repeated wave erosion cycles, modified from Jara-Munoz et al., (2016).

Wave-cut platforms and notches (Fig. 2.2a, b) predominantly form in the intertidal zone, which represents the area of the shore washed by waves from low tide to high tide. Both the wave-cut platform and the palaeoshoreline/notch may display preserved erosional features and fossil assemblages that are characteristic of the environment within the intertidal zone. Surface features on wave-cut platforms, such as millholes/potholes (Fig. 2.2d), record the effect of physical erosion. These features are circular depressions in the platform caused by pebbles scouring the surface as a result of wave action (Miller and Mason, 1994; Griggs and Trenhaile, 1994; Pirazzoli, 2013). The effects of bioerosion on the notches and wave-cut platforms are from burrowing, boring and grazing organisms that leave their mark in the form of borings and fossil shells (Scheffers et al., 2012). Borings are typically visible from sponges and the bivalve *Lithophaga lithophaga*, which tunnels into the rocky substrate to form smooth holes up to 9 cm deep (Peharda et al., 2015) (Fig. 2.2c). Lines of lithophagid borings have been observed within present day and fossil sea-level notches (e.g. De Guidi et al., 2003; Cooper et al., 2007; Roberts et al., 2009; Shaw et al., 2010; Evelpidou et al., 2012: Meschis et al., 2018).

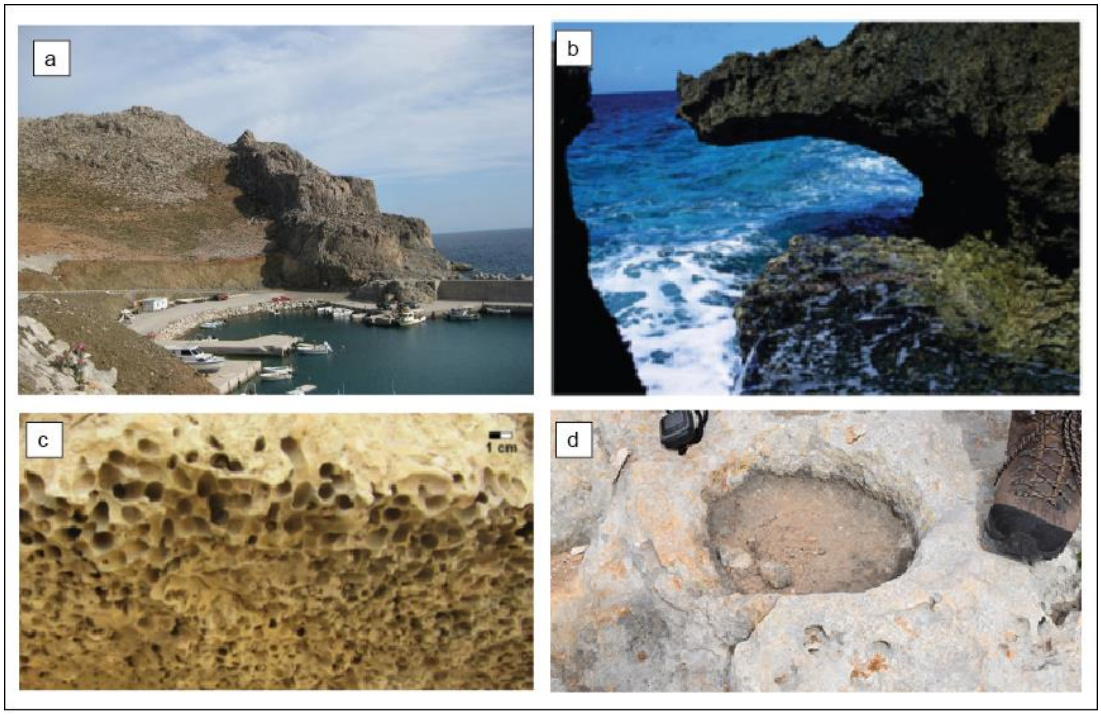

Figure 2.2: (a) Sequence of erosional palaeoshorelines from Lentas, Crete (Sean Gallen) (https://sites.google.com/site/theseanswebsite/current-research/crete-greece) (b) Tidal notch along southern Crete, Greece (from Scheffers et al., 2012); (c) lithophagid borings (from Falkenroth et al., 2020), (d) Millhole with lithophagid borings on the outer edges on the Peloponnese (author's own photograph from the Western Peloponnese).

Along coastal sections where softer less-lithified sediments dominate, wave-cut platforms may form on marine shoreface sediments that were laid down during the sea-level transgression associated with a highstand. In some studies, these marine shoreface sediments are referred to as 'caprock'. This 'caprock' is typically a thin layer (a few meters thick) of marine deposits, that unconformably overlie the strata that were in place prior to palaeoshoreline formation (e.g. Doutsos and Piper, 1990; Armijo et al., 1996; Gaki-Papanastassiou et al., 2011). The marine deposits that comprise the 'caprock' may represent progradational sequences that coarsen up from sandstones to beach or shoreface conglomerates (e.g. Doutsos and Piper, 1990; Armijo et al., 1996 *and references therein*).

Palaeoshorelines may be wholly erosional or associated with down-dip sediments and/or constructional coral and algal growths (e.g. Roberts et al., 2009; Matsur'ura et al., 2014; Jara-Munoz and Melnick, 2015). Moreover, predominantly erosional palaeoshorelines, where wave-cut platforms and notches occur, have been shown to be located along strike and contemporaneous with palaeoshorelines that display more depositional characteristics (e.g. Roberts et al., 2009; Matsur'ura et al., 2014; Jara-Munoz and Melnick, 2015). One such example is documented in Roberts et al. (2009) in the Gulf of Corinth, Greece, where wave-

cut platforms that are cut into limestones, volcanics or Quaternary conglomerates can be mapped along strike into shallow marine shoreface sediments that form layered deposits comprised of lower shoreface silts, medium to coarse-grained sand, and upper shoreface pebble to cobble-grade conglomerates. Such settings are suggested to be dependent on variable wave erosion linked to the geometry of the coastline (Trenhaile, 2002) where, for instance, stacked sediment accumulation may occur in bays while headlands develop wave-cut platforms (Fig. 2.3). The observed lateral variation between layered successions and sequences of wave-cut platforms is an example of the complexity of palaeoshoreline formation.

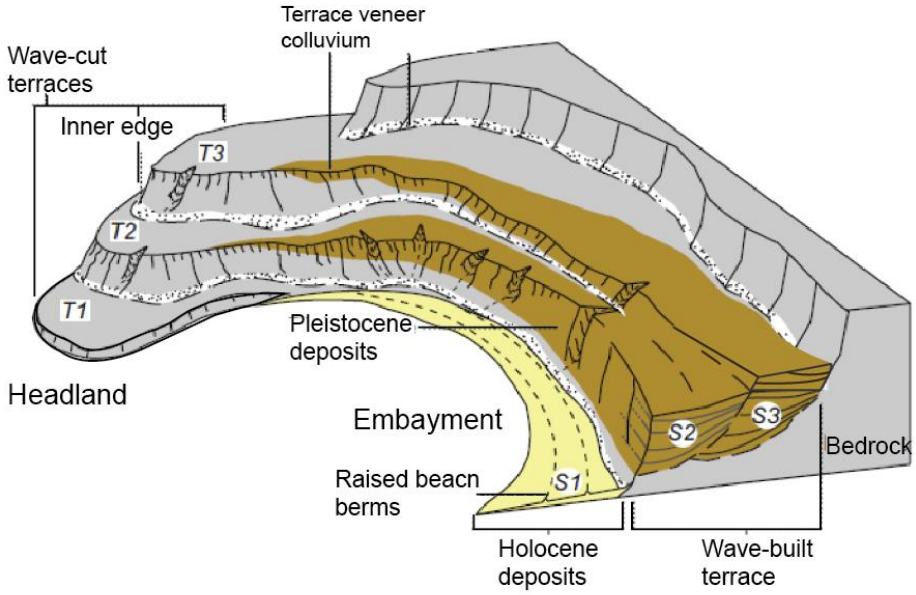

Figure 2.3: Potential spatial relationships between wave-cut platforms and depositional palaeoshorelines as per Trenhaile (2002) (modified from Jara-Munoz and Melnick, 2015).

2.1.2 Late Quaternary sea level variation

Understanding historical sea level is necessary in order to use palaeoshorelines to investigate fault-related uplift. Throughout the late Quaternary, changes in the volume of global ice, driven by long-term climatic cycles that are themselves driven by orbital parameters (Peltier, 1998; Kominz, 2009), are the dominant control on global sea-level (typically referred to as eustatic sea-level, Rovere et al., 2016a). These orbital parameters relate to variations over time in the shape of the Earth's orbit, the angle of tilt of the axis and the direction that the axis of rotation is pointed (Berger, 1988; Berger, 2013), and have resulted in changes to the

effective solar insolation that reaches the Earth's surface (Lambeck et al., 2002) through time. Specifically, variations in the Earth's orbit around the sun have been strongly linked to Pleistocene changes in continental ice volume (Peltier, 1998) over ~100 kyr cycles for the past 1 Myr (Lambeck et al., 2002).

Glacial and interglacial periods represent periods of high ice extent, low temperatures and low sea-level versus warmer temperatures, low ice extent and higher sea-level, respectively (Past Interglacials Working Group of PAGES, 2016). Interglacial periods host sea-level highstands seen as peaks on a sea-level curve (Fig. 2.4) (e.g. Siddall et al., 2003; Railsback et al., 2015). Numerous studies have investigated historic sea-levels and constructed sea-level curves that document the elevation changes of sea level over the Pleistocene and beyond (e.g. Lambeck and Chappell, 2001; Waelbroeck et al., 2002; Siddall et al., 2003; Bintanja and van de Wal, 2008; Rohling et al., 2009, 2014; De Boer et al., 2010; Grant et al., 2014; Past Interglacials Working Group of PAGES, 2016; Spratt and Lisiecki, 2016). Each of the peaks (highstands) and troughs (lowstands) in sea-level curves relates to a stage or sub-stage (e.g. Emiliani, 1995; Shackleton, 1969; Railsback et al., 2015), these oxygen isotope stages are known as Marine Isotope Stages (MIS).

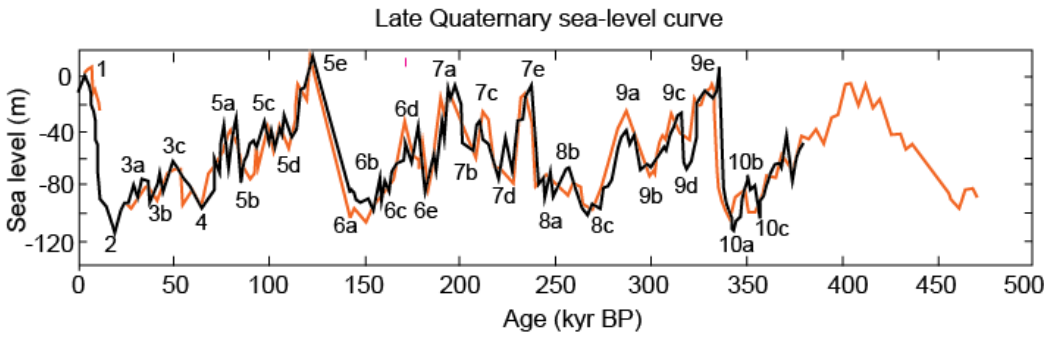

Figure 2.4: Eustatic sea-level curve from ~400 ka to the present day, modified from Siddall et al. (2003), black and orange lines represent two different cores used in the study. Each of the peaks (highstands) and troughs (lowstands) relates to a Marine Isotope Stage (MIS) given here as per Railsback et al. (2015).

On Late-Quaternary timescales, the elevations of past sea level highstands have predominantly been derived using local observations on dated benchmarks (e.g. sand-barrier shorelines, coral reefs, speleothems), the variation of oxygen isotopes in marine sediments, and reconstructions of past ice sheets (Siddall et al., 2007 and *references therein*); these methods are explored below. Sea level estimates derived using benchmarks rely on the assumption that the sample has been removed from a tectonically stable coastline (e.g. Hearty et al., 1999; Muhs et al., 2011) and on accurate ages from, for instance, OSL and U-series dating on corals, fossils, marine sediment and speleothems (e.g. Richards et al., 1994;

Hilliare-Marcel et al., 1996; Muhs et al., 2011; Simms et al., 2011; Hibbert et al., 2016). Of all of these methods, $^{234}U/^{230}Th$ on corals has been the dominant approach, such that over the past ~30 years, a large dataset of coral sea-level benchmarks (Medina-Elizalde, 2013; Hibbert et al., 2016 *and references therein*) and knowledge about the growth of constructional marine terraces from coral reefs during highstands (e.g. Burbank and Anderson, 2013) have allowed both highstand-specific and late Quaternary sea-level curves to be developed (Chappell, 1974; Stirling et al., 1998; Bard et al., 1990; Hearty et al., 2007; Dutton et al., 2009; Dutton and Lambeck, 2012; O'Leary et al., 2013). The success of coral benchmarks as sea-level indicators is partly as a result of the reliability and precision of the $^{234}U/^{230}Th$ method.

Marine oxygen isotopes have been shown to vary throughout climatic cycles associated with sea-level highstands and lowstands (Imbrie et al., 1984). Using oxygen isotope records from marine sediment cores to establish eustatic highstand and lowstand timing (e.g. Siddall et al., 2003; Rohling et al., 2009, 2014) is dependent on our understanding of the behaviour of ^{18}O and its lighter isotope, ^{16}O, specifically, that the ratio of $^{16}O/^{18}O$ in ice sheets is different compared to the ocean. During glaciation, preferential evaporation of ^{16}O leaves the ocean enriched in ^{18}O, whereas condensation and precipitation preferentially removes ^{18}O from water vapour, such that when the vapour arrives at the poles it is significantly enriched in ^{16}O. Consequently, the ice sheets that form at the poles are isotopically light in comparison to sea water; the higher the volume of ice stored on land, the higher the concentration of ^{18}O in the open ocean (Fig. 2.5). Small organisms (foraminifera/ostracods) that have grown in the oceans over time reflect the isotopic signal of the sea water in which they grew yielding records of $\delta^{18}O$ of calcite which can be used to construct sea-level curves (e.g. Lisiecki and Raymo, 2005). However, comparison of the sea-level estimates derived from coral datasets compared with $\delta^{18}O$ records revealed a mismatch between the two datasets (Chappell and Shackleton, 1986), which has been postulated to be linked to variations in deep water temperature (Chappell and Shackleton, 1986; Shackleton, 1987), temporal differences in the isotopic composition of meltwater (Marshall and Clarke, 2002) and possible variations regarding the preferential evaporation of ^{16}O, and therefore the ^{18}O incorporated into ice sheets (Bintanja et al., 2005). Despite their lack of direct agreement, both methods provide valuable insight into the elevations of past sea-levels.

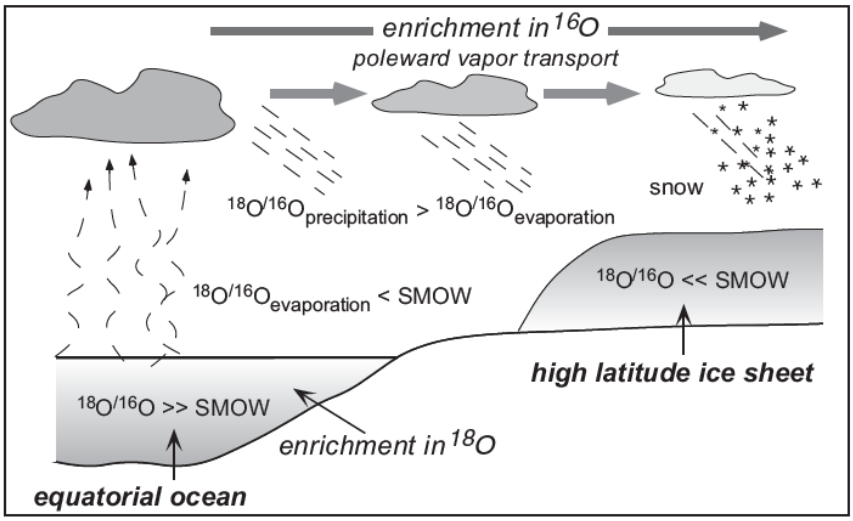

Figure 2.5: Isotopic changes during glaciation, where SMOW refers to Standard Mean Ocean Water (from Burbank and Anderson, 2013).

Oxygen isotope data from benthic foraminifera provide constraints on deep sea temperature, continental ice volume, and high latitude sea surface temperatures (Zachos et al., 2001). However, the oxygen isotope data from foraminifera shells is complex to interpret because both temperature and the process of ice-sheet growth and decay outlined above have been shown to impact the degree of fractionation of $^{18}O/^{16}O$ (Zachos et al., 2001 *web note 2*). Therefore, oxygen isotope data from marine organisms are commonly combined with proxies that are used to independently constrain the ocean temperature component (Dutton et al., 2015). These proxies include are outlined in more detail below.

(i) Using geochemical data, such as Mg/Ca ratios, measured from calcite belonging to benthic foraminifera (e.g. Elderfield et al., 2012) and ostracods (e.g. Dwyer et al., 1995) to determine the temperature component of deep seawater, while the temperature of shallow seawater is obtained from planktonic foraminifera (e.g. Lea et al., 2002; Shakun et al., 2015). Mg/Ca ratios can be used to estimate the calcification temperature, because the calcification temperature is imprinted on a shell at the same time as the $\delta^{18}O$ (Lea et al., 2002 *and references therein*). Thus, the temperature influence on the calcite can be measured using the Mg/Ca proxy; once this influence is known the signal is subtracted from the $\delta^{18}O$ of the calcite to leave a residual value which represents the $\delta^{18}O$ of the seawater (Shakun et al., 2015).

ii) Using the $\delta^{18}O$ from deep sea sediments and $\delta^{18}O$ signals from atmospheric gas in ice cores to identify the common ice-volume component through time (Shackleton, 2000). Measurements of the $\delta^{18}O$ from air bubbles within the Antarctic Vostok ice cores provide a

record of atmospheric oxygen throughout the late Quaternary, these records display variations that occur in response to changes in the $\delta^{18}O$ of ocean water and show similarity with the results obtained from $\delta^{18}O$ benthic records.

(iii) Ice-sheet-ocean-temperature models from benthic $\delta^{18}O$ records (Bintanja et al., 2005; Bintaja and van de Wal, 2008; De Boer et al., 2010). This approach is based upon the assumption that the Northern Hemisphere ice-sheet isotope content and the local deep sea temperature are the main contributors to the mean benthic oxygen isotope record, and that both of these signals are directly linked to Northern Hemisphere mid-latitude to sub polar surface air temperature. The result of the direct relationship between these signals allowed the surface air temperature to be derived, which, in turn, was used to simultaneously separate the ice-sheet and deep water components.

(iv) Hydraulic models from semi-isolated basins (e.g. Red Sea and Mediterranean Sea) (Siddall et al., 2003; Rohling et al., 2009; Grant et al., 2014; Rohling et al., 2014) allow relative sea level to be scaled to eustatic sea level. In Siddall et al. (2003) this approach determined water residence times obtained from oxygen isotopes removed from sediment cores, following which, the depth of the sill that controlled water exchange between the restricted basin and open ocean was calculated over 470 ka. These calculations relied upon a hydraulic model developed from cross sections of the inlet channel into the Red Sea and assumptions based upon the inflowing and outflowing of layers of water (Siddall et al., 2002) throughout different seasons.

(v) High resolution coral datasets combined with benthic $\delta^{18}O$ records from a number of sedimentary cores were fitted together using polynomial regressions (using the relationship between the independent and dependent variables) to produce a Last Interglacial composite sea-level curve; this curve was then extended in time using the known relationships between two datasets as a proxy (e.g. Waelbroeck et al., 2002).

(vi) A similar approach to (v) without the use of corals involved using different benthic $\delta^{18}O$ records was adopted by Siddall et al. (2010) and Bates et al. (2014).

(vii) Principal component statistical analyses that allow the common key trends from numerous sea-level datasets to be identified resulting in the production of a sea-level stack (Spratt and Lisiecki, 2016), which was then scaled to eustatic sea level. In constructing the stack, this approach evaluates the differences between the reconstruction techniques.

As a result of the construction of sea-level curves based upon different approaches, variation exists on the exact timing of sea-level highstands and the elevation of sea levels during the highstands (Fig. 2.6) (e.g. Caputo et al., 2007; de Gelder et al., 2020), the impact of which is explored in Chapter 5. Despite the differences between individual sea-level curves, an overall pattern of eustatic sea-level fluctuation between 5 m and -120 m, relative to today's sea level, has been observed over lowstand and highstand periods since ~500 ka (e.g. Siddall et al., 2003; Rohling et al., 2009, 2014) (Fig. 2.4).

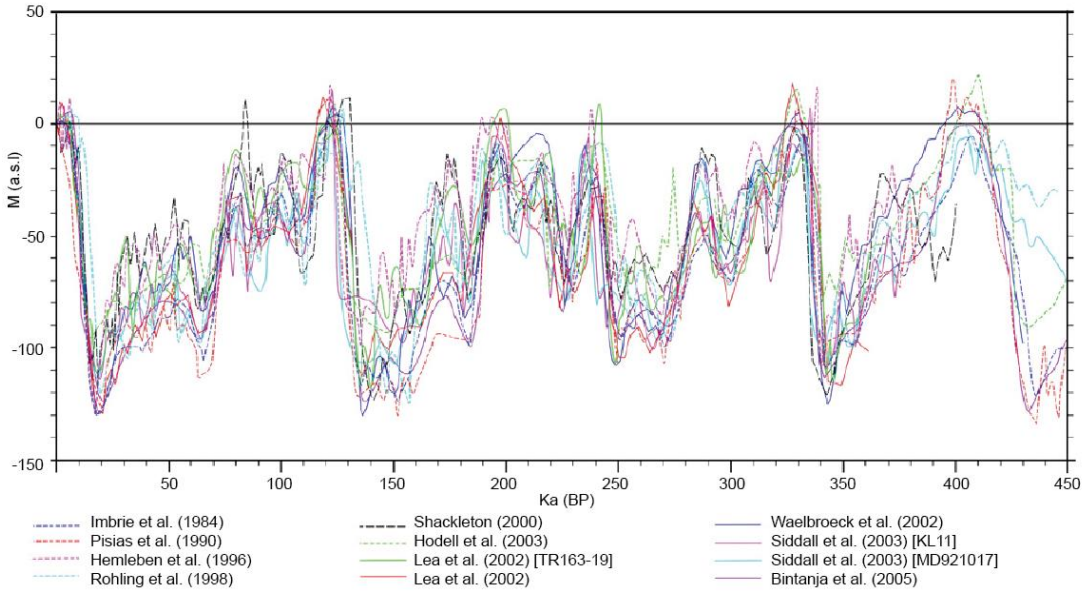

Figure 2.6: Selection of sea-level curves over the late Quaternary (modified from Caputo et al., 2007).

Key observations of the sea level curves are that the maximum sea-level elevation of successive highstands has not been consistent over time, and that highstands occur at unevenly-spaced time intervals (Fig. 2.4). Specifically, the relative elevation difference between two subsequent highstands can be as much as 35 m (i.e. from the 175 ka (MIS 6d) highstand to the 125 ka highstand (MIS 5e), Fig. 2.4). Major highstands are those that have sea-level elevations close to or in excess of the present day value. According to Siddall et al. (2003) the maximum elevations of the 125 ka, 240 ka and 340 ka highstands (relative to present day sea level) are 5 m, -5 m and 5 m, respectively, compared to -30 m, which is the suggested elevation of the minor highstands (175 ka, 217 ka, 285 ka). These sea-level elevation differences are reflected in sequences of palaeoshorelines, and are important in the correlation of undated palaeoshorelines to sea-level highstands.

2.1.3 Preservation of palaeoshoreline and marine terrace sequences

The preservation of sequences of terraces and palaeoshorelines was explored in detail by Lajoie (1986) who explained that the role of fluctuating sea-level and a rising coastline are the reason that preserved sequences of palaeoshorelines occur. In Section 2.1.2, large-scale sea-level fluctuations of ~120 m over late Quaternary glacial cycles are highlighted (e.g. Anderson et al., 1999; Siddall et al., 2003; Rohling et al., 2009, 2014); this means that on uplifting coastlines, palaeoshorelines may only be preserved if their uplift brings them to elevations above the sea-level of future highstands (Fig. 2.4). Thus, the uplift value is one of the key controlling factors that defines palaeoshoreline preservation (Fig. 2.7).

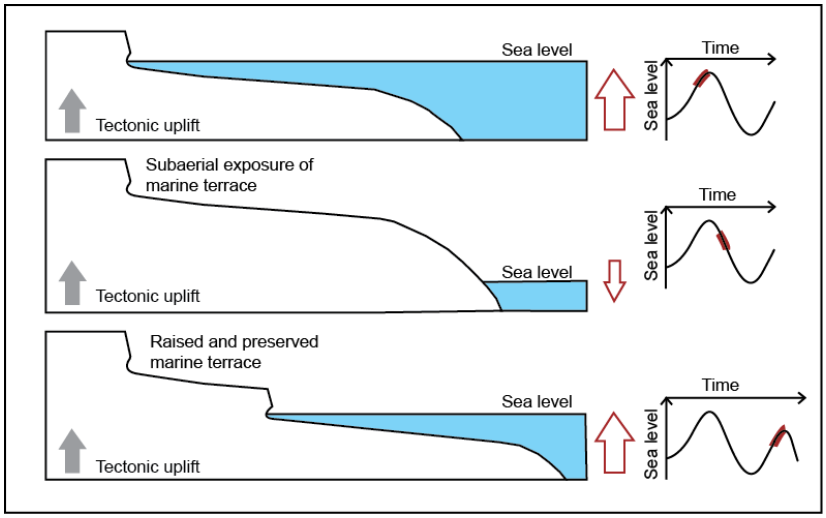

Figure 2.7: Cartoon of the formation, uplift and subsequent preservation of marine terraces and palaeoshorelines in relation to eustatic sea-level change over time, modified from Nalin et al. (2007).

Observations on uplifting coastlines throughout the world reveal that relatively low uplift rates result in fewer palaeoshorelines, whereas relatively high uplift rates result in a higher number of preserved palaeoshorelines (e.g. Lajoie, 1986; Leonard and Wehmiller, 1992; Westaway, 1993; Saillard et al., 2009; Pedoja et al., 2018; de Gelder et al., 2020). The preservation of relatively low uplift-rate settings is explained by terrace and/or palaeoshoreline reoccupation, whereby younger, eustatic highstands overprint and destroy older palaeoshorelines (Fig. 2.8) (e.g. Roberts et al., 2009; Jara-Munoz and Melnick, 2015; Pedoja et al., 2014, 2018; Normand et al., 2019). This process occurs when the tectonic uplift is lower than the amount of sea-level rise associated with highstands. As an example, a palaeoshoreline formed during the 175 ka highstand when the sea-level elevation relative to today was ~-30 m would need to be uplifting at a rate >0.69 mm/yr to prevent it being reoccupied by the 125 ka highstand (relative sea-level elevation 5 m) (Fig. 2.8). At uplift rates below 0.69 mm/yr, the 125 ka highstand would cut into and erode the 175 ka palaeoshoreline (Fig. 2.8). Where uplift rates are very low (<0.2 mm/yr) the process of

terrace reoccupation results in few but large composite terraces (e.g. Pedoja et al., 2018). Studies show that uplift rates ≤1 mm/yr, will typically result in preservation of the major highstands (125 ka, 240 ka and 340 ka) and overprinting of the minor highstands (175 ka, 217 ka and 285 ka) (e.g. Merrits and Bull, 1989; Roberts et al., 2009; de Gelder et al., 2020). This is due to the relative differences in highstand sea-level maxima (Fig. 2.4).

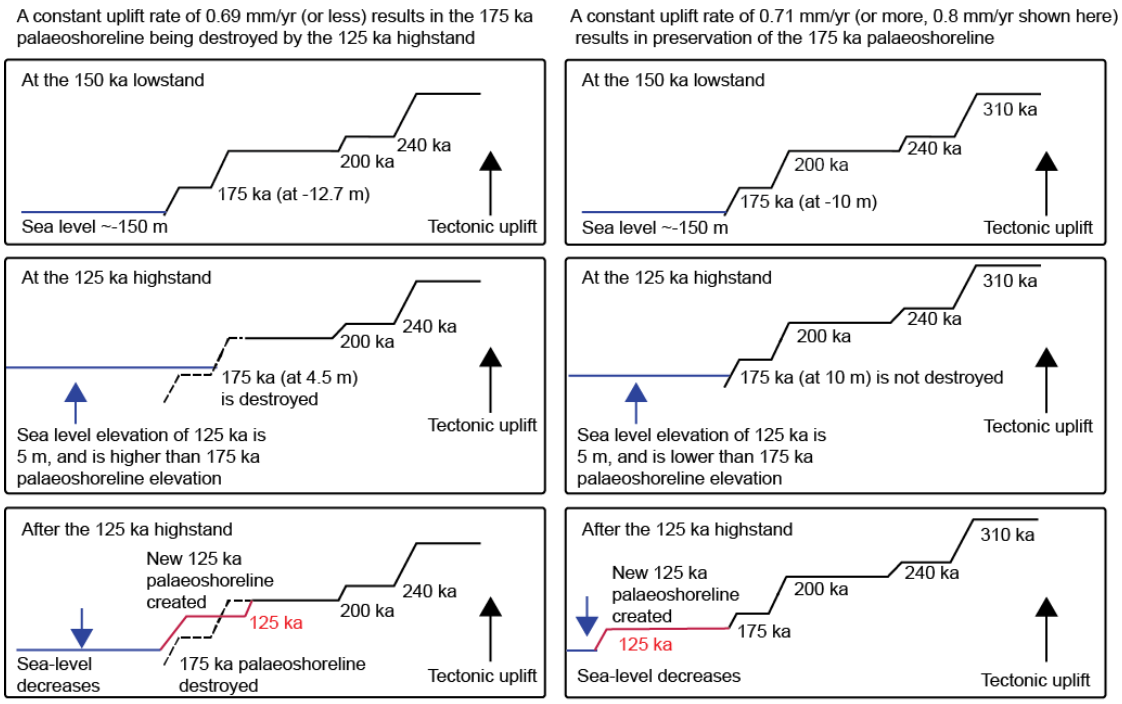

Figure 2.8: Cartoon demonstrating palaeoshoreline destruction of the one of the minor sea-level highstands (175 ka) at uplift rates below 0.69 mm/yr. At uplift rates above this (0.8 mm/yr is shown) the 175 ka palaeoshoreline is not destroyed (using sea-level data from Siddall et al. (2003)).

The steady uplift of palaeoshorelines will place them at elevations that are too high for future sea-level highstands to destroy them, however, these palaeoshorelines are subject to other erosive forces that act to remove or obscure them. For example, fluvial incision (Pope et al., 2016, *and references therein*) may result in the slow destruction of palaeoshorelines such that landward (older and higher) terraces become more and more dissected (Anderson et al., 1999). Alluvial fan deposits have been shown to obscure, or partially obscure, palaeoshorelines, such that a sequence may not be wholly visible (e.g. Pope et al., 2008; Gallen et al., 2014; Pope et al., 2016; Mouslopolou et al., 2017; Ott et al., 2019). Correlating preserved palaeoshorelines to sea-level highstands is particularly challenging where palaeoshorelines are obscured or destroyed, thus it is important that geologists do not assume that all eustatic highstands will be preserved in a sequence of terraces.

2.1.4 Absolute dating of palaeoshorelines, marine terraces and wave-cut platforms

Uplift rates from palaeoshorelines are obtained via a combination of relative and absolute dating, knowledge of palaeoshoreline elevations and the process of matching sea-level highstands to undated palaeoshorelines using data from Late-Quaternary sea-level curves (e.g. Armijo et al., 1996; Roberts et al., 2009, 2013; Matsu'ura et al., 2014, 2015; Jara-Munoz and Melnick, 2015; Meschis et al., 2018). There are studies that assign terrace ages to sea-level highstands using stratigraphy, tephrostratigraphy and index fossils such as Strombus bubonius (which are known to characterise MIS 5e) (e.g. Muhs, 2013; Matsu'ura et al., 2015; Sivan et al., 2016). However, direct correlation of palaeoshorelines to interglacial highstands is particularly reliable using absolute age constraints (Karymbalis et al., 2013); an excellent example of this is where coral reef palaeoshorelines are uplifted and allow absolute dating of all palaeoshorelines (Fig. 2.9) (e.g. Huon Peninsula, Papua New Guinea) (Chappell, 1974).

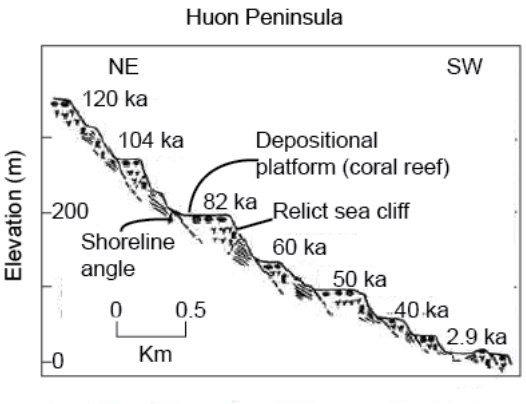

Figure 2.9: Example of a set of coral reef palaeoshorelines, each dated using U-series methods on fossil corals (modified from Chappell, 1974).

The type of absolute dating employed is dependent on the type of palaeoshoreline and palaeoshoreline features present. Herein, the focus is on erosional wave-cut terraces that may have a thin veneer of sedimentary cover associated with the palaeoshoreline on parts or all of the terrace or no cover at all, where the abrasive action of waves and rock fragments have cut a surface into bedrock (Bird, 2011). In the Western Mediterranean locations studied herein, large constructional coral reefs do not dominate and so, unlike the example in Fig. 2.9, it is not realistic to obtain absolute age controls on all palaeoshorelines within a sequence, so studies typically employ an approach where-by few age controls on one or two terraces provide age constraints.

Absolute controls on erosional palaeoshorelines may be derived from: (i) the syn-sedimentary deposits associated with the palaeoshoreline, using, for instance, OSL dating (e.g. Gallen et al., 2014; Ott et al., 2019); (ii) fossils preserved within sedimentary deposits or cemented on the wave-cut bedrock of the platform/within the notch using ^{14}C (e.g. Shaw et al., 2008), $^{234}U/^{230}Th$ (e.g. Stirling et al., 1998), $^{238}U/^{206}Pb$ (e.g. Quigley et al., 2012), electron spin resonance (ESR) and amino-acid racemisation (AAR) (see Schellmann and Radtke, 2000 *and references therein for these latter two methods*); and (iii) *in-situ* cosmogenic exposure dating using ^{36}Cl or ^{10}Be to date wave-cut platform surfaces associated with palaeoshorelines (Cockburn and Summerfield, 2004; Ivy-Ochs and Kober, 2008; Dunai, 2010). ^{36}Cl exposure dating offers an excellent opportunity to date erosional palaeoshorelines composed of carbonate lithologies, however, as detailed in Chapter 1, there are challenges associated with this method and it is yet to be shown to be a reliable approach to use on Quaternary wave-cut platforms. As this thesis focuses on ^{36}Cl exposure dating in combination with $^{234}U/^{230}Th$ coral age dating, these techniques are further explored below.

2.1.4.1 $^{234}U/^{230}Th$ dating

During the formation of carbonates, uranium (U) is absorbed from the surrounding water, which decays through its decay chain to the long-lived isotope thorium (Th), which is not soluble in water (Fig. 2.10a). This decay process serves as a clock, allowing geochronologists to measure the formation age of fossils and algal growths (Scholz and Hoffmann, 2008; Dutton, 2009) (Fig. 2.10b). In more detail, as the carbonate forms it incorporates mobile uranium into its lattice (and typically trace values of thorium), thus the carbonate will have the same $^{234}U/^{238}U$ ratio of the fluid in which it grew. Secular equilibrium will be reached in a steady state situation provided the system remains closed such that quantities of the daughter isotope ^{230}Th will increase systematically once the carbonate has formed. However, U-series disequilibrium may occur as a result of processes that create a non-steady state condition. For example, the decay of ^{238}U through its decay chain to ^{234}U (Fig. 2.10a) results in the emission of one alpha and two beta particles which damages the crystal lattice surrounding the ^{238}U. The ^{234}U daughter isotope is susceptible to being removed from the damaged lattice by leaching during weathering (Dutton, 2015). Processes that result in disequilibrium need to be taken into consideration during age calculations.

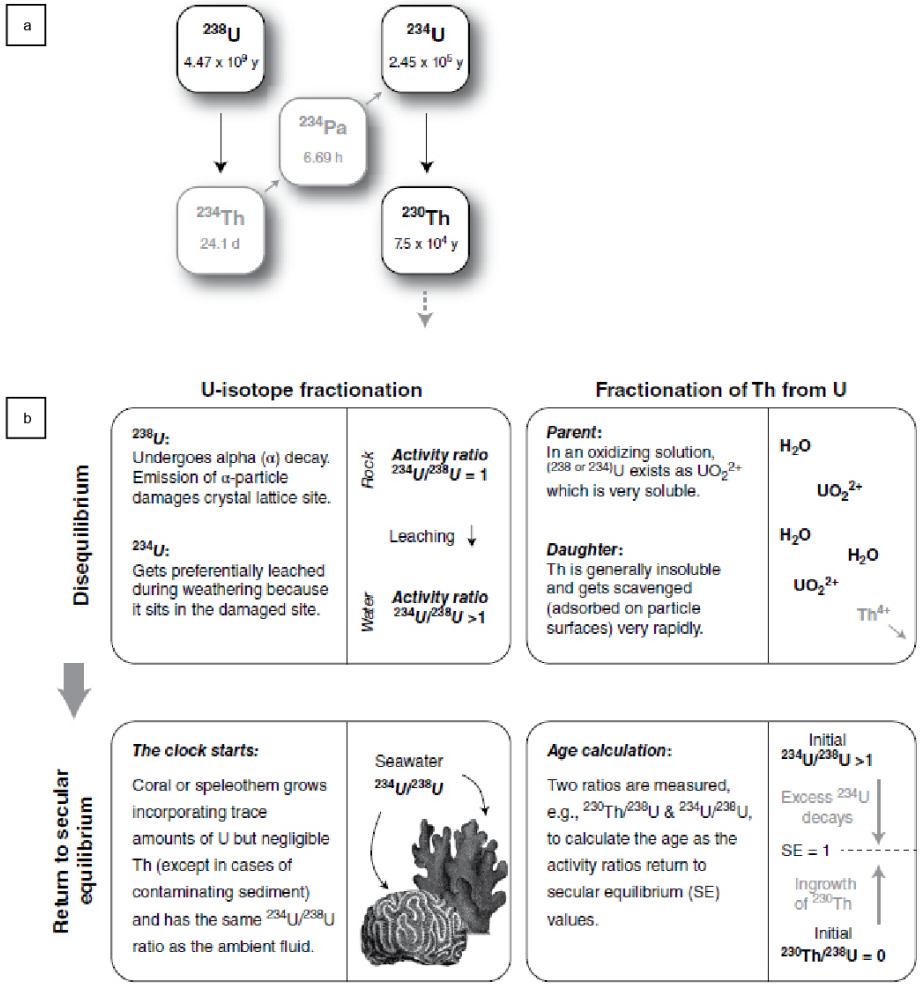

Figure 2.10: (a) Isotopes and their half-lives for ^{238}U decay chain, ^{238}U, ^{234}U and ^{230}Th form the basis of the U-series dating technique. The half-lives of ^{234}Th and ^{234}Pa are so short that are usually ignored in carbonate dating. (b) The premise of U-series dating techniques based on fractionation of isotopes (modified from Dutton, 2009).

In order to obtain accurate ages, knowledge of the decay constants (the rate at which the population of radioactive atoms decreases because of decay) for nuclides of ^{234}U, ^{238}U and ^{230}Th is required; these decay constants are continuously being improved over time (e.g. Cheng et al., 2013). It is also important that ^{230}Th was not present on formation because it will lead to erroneous age calculations, and in ideal circumstances as shown above, that the U-series decay chain has remained closed, such that that no loss or gain of nuclides since deposition has occurred (e.g. Dutton, 2009; Dutton, 2015). These factors can be investigated by screening the results of U-series dating on the samples in question (Fig. 2.11) based upon the concentrations of ^{238}U and ^{232}Th (or using the activity ratio of ^{230}Th/^{232}Th) and the initial activity ratio ^{234}U/^{238}U (^{234}U/^{238}U$_i$) in order to determine whether open system or closed system behaviour has occurred; where t is the age of the sample and λ_{234} is the decay constant of 2.82206 x 10^{-6}:

$$\left[\left({}^{234}U \div {}^{238}U\right)i - 1\right] = \left[\left({}^{234}U \div {}^{238}U\right)t - 1\right]e^{\lambda^{234}t}$$

In this thesis, activity ratios are displayed in parentheses, and the initial activity ratio of $^{234}U/^{238}U$ is reported in delta notation ($\delta^{234}U_i$) (Section 3.4.3).

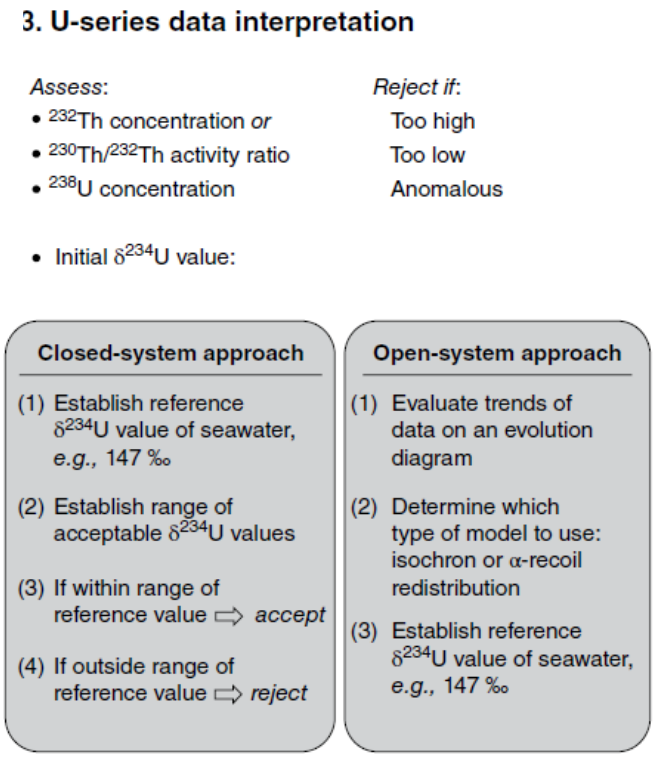

Figure 2.11: Interpreting U-series data using closed and open system approaches (modified from Dutton, 2015).

A $\delta^{234}U_i$ equivalent to that of present-day homogenous oceanic water of ~147 ± 10‰ (e.g. Stirling and Anderson, 2009; Medina-Elizalde et al., 2013) is used to suggest that the carbonate exhibits closed system conditions, and therefore, that the age obtained is reliable. Outside of the factors in Fig. 2.11, the reliability of ages is based on the assumption that the carbonate formed in seawater with $\delta^{234}U_i$ that is (a) homogenous and (b) has not changed through time. This latter point was thought to be well known as a result of the long residence time of U (~400 ka) (e.g. Hamelin et al., 1991, Henderson et al., 1993), however, relatively recent studies on corals (e.g. Robinson et al., 2004; Esat and Yokoyama, 2006; 2010) show that variation of the measured $\delta^{234}U_i$ has occurred on glacial to interglacial timescales as a

result of rising sea-levels mobilising and transporting U with excess ^{234}U into the oceans, and that this may also be observed on centennial timescales.

$^{234}U/^{230}Th$ dating has been applied to carbonate deposits including molluscs (e.g. Magnani et al., 2007), cyanobacterial mounds (i.e. bioherms) (Portman et al., 2005), speleothems (e.g. Moriaty et al., 2000) and corals (e.g. Stirling et al., 1998). $^{234}U/^{230}Th$ dating of molluscs predominantly reflect the fact that they display open system behaviour, and their reliability has therefore been doubted (McLaren and Rowe, 1996; Labonne and Hillaire-Mercel, 2000; Azougagh et al., 2001; Yaltirak et al., 2002). Specifically, in common with other molluscs, $^{234}U/^{230}Th$ dating on Pleistocene lithophagid samples show evidence of exchange of uranium from groundwater and geochemical alteration and cannot be used to determine ages and crustal uplift older than Holocene samples (Rowe et al., 2015).

Closed system behaviour has been demonstrated in some coral samples, which, in combination with the relatively large concentrations of uranium they store in comparison to other carbonates, makes them one of the most reliable materials for U-series dating (Burnett and Veeh, 1992). Consequently, they have been instrumental in determining uplift rates on palaeoshorelines throughout the World (Medina-Elizalde, 2013 *and references therein*). However, this approach suffers from two issues, firstly there is a recognised lack of palaeoshorelines with coralliferous deposits in the Western Mediterranean (McLaren and Rowe, 1996). Secondly, plots of coral age versus $\delta^{234}U_i$, such as those from the last interglacial, reveal increasing scatter of $\delta^{234}U_i$ with age which is interpreted to represent unreliable ages, possibly as a result of post-depositional diagenesis (Stirling et al., 1998; Hamelin et al., 1991; Stirling and Anderson, 2009; Medina-Elizalde, 2013); yet studies that obtain corals with elevated $\delta^{234}U_i$ also result in ages that match known sea-level highstands, agree with other age controls and with the expected geomorphology of the area in question (e.g. Poole et al., 1990; Muhs et al., 1994; Bard et al., 1996; Roberts et al., 2009; Roberts et al., 2013). For example, of the 19 corals dated from Sumba (Indonesia) by Bard et al. (1996), 13 displayed $\delta^{234}U_i$ values outside the 147 ± 10‰ range but were dated to known Quaternary sea-level highstands. Analysis by Esat and Yokoyama (2010) examined coral data and showed that samples that passed screening tests to assess for thorium and uranium concentrations (e.g. Fig 2.11) still display variable $\delta^{234}U_i$. These authors suggest that near to coastlines where many of the dated corals grew, $^{234}U/^{238}U$ ratios vary spatially and temporally because they grew in waters that were variably mixed with ^{234}U-enriched surface plumes. Esat and Yokoyama (2010) went on to suggest that the age versus $\delta^{234}U_i$ scatter, such as that observed

throughout the last interglacial, may be systematic in nature. These authors recognised that in order to adequately investigate any spatial or temporal variations of $\delta^{234}U_i$ in corals, attention should be paid to: (i) sedimentary and stratigraphic evidence alongside the interpretation of U-series data from corals (e.g. Speed and Cheng, 2004); (ii) employment of an approach that involves analysing multiple samples from the same stratigraphic unit; and (iii) undertaking multiple analyses on individual corallite samples in order to check for consistency between the ages and $\delta^{234}U_i$ values of corals (Esat and Yokoyama, 2010; Dutton, 2015). A study by Roberts et al. (2009) in the Gulf of Corinth dated corals and analysed the reliability of coral ages based upon their locations in sedimentary successions and on sequences of palaeoshorelines; these authors also sampled multiple corallites from layers that were expected to be the same age and in a few cases undertook multiple analyses on the same corallite sample. They showed that $\delta^{234}U_i$ values were elevated but that coral growth ages agreed with the timing of eustatic sea-level highstands and expected age relationships given their stratigraphic, tectonic or palaeoshoreline setting.

2.1.4.2 Cosmogenic ^{36}Cl exposure dating

Cosmogenic exposure dating has been recognised as a powerful tool within Quaternary geochronology (Ivy-Ochs and Kober, 2008) having undergone significant analytical and theoretical developments since the application of accelerator mass spectrometry (AMS) in the 1980s (Gosse and Phillips, 2001). Cosmogenic exposure dating is reliant on knowledge of the behaviour of cosmic rays, that is, high-energy, charged particles, that impinge upon the Earth (Dunai, 2010). Originating from supernova explosions (Diehl et al., 2006), cosmic rays undergo reactions upon entering the Earth's atmosphere resulting in a nuclear cascade of protons, neutrons, alpha particles, pions and muons (Gosse and Phillips, 2001; Dunai, 2010) (Fig. 2.12).

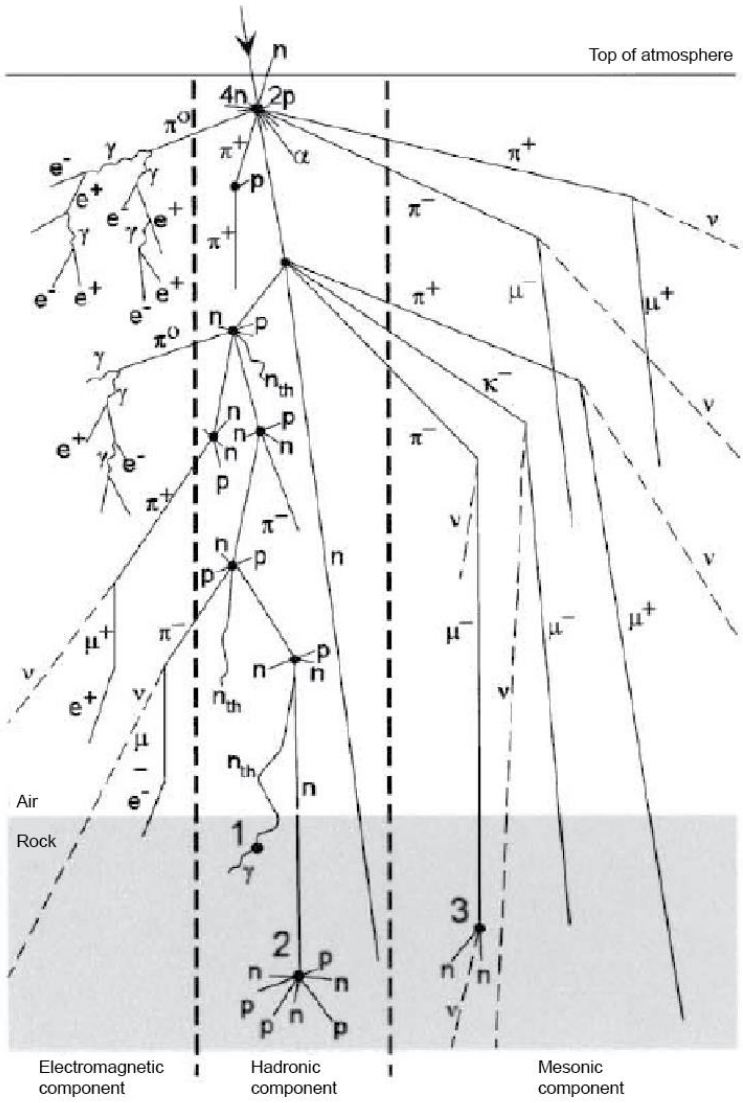

Figure 2.12: The major components of a cosmic-ray cascade, showing secondary production of particles in the atmosphere and rock: n = nucleogenic/nuclide, μ = muon; numbers represent in-situ cosmogenic nuclide interaction with: 1 = ^{35}Cl and ^{36}Cl; 2 = ^{16}O and ^{10}Be, and 3 = ^{28}Si, 36Al. Vertical scale not linear (from Gosse and Phillips, 2001).

Ages derived from cosmogenic exposure dating require measurement of the abundance of cosmogenic isotopes in a given rock sample and knowledge of the production rate of the cosmogenic isotopes. When the carbonate wave-cut platforms that are the focus of this thesis are exposed to cosmic rays (due to sea-level change and tectonic uplift) the target elements of ^{40}Ca, ^{35}Cl and ^{39}K are responsible for producing ^{36}Cl (Schlagenhauf et al., 2010). ^{36}Cl is suited to date Late-Quaternary carbonate wave-cut platforms because it has a half-life of 3.01x10^{5} years (Dunai, 2010). The production pathways for ^{36}Cl involve: (i) spallation of target elements (^{40}Ca and ^{39}K) which occurs when high energy neutrons impact the Earth's surface and collide with the nuclei of atoms; (ii) slow negative muon capture by ^{40}Ca and ^{39}K; and (iii) low energy neutron capture by ^{35}Cl, which is an important and complex pathway

because ^{35}Cl is the dominant naturally occurring Cl isotope but is particularly sensitive to the concentration of hydrogen from, for instance, pore waters and snow cover (Phillips et al., 2001; Schimmelpfennig et al., 2009). The contribution from each production mechanism depends on the concentrations of the target element in the rock sample and also on surface geometry, the incoming cosmic-ray flux (which is dependent on geographic position and time) and depth of the sample, whereby the total production rate typically decreases with increasing depth (Gosse and Phillips, 2001; Marrero et al., 2016a, 2016b). There are notable differences between the dominant production mechanisms as a function of depth (Fig. 2.13); at the surface of the Earth thermal neutron capture and spallation are the dominant mechanisms, specifically spallation is mostly limited to the upper 2 m of rock below exposed surfaces, decreasing exponentially with depth (Licciardi et al., 2008). Whereas, production of ^{36}Cl by muons is small when measured at or near the exposed surface but its relative contribution increases with depth because muons have been shown to penetrate deeply into the subsurface as they do not interact with atoms in the same way as high energy neutrons (Heisinger et al., 2002a, 2002b; Schlagenhauf et al., 2010).

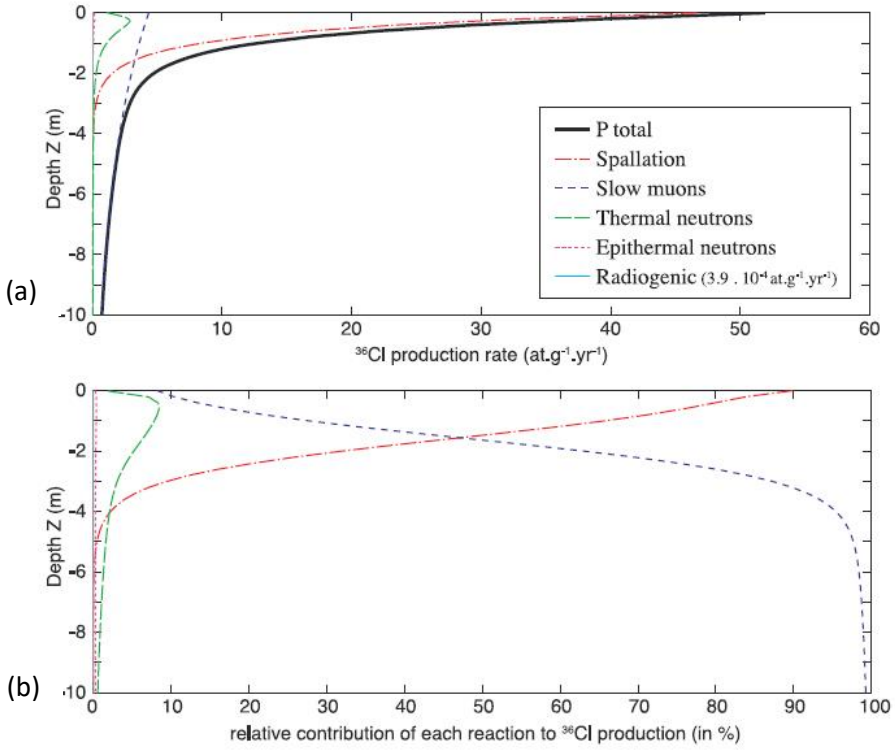

Figure 2.13: Contribution of the sources in the production of in situ 36Cl in the upper 10 m for a horizontal surface composed of limestone (a) production rates, (b) relative (percentage) contribution of each production source (from Schlagenhauf et al., 2010).

The varying depth-dependent production rates for each of the pathways mean that if erosion has been significant since initial exposure, the exposure ages obtained may be incorrect because, rather than reflecting dominantly spallation-caused ^{36}Cl they may reflect production rates associated with muons (Stone et al., 1998). As a very simplistic example, if a sample that is assumed to have experienced minimal erosion has, in fact, experienced 1 m of erosion, the production rate applied of 47-52 atoms $g^{-1} yr^{-1}$ will be significantly higher than the actual rate of ~20 atoms $g^{-1} yr^{-1}$ (Fig 2.13a) reflective of a 1 m eroded sample; when applied over hundreds of thousands of years this has the capacity to produce ages that may significantly vary from the actual exposure age. Age determinations using ^{36}Cl exposure dating can accommodate erosion within the modelling (Marrero et al., 2016a), but this relies on accurate quantification of erosion rates.

Stone et al. (1996) was one of the first published studies to document application of ^{36}Cl to date a Holocene wave-cut platform, located in Scotland, which they interpreted to be successful because multiple exposure ages on the same platform were in agreement. However, attempts to use ^{36}Cl exposure dating on exposed bedrock to determine the age of Pleistocene wave-cut surfaces have been reported in PhD theses and show mixed results (Wegmann, 2008; Spampinato, 2011; de Gelder, 2017; Meschis, 2019), these are each outlined below. Wegmann (2008) sampled the vertical walls above four wave-cut notches in south-east Crete (Table 2.1) and attempted to calibrate his results against the ^{14}C shell ages removed from the same platforms. Three of the ^{36}Cl samples from Wegmann (2008) suggest Holocene ages and one a Late-Quaternary age, but these ages were not in agreement with those that Wegmann (2008) obtained using ^{14}C and so he rejected them. Potential issues with the approach by Wegmann (2008) are that he assumed that the outer 1-2 mm of all of the samples were removed by abrasion, given that samples vary between 9-71 m in elevation with an age difference of ~30 ka (based upon the ^{14}C ages) it would be expected that their total erosion values would not be the same. Furthermore, Wegmann (2008) noted that the exposure ages were calculated without consideration of low-energy neutron capture. It is, however, interesting that the four ^{36}Cl exposure samples and the number of ^{36}Cl atoms/g from Wegmann (2008) increase with elevation as is expected of the ages of the wave-cut platforms.

Sample	^{36}Cl atoms/g	Elevation (m asl)	Exposure age (yrs)	^{14}C age (yrs)
050906-8	109000	9	8810 ± 350	44500 ± 500
050906-5	170000	15	13430 ± 2550	50330 ± 1430
050906-6	238000	31	19230 ± 590	60000 ±2000
060906-7	640000	71	50170 ± 1660	77500 ± 2000

Table 2.1: ^{36}Cl exposure ages compared to ^{14}C ages of shells from the same wave-cut platforms (from Wegmann, 2008)

de Gelder (2017) carried out ^{36}Cl exposure dating on wave-cut platforms comprised of abraded limestone bedrock from eastern Crete. His sampling approach was to sample the bedrock from the most elevated parts of a number of terraces, away from the eroding cliffs, avoiding outcrops with karstification, chemical alteration or coastal deposits; with calculated ages derived assuming negligible sub-aerial erosion. The exposure ages obtained by de Gelder (2017) for each terrace are as follows: terrace 2 (elevation 15-27 m) 83-306 ka, terrace 3 (elevation 37-41 m): 91-108 ka, terrace 4 (elevation 49-71 m): 91-153 ka, terrace 5 (elevation 116-117 m): 142-296 ka, and terrace 8 (124-154 m): 80-136 ka (Table 2.2). If these exposure ages were to be considered as reliable, then it would be expected that multiple ages from the same terrace should agree with one another, but this is not the case (e.g. terrace 2N has exposure ages of 103-306 ka). Furthermore, the broad range of exposure ages for individual terraces makes these ages difficult to decipher in terms of allocating palaeoshorelines to sea-level highstands, and there is no apparent relationship between the number of ^{36}Cl atoms/g and elevation. These lines of evidence may indicate that samples may have experienced significant erosion. de Gelder (2017) did not report any specific surface features that provide further understanding of the levels of erosion for any of the samples or evidence of low erosion.

Sample	^{36}Cl atoms/g	^{36}Cl conc. (ppm)	Erosion rate (mm/ky)	Exposure age (yrs)	Total uncertainty (yrs)	Elevation (m)	Terrace	Lithology	Lithology age
5	1620000	94	Negligible	103000	14000	16	2N	bedrock	Cretaceous
6	2740000	181	Negligible	168000	27000	19	2N	bedrock	Cretaceous
7	4600000	238	Negligible	306000	63000	15	2N	bedrock	Cretaceous
4	2020000	20	Negligible	113000	15000	27	2S	bedrock	Eocene
15	1460000	10	Negligible	83000	11000	27	2S	bedrock	Eocene
16	1730000	43	Negligible	92000	12000	27	2S	amalgamate	Eocene
17	2550000	34	Negligible	146000	20000	27	2S	bedrock	Eocene
1	1860000	23	Negligible	106000	14000	41	3S	bedrock	Eocene
2	1890000	22	Negligible	108000	15000	37	3S	bedrock	Eocene
3	1600000	21	Negligible	91000	12000	37	3S	amalgamate	Eocene
9	1710000	10	Negligible	109000	15000	49	4N	bedrock	Cretaceous
10	1080000	22	Negligible	153000	22000	49	4N	bedrock	Cretaceous
13	1620000	0.33	Negligible	91000	13000	71	4S	bedrock	Eocene
14	2030000	8	Negligible	116000	16000	74	4S	bedrock	Eocene
14R	2180000	13	Negligible	124000	17000	74	4S	bedrock	Eocene
11	5660000	136	Negligible	296000	47000	116	5S	bedrock	Cretaceous
12	2400000	9	Negligible	142000	20000	117	5S	bedrock	Cretaceous
18	2070000	22	Negligible	117000	16000	127	8N	bedrock	Cretaceous
19	1980000	25	Negligible	111000	15000	124	8N	bedrock	Cretaceous
20	2430000	36	Negligible	136000	18000	126	8N	bedrock	Cretaceous
21	1500000	15	Negligible	80000	11000	150	8N	bedrock	Cretaceous
22	1910000	30	Negligible	101000	13000	154	8N	bedrock	Cretaceous

Table 2.2: ^{36}Cl exposure ages and analytical results for palaeoshorelines along E. Crete (modified from de Gelder, 2017). Samples were removed from wave-cut platforms (terraces) at different elevations, de Gelder (2017) assumed negligible erosion for all samples. If the exposure ages were reliable then ages from individual terraces should agree but exposure ages for each terrace are shown to vary significantly (e.g. those from terrace 2N range from 103-306 ka). There is no apparent relationship between the reported ^{36}Cl atoms/g for samples removed from similar elevations (which should increase with elevation); this may be suggestive that some samples have been significantly eroded. As such, determining the actual age of each terrace was not possible.

Analysis of the ^{36}Cl exposure results from Spampinato (2011) and Meschis (2019) will be considered together as they dated locations in eastern Sicily with some overlap of sample sites (samples C5 and C9 from Spampinato (2011) are 300 m away from samples 1-3 of Meschis, 2019). The ^{36}Cl exposure ages obtained by Spampinato (2011) (Table 2.3) and Meschis (2019) (Table 2.4) are recognised by both authors as erroneously low. Meschis (2019) identifies that the expected age of the 14 m palaeoshorelines he dated to be ~125 ka, but he obtains maximum ages of 31 ka; Spampinato (2011) obtains ages between 37-75 ka on similar palaeoshorelines. Both authors recognise that high erosion is likely to be the cause of such low ages citing possible values between 8 mm/ky and 11 mm/ky equating to between 1-1.3 m of total erosion, assuming the 125 ka expected age is accurate. Furthermore, comparing ^{36}Cl samples from the same locations between both studies (C5 and C9 Spampinato, 2011 and 1, 2, 3 Meschis, 2019), shows an order of magnitude difference between the ^{36}Cl atoms/g in the two studies. Assuming there is no lithological variation in the 300 m difference between the locations, this is difficult to understand. In the selection of their sample sites, Spampinato (2011) appears to sample from the tops of small pinnacles,

while Meschis (2019) selected the locations of samples 1-3 based upon the presence of millholes, sampling at the edges.

Sample	^{36}Cl atoms/g	Exposure age (kys)	Total uncertainty (yrs)	Elevation (m)
C1	1490000	75311	7146	80
C2	1250000	62878	6118	46
C3	1020000	37282	3514	412
C4	1340000	61159	6049	162
C5	1220000	61809	6110	37
C6	1450000	72656	7155	64
C7	1250000	62816	6164	133
C8	1370000	65144	6375	101
C9	1090000	56262	5429	27

Table 2.3: ^{36}Cl exposure ages and analytical results for palaeoshorelines along E. Sicily (from Spampinato, 2011). Spampiniato (2011) suggests that the exposure ages obtained are erroneously young as a result of erosion since formation.

Sample	^{36}Cl atoms/g	Erosion rate (cm/ky)	Exposure age (yrs)	Total uncertainty (yrs)	Elevation (m)
1	444513	8	31100	7400	36
2	501753	8	35200	8600	36
3	529941	8	35700	8600	35
5	377426	8	22500	5500	139
6	435056	8	29100	6500	14
7	378052	8	25100	5600	14
8	144168	8	14300	3200	14
9	452615	8	32500	7500	14
10	113835	8	10700	2300	14
11	413139	8	27700	6300	14
12	444513	8	31100	7400	14

Table 2.4: ^{36}Cl exposure ages and analytical results for palaeoshorelines along E. Sicily (from Meschis, 2019). Meschis (2019) notes that the ages presented are very young compared to those expected (highstands at 20-30 ka are not observed on sea-level curves). This is also evident from similar exposure ages obtained from terraces at 14 m, 36 m and 139 m which should not be the case because palaeoshoreline age in this location should increase with elevation.

One of the expectations from ^{36}Cl exposure dating on a sequence of wave-cut platforms composed of the same lithology is that the concentration of measured ^{36}Cl from samples (reported as number of atoms of ^{36}Cl/g of sample) should increase with elevation, this is because the wave-cut platforms from higher terraces have been exposed to bombardment of high-energy neutrons from the atmosphere for longer periods of time, but this has not yet been proven. However, where significant, but unknown, erosion has taken place the sample will contain fewer ^{36}Cl atoms owing to lower production rates from spallation and production

dominated by muon capture (Fig. 2.13). In these instances, it follows the lower number of atoms of ^{36}Cl/g would result in sample ages that are erroneously young and do not represent the actual age of the dated surface. With the exception of Meschis (2019), sample site selection did not appear to be based upon the presence of erosional features, such as millholes and borings, that are indicative of low erosion and allow such values to be constrained.

In summary, the four studies appear to have obtained ^{36}Cl exposure ages that are limited in their ability to provide reliable age constraints on the wave-cut platforms that they have dated, possibly as a result of difficulty constraining the rates of erosion since formation. While the results of attempts to date wave-cut platforms using ^{36}Cl exposure dating within the studies of Wegmann (2008), Spampinato (2011), de Gelder (2017) and Meschis (2019) that are discussed above appear to be limited, ^{36}Cl exposure dating applied to other geomorphic features, such as fault scarp dating (e.g. Schlagenhauf et al., 2010) and boulder/bedrock dating to explore glaciation timings (e.g. Ivy-Ochs et al., 2006), have yielded results that are interpreted to be acceptable. The strength of these studies is that they are able to a) confidently constrain minimal erosion using observations (i.e. striations) on the fault scarps and boulder deposits, and b) know that the total values of erosion are not such that they approach the depths where the production rates and mechanisms will significantly differ (Fig. 2.13b). However, with knowledge of the erosion rates of sample locations, ^{36}Cl exposure dating has the potential to be a powerful tool to derive the ages of Quaternary wave-cut platforms that may not be amenable to other dating methods.

2.1.5 Correlating preserved palaeoshorelines to eustatic sea-level highstands

The process of determining uplift rates from deformed palaeoshorelines is dependent on correlations between measured palaeoshoreline elevations and historic sea levels. However, as Anderson et al. (1999) described: “erosional systems [such as palaeoshorelines] are imperfect recorders of past events… this is part of their charm and attraction”. The process of correlation is complex due to variable palaeoshoreline preservation, incomplete knowledge of sea-level histories and availability of absolute ages, as discussed in previous sections.

Two approaches have been employed in order to correlate eustatic highstands with undated palaeoshorelines, namely sequential correlation (e.g. Armijo et al., 1996; De Martini et al., 2004) and synchronous correlation (e.g. Houghton et al., 2003; Roberts et al., 2009; Roberts

et al., 2013; Meschis et al., 2018). When evaluating along-strike changes in deformation, these approaches rely upon knowledge of the palaeoshoreline elevations along the strike (length) of a set of sequences, obtained through detailed field mapping, interrogation of DEMs or high resolution photographs, ideally in combination with at least one absolute age control (e.g. Armijo et al., 1996; Palamara et al., 2007; Saillard et al., 2009, 2011; Roberts et al., 2009, 2013; Binnie et al., 2016; Meschis et al., 2018; de Gelder et al., 2019; Jara-Munoz et al., 2019). When the age of one (or more) palaeoshorelines is known, sequential correlation allocates undated palaeoshorelines to highstands based upon the assumption that lower and higher palaeoshorelines can be allocated, in turn, to the successive and preceding highstands, respectively (Fig. 2.14). The outcome of this method of correlation is that each palaeoshoreline is tied to a highstand, which allows an uplift rate to be calculated for that individual palaeoshoreline (Fig. 2.14). This method may be successfully applied where sufficiently high rates (>1 mm/yr) of uplift occur such that the palaeoshorelines produced by all eustatic highstands are expected to be preserved (Pirazzoli, 2013). However, criticism of this method (e.g. Westaway et al., 2002; Roberts et al., 2009) is centred upon the fact that for low uplift rates not all palaeoshorelines will be preserved, either due to sub-aerial erosion or overprinting, and therefore one or many palaeoshorelines may be allocated to the wrong highstand. Consequently, uplift rates that are calculated for each individual palaeoshoreline-to-highstand correlation may also be erroneous, and suggestive of uplift rates that change through time (see Roberts et al., 2013 for an example of this). The ramifications of erroneous uplift rates stand to be significant if they are interpreted as a change in uplift-rate due to some assumed large-scale tectonic event (e.g. Gallen et al., 2014).

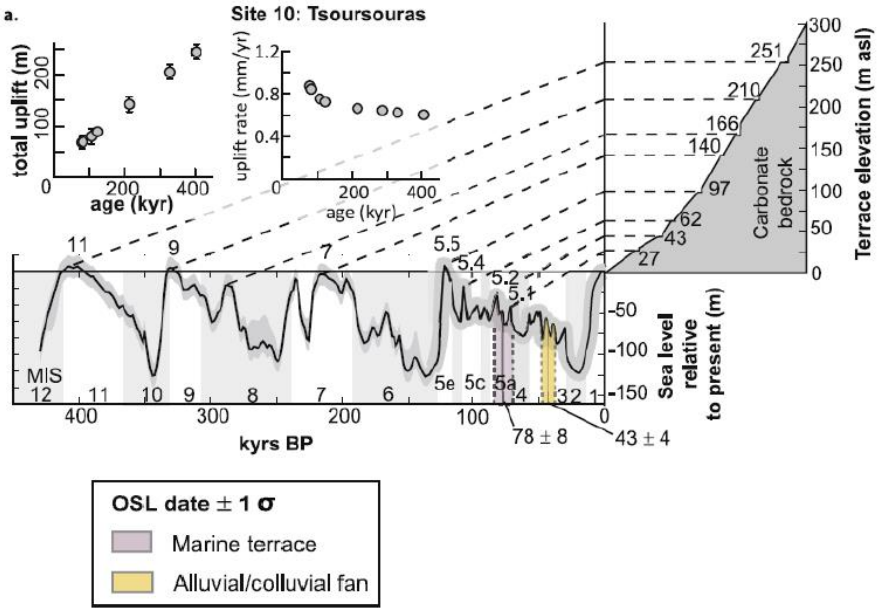

Figure 2.14: Graphical correlation of sea-level highstands with uplifted palaeoshorelines based upon an age control and sequential correlation approach (modified from Gallen et al., 2014).

In contrast, synchronous correlation (Houghton et al., 2003; Roberts et al., 2009) (Fig. 2.15) makes use of the fact that Quaternary sea-level highstands are unevenly spaced in time and hence if uplift rates are constant through time the elevation unevenness of the palaeoshorelines will mirror the highstand elevation unevenness (Fig. 2.4). If age constraints are available, the absolute age of one or more palaeoshorelines is used to drive the simplest hypothesis, that of a constant uplift rate throughout time, though more complex uplift scenarios can also be tested. The age determination allows the uplift rate of the dated palaeoshoreline to be identified. In turn, this uplift rate is applied to the entire sequence of palaeoshoreline elevations along a topographic profile obtained from field or DEM measurements. This tests whether the elevations of undated palaeoshorelines can be explained by the uplift rates implied by the elevations of dated palaeoshorelines (Fig. 2.15b). The calculation is facilitated by a 'Terrace Calculator' in Excel (Chapter 3), populated with data from sea-level curves (Section 2.1.2). The calculator uses an iterated uplift rate to calculate predicted elevations of all highstands, thus, it is possible to visualise which palaeoshorelines will be preserved or overprinted using the uplift rate from the dated platform (Fig. 2.15c) and perform regression analysis between predicted and measured palaeoshoreline elevations (Fig. 2.15d). A successful correlation is characterised by (a) an elevation correlation between all measured palaeoshorelines and all palaeoshorelines expected, given the overprinting problem, and (b) a perfect statistical match between the elevations of measured and predicted palaeoshorelines, for example, an R^2 value = 1. In practise, a perfect correlation may not be achieved due to (i) error in elevation identification

or measurement, (ii) error in the absolute elevation of palaeo- sea-levels, and (iii) local geomorphic processes that conspire so that a palaeo- sea-level does not produce a palaeoshoreline that is recognisable in the geomorphology. However, the level of success can be quantified with values such as R^2 values, and this can also guide future fieldwork priorities. Alternatively, if a constant uplift-rate through time cannot explain the measured palaeoshorelines, a time-varying uplift can then be explored, as was shown by Roberts et al. (2009) for the South Alkyonides Fault System (SAFS) in the Gulf of Corinth (e.g. Fig. 2.15e). If multiple profiles along strike area available, time-varying uplift-rate scenarios can be viewed as having greater certainty if they can explain multiple profiles along strike. The synchronous correlation method was applied in Roberts et al. (2013) in Calabria (Italy) and showed that sequentially-correlated palaeoshorelines previously interpreted as displaying late Quaternary temporally variable uplift rates (Tortorici et al., 2003; Bianca et al., 2011), in fact, displayed temporally constant uplift rates when the synchronous method was used to correlate palaeoshorelines to highstands.

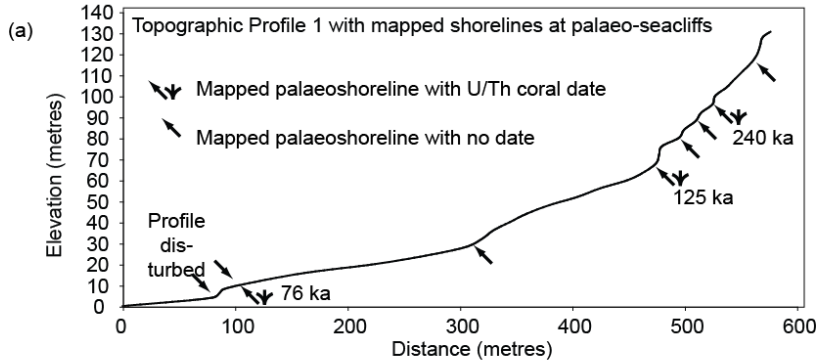
(a)
Topographic Profile 1 with mapped shorelines at palaeo-seacliffs
Mapped palaeoshoreline with U/Th coral date
Mapped palaeoshoreline with no date
Profile dis-turbed
76 ka
125 ka
240 ka
Elevation (metres)
Distance (metres)

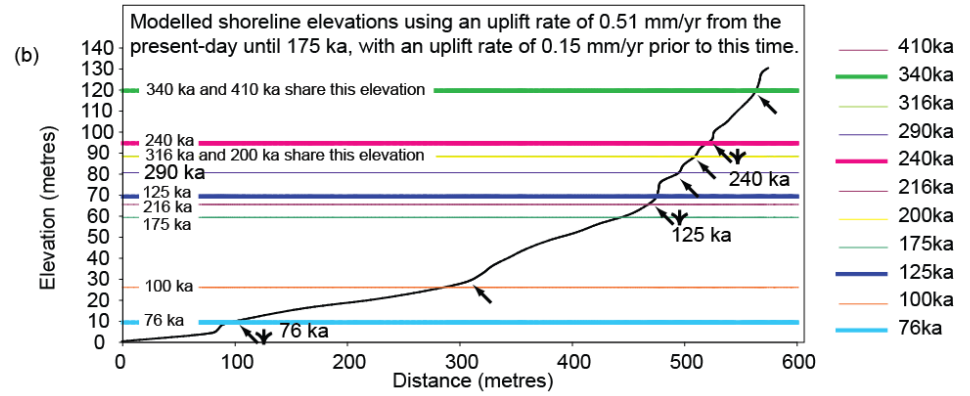
(b)
Modelled shoreline elevations using an uplift rate of 0.51 mm/yr from the present-day until 175 ka, with an uplift rate of 0.15 mm/yr prior to this time.
340 ka and 410 ka share this elevation
240 ka
316 ka and 200 ka share this elevation
290 ka
125 ka
216 ka
175 ka
100 ka
76 ka
240 ka
125 ka
76 ka
410ka
340ka
316ka
290ka
240ka
216ka
200ka
175ka
125ka
100ka
76ka
Elevation (metres)
Distance (metres)

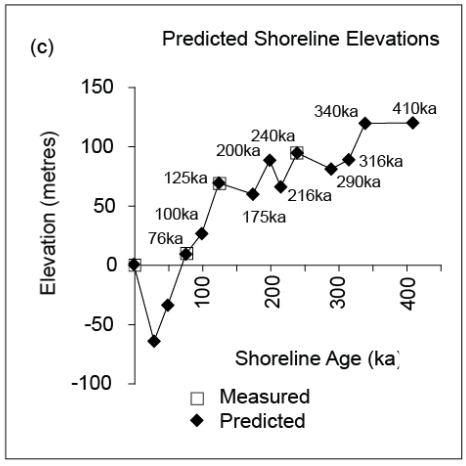
(c)
Predicted Shoreline Elevations
410ka
340ka
240ka
200ka
316ka
290ka
125ka
216ka
175ka
100ka
76ka
Elevation (metres)
Shoreline Age (ka)
Measured
Predicted

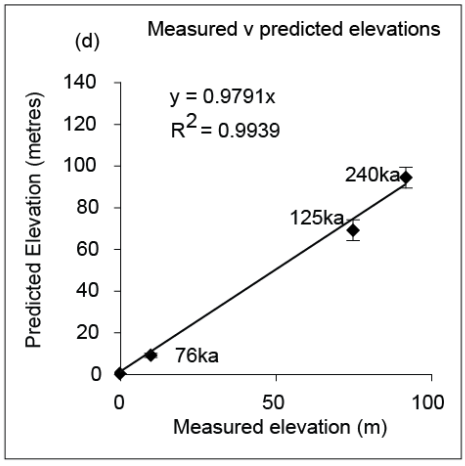
(d)
Measured v predicted elevations
y = 0.9791x
R2 = 0.9939
240ka
125ka
76ka
Predicted Elevation (metres)
Measured elevation (m)

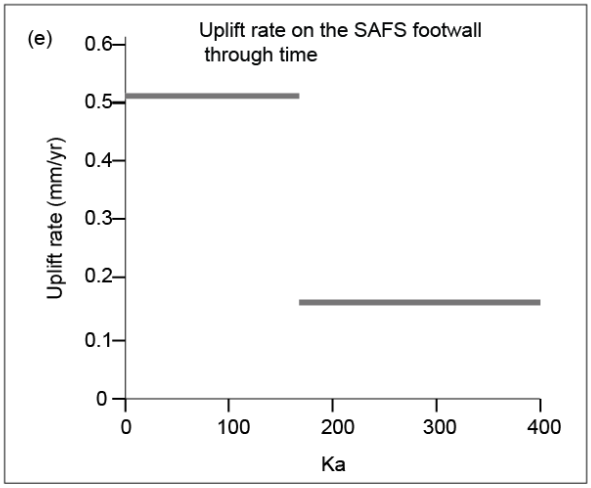
(e)
Uplift rate on the SAFS footwall through time
Uplift rate (mm/yr)
Ka

Figure 2.15: (a) Mapped and dated palaeoshorelines from a profile on Perachora peninsula, Gulf of Corinth (Greece); (b) modelled (predicted) elevations of palaeoshorelines obtained using the terrace calculator, which match measured and dated palaeoshorelines. Note the elevations of 175 ka, 216 ka, 290 ka and 316 ka are predicted to be below palaeoshoreline elevations from younger highstands, this is reflected in (c). (c) Palaeoshorelines expected to be preserved and destroyed based upon the uplift rate used in (b). (d) Plot comparing predicted and measured palaeoshoreline elevations. (e) Plot of the South Alkyonides Fault System footwall uplift rate through time (modified from Roberts et al., 2009).

In summary, the key difference between these two methods is that in sequential correlation, the uplift rates of palaeoshorelines are considered individually and the only way to identify which palaeoshorelines have been overprinted is to date all of the associated marine terraces. In contrast, synchronous correlation derives an uplift rate for an entire sequence and can therefore identify palaeoshorelines that may be liable to be overprinted (Fig. 2.15c). Successful correlation of palaeoshorelines to sea-level highstands at multiple locations along the strike of a set of palaeoshorelines allows for detailed analysis of the spatial variation of uplift rates, which in turn can be used to explore the tectonic causes of the observed deformation patterns (e.g. Roberts et al., 2009; Roberts et al., 2013; Meschis et al., 2018, 2019; Normand et al., 2020).

2.2 FAULT-RELATED DEFORMATION AND ITS IMPACT ON PALAEOSHORELINE SEQUENCES

Spatially variable uplift rates provide evidence of tectonic deformation imprinted onto a set of palaeoshorelines and terraces. The pattern and length-scale of the observed deformation can be used to interrogate the tectonic processes that are responsible. For instance, normal faults result in shorter length-scales of deformation (~30km) (e.g. Armijo et al., 1996, Roberts et al., 2009, 2013; Meschis et al., 2013) compared to longer length scales of deformation caused by slip on a subduction interface (e.g. Subarya et al., 2006; Ozawa et al., 2011; Vigny et al., 2011); this variation is further explored in this section, but it is first it is necessary to provide a brief overview of normal faults as they are the focus of this thesis.

2.2.1 Normal faulting

Coseismic rupture of a normal fault results in uplift of the footwall and subsidence of the hangingwall (e.g. Stein and Barrientos, 1985; Papanikolaou et al., 2010) (Fig. 2.16a). It is generally accepted, and has been demonstrated from analysis of the coseismic footwall and hangingwall motion following the Borah Peak earthquake (Stein and Barrientos, 1985), that deformation in the footwall and hangingwall of normal faults extends to distances approximately half of the fault rupture length perpendicular to the strike of the fault (e.g.

Fig. 2.16a). Through time, normal faults accumulate displacement as a result of cumulative earthquakes (Cowie and Scholz, 1992a), however, this displacement varies along the strike of the fault as a result of differential uplift between the centre (maximum displacement) and tips (minimum displacement) of the faults (Fig. 2.16b) (Schlische et al., 1996). Displacement may be expressed as a gradient using knowledge of fault dimensions (length) and maximum observed displacement (Walsh and Watterson, 1989). Comparison between displacement gradients is a fundamental approach used to investigate possible fault interaction between the tips of normal faults (Section 2.2.3).

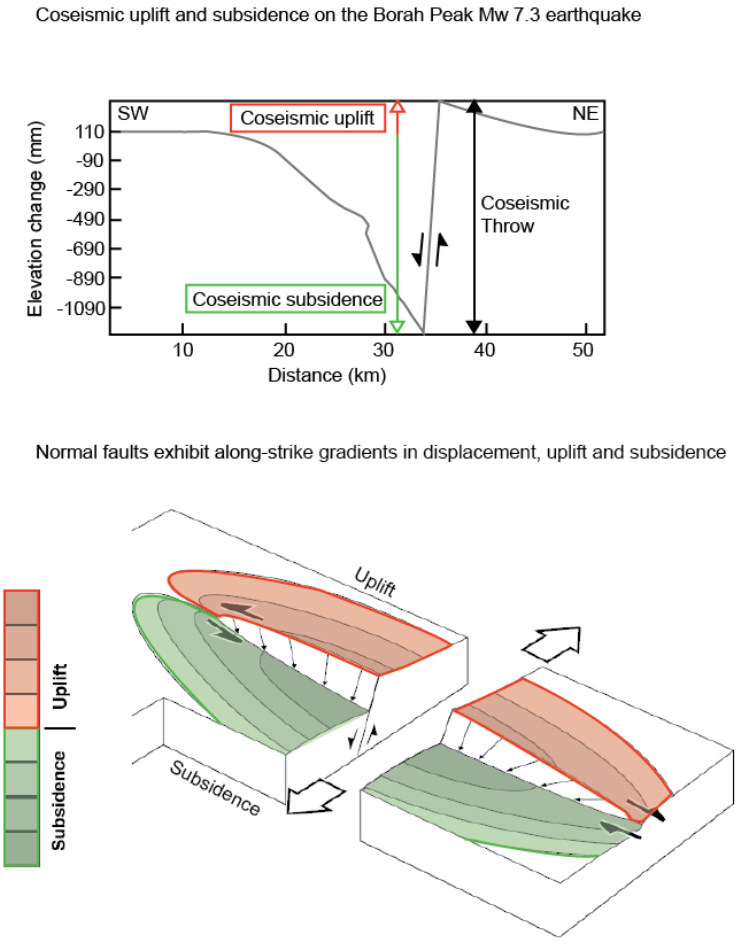

Figure 2.16: (a) Coseismic footwall and hangingwall offset following the Borah Peak earthquake showing the coseismic uplift, subsidence and throw (modified from Stein and Barrientos, 1985). (b) Schematic view of normal fault displacement where uplift in the footwall and subsidence in the hangingwall occur as a result of along-strike displacement being greater in the middle of the fault compared to the tips (modified from Roberts et al., 2007).

Correlation between the lengths and displacement of normal faults has been observed, whereby faults that are tens of km long typically have displacements that are hundreds of meters, and faults that are a few meters long display displacements of a few centimetres (Cowie and Scholz, 1992b). This correlation has been expressed as a scaling relationship between the length (L) and displacement (d) where a value of γ* (usually between 0.001-0.1)

represents variations along normal faults such as local rock type and friction on the fault surface (Cowie and Scholz, 1992b):

$$d = \gamma^* L$$

If displacement of a normal fault (also known as vertical offset or throw) (O) and the time over which the displacement has formed (t) is known, then the throw rate can be calculated; furthermore, if the dip of the fault is also known, the slip rate can be calculated by substituting vertical offset for the value of slip on the actual fault plane (S).

$$Throw\ rate = O/t$$

$$Slip\ rate = S/t$$

In extensional fault systems, multiple normal faults that are closely spaced across and along strike (e.g. central and southern Apennines: Roberts and Michetti, 2004; Papanikolaou and Roberts, 2007; Gulf of Corinth: Roberts and Koukouvelas 1996; Nixon et al., 2016) have been shown to accommodate horizontal extension linked to regional strain (e.g. Faure Walker et al., 2012). If faults are closely spaced along strike such that their tips overlap (en-echelon) then structures called relay ramps develop (Fig. 2.17). These structures transfer displacement between the overlapping faults and may occur between crustal-scale faults (referred to as persistent segment boundaries) or on faults that are segmented at the surface but linked at depth (see Roberts and Koukouvelas, 1996 for examples of both).

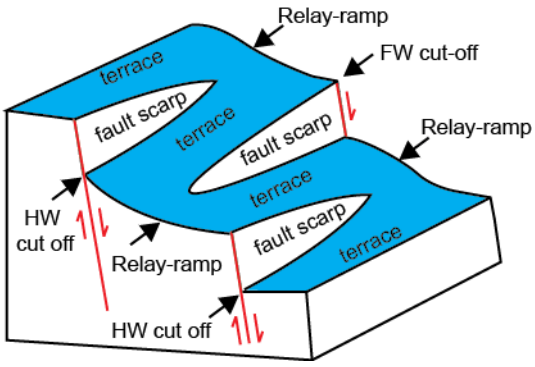

Figure 2.17: Example of relay ramps that form between the overlapping tips of normal faults on a faulted marine terrace. Note that the throw of each fault decreases to nil at the tips (modified from Robertson et al., 2020).

2.2.2 Palaeoshoreline deformation

Quaternary uplifted marine terraces and their preserved palaeoshorelines provide a record of surface uplift (vertical motion of the surface with respect to the geoid) over long-term timescales of tens to hundreds of thousands of years (Muhs, 2013). Interrogation of the uplift recorded by sequences of palaeoshorelines provides the basis for studies that investigate deformation in collisional, extensional and strike-slip tectonic settings throughout the world (e.g. Valensise and Ward, 1991; Muhs et al., 1992; Westaway, 1993; Berryman et al., 1993; Armijo et al., 1996; Roberts et al., 2009; Saillard et al., 2009; Roberts et al., 2013; Matsu'ura et al., 2014, 2015; Binnie et al., 2016; Meschis et al., 2017). For the example of subduction zones, palaeoshorelines uplifted by tectonic processes (as opposed to post-glacial isostatic rebound, which is not investigated in this thesis) are predominantly found in the upper plate. Palaeoshorelines above the leading edge of subduction zones may be linked to slip on the subduction interface, normal faulting as a response to forearc extension in the upper plate, reverse faulting in the upper plate, sediment underplating, interseismic loading during the earthquake cycle or a combination of these (e.g. Muhs et al., 1990, 1992; Byrne et al., 1992; Sato and Matsu'ura, 1992; Berryman, 1993; McNeill et al., 1999; Marquardt et al., 2004; Shaw et al., 2008; Sieh et al., 2008; Saillard et al., 2009; Roberts et al., 2013; Gallen et al., 2014; Strobl et al., 2014; Binnie et al., 2016; Jara-Munoz et al., 2017; Meschis et al., 2018; Ott et al., 2019; Litchfield et al., 2020). Palaeoshorelines also occur within established zones of intra-continental active rifting, located in coastal marine settings, where normal faults accommodate high rates of extensional strain (e.g. McNeil and Collier, 2004; Armijo et al., 1996; Monaco and Tortorici, 2000; Leeder et al., 2005; Roberts et al., 2009).

Patterns of uplift and subsidence associated with faulting may be imprinted onto deforming palaeoshorelines. For instance, where uplift is predominantly caused by upper-plate normal faults located offshore but close (≤ ~10 km) to the coastline the maximum length of palaeoshoreline deformation will be influenced by to the length of the fault, which is dictated by the depth of the seismogenic layer (Jackson and White, 1989) and assumed to be ~15 km. This results in faults with lengths in the region of 30 km and palaeoshoreline deformation that corresponds to these lengths (e.g. McNeill and Collier, 1994; Armijo et al., 1996; Papanikolaou, D. et al., 2007; Roberts et al., 2009; Roberts et al., 2013; Meschis et al., 2018). This is in contrast to uplift caused by slip on a subduction interface where fault rupture length can be in the region of hundreds of km, exceeding 1000 km in the case of megathrust

earthquakes. In such situations longer length scales of palaeoshoreline deformation dominate (e.g. Barrientos and Ward, 1990; Stein and Okal, 2005; Subarya et al., 2006; Papadimitriou and Karakostas, 2008; Ozawa et al., 2011; Vigny et al., 2011).

Where sequences of palaeoshorelines occur, the analysis of uplift rates along the lengths (herein referred to as strike) of palaeoshorelines has proven important in order to temporally and spatially evaluate uplift rates (e.g. Armijo et al., 1996; Roberts et al., 2009; Saillard et al., 2011; Roberts et al., 2013; Meschis et al., 2018), which should differ in accordance with fault displacement. One such example is within the Gulf of Corinth, Greece, where active extension has resulted in sequences of palaeoshorelines in the footwalls of normal faults (e.g. McNeill and Collier, 1994; Armijo et al., 1996; Roberts et al., 2009). Analyses of a set of deformed palaeoshorelines located in the footwall of the South Alkyonides normal fault in the Gulf of Corinth was carried out by Roberts et al. (2009) and revealed that palaeoshoreline elevations increased along strike recording the footwall uplift linked to faulting over 100s kyrs (Fig. 2.18), furthermore, the palaeoshorelines provided a record of non-steady uplift whereby a three-fold increase in the uplift rate, and therefore the inferred slip rate of the fault in question, occurred at ~175 ka.

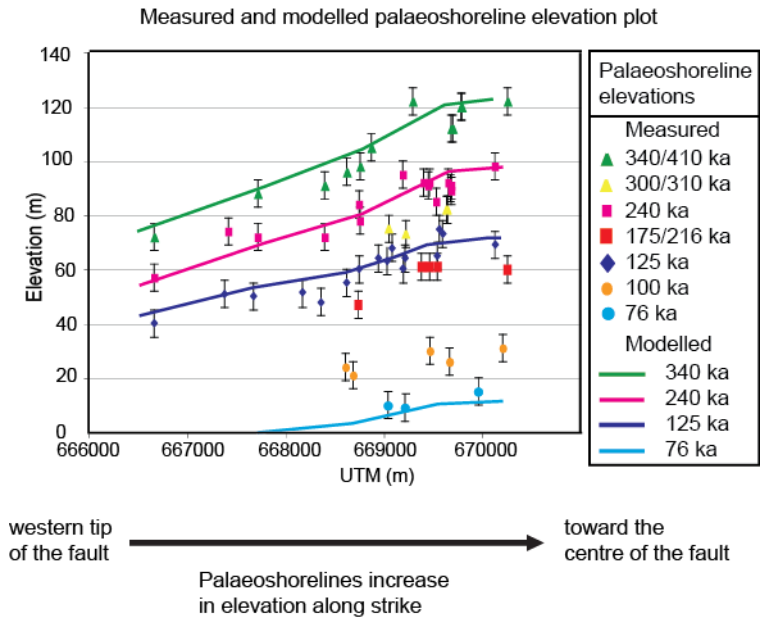

Figure 2.18: (a) Analysis of palaeoshoreline elevations in the footwall of the South Alkyonides fault (Gulf of Corinth) show an increase in palaeoshoreline elevation from the tip of the fault (UTM 666500) toward the centre of the fault (UTM 670200) (modified from Roberts et al., 2009).

In-depth analysis of palaeoshorelines shows that differential displacement related to faulting results in the variable preservation of palaeoshorelines along strike. In the footwall of normal

faults more palaeoshorelines will be preserved in the centre compared to fewer shorelines preserved in the tips (e.g. Armijo et al., 1996; Roberts et al., 2009; de Gelder et al., 2019) (Fig. 2.20). Where faulting is onshore, adjacent to the coast and offsets sequences of palaeoshorelines (e.g. Skourtsos et al., 2007; Tsimi et al., 2007; Gaki-Papanastassiou et al., 2009; Saillard et al., 2011; Roberts et al., 2013, Gallen et al., 2014; Meschis et al., 2018) the hangingwall will host fewer preserved palaeoshorelines in the centre compared to more shorelines preserved in the tips (e.g. Roberts et al., 2013; Meschis et al., 2018) (Fig. 2.19a). Moreover, where onshore faulting offsets palaeoshorelines, the presence of hangingwall palaeoshorelines alludes to additional tectonic processes that are responsible for uplifting the subsiding hangingwall such that palaeoshorelines may be preserved.

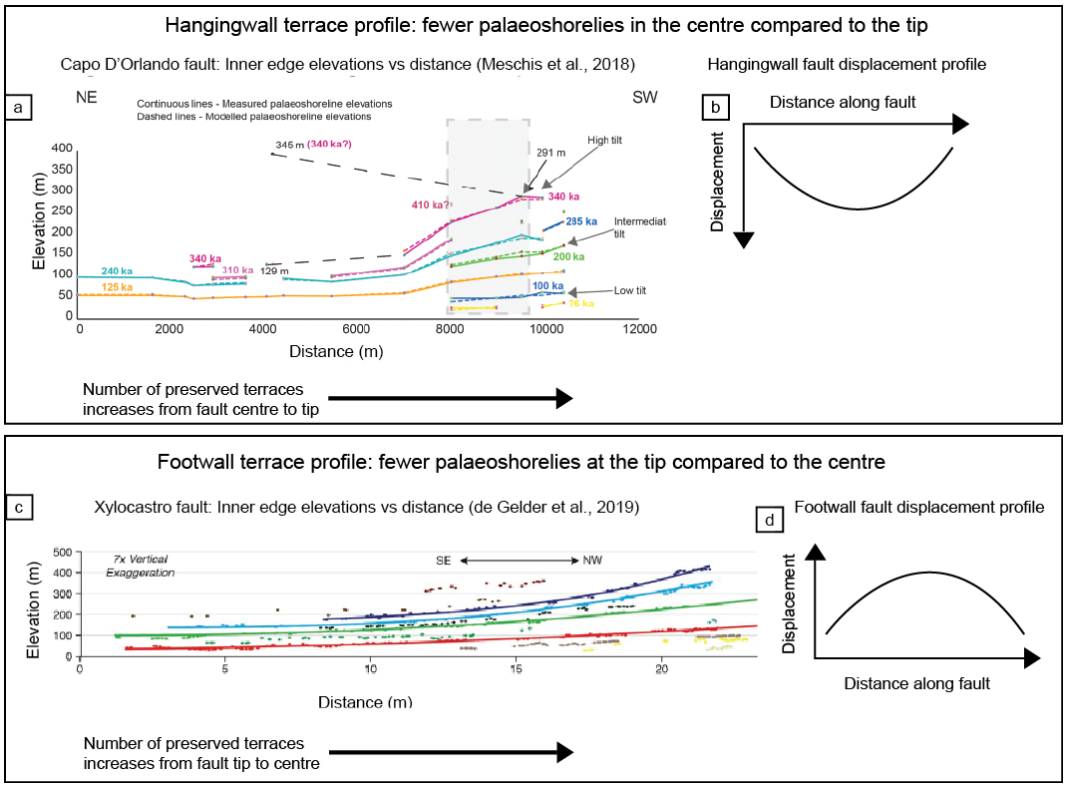

Figure 2.19: (a) In the hangingwall of a normal fault, fewer palaeoshorelines are preserved from the centre to the tip (modified from Meschis et al., 2018), in this situation the hangingwall is uplifted due to background regional uplift. (b) Schematic diagram of the fault displacement in the hangingwall of a normal fault where subsidence is higher in the centre of the fault compared to the tips. (c) In the footwall of a normal fault, fewer palaeoshorelines are visible in the tip compared to the centre (modified from de Gelder et al., 2019). (d) Schematic diagram of the fault displacement in the footwall of a normal fault where uplift is higher in the centre of the fault compared to the tips.

Palaeoshorelines have been shown to exhibit tilting parallel to the strike of the fault (Figs. 2.19, 2.20). When the values of tilt for individual palaeoshorelines are compared, higher, older palaeoshorelines exhibit higher along-strike tilt angles (Fig. 2.20) (Armijo et al., 1996; Ortlieb et al., 1996; Roberts et al., 2009; Meschis et al., 2018; Normand et al., 2019). The

reason why these higher tilt angles form is linked to fault displacement gradients, where the largest fault displacement is located at the centre of the fault. The older palaeoshorelines have been subjected to more earthquakes and have therefore experienced larger values of displacement in the centre compared to at the tips.

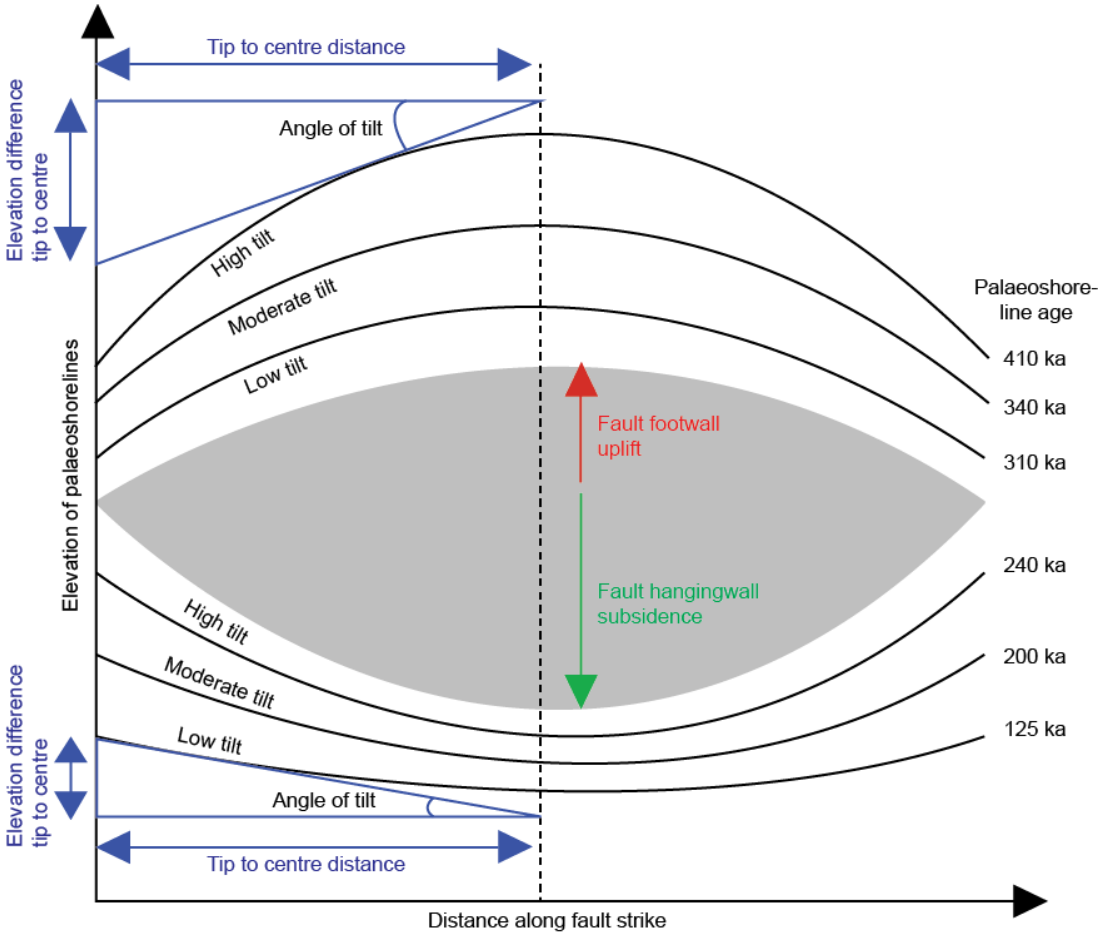

Figure 2.20: Schematic diagram of the expected patterns of tilt angle variation in the hangingwall and footwall of a fault where greater tilt is expected for older palaeoshorelines in both the hangingwall and footwall. The tilt angles are calculated using trigonometry and measurements of the distance from the centre to the tip of the fault and the elevation difference between the centre and the fault tips. Hangingwall palaeoshoreline preservation is expected to predominantly occur if there is offshore uplift (from upper-plate faulting or regional processes).

Spatial analysis of uplift rates along the strike of the palaeoshorelines reveals patterns of uplift that can be used to reconcile the kinematics of faults that are challenging to observe (i.e. offshore or low slip rate) (e.g. Armijo et al., 1996; Roberts et al., 2013; Meschis et al., 2018, 2019). This is particularly important where sequences of palaeoshorelines are observed above subduction zones; in these types of settings fault-related uplift may be complex (Fig. 2.21) because of multiple potential causes (i.e. slip on the subduction interface, sediment underplating, interseismic loading, normal faulting). The problem is that these potential uplift forming processes are typically unobservable because they are located

offshore, so deciphering the individual or combined causes of deformation is difficult. The observation of deformed palaeoshorelines above subduction zones has caused some researchers to directly link coastal uplift to slip on the subduction interface and use this uplift to make inferences as to the potential slip distribution on the subduction interface (e.g. Nalbant et al., 2013; Sato et al., 2016). In the instance of Nalbant et al. (2013), they reconstructed past subduction zone earthquakes using uplifted coral build ups located offshore Sumatra; their findings are based on assumptions that these coral build ups could have only been uplifted as a consequence of slip on the subduction interface since ~1790.

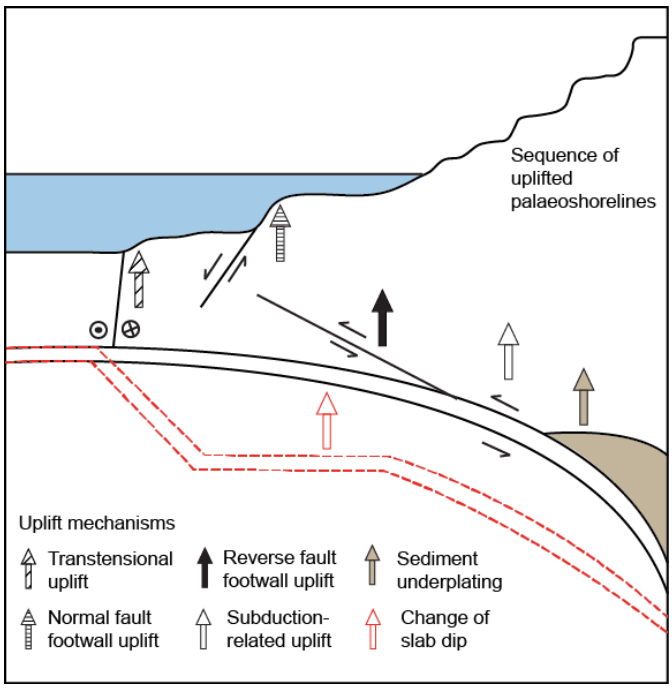

Figure 2.21: Cartoon of possible uplift mechanisms that may contribute to uplifted palaeoshorelines within a subduction zone setting (modified from Robertson et al., 2019).

Another scenario of complex spatial deformation on palaeoshorelines above subduction zones, is where compression-related uplift (sometimes referred to as 'regional' uplift) may be combined with the effects of upper-plate extensional faults which has been postulated and in some places observed in subduction zones in Greece, Italy, Chile, Peru, Western USA, Japan and New Zealand (e.g. McNeill et al., 1999; Saillard et al., 2009; Imanishi et al., 2012; Roberts et al., 2013; Matsu'ura et al., 2014, 2015; Howell et al., 2017; Ott et al., 2019; Litchfield et al., 2020). Specific examples of this are illustrated in Roberts et al. (2013) and Meschis et al. (2018) who used sequences of deformed palaeoshorelines to constrain the throw rate of normal faults and quantify regional uplift rates in Calabria and northern Sicily (e.g. Fig 2.19a), respectively.

Constraining the existence, location, deformation rates and geometry of extensional faults is important for seismic hazard assessment. Specifically: (i) deformation rates calculated using data recorded from faults are a key input parameter within PSHA (Chapter 1), and are used to estimate the recurrence intervals of an earthquake and ground-shaking exceedance probabilities in given time periods (e.g. 50 years, 100 years etc.) at a location based upon all possible earthquake sources (Pace et al., 2016; Faure Walker et al., 2019); (ii) subduction zone earthquakes have the capacity to coevally rupture extensional faults in their upper plate, as seen in the Chile, 2010 and Japan, 2011 megathrust events (Bottner et al., 2018); and, (iii) knowledge of the locations and lengths of upper-plate faults allows for their seismic potential (Section 2.2.4) to be defined, which is vital for local populations and critical facilities.

2.2.3 Fault interaction

Normal faults may exist in isolation, but commonly occur in fault systems with other normal faults located across- and along-strike (Section 2.2.1) where they interact through their stress fields. The interaction between faults that deform or offset palaeoshorelines has the capacity to influence the observed deformation patterns associated with the palaeoshorelines, therefore this concept is key to explore further. When a fault ruptures, it results in an increase or reduction in the stress of the surrounding rock. Where other faults are located close by to a rupturing fault (either along strike or across strike), this change in stress, also known as Coulomb stress change, leads to changes in the stress state on the adjacent faults, either bringing them closer to failure or placing them in a stress shadow such that stress decreases and they move away from failure (Fig. 2.22) (King et al., 1994; Hodgkinson et al., 1996; Harris, 1998; Toda et al., 2005). The critical spacing of faults dictates whether interaction may occur and varies with fault length and displacement; for example, larger faults perturb the stresses of a wider area compared to smaller faults (Fossen and Rotevatn, 2016).

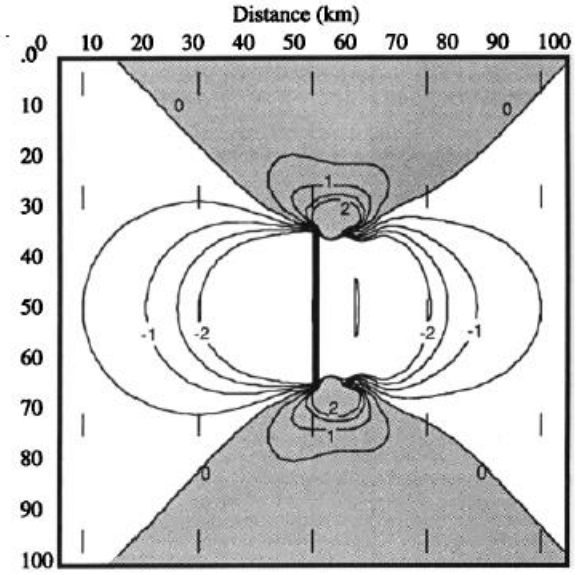

Figure 2.22: Coulomb stress changes associated with 1 m of slip on a normal, 60˚ dipping fault, stress changes are contoured at $0.5x10^5$ Pa intervals, negative numbers suggest stress reduction, positive numbers suggest stress enhancement (modified from Hodgkinson et al., 1996).

An example of fault interaction occurred as a result of the 1992 Landers and Joshua Tree earthquakes (California, USA) whereby an area that was modelled to have experienced high Coulomb stress change went on to rupture 3.26 hrs after the Landers rupture (the Big Bear earthquake, Mw 6.5) (Fig. 2.23).

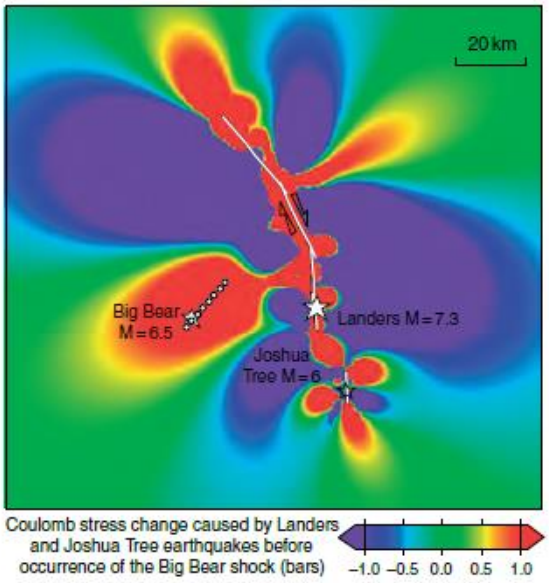

Figure 2.23: Map view of Coulomb stress changes caused by the 1992 Joshua Tree and Landers earthquakes. The Big Bear earthquake occurs in an area of high Coulomb stress change (from King et al., 1994).

The example from California highlights the impact of Coulomb stress change over very short timescales (hours); similar studies have carried out Coulomb stress change analysis to show

that earthquakes have occurred in response to positive Coulomb stress change from days to years (e.g. Chile: Lemoine et al., 2001; central Apennines: Mildon et al., 2017).

Over the time periods of 10^{1-3} years the effect of fault interaction has been suggested to result in a sharing of the slip between more than one fault in order to accommodate regional strain rates (e.g. Dolan et al., 2007; Luo and Liu, 2012, Cowie et al., 2013, 2017). In such instances, faults that are closely-spaced across strike show evidence that clusters of earthquakes occur on one fault while the other experiences a period of quiescence. The length of these clusters and quiescent periods may depend on the overall strain rate being accommodated in the fault system; for instance, along the fast moving San-Andreas fault, earthquakes within clusters may be separated by several decades with each cluster separated by periods of quiescence in the region of 2-3 centuries (Sieh et al., 1989). In regions of comparable slower deformation, for example the central Apennines (Italy), the recurrence of earthquakes within clusters is suggested to be in the order of centuries, whole clusters lasted 1-2 kyrs and periods of quiescence were up to 5 kys (e.g. Schlagenhauf et al., 2011; Benedetti et al., 2013). Similar lengths of periods of clusters were reported by Rockwell et al. (2000) for the active faults in the so-called California shear zone. This evidence suggests that where fault interaction is possible, slip rates over multiple millennia may vary significantly depending on whether the fault in question is experiencing a cluster or anticluster. This is in contrast to the suggestion by Luo and Liu (2012) that on longer cycles slip rates should be able to be treated as steady state, and one of the reasons that long-term slip rates may provide a broader view of fault activity compared to short-term slip rates.

Studies that examine possible fault interaction over multiple millennia also examine the process of along-strike fault interaction. For example, on the Rangitaiki fault (New Zealand), Bull et al. (2006) observed temporal and spatial variability in incremental displacements associated with slip events is as a result of fault linkage at the overlapping tips of normal fault segments. A model of normal fault interaction, developed by Gupta and Scholz (2000) (Fig. 2.24) illustrates this process. One of the interesting observations of this study was the process that happens when moderate interaction occurs (prior to hard linkage between two faults), whereby the displacement profile (Section 2.2.1) of the adjacent tips steepens as a result of anomalously high slip in the tips zones of the faults (2.24c, d). The reason this is interesting is two-fold in the context of seismic hazard assessment, firstly because it suggests that slip-rate changes may occur over long timescales and secondly, it suggests that in interacting fault systems, the extent of fault interaction can be examined from the geometry

of the fault displacement gradient provided that there is knowledge of time over which the displacement occurred. While steeper tip zone displacement has been observed from outcrop scale (mm to m) to <10 km scale (e.g. Walsh and Watterson, 1990; Huggins et al., 1995; Schlische et al., 1996; Cartwright and Mansfield, 1998), there are few observations of this process from crustal scale active faults (e.g. Ferrill et al., 1999). This is likely explained by the difficulty in observing these processes because they occur over the long term, though such observations are made using subsurface seismic investigations from previously extending basins (e.g. Giba et al., 2012). Fault interaction has been shown to affect the deformation of palaeoshorelines and is therefore important to consider in studies that use palaeoshorelines to investigate upper-plate faulting.

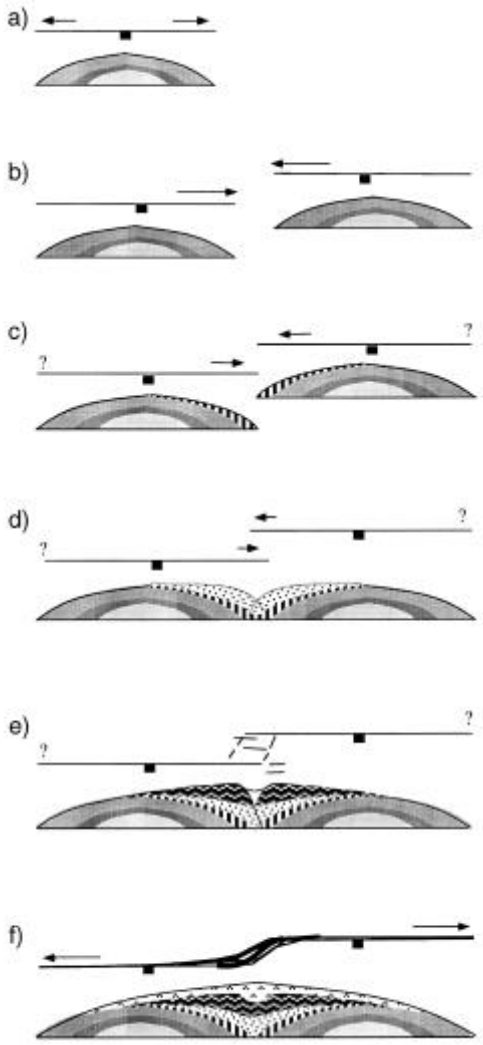

Figure 2.24: Conceptual model showing the interaction of two sub-parallel normal faults from no interaction (a) to full interaction (f). Each diagram (a)-(f) is comprised of a map view (top of each diagram) and a vertical cross section (bottom of each diagram) of two normal faults as they grow in length at their tips and experience increasing displacement, changing from two single faults to one linked fault. Shading represents different periods of displacement accumulation with time. (a) Pre-interaction - map view (arrows indicate propagation direction), symmetrical D±L profile is shown below. (b) Weak interaction – while underlapping, an increase in shear stress near tips may drive faults to accelerate towards each other, until a stress drop region is reached. Underlapping faults are rarely observed. (c) Moderate interaction - after entering the stress shadow, propagation decelerates and displacement begins to accumulate near interacting tips, and steep profiles develop on interaction ends. (d) Strong interaction - any propagation is slow, displacement profiles near interacting tips steepen. Individual profiles are now very different from the characteristic profile and the composite profile is closer to the characteristic profile. (e) Linkage - once critical stress drop is reached, propagation stops, minor linkage structures form, displacement accumulates in the linkage region, and the summed profile approaches that of a single fault. (f) Coalescence - linkage is complete, the displacement profile is now appropriate for a single long fault. Propagation of distal ends resumes, leaving segment boundary behind. Portions of the overlap zone may now become part of the fault gouge (from Gupta and Scholz, 2000).

Interaction between multiple faults has previously been explored using Coulomb 3.4 (Toda et al., 2011), a software package designed to allow the user to interrogate the Coulomb stress transfer imparted from rupturing a source fault onto adjacent receiver faults. In Coulomb 3.4 the user defines the geometry and kinematics of a source fault and ruptures the fault (see

Section 3.5.2 for detail). The Coulomb stress transfer imparted from the rupture of the source fault onto one or many receiver faults can then be examined in order to evaluate whether adjacent faults experience stress enhancement or a stress shadow (e.g. Fig. 2.23). The results of such analyses can be used to examine the effects of Coulomb stress transfer on earthquake probabilities. For example, Toda et al. (1998) undertook an analysis of the Coulomb stress transfer following the 1995 Mw 6.9 Kobe earthquake (Japan) and showed that regions of stress increase and stress decrease were probable given the earthquake, estimating that a 3-bar increase on some faults results in a fivefold increase in the 30-year probability of an earthquake, while other faults experienced a reduction in probability. Moreover, analyses of Coulomb stress transfer may also provide an understanding of the long-term behaviour of a fault, for instance, in line with Fig. 2.24 where it is expected that interaction between along-strike faults may result in anomalous displacement gradients as a result of stress enhancement at the tips of rupturing normal faults (Fig. 2.22). Coulomb software can be used to gain an understanding of the effects of coseismic faulting which can be extrapolated over the long-term in order to compare to observed patterns of palaeoshoreline deformation.

2.2.4 Application to seismic hazard

Chapter 1 highlighted that long term throw/slip rates and recurrence intervals (see below) can be obtained via studies of deformed palaeoshorelines. Slip/throw rates are essential input parameters into PSHA and allow calculation of recurrence intervals and the probability of exceedance of ground motion, in given time periods, using known seismic sources (Pace et al., 2016). However, variations in slip rate have been shown to be one of the main sources of uncertainty in calculating earthquake probabilities (Field et al., 2014). Such uncertainties arise as a result of earthquake clustering and quiescence and assumptions based on the slip/throw rate along the strike of a fault (e.g. Dolan et al., 2007; Faure Walker et al., 2019). Specifically, temporal earthquake clustering has the potential to introduce bias into fault slip rate where the measured slip rates may not be representative of the long term behaviour of a fault. Furthermore, Faure-Walker et al. (2019) highlight that detailed fault data reflective of how fault/slip rates may vary along a fault are rare, and that consequently in PSHA, artificially simplified shapes of along-strike slip/throw rates are used based upon one or few measurements. This is problematic because throw/slip rates along a fault have been shown to be highly variable as a result of changes in the geometry of the fault and fault interaction that may, for instance, load part of a fault and result in partial fault ruptures (e.g. Faure

Walker et al., 2009; Mildon et al., 2017; Iezzi et al., 2018, 2019, 2020) or result in increased displacement gradients towards the tips (Walsh and Watterson, 1989; Gupta and Scholz, 2000). The impact of using an along strike slip/throw rate that is in error has the potential to significantly affect the key outputs from PSHA models, resulting in variation of recurrence intervals and ground shaking intensities. In this regard, Faure Walker et al. (2019) showed that using simplified throw rate profiles for a Mw 5.1 on the Parasano-Pescina normal fault (Italy) resulted in differing recurrence intervals of 420, 465, 262 and 524 years when different fault profiles and completeness of throw data was used (Fig. 2.25). Thus, it is beneficial to obtain slip/throw rates from a number of points along a fault in order that PSHA will be as accurate as possible.

-

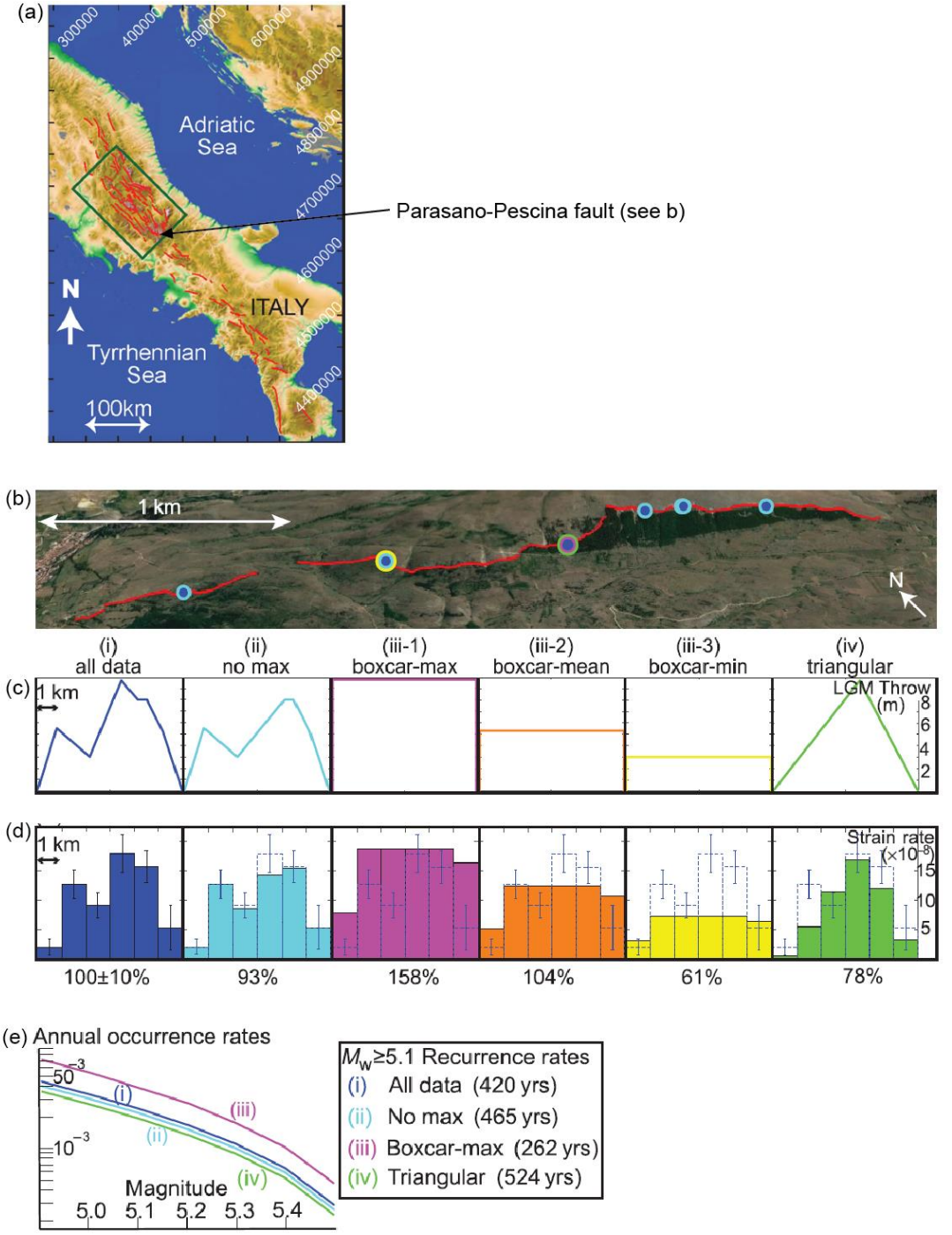

Figure 2.25: Overview of the work of Faure Walker et al. (2019) to investigate the effects of using different fault throw profiles to calculate rates of earthquake occurrence on the Parasano-Pescina fault, Italy. (a) Map of the faults in the central Apennines (Italy) and the location of the Parasano-Pescina fault shown in (b). (b) View of the Parasano-Pescina fault trace from Google Earth. Circles show sites of postglacial throw measurements, the colours correspond to which models (i-iv) the throw measurements were used in. (c) Throw profiles along the fault for each of the models assuming either a triangular or 'boxcar' profile (where a 'boxcar' profile represents a singular constant throw value along the entire fault) and (d) strain rates with 1 km x 2 km grid boxes along the fault; (i) 'all data' uses the all data from seven data collection sites along the fault; (ii) 'no max' uses all the data except from the throw-rate data from the site of maximum 15 Ka throw; (iii-1) 'boxcar-max' only uses the throw data from the maximum throw-rate site; (iii-2) 'boxcarmean' uses the average 15 ka throw, slip vector, azimuth and plunge; and (iii-3) 'boxcar-min) uses only data collected from the minimum throw-rate site, but in this

scenario the throw rate decreases linearly from the maximum to zero at each tip, forming a triangular throw-rate profile along the fault. Error bars and dashed bar plots shown in each plot are for the (i) all data case. Percentage values in the boxes give the total strain rate across the fault relative to the (i) all data case. This shows that (ii) degrading data by excluding a single data point or (iii, iv) extrapolating a single throw value along a fault changes calculated strain rates across the fault. (e) Frequency-magnitude semilog plots for Mw 4.9-5.5 for the four throw profile scenarios along the Parasano-Pescina fault. Graphs compare (i) all data sites included in the all data throw profile with three sets of degraded data. The three sets of degraded data are created by: (ii) leaving out the maximum throw point in the no max profile but including the other measurements; (iii) extrapolating the maximum throw along the whole fault in a boxcar-max profile; and (iv) extrapolating throw along the fault by decreasing the maximum throw linearly to the fault tips in a triangular profile. Calculated earthquake >Mw 5.1 recurrence intervals are 420, 465, 252 and 524 yrs for cases (i)-(v), respectively. This example shows that using simplified throw-rate profiles can change calculated recurrence intervals that are used to inform probabilistic seismic hazard assessment.

Along faults where Holocene slip/throw rates are not known, slip rates are low or where faults are offshore, deformed palaeoshorelines are one of few ways to determine the recurrence intervals. The recurrence interval can be calculated in two ways using information from deformed palaeoshorelines. In situations where a fault is located onshore and offsets palaeoshorelines in its footwall and hangingwall, knowledge of the total fault offset (*FO*) over a specified time period (*T*) and the modelled coseismic uplift (*CU*) (using Coulomb 3.4, see above) can be used to gain the total number of earthquakes (*E*) and thus the long-term recurrence interval:

$$Recurrence\ interval = \frac{T}{E} \text{ where, } E = \frac{FO}{CU}$$

Secondly, where the fault is offshore, knowledge of the age of a palaeoshoreline (*A*) and its total uplift from its initial elevation (*O*), which is calculated using the elevation of the sea-level highstand relative to today (*HE*) and the present day elevation of the palaeoshoreline (*PE*), can be used to determine the long-term recurrence interval:

$$Recurrence\ interval = \frac{A}{\left(\frac{O}{CU}\right)} \text{ where } O = HE + PE$$

Defining the maximum magnitude that is possible on a fault is of particular importance in understanding its potential seismic hazard because it is one of the parameters used to calculate possible ground motion associated with a fault (Thenhaus and Campbell, 2003). Wells and Coppersmith (1994) identified empirical fault-scaling relationships that relate parameters of fault ruptures with the maximum magnitude of an earthquake. In particular, Wells and Coppersmith (1994) used log-linear regressions to show that earthquake magnitude and surface and sub-surface rupture length are well correlated, suggesting a scaling relationship between the fault length and the maximum magnitude (Fig. 2.26). This relationship allows estimation of the potential magnitude (M) of an earthquake based upon

the length of the fault using the following equation where *SRL* corresponds to surface rupture length (which can be obtained from field measurements, geological maps or databases of active faults):

$$M = 5.08 + 1.16 * \log(SRL)$$

For instance, using Fig. 2.26, a normal fault that is 30 km in length has the potential to cause a maximum Mw ~6.7 earthquake. If the fault accommodates displacement along a number of segments that are linked at depth, it is possible to consider the maximum magnitudes for different rupture scenarios of one, multiple or all segments.

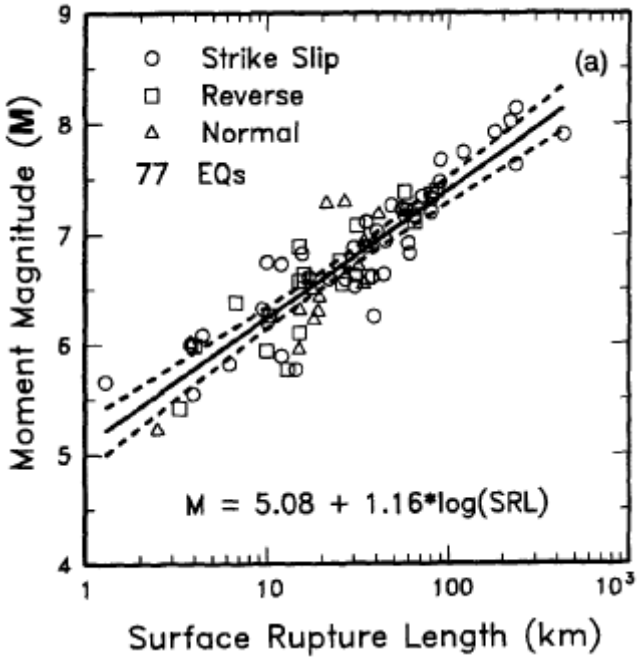

Figure 2.26: Fault scaling relationship between surface rupture length (SRL) and moment magnitude (M) (from Wells and Coppersmith, 1994).

Fault-scaling relationships, such as those detailed in Wells and Coppersmith (1994), form the basis for exploring and understanding the coseismic deformation caused by faulting using elastic half-space modelling. Coulomb 3.4 (Toda et al., 2011) introduced in Section 2.2.3, can also be used to model the rupture on a fault (see Section 3.5.2 for detail) in order to examine the coseismic uplift and subsidence that occur along strike in the footwall and hangingwall of the fault. The coseismic patters of uplift and subsidence are particularly useful because they allow long-term patterns of fault deformation to be extrapolated using the coseismic patterns (this is based on the fault hosting similar ruptures throughout time). Furthermore, this modelling provides absolute values of footwall and hangingwall coseismic vertical

movement caused by faulting, which can be used in combination with palaeoshoreline deformation to determine long-term recurrence intervals and deformation associated with individual earthquakes. Meschis et al. (2019) use the basis of this approach to determine the geometry and kinematics of the offshore fault linked to the 1908 Messina earthquake (Italy) that was responsible for >80,000 deaths. These authors used measurements of the coseismic vertical deformation on footwall palaeoshorelines compared to tests of fault ruptures using variable geometries of the fault in question modelled in Coulomb 3.4 (Fig. 2.27).

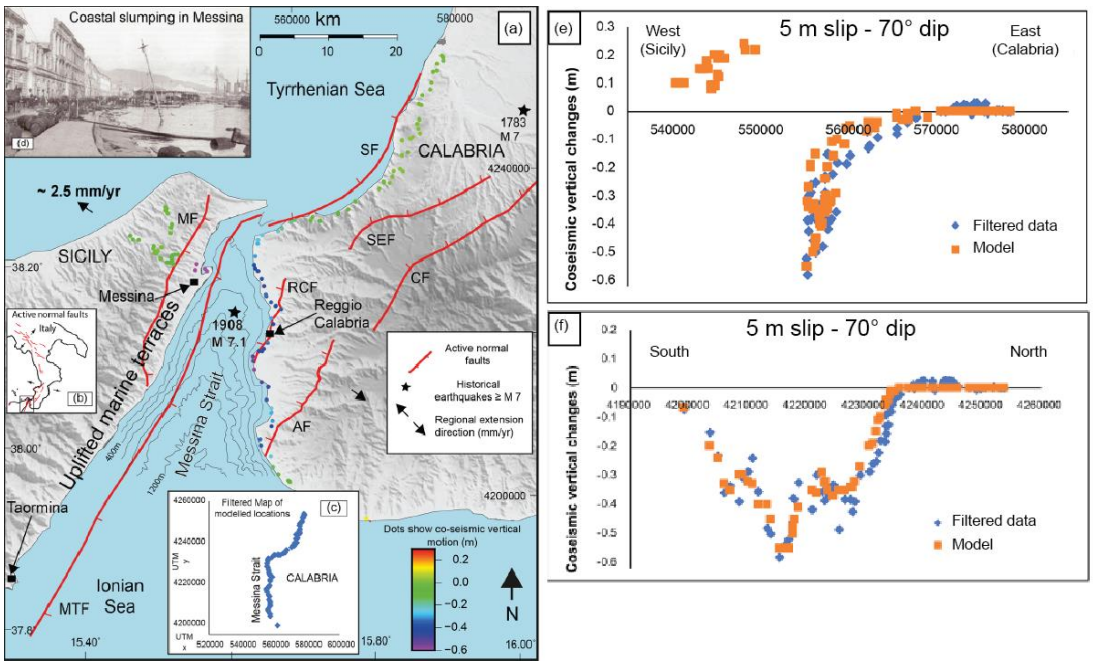

Figure 2.27: Map of the Messina Strait and Quaternary faults, coloured dots represent co-seismic vertical movement mapped by Loperfido (1909). Messina Fault (MF); Messina-Taormina Fault (MTF); Armo Fault (AF); Reggio Calabria Fault (RCF); Sant'Eufemia Fault (SEF); Cittanova Fault (CF); Scilla Fault (SF). Panel (a) is located in (b). (c) Filtered levelling data used in the modelling. (d) Port of Messina town affected by coastal slumping after the earthquake. Models of the coseismic modelled deformation (using Coulomb 3.4) for a south east 70˚ dipping fault with 5 m of slip (orange) compared to filtered data obtained from Loperfido (1909) (blue) plotted (e) east-west plot and (f) north-south.

The approach to use modelled coseismic deformation as a proxy for long-term deformation requires consideration of the impact of post-seismic deformation, where a viscous response occurs in the crust and upper mantle following an earthquake (Shen et al., 1994), that can result in continued deformation (subsidence or uplift) in the hangingwall and footwall for tens of years after the earthquake (e.g. Barrientos et al., 1992). The unknown factor associated with post-seismic deformation is what timescales it may last over; evidence in the literature suggest timescales of tens of years to a few hundreds of years (e.g. Kenner and Segall, 2000; Jacobs et al., 2002; Hu et al., 2004) so it is not considered to be particularly relevant to the studies herein, which examine deformation in the order of hundreds of

thousands of years. In any case, whether differentiation of uplift caused coseismically versus post-seismically is not essential for the purpose of gaining the long-term rate because: (a) the measured deformation includes post-seismic and coseismic deformation, and (b) Wells and Coppersmith (1994) include post-seismic deformation as many of the earthquakes were studied years after the coseismic measurements were obtained.

2.3 INTRODUCTION TO THE GEOLOGICAL LOCALITIES

The key geological localities within this thesis are briefly introduced here; in-depth exploration of each of these areas is provided in the appropriate chapters within the thesis.

2.3.1 South Crete, Greece

The presence of sequences of palaeoshorelines cut into carbonate lithologies along the south of Crete was first documented in detail by Kelletat et al. (1976). Such sequences of palaeoshorelines were selected for this study as they provide the opportunity to test the use of cosmogenic ^{36}Cl exposure dating owing to the presence of pre-existing age controls from OSL dating and limestone wave-cut platforms. Complex tectonics also mean that this area would benefit from examination of the temporal and spatial variation of uplift rates using the approach outlined herein.

Crete lies in the forearc of the western Hellenic subduction zone (WHSZ) (Fig. 2.28, 2.29), which is over 1,200 km long and is one of the most seismically active regions on Earth (Becker & Meier, 2010) (Fig. 2.29a). The variation of lithologies observed on Crete (carbonite Plattenkalk unit, phyllite quartzite unit, limestones of the Gavrovo-Tripolitza zone, marine sediments of the Pindos unit, marine marls and ophiolites) occur predominantly as a result of deformation that has occurred throughout the Oligocene to the early Miocene in the form of south-directed thrusting (Fassoulas et al., 1994, and references therein; Papanikolaou & Vassilakis, 2010). The result of this compression was stacking of the internal and external nappe zones (IGME map sheets Ano Viannos 1:50,000; IGME Akhendhrias 1:50,000).

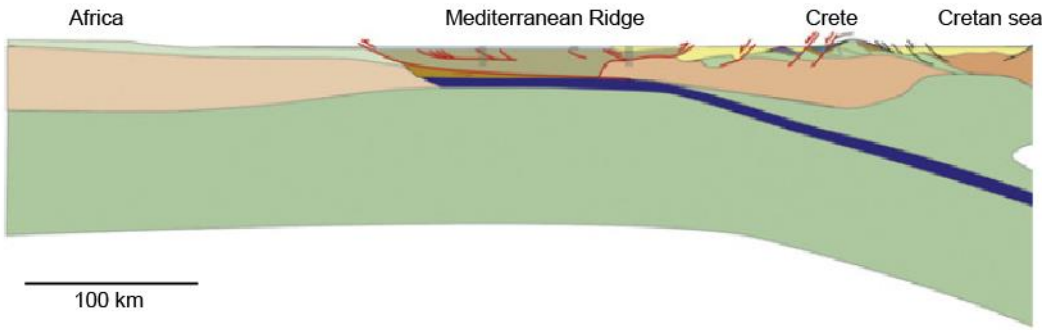

Figure 2.28: Lithospheric-scale cross section of African passive margin to the Cretan sea (from Jolivet et al., 2013)

Crete accommodates convergence between the Eurasian and African plates at a rate of ~35–40 mm/year (Nocquet, 2012; Fig. 2.29b), with much of this convergence occurring as a result of subduction rollback and the southward motion of the Eurasian plate (Jackson, 1994; Kreemer and Chamot-Rooke, 2004; Nyst and Thatcher, 2004; Jolivet et al., 2013). Studies of the WHSZ crustal stress field using earthquake focal mechanisms reveal that strike slip faulting dominates along the north west of Hellenic trench, transitioning to extension in the south western Peloponnese and the southern coast of Crete (Chousianitis et al., 2015; Konstantinou et al., 2016).

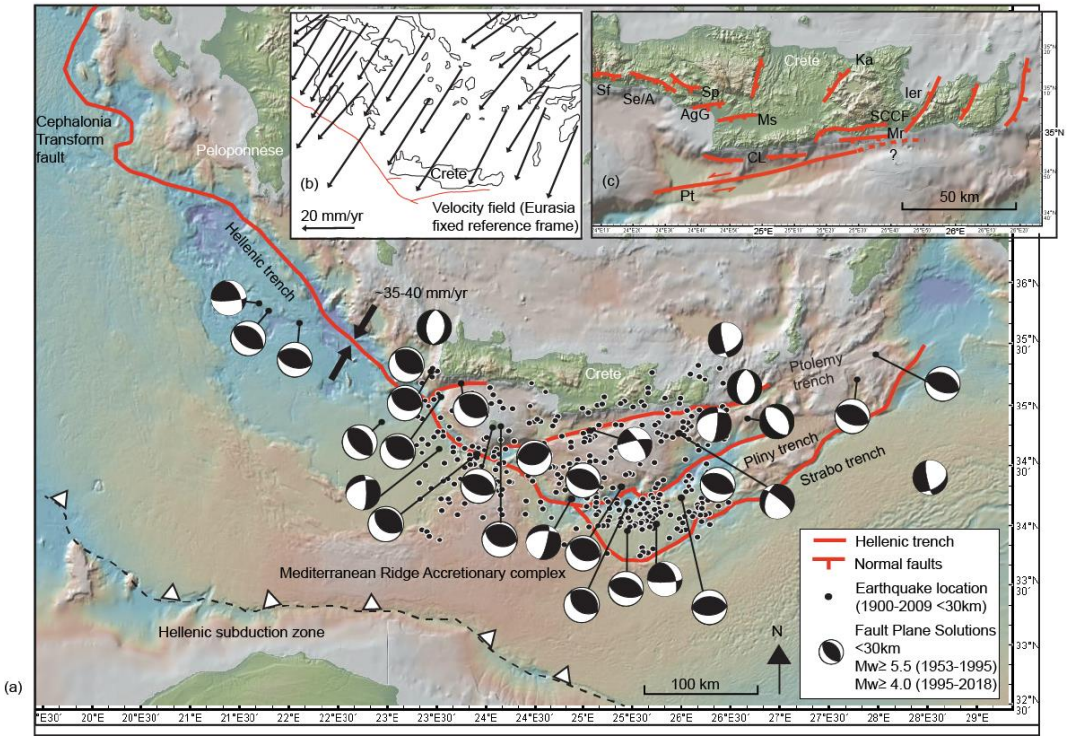

Figure 2.29: (a) Tectonic setting of Crete, Greece. GPS data are from Nocquet (2012). The location of the Hellenic subduction zone is taken from Kreemer & Chamot-Rooke (2004). Dots show earthquakes between 1900 and 2009 >Mw 4, constrained to a depth ≤30 km (Makropoulos et al., 2012); fault plane solutions for earthquakes constrained to a depth ≤30 between 1953 and 1995 (solutions for earthquakes constrained to a depth ≤30 between 1953 and 1995 (Mw ≥ 5.5; Papazachos et al., 1998) and 1995 and 2018 (Mw ≥ 4; CMT Catalogue: Dziewonski et al., 1981; Ekström et al., 2012). (b) Velocity field for Greece (Nocquet, 2012); (c) map of Crete with possible active arc normal upper-plate faults labelled: Ka = Kastelli fault (Caputo et al., 2010); Sf = Sfakia (Caputo et al., 2010); Se/A = Sellia/Asomatos (Caputo et al., 2010); Sp = Spilli (Monaco & Tortorici, 2004); Caputo et al., 2010); AgG = Agia Galini (Caputo et al., 2010; Monaco & Tortorici, 2004); Ier = Ierapetra (Caputo et al., 2010); Ms = Messara (Fassoulas, 2000); CL = Cape Lithino (Caputo et al., 2010); Mr = Mirto (Caputo et al., 2010) SCCF = South Central Crete Fault (Gallen et al., 2014); Pt = Ptolemy trench fault (Mascle et al., 1982; Becker et al., 2006, 2010; Kokinou et al., 2012).

A number of authors suggest that Crete represents a horst structure that has been uplifting since the Miocene (Bohnhoff et al., 2001; Meier et al., 2007; Papanikolaou & Vassilakis, 2010; Ten Veen & Meijer, 1998). There is evidence of megathrust earthquakes along the area to the south of Crete, namely the C.E 365 and 1303 earthquakes (Ambraseys, 2009). However, debate continues as to whether these earthquakes ruptured along the subduction interface (e.g. Papadimitriou and Karakostas, 2008; Ganas and Parsons, 2009) or on upper-plate reverse faults that are suggested to splay from the subduction interface (e.g. Shaw et al., 2008, 2010). Convergence-based tectonic models for the south of Crete have suggested slip on shallow splay or steeply dipping thrust faults beneath Crete as the cause of coastal uplift; these are predominantly based on coastal observations along south western Crete linked to

the 365 C.E. earthquake (Taymaz et al., 1990; Shaw et al., 2008; Tiberti et al., 2014; Mouslopoulou et al., 2015b). However, such convergence-based models have been extended throughout south Crete to explain the observed coastal topography (Mouslopoulou et al., 2015a) without considering the impact of extensional faults within their analyses.

While thrust faulting dominates the offshore of southern Crete at depths above and along the subduction interface, shallower depths of <15 km and closer to the southern shoreline of Crete are predominantly characterised by normal and transtensional faulting (Papazachos, 1990; Ten Veen & Kleinspehn, 2003; Alves et al., 2007; Kokinou et al., 2012). Onshore, normal faulting is prevalent, with the strikes of these dip-slip faults having multiple directions suggesting a complex extensional regime (Caputo et al., 2010; Ganas et al., 2017; Mercier et al., 1987; Zygouri et al., 2016). The active normal faults broadly trend E-W or N-S with the exception of the Ierapetra and Kastelli faults, which trend NE-SW (Strobl et al., 2014) (Fig. 2.29c). Offshore southern Crete, the coast is bounded by three "trench" faults. The Ptolemy, Pliny, and Strabo trenches are upper-plate faults that do not represent the subduction trench of Crete (Fig. 2.29), which is buried under up to 10 km of sediments belonging to the accretionary prism (Chaumillon & Mascle, 1997). The Ptolemy fault is of interest because it is the mostly closely located of the trench faults, ~10 km away from the shoreline of south central Crete (Fig. 2.29). Analysis of the microseismicity within the area of the Ptolemy trench reveals that this fault is active and has been shown to extend to the subduction interface (Fig. 2.30) (Meier et al., 2004; Becker et al., 2010).

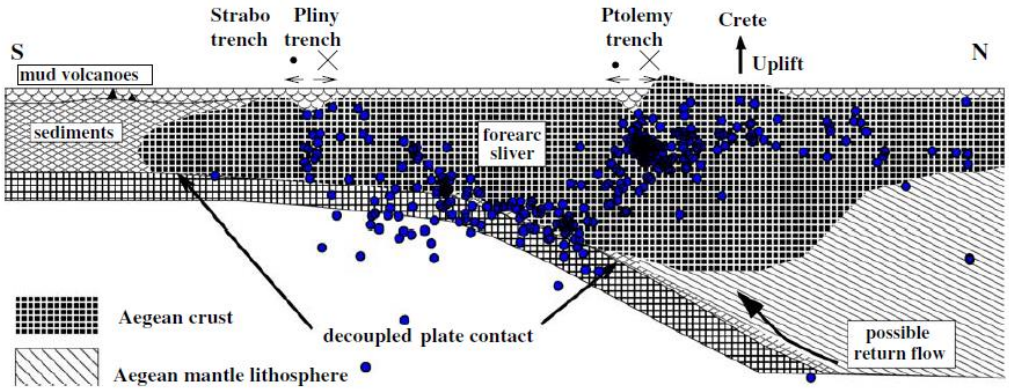

Figure 2.30: Location of the seismogenic zones of the Hellenic forearc south of central and eastern Crete. Blue circles represent microseismicity (from Becker et al., 2010).

Pleistocene uplift is visible in sequences of preserved palaeoshorelines seen throughout the eastern and southern coasts of Crete (Angelier, 1979b; Gaki-Papanastassiou et al., 2009; Gallen et al., 2014; Peterek and Schwarze, 2004; Pirazzoli et al., 1982; Strobl et al., 2014).

Uplift continues into the present day, evidenced by raised Holocene notches and raised beach deposits, which are predominantly seen in Western Crete and linked to suggested coseismic uplift caused by the C.E. 365 earthquake (Pirazzoli et al., 1982; Postma and Nemec, 1990; Shaw et al., 2008; Stiros, 2001, 2010). Uplifted Holocene beachrocks are also reported on the footwall of the Ierapetra fault toward the south east of the island (Figure 2.29c; see Gaki-Papanastassiou et al., 2009, *and references therein*). Along parts of the south coast of Crete, east-west trending normal faults display uplifting palaeoshorelines in their subsiding hangingwalls, suggestive of offshore uplift, but the cause of such uplift is debated and linked to regional deformation, slip on upper-plate reverse faults, and normal faults (e.g. Alves et al., 2007; Shaw et al., 2008; Kokinou et al., 2012; Gallen et al., 2014, 2017; Mouslopolou et al., 2015; Ott et al., 2019). The research in this thesis focuses on the south central area of Crete, where palaeoshorelines occur along the length of the coast and the coastline is intersected by a normal E-W trending fault that also offsets palaeoshorelines and displays uplift in its hangingwall. The presence of existing age controls along shorelines in the south central area allows testing of ^{36}Cl exposure dating and analysis of possible uplift mechanisms using elastic half-space modelling (Chapter 4) and sensitivity testing of the use of different sea-level curves to determine deformation rates (Chapter 5).

2.3.2 Gulf of Corinth, Greece

The Perachora Peninsula, located within the eastern Gulf of Corinth (Fig. 2.31), provides an excellent opportunity to carry out cosmogenic ^{36}Cl exposure dating on wave-cut platforms at different elevations comprised of variable carbonate lithologies. There are existing coral growth ages on parts of the peninsula, providing insights into the along-strike variation in uplift along the South Alkyonides fault. However, an area at the western tip of the fault (Cape Heraion) with excellent wave-cut platforms cut into carbonates has been identified where existing coral ages are insufficient to provide robust enough evidence to determine whether the wave-cut platforms represent a faulted single terrace or a sequence of Late-Quaternary platforms and palaeoshorelines. Locations on Cape Heraion amenable to ^{36}Cl exposure dating and new coral sampling sites have been identified, so this location allows new age controls to be used to test between the two published hypotheses (Chapter 6), this in turn allows the cause of observed uplift to be determined between localised normal faulting (e.g. Roberts et al., 2009) versus uplift resulting from regional subduction-related processes (Leeder et al., 2003; 2005). Furthermore, the presence of new coral ages and a significant number of existing coral growth ages obtained using ^{234}U/^{230}Th from the wider Gulf of

Corinth provide the opportunity to examine the application of $\delta^{234}U_i$ as a method of determining the reliability of coral ages from coastal margins (Chapter 7).

The Gulf of Corinth (Fig. 2.31) represents an intra-continental rift that is seismically active and is thought to have initiated <5 Ma (Ori, 1989). It formed as a result of normal faulting in response to high N-S extensional strain rates across central Greece and is one of the world's fastest extending rift systems, with geodetic extension rates between <5 mm/yr and 10-15 mm/yr (Davies et al., 1997; Clarke et al., 1998; Briole et al., 2000). Late Quaternary rift extension has been derived from extensive offshore studies (e.g. Sachpazi et al., 2003; Sakellariou et al., 2007; Bell, 2008, 2009, 2011; Taylor et al., 2011; Charalampakis et al., 2014) using marine seismic data.

The presence of a complex basin structure (e.g. Moretti et al., 2003; Sachpazi et al., 2003; McNeill et al., 2005; Sakellariou et al., 2007; Bell et al., 2009; Nixon et al., 2016; Gawthorpe et al., 2018) is a consequence of extension predominantly accommodated along north-dipping faults that bound the southern margin of the gulf (Sakellariou et al., 2007; Bell et al., 2009; Roberts et al., 2009; Nixon et al., 2016). From the Late Quaternary to the present day, north-dipping faults located along the rift system that borders the south of the gulf are predominately responsible for extension, with other faults less active or ceasing activity (Sakellariou et al., 2007; Bell et al., 2009; Roberts et al., 2009; Nixon et al., 2016; Fernandez-Blanco et al., 2019). The north-dipping faults have been shown to have started to dominate the deformation between 340-175 ka (Roberts et al., 2009; Nixon et al., 2016).

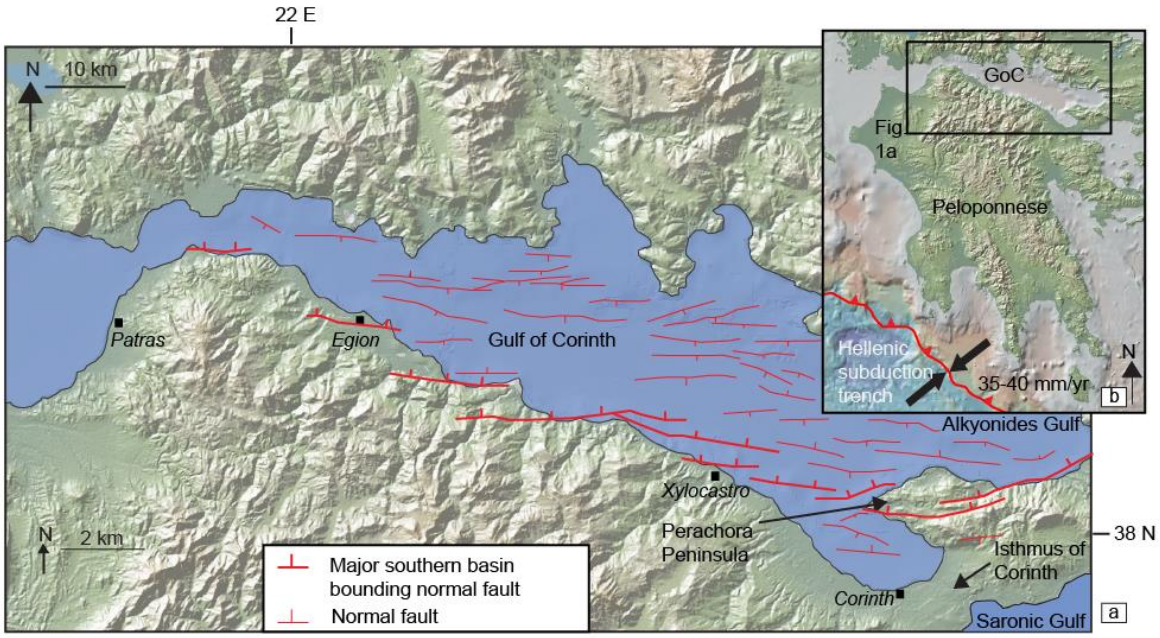

Figure 2.31: (a) Map of the Gulf of Corinth showing normal faults as per Nixon et al. (2016). (b) Location of the Gulf of Corinth within Greece, GPS velocities from Nocquet et al., 2012.

Marine terraces and their palaeoshorelines are located throughout the southern and eastern margin of the Gulf of Corinth where, detailed mapping of palaeoshoreline sequences alongside uplift rates from $^{234}U/^{230}Th$ coral growth ages provide evidence of spatially variable uplift caused by footwall uplift during normal faulting (e.g. McNeill and Collier, 1994; Armijo et al., 1996; Houghton et al., 2003; De Martini et al., 2004; Roberts et al., 2009). The Perachora Peninsula, in the east of the gulf, accommodates the South Alkyonides Fault System (SAFS), which reaches its western tip in the west of the Peninsula known as Cape Heraion. This western tip of the Perachora Peninsula has been referred to as the Perachora Fault Segment Boundary (PFSB) by Morewood and Roberts (1997, 1999) because it marks the location where two crustal-scale faults overlap at their tips (Fig. 2.31) and has been suggested to accommodate contemporaneous N-S and E-W faulting over the past 125 ka.

Given the background presented above, the next chapter will provide an overview of the general methods applied throughout this thesis in order to investigate the deformation on late Quaternary palaeoshorelines by applying and testing ^{36}Cl exposure dating on wave-cut platforms, such that the dominant tectonic processes can be explored and considered in the context of seismic hazard analysis.

3 CHAPTER 3: METHODS

This chapter details the principal methods employed in this thesis that are essential to investigating palaeoshorelines and determining deformation rates in order to examine the long-term behaviour of faults: (1) identifying and measuring marine terraces, wave-cut platforms and their associated palaeoshorelines using field observations and a DEM; (2) correlating palaeoshorelines with sea-level highstands using the synchronous method; (3) sampling and sample preparation for ^{36}Cl cosmogenic exposure dating and $^{234}U/^{230}Th$ coral age dating, (4) mapping normal faults and using elastic half-space deformation to explore long-term patterns of uplift associated with faulting. Other methods employed that are relevant to individual chapters are detailed in those chapters.

3.1 IDENTIFICATION AND MEASUREMENT OF PALAEOSHORELINES

Understanding of the formation of palaeoshorelines and their associated features outlined in Chapter 2 informs the approach to identifying, locating and measuring palaeoshoreline elevations employed within this thesis. Field investigations were the preferred approach to map palaeoshorelines, however, in order to investigate the longer length-scale deformation of sequences of palaeoshorelines that may occur over tens of km, high resolution (5 m) DEMs were also employed.

3.1.1 Interrogation of palaeoshorelines using DEMs

Palaeoshorelines were initially investigated using a 5 m DEM (Fig. 3.1a) (produced by Ktimatologio SA from air-photo stereopairs), provided as .tif files (from Dr Athanassios Ganas, National Observatory Athens) and loaded and interrogated in ArcGIS. The 'hillshade' function was used in ArcGIS to produce a 3D greyscale representation of the surface such that changes in topography (i.e. palaeoshorelines) were visible. In the case of the study of south central Crete (Chapter 4), a sequence of palaeoshorelines along a strike of ~50 km were analysed. As palaeoshorelines are being used to investigate deformation that is expected to be concordant with the displacement along faults (Section 2.2.2), serial topographic profiles were taken along the strike of the faults in question from the tip to the centre of the fault. This approach is in line with existing studies of palaeoshoreline deformation (Armijo et al., 1996; Roberts et al., 2009, 2013; Gallen et al., 2014).

The location of the onshore South Central Crete Fault (SCCF) was identified using geological maps (IGME map sheets: Ano Viannos 1:50,000; IGME Akhendhrias 1:50,000), these maps also outlined the locations of Quaternary palaeoshorelines and their associated deposits. The palaeoshorelines throughout south central Crete were initially identified using the 'hillshade' layer (Fig. 3.1a) on the DEM and then further assessed using 'slope' function (Fig. 3.1b) within ArcGIS. The slope function displays changes in elevation represented by colour change; red colours indicate steeper topography, yellow to green represent progressively shallowing terrains (Fig 3.1b). Steeper topography that runs parallel/sub-parallel to the coastline was taken to indicate the palaeoshoreline and back wall, shallower topography indicated the wave-cut platform (Fig. 3.1b). Analysis of the DEM revealed that palaeoshorelines in south central Crete were broadly continuous along strike and as such were mapped along their length.

When deciding on the locations of multiple topographic profiles areas near river incision were avoided to ensure marine and not fluvial features were measured. 2D topographic profiles across a sequence of palaeoshorelines revealed a staircase-like morphology (Fig. 3.1c); the inflection point between the sub-horizontal surface and the back wall of the palaeoshoreline was taken as the elevation of the palaeoshoreline and measured using the '3D analyst' function in ArcGIS, the errors associated with the DEM were ± 4 m (at 95% confidence level). Palaeoshorelines observed on the DEM were subsequently investigated in Google Earth to check that the breaks of slope were not associated with "human-made" features and on geological maps to ensure they did not represent lithological changes or faults. Importantly, studies of the DEM and Google Earth were used as the basis to inform field mapping, where palaeoshoreline and fault locations along with their elevations were verified, this is discussed below.

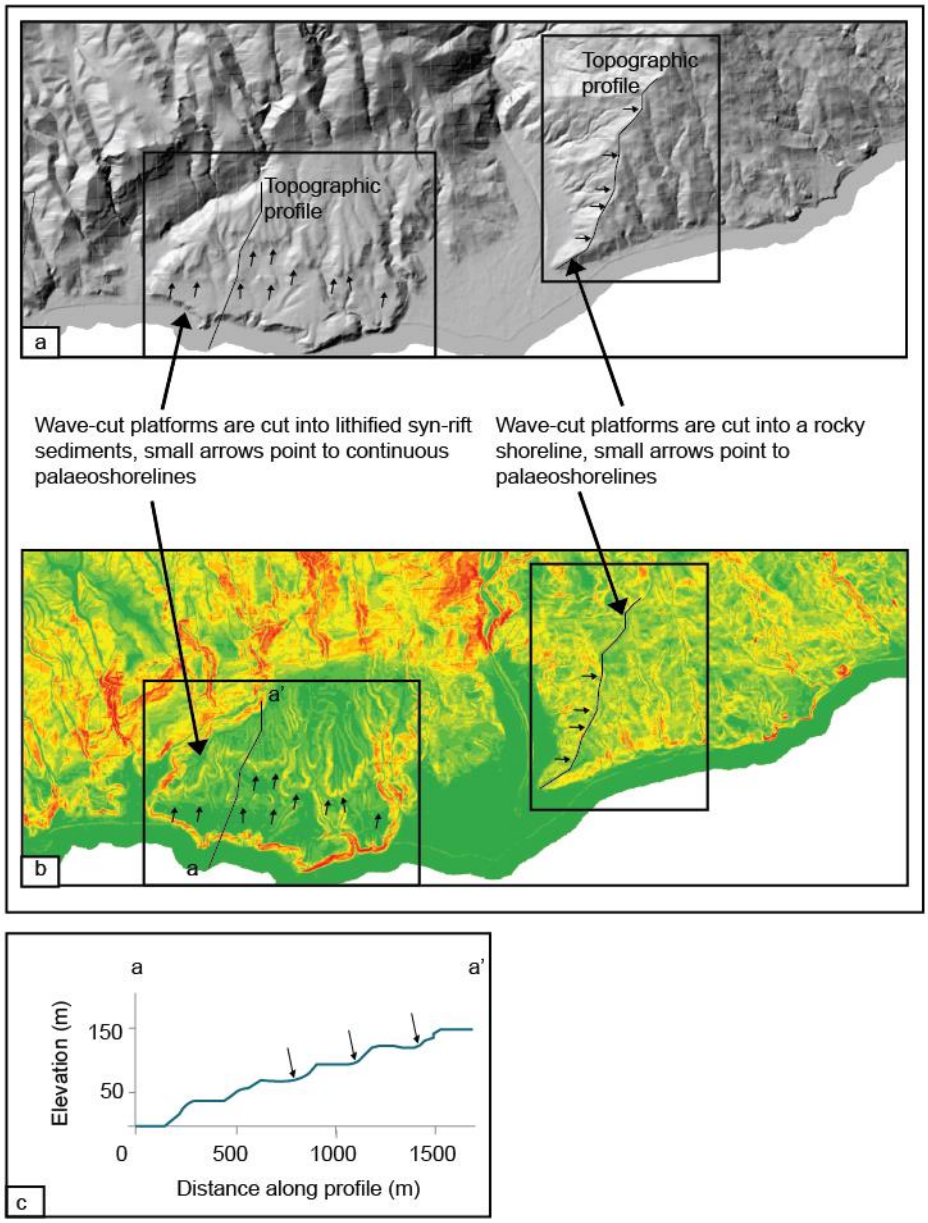

Figure 3.1: (a) 5 m DEM with 'hillshade' showing palaeoshorelines located on syn-rift sediments and on a rocky shoreline. (b) as (a) but with a 5 m DEM showing 'slope analysis' used to help identify palaeoshorelines and wave-cut surface. Topographic profile lines are shown in (a) and (b). Small arrows in (a) and (b) point to palaeoshorelines. (c) example 2D topographic profile, small arrows point to palaeoshoreline inner edges, flat surfaces are wave-cut platforms.

The use of the DEM for investigations on Cape Heraion, Perachora Peninsula (Gulf of Corinth) was to provide spot elevation measurements above and below the offsets debated to be palaeoshorelines or faults. As the mapped area for Cape Heraion was relatively small (~1 km^2) the majority of elevation measurements were made in the field (Section 3.1.2), thus DEM measurements were used in order to supplement the field-based elevation measurements. These spot elevations were carried out using the '3D analysis' function in ArcGIS and were taken on flat surfaces away from drainage.

3.1.2 Field observations

The aims of field observations in this thesis were to: (i) identify the presence of palaeoshorelines and measure their elevations, (ii) identify the locations of faults and where possible measure their hangingwall and footwall elevations to derive the vertical offset (throw) and, (iii) to identify locations suitable for sampling and sample wave-cut platforms for ^{36}Cl exposure dating and corals for $^{234}U/^{230}Th$ dating. All field elevation measurements were made using a *Garmin eTrex 30x* handheld barometric altimeter, with a horizontal error of ± 3 m and a published vertical error of ± 3 m, though repeated measurements in the same location suggest that the vertical error is less than 1 m. The barometric altimeter was regularly recalibrated to sea level to ensure the accuracy of elevation measurements.

3.1.2.1 Identifying and measuring palaeoshoreline elevations

Along rocky coastlines in the Mediterranean, where the normal tidal range is expected to be ~10-20 cm (Bonaduce et al., 2016), the primary field-based geomorphological indicators used to identify palaeoshorelines are notches, palaeo cliffs or caves, or a combination of these (e.g. Pirazzoli, 1986; Ferranti et al., 2006; Shaw et al., 2008; Roberts et al., 2013; Gallen et al., 2014; Antonioli et al., 2015; Boulton and Stewart, 2015; Rovere et al., 2016b). A notch is a groove formed in the bedrock (Kershaw and Guo, 2001) as a result of wave action involving the abrasion of the bedrock by sand/pebbles, chemical dissolution and/or biological abrasion (Section 2.1.1). Notch morphology has been shown to vary depending on the dominant cause of formation, which in turn is related to local conditions such as wave energy (Pirazzoli, 1986, Rust and Kershaw, 2000) and bedrock heterogeneity (Kersaw and Guo, 2001). Specifically, Pirazzoli (1986) showed that the elevation of the notch relative to mean sea level during formation may vary depending on how sheltered or exposed the notch sites were (Fig. 3.2). In this thesis, where notches were observed in the field, the elevation of the inflection point within the notch was accepted as representative of palaeo-sea level (Schneiderwind et al., 2016) (Figs. 3.2, 3.3). The small elevation differences observed by Pirazzoli (1986) linked to variations in the exposure of the setting (Fig. 3.2) are less of a concern to the work herein because they are accounted for within the measured uncertainty (± 3 m) associated with using the barometric altimeter.

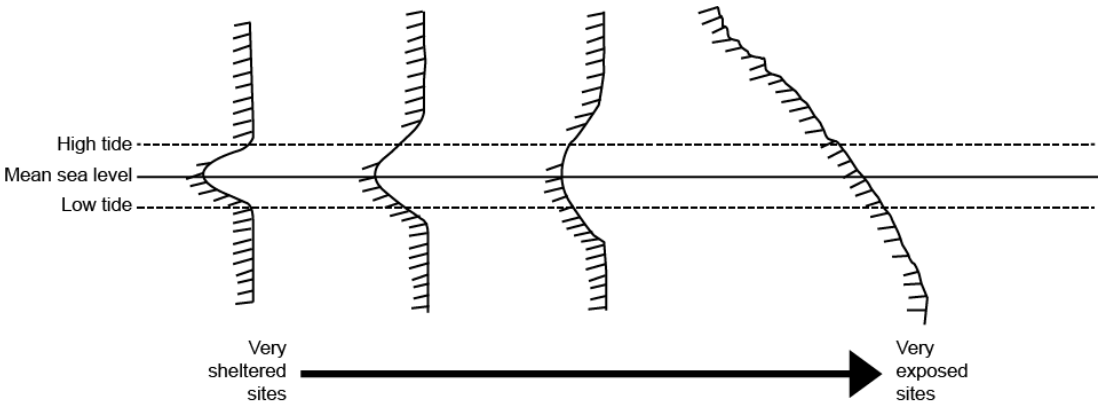

Figure 3.2: Cross sections of notch profiles showing the effect of variations on coastal wave energy on notch formation (modified from Pirazzoli, 1986).

Caves are also known to form at sea level during sea-level highstands from mechanical abrasion processes in combination with bioerosion and chemical dissolution processes (Carobene, 2015; Rovere et al., 2016b). Where caves were used to identify the palaeo-sea-level within this thesis, the elevation of the levelled floor at the entrance of the cave was taken as this is often associated with abrasion notches and provides a marker for relative sea level (Pirazzoli, 2005; Rovere et al., 2016b). Where there was an absence of notches and caves along a rocky shoreline, the palaeo-cliff (back wall) of a wave-cut platform served as an indicator of palaeo-sea level, elevation measurements were recorded using the intersection between the sub-horizontal platform and palaeo-cliff if a notch or cave was not present.

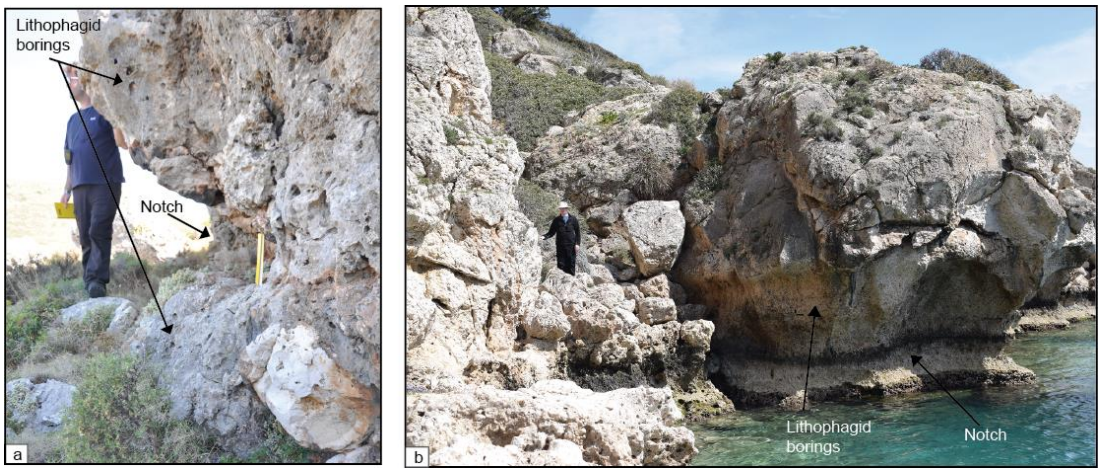

Figure 3.3: Notch examples: (a) notch cut into a back wall on the Paliki Peninsula, Cephalonia (UTM: 443228/4225548); (b) Holocene notches, south Perachora Peninsula, the most recent notch is labelled and horizontal lines of lithophagid borings are visible in upper notches (UTM: 4210451/662493) (images author's own).

Fixed biological indicators (FBI) are organisms that reside close to sea level. They typically live fixed to a rocky substrate such as a wave-cut surface, notch, cave or palaeo-cliff. The living range of these organisms varies (Fig. 3.4) but their upper limit is typically located at sea level (Stephenson and Stephenson, 1949; Laborel, 1986; Laborel and Laborel-Deguen, 2005; Rovere et al., 2015) and as such they provide a reliable indication of palaeo-sea level. FBI have been suggested to enhance the reliability of palaeo-sea level elevation measurements where notches, caves and paleo-cliffs occur, and in the absence of these features, multiple FBI can be used to indicate that a location is representative of palaeo-sea level (Rovere et al., 2015, 2016b). The presence of FBI (Fig. 3.4) were used in this thesis alongside notch, cave and palaeo-cliff observations to identify shallow marine environments indicative of shoreface settings and provide confidence in the measured palaeo-sea level elevations. This was particularly necessary in investigations on Cape Heraion (Perachora) where, as a result of faulting, notches and wave-cut platforms were vertically offset by faults. The relevant individual indicators are discussed further below using examples from the literature and observations from the field studies herein.

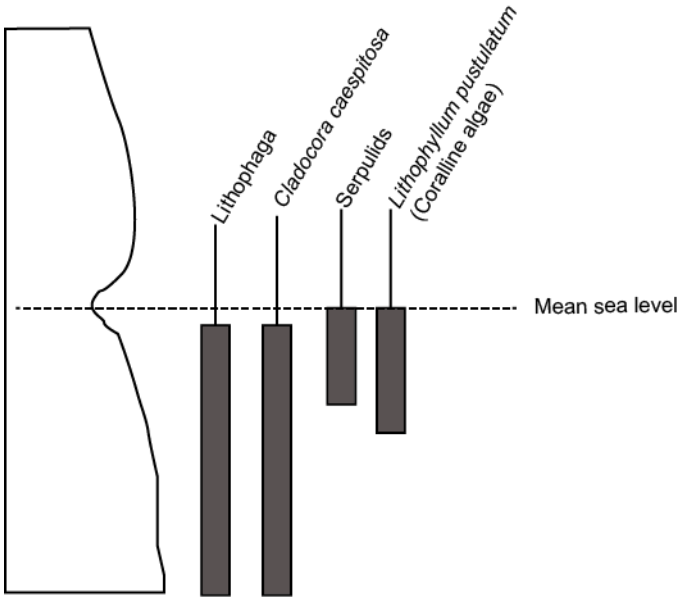

Figure 3.4: Cross section showing a relative Indication of the depths of key FBI featured in this thesis (modified from Rovere et al., 2015). See text for details.

Examples of FBI include corals, vermetid reefs, serpulid reefs, coralline algae, sponge borings and *Lithophaga* borings (Rovere et al., 2015) (Fig. 3.4). Changes in relative sea-level following a still-stand typically results in the death of these organisms leaving fossil remains. Small scale constructional features are formed by reef-forming organisms such as corals, serpulids and algae. Corals are an extensively used FBI in tropical and subtropical areas. The temperate

coral *Cladocora caespitosa* (Fig. 3.5a-d) is known to exist within the Mediterranean (e.g. Hearty et al., 1986; Kershaw et al., 2005; Roberts et al., 2009; Gaki-Papanastassiou et al., 2009; Houghton, 2010) and provides excellent dating opportunities using $^{234}U/^{230}Th$ but also an indication of relatively shallow depths associated with proximity to a palaeoshoreline. While colonies of *Cladocora caespitosa* have been reported at depths of -40 m, they are more commonly observed at depths between 4-10 m (Peirano et al., 2004). Coralline algae are calcareous deposits known to colonise rocky substrates, they are characterised by a hard outer thallus which consists of filaments of cells joined together and grow to form a coherent mass (Adey, 1986; Braga, 2011) (Fig 3.5c, d). Coralline algae have been reported to depths up to 35 m (Rasser and Piller, 1997) but knowledge of the specific species may provide a smaller ranges of depths, for instance, the presence of the species *Lithophyllum pustulatum* approximates depths of less than 10-15 m (Adey, 1986; Kershaw et al., 2005). Serpulids have calcareous habitation tubes (Fig. 3.5c, d) and are most commonly found in enclosed embayments, but can also withstand brackish conditions typical of lagoons and estuaries (Rovere et al., 2015). Frequently, small-scale constructional reefs are comprised of a combination of organisms where serpulids act as binders or secondary builders, cementing rubble in coral or coralline algal reefs. An excellent example of this is at Mavra Litharia, in the Gulf of Corinth, Greece, where a coral-algal reef has encrusted limestone bedrock. The reef is comprised of the coral *Cladocora caespitosa,* coralline algae and serpulids, and has been latterly bored by *Lithophaga* (Kershaw et al., 2005). Kershaw et al. (2005) suggested that this combination of reefal organisms was evidence for shallow formation in ~10 m of water depth.

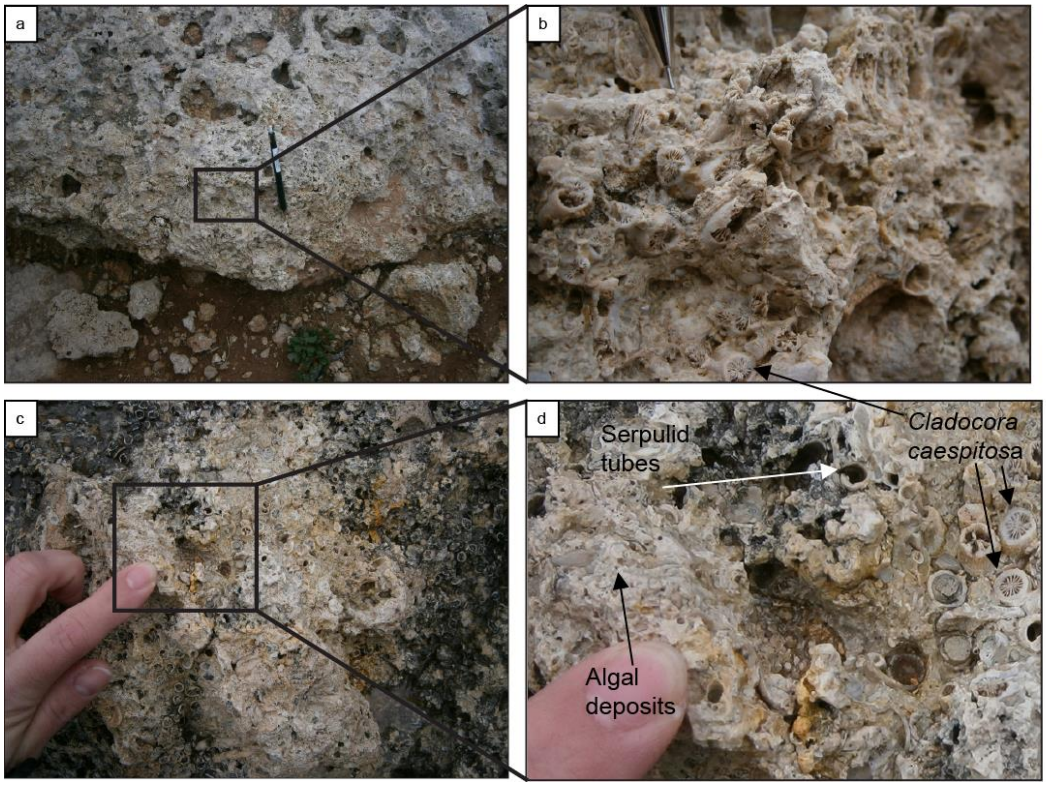

Figure 3.5: Field views of reef-frame constructors: (a) Cladocora caespitosa in a bioclastic matrix, branching Cladocora caespitosa colony can be seen in-life position below the black box. (b) Close up of (a). (c) Algal serpulid coral reef, seen close up in (d). All images taken from wave-cut platform deposits at 7m on Cape Heraion (Chapter 6).

On Cape Heraion, Gulf of Corinth, wave-cut platforms were composed of algal-bioclastic sediments (similar to those identified by Kershaw et al., 2005), occasionally baffled between in-life position *Cladocora caespitosa*. Thin section analysis of these palaeoshoreline deposits was carried out to identify the composition and revealed that the sediments were comprised of fine grained bioclastic debris (Fig. 3.6a-c), *Cladocora caespitosa* corals (3.6a) and *Lithophyllum pustulatum* (the latter identified by H. Sombroek, Birkbeck College) (Fig 3.6c-d), indicative of shallow water conditions in a marine setting. Furthermore, fossil assemblages apparent on the wave-cut platforms were used to indicate the relative energy within the environments, specifically death assemblages featuring broken and disarticulated bivalves, oyster shells, pectin, single corallites of *Cladocora caespitosa* and bryozoan fragments were observed and associated with a beach environment (as per Roberts et al., 2009).

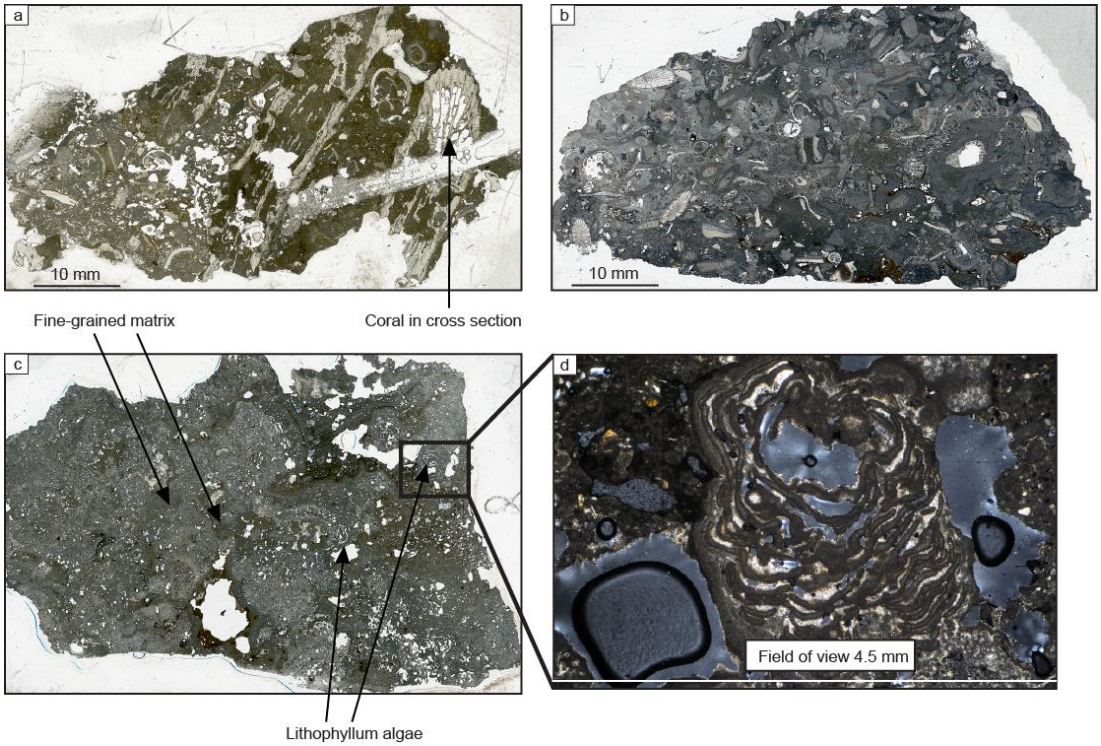

Figure 3.6: Thin sections of samples from wave-cut platforms on Cape Heraion (Chapter 6): (a) Corals in a fine-grained matrix. (b) bioclastic assemblage; (c) Lithophyllum algae in a fine-grained matrix, with a close up of the lithophyllum in (d).

Evidence from sponges and *Lithophaga* leave their mark as borings into rocky substrates such as a notch, palaeo-cliff, carbonate wave-cut platforms or carbonate pebbles within a conglomerate. The highest concentrations of *Lithophaga* borings are frequently observed within the top few meters of sea level (Rovere et al., 2015) where horizontal bands of borings occur (e.g. Fig 3.7). In the fieldwork conducted, where present, the upper limit of horizontal lines of lithophagid borings within a palaeo-cliff, cave or notch, was used as an indicator of palaeoshoreline elevation, as this serves to act as an excellent sea-level index point (Laborel and Laborel-Deguen, 1994; Pirazzoli, 1996; Carobene, 2015). Abundant borings on wave-cut surfaces were also used to indicate proximity to the palaeoshoreline where notches or caves were not present. Furthermore, the presence of lithophagid borings was particularly important for selecting ^{36}Cl exposure dating sampling locations on wave-cut platforms (see below) indicative of low erosion (e.g. Fig 3.7c).

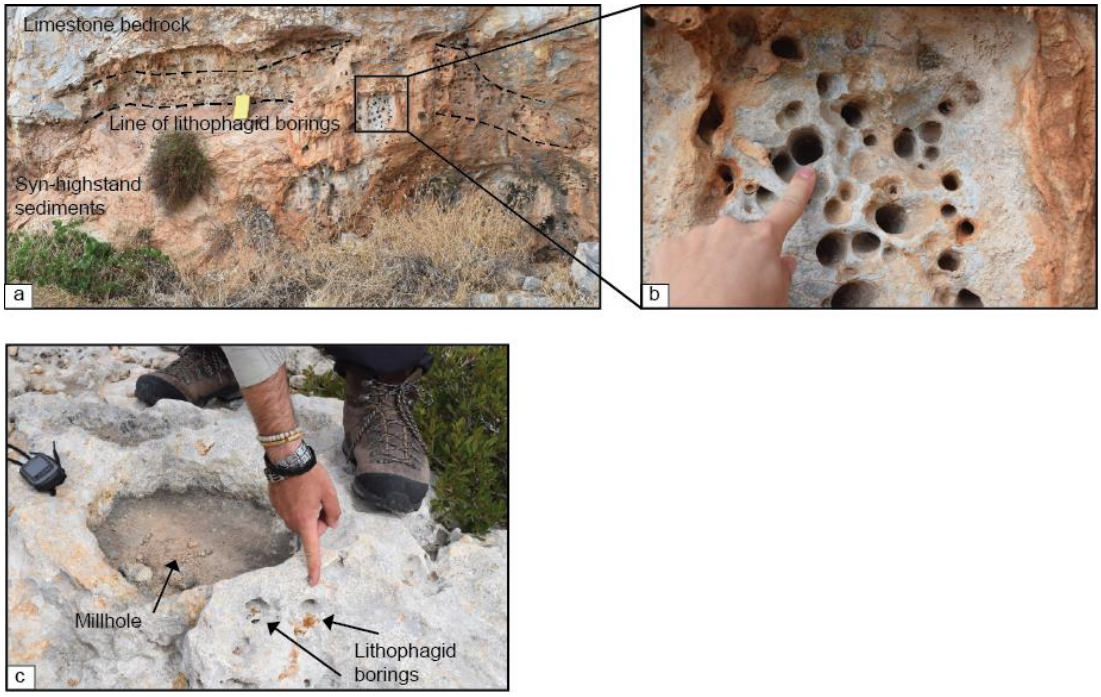

Figure 3.7: (a) Lines of lithophagid borings along a back wall, close up shown in (b); (c) Millhole on a wave-cut platform with lithophagid borings present on the edge of the millhole. (Photographs taken in Greece, authors own).

Cemented beach deposits were interpreted to represent the upper shoreface environment (Roberts et al., 2009) as they were observed as partial veneers on bedrock wave-cut platforms (Fig. 3.8a, b) or emplaced onto softer less-lithified sediments. Along south central Crete (Chapter 4), the cemented beach deposits were comprised of well to moderately sorted, rounded to sub-rounded carbonate, phyllite, quartzite and sandstone cobble- and pebble-grade conglomerates (Fig. 3.8c, d); oyster and pectin shells were frequently observed adhered to the wave-cut surfaces of these conglomerates. Cement between the pebbles and cobbles was comprised of gravel to coarse sands. The presence of layered marine deposits below the upper shoreface conglomerates was interpreted to represent conformable syn-wave-cut platform deposits. Elevation measurements on palaeoshorelines comprised of cemented beach deposits were taken as close to the palaeoshoreline location as possible; away from rocky shorelines the palaeoshorelines were often represented as a vertical cutting.

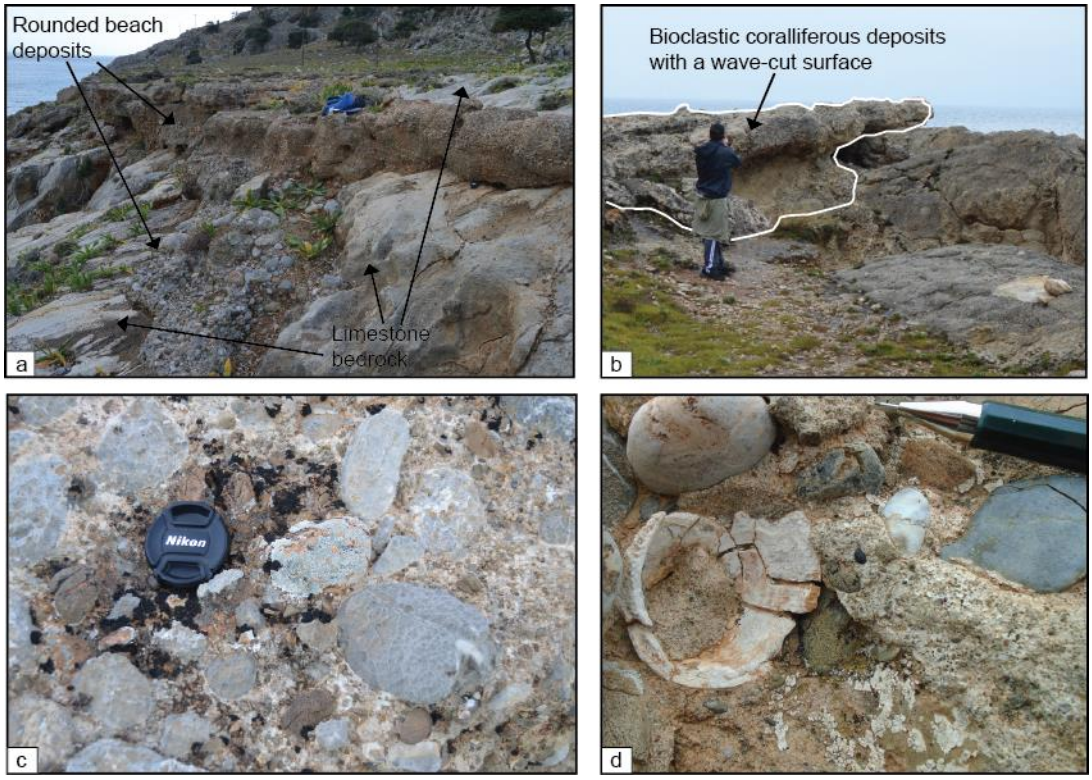

Figure 3.8: (a) Rounded beach deposits directly above a limestone wave-cut platform (Crete); (b) Bioclastic coralliferous deposits (e.g. Figs 3.5 and 3.6) that were emplaced atop algal bioherm deposits, wave-cut features were apparent on the surface of the bioclastic deposits (Cape Heraion); (c and d) Flat-topped beach conglomerate in Crete, with (d) showing part of a bivalve shell cemented to the surface.

The wave-cut platform itself is located a few meters to decimetres downdip of the palaeoshoreline; it exhibits a sub-horizontal seaward dip and may be comprised of planed-off bedrock or planed off bioclastic sandstone/conglomeritic surfaces (Fig. 3.8). In addition to using the presence of FBI on the wave-cut platform to confirm close proximity to palaeo-sea level, observations of small-scale erosional structures, named millholes/potholes (Fig. 3.7c), were also employed. These millholes are circular depressions made in the wave-cut platform caused by pebbles scouring the surface as a result of wave action in the shallow shoreface area (Laborel and Laborel-Deguen, 1994; Miller & Mason, 1994; Roberts et al., 2009; Bird, 2011). They have been observed on wave-cut platforms elsewhere in the Mediterranean (e.g. Laborel and Laborel-Deguen, 1994) and are typically located decimetres down-dip from the palaeoshoreline. In this thesis the presence of millholes was used as evidence of being in closely located to the palaeoshoreline (Laborel and Laborel-Deguen, 1994; Miller & Mason, 1994; Roberts et al., 2009). Millholes were of importance when choosing ^{36}Cl exposure dating sample sites because, like lithophagid borings, their presence is supportive of minimal erosion since their formation during the highstand. Section 2.1.1 highlighted that millholes form in the intertidal zone. The formation of the millhole can be

directly linked to the formation of the wave-cut platform that occurred prior to the millhole being removed from the erosive action of the waves - either as a result of sea-level fall during a highstand and/or uplift coeval to the highstand. As such, surface exposure dating associated with the millhole should provide an age that can be directly linked to the sea-level highstand.

In summary, the palaeoshoreline itself is commonly a break of slope marking a palaeo-rocky shoreline or a palaeo-sea cliff that exists a few decimeters to meters updip of either a wave-cut platform or outcrops of shallow marine sediment (Fig 3.9). Where a notch was present, the measured palaeoshoreline elevation was taken from the middle of the notch. If a notch was not present, the palaeoshoreline elevation was taken from either the base of a cave (as per Pirazzoli, 2005), the intersection between the sub-horizontal platform and the palaeo-cliff or, if present, the uppermost line of lithophagid borings on the palaeo-cliff (Laborel and Laborel-Deguen, 1994). The presence of FBI in all of the examined field locations was noted, along with their elevations and descriptions; particular importance was placed on these observations to contribute to the identification of proximity to palaeoshorelines where wave-cut features were less clear in the landscape.

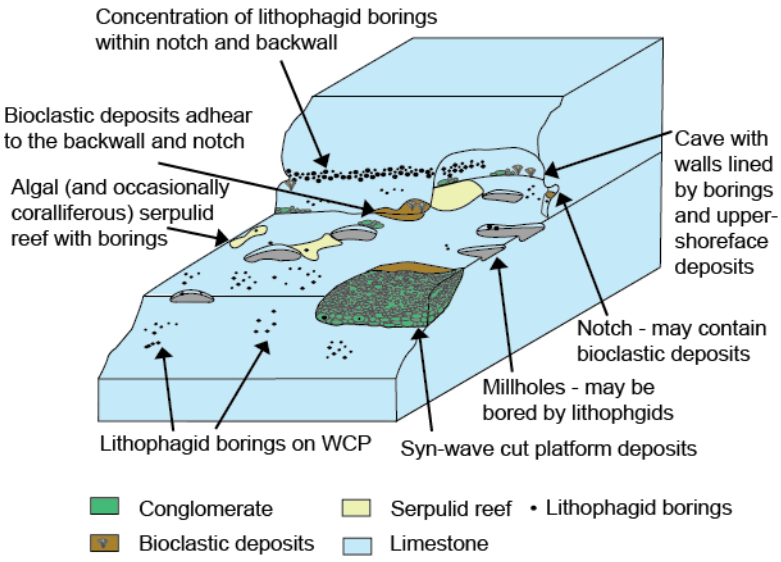

Figure 3.9: Schematic cartoon of types of features used to identify palaeoshorelines and wave-cut platforms (modified from Robertson et al., 2019)

3.1.3 Along-strike palaeoshoreline measurements

In order to examine the deformation of palaeoshorelines along the strike of a fault(s), the elevations of sequences of palaeoshorelines and of offset palaeoshorelines were mapped

along their length using serial topographic profiles (Section 3.1.1). Detailed field mapping was undertaken to document the palaeoshoreline features present, and obtain elevation measurements of palaeoshorelines. On Cape Heraion (Perachora), the field area was less than 1 km^2, thus very accurate field mapping was possible and was the preferred mechanism for the collection of elevations. In this location, the vertical offsets of wave-cut platforms were examined in order to determine whether they changed according to expected patterns of fault displacement or whether they were continuous and indicated Quaternary palaeoshorelines. Elevation measurements were taken at the same location above and below an offset (using two people, with two calibrated barometric altimeters) in order to derive the along-strike patterns of offset (Fig 3.10). Areas that were inaccessible, particularly at the highest elevations, were supplemented by elevation measurements from the DEM. Once all of the elevations were obtained, they were used to derive the offset values at multiple points on the displaced surfaces (Fig. 3.10b), which were then plotted onto a graph (Fig. 3.10c). Fault identification was made on the basis of offsets that were higher in the centre and decreased to zero, suggestive of normal faulting where the throw decreased to zero at the fault tips (Figs. 2.16, 2.17, 3.10); this was clear in the field because it was possible to walk continuously along a surface, around the tip, up a relay ramp and onto a higher wave-cut surface. The cumulative throw values along the study area were obtained from 58 serial topographic profiles that were taken perpendicular to the strike of the faults where individual offsets along each profile line were summed (Fig. 3.10a), more detail on this is provided in Chapter 6.

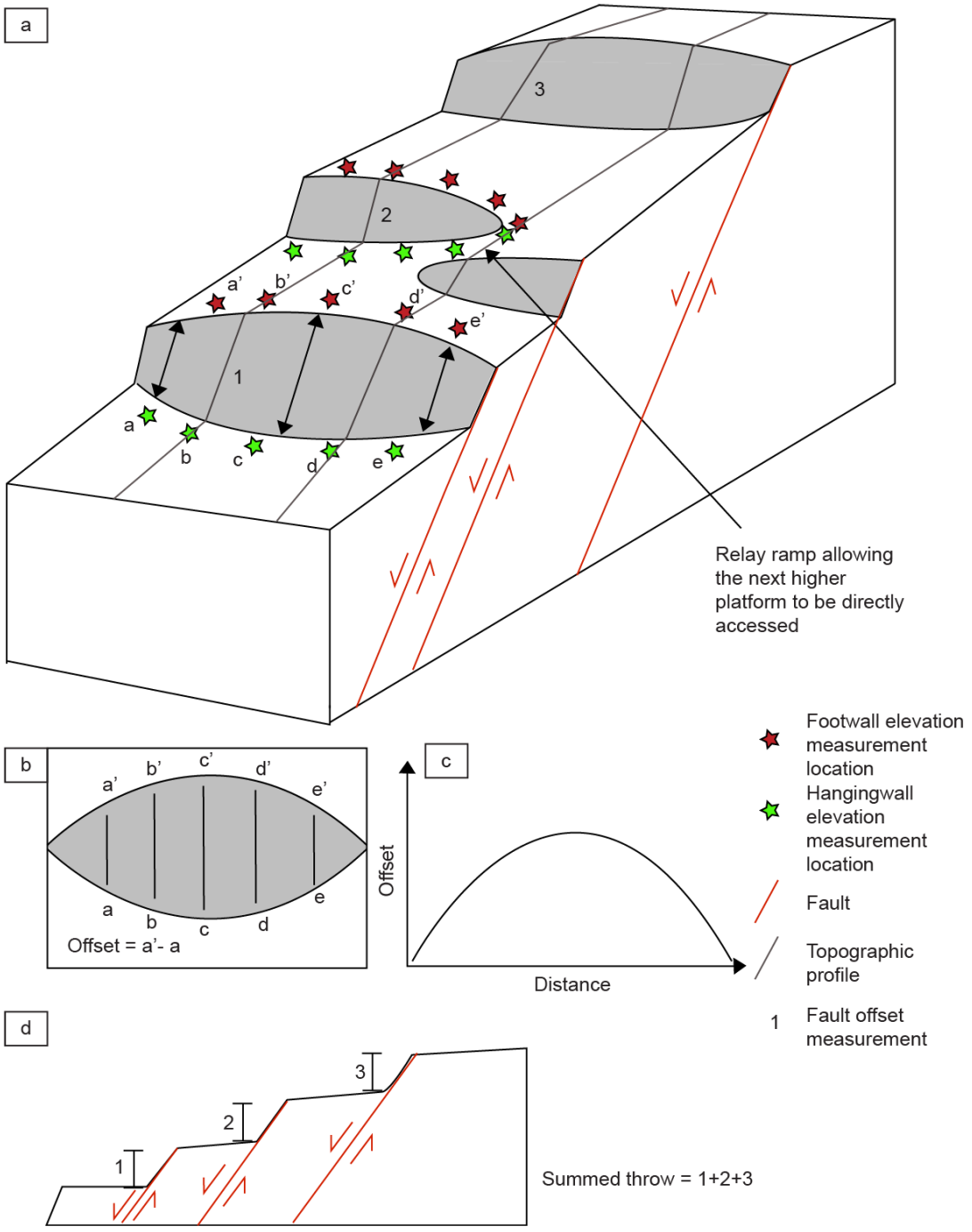

Figure 3.10: (a) Schematic diagram to show the locations of elevation measurements in order to calculate whether offsets change along strike and topographic profiles relative to the fault locations; (b) Calculation of offsets, along strike of a fault, these values are expected to change, as shown in (c); (d) Topographic profile across numerous faults showing how the summed throw for each profile is calculated.

In southern Crete, where sequences of palaeoshorelines were investigated, the aim was to field-measure entire sequences of palaeoshorelines from the lowest, close to sea level, to as high as possible along the length of the field area. In some locations, wave-cut platforms and marine terraces were used to house large greenhouse structures such that direct mapping was limited. DEM-based measurements along southern central Crete were also essential

owing to the large area being mapped and the inaccessibility of higher palaeoshorelines. DEM elevations were taken from the same locations as field-based elevations in order to cross check the accuracy of DEM data. This was carried out using plots of DEM versus field elevation measurements and R^2 goodness-of-fit analysis, which is an indication of the variance between two variables (Fig. 3.11).

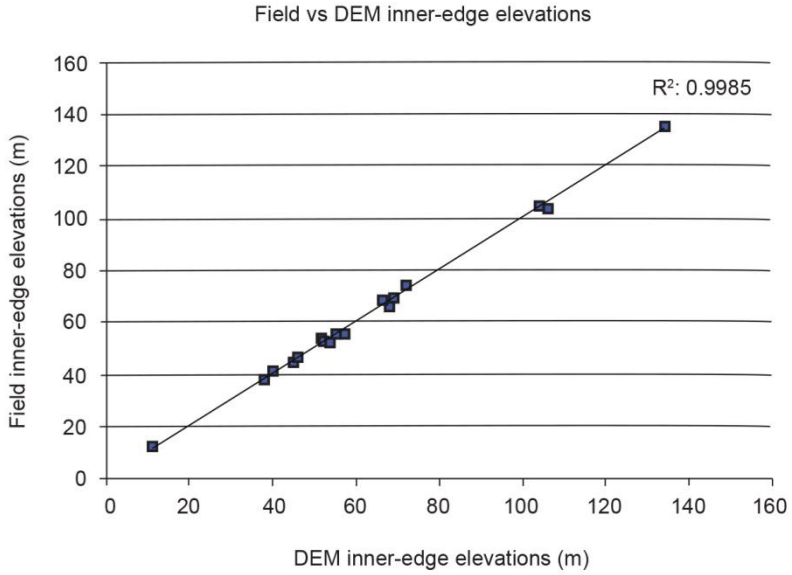

Figure 3.11: Plot and R^2 of DEM versus field palaeoshoreline elevations (Crete) (from Robertson et al., 2019).

The elevation measurements made with a barometric altimeter were accurate to ~ 1 m. In this thesis, particularly along southern Crete, the aim is to derive uplift rates using the palaeoshoreline elevation measurements. Such calculations are reliant on existing data of historic sea-level elevations, relative to today, that are obtained from sea-level curves. These sea-level curves have minimum uncertainties of ±~12 m, so very precise measurements of palaeoshoreline elevations are not necessary. The uncertainties associated with sea-level highstand data (age and relative sea-level elevation), field and DEM elevations were propagated to derive uplift uncertainties (Section 3.2).

3.2 SYNCHRONOUS CORRELATION APPROACH

In order to derive uplift rates from a sequence of palaeoshorelines, it is necessary to correlate eustatic highstands to both dated and undated palaeoshorelines. This thesis uses the synchronous correlation approach, developed by Houghton et al. (2003) (Section 2.1.5), whereby the uplift rate obtained from a dated palaeoshoreline is applied to all

palaeoshorelines from the same topographic profile (Section 3.1.1). The 'Terrace Calculator', an excel spreadsheet, is used to facilitate uplift determinations (Fig. 3.12).

The calculator uses an input uplift rate (*u*), which is iterated such that the elevation of the dated palaeoshoreline is a match to the predicted elevation for the same age of highstand. In turn this results in calculation of the predicted elevations (*Epred*) of all highstands (along the topographic profile in question) using the age of the highstands (*T*) and the sea level elevations (*SL*) of the highstands relative to today's sea level:

$$E_{Pred} = (T \times u) + SL$$

For this thesis the author extended the Terrace Calculator beyond 410 ka (compare with the version provided by Houghton et al., 2003, Roberts et al., 2009, 2013) to include highstands to 980 ka (Siddall et al., 2003, to 410 ka and Rohling et al., 2014, beyond 410 ka) so that the uplift further back in time can be explored. The output of the Terrace Calculator, given iteration of the uplift rate, is a set of predicted elevations for all sea level highstands along the topographic profile in question, which are then matched if they are ±10 m of the measured elevations, allowing palaeoshorelines to be assigned to highstand ages (Fig. 3.12). The fit between the two data sets (predicted vs. measured elevations) was evaluated using R^2 and the Root Mean Square Error (RMSE).

An attempt is made to maximise the number of palaeoshorelines identified, taking particular care to make sure that palaeoshorelines that tend to have prominent geomorphology, such as those from 125, 240, and 340 ka, are identified (Section 2.1.2). However, not all highstands will result in preserved palaeoshorelines, either because they have been subaerially eroded or eroded as a consequence of overprinting of older terraces by younger sea level highstands (Roberts et al., 2013; Pedoja et al., 2014; Jara-Muñoz & Melnick, 2015; Jara-Muñoz et al., 2017; Pedoja et al., 2018) (Section 2.1.3). This is visible on Fig. 3.12c where the Terrace Calculator shows which palaeoshorelines are likely to have been destroyed for a topographic profile with an uplift value of 0.37 ± 0.09 mm/year; palaeoshorelines at 175, 217, and 285 ka are particularly prone to being overprinted.

To assign highstand ages to undated palaeoshorelines on topographic profiles that do not have absolute age controls, two methods were employed, the first is where all palaeoshorelines with absolute age controls were identified in the DEM and the dated palaeoshorelines were laterally traced across strike. Where topographic profiles intersected

a dated palaeoshoreline, the age control was used to identify the uplift rate, which was then applied to the entire topographic profile and measured palaeoshoreline elevations were then matched to the elevations predicted by the Terrace Calculator, as detailed above. However, the variable lithology observed along south central Crete meant that occasionally palaeoshoreline preservation was poor and tracing a dated palaeoshoreline along strike was not possible. Where this was the case, an alternative method was applied whereby topographic profiles were tested for all uplift scenarios based on the measured palaeoshoreline elevations. This involved in turn, allocating the lowest measured palaeoshoreline to each highstand in the calculator, applying the resultant uplift rate to the entire topographic profile and counting the matches between the predicted palaeoshoreline elevations and the measured elevations. The number of matches between measured and predicted palaeoshoreline elevations, and the R^2 and RMSE values of the predicted and measured values were used to identify the best fit.

For all topographic profiles, exact uplift rates were obtained by iterating the uplift values from 0.1 to 1.0 mm/year at intervals of 0.05 mm/year and plotting the RMSE values obtained from comparing the predicted versus measured elevation values. The uplift value with the lowest RMSE was applied to the topographic profile (see Fig. 3.12d for an example).

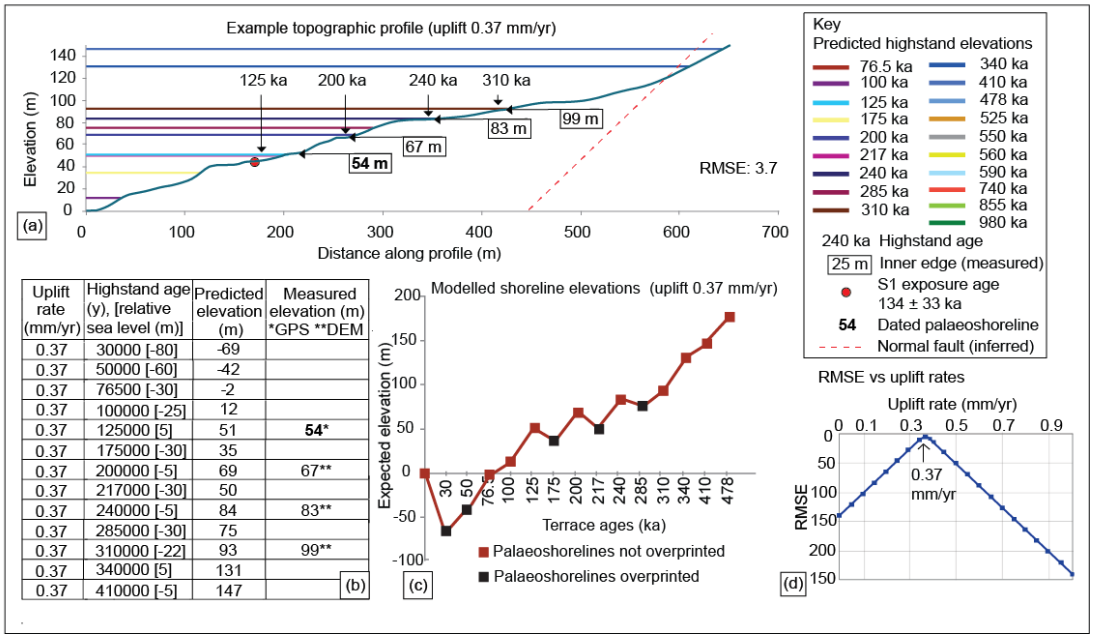

Uplift rate (mm/yr)	Highstand age (y), [relative sea level (m)]	Predicted elevation (m)	Measured elevation (m) *GPS **DEM
0.37	30000 [-80]	-69	
0.37	50000 [-60]	-42	
0.37	76500 [-30]	-2	
0.37	100000 [-25]	12	
0.37	125000 [5]	51	**54***
0.37	175000 [-30]	35	
0.37	200000 [-5]	69	67**
0.37	217000 [-30]	50	
0.37	240000 [-5]	84	83**
0.37	285000 [-30]	75	
0.37	310000 [-22]	93	99**
0.37	340000 [5]	131	
0.37	410000 [-5]	147	

Figure 3.12: An overview of the method used to allocate highstand ages to palaeoshoreline elevations for each topographic profile. (a) Topographic profile example with an uplift rate of 0.37 mm/year. Horizontal coloured lines show the predicted elevations of highstands obtained using the Terrace Calculator, which shows some older highstands overprinted by younger highstands; this is clear in (c). Tie points between observed (field or digital elevation model) palaeoshorelines and those predicted are marked. Initial uplift value is derived from the terrace with an age control. (b) Terrace calculator data for example topographic profile. (c) Predicted highstand elevations for example topographic profile; graph shows the highstands that would not be preserved (black squares), given the 0.37 mm/year uplift rate. (d) Root mean square error (RMSE) values for all uplift scenarios from 0 to 1 mm/year at intervals of 0.05 mm/year when the 125-ka highstand is tied to the 54-m palaeoshoreline. (From Robertson et al., 2019).

Sea level curve uncertainties vary depending on the sea level curve employed. For the Siddall et al. (2003) curve, the reported uncertainty on the sea level is ±12 m compared to the reported uncertainty of ±6 m for the Rohling et al. (2014) curve. The uncertainty values on the age of the sea level highstands are reported to be ±4 kyr from Rohling et al. (2014) but are not defined by Siddall et al. (2003). This value is needed in order to propagate uplift rate errors, so the value obtained by Rohling et al. (2014) was used as this later work builds upon research initially based upon the Siddall et al. (2003) data. The equation for standard error (SE) is used to propagate uplift value errors:

$$SE\ (u)^2 = u^2 \left(\left(\frac{\sigma_{H^2}}{(H_T - H_{SL})^2} \right) + \left(\frac{\sigma_{T^2}}{T^2} \right) \right)$$

where *SE* is the standard error, *u* is the uplift rate, *σH* is the combined uncertainty for measured palaeoshoreline elevation and sea level relative to today, *HT* is the measured palaeoshoreline elevation, *HSL* is the sea level for the highstand in question, and *T* is the

highstand age related to the terrace formation. Typical propagated uncertainties associated with uplift rates are in the region of 0.02-0.11 mm/yr.

3.3 ^{36}Cl COSMOGENIC EXPOSURE DATING APPROACH

3.3.1 Sampling protocol

The production rate of ^{36}Cl has been shown to vary with depth (Section 2.1.4.2), meaning that high levels of erosion have the capacity to significantly affect the exposure ages obtained. Other factors also cause variation in the production rate and are important to consider when identifying sampling sites and collecting data used in exposure age determinations (Marrero et al., 2016a, 2016b). These factors are: (i) altitude, whereby cosmic-rays lose energy when travelling through greater thicknesses of atmosphere, such that samples removed closer to sea-level will have experienced a lower cosmic-ray flux compared to samples removed from higher altitudes; (ii) topographic shielding, which acts to decrease the production rate because the sample location may not be exposed to the total cosmic-ray flux; and, (iii) latitude, because cosmic-ray flux is lower at equatorial latitudes and increases at higher latitudes due to the effect of the Earth's magnetic field lines. Variations of the magnetic field over short time periods (~7-15 ka) have also been shown to impact the production rate, but over longer time periods in the region of 100 ka, the effect is minimal.

In light of this knowledge, the application of ^{36}Cl cosmogenic exposure dating to carbonate wave-cut platforms is reliant on the accurate collection of field-measured data relating to sample elevation, longitude and latitude, topographic shielding and erosion rate. The selection of sample locations should be made on the basis of sites that have experienced minimal erosion that can be quantified, and have not been too shielded by the surrounding topography or experienced pre-exposure to cosmic rays. Furthermore, samples should be located out of the wave-splash zone and away from locations that may have been covered by sediment. These factors are discussed below in the context of the sampling approach for ^{36}Cl applied herein.

3.3.1.1 Pre-exposure shielding and topographic shielding

Dunai et al. (2010) highlights that topographic shielding and pre-exposure shielding are important to consider when sampling for ^{36}Cl exposure dating on wave-cut surfaces.

Specifically, topographic shielding is a measure of the amount of shielding at a sample site from the surrounding topography, this is important because the presence of topography has the capacity to impact the cosmic ray influx. The cosmic ray flux is shown to decrease as a result of steeper local topography surrounding the sample site (Darvil, 2013). Topographic shielding can be calculated from field measurements at the time of sampling and is necessary in order to obtain ^{36}Cl age calculations (Gosse and Phillips, 2001; Marrero et al., 2016a, 2016b). In this thesis, shielding measurements for all sample sites were obtained in the field by measuring the inclination (in degrees) of the exposure of the sample site to a full hemisphere of open sky (Fig. 3.13) (Balco et al., 2008). This measurement was made using a clinometer every 30˚ for a full 360˚. The shielding value was calculated by inputting all of the measured angles of inclination into a shielding calculator (Tibor Dunai, Pers. Comms. 2016).

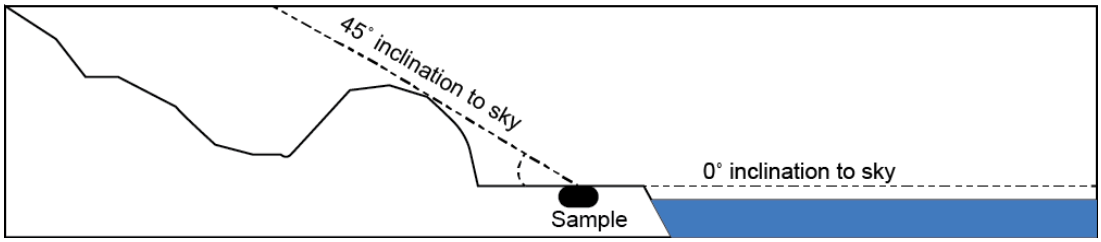

Figure 3.13: Schematic 2D representation of taking shielding measurements from a ^{36}Cl exposure sample site. Measurements are taken every 30˚ for a full 360˚ from the location of the sample site.

In order to obtain accurate exposure ages on wave-cut surfaces, the surface in question must have been sufficiently shielded from cosmic rays prior to excavation to ensure that the ages obtained are reflective of the exposure age of the platform and not a factor of inheritance associated with pre exposure (Dunai, 2010). This is done via consideration of the location of sampling on a wave-cut platform with regard to the overburden, whereby samples closer to the palaeoshoreline would have been covered by a thicker overburden of rock (Fig. 3.14) and are thus more protected from pre-exposure cosmic rays. Furthermore, the presence of an inherited nuclide component would be apparent in the ages obtained as it would yield an anomalously old age for a sample, such anomalous ages would be clear when considered within the context of the ages of other nearby ^{36}Cl samples and age controls obtained from other dating methods (Darvil, 2013).

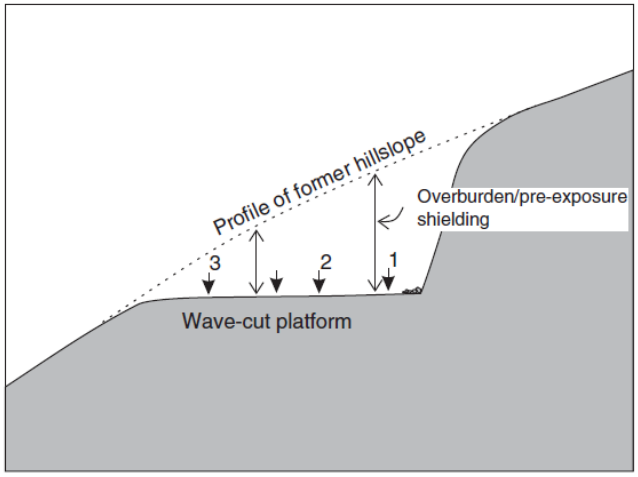

Figure 3.14: Pre-exposure shielding of a wave-cut platform depends on the position of the sample site on the platform. Samples near the cliff are expected to have more pre-erosional shielding compared to those further away from the cliff, represented by numbers 1, 2 and 3 (from Dunai, 2010).

3.3.1.2 Post-formation sediment cover

Evaluation of the surrounding areas of sample locations was undertaken to attempt to establish whether or not the sample could have been covered by sediments and latterly exposed. If this were the case it would lead to a complex exposure-covering re-exposure history and the sample in question may produce an erroneously young age, more representative of when the covering sediment was removed from the sample site. An example of this is discussed in Chapter 4, where a sample removed from a wave-cut platform in south central Crete yielded an age of ~40 ka. A sea-level highstand is not visible on the sea-level curve at this time, and the age was not in agreement with a second ^{36}Cl exposure age nor from an OSL-derived age obtained by Gallen et al. (2014) from the same wave-cut platform. Post-sampling investigations of this location revealed the presence of syn-wave-cut platform sediments very close by, so it is expected that this location was not exposed in accordance with sea-level fall after a highstand but instead by later subaerial erosion of undefined timing and extent.

3.3.1.3 Consideration of the wave-splash zone

The impact of sampling for ^{36}Cl exposure dating close to the present wave-splash zone (taken to be ~ 8-10 m) was considered in this thesis because the wave-cut platforms sampled were located along coastal regions and near to the sea; it was initially unknown if thousands of years of sample exposure to Cl from sea-splash would impact the possible ^{36}Cl exposure age. Ten wave-cut platform samples were removed from within the splash zone (<10 m) (Locality

c, Fig. 6.4) and 11 samples removed from higher elevations outside of the splash zone (>42 m) on Cape Heraion. Of these samples, five (two from a 7 m platform and three from ~60 m platform) were analysed for measureable sea salt using a Jeol8100 Superprobe (WDS) with an Oxford Instrument INCA microanalytical system (EDS) at Birkbeck College to evaluate the Na and Cl peaks of all samples. The results showed that samples collected from within the sea-spray zone (n = 2) had measureable Na and Cl peaks but those from above 10 m (n = 3) did not. The sea-spray samples were then washed in an ultrasonic bath for 3 x 6 minute intervals and left to air dry before being re-analysed using the microprobe; this resulted in removal of the observed Na and Cl peaks and informed the decision to wash all ^{36}Cl exposure samples prior to preparation for AMS (see below). Further analyses of the two sea-spray samples (Ch6 and Ch7, sampled from a wave-cut platform at 7 m, Locality c, Fig. 6.4) were undertaken to investigate Cl quantities using X-ray fluorescence (XRF) prior to AMS analysis. XRF was undertaken using 32 mm diameter pressed powder pellets (produced from mixing 1.5 g fine ground sample powder with 6.0 g of Paraffin Wax pressed at 10 tons per sq. inch) on a PANalytical Axios Advanced XRF spectrometer at the University of Leicester; Cl spike base material (blanks), were 90 ppm. The results of this analysis showed elevated Cl values of 109.8 ± 3.4 ppm and 191.8 ± 3.5 ppm for samples Ch6 and Ch7, respectively. These elevated Cl values were also confirmed from the AMS (see below) possibly suggesting that initial values of ^{35}Cl were high. This is discussed further in Section 3.3.3.

3.3.1.4 Identifying low-erosion sample sites

Erosion of surfaces since initial exposure will lower the measured cosmogenic nuclide concentrations in samples because it brings material to the surface that has previously been partially shielded by cosmic rays (Dunai, 2010). Constraining the erosion rates is therefore of particular importance in order to be able to calculate accurate ages. Chapter 2 (Section 2.1.4.2) highlighted that there are a number of natural pathways capable of producing ^{36}Cl in carbonates and that both the dominant pathway and production rate varies with depth. Spallation of ^{40}Ca and ^{39}K atoms is the dominant production mechanism in the top 2 m of rock beneath exposed carbonate surfaces (Licciardi et al., 2008), while beyond this depth, production of ^{36}Cl is predominantly by muons at much lower production rates when compared to that of spallation (Fig 2.13) (Schlagenhauf et al., 2010). Sample sites were, therefore, selected based upon observations that indicate minimal erosion of the wave-cut surface and, allow the rates of erosion to be approximately constrained. This approach

allowed: (i) the estimation of erosion rates, which were essential because they mean that the calculation of exposure ages was adjusted to take into account the erosion through time since initial exposure and, (ii) confidence that the dominant production mechanism was expected to be from spallation.

Observations of minimal erosion were made through the presence of preserved lithophagid borings and millholes, because they are strong indicators that erosional values have been low since formation and allow erosion rates to be approximately constrained. Lithophagid borings are between 3 and 9 cm deep when formed (Peharda et al., 2015), though research by Devescovi and Iveša (2008) suggests an average value closer to 6 cm is common. This suggests that the preservation of lithophagid borings with depths of 2-3 centimetres indicates total erosion of between 3-6 cm since their formation. This value is minimal in the context of the depth dependency of the production pathways. Similar values of a few cm of erosion on preserved millholes have also been observed. This is evidenced by examining the morphology of the millholes. These features are formed by the agitation of pebbles during wave action, they erode a circular depression into the wave-cut platform that results in a millhole with a 2D profile displaying a wider base compared to narrower surface hole with a slight overhang from the surface to the base (Fig. 3.15a). The preservation of this morphology is taken to be indicative that erosion has been minimal (<2-3 cm when the overhang at the top of the millhole is preserved) (Fig. 3.15b). Thus, evidence of preserved lithophagid borings and millholes on a wave-cut platform suggests that erosion values of a few cm or less since palaeoshoreline formation can confidently be ascertained.

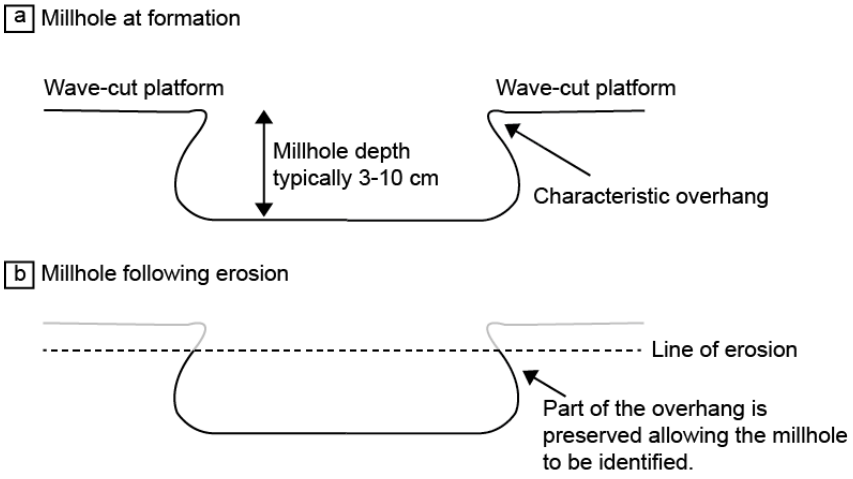

Figure 3.15: Schematic cross sections of a millhole at (a) the time of formation and (b) after erosion where the millhole is still recognisable from its profile.

Sampling followed a process whereby the immediate geology and wave-cut features were mapped and photographed, and the UTM (Universal Transverse Mercator) and elevation of the sample and palaeoshoreline were recorded. Samples were removed from a variety of lithologies using a mallet and chisel, with photographs taken prior to and following sample removal. Shielding values were noted every 30˚ of azimuth as per the method in Dunai (2010) (Section 3.3.1.1). Prior to ^{36}Cl sample preparation, non-bedrock samples were analysed as thin sections to accurately determine their lithologies. Taken together, the approach herein means that carbonate wave-cut platforms, displaying preserved lithophagid borings and/or millholes are suitable targets for ^{36}Cl exposure sampling.

3.3.2 Sample preparation

All samples were washed in distilled water in an ultrasonic bath. Samples were initially crushed to a 'gravel-sized' fraction using a jaw crusher and subsequently milled to a 125-250 µm fraction using a disc mill at both the Scottish Universities Environmental Research Centre (SUERC) and University College London (UCL) by the author. Both machines were cleaned between each sample processing using a hoover and thoroughly wiped down with acetone. The ^{36}Cl sample preparation method and production of targets from crushed fractions prior to accelerator mass spectrometry was completed as per the method outlined by Schimmelpfennig et al. (2009) by Dr Delia Gheorgiou at SUERC. The accelerator mass spectrometry was carried out at SUERC.

3.3.3 Age determination

Following accelerator mass spectrometry and analysis using inductively coupled plasma optical emission spectrometry (ICP-OES) a set of data was provided for each sample. This dataset showed the concentration of ^{36}Cl atoms per gram of sample, the bulk rock weight of key oxides (Ca, Na, K and P) and chemical elements and the analytical uncertainties associated with all reported values. Screening of all samples prior to age determination was carried out, because high values of bulk rock Cl (> 80 ppm) have been shown to result in ^{36}Cl exposure ages that should be interpreted with extreme caution (Marrero et al., 2016b). Therefore, all samples are screened for high Cl prior to age determination. All ^{36}Cl exposure results presented in the results chapters within this thesis (Chapters 4 and 6) have bulk rock Cl values <80 ppm. The results of two samples from Cape Heraion (Perachora) showed very high Cl values and were excluded from further analysis. These samples (CH6 and CH7) were

collected from a wave-cut platform at 7 m, within the sea-spray zone identified (Section 3.3.1) (Locality C, Fig. 6.4) and were comprised of bioclastic debris and algal deposits in a micritic cement, they were closely located (1-3 m) to the in-life positions of colonies of the coral *Cladocora caespitosa*. Samples CH6 and CH7 have bulk rock Cl values of 103 and 198 ppm, respectively (Table 3.1) which far exceeds the 80 ppm value recommended by Marrero et al. (2016b). The reason for their high Cl values is unknown, however, it could be speculated that they were related to the presence of sea-salt from sea spray that survived the washing process or from high values of water content in the samples (Marrero et al., 2016b). Alternatively, if the bioclastic debris in these samples were comprised of unidentifiable minute coral remains, then it has been suggested that high Cl content could be related to relatively high concentrations of uranium, which is naturally abundant in corals. Decay of uranium results in alpha particles, which can react with the light nuclei in the rock to produce low energy neutrons, these neutrons are then available to react with the target elements in the rock to produce ^{36}Cl (Marrero et al., 2016a). However, if the cause of increased Cl is as a result of abundant uranium in samples CH6 and CH7 then one may question whether the decay of uranium is sufficient to raise the Cl concentration by values of 20-110 ppm. What is clear at the moment is that the causes of the elevated Cl in low elevation samples are unknown and would benefit from further research.

Sample reference	Sample elevation (m)	Concentration of ^{36}Cl atoms/g	Bulk rock Cl (ppm)
CH6	7	708221	103.10
CH7	7	1255949	198.48

Table 3.1: ^{36}Cl exposure results of samples CH6 and CH7 from Perachora at 7 m. These results were disregarded as a result of the high values of Cl in excess of 80 ppm.

The exposure ages of samples were determined using the CRONUScalc programme (Marrero et al., 2016a), which is an online tool that calculates concentrations using the known production pathways and other variables to determine the exposure age. CRONUScalc (http://cronus.cosmogenicnuclides.rocks/2.0/) (Marrero et al., 2016a) requires an input file that contains data about the sample such as longitude, latitude, elevation, pressure, sample thickness and density, the shielding factor, and elemental data alongside ^{36}Cl concentration measured during AMS and ICP-OES analysis. Where input data is associated with a measured value obtained during sampling, the uncertainties linked to the measurement are also included. The output from CRONUScalc is an exposure age and internal and external uncertainties associated with that age. Internal uncertainty values are linked only to

analytical uncertainties from AMS and result in a minimum uncertainty age value. External uncertainties are calculated by propagating the production-rate and measured uncertainties and combining them with the analytical uncertainty (Marrero et al., 2016a). When examining the potential uncertainties associated with ^{36}Cl age determinations, Marrero et al. (2016b) observed uncertainty values of up to 20% of the age. Marrero et al. (2016b) discuss such large uncertainties and highlight a number of reasons. (1) Underestimation of the actual analytical uncertainties – where laboratory-reported uncertainties may significantly underestimate the spread of cosmogenic-nuclide analytical uncertainties. (2) Spatial-scaling errors as a result of location and elevation, because individual scaling models may not accurately predict the global pattern of nuclide production. (3) Factors that are specific to individual sites such as erosion rates and covering from soil/snow cover.

While internal uncertainties alone may underestimate realistic uncertainties, especially when comparing the age determinations to other dating techniques or when samples are compared between different temporal timescales or geographical locations, the total uncertainties may represent an overestimation when the uncertainties are not independent (Marrero et al., 2016a). In other words, where ^{36}Cl exposure ages are derived from the same geographical location (with expected similar production rate values), the calculated external uncertainties may exceed true uncertainties. Regardless of this, the resultant ages are suggested to be able to be compared to one another (Marrero et al., 2016b). Considering these complexities, full uncertainties are advised to be used (Marrero et al., 2016a) and are quoted throughout this thesis.

While the broader uncertainties are listed above, it is worth exploring the primary unknowns associated with ^{36}Cl exposure dating in more detail, namely the production rates and erosion rates (Marrero et al., 2016). Specifically, uncertainties associated with the relative contribution of each of the production mechanisms (spallation, thermal neutron capture and muons) occur because individual production rates are difficult to measure (Schlagenhauf et al., 2010). Moreover, the spallation production rate from ^{40}Ca has been suggested to vary between 48.8 ± 3.5 and 66.8 ± 4.4 atoms of ^{36}Cl per gram of Ca per year (Schimmelpfennig et al., 2009; Marrero et al., 2016b). As this thesis uses CRONUScalc to derive the exposure ages of the samples, the calibration approach applied in the CRONUScalc code is of interest. Large-scale calibration of ^{36}Cl production rates was completed within the CRONUS-Earth project using multiple high-quality calibration sites throughout the world in Scotland, Peru and Utah (Marrero et al., 2015b). The study of Marrero et al. (2015b) includes a large number

of sites representing a range of latitudes, longitudes and elevations and resulted in a single coherent set of production parameters for ^{36}Cl that are incorporated into the CRONUScalc programme.

Erosion rates represent a significant uncertainty in age determinations of ^{36}Cl if they cannot be constrained. The approach outlined in this thesis details that high importance is placed on sampling from locations where palaeoshoreline indicators are present, specifically millholes and lithophagid borings. The importance of these features can be emphasised by discussing attempts to undertake ^{36}Cl exposure dating on horizontal to sub-horizontal bedrock surfaces associated with high palaeoshorelines (336-406 m) located in the footwall of the SCCF in Crete. While palaeoshoreline evidence was still clear at the high elevations (Fig. 3.16) (notches, syn-wave cut platform upper shoreface and algal deposits and lithophagid borings on palaeo-cliffs), the assumed wave-cut platform surfaces did not display low erosion features such as millholes and lithophagid borings.

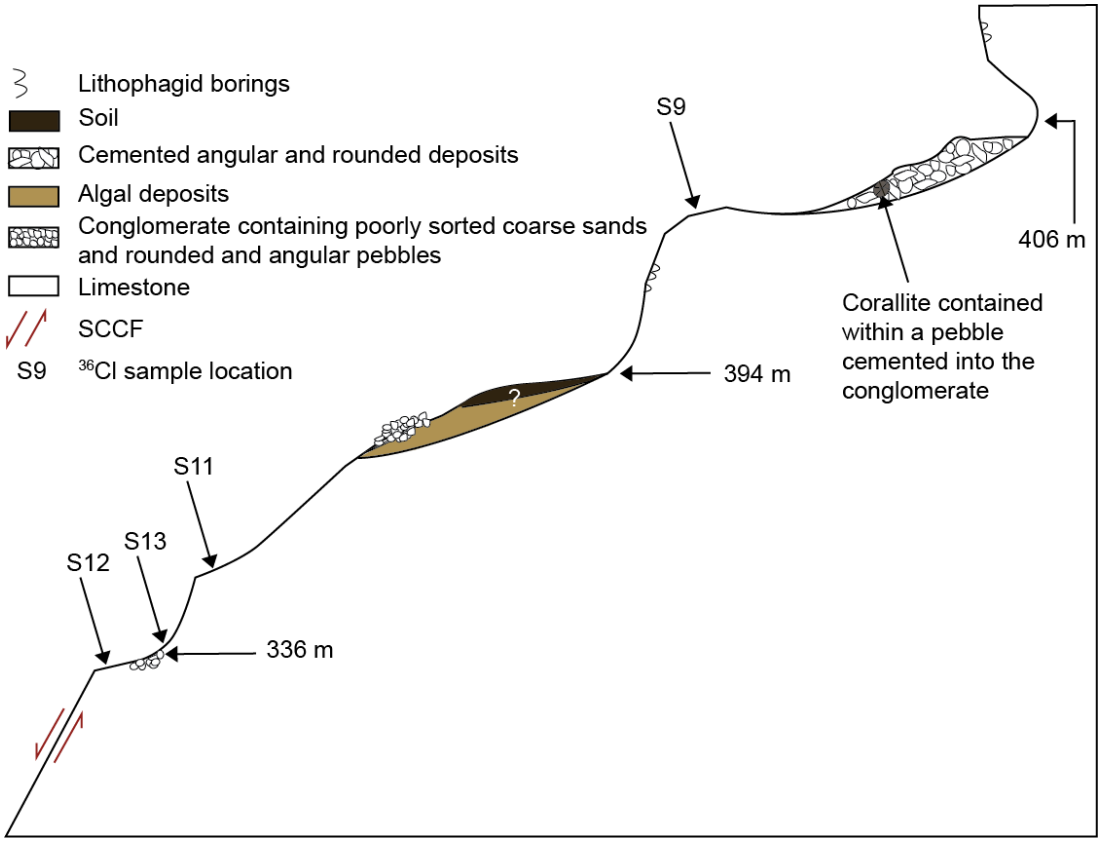

Figure 3.16: Schematic diagram of the palaeoshorelines in the footwall of the South Central Crete Fault and the features observed along profile 14 (Fig. 4.4a). The locations of samples for ^{36}Cl exposure dating are shown, the results of this dating are detailed in Table 3.2.

The results of ^{36}Cl exposure dating from the assumed wave-cut surfaces resulted in ages in the region of 33.8 – 65 ky (Table 3.2), using erosion rates (0.1 mm/ky) that were the same as those applied to limestone surfaces elsewhere on Crete (Section 4.4.2). However, Tucker et al. (2011) showed a connection between climatic cooling during periods of glaciation and increased rates in hillslope erosion at higher elevations, particularly where rocky landscapes occur that are not protected by soil, such as those in the footwall of the SCCF. This implies that erosion rates in the footwall are expected to be higher than those in the hangingwall because: (i) they are at higher elevations and, (ii) the fact that they are expected to be older and would have experienced more periods of glaciation. Based upon this, higher rates of erosion (4.0, 6.0 and 8.0 mm/ky) were applied to the footwall samples when calculating their exposure ages in CRONUScalc (Section 3.3.3). The results of this test (Fig. 3.17) show that the maximum age reached is 118 kyrs. Chapter 4 will show that these ages are uncharacteristically young in comparison to those obtained in the hangingwall. It is not plausible that the palaeoshorelines in the footwall of a normal fault can be younger than those in the hangingwall. It is, therefore, concluded that the absence of low-erosion features alongside erroneously young ^{36}Cl exposure ages suggests that the sample sites have experienced significant erosion; in light of this evidence their ages were rejected. The value of erosion input into CRONUScalc throughout this thesis is discussed within the context of the lithology and observed wave-cut platform features for each sample in Chapters 4 and 6.

Sample reference	Latitude (°)	Longitude (°)	P'shoreline elevation (sample elevation) (m)	Cl (p.p.m)	±	^{36}Cl (g of rock)	±	CaO (wt%)	±	Erosion rate (mm/kyr)	Age (kyr)	Internal uncertainty (kyr)	Total uncertainty (kyr)
S9	35.00268	25.45582	406 (397)	18.41	0.35	1430271	41051	50.06	1.32	0.1	65	1.96	15
S11	35.00592	25.45144	394 (349)	15.97	0.29	1119629	32694	47.50	1.25	0.1	54	1.76	13
S12	35.00515	25.45003	336 (328)	14.41	0.26	811964	23111	50.29	1.22	0.1	39.5	1.04	8.2
S13	35.00515	25.45003	336 (336)	5.80	0.10	674158	16674	50.15	1.26	0.1	33.8	0.79	7.2

Table 3.2: ^{36}Cl exposure dating results for footwall samples in Fig. 3.16, the erosion rate of 0.1 mm/ky applied here was the same as that shown to be applicable to lower bedrock samples in the study area (Section 4.4.2). Ages calculated using CRONUScalc input data detailed in Appendix 1.

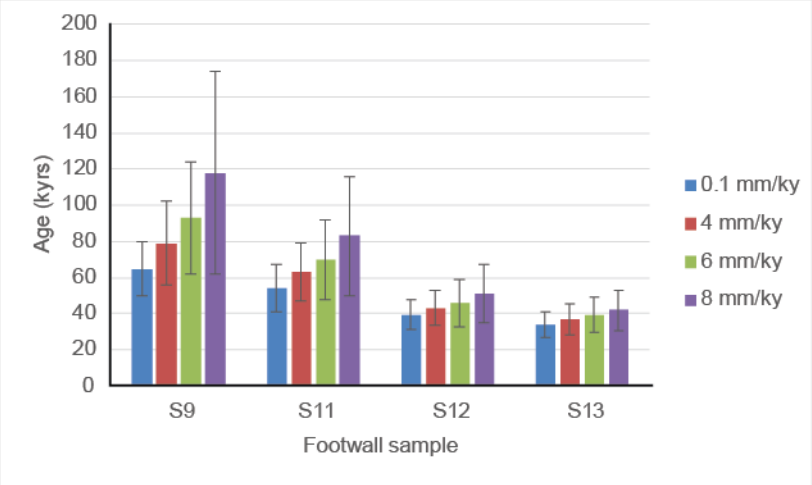

Figure 3.17: Plots to show the ^{36}Cl exposure ages for SCCF footwall samples given erosion rates of 0.1, 4, 6 and 8 mm/ky. Error bars represent the total uncertainties from CRONUScalc. A rate of 10 mm/yr of erosion was also tested but resulted in errors that exceeded the age obtained.

3.3.4 Examining the reliability of ^{36}Cl exposure age controls on wave-cut platforms

One of the aims in this thesis (Section 1.4) is to establish the reliability of ages obtained from ^{36}Cl exposure dating on Late-Quaternary wave-cut platforms. Given the discussion above with regard to the potential uncertainties on the ages, it is important to show how the age determinations from ^{36}Cl exposure dating will be evaluated in terms of their reliability. These are outlined below.

1. Does the ^{36}Cl age determination agree with existing age controls obtained from the vicinity of the ^{36}Cl exposure age (i.e. the same wave-cut platform within a few tens to a few hundreds of meters from one another), or from existing age controls obtained from the same palaeoshoreline that can be traced along strike. The age controls should be from other independent methods, specifically in this thesis they are from OSL on syn-wave-cut platform sediments and ^{234}U/^{230}Th dating on corals associated with the palaeoshoreline formation.
2. The ^{36}Cl exposure ages (within uncertainties) should agree with the timing of sea-level highstands obtained from sea-level curves.
3. ^{36}Cl exposure samples removed from a sequential set of palaeoshorelines should result in:
    a. age determinations that show a relative increase in age and the concentration of ^{36}Cl atoms/g with increasing palaeoshoreline elevation, and,

b. in palaeoshoreline ages that are in agreement with modelled ages obtained from the Terrace Calculator (Section 3.2).

4. ^{36}Cl exposure ages removed from wave-cut platforms that have been offset from faulting should result in ages in the hangingwall and footwall of the faults that can be associated with the same palaeoshoreline (within uncertainties).

3.4 ^{234}U/^{230}TH CORAL AGE DATING APPROACH

3.4.1 Sampling protocol

Cladocora caespitosa corals sampled in this thesis have been shown to predominantly grow in depths of up to -10 m but have been reported down to -40 m (Peirano et al., 2004). Therefore, where coral ages were used to determine the formation age of a wave-cut platform in this thesis, they were only sampled if they could be correlated along-strike and up-dip into palaeoshorelines. Furthermore, the corals were sampled on the basis that they could be mapped into the wave-cut platforms that were being dated using ^{36}Cl exposure dating. Correlation of coral sampling to wave-cut platforms and palaeoshorelines was achieved though detailed mapping; in detail, the corals dated in Chapter 6 (S6U/TH and S7U/TH) were selected because they were located on a wave-cut platform that could directly be mapped into a palaeoshoreline marked by a cave, notch and abundant lithophagid borings. The sampled corals were located ~20 m to the south-west of the palaeoshoreline along a sub-horizontal platform composed of bioclastic sediments, thus the evidence strongly supported coral growth coeval with the highstand that formed the cave, borings and wave-cut platform.

Some corals in the literature have been sampled from sedimentary sections, where deposits and coral remains are stacked atop one another and result in younger deposits located toward the top of the sections (e.g. Roberts et al., 2009; Houghton, 2010). The corals sampled for Chapter 7 bear some similarities to a sedimentary section as they were sampled from a human-made sub-surface cistern below an existing dated wave-cut platform surface; these corals were not in life position suggesting they had been reworked into the sediment they were located within.

Where corals were sampled, detailed mapping of the local area was carried out prior to removal, with the elevation, UTM and surrounding lithology recorded. Multiple coral samples from each location were removed such that the coral ages at each location can be compared. Corals that could be sampled from their surrounding sediment without any risk of damage to the delicate corallite were removed. Where the corals were enclosed within lithified sediments, a sample of the lithified rock containing the corals was removed using a hammer and chisel.

3.4.2 Sample preparation

Ideally, pristine, whole coral corallite samples were selected for age dating, but some corals selected in Chapter 7 were part of a death assemblage and had been broken so fragments from whole corallites were used. These fragments were only sampled if they had intact walls and septa that allowed formal identification. Cleaning and sample preparation of corallites was carried out by the author as per the approach in Roberts et al. (2009) and Houghton (2010). Each corallite sample was washed in ultrapure water in an ultrasonic bath for 1-2 minutes. The corallites were left to dry and then split and the septa removed and discarded as septa have been shown to experience greater post-depositional alteration because they are significantly thinner than the corallite walls (Roberts et al., 2009; Houghton, 2010). Individual samples were then fragmented and analysed under a binocular microscope for signs of alteration that appear as patches of brown colouration and small crystal growths. The corallites were physically cleaned using a scalpel to remove areas of alteration and any sediment and then placed in 10% hydrochloric acid for 2-3 seconds after which they were immediately rinsed in ultrapure water. This process was repeated until all signs of alteration were removed. Following this process fragments from each corallite were analysed for $^{234}U/^{230}Th$ by Dr Diana Sahy at the British Geological Survey (BGS), Keyworth, as per the method detailed in Crémière et al. (2016) and Teichert et al. (2003).

Typically, when corals are dated using U-series dating, mineralogical analysis is carried out using X-ray diffraction (XRD) to determine the calcite content of the coral and assess whether the samples have been recrystallised. The approach adopted herein, to date multiple sub-samples of the same corallite, means that it was not possible to analyse the same coral sub sample for XRD in addition to U-series, so it would not be clear if the calcite content of the XRD was representative of the volume used for U-series. Furthermore, the small quantities of coral fragments that were of acceptable quality for $^{234}U/^{230}Th$ mean that each coral sub

sample was very small. The detection limit for any particular minerals using quantitative XRD is ~3-5%, and such small coral samples may not yield reliable data. Attention was instead focused on screening the U-series data (Section 2.1.4.1) and analysing whether $\delta^{234}U_i$ values for each corallite clustered (Chapter 7) as a way of inferring whether the corals had been subjected to open or closed system conditions.

3.4.3 Age calculation

The basis of $^{234}U/^{230}Th$ coral age dating is that the radioactive system in question is attempting to return to secular equilibrium, where the activity of all nuclides in the decay chain are equal. Therefore, measurement of the ingrowth relationships between ^{238}U, ^{234}U and ^{230}Th allow for the calculation of time since growth (Dutton, 2015). Age calculation requires the measurement of two ratios: $^{230}Th/^{238}U$ and $^{234}U/^{238}U$ and relies on knowledge of the decay constants of ^{234}U, ^{238}U and ^{230}Th. $^{234}U/^{230}Th$ coral age calculations within this thesis were undertaken by Dr Diana Sahy (BGS), the decay constants of Cheng et al. (2013) were applied. Activity ratios were corrected for ^{230}Th, ^{234}U and ^{238}U contribution from the synthetic ^{236}U–^{229}Th tracer, instrument baselines, mass bias, hydride formation and tailing. ^{230}Th blanks amounting to 0.15 ± 0.03 fg were subtracted from each sample. ^{238}U blanks were on the order of 10 pg, and were negligible relative to sample size. Age and $\delta^{234}U_i$ data were corrected for the presence of initial ^{230}Th assuming an initial isotope composition of ($^{232}Th/^{238}U$) = 1.2 ± 0.6, ($^{230}Th/^{238}U$) = 1 ± 0.5 and ($^{234}U/^{238}U$) = 1 ± 0.5 (all uncertainties quoted at the 2σ level) (Diana Sahy, 2019, Pers. Comms). Uncertainties for $^{234}U/^{230}Th$ coral growth ages comprised counting statistics from the analytical instrument, external reproducibility for U and Th isotope ratios obtained from measuring certified reference material and a propagated uncertainty from the initial Th correction carried out using Monte Carlo simulation (Diana Sahy, 2019, Pers. Comms). The $^{234}U/^{238}U$ isotope initial activity ratio ($^{234}U/^{238}U_i$) in this thesis is reported in standard delta notation relative to secular equilibrium ($\delta^{234}U_i$) (Chutcharavan et al., 2018) where:

$$\delta^{234}U_i\,(‰) = \left[\left(^{234}U \div {}^{238}U\right)i - 1\right] \mathrm{x}\, 1000$$

Following age determination, evaluation of the reliability of the coral ages was considered based upon uranium concentrations, which should be between ~2-3.5 ppm (Shen and Dunbar, 1995) and values of $^{230}Th/^{232}Th$, which should be >100 (van Calsteren and Thomas, 2006) (Section 2.1.4.1). The use of $\delta^{234}U_i$ to determine age reliability is the subject of Chapter

7 and, as such, is discussed in detail within that chapter. However, it is important to note that it is now routine to assess whether coral U-series geochemistry has been impacted by open system conditions by back calculating $\delta^{234}U_i$ (Chutcharavan et al., 2017, *and references therein*). This approach assumes that the corals have grown in water with an $^{234}U/^{238}U$ initial activity ratio that is similar to current values associated with homogenous sea water, such assumptions that are questioned within Chapter 7.

3.5 FAULT ANALYSIS

3.5.1 Mapping normal faults

The location of mapped normal faults in the field areas of investigation were initially identified using existing geological maps obtained from the Institute of Geology and Mineral Exploration (IGME), Greece, and investigated through detailed fieldwork, examination of Google Earth and DEM. Where possible, the offset caused by crustal-scale normal faults was measured from topographic profiles in the DEM that were taken perpendicular to the strike of the fault and using the geological maps. During field campaigns, fault traces were annotated on Google Earth base maps and structural measurements taken from the fault plane, recording also the exact elevation using a barometric altimeter and the UTM location. Structural measurements were taken using a compass clinometer and include the strike and dip of the fault plane and slip vector azimuth and plunge of kinematic indicators such as slip striations.

3.5.2 Elastic half-space modelling to investigate co-seismic fault motion and Coulomb stress transfer

Coulomb 3.4 (Toda et al., 2011) is a software programme, hosted in Matlab, that allows analysis of displacements, strains and stresses caused by fault slip (Sections 2.2.3 and 2.2.4). In this thesis Coulomb 3.4 was used in two ways: firstly, to investigate the patterns and absolute values of the expected coseismic uplift and subsidence from a fault rupture; and secondly to examine the Coulomb stress transfer imparted from rupturing source faults onto surrounding receiver faults.

The approach and updated code of Mildon et al. (2016) within Coulomb 3.4 was employed, this allowed strike-variable faults to be used, as Coulomb stress transfer is particularly

sensitive to changes in the strike of receiver faults (Mildon et al., 2016). A fault input file was created using an accurate fault trace drawn from Google Earth, fault parameters (dip, facing direction, rake), the amount of slip at depth and the amount of slip at the surface. The amount of slip at depth was iterated in order to produce an earthquake that matched the maximum magnitude expected given the length of the fault (the maximum magnitude was calculated using the fault-scaling equation in Section 2.2.4). The slip at the surface was set at 0.1 (10%), this value was based upon the relationship between surface slip (Vittori et al., 2011) and maximum slip at depth (Wilkinson et al., 2015) for the 2009 Mw 6.3 L'Aquila earthquake (Italy). Once the fault was ruptured in the programme (Fig. 3.18a), interrogation of the vertical deformation, using the Coulomb 3.4 function 'vertical displacement', reveals contours that relate to absolute values of off-fault uplift and subsidence (Fig. 3.18b), this output file was then overlaid onto Google Earth.

Coulomb stress transfer analysis (Section 2.2.3) requires construction of the fault input file and rupturing in the same way as outlined above, but in addition to the rupturing source fault, a receiver fault is also built based upon the same parameters outlined above. The Coulomb 3.4 function 'Calculate stress on fault' is used to model the Coulomb stress change imparted from a rupture on the source fault to the receiver fault (Fig. 3.18c), represented by colour change from blue through yellow to red (stress reduction to stress enhancement). Greater detail is provided within the chapters where Coulomb 3.4 is applied.

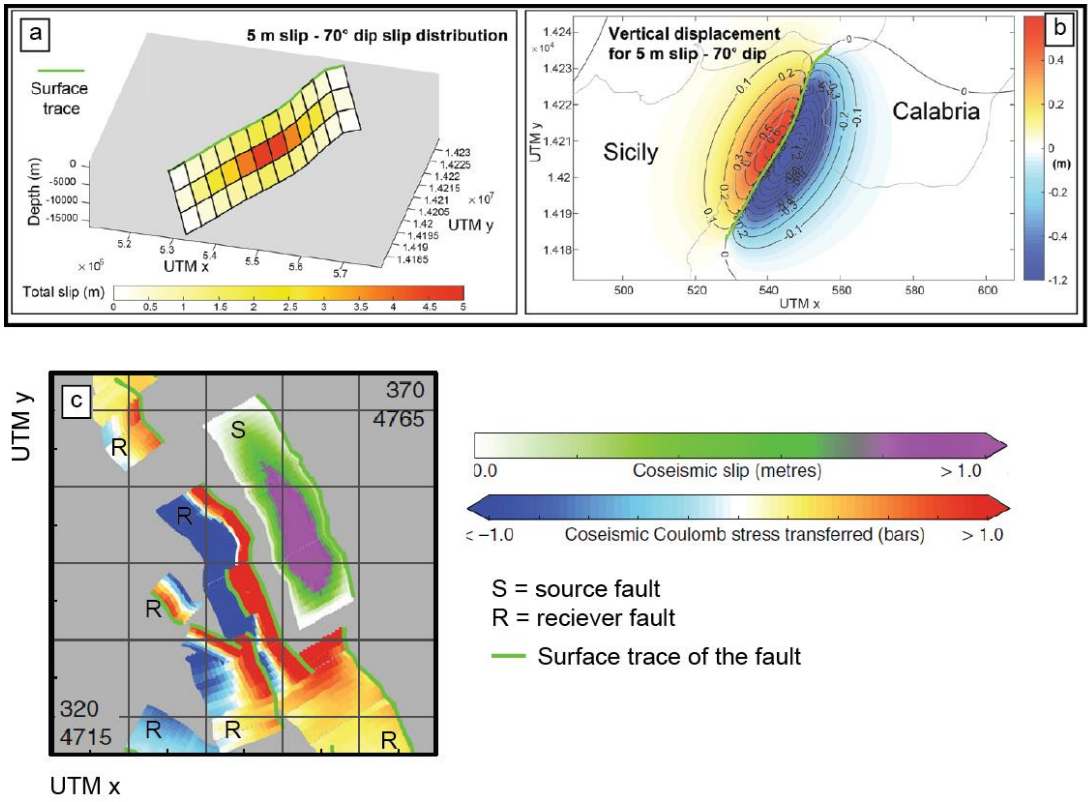

Figure 3.18: Slip on the Messina normal fault (a) and (b) vertical displacement following a rupture on the same fault (modified from Meschis et al., 2019). (c) Coulomb stress change imparted onto surrounding normal faults following the 30 Oct 2016 Vettore (Italy) earthquake (modified from Mildon et al., 2019).

To conclude, this chapter outlines the approach and detailed methods relating to the identification and measurement of palaeoshorelines, their correlation and dating techniques applied herein, in addition to detailing how normal faults were mapped in the field and their behaviour modelled using elastic half-space modelling. Where necessary, other minor methods are introduced in the coming chapters.

4 CHAPTER 4: TEMPORALLY CONSTANT QUATERNARY UPLIFT RATES AND THEIR RELATIONSHIP WITH EXTENSIONAL UPPER-PLATE FAULTS IN SOUTH CRETE, CONSTRAINED WITH ^{36}CL COSMOGENIC EXPOSURE DATING

4.1 SUMMARY

This chapter aims to apply a novel approach to interrogate Late-Quaternary palaeoshorelines, specifically using ^{36}Cl exposure dating on a number of limestone wave-cut platforms to derive spatial patterns of uplift rates which can be used to investigate fault-based uplift mechanisms and determine long-term deformation rates of the fault(s). The south of Crete provides an excellent opportunity to investigate uplift along sequences of deformed palaeoshorelines and carry out ^{36}Cl exposure dating on bedrock surfaces eroded during the formation of the palaeoshorelines. In this chapter a key location along the south central coast of Crete, where a normal fault (South Central Crete Fault—SCCF) crosses the coastline is investigated. The broader location, in the forearc of the Western Hellenic Subduction Zone (WHSZ), means palaeoshoreline deformation is complex and could occur due to more than one tectonic mechanism. The focus of this chapter is three-fold: (i) to determine whether ^{36}Cl exposure dating of wave-cut platforms reveal ages that are in agreement with existing age constrains on palaeoshorelines and with known sea-level highstands; (ii) to explore the spatial variation of uplift rates and use these data in order to determine the dominant fault process responsible for uplift in the upper-plate of a subduction zone, and (iii) determine long-term deformation rates (throw and slip rates and recurrence intervals) on the faults in question.

This chapter documents the application of ^{36}Cl exposure dating on wave-cut platforms that are interpreted to provide reliable age constraints that are used to guide a correlation of palaeoshorelines to eustatic sea-level highstands from 76.5-900 ka; the results of which suggest that uplift rates vary along fault strikes but have been constant for 900-600 ka in places. Correlation of palaeoshorelines across the SCCF results in a throw-rate of 0.41 mm/year and, assuming repetition of 1.1-m slip events, a fault-specific earthquake recurrence interval of approximately 2,700 years. Elastic-half-space modelling implies that coastal uplift of the study area is related to offshore upper-plate extensional faults, likely

dominated by the Ptolemy Trough fault, which is suggested to have a minimum mean recurrence interval in the region of ~ 550 years. These upper-plate faults may be responsible for perturbing the uplift rate signals in the south central Crete area. The findings presented suggest that where uplifted palaeoshorelines are used to make inferences about the mechanisms responsible for uplift throughout the Hellenic Subduction Zone, and other subduction zones worldwide, the impact of upper-plate extensional faults over multiple seismic cycles should also be considered.

The findings of this chapter are published in Robertson et al. (2019) in *Tectonics*.

4.2 INTRODUCTION

As a result of its location above the WHSZ, Crete (Fig. 4.1) has been used to study the relationship between uplift and slip associated with the WHSZ (Papadimitriou & Karakostas, 2008; Shaw et al., 2008; Shaw & Jackson, 2010; Gallen et al., 2014; Strobl et al., 2014). Observations from uplifted palaeoshorelines (e.g. Pirazzoli et al., 1982; Tsimi et al., 2007; Shaw et al., 2008; Gallen et al., 2014; Mouslopoulou et al., 2015a, 2015b), Paleolithic sites (Strasser et al., 2011), alluvial fans (Pope et al., 2008; Mouslopoulou et al., 2017), and other geomorphological and biological features (Kelletat, 1991; Shaw et al., 2010) along its south and west coasts have been used to discuss the relationships between slip on the subduction interface, thrust faults in the overlying wedge, and historic tsunamigenic earthquakes (Ganas & Parsons, 2009; Shaw et al., 2008; Shaw & Jackson, 2010; Stiros, 2010). However, less attention has been given to the role of active normal faulting in influencing uplift, a phenomenon that is widespread on Crete (Angelier, 1979a; Armijo et al., 1992; Caputo et al., 2010; Gallen et al., 2014; Ganas et al., 2017).

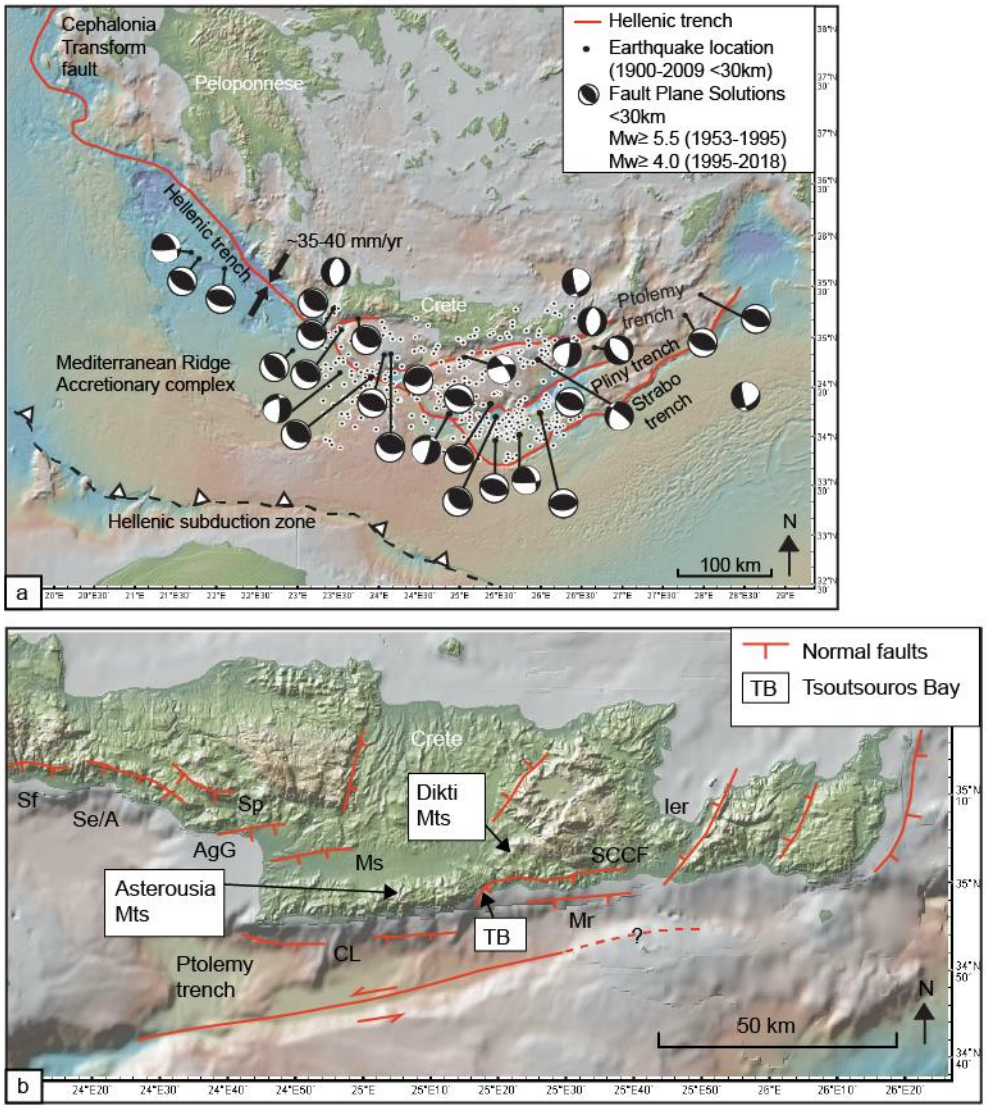

Figure 4.1: (a) Tectonic setting of Crete, Greece. GPS data are from Nocquet (2012). The location of the Hellenic subduction zone is taken from Kreemer & Chamot-Rooke (2004). Dots show earthquakes between 1900 and 2009 >Mw 4, constrained to a depth of <30 km (Makropoulos et al., 2012); fault plane solutions for earthquakes constrained to a depth of <30 km between 1953 and 1995 (Mw >5.5; Papazachos et al., 1998) and 1995 and 2018 (Mw >4; CMT Catalogue: Dziewonski et al., 1981; Ekström et al., 2012). (b) map of Crete with possible active arc-normal upper-plate faults labelled: Ka = Kastelli fault (Caputo et al., 2010); Sf = Sfakia (Caputo et al., 2010); Se/A = Sellia/Asomatos (Caputo et al., 2010); Sp = Spilli (Monaco & Tortorici, 2004); Caputo et al., 2010); AgG = Agia Galini (Caputo et al., 2010; Monaco & Tortorici, 2004); Ier = Ierapetra (Caputo et al., 2010); Ms = Messara (Fassoulas, 2000); CL = Cape Lithino (Caputo et al., 2010); Mr = Mirto (Caputo et al., 2010) SCCF = South Central Crete Fault (Gallen et al., 2014); Pt = Ptolemy trench fault (Mascle et al., 1982; Becker et al., 2006, 2010; Kokinou et al., 2012); TB = Tsoutsouros Bay. (From Robertson et al., 2019)

The upper plates of subduction zones throughout the world have been shown to host onshore and offshore upper-crustal normal faults, identified from studies of deformed palaeoshorelines, high resolution seismic data and detailed structural fault mapping (e.g. Cashman & Kelsey, 1990; McIntosh et al., 1993; Wessel et al., 1994; Monaco & Tortorici, 2004; Papanikolaou et al., 2007; Saillard et al., 2011; Binnie et al., 2016; Howell et al., 2016;

Böttner et al., 2018; Meschis et al., 2018). Where extensional faults occur near to the coastline they leave clear geomorphic signatures of the variable deformation that they cause as a result of displacement gradients that change along the strike of the fault (Sections 2.2.1, 2.2.2) (Wessel et al., 1994; Armijo et al., 1996; Papanikolaou. D. et al., 2007; Roberts et al., 2013; Meschis et al., 2018). It follows, therefore, that onshore and offshore extensional faults in the upper plates of subduction zones may have the capacity to influence coastal uplift, and that uplift rates inferred using coastline data may represent a combination of mechanisms including upper-plate extensional faulting (McNeill et al., 1999). Chapter 2 highlighted that deformed palaeoshorelines can be used to determine the dominant cause of tectonic uplift observed on coastlines and quantify deformation rates linked to upper-plate faults. In detail, this is done by examining the length scale of deformation and patterns of uplift that may occur along the strike of a sequence of palaeoshorelines, which may reveal displacement gradients along specific faults and indicate whether uplift rates remain constant through time (e.g. Roberts et al., 2013) or change through time due to fault interaction (e.g. Roberts et al., 2009). Using deformed palaeoshorelines to infer the dominant cause of uplift and time-averaged deformation rates over multiple seismic cycles requires robust dating techniques, which extend into the Late Quaternary. Presently, there are few sets of existing dates from the south central area of Crete.

This chapter investigates a key location in south central Crete, where a normal fault (SCCF) crosses the coastline, producing differential uplift, with Quaternary palaeoshoreline and marine terrace deposits at elevations that vary along the coast (Gallen et al., 2014). To the west where the SCCF crosses the coast at Tsoutsourous Bay (TB; Fig. 4.1 and 4.2), palaeoshorelines are cut into a steep, high relief coastal area with greater vertical spacing between them in comparison to those to the east of TB where the palaeoshorelines are more closely spaced together in elevation and cut into a low relief coastal plain. Owing to the variation in geology, relief, and elevation of Quaternary palaeoshorelines, and the fact that the SCCF has a Holocene scarp with dramatic fault planes exposed near Arvi (Fig. 4.2a), it is likely to be an active fault, capable of hosting destructive earthquakes. The application of a new dating approach allows important new insights. The preservation of geomorphological features associated with wave-cut platforms provides evidence of minimal erosion, thus facilitating the use of in situ ^{36}Cl cosmogenic exposure dating. ^{36}Cl exposure ages from five wave-cut platform sites have been obtained, providing dates for palaeoshorelines that would not be amenable to conventional optically stimulated luminescence (OSL) sediment dating or Uranium-series coral dating. These new ^{36}Cl exposure ages alongside synchronous

correlation modelling using sea-level curve data provide new insights that allow an understanding of how uplift rates change spatially and temporally, and the quantification of deformation rates obtained using synchronous correlation modelling. Elastic-half space modelling allows comparison of the observed and modelled patterns of uplift rates in order to establish the significance that extensional upper-plate faults have with regard to coastal uplift. Finally, the implications of the findings from the study are considered within the context of seismic hazard, and local and broader tectonic regimes of the WHSZ and suggest that as coastal uplift along the south of Crete appears to be dominated by extensional faulting, this may also be true of the rest of the WHSZ.

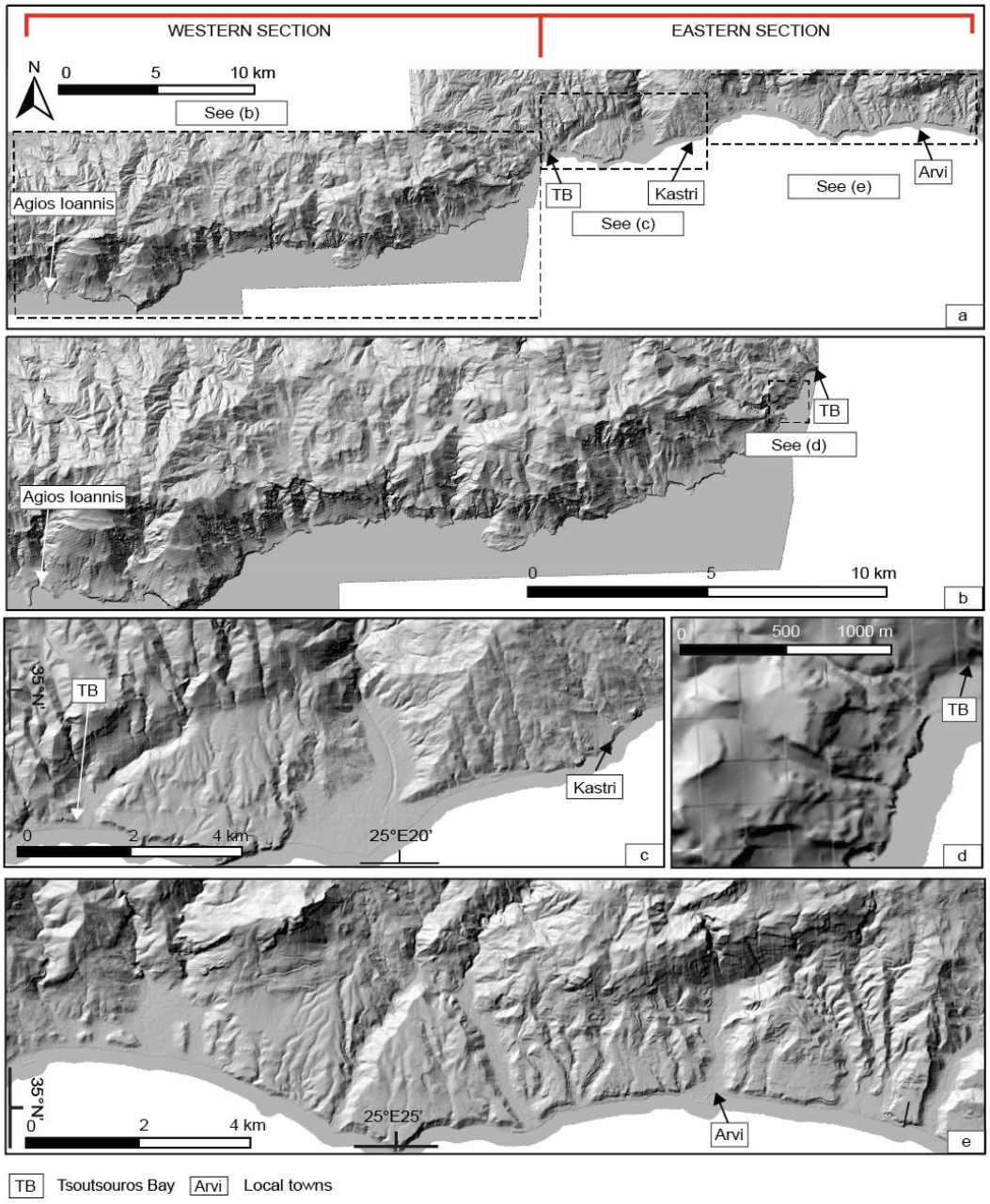

Figure 4.2: Five-meter digital elevation models of (a) the research area showing the western and eastern sections referred to throughout the text, and (b-e) detailed views of the digital elevation models (from Robertson et al., 2019). An interpreted version is shown in Fig. 4.4.

4.3 BACKGROUND

4.3.1 South central Crete geology

The south-central Crete area is bounded by two mountain ranges: the Asterousia mountains in the west and the Dikti mountains in the east (Figure 4.1b). The hangingwall of the SCCF, which is bounded by the Dikti mountain range to the north, is predominantly comprised of

middle-upper Miocene sediments juxtaposed with ophiolitic and flysch deposits from the internal and external zones nappes (IGME Ano Viannos 1:50,000). To the west, beyond the western tip of the SCCF, the lithology is dominated by limestones of variable age (Mesozoic to Tertiary), and their unconsolidated and consolidated scree deposits that make up the Asterousia mountain range (IGME map sheet Akhendhrias 1:50,000). The palaeoshorelines studied in this chapter are broadly parallel to the coastline and in the case of the SCCF, parallel to the strike of the fault. Marine terrace deposits are reported throughout the area and are seen as conglomeratic beach rocks, gravels, and sands, which unconformably overlie eroded Miocene sediments and limestone surfaces (Gallen et al., 2014). Quaternary and Holocene alluvial fan deposits are common throughout the study area, especially along the hangingwall of the SCCF (Gallen et al., 2014).

4.3.2 Upper-plate faults and their context within a converging zone

The E-W-trending faults present along the south of central Crete (Fig. 4.1) accommodate arc-perpendicular extension and are observed both onshore and offshore; these faults are the subject of this study. Onshore E-W-trending normal faults show uplift in their footwalls, as expected, but also uplift in their hangingwalls, indicated by preserved palaeoshorelines, despite the subsidence they are experiencing as a result of faulting. The hangingwall subsidence is counteracted by uplift, presumably related to the subduction interface and/or thrust faults in the overlying wedge and/or footwall uplift from offshore, E-W striking extensional faults. Uplift in the hangingwall of normal faults is observed along the south coast of Crete, namely, the Sfakia fault, SW Crete (Skourtsos et al., 2007; Tsimi et al., 2007), the Ierapetra fault, SE Crete (Gaki- Papanastassiou et al., 2009), and the SCCF (Angelier, 1979b; Gallen et al., 2014; Gallen & Wegmann, 2017).

The focus of this chapter is the onshore SCCF along the southern central area of Crete (Fig. 4.1b), because it crosses the coast and appears to control differential uplift that can be explored through mapping and dating of wave-cut platforms. Limestone fault scarps are visible along all four of its south-dipping segments and have an average dip of 45˚ (Gallen et al., 2014). Converging slip vectors reported along its ~45-km onshore length (Gallen et al., 2014) suggest that the segments represent one fault at depth (Michetti et al., 2000; Roberts, 1996a, 2007; Roberts & Ganas, 2000). The western section of the SCCF fault exhibits a change in strike as it curves toward the coastline and displacements appear to decrease towards a fault tip offshore, identified by a decrease in topographic and bathymetric relief (Figs. 4.2).

Analysis of bathymetry defines the approximate offshore extent of this fault as ~2.5 km south of the coastline (Alves et al., 2014; Kokinou et al., 2012). This interpretation contrasts with the suggestion by Gallen and Wegmann (2017) where the SCCF represents the onshore extension of the Ptolemy fault, which they suggest has a normal motion, implying an intraplate normal fault, which is ~124 km in length. This length is at odds with the notion that maximum fault length is about twice the depth of the seismogenic layer of 12–15 km (Jackson & White, 1989), so the interpretation of a ~45-km fault is preferred.

Offshore, the southern coast of Crete is bounded by active normal faults and three "trench" faults (Section 2.3.1, Fig. 2.30). The normal faults, the Cape Lithino faults, and the Mirto fault (Caputo et al., 2010) (Fig. 4.1b) have a dip to the south, synthetic to the SCCF. Investigations using bathymetry, seismic reflection, and sediment core data by Alves et al. (2007) and Kokinou et al. (2012) showed that the faults are active and control basin development. Of the three trench faults (Ptolemy, Pliny and Strabo) (Fig. 4.1a), the Ptolemy fault is closest to the southern Crete shoreline. The Ptolemy fault trends NE to NNE (Angelier et al., 1982) and extends ~90 km along strike (Fig 4.1a). The motion on this fault has been the subject of much debate with earlier studies suggesting that it either accommodates convergence as a transform/thrust fault (McKenzie, 1978; Mascle et al., 1982; Taymaz et al., 1990), is a strike-slip fault (le Pichon & Angelier, 1979; Chaumillon & Mascle, 1997; Huguen et al., 2001), or is a normal fault (Gallen et al., 2014; Gallen & Wegmann, 2017). However, evidence from microseismicity, bathymetry, and seismic reflection and analysis of fault-plane solutions suggest that the active fault cuts through the entire upper plate; is south dipping, near vertical (85˚); and records sinistral transtensional motion that has resulted in the development of a wedge-shaped sedimentary basin approximately 4 km thick (Bohnhoff et al., 2001; Meier et al., 2004; Becker et al., 2006; Kokinou et al., 2012). In summary, there is compelling evidence that the area immediately offshore of the south of the south central Crete area is dominated by extensional tectonics in the form of numerous upper-plate normal faults and the Ptolemy transtensional fault.

4.3.3 Crete uplift

The cause of uplift on Crete is debated and suggested to result from underplating on the subduction interface, reverse motion on the megathrust, thrusting and oblique slip faulting in the forearc, and active normal faulting (Angelier et al., 1982; Taymaz et al., 1990; Meier et al., 2007; Shaw et al., 2008; Ganas & Parsons, 2009; Caputo et al., 2010; Gallen et al., 2014;

Strobl et al., 2014; Tiberti et al., 2014; Mouslopoulou et al., 2015a). Geodetic, seismological, and geological evidence suggests compressional, extensional, and strike-slip tectonics onshore and offshore southern Crete as seen by the analysis of fault plane solutions and microseismicity studies (Papazachos, 1990; Taymaz et al., 1990; Doutsos & Kokkalas, 2001; Bohnhoff et al., 2005; Meier et al., 2007; Becker et al., 2010; Caputo et al., 2010; Shaw & Jackson, 2010; Kokinou et al., 2012; Howell et al., 2017). These studies show that thrust faulting occurs as a result of forearc normal compression at depths linked to subduction to the south of Crete; additionally, Shaw et al. (2008) suggested that reverse (high-angle) splay faults may cut the upper crust in western Crete; however, their existence was debated by Ganas and Parsons (2009) on the basis of a lack of compatible seismological data. The E-W and N-S trending normal faults accommodate arc-normal and arc-parallel extension (Angelier, 1979a; Armijo et al., 1992; Fassoulas, 2000; Peterek & Schwarze, 2004; Caputo et al., 2006; Snopek et al., 2007; Caputo et al., 2010; Floyd et al., 2010; Kokinou et al., 2012; Gallen et al., 2014; Gallen & Wegmann, 2017; Ganas et al., 2017; Howell et al., 2017)**,** which is also reflected in Eurasian (upper) plate GPS motions that increase toward the southern edge of the plate in the location of Crete (McClusky et al., 2000; Floyd et al., 2010) and are quantified by Nocquet (2012) as ~10 mm/year.

Investigations using uplifted hangingwall and footwall marine terraces, 2-D viscoelastic modelling, and sedimentary correlations have led to a large variety of uplift estimates along the south coast of Crete from 0.2 to 7.7 mm/year over timescales since the late Quaternary (~600 ka) to the present day (Meulenkamp et al., 1994; Skourtsos et al., 2007; Shaw et al., 2008; Gaki-Papanastassiou et al., 2009; Strasser et al., 2011; Gallen et al., 2014; Strobl et al., 2014; Tiberti et al., 2014; Mouslopoulou et al., 2015a; Mouslopoulou et al., 2015b; Gallen & Wegmann, 2017; Mouslopoulou et al., 2017; Ott et al., 2019). Additionally, some authors propose that uplift rates have varied over time (Gallen et al., 2014; Tiberti et al., 2014; Mouslopoulou et al., 2015b). For example, in the south west of Crete, Tiberti et al. (2014) propose subsidence rates of 2.6-3.2 mm/yr between 42-23 ka and from 23 ka to present, an uplift rate of 7.7 mm/yr; over longer timescales, in the area of south central Crete, Gallen et al. (2014) propose an increase from 0.55 mm/yr to 0.8 mm/yr during the period from 350 ka to 76 ka. Studies to determine uplift rates have employed a mixture of dating techniques with many attempting to explore long-term uplift using ^{14}C radiocarbon dating on marine shells (Shaw et al., 2008, 2010; Strasser et al., 2011; Shaw, 2012; Tiberti et al., 2014; Mouslopoulou et al., 2015a; Mouslopoulou et al., 2015b) other methods include ^{10}Be exposure dating on wave-cut platforms (Strobl et al., 2014), OSL geochronology (Gallen et

al., 2014), and U-Series measurements on corals (Angelier, 1979b; Gaki-Papanastassiou et al., 2009). The half-life of ^{14}C is relatively short (5,730 years), but ^{14}C has been used to date organic material up to 70 ka (Peppe et al., 2013). However, Ott et al. (2019) query the reliability of ^{14}C radiocarbon dating as a method to explore Late-Quaternary uplift, owing to the fact that there is evidence to suggest that radiocarbon ages from fossils founds on palaeoshorelines older than 40-50 ka yield unreliable ages because of possible contamination by young meteoric carbon (see also Busschers et al., 2014). Ott et al. (2019) identify that significant temporally variable rates of vertical deformation that vary on ten-thousand-year timescales are apparent in studies that make use of radiocarbon-derived ages older than ~40 ka (e.g. Tiberti et al., 2014; Mouslopoulou et al., 2015a). Thus, there is a clear lack of agreement as to the magnitude and temporal behaviour of uplift rates along southern Crete, and therefore the potential cause of such uplift, in part linked to the reliance of using age controls from ^{14}C radiocarbon dating. This needs further investigation, using age controls that are reliable over Late-Quaternary timescales.

The pattern of uplift described within published works is further complicated with regard to attempting to identify regional uplift rates, because much of the south and west of Crete is affected by onshore and offshore faulting (Fig. 4.1b) with the west of the island uplifted as a result of several Holocene earthquakes (Pirazzoli et al., 1996; Stiros, 2001; Shaw et al., 2008; Stiros, 2010). As such, Strobl et al. (2014) commented that the upper values of uplift are likely to be representative of the short term (i.e. Holocene) and significantly overestimate the Pliocene- Quaternary uplift rate. Thus, there is an expectation that the Late-Quaternary uplift rates derived from along southern Crete should be lower than those observed throughout the Holocene (Strobl et al., 2014; Ott et al., 2019); this can be measured using deformed palaeoshorelines, but the successful application of this approach requires consideration of the extensional faults that are known to exist offshore prior to considering the 'regional' explanation.

4.3.4 Previous studies on the SCCF

This chapter revisits known palaeoshorelines in southern Crete, previously investigated by Angelier (1979b) and Gallen et al. (2014), in order to conduct a reappraisal of palaeoshoreline ages and uplift rates. Gallen et al. (2014) conducted along strike analysis of the deformation on palaeoshorelines in the south central Crete area (Fig 4.3a) using field mapping to obtain the elevations of sequences of palaeoshorelines, and age controls from OSL dating on

sediments associated with Late-Quaternary palaeoshorelines. The age controls from Gallen et al. (2014) (Fig. 4.4b–4.4d) provide two ages that constrain the 76.5-ka highstand (LS1251 and LS1254) and one age that constrains the 125- ka highstand (LS1255) (Gallen et al., 2014). The palaeoshoreline elevations and OSL age controls were used by Gallen et al. (2014) alongside sequential correlation (Section 2.1.5) to derive uplift rates for 18 Profiles, 12 of which are located in the same geographic area as investigated in this chapter (Fig 4.3a). The results of their correlation and uplift analysis show that the uplift rates vary along-strike, increasing from west to east until the SCCF is intersected, when they decrease significantly (Fig. 4.3b) (Gallen et al., 2014). Sequential correlation conducted by Gallen et al. (2014) suggests that uplift rates temporally vary through time at all 18 localities, increasing from 400 ka to the present day (Fig 4.3c). Gallen et al. (2014) recognise the role of the SCCF in deforming the hangingwall palaeoshorelines and explain the presence of hangingwall palaeoshorelines above sea level as a result of regional uplift associated with crustal thickening. They suggest Late-Quaternary regional values of 0.55-0.8 mm/year. This value was obtained by first modelling the expected elevations of palaeoshorelines in the SCCF hangingwall given knowledge of the sea-level elevations at the time of palaeoshoreline formation and the throw rate of the fault, assuming there were no other uplift sources; to do this they assumed a fault-related subsidence versus uplift ratio of 4:1. These modelled hangingwall elevations were then compared to the measured hangingwall elevations, and the difference was inferred to represent regional values. However, the impact in terms of uplift associated with the offshore upper-plate faults was not considered within their analysis, and as will be shown below, their time varying uplift and uplift values rely on ages they assigned to palaeoshorelines, some of which are questioned.

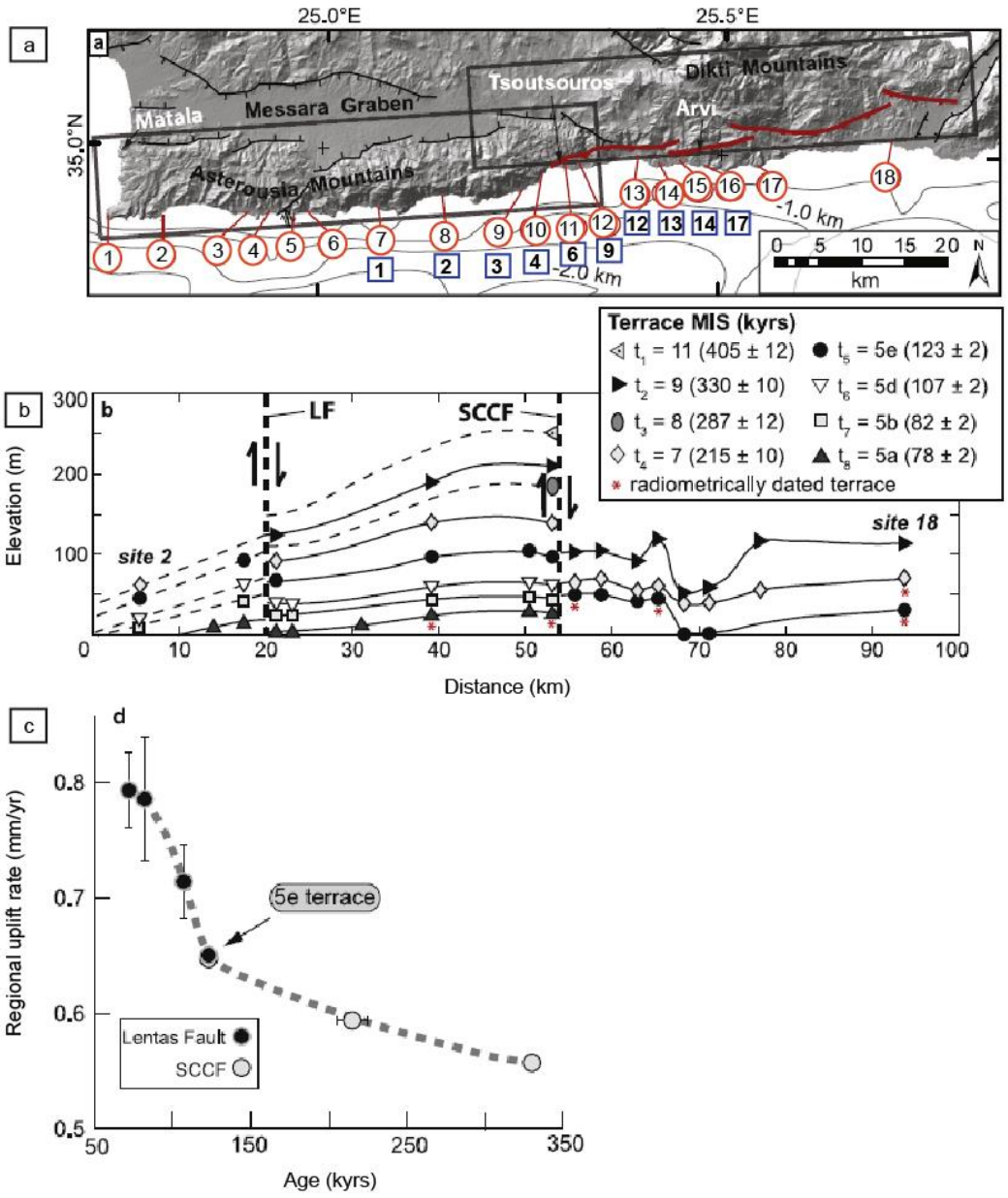

Figure 4.3: (a) Locations of palaeoshoreline sequence profiles from Gallen et al. (2014) in red circles, compared to the location of profiles in this chapter (blue squares). (b) Palaeoshoreline elevations along the study area from Gallen et al. (2014), LF refers to the Lentas Fault, located outside the study area of this chapter. (c) Uplift rate through time according to Gallen et al. (2014).

The reappraisal of palaeoshoreline ages and temporal and spatial patterns of uplift rates conducted herein is undertaken as a result of additional palaeoshoreline elevations measured from the DEM, new ages from ^{36}Cl exposure dating and the application of the synchronous correlation method to allocate undated palaeoshorelines to sea-level highstands, because it has been shown that sequential correlation may result in uplift rates that change through time which are latterly disputed when the synchronous approach is applied (e.g. Roberts et al., 2013; Meschis et al., 2018). Where possible, the topographic

profiles constructed in this chapter are done so in locations close or identical to those of Gallen et al. (2014) (Fig 4.3a) to allow direct comparison of palaeoshoreline elevation and uplift rates; of the 17 topographic palaeoshorelines in this chapter, 10 were taken from close to the locations of Gallen et al. (2014). The results of DEM analysis, extensive field campaigns conducted over 2015-2016, ^{36}Cl exposure ages, synchronous correlation of palaeoshoreline elevations to sea-level highstands, and the spatial and temporal uplift rate analyses are presented below and discussed in the context of the results from Gallen et al. (2014).

4.4 RESULTS

This section applies the method (Chapter 3) to correlate sea level highstand ages and palaeoshoreline elevations with absolute dating provided by ^{36}Cl exposure dating of wave-cut platforms and published ages from Gallen et al. (2014). A review of the along-strike variation of palaeoshoreline elevations between the topographic profiles is undertaken followed by evaluation of the temporal and spatial variation of uplift values. These data are then used in combination with the palaeoshoreline elevations of offset terraces on the footwall of the SCCF to derive deformation rates associated with the fault(s).

4.4.1 Field mapping and palaeoshoreline elevations

Palaeoshoreline elevations along 17 serial topographic profiles (Fig. 4.4a) were obtained from the DEM (Section 3.1.1) and from fieldwork (Section 3.1.2). 74 DEM elevations were measured from 2D topographic profiles and cross checked with Google Earth and then, where possible, in the field. It was preferable to take field-based palaeoshoreline elevations and DEM palaeoshoreline measurements from topographic profiles that are located close to those of Gallen et al. (2014) to allow palaeoshoreline elevations and calculated uplift rates to be directly compared.

Detailed field mapping of the study area reveals a set of palaeoshorelines that are also observed on the DEM (Fig. 4.4). The field observations below are firstly described for the western field section then for the eastern field section, the locations of which are defined by where the western onshore tip of the SCCF intersects the coastline (Fig 4.4a). The western section of the study area represents palaeoshorelines cut into Mesozoic bedrock, while the eastern section hosts palaeoshorelines cut into softer, less lithified sediments located in the hangingwall of the SCCF (Fig. 4.4a).

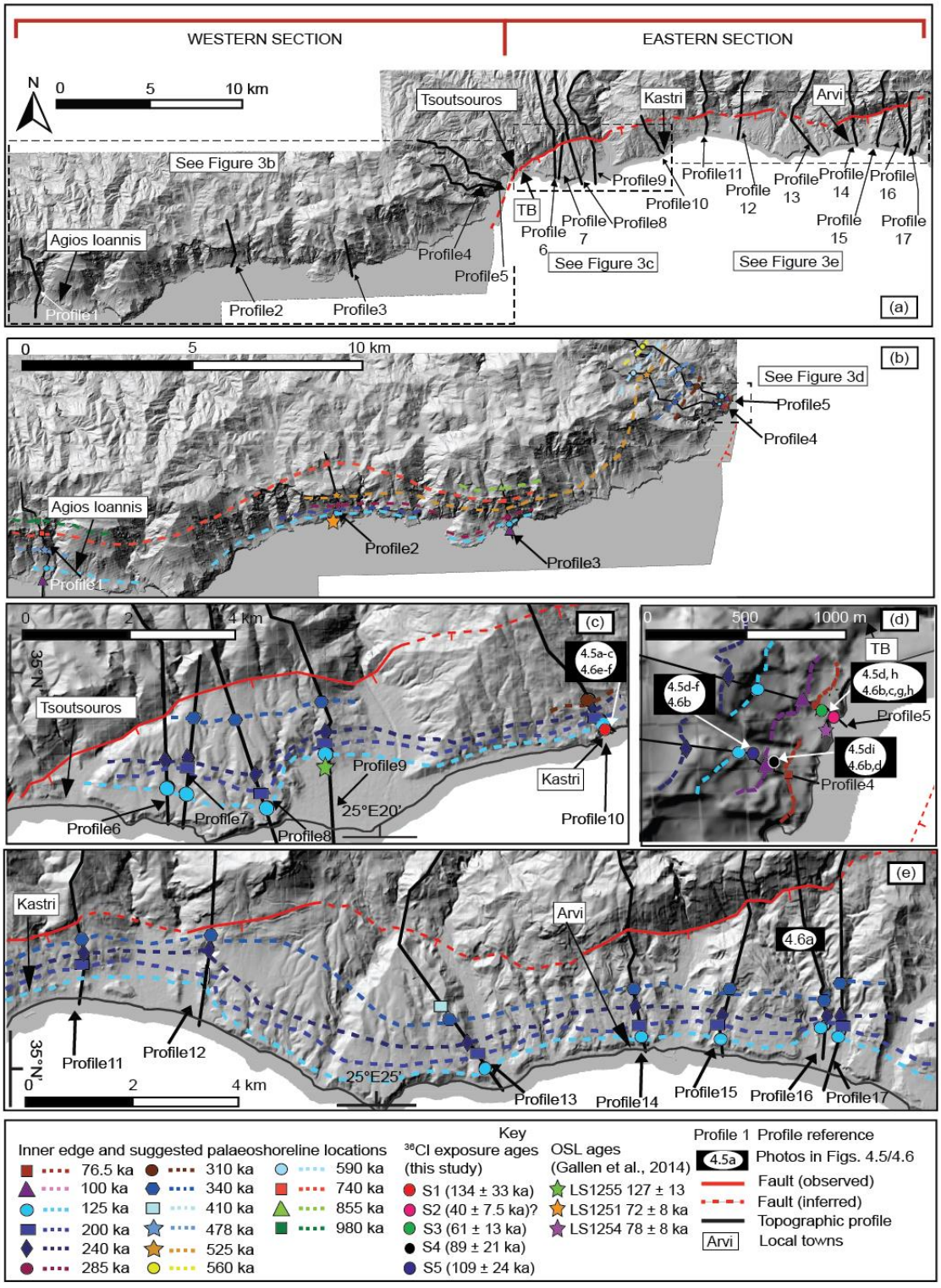

Figure 4.4: Five-meter digital elevation models: (a) location of topographic Profiles (numbered) and western and eastern sections referred to in the text. Observed fault location from fieldwork during 2015 and 2016; inferred fault location is obtained from IGME Ano Viannos 1:50,000 map. Locations of panels (b), (c), and (e) are shown by dashed boxes in (a). (b) Western section of the study area from Profile 1 (Agios Ioannis) to Profile 5 (Tsoutsouros); inset location is shown in detail in (d). (c) Eastern study area from Profile 6 (Tsoutsouros) to Profile 10 (Kastri). (d) Detailed view of west of Tsoutsouros Bay (TB). (e) Eastern study area from Profile 11 (Kastri) to Profile 17 (Arvi). Dating locations using 36Cl (this study) and optically stimulated luminescence (OSL; Gallen et al., 2014) are shown. Locations of photographs featured in (Figs 4.5 and 4.6) are marked (from Robertson et al., 2019).

The western section (Fig. 4.4b, Profiles 1–5) displays excellent palaeoshoreline features cut into Mesozoic bedrock (Fig. 4.5d-i; 4.6b-d, g and h; Table 4.1) including wave-cut platforms, notches and shoreline caves, many of which contain abundant lithophagid borings. Syn-wave-cut platform deposits are rarely preserved, except as patches on the lower platform of Profiles 4 and 5, where cemented marine sands and conglomeritic deposits comprised of rounded limestone beach pebbles and cobbles occur (Fig. 4.5h), these deposits are present toward the outer edge of the wave-cut platform and have been bored by lithophagids. Preserved serpulid algal reefs are evident on the wave-cut platforms; in some places they are observed as small patches, for example close by to where Sample 4 was removed algal reef deposits are 10-20 cm wide (Fig 4.5d, i), this is compared to a significant reef ~ 2 m tall located adjacent to the platform where Sample 3 was removed (Fig 4.5d). Lithophagid borings are visible in the algal deposits, significantly so on the larger reef. The wave-cut platforms are extensive and can be mapped for tens to hundreds of meters along strike, they form laterally persistent features in the landscape, and kilometres along strike on DEMs (Fig. 4.4, 4.6a, and 4.6b). Up to eight palaeoshorelines are observed throughout the western section, with the greatest number present in the areas of Profiles 4 and 5 (Fig 4.4b, d), where the ages of three palaeoshorelines were obtained using ^{36}Cl exposure dating (Fig. 4.5d) (Section 4.4.2).

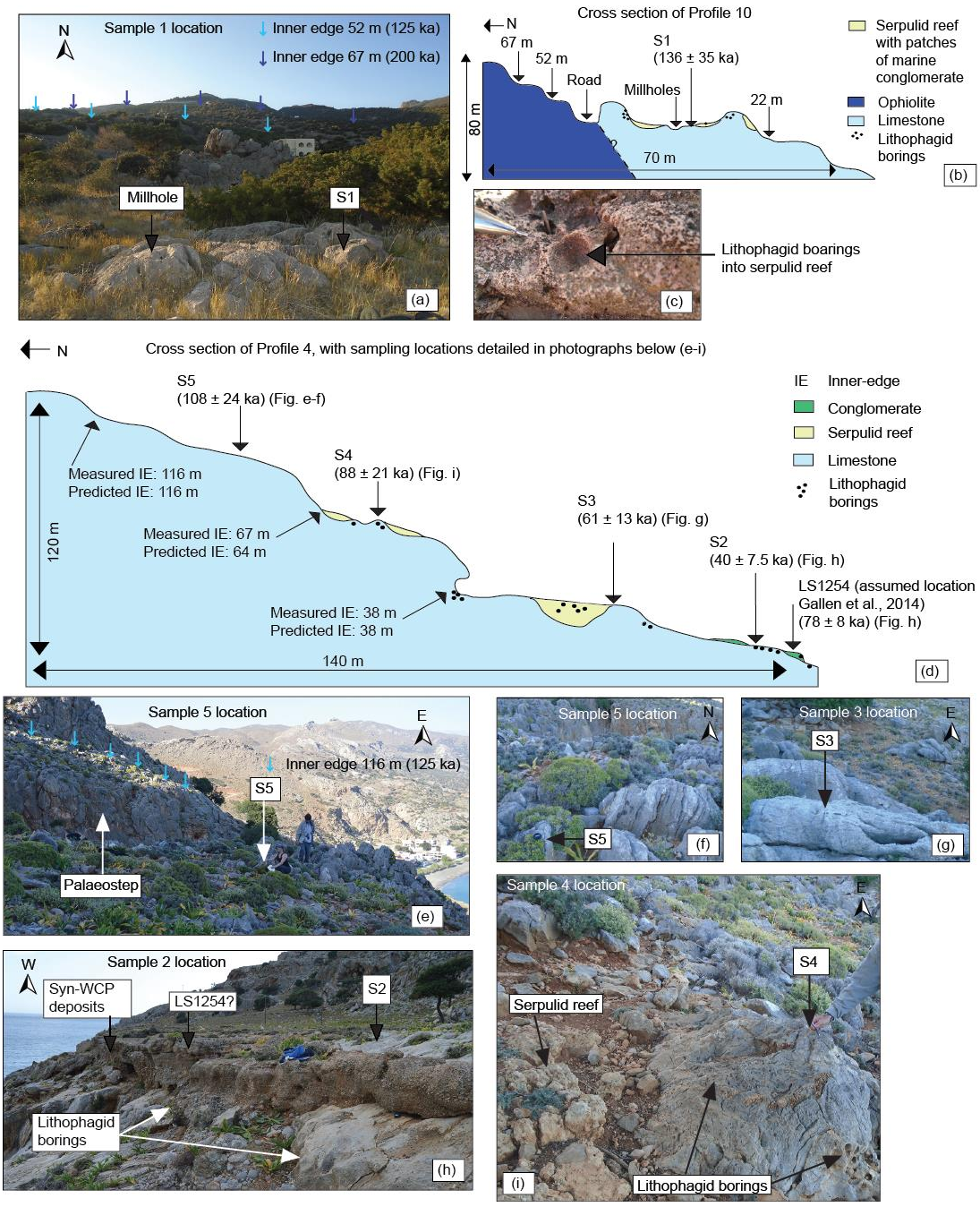

Figure 4.5: ^{36}Cl exposure dating location photographs and cross-section illustrations showing palaeogeological evidence for sample locations S1 (a–c), S2 (d and h), S3 (d and g), S4 (d and i), and S5 (d–f). Palaeoshorelines are marked by arrows on (b and d). (From Robertson et al., 2019). The results of ^{36}Cl exposure dating are shown in Table 4.2.

Sample reference (profile)	Sample elevation (m)	Geomorphological description	Palaeoshoreline elevation (m)
S1 (Profile10)	52	Limestone WCP showing evidence of a palaeolagoon environment: marine conglomerate is overlain by an algal serpulid reef into which lithophagids have bored. The limestone front and back wall of the lagoon also contains numerous lithophagid borings and milholes are evident in the limestone surfaces (Figures 4.5a-c, 4.6e, f)	54
S2 (Profile5)	20	Outer edge of a limestone WCP, small lithophagid borings <1 cm deep, 1 m from the sample site a syn-WCP conglomeratic beach deposits overlie the limestone WCP, some of the cobbles/boulders in the beach deposits contain larger lithophagid borings (~2.5 cm) (Figures 4.5d, h, 4.6b, c, h). See sample 3 for inner edge details.	38
S3 (Profile5)	34	Sample removed 30 m south of the inner edge from a pinnacle above a 4 m palaeostep which leads down to the location of sample 2. The palaeoshoreline is represented by a cave with a notch, a ~1-2 m thick algal serpulid reef overlies the limestone; lithophagid borings were present throughout the platform - bored into the algal serpulid reef, along the notch, within the inner and external cave walls (Figures 4.5d, g, 4.6b).	38
S4 (Profile4)	64	Limestone in this location contains abundant lithophagid borings surrounding the sample location which vary in size from 1-3 cm diameter, near to the sample site are the remnants of a millhole. Thin (~20 cm) patches of algal serpulid reef overlies the limestone in places (Figures 4.5d, f, 4.6b, d, i)	67
S5 (Profile4)	80	Few, poorly preserved lithophagid borings, sample removed from high pinnacle at the outer edge of the terrace (Figures 4.5d, e, f, 4.6b)	116

Table 4.1: Geomorphological features for each ^{36}Cl sampling location

Within the eastern section (Fig. 4.4a), east of where the SCCF fault crosses the coast (Fig. 4.4c and 4.4d), significant fluvial incision exists in the softer lithified syn-rift hangingwall sediments resulting in the creation of interfluves clearly visible in the DEM (Figs. 4.2c, e, 4.4c, e and 4.6a). The palaeoshorelines in the soft sediments are preserved as breaks of slope, especially on interfluves, and these can be mapped between topographic profiles both in the field and on the DEM. Flat surfaces a few decimetres to meters down dip of the palaeoshorelines are wave-cut surfaces cut into either: (i) compositionally immature conglomerates comprised of carbonate, phyllite, quartzite and sandstone pebbles and

cobbles, containing bioclastic debris including marine oyster shells (see also Fig. 3.8c and d), or (ii) a shallow succession of well sorted coarse grained sand, pebbles and cobbles with infrequent marine fossils. The tops of such deposits frequently reveal planed-off surfaces. In places within the eastern section, bedrock limestone occurs as wave-cut platforms with associated algal and beach conglomerate deposits (Figs. 4.5a-d and 4.6e) or as sea stacks, which represent inliers within the shallow marine hangingwall sediments. These bedrock inliers display palaeoshoreline features including horizontal stripes of lithophagid borings on limestone palaeo-cliffs and sea stacks, and lithophagid borings and millholes (Fig. 4.6i) on flat wave-cut surfaces. The wave-cut surfaces of one of the inliers was the location of ^{36}Cl Sample 1 (Fig 4.5b).

During fieldwork, it was not possible to visit all of the locations where DEM palaeoshoreline elevations were measured, owing to the broadness of the area being investigated, land ownership restrictions and accessibility issues (particularly on the higher palaeoshorelines). Measurements of as many field-based palaeoshoreline elevations that could be accessed took place allowing ~30% of DEM palaeoshorelines to be verified in the field. Section 3.1.3 outlines that the validity of the DEM measurements can be tested by plotting the measured palaeoshoreline elevations from the DEM against elevations measured at the same locations in the field and analysing the goodness of fit between the two datasets using R^2, the closer this value is to 1 provides an indication that the two datasets are in good agreement. The field and DEM elevations were well correlated with an R^2 of 0.9985 (Fig. 3.11), and this is interpreted to suggest that the DEM dataset is reliable. Thus, there is a robust regional coverage of palaeoshoreline elevations from combined field and DEM studies.

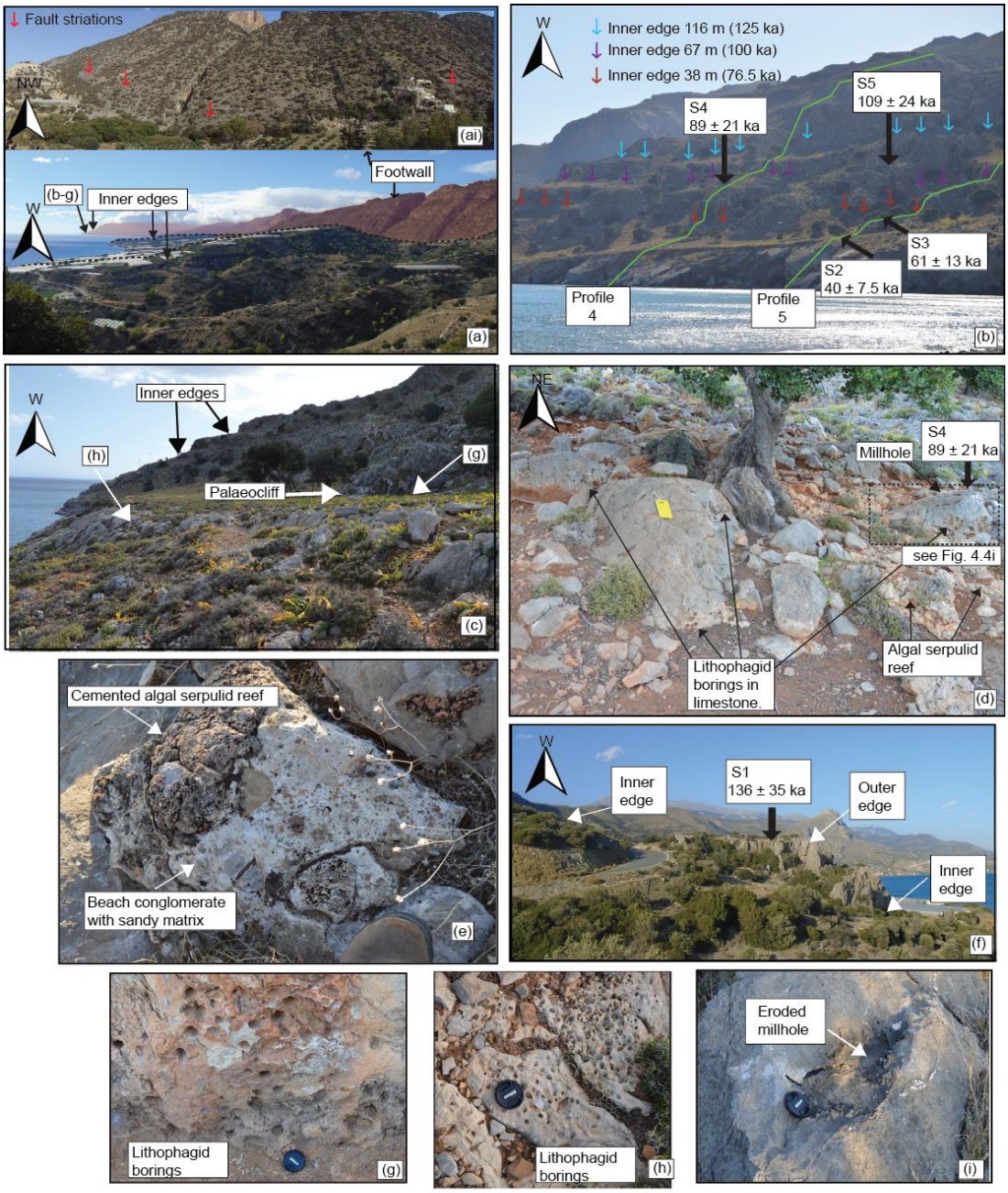

Figure 4.6: Field photographs (see Fig. 4.4 for locations). (a) Photograph of hangingwall terraces cut into Miocene sediments against the limestone fault scarp and footwall; (ai) shows a close-up of the slot gorge near to Arvi (Fig 4.4, Profile 14) with visible bedrock scarps identified by red arrows. (b) Overview of the Profiles 4 and 5 areas and the locations of ^{36}Cl samples S2–S5. Arrows show the palaeoshorelines of the 76.5-, 100-, and 125-ka highstands based on the age results obtained herein. (c) Profile 4, lower terrace (76.5 ka). Lithophagid borings are visible on the limestone outer edge (h). (d) Detailed view of the S4 sample site at 60 m on Profile 4; lithophagid borings in limestone are clear and remains of a serpulid algal reef surround part of the limestone. (e) Profile 10 at 43-m contact between algal serpulid reef and beach conglomerate both deposited during the 125-ka highstand allocated to this elevation. (f) Overview Profile 10 palaeoshoreline at 54 m and associated wave-cut platform; ^{36}Cl sample S1 was removed from this location. (g and h) Lithophagid borings along Profile 4 (i). Profile 10 at 43 m, an eroded millhole cut into limestone within 1 m of the sampling location for S1. (From Robertson et al., 2019)

Fault scarps belonging to the SCCF are clear in the field (Fig. 4.6a, ai) and on the DEM (Fig. 4.4c and 4.4e) separating the hangingwall marine sediments from uplifted basement rocks.

Specifically, fault scarps in the field were observed from the western extreme of the fault before it moves offshore and throughout most of the field area along Profiles 6, 7, 8, 11, 12, 14, 15, 16, and 17 (Fig. 4.4), which coincides with the presence of scarps comprising Mesozoic limestones (IGME map sheet Ano Viannos 1:50,000). In places kinematic indicators such as fault striations are present on the bedrock scarps, with excellent preservation of these in the centre of the SCCF (Fig 4.6ai). Along the remaining profiles, the fault is less apparent in the landscape, probably because of the limited preservation potential within the flysch and ophiolitic lithologies that comprise some of the footwall area (Profiles 9, 10, 13) (IGME map sheet Ano Viannos 1:50,000). The fault offsets steadily increase from the western part of the SCCF, where a fault offset of ~87 m can be measured using the DEM, to centre of the fault which displays an offset of ~290 m.

In summary, the palaeoshorelines were mapped and their elevations measured from the DEM and during field campaigns alongside observations made on visible fault scarps. In addition to the existing age controls from Gallen et al. (2014), five absolute ages from ^{36}Cl exposure dating place further constraints on the ages of the palaeoshorelines – these are discussed below.

4.4.2 ^{36}Cl exposure dating results

Absolute dating of the wave-cut platforms was carried out using ^{36}Cl exposure dating. Five localities were sampled; the geomorphology of each sample location is detailed in Table 4.1 and shown in Figures 4.5b and d. The ^{36}Cl exposure age values for each sample are reported along with their external errors in Figure 4.7a and Table 4.2 (see Appendix 1 for all input data used to obtain ^{36}Cl exposure ages). Age results suggest that four of the five ^{36}Cl determinations provide exposure ages that can be assigned to sea-level highstands, whereas the fifth was probably covered by sediment at some point and a complex exposure-covering re-exposure history results in an anomalously low ^{36}Cl concentration. The four exposure ages assigned to sea level highstands are S1, 134 ± 33 kyr; S3, 61 ± 13 kyr; S4, 88 ± 21 kyr; and S5, 108 ± 24 kyr. The fifth ^{36}Cl determination, S2, implies an exposure age of 40 ± 7.5 kyr, but this age is rejected because (a) there is no clear sea level highstand at this time on the sea level curve (Fig. 4.6b) and (b) re-examination of field photographs shows that the sample was taken close to syn-wave-cut platform sediments dated by Gallen et al. (2014) as 78 ± 8 ka using OSL, and it is now suspected that the sample was covered by this sediment before erosion (Fig. 4.4h), producing a low ^{36}Cl concentration and hence age.

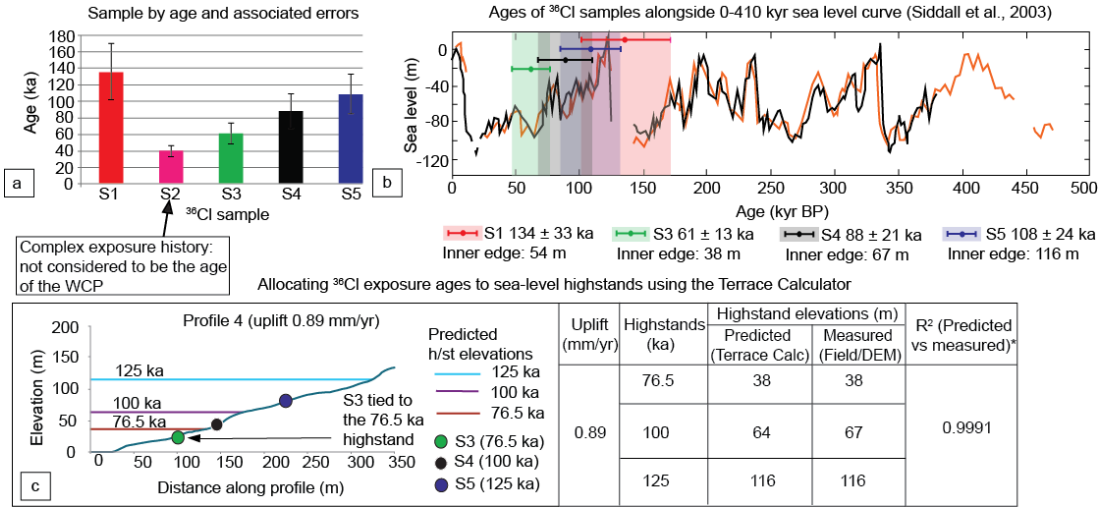

Uplift (mm/yr)	Highstands (ka)	Highstand elevations (m)		R^2 (Predicted vs measured)*
		Predicted (Terrace Calc)	Measured (Field/DEM)	
0.89	76.5	38	38	0.9991
	100	64	67	
	125	116	116	

Figure 4.7: (a) ^{36}Cl sample ages and associated errors. (b) Ages and errors plotted onto the Siddall et al. (2003) sea level curve; the two lines represent two cores used in their study. (c) Preferred uplift scenario of 0.89 mm/yr on Profile 4 achieved by tying S3 to the 76.5-ka highstand. Note that while only the allocation to highstands 76.5, 100, and 125 ka are shown in (c), matches between measured inner-edge elevations and predicted inner-edge elevations up to 980 ka were carried out (detailed in Fig.4.8). Predicted versus matched elevations were evaluated using R^2 and showed excellent agreement between the predicted and measured datasets (R^2 = 0.9991). (From Robertson et al., 2019)

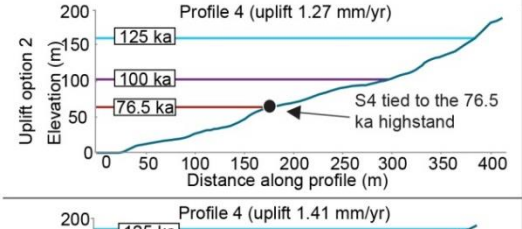

Uplift (mm/yr)	Highstands (ka)	Highstand elevations (m)		R^2 (Predicted vs measured)*
		Predicted	Measured	
1.27	76.5	67	67	
	100	102	No inner-edge here	0.9989
	125	164	No inner-edge here	
1.41	76.5	78	No inner-edge here	
	100	116	116	0.9995
	125	181	No inner-edge here	

* R^2 values are for all measured palaeoshoreline values compared to predicted values (to 980 ka)

Figure 4.8: Alternative 36Cl exposure age allocation scenarios to the preferred scenario in Fig. 4.7c: (a) S4 (palaeoshoreline of 67 m) allocated to 76.5 ka highstand (as opposed to the 100 ka highstand). (b) S5 (palaeoshoreline 116 m) allocated to the 100 ka hi highstand (as opposed to the 125 ka highstand). Note that while only the allocation to highstands 76.5, 100 and 125 ka are shown here, matches between measured palaeoshoreline elevations and predicted palaeoshoreline elevations up to 980 ka were carried out (Table 4.3).

While the value of the uncertainties on the ^{36}Cl exposure age determinations are relatively large compared to other dating techniques (see Section 3.3.3 for further discussion), it is important to note that these are likely to be overestimated when comparing between groups of samples from a single geographic location where the uncertainties are not independent (Marrero et al., 2016a). At first glance the reliability of the ^{36}Cl exposure ages may be

questioned, owing to the uncertainties reported. However, note that Table 4.2 shows that for the samples from close to Tsoutsouros Bay (Figs. 4.4d, 4.7), the concentration of ^{36}Cl atoms/g in the footwall samples (Fig 4.4, S3–S5 from Profiles 4 and 5; Table 4.2) increase with elevation, as would be expected if the rocks were incrementally lifted out of the sea, suggesting a correlation of palaeoshoreline age with elevation. Furthermore, as will be shown below, the ^{36}Cl exposure ages agree with ages obtained using OSL dating and with the expected elevations of palaeoshorelines based upon field observations and modelling. Very precise ages are of less importance when dating palaeoshorelines because their formation occurs over a number of thousands of years; it is, therefore, more important that ages to date palaeoshorelines can be attributed to sea-level highstands.

The wave-cut platforms and associated palaeoshorelines are likely to have been formed during Late-Quaternary sea level highstands, which occurred at 76.5, 100, 125, 175, 200, 240, 310, 340, and 410 ka (Siddall et al., 2003) (Fig. 4.7b); the question is which of these is the highstand for each wave-cut platform? Plotting the exposure ages against the sea level curve shows that samples could be allocated to more than one sea level highstand (Fig. 4.7b): S3 (61 ± 13 ka), inner edge 38 m, could be allocated to the 50- or 76.5-ka highstands; S4 (88 ± 21 ka), inner edge 67 m, could be allocated to the 76.5- or 100-ka highstands; S5 (108 ± 24), inner edge 116 m, could be allocated to the 100- or 125-ka palaeoshoreline; and, S1 (134 ± 33 ka), inner edge 54 m, could be allocated to the 125 ka highstand.

Sample reference (Profile)	Latitude (°)	Longitude (°)	P'shoreline elevation (m) (Sample elevation (m))	Erosion rate (mm/kyr)	Total erosion (mm)	Cl (p.p.m)	±	^{36}Cl (g of rock)	±	CaO (wt%)	±	Age (kyr)	Internal uncertainty (kyr)	Total uncertainty (kyr)
S1 (10)	34.98335	25.34718	54 (43)	0.1	13.4	26.75	0.63	2137936	74973	50.84	1.17	134	0.92	33
S2 (4)	34.98417	25.28201	38 (20)	0.1	4	40.54	1.19	677147	21952	49.45	1.21	40	0.22	7.5
S3 (4)	34.98303	25.27876	38 (34)	0.1	6.1	41.05	1.20	1027505	33320	49.58	1.28	61	0.4	13
S4 (5)	34.98106	25.27817	67 (65)	0.1	8.8	29.49	0.72	1464291	44509	50.15	1.14	88	0.52	21
S5 (5)	34.98207	25.27847	116 (80)	0.1	10.8	33.00	0.87	1770564	53271	48.57	1.21	108	0.66	24

Table 4.2: ^{36}Cl data for samples (from Robertson et al., 2019), see Appendix 1 for all ^{36}Cl exposure data and Section 3.3.3 for detail on internal versus external uncertainties.

Samples S3, S4 and S5 were sampled from close to Tsoutsouros Bay along Profiles 4 and 5 (Figs. 4.4d, 4.5d, 4.6b and 4.7) from three sequentially higher wave-cut platforms with palaeoshorelines at 38 m, 67 m and 116 m, respectively. The palaeoshorelines along Profiles 4 and 5 form a set of continuous palaeoshorelines situated ~50 m apart along strike (Fig. 4.4d and 4.6b). Samples S3, S4 and S5 are interpreted to represent three successive wave-cut platforms, there is no evidence of additional palaeoshorelines existing between these elevations (see Figs. 4.4d and 4.6b). Having identified the possible highstands each sample

might belong to (Fig. 4.7b), all synchronous correlation uplift-rate scenarios were tested (Section 3.2) and revealed that one uplift solution of 0.89 ± 0.09 mm/year results in the allocation of all of the exposure ages and their palaeoshorelines to three sequential highstands, the 76.5, 100, and 125 ka along Profile 4 (Fig. 4.7c). In the uplift solution of 0.89 mm/yr along Profile 4 there were 7 matches between predicted palaeoshoreline elevations and measured palaeoshoreline elevations, these 7 matches resulted in an R^2 of 0.9991 and RMSE of 7.6 suggesting the two datasets were in good agreement (Fig. 4.7c, Table 4.3). In comparison, the results of the other tested scenarios (Figure 4.8, Table 4.3) revealed fewer (3 and 4) matches between predicted and measured palaeoshoreline elevations for highstands up to 980 ka and RMSE of between 8.4 and 12.4. Furthermore, the allocation of the lowest palaeoshoreline to the 76.5-ka highstand is in agreement with the OSL age from syn-wave-cut platform deposits obtained by Gallen et al. (2014) (sample LS1254). However, the two studies do not agree with regard to the palaeoshoreline elevation for this location (27 m from Gallen et al. (2014) and 38 m this study). Approximately 15 m inland from where sample S2 (Fig 4.5d) was removed there is a limestone wall (~3 m high) which displays lithophagid borings and intersects the wave-cut platform at ~27 m, this feature appears to be discontinuous along strike and so was not recognised as a palaeoshoreline in this study. Moreover, the age constraints for this palaeoshoreline support that a wave-cut platform extending from 24 m to 38 m belongs to the 76.5 ka palaeoshoreline, whereby both ^{36}Cl exposure sample S3 (removed from 34 m, up-dip of the limestone wall) and sample LS1254 (removed from 25 m, down-dip of the limestone wall) (Gallen et al., 2014) are linked to the 76.5 ka highstand (Fig. 4.5d).

Exposure age (ka) (Sample ref)	Palaeoshoreline elevation (m)	Highstand age allocation tested (ka)	Uplift (mm/yr)	Number of predicted to measured palaeoshoreline matches	RMSE
61 ± 13 (S3)	38	50	1.95	4	8.41
61 ± 13 (S3)	38	76.5	0.89	7	7.6
88 ± 21 (S4)	67	76.5	1.27	3	11.6
88 ± 21 (S4)	67	100	0.89	7	7.6
109 ± 24 (S5)	116	100	1.41	3	12.4
109 ± 24 (S5)	116	125	0.89	7	7.6

Table 4.3: Results of test to check the allocation of 36Cl exposure ages to highstands along Profile 4.

For ^{36}Cl sample S1, sampled from 43 m along profile 10 in the hangingwall (Fig. 4.4c) (7 km east of samples S2-5), the exposure age of 134 ± 33 suggests that it should be allocated to the 125 highstand, which requires an uplift value of 0.37 mm/year ± 0.09. This is in agreement with the 125-ka OSL age obtained by Gallen et al. (2014) (sample LS1255) for the same palaeoshoreline, located 3 km to the west of sample S1 (Fig. 4.4c). Calculation of the ^{36}Cl exposure ages using CRONUScalc (Section 3.3.3) requires an erosion rate for each sample (Marrero et al., 2016a). Based on the fact that all of these samples are from the same bedrock limestone lithology, with widespread preservation of lithophagid borings that are 6-9 cm centimetres deep when formed (Section 3.3.1) (Devescovi and Iveša, 2008; Peharda et al., 2015) the same erosional rate of 0.1 mm/ka was applied. Over 125 kyrs, ~1.25 cm would be eroded, consistent with the preservation of lithophagid borings; it is accepted that this rate may be marginally higher where total erosion may equal up to 3 cm (based on observations of lithophagid borings), this equates to erosion rates of 0.24 mm/ky for 125- ka aged samples, 0.3 mm/ky for 100- ka samples and 0.39 mm/ky for 76.5- ka aged samples. Application of these slightly higher erosion rates to samples S3 (0.39 mm/ky), S4 (0.3 mm/ky) and S5 (0.24 mm/ky) in CRONUScalc only changes the ages shown in Fig. 4.7a and Table 4.2 by a maximum of 1 ky.

In summary, with the exception of Sample S2, the ages obtained from ^{36}Cl exposure dating of the bedrock wave-cut platforms are indicative of Late-Quaternary highstand ages and in agreement with the elevations expected obtained from synchronous correlation; furthermore, they are in agreement with all existing OSL ages from Gallen et al. (2014).

4.4.3 Analysis of uplift rates

Absolute ages in combination with the Terrace Calculator are used to iterate uplift rates to produce a correlation between mapped palaeoshorelines to expected highstand elevations for undated palaeoshorelines. For each topographic profile where the absolute age of a palaeoshoreline is known, the dated palaeoshoreline is used to obtain the uplift rate within the Terrace Calculator, which is then applied to the entire topographic profile. This results in a set of predicted elevations for each highstand, which are then matched to measured palaeoshoreline elevations (see Sections 2.1.5 and 3.2 for more detail). An outcome of this correlation is that measured palaeoshorelines are allocated to sea-level highstands, with an uplift rate produced for each of the 17 topographic profiles (Fig. 4.9, Table 4.4). The goodness of fit between predicted and measured palaeoshorelines is examined using R^2 and RMSE (Fig. 4.10, Table 4.4). The results of correlation and uplift rates through time obtained here are discussed within the context of those from Gallen et al. (2014); plots of the palaeoshoreline age versus elevation are used to examine the temporal behaviour of the uplift rate for each of the profiles (Fig. 4.11).

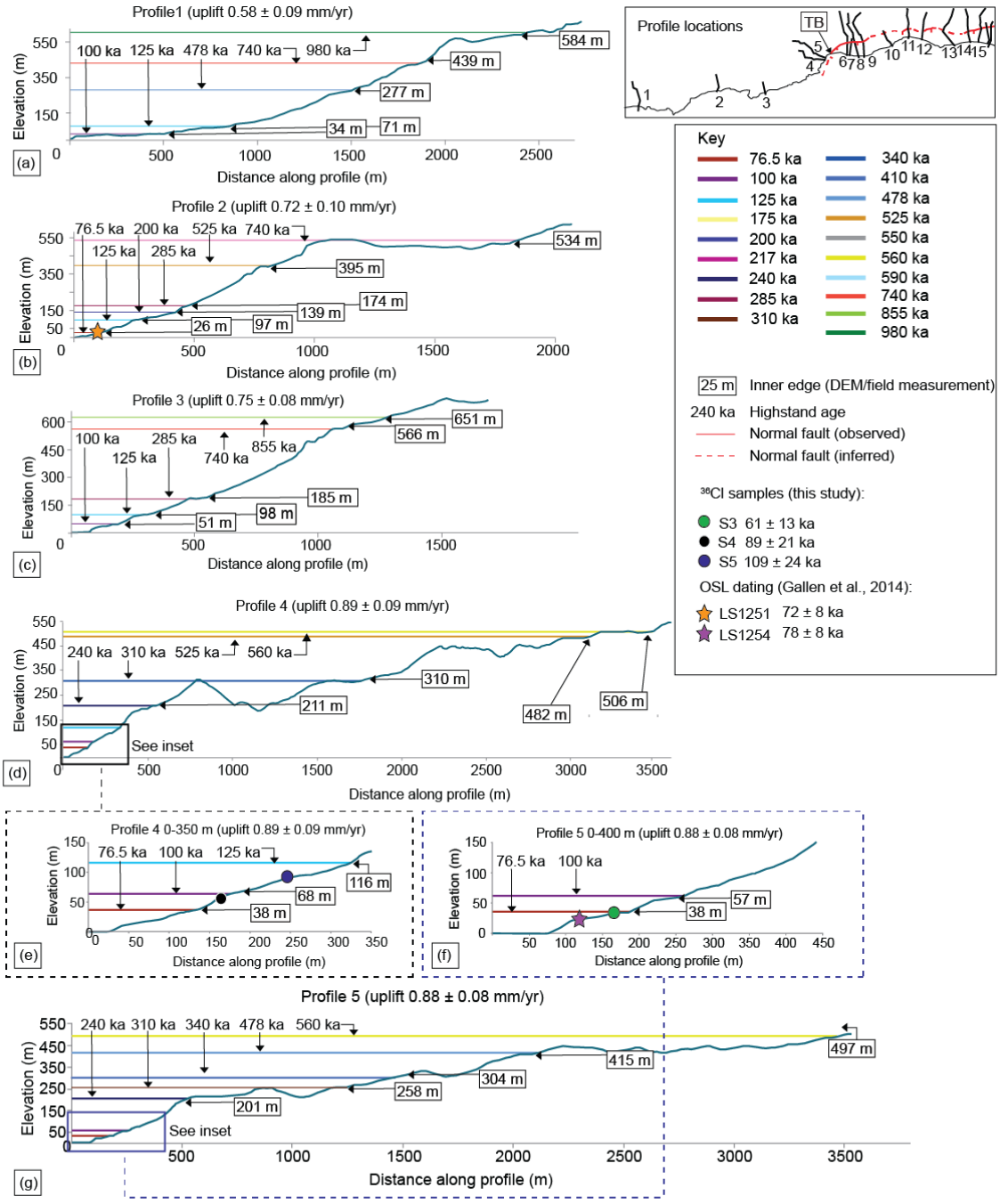
Profile1 (uplift 0.58 ± 0.09 mm/yr)
100 ka 125 ka 478 ka 740 ka 980 ka
584 m
439 m
277 m
34 m
71 m
(a)
Elevation (m)
Distance along profile (m)
Profile 2 (uplift 0.72 ± 0.10 mm/yr)
76.5 ka 200 ka 525 ka 740 ka
125 ka 285 ka
534 m
395 m
174 m
139 m
26 m
97 m
(b)
Profile 3 (uplift 0.75 ± 0.08 mm/yr)
100 ka 285 ka 855 ka
125 ka 740 ka
651 m
566 m
185 m
98 m
51 m
(c)
Profile 4 (uplift 0.89 ± 0.09 mm/yr)
240 ka 310 ka 525 ka 560 ka
310 m
211 m
482 m
506 m
See inset
(d)
Profile 4 0-350 m (uplift 0.89 ± 0.09 mm/yr)
76.5 ka 100 ka 125 ka
116 m
68 m
38 m
(e)
Profile 5 0-400 m (uplift 0.88 ± 0.08 mm/yr)
76.5 ka 100 ka
57 m
38 m
(f)
Profile 5 (uplift 0.88 ± 0.08 mm/yr)
240 ka 310 ka 340 ka 478 ka 560 ka
497 m
415 m
304 m
258 m
201 m
See inset
(g)
Profile locations
TB
Key
76.5 ka
100 ka
125 ka
175 ka
200 ka
217 ka
240 ka
285 ka
310 ka
340 ka
410 ka
478 ka
525 ka
550 ka
560 ka
590 ka
740 ka
855 ka
980 ka
25 m Inner edge (DEM/field measurement)
240 ka Highstand age
Normal fault (observed)
Normal fault (inferred)
36Cl samples (this study):
S3 61 ± 13 ka
S4 89 ± 21 ka
S5 109 ± 24 ka
OSL dating (Gallen et al., 2014):
LS1251 72 ± 8 ka
LS1254 78 ± 8 ka

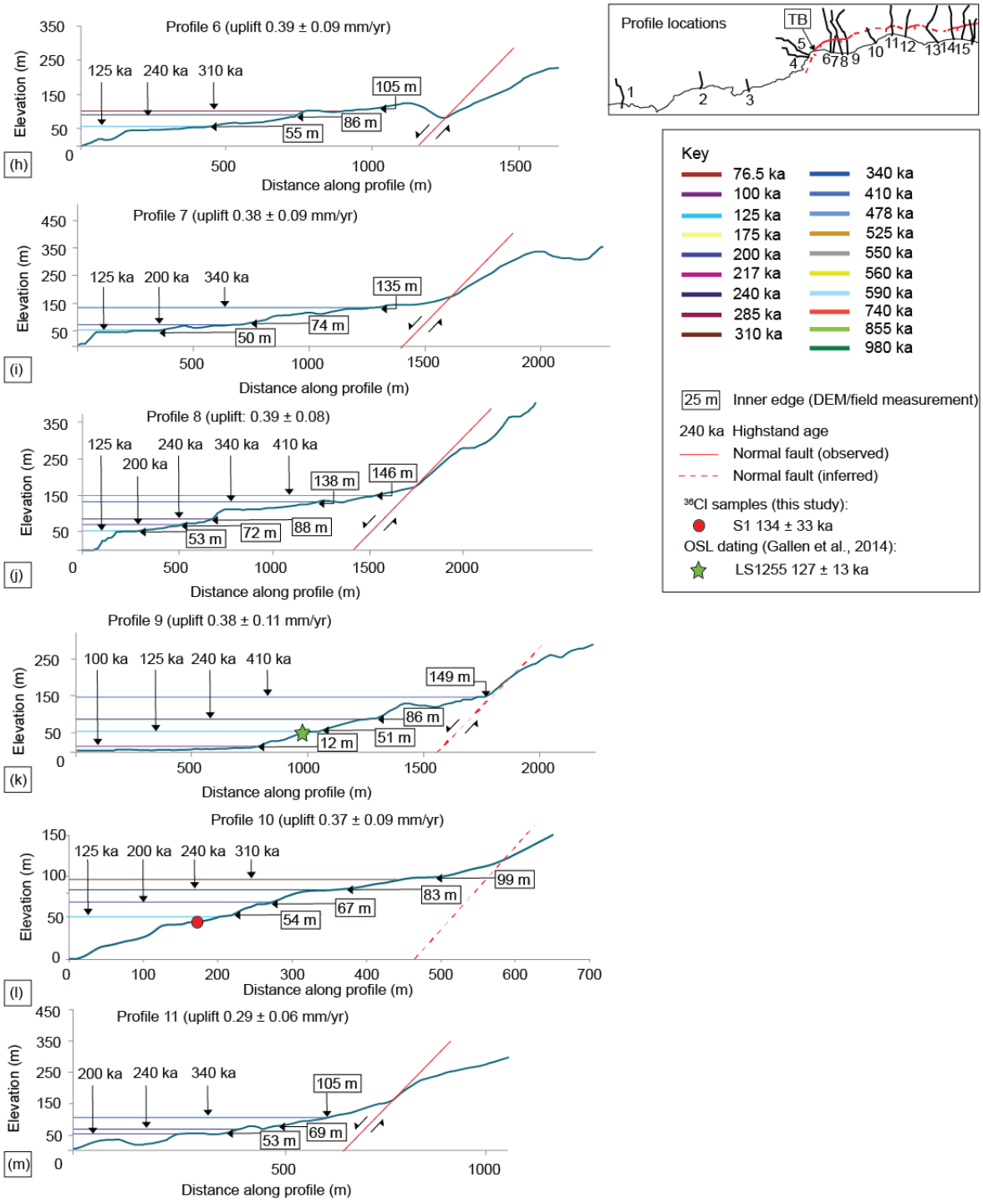
Profile 6 (uplift 0.39 ± 0.09 mm/yr)
125 ka 240 ka 310 ka
105 m
86 m
55 m
(h)
Profile 7 (uplift 0.38 ± 0.09 mm/yr)
125 ka 200 ka 340 ka
135 m
74 m
50 m
(i)
Profile 8 (uplift: 0.39 ± 0.08)
125 ka 200 ka 240 ka 340 ka 410 ka
138 m
146 m
88 m
72 m
53 m
(j)
Profile 9 (uplift 0.38 ± 0.11 mm/yr)
100 ka 125 ka 240 ka 410 ka
149 m
86 m
51 m
12 m
(k)
Profile 10 (uplift 0.37 ± 0.09 mm/yr)
125 ka 200 ka 240 ka 310 ka
99 m
83 m
67 m
54 m
(l)
Profile 11 (uplift 0.29 ± 0.06 mm/yr)
200 ka 240 ka 340 ka
105 m
69 m
53 m
(m)
Elevation (m)
Distance along profile (m)
Profile locations
TB
Key
76.5 ka
100 ka
125 ka
175 ka
200 ka
217 ka
240 ka
285 ka
310 ka
340 ka
410 ka
478 ka
525 ka
550 ka
560 ka
590 ka
740 ka
855 ka
980 ka
25 m Inner edge (DEM/field measurement)
240 ka Highstand age
Normal fault (observed)
Normal fault (inferred)
36Cl samples (this study):
S1 134 ± 33 ka
OSL dating (Gallen et al., 2014):
LS1255 127 ± 13 ka

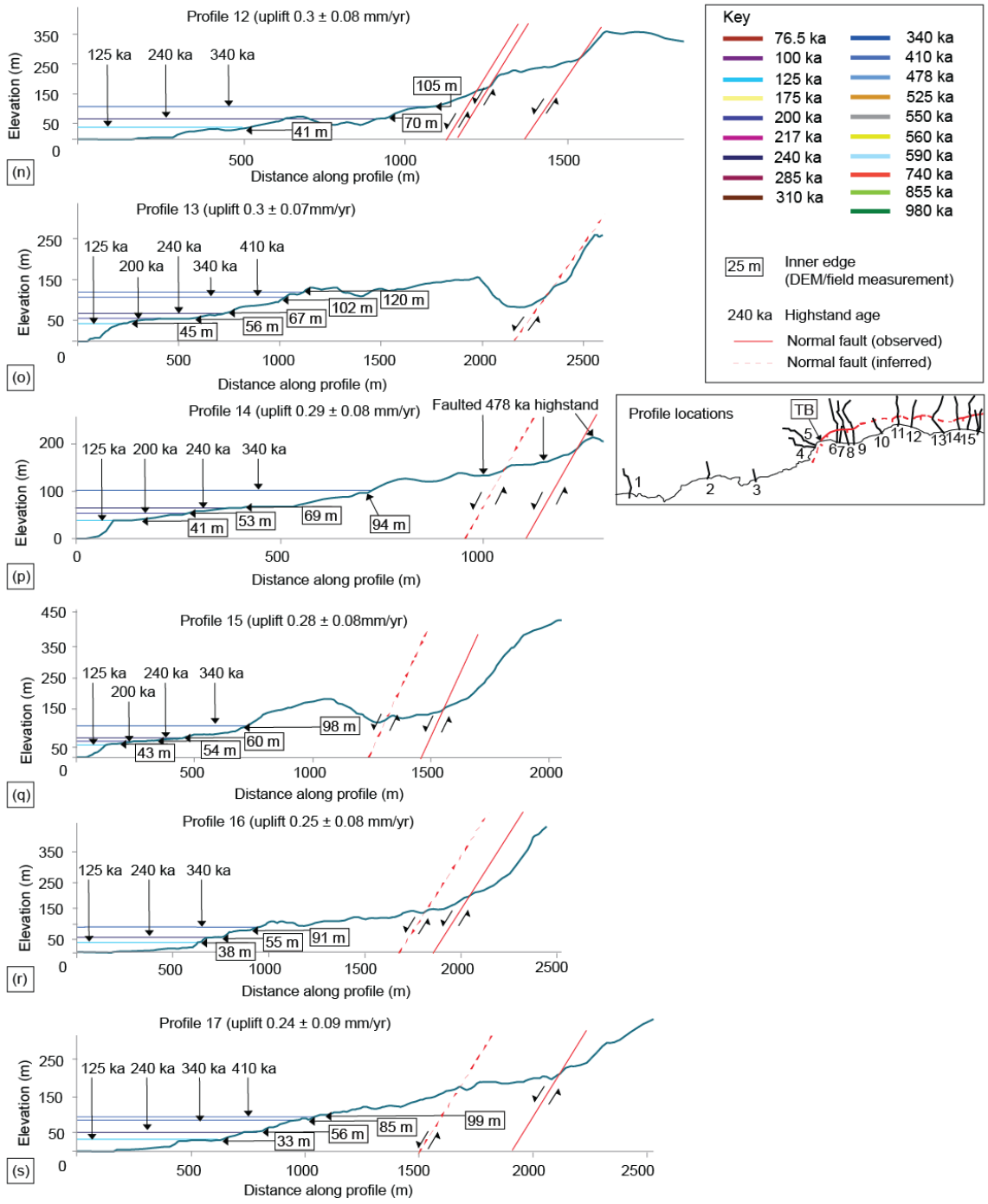

Figure 4.9: Topographic profiles for all profile lines, which run perpendicular to the strike of the SCCF (see Fig. 4.4 for locations of profile lines) obtained from 5-m DEMs. Measured (DEM or field) palaeoshoreline elevations are matched against highstand elevations predicted by the Terrace Calculator given an iterated uplift value (Section 3.2). Locations of ^{36}Cl-dated samples (this study) and OSL-dated samples (Gallen et al., 2014) are shown alongside the ages obtained. Detailed topographic profiles are shown for 0–400 m for Profiles 5 (f) and 4 (e). See text for an explanation of along-strike correlation between palaeoshorelines. Panels (a–g) show profiles in the footwall of an offshore fault; panels (h–s) are in the hangingwall of the SCCF onshore fault (from Robertson et al., 2019).

In general, palaeoshorelines are at the elevations expected given the preferred uplift rate scenarios. The most prominent highstands on the sea level curve (125, 200, 240, and 340 ka) predominantly fall on clear geomorphic palaeoshorelines on the topographic profiles, and

other more-subtle sea level highstands (e.g. 76.5 and 410 ka) are also matched to observed palaeoshorelines. Cross-plots of all measured palaeoshoreline elevations against predicted inner-edge elevations from the Terrace Calculator (Fig. 4.10) show an R^2 value of 0.9996; while R^2 and RMSE analysis for each topographic profile are indicative of excellent correlation (Table 4.4). These values confirm that the fits between highstands and palaeoshorelines are good, giving confidence to the uplift rates. The correlations shown in Figs. 4.9, 4.10 and Table 4.4 show that constant uplift rates through time produce excellent fits between measured and predicted palaeoshoreline elevations, along all topographic profiles.

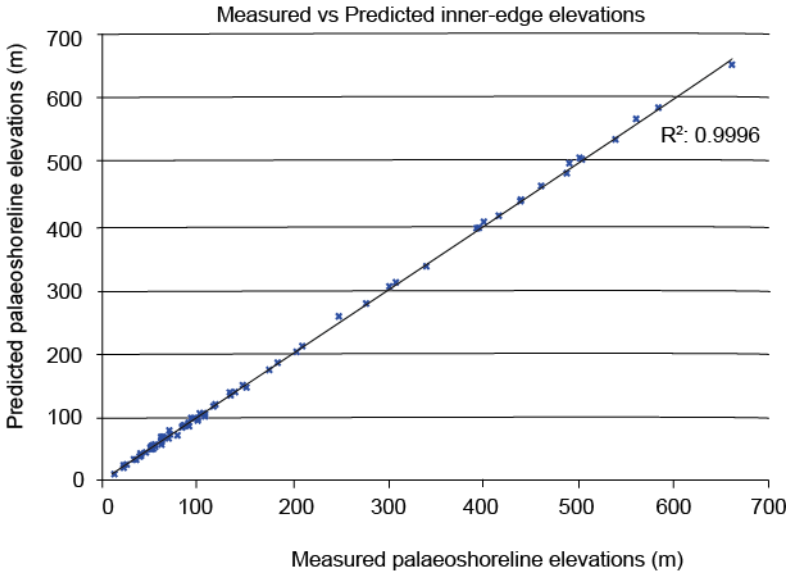

Figure 4.10: Measured (DEM and field) versus predicted palaeoshoreline elevations from the Terrace Calculator; error values are small and contained within the size of the symbols, which represent each data point (from Robertson et al., 2019).

Profile reference	Uplift (mm/yr)	RMSE and R^2	UTM of altimeter msmts		Allocated highstand age (ka)	Predicted palaeoshoreline elevations (m)	DEM palaeoshoreline elevations (this study) (m)	Barometric altimeter palaeoshoreline elevations (this study) (m)	Gallen et al. (2014) profile ref	Measured palaeoshoreline elevations (Gallen et al, 2014) (m)
			Easting	Northing						
1	0.58 ± 0.09	9.01 0.9998			76.5	14			7	13
					100	33	34			
					125	78	71			
					478	277	277			
					740	439	439			
					980	584	584			
2	0.72 ± 0.10	4.71 1			76.5	25	26		8	**25**
					125	95	97			96
					200	139	139			
					285	175	174			
					525	395	395			
					740	538	534			
3	0.75 ± 0.08	7.75 0.996			76.5	27			9	30
					100	50	51			65
					125	99	98			103
					285	184	185			
					740	560	566			
					855	661	651			
4	0.89 ± 0.09	7.63 0.9997			76.5	38	38		10	**27**
			342710	3872265	100	64	**68**	67		62
					125	116	**116**			97
					200	173				140
					240	209	211			
					285	224				166
					340	308	310			210
					410	360				251
					525	487	482			
					560	501	506			
5	0.88 ± 0.08	12.56 0.999	342882	3872461	76.5	38	38	**38**	NA	
					100	62	57			
					115	70	79			
					240	204	201			
					310	248	258			
					340	301	304			
					478	416	415			
					560	490	497			
6	0.39 ± 0.09	4.55 0.9745			125	55	55		11	50
					200	75				65
					240	91	86			
					340	102	105			103
7	0.38 ± 0.09	2.7 0.9963			125	53	50		NA	
			345779	3873003	200	71	72	74		
			345763	3873855	340	134	134	136		
8	0.39 ± 0.08	4.23 0.9939			125	53	53		NA	
					200	71	72			
					240	86	88			
					340	134	138			
					410	151	146			
9	0.38 ± 0.11	3.04 0.9995	347082	3873046	100	12	11	12	12	
					115	22	25			
					125	51	51			**50**
					200	69				70
					240	84	86			
					340	131				105
					410	147	149			
10	0.37 ± 0.09	4.51 0.9886			115	22	22		NA	
			349877	3873397	125	51	54	**54**		
					200	69	67			
					240	84	83			
					310	93	99			
11	0.29 ± 0.06	2.92 1			200	55	53		NA	
			352204	3874596	240	67		69		
			352238	3874670	340	107	104	105		
12	0.3 ± 0.08	2.12 0.9943	353581	3874152	125	43		41	13	42
					200	55				55
			353707	3874364	240	67	69	70		
			353789	3874574	340	105	106	105		92
13	0.3 ±0.07	6.52 0.9929	356636	3873273	125	45	45	45	14	45
			356352	3873458	200	55	55	56		61
			355492	3873344	240	67	67	68		
					340	107	102			114
					410	118	120			
14	0.29 ± 0.08	6.42 0.9692	358624	3873366	125	40	40	41	15	1
			358618	3873493	200	51	53	53		39
					240	62	69			
					340	100	94			50
15	0.28 ± 0.08	4.9 0.9944			125	40	43		NA	
					200	51	54			
					240	62	60			
					340	100	98			
16	0.25 ± 0.08	1.84 0.9988	360348	3873126	125	36		38	NA	
			359983	3873325	240	55	57	55		
					340	90	91			
17	0.24 ± 0.09	6.72 0.9853			125	35	33		16	2
					200	43				40
			361216	3872978	240	53	55	56		
			361280	3873130	340	87		85		59
					410	93	99			

Table 4.4: Predicted and measured palaeoshoreline elevation data from this study and Gallen et al. (2014) for 17 profiles (see Fig. 4.4). All easting and northing references are in zone 34S. Bold numbers refer to palaeoshoreline elevations with age constraints from this study or Gallen et all. (2014). (From Robertson et al., 2019)

The constant uplift rate finding presented above contrasts with the interpretation from Gallen et al. (2014) who suggest uplift rates increased through time. The contrast in temporal uplift rate explanations between Gallen et al. (2014) and those in this chapter may be due to differences between the two studies. Specifically: (i) where there is variation between the palaeoshoreline elevations measured in each study; (ii) the application of different correlation methods; and (iii) as a consequence of the use of different sea-level curve data. Each of these factors is discussed in turn below.

Analysis of the measured palaeoshoreline elevations in this chapter compared to Gallen et al. (2014) shows that 50% of measurements from this study are within ±7 m of those from Gallen et al. (2014), suggesting generally good agreement between the measured palaeoshoreline elevations of the two studies. Gallen et al. (2014) used differential GPS to measure palaeoshoreline elevations, and reported uncertainties of 0.1–4 m; these values are within the same magnitude as those obtained from palaeoshoreline elevations within this study of 1–4 m, suggesting that variation of measurements between the two studies are unlikely to be as a result of the methods used to obtain elevations. Where possible, palaeoshoreline elevation measurements were taken from along the same profiles as Gallen et al. (2014); however, this was challenging because the longitude and latitude of all palaeoshoreline elevation measurements made by Gallen et al. (2014) were not published, only of the lowest elevation within a profile. Therefore, elevation variations are plausible throughout the study area depending on exactly where the palaeoshorelines were measured. Furthermore, it is possible that identification of the palaeoshorelines cut into the softer, less lithified hangingwall sediments may be open to different interpretations leading to varying measurements of palaeoshoreline elevations.

There are significant differences between the sequential correlation approach employed by Gallen et al. (2014) and synchronous correlation applied in this chapter (Section 2.1.5). As an overview, sequential correlation involves the allocation of undated palaeoshorelines to sea-level highstands based on the relative position of the undated palaeoshorelines to one where the palaeoshoreline age is known. This method does not take into account the potential for younger highstands to overprint and destroy older palaeoshorelines, so at low uplift rates it is possible that correlation between palaeoshorelines and highstands may be in error. The major consequence of the sequential approach is that uplift rates are calculated for each palaeoshoreline within a topographic profile. Any incorrect allocation between palaeoshorelines to highstands may result in an apparent variation between uplift rates

along one topographic profile, which could be erroneous. Comparison of the palaeoshoreline to highstand correlations made by Gallen et al. (2014) to those in this chapter can be carried out along ten topographic profiles that are taken from the same (or close to) locations as those in Gallen et al. (2014) (Fig. 4.3a, Table 4.4). Comparing the palaeoshoreline to highstand correlations along these 10 profiles shows differing highstand to palaeoshoreline correlations on seven of the topographic profiles (Table 4.4) alongside some variation between the measured palaeoshoreline elevations. In detail, differing correlations are particularly visible along Profiles 4, 14, and 17. Specifically, along Profile 4 the 125-, 200-, 285-, 340-, and 410-ka highstands are allocated to palaeoshoreline elevations at 116, 173, 224, 310, and 360 m. Along the same profile, Gallen et al. (2014) allocated the following palaeoshoreline elevations to the same highstands, respectively, 97, 140, 166, 210, and 251 m. For Profile 14, the 125-, 200-, and 340- ka palaeoshorelines are placed at 41, 53, and 94 m, respectively, while Gallen et al. (2014) have the same palaeoshoreline ages allocated to palaeoshoreline elevations of 1, 39, and 50 m. There is a similar pattern along Profile 17 where the 125-, 200, and 340-ka highstands are allocated to 33, 43, and 85 m and Gallen et al. (2014) suggest the same highstands are at 2, 40, and 59 m. For Profiles 9, 12 and 13 the variation between the two studies is apparent for older highstand allocations and may be related to the different correlation methods in combination with a lack of agreement of the elevation of higher palaeoshorelines between the two studies (Table 4.4). Specifically, for Profile 13, Gallen et al. (2014) allocates their 114 m palaeoshoreline to the 340 ka highstand, in comparison to the 410 ka highstand allocation made using synchronous correlation. For Profiles 9 and 12 the elevations of highest palaeoshorelines observed by Gallen et al. (2014) do not agree with any of those observed along the respective topographic profiles herein. To summarise, the result of this comparison identifies some variation between the two studies that is caused by differing palaeoshoreline elevation measurements, however it is also observed that differences in the allocation of undated palaeoshorelines are more apparent in the eastern section of the research area (Profiles 6-17), suggesting that the effect of the application of sequential versus synchronous correlation are apparent where low uplift rates dominate toward the centre of the SCCF hangingwall SCCF (eastern section of the research area, Fig. 4.4).

It is also plausible that the use of different sea level curves for 0–450 ka between the two studies (Siddall et al., 2003, for this study; Lambeck & Chappell, 2001, for 0–125 ka; and Waelbroeck et al. 2002, for 125–410 ka; Gallen et al., 2014) has an impact on the differing uplift scenarios. For instance, comparing the sea-level elevations between Siddall et al.

(2003) and Lambeck and Chappell (2001) shows significant differences between the two sea-level curves (relative to today) for the 76.5 ka and 100 ka highstands, where Siddall et al. (2003) proposed elevations of -30 m and -25 m, respectively, compared to the -50 m and -41 m elevations, respectively, of Lambeck and Chappell (2001). The effect of these varying relative sea-level elevations is that any uplift rates calculated using Lambeck and Chappell (2001) will be comparatively higher for the 76.5 and 100 ka highstands than those of Siddall et al. (2003) (this is shown in a worked example in Table 4.5). This is because uplift rate is calculated using the total uplift (TU) since formation and the age (A) of the highstand in question, where TU is calculated using the elevation of the sea-level highstand relative to today (*HE*) and the present day elevation of the palaeoshoreline (*PE*):

$Uplift\ rate = \frac{TU}{A}$ where $TU = HE + PE$

Measured palaeoshoreline elevation (m) (from Profile 9 of Gallen et al. (2014))	Siddall et al. (2003) Highstand (ky)	Siddall et al. (2003) Sea-level relative to today (mm)	Uplift rate (mm/yr) using Siddall et al. (2003)	Lambeck & Chappell (2001) Highstand (ky)	Lambeck & Chappell (2001) Sea-level relative to today (mm)	Uplift rate (mm/yr) using Lambeck & Chappell (2001)
30	76.5	-30000	0.78	77	-50000	1.04
65	100	-25000	0.9	100	-41000	1.06
103	125	5000	0.78	119	4000	0.83

Table 4.5: Comparison of the uplift rates derived from sea-level curves of Siddall et al. (2003) and Lambeck and Chappell (2001) using elevation data from Profile 9 of Gallen et al. (2014) (Profile 3 in this study, Fig. 4.3a).

Considering that the sea-level curve of Waelbroeck et al. (2002) is applied in Gallen et al. (2014) after 125 ka, comparison between Siddall et al. (2003) and Waelbroeck et al. (2002) is also necessary (Table 4.6). This comparison is examined for an uplift scenario in the hangingwall of the SCCF (Profile 12 in Gallen et al. (2014), Profile 9 in this study) and shows that sea-level elevations between the two studies are broadly similar and that the values of calculated uplift rates do not change too greatly between the application of the different sea-level curves.

Measured palaeoshoreline elevation (m) (from Profile 12 of Gallen et al. (2014))	Siddall et al. (2003) Highstand (ky)	Siddall et al. (2003) Sea-level relative to today (mm)	Uplift rate (mm/yr) using Siddall et al. (2003)	Lambeck & Chappell (2001) /Waelbroeck et al. (2002) Highstand (ky)	Lambeck & Chappell (2001)/ Waelbroeck et al. (2002) Sea-level (mm)	Uplift rate (mm/yr) using Lambeck & Chappell (2001)/ Waelbroeck et al. (2002)
50	125	5000	0.36	119 (L&C)	4000	0.39
70	200	-5000	0.38	213 (W)	-3000	0.34
105	340	5000	0.29	331 (W)	4000	0.31

Table 4.6: Comparison of the uplift rates derived from sea-level curves of Siddall et al. (2003) and Lambeck and Chappell (2001) (L&C)/Waelbroeck et al. (2002) (W) using elevation data from Profile 12 of Gallen et al. (2014) (Profile 9 in this study, Fig. 4.3a).

From the analysis in Tables 4.5 and 4.6, it is possible to summarise that where uplift rates in the research area are higher (such as along Profiles 1-5 (Table 4.5) in the western section (Fig. 4.4a)), the application of Lambeck and Chappell (2001) to calculate uplift rates on palaeoshorelines younger than 125 ka is expected to be at least partly responsible for the different temporal uplift-rate interpretations. Whereas, in the hangingwall of the SCCF (the eastern section, Fig 4.4a), the effect of the application of Lambeck and Chappell (2001) sea-level data is minimal because low uplift rates mean that the 76.5 ka and 100 ka palaeoshorelines are rarely, if at all, preserved and uplift rate calculations using Waelbroeck et al. (2002) are similar to those from Siddall et al. (2003). This brief analysis inspired a detailed examination of the effect of different sea-level curve data on the calculation of uplift rates; this is explored in Chapter 5.

To further explore the constant uplift rate proposed in this chapter, each profile's highstand ages versus measured elevations were plotted (obtained from Table 4.4). Constant uplift rate scenarios would be expected to plot as straight lines (or near straight lines as perfectly-straight lines are not expected due the variations in palaeo-sea level between highstands). These plots result in near-straight lines for all of the 17 profiles, which strongly support temporally constant uplift (Fig 4.11). For the topographic profiles along the western footwall section (Profiles 1–5, Figs 4.11a-e), constant uplift rates are implied to 600 ka and, in the case of Profile 1, up to ~900 ka. Along the hangingwall section (Profiles 6–17, Figs. 4.11f-p), constant uplift rates are implied up to 410 ka. The noticeable kink along on Profile 9 for the 100 ka highstand (Fig. 4.11i) is suggested to be as a result of the measured palaeoshoreline elevation for the 100 ka highstand in soft less-lithified sediments where the original palaeoshoreline elevation may have been slightly eroded.

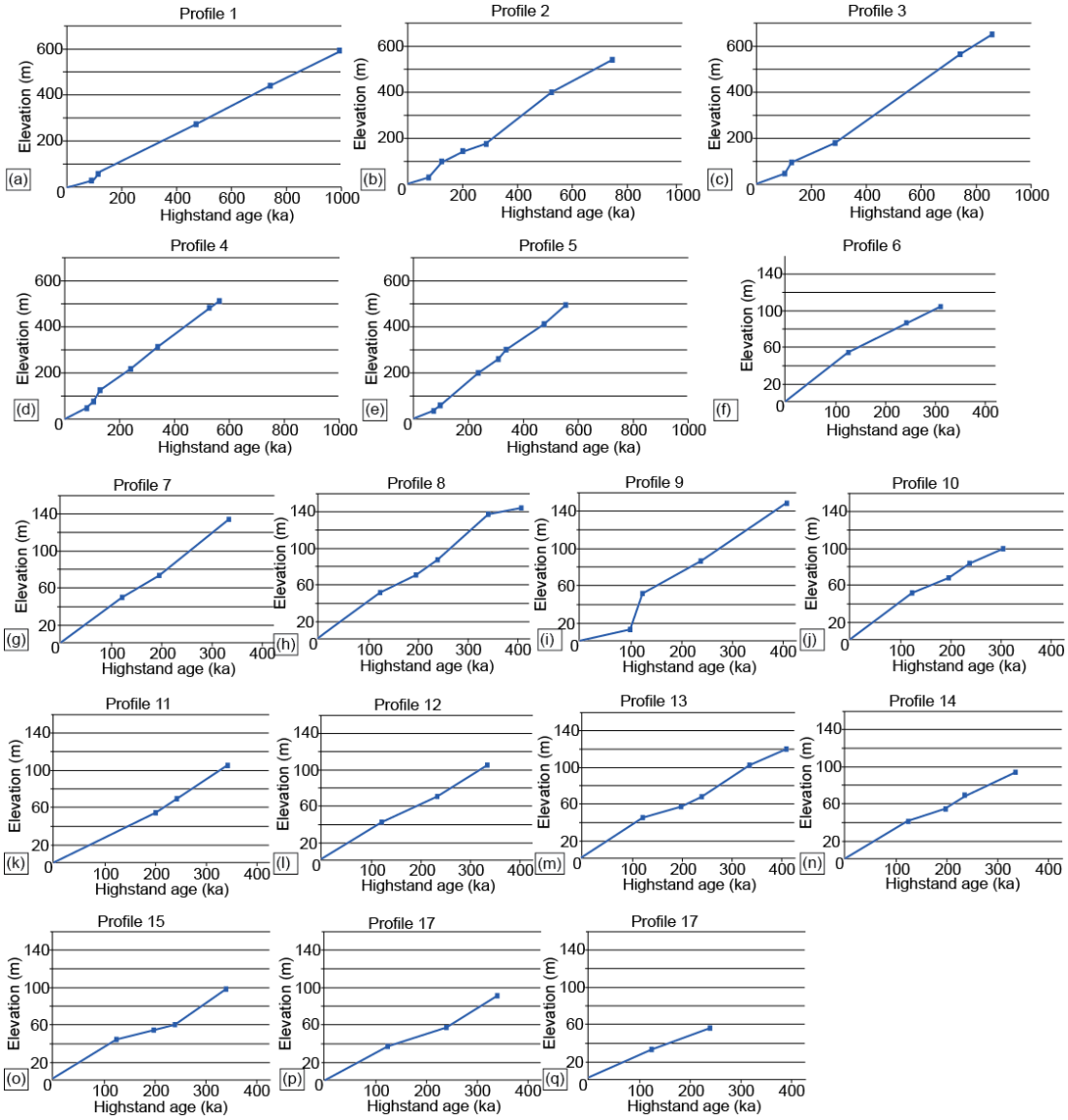

Figure 4.11:(a–q) Elevation of measured inner-edge elevations plotted against highstand age for each topographic profile; elevation error values are small and contained within the size of the symbols, which represent each data point. (From Robertson et al., 2019)

The constant uplift rate interpretation from this chapter is preferred because (a) it is simpler, (b) it identifies geomorphic features that are consistent with both the prominent and less prominent sea level highstands, (c) a greater number of palaeoshoreline elevations using the high-resolution DEM have been mapped and (d) new cosmogenic exposure ages from near to Tsoutsourous Bay (Fig. 4.4) provide age constraints on palaeoshorelines whose elevations

are in agreement with constant uplift rates modelled using the synchronous correlation approach.

4.4.4 Along strike variation of palaeoshoreline elevations and uplift

When the elevations for the palaeoshorelines are plotted along strike across the entire area, the variation in uplift either side of the western tip of the SCCF along the western and eastern sections (Fig. 4.4a) is clearly visible (Fig. 4.12, 4.13, 4.14a, b), also pointed out by Gallen et al. (2014). Palaeoshorelines in the hangingwall of the SCCF along strike (eastern section), east of ~22.5 km (Fig. 4.12) (longitude 25.28°), are relatively low and closely spaced in elevation, while those to the west in the adjacent footwall and beyond the SCCF fault tip (western section) are higher and more widely spaced with elevation.

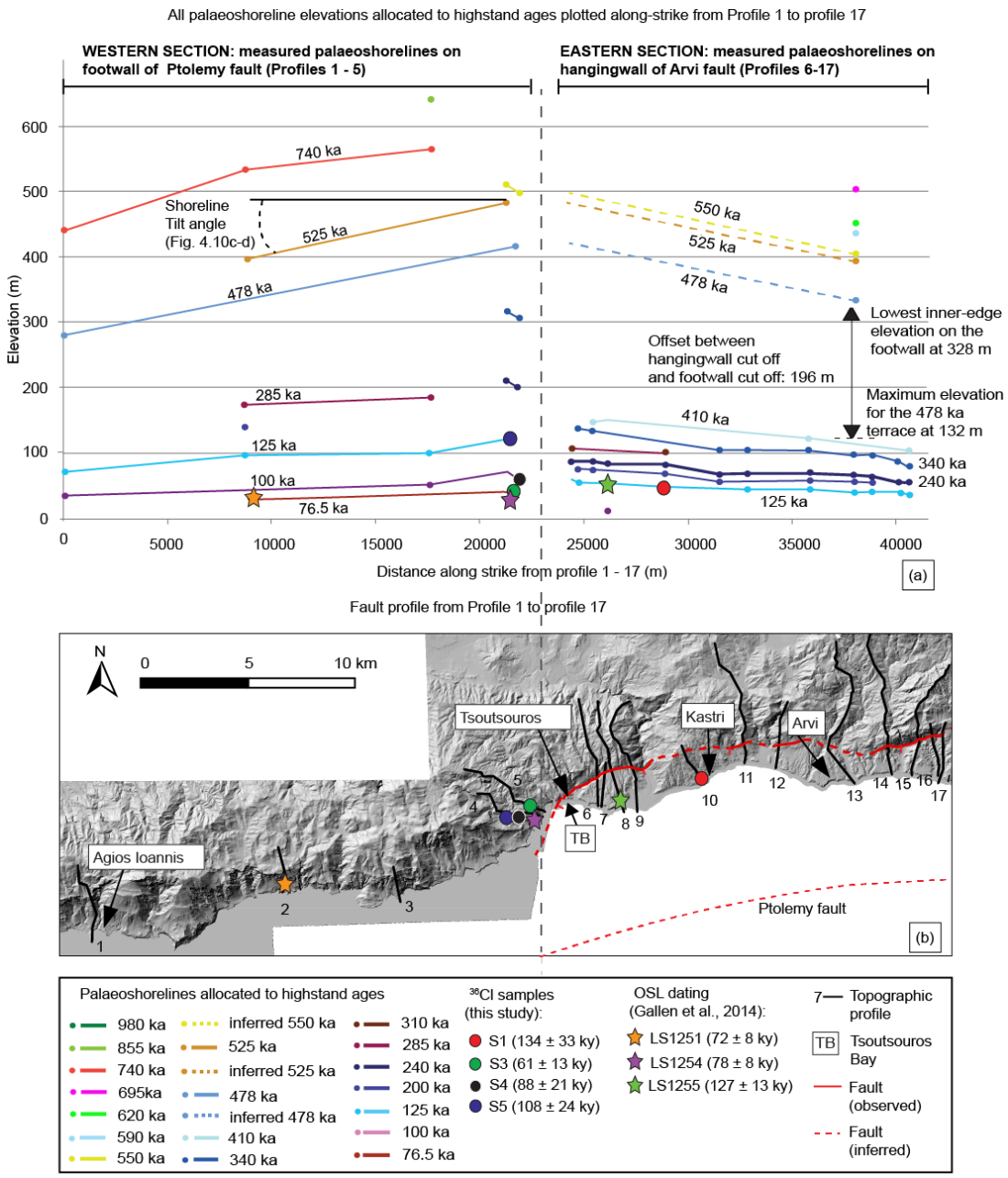

Figure 4.12: (a) Along-strike palaeoshoreline elevations for the western section (footwall of the Ptolemy fault) and eastern section (SCCF hangingwall terraces) (see Fig. 4.4a for locations). Vertical dashed line indicates point at which the curving SCCF fault trace is crossed. (b) Location of the offshore Ptolemy fault and the onshore SCCF with dating locations (this study and Gallen et al., 2014) also marked. FW = footwall; HW = hangingwall; SCCF = South Central Crete Fault; TB = Tsoutsouros Bay. (From Robertson et al., 2019).

Within the western section, elevations, and therefore uplift (Fig. 4.12 and 4.14a), increase across Profiles 1 to 5 (from west to east) where it reaches a peak at 0.89 ± 0.09 mm/year. This pattern of uplift is particularly reliable given that there are age controls at the western and eastern areas within this area (see samples LS1251 and S3 on Figure 4.12a). The spatial variation in the uplift rates along the western section is interpreted as footwall uplift.

For the SCCF, the transition from footwall to hangingwall at TB results in uplift rates decreasing from 0.88 ± 0.08 mm/year (Profile 5) to 0.39 ± 0.08 mm/year (Profile 6; Figs. 4.12, 4.14a, b; Table 4.4). They continue to decrease to the east toward the centre of the SCCF at Profile 17; the lowest palaeoshoreline allocated to the 125-ka highstand decreases in elevation from 55 to 33 m. Uplift rates decrease from 0.39 ± 0.08 to 0.24 ± 0.09 mm/year, with lowest values between Profiles 14 and 17 at the centre of the fault where the displacement, and hence the component of hangingwall subsidence, is presumably at its greatest. This deformation suggests a component of hangingwall subsidence as a result of normal-slip motion of the SCCF, but as the hangingwall terraces are above current sea level, it can be concluded that this area is being uplifted by a background value, perhaps related to the subduction interface, thrust faulting in the wedge above the subduction interface, or offshore upper-plate faults, which exceeds the subsidence value linked to the SCCF.

The variation of uplift rates between the western (Fig. 4.14a) and eastern (Fig. 4.14b) sections is a clear indication that the SCCF has been active in the Late Quaternary because faulting has actively downthrown the hangingwall. One of the geomorphic effects of continued faulting along the SCCF throughout the late Quaternary is that palaeoshorelines in the hangingwall and footwall experience cumulative fault offset in accordance with along-strike fault displacement gradients, where offset is greater in the centre of the fault compared to the tips of the fault. Through time (over hundreds of ka), older palaeoshorelines would therefore experience more deformation. Due to variation in displacement gradients along fault strike, older palaeoshorelines are expected to be more steeply tilted along-strike than younger, lower palaeoshorelines (Section 2.2.2, Figs. 2.19, 2.20). Analysis of the values of tilt for all palaeoshorelines in the western and eastern sections (Fig. 4.4a) are obtained using trigonometry where, for each palaeoshoreline, the along-strike distance from the tip to the centre and the elevation variation of palaeoshorelines from the tip to the centre allow calculation of the angle of dip using the inverse tangent (atan) rule (Fig. 2.20). These data for measured tilt angles are plotted for each palaeoshoreline on the footwall and adjacent hangingwall (Figs. 4.13, 4.14c and d, respectively).

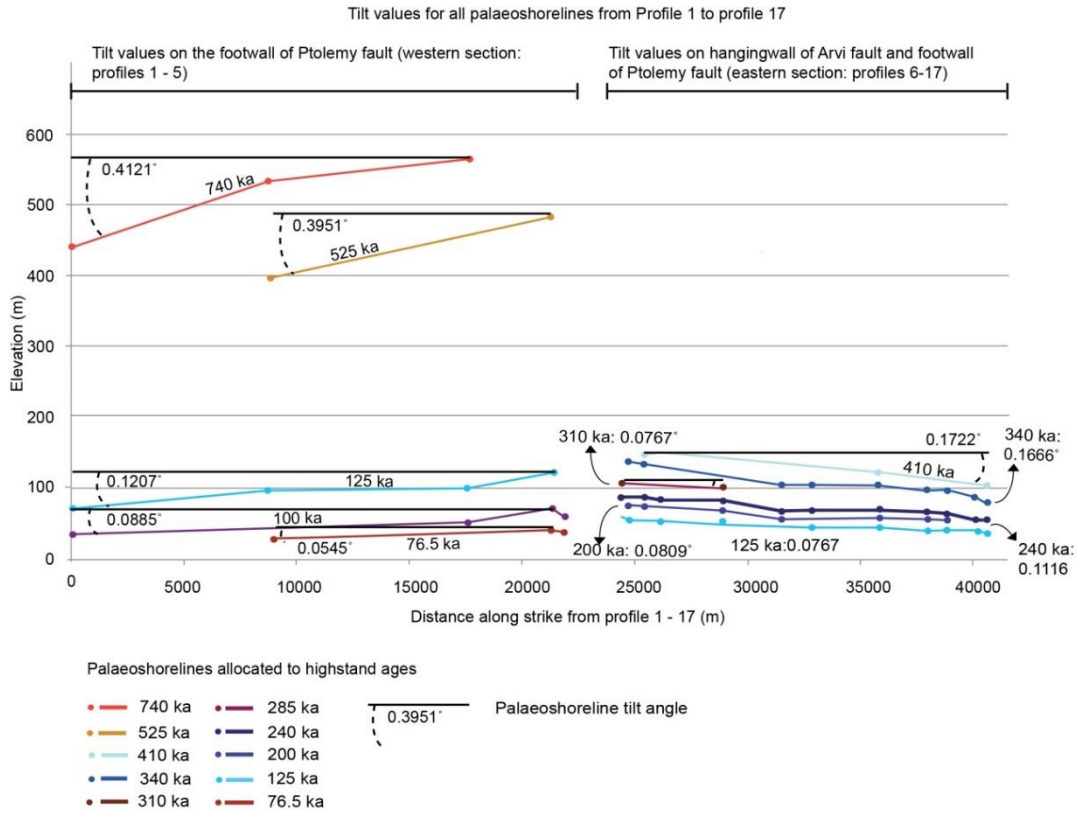

Figure 4.13: Tilt angles for all palaeoshorelines in the (a) footwall and (b) hangingwall. See Section 2.2.2 for an overview of palaeoshoreline tilt angles.

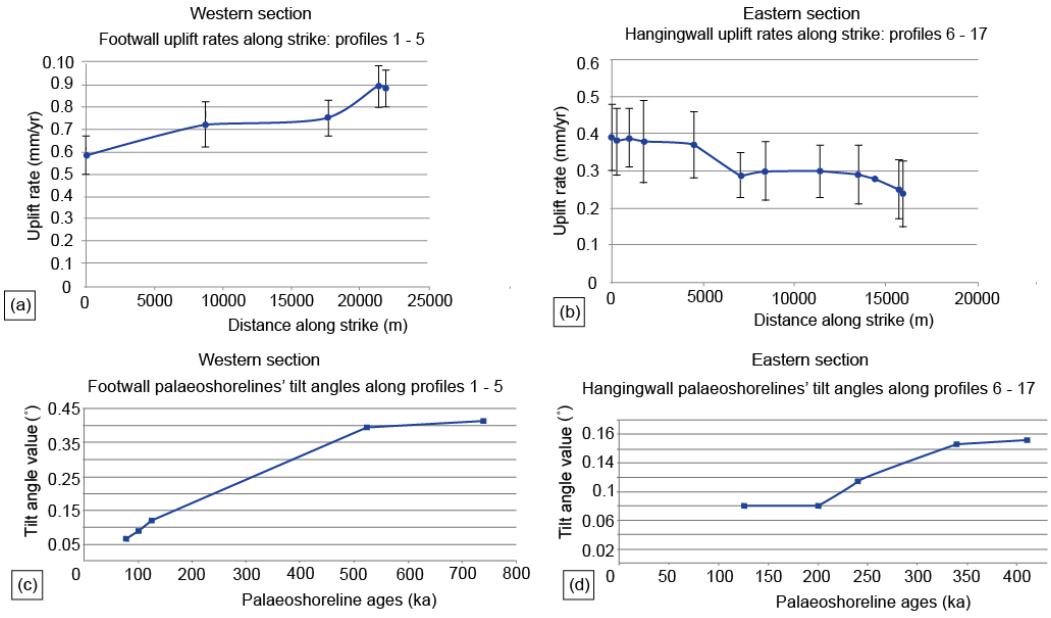

Figure 4.14: (a) Footwall (Profiles 1–5) and (b) hangingwall (Profiles 6-17) uplift along strike. The error bars on (a) and (b) are obtained from propagating the uncertainties as per Section 3.2. (c) Tilt angles of footwall terraces from Profiles 1–4 (tip to the highest point of the fault). (d) Tilt angles of hangingwall terraces from Profiles 6–17 (tip to the lowest point of the fault; see Fig. 13 for actual tilt values). (From Robertson et al., 2019).

The tilt values increase with palaeoshoreline age, suggesting that the older palaeoshorelines have experienced more fault-related deformation (uplift in the case of the footwall (Fig. 4.14c); subsidence, in addition to some uplift component, in the case of the hangingwall (Fig. 4.14d)). Note that the values of tilt observed for the footwall and hangingwall are similar, which is perhaps unexpected given the fact that observations from other normal fault systems suggest the amplitude of deformation tends to be greater in the hangingwall compared to the footwall (Section 2.2.1, Fig. 2.16), with ratios in the order of ~1:2–3 uplift to subsidence (McNeill & Collier, 2004; Papanikolaou, I. et al., 2010). When the hangingwall tilt angles for the SCCF (0.16 along the 340-ka terrace, Fig. 4.14c) are compared to other hangingwall tilt angle values from elsewhere in the Mediterranean: 0.93 and 2.14 along the 340 ka terraces belonging to the Capo D'Orlando fault, Sicily (Meschis et al., 2018), and the Vibo fault, Calabria (Roberts et al., 2013) respectively, the SCCF has anomalously low values (Figs. 4.14, 4.15). As all normal faults ought to have similar displacement gradients (e.g. Schlische et al., 1996), this is unusual. The reasons for variation between these angles is unknown but may relate to fault interaction and/or a difference in slip rates; this topic is explored further in Section 4.5.

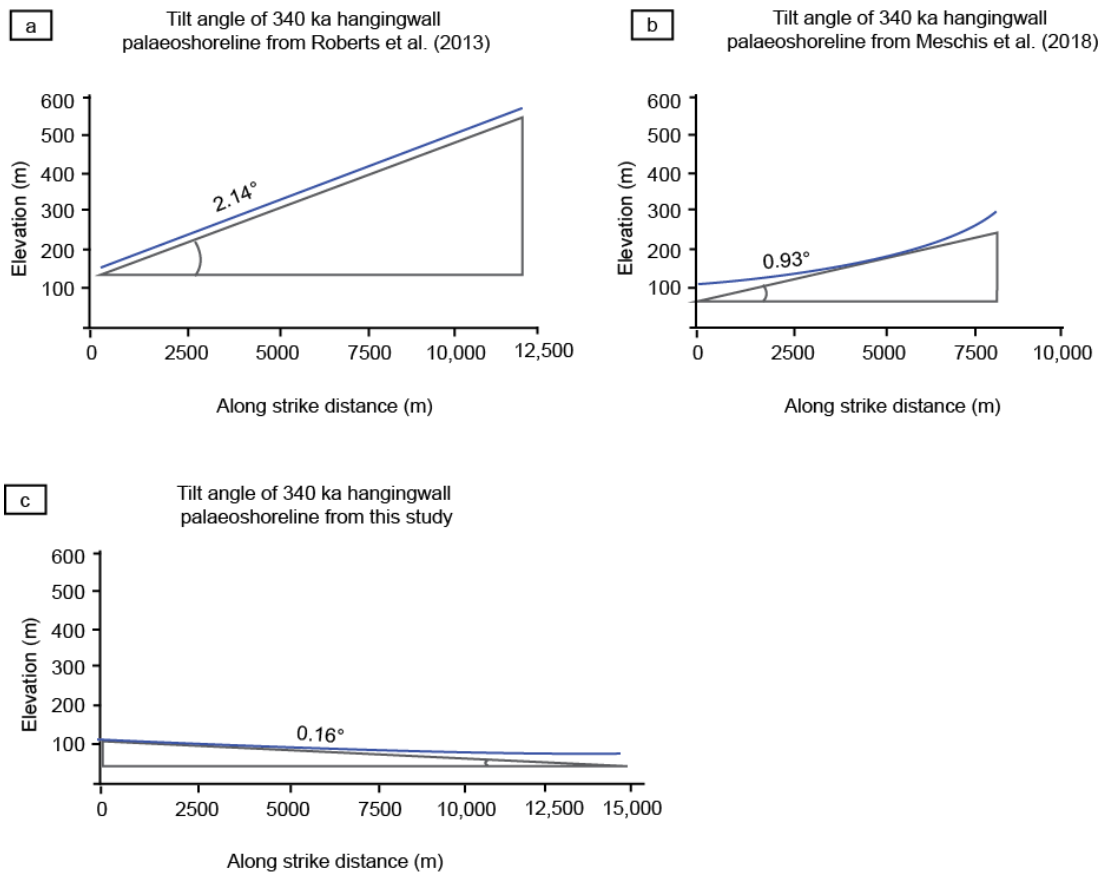

Figure 4.15: Tilt angle variation between the 340 ka palaeoshorelines in the hangingwalls of the: (a) Vibo fault, Italy (Roberts et al., 2013); (b) Capo D'Orlando fault, Sicily (Meschis et al., 2018); (c) SCCF, this study. See Fig. 2.21 for information on calculating palaeoshoreline tilt angles.

4.4.5 Calculating the throw rate of the SCCF

The hangingwall exposure ages and along-strike highstand-to-palaeoshoreline allocation can be used to investigate faulting activity on the SCCF. Profile 14 (Fig. 4.16) is located toward the centre of the SCCF (Fig. 4.4e) along an interfluve that abuts against the fault scarp (Fig. 4.6a and 4.8p). In the hangingwall of the fault along Profile 14 there are four preserved palaeoshorelines. The lowest palaeoshoreline at 40 m can be laterally traced in the DEM from Profile 14 to Profile 10 where the palaeoshoreline is at 54 m and has been dated to the 125 ka highstand (Figs. 4.4c, e, 4.8l and 4.12a); this provides the age constraint for Profile 14 (Fig. 4.16). The oldest and highest marine terrace on the hangingwall along Profile 14 is modelled to extend from ~130 to ~162 m in elevation and belong to the 478-ka highstand. This terrace has experienced faulting, as indicated by lithological variation across the fault (IGME map sheet Ano Viannos 1:50,000), and the Terrace Calculator predicts that the 478 ka palaeoshoreline elevation is suggested to be at an elevation where the main fault scarp of the SCCF is observed. These observations indicate that the 478-ka terrace may have been

offset by the SCCF placing the 478-ka palaeoshoreline on the uplifted footwall, if this can be proven it would allow calculation of the throw rate of the SCCF since 478 ka.

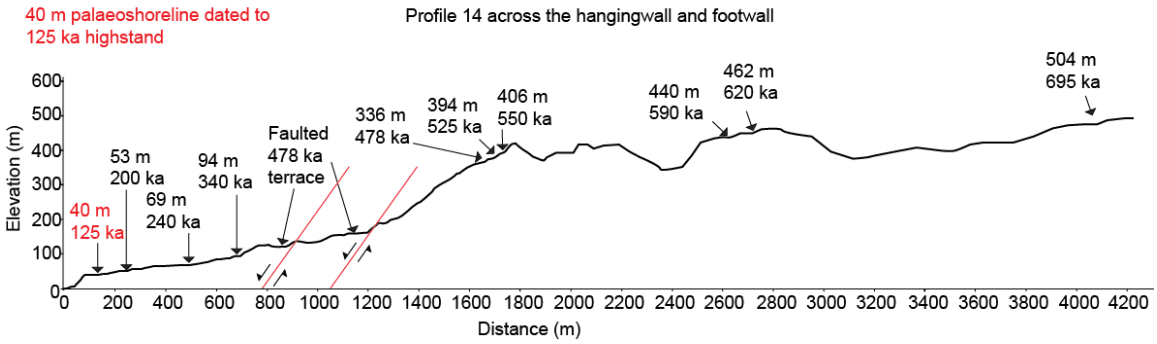

Figure 4.16: Topographic profile 14 across palaeoshorelines in the hangingwall and footwall of the SCCF.

Directly above the scarp along Profile 14, six footwall palaeoshorelines are visible from the DEM topographic profile; the lower three of these footwall palaeoshorelines were explored during fieldwork and show wave-cut platform evidence including syn-wave-cut platform deposits, lithophagid borings in the palaeo-cliffs, and a notch (Figs 3.16, 4.16). As the elevations of palaeoshorelines on the footwall above the scarp in this location have been measured (Fig. 4.16), the Terrace Calculator can be used to test whether it is plausible that the 478-ka and older palaeoshorelines are located on the footwall. The approach to do this is similar to the method applied to allocating undated palaeoshorelines to highstands along hangingwall profiles that do not have age constraints (Section 3.2). Briefly, it involves the lowest observed footwall palaeoshoreline (336 m, visible on the DEM and in the field, Figs. 3.16 and 4.16) being allocated to highstands in the Terrace Calculator, in turn, starting with the 478 ka highstand. The uplift rate is then iterated so that the measured palaeoshoreline elevation matches the predicted palaeoshoreline elevation and the iterated uplift rate is then applied to the whole topographic profile. Analysis of the number of measured to predicted palaeoshorelines matches, R^2 and RMSE are used to identify the best-fit solution.

The results of this analysis are shown in Table 4.7 and reveal that allocating the lowest palaeoshoreline at 336 m to the 478 ka highstand allows for all six of the measured palaeoshoreline elevations along this profile to be allocated to sea-level highstands (Tables 4.7 and 4.8). Furthermore, this solution results in the best fit R^2 value. Details of each of the measured and predicted palaeoshoreline elevations using the uplift rate of 0.71 mm/yr from Table 4.7 are shown in Table. 4.8.

Highstand allocated to 336 m (ka)	Required Uplift (mm/yr)	Number of matches	R^2	RMSE
478	0.71	6	0.9998	7.16
525	0.6	4	0.9911	9.75
550	0.59	3	0.9888	9.37
560	No solution due to overprinting			
590	0.535	3	0.9987	6.89
620	0.51	2	0.9862	4.21
695	0.47	2	0.9838	0.96
740	0.445	3	0.9882	5.76
800	0.395	2	0.9837	4.31
855	0.37	2	0.9818	5.24

Table 4.7: Terrace calculator solutions for the palaeoshoreline analysis in the footwall of the SCCF (from Robertson et al., 2019).

Uplift (mm/yr)	R^2	RMSE	UTM of altimeter		Allocated highstand age (ka)	Predicted palaeoshoreline elevations (m)	DEM palaeoshoreline elevations (m)	Barometric altimeter palaeoshoreline elevations (m)
			Easting	Northing				
0.71 ± 0.02	0.9998	7.16	358496	3874675	478	339	336	336
			358995	3874892	525	393	395	394
			358840	3874889	550	401	405	406
					560	401		
					590	439	440	
					620	460	462	
					695	503	504	

Table 4.8: Highstand allocation, uplift and elevation measurements for footwall palaeoshorelines on Profile 14 (from Robertson et al., 2019).

The correlations shown in Tables 4.7 and 4.8 strongly suggest that that the 478-ka palaeoshoreline is the lowest observed shoreline in the SCCF footwall along Profile 14, and that the 478 ka terrace has been offset by the SCCF along Profile 14. Consequently, the 196 m of measured vertical fault displacement can be used (Fig. 4.12a) to calculate a throw rate of 0.41 mm/year, which equates to a slip rate of 0.58 mm/year (the average dip of the fault is 45°) since 478 ka. The throw rate value, in addition to the expected coseismic displacement obtained from empirical fault-scaling relationships (Wells & Coppersmith, 1994), can be used to calculate the time-averaged recurrence interval on the fault (Section 2.2.4). A typical (also referred to as a standard) Mw 6.7 earthquake along the entire western segment of the SCCF

(29 km long) would result in a maximum coseismic vertical surface displacement of ~1.1m (Wells & Coppersmith, 1994). Knowledge of the maximum coseismic displacement value of 1.1 m and the total displacement of 196 m allows calculation of the approximate number of earthquakes since 478 ka as 178, assuming that previous earthquakes rupture the entire western segment of the fault. This information can be used to calculate a recurrence interval over 478 ka. As the maximum coseismic displacement is assumed, the number of earthquakes (178) is a minimum value, such that more but smaller earthquakes may be responsible for the observed offset; however, it is impossible to calculate recurrence intervals based upon any combination of large and small magnitude earthquakes through time. Thus, the calculated recurrence interval (178 earthquakes over 478 ka) of ~2,685 years is used herein, and represents a maximum recurrence value.

4.5 DISCUSSION

This section will outline the major findings from this chapter and explore the questions that arise from these findings. Particular focus is given to: (i) the temporal uplift rate differences observed between this chapter and the findings of Gallen et al. (2014) and (ii) exploring the cause of the observed patterns of uplifted palaeoshorelines in the western and eastern field sections using fault deformation modelling in Coulomb 3.4.

A key finding from within this chapter is that limestone wave-cut platforms, which display features suggesting minimal erosion, can be used to provide cosmogenic exposure ages that correlate with highstands from Quaternary sea level curves and hence constrain the rates of uplift. The results of this study show that the success of the ^{36}Cl approach relies on careful site selection to ensure that samples are removed from locations that display features indicative of minimal erosion such as lithophagid borings and millholes with further consideration as to the possibility of sedimentary cover. The application of ^{36}Cl exposure dating on wave-cut platforms is further explored in Section 8.2.

4.5.1 Constant versus variable uplift rates through time

This chapter has shown that the spatially variable uplift observed along the south central area of Crete appears to have been temporally constant between 76.5–980 ka; this is in contrast with the findings of Gallen et al. (2014). Section 4.4.3 explored the reasons for the differing temporal uplift rate observations between each study and outlined that where high

uplift rates occur (such as the western footwall section, Figs. 4.12a, 4.14a) the application of different sea-level curves may, in part, be responsible. Furthermore, a comparison of the results of palaeoshoreline to highstand correlation obtained from synchronous correlation in this study to those from sequential correlation (Gallen et al., 2014) also revealed differences between the two studies, particularly toward the centre of hangingwall of the SCCF (Profiles 12-17) where lower uplift rates prevail and overprinting of palaeoshorelines has occurred. These results raise the question as to what extent the temporal uplift rate variability suggested by Gallen et al. (2014) may have been a result of the application of the sequential method of correlation. Two previous studies (Roberts et al., 2013, Meschis et al., 2018) have applied synchronous correlation to deformed palaeoshorelines in Italy and Sicily, respectively, revising the chronology of palaeoshorelines previously investigated using sequential correlation. The studies of Roberts et al. (2013) and Meschis et al. (2018) both show that where sequential correlation has resulted in temporally-variable uplift rates, the results of synchronous correlation reveal that temporally constant uplift rates dominate.

If temporally variable uplift rates that increase toward the present day exist along south central Crete (as per Gallen et al., 2014), it is expected that uplift rate changes through time would be reflected on all profiles from Gallen et al. (2014). In order to examine this, the uplift rates for each palaeoshoreline along each profile in the hangingwall of the SCCF (eastern section, Profiles 6-17, Fig. 4.4) have been calculated using measured elevations from Gallen et al. (2014) and plotted against palaeoshoreline age (Fig. 4.17). This analysis is focused on the hangingwall palaeoshorelines because Section 4.4.3 showed that the effects of sequential versus synchronous correlation are apparent on areas of low uplift.

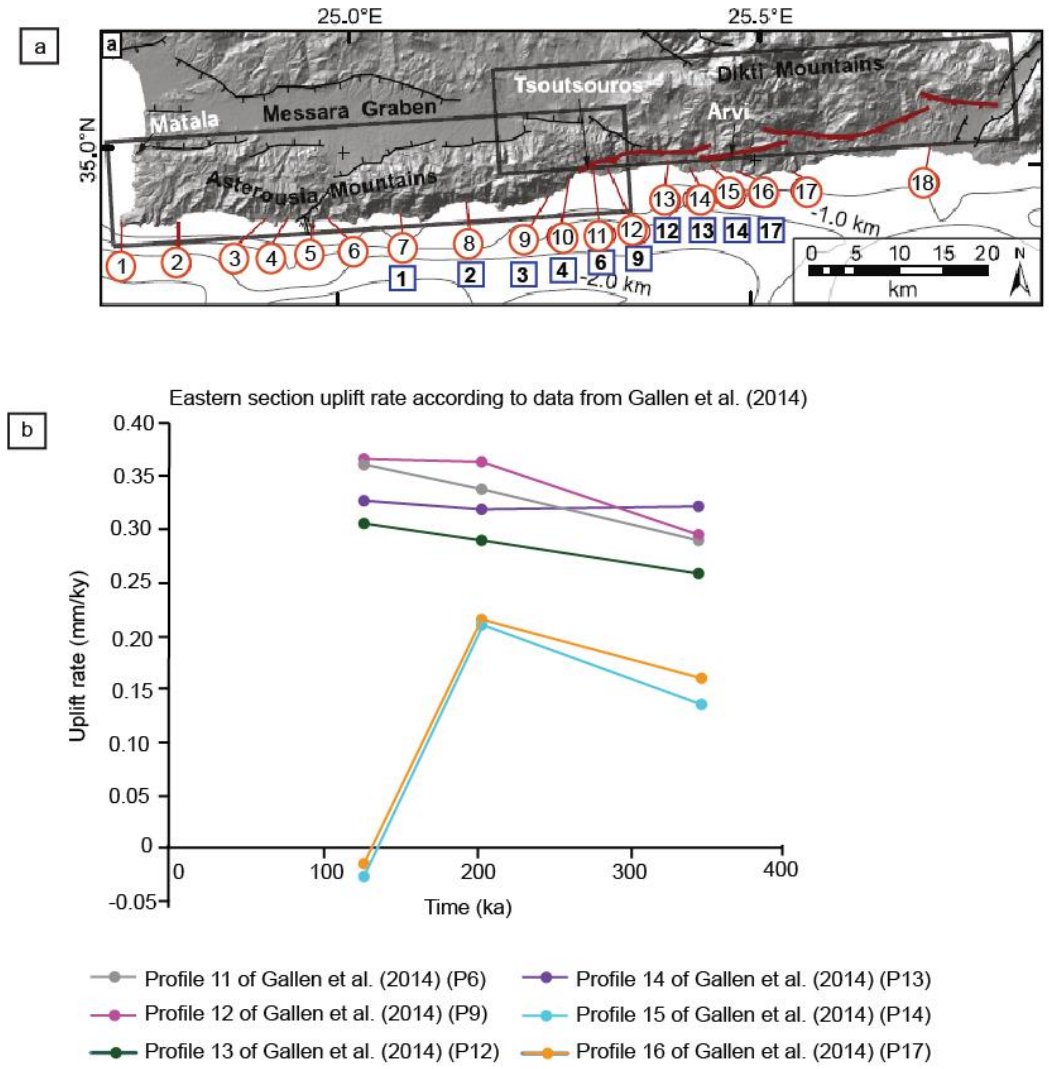

Figure 4.17: (a) Location of profiles from Gallen et al. (2014) in red circles and this study (blue squares); (b) Uplift against highstand age for profiles in the eastern section (Profiles 6, 9, 12, 13, 14 and 17 of Gallen et al., 2014). Uplift rates are calculated using the measured palaeoshoreline elevation plus the sea-level elevation (relative to today) for a given highstand and the age of the highstand from Gallen et al. (2014)).

The uplift rates plotted on Fig. 4.17 reveal inconsistencies, whereby uplift-rate patterns between 125 ka and 340 ka do not all appear to agree with the overall suggestion that uplift rates have increased through time (Gallen et al., 2014). Specifically, for profiles 15 and 16 (of Gallen et al., 2014) the uplift rate is suggested to decrease from 200 ka to 125 ka. This brief investigation allows for the tentative suggestion that extent of the uplift rate variations observed by Gallen et al. (2014), specifically in the hangingwall of the SCCF, may not be representative, and could thus be interpreted to be a factor of the application of the sequential correlation method in an area of low uplift where palaeoshoreline overprinting has occurred throughout the late Quaternary.

4.5.2 Investigating the causes of uplift along south central Crete

This chapter has shown that the uplift rate has been observed to vary along the strike of a mapped fault, and across the fault as seen through a change in uplift rates between the western footwall section and hangingwall of the SCCF (the eastern section) (Figs. 4.12, 4.14). This latter point provokes questions investigated in this section that are associated with the cause of the deformation observed in the findings, specifically whether the uplift and pattern of deformed palaeoshorelines in the hangingwall of the SCCF and the east-to-west decrease in uplift rates in the western section (Fig. 4.12) are representative of regional uplift, as per Gallen et al. (2014), or could be explained from other mechanisms.

Sections 2.3.1 and 4.3.2 showed that the offshore area of south central Crete hosts upper-plate extensional and transtensional faults. The question, therefore, is whether it is possible to determine if the observed patterns of deformation (Fig. 4.12) can be linked to these offshore upper-plate faults. There are two aspects of the findings presented herein that are of particular interest to examine. First, uplift of the western section of the coast, between Profiles 1–5, is up to ~20 km away from the SCCF, so footwall uplift as a consequence of the SCCF alone is perhaps unlikely to explain all the observed uplift. Second, it is noted that the along-strike tilt angles for the palaeoshorelines in the hangingwall of the SCCF are very low compared to other examples (Section 4.4.4, Fig. 4.15) (Roberts et al., 2013; Meschis et al., 2018). If the uplift observations along the eastern and western sections can be explained by modelling the uplift in response to offshore extensional faulting, then it would provide evidence that coastal uplift is perturbed by upper-plate faulting; this is examined using Coulomb 3.4 to model the expected uplift patterns associated with the offshore faults.

Coseismic uplift from earthquake ruptures, modelled using Coulomb 3.4 software, allows the user to explore vertical off-fault related deformation using inputs from multiple faults (Lin & Stein, 2004; Toda et al., 2005; Mildon et al., 2016), which acts as a proxy for the long-term patterns of uplift (e.g. Section 2.2.4). Details of the steps required to model the off-fault deformation in Coulomb 3.4 can be found in Section 3.5.2. Briefly, it involves fault inputs (Table 4.9) of: (i) fault traces; (ii) fault geometry parameters; and (iii) subsurface slip value for each fault, a value that is iterated until the modelled maximum earthquake Mw matches that obtained from total fault-length scaling relationships (Section 2.2.4) (Wells and Coppersmith, 1994). The Coulomb 3.4 software models an earthquake rupture using the fault input parameters and provides an output of a map-view model of 3-D deformation

shown as vertical contours (Fig. 4.18). It is recognised that this approach does not take into account post-seismic deformation as a consequence of faulting (Section 2.2.4). However, it is suggested that post-seismic deformation increases the magnitude of vertical motions by at most a few tens of percent of the coseismic values and that post-seismic vertical motions share similar spatial variation patterns as coseismic motions (Atzori et al., 2008; D'Agostino et al., 2012).

An earthquake rupture on each of the offshore faults in Fig. 4.1b was modelled in Coulomb 3.4 (Fig. 4.18). In terms of modelling the Ptolemy fault, Section 2.2.2 highlighted that the depth of the seismogenic layer is typically accepted to be ~15 km (Jackson and White, 1989), however, the Ptolemy trench fault has been modelled with seismogenic layer depth of 30 km because examinations of the microseismicity associated with the Ptolemy fault (Fig. 2.2.9) reveal that the fault is active down to the subduction interface at depths of ~30 km (Meier et al., 2004; Becker et al., 2010). As a check on the impact of a 15 km versus 30 km seismogenic depth, both values were used to model a Ptolemy fault rupture – the footwall vertical deformation between the two models was similar so results of the 30 km model are shown (Fig. 4.18) as this depth is expected to be an accurate reflection of depths of seismicity for this fault (Becker et al., 2010). Two iterations for the offshore Mirto fault were also tested – as one fault, and also as two separate faults because there is a lack of clarity in the literature (Caputo et al., 2010; Kokinou et al., 2012). Modelling the footwall uplift in Coulomb 3.4 for both fault options results in a coseismic uplift value of ~0.07 m (combined faults) versus ~0.02 m (two separate faults) at Profile 10, as these values are in the same order of magnitude, the combined fault model is used in the following analysis.

4.5.2.1 Uplift of the western section (Profiles 1-5)

The uplift rates of palaeoshorelines in the western section (Fig 4.4a) decrease from Profile 4 westwards to Profile 1 (Fig. 4.12a) and have been suggested to represent a pattern of footwall uplift (Section 4.4.4). The results from the Coulomb modelling show that rupturing the Ptolemy fault (maximum Mw of 7.3, subsurface slip of 4.3 m, Table 4.9) and rupturing the Cape Lithino faults (maximum Mw of 6.2, subsurface slip of 1 m, Table 4.9) both result in coseismic uplift patterns that appear to decrease from Profile 4 toward the west (Fig. 4.18). So this initial test appears to show that ruptures on both faults may be capable of producing the patterns of uplift observed on the palaeoshorelines. It is possible to attempt to differentiate between which of these two faults may be responsible for uplift of the western

section by calculating the implied recurrence interval for uplift events using the total uplift of palaeoshorelines and the single earthquake uplift contours modelled in Coulomb (Fig. 4.18a and 4.18b) (Section 2.2.4). At Profile 2 on Fig. 4.18a and 4.18b the 26-m palaeoshoreline has been allocated to the 76.5-ka highstand (using OSL dating of sample LS1251 from Gallen et al., 2014); since the sea-level elevation during the 76.5 ka highstand was at -30 m (relative to present day, Siddall et al., 2003), there has been total uplift of 56 m. Solely rupturing the Ptolemy fault results in 0.4 m of uplift at Profile 2 (Fig. 4.18a); over the period of 76.5 ka, 140 standard earthquakes would be required for this palaeoshoreline to reach its 26-m elevation; this results in a time-averaged recurrence interval of 546 years (Fig. 4.18c) for Mw 7.3 events. The same analysis was carried out using the uplift produced by rupturing the western and eastern Cape Lithino faults, which results in 0.018-m uplift per earthquake at Profile 2 (Fig. 4.18b). Over 76.5 ka 3,122 earthquakes would be required to uplift the palaeoshoreline to 26 m, which results in a time-averaged recurrence interval of 24.5 years (Fig. 4.18d) for Mw 6.1 (western fault) and Mw 6.25 (eastern fault) events (Table 4.9).

Fault name	Fault information (fault trace, kinematics)	Length (km)	Depth of seismogenic zone (km)	Dip °	Facing direction °	Rake °	Sub-surface slip value (m)	Max. Mw
Ptolemy trench	Kokinou et al., 2012; Becker et al 2006, 2009; Meier et al., 2004, Ozbakir et al., 2013	94	30	85	150	-40	4.3	7.3
Offshore normal faults:	Kokinou et al., 2012; Mascle 1982; Caputo et al., 2010; Gallen et al., 2014							
Fault 1 (aka. Lithino fault)		14.8	15	60	180	-90	0.75	6.1
Fault 2 (aka. Lithino fault)		18.2	15	60	180	-90	1	6.2
Fault 3 (aka. Mirto fault)		13	15	60	170	-90	0.6	6
Fault 4 (aka. Mirto fault		19	15	60	170	-90	1	6.2
Fault 3&4 (aka. Mirto fault)		37	15	60	155	-90	2.2	6.7

Table 4.9: Fault data used for coulomb modelling. 'Facing direction' is an input value in the code of Mildon et al. (2016) and refers to the direction that the fault faces toward the direction of slip. Slip at the surface is set at 0.1 (10%) of the slip value at depth. This is based upon the relationship between surface slip (Vittori et al., 2011) and maximum slip values at depth (Wilkinson et al., 2015) for the Mw 6.3 2009 L'Aquila Earthquake, Italy (from Robertson et al., 2019).

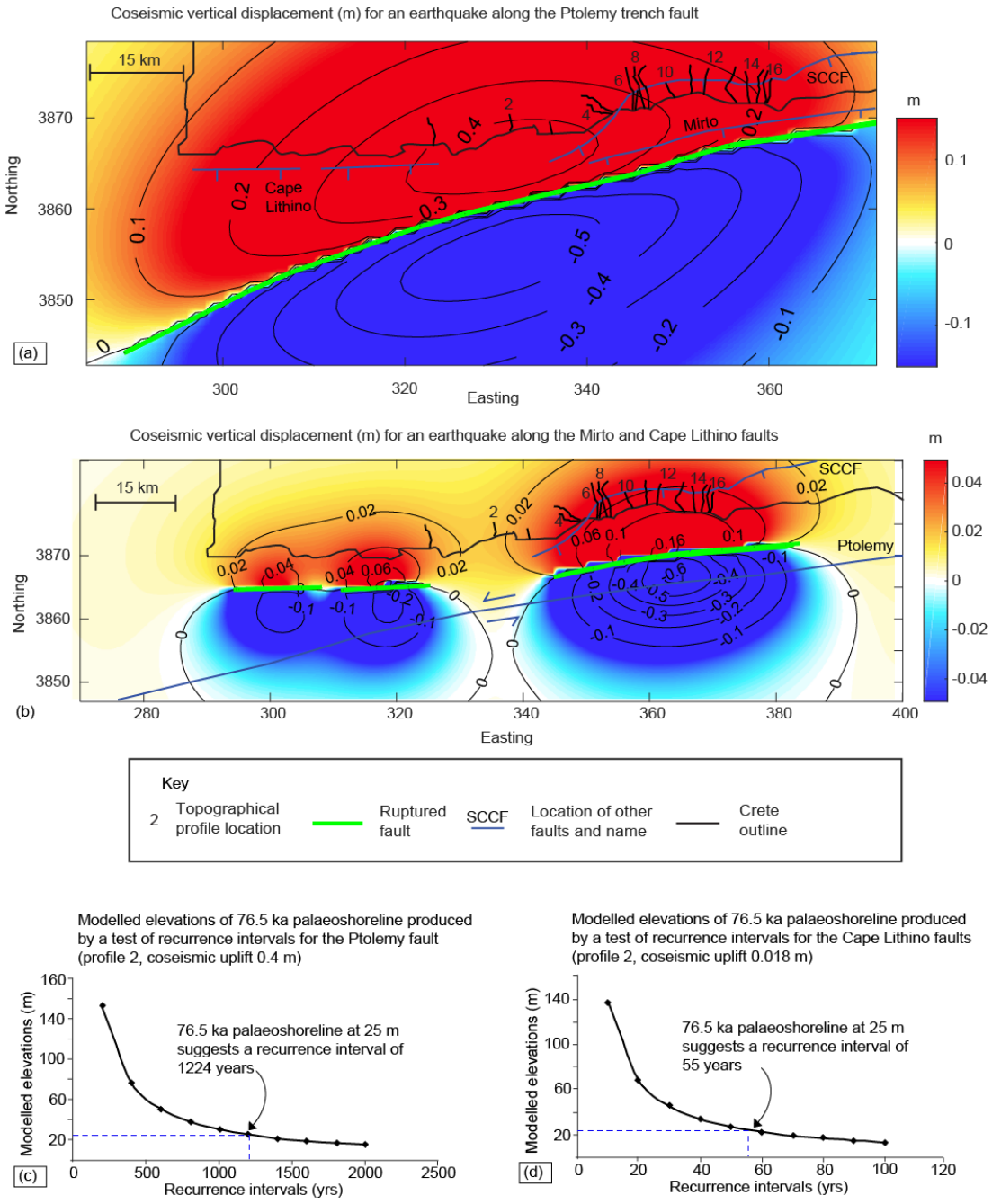

Figure 4.18: Coulomb models of the vertical deformation (m) caused by offshore upper-plate faults as a result of an earthquake (see Table 4.9 for input values). Crete coastline is outlined in black with the profile lines (numbered every alternate profile); blue lines are faults; green lines represent the faults modelled; contours represent uplift [red] and subsidence [blue] at the surface). (a) Modelling only the Ptolemy fault results in a maximum value of 0.4 m of coseismic uplift at Profile 2 where the 76.5-ka palaeoshoreline is at 26 m (total uplift 56 m since 76.5 ka) (Table 4.4); (b) modelling the offshore normal Cape Lithino and Mirto faults (see Table 4.9 for input values) results in 0.01–0.02 m of coseismic uplift at Profile 2 where the 76.5-ka palaeoshoreline is at 26 m (total uplift 56 m since 76.5 ka) (Table 4.4). Tests to obtain the recurrence intervals for the 26m, 76.5-ka palaeoshoreline at Profile 2 are shown in (c) for coseismic uplift along the Ptolemy fault and (d) for coseismic uplift for the Cape Lithino faults. SCCF = South Central Crete Fault. (From Robertson et al., 2019).

An analysis of the instrumental seismology for depths <30 km reveals a small number of moderately sized earthquakes (~Mw 5), which could be attributed to the Cape Lithino faults from a record that is thought to be complete since ~1900 (Dziewonski et al., 1981; National

Observatory of Athens (NOA) 1997; Papazachos et al., 1998; Ekström et al., 2012; Makropoulos et al., 2012; International Seismological Centre, 2016), but there is no instrumental evidence of earthquakes >Mw 6.1 during this period. It is, therefore, possible that the Ptolemy fault could solely be responsible for uplifting the western section, because it is plausible that the Ptolemy fault may not have ruptured in this time period (recurrence interval of 546 years) (i.e. 1900–2018). However, it appears that the normal offshore Cape Lithino faults alone cannot because the instrumental and historical seismicity does not support such a frequent earthquake recurrence (24.5 years) on these faults. In light of this finding, the calculated inferred recurrence interval (546 years) on the Ptolemy fault may be taken as a representative of a minimum interval value since 76.5 ka; however, it is acknowledged that it is likely that some component of the recorded uplift may be linked to background regional values/other upper-plate faults and this recurrence interval may be longer.

4.5.2.2 Uplift along the hangingwall of the SCCF (eastern section)

The variation in uplift-rates along strike of the SCCF (Figs. 4.12, 4.14b) is reminiscent of similar hangingwall observations for other active normal faults (e.g. Cucci et al., 1996; Roberts et al., 2013; Meschis et al., 2018) where greater subsidence results in lower uplift rates recorded in the centre of the fault compared to higher uplift rates (less subsidence) toward the fault tips. However, analysis of the tilt values of palaeoshorelines in the hangingwall of the SCCF (Profiles 6–17) (Section 4.4.4) revealed that the tilt angles appear to be anomalously low compared to the measured hangingwall tilt angles from other normal faults. In detail, the 340 ka palaeoshoreline in the hangingwall of the SCCF exhibits a 0.16˚ along-strike tilt (Figs. 4.13, 4.14d, 4.15c) compared to the tilt angles on other 340-ka palaeoshorelines in Italy (Vibo fault, Calabria) and Sicily (Capo D'Orlando fault), which have values of 2.15˚ (Roberts et al., 2013) and 0.93˚ (Meschis et al., 2018), respectively (Figs. 4.15a, b). But the reason for the low tilt angles in the hangingwall of the SCCF are unknown. The question that this section seeks to address is whether it is possible that the low tilt angles in the hangingwall of the SCCF may be linked to the presence of offshore faults directly south of the SCCF (Mirto fault and Ptolemy fault, Figs 4.1b, 4.15a), whereby the hangingwall of the SCCF could be uplifted because it is located in the footwall of the Mirto and Ptolemy faults (Fig. 4.19). To explore the impact of cumulative earthquakes along the offshore south-dipping normal Mirto fault and the transtensional Ptolemy fault on the tilt angles of the

palaeoshorelines in the hangingwall of the SCCF (Profiles 6–17), the coseismic uplift pattern for the Mirto and Ptolmey faults along Profiles 6–17 was interrogated (Fig. 4.16a, b, 4.18).

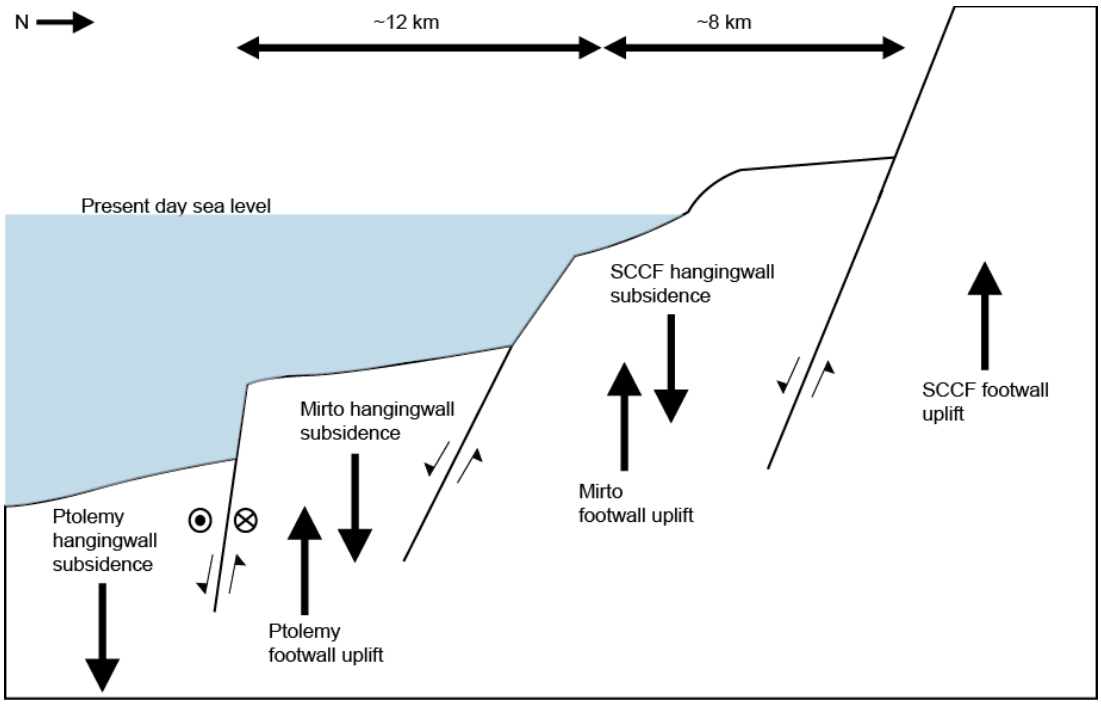

Figure 4.19: Schematic cross section across the south central area of Crete to show the locations of the SCCF, Mirto and Ptolemy faults relative to one another and the effects of footwall uplift and hangingwall subsidence.

The observed shallowing of tilt angles along the SCCF hangingwall palaeoshorelines are explored from its western tip (Profile 6) toward its centre (Profile 17). The patterns of coseismic uplift associated with ruptures along the Mirto and Ptolemy faults show that when footwall uplift caused by slip along the Ptolemy fault is compared to the Mirto fault, both result in spatially variable uplift but the magnitude and pattern of uplift differs (Figs. 4.18, 4.18). Uplift in the footwall of the Ptolemy fault results in maximum uplift values (~0.3-0.4 m) in its centre, which is co-located near to the western tip of the SCCF hangingwall (Profile 6) (Fig. 4.18a, 4.20b). Ptolemy fault footwall uplift decreases eastward from Profile 6 toward Profile 17, where footwall uplift values are in the region of 0.2-0.1 m. The coseismic uplift observed in the footwall of the offshore Mirto fault is highest in the centre of the Mirto fault (0.1 m), which is approximately co-located with the centre of the SCCF (Fig. 4.18b, 4.20c). Mirto footwall uplift then decreases from Profile 17 toward Profile 6 in the west, where coseismic uplift values are in the region of 0.06-0.02 m.

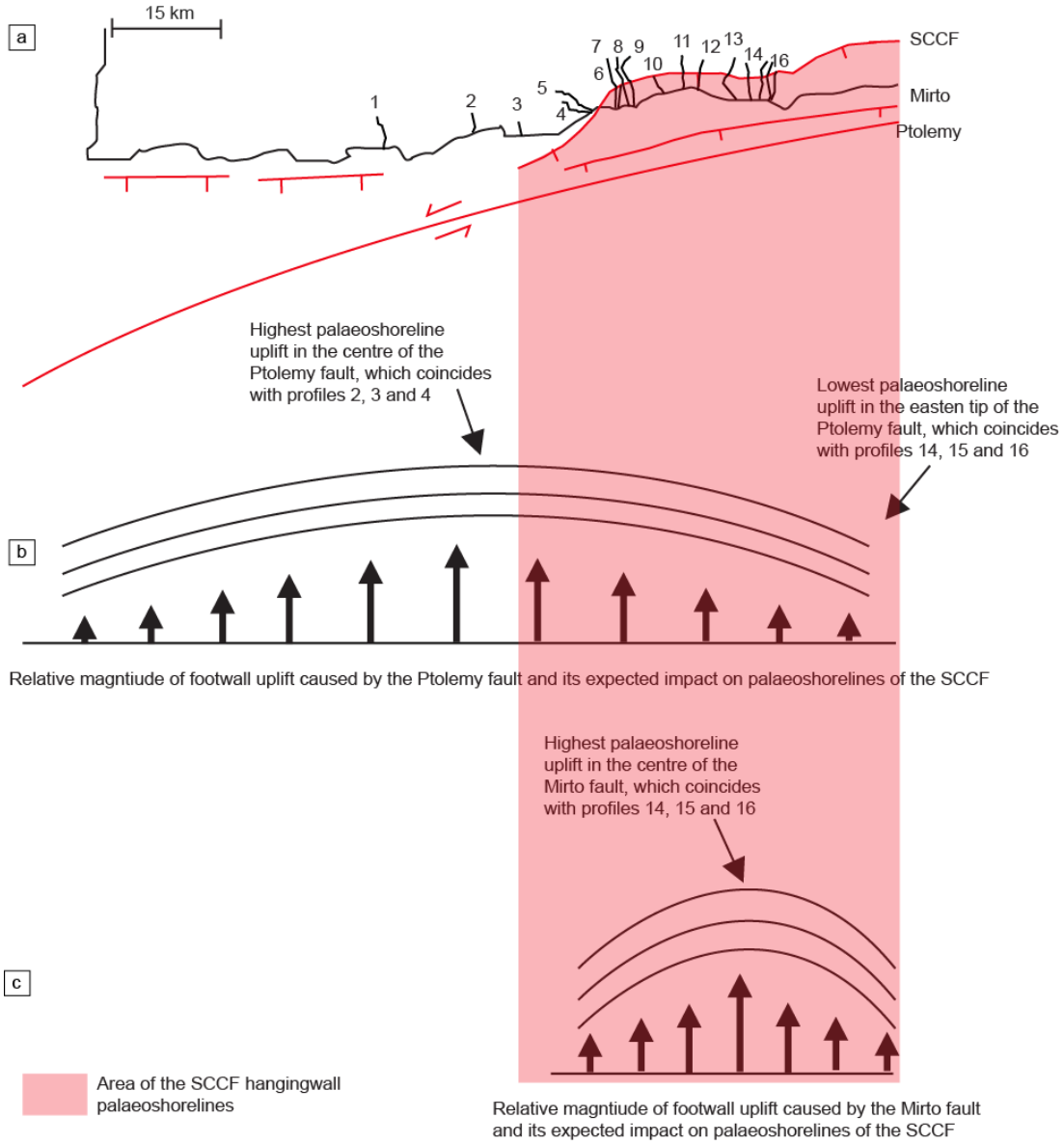

Figure 4.20: (a) Locations of the faults along south central Crete and a schematic diagram to show how the relative magnitude of uplift caused by the (b) Ptolemy and (c) Mirto faults varies along parts of the southern Crete coastline in relation to the location of the SCCF. The relative magnitudes are obtained from the results of Coulomb vertical motion modelling shown in Fig. 4.18

Figure 4.20 shows that the footwall uplift patterns from the Ptolemy fault would act to increase the elevation of palaeoshorelines at the western tip of the SCCF (Fig 4.20b), this motion would increase the tilt angle of the SCCF hangingwall palaeoshorelines. Conversely, footwall uplift patterns from the Mirto fault would act to increase the elevation of palaeoshorelines in the centre of the hangingwall of the SCCF (Fig. 4.20c) which could act to reduce the tilt angles of the hangingwall palaeoshorelines. In the context of the shallow tilt angles observed along the hangingwall of the SCCF it can be inferred that the shallower tilt of the SCCF hangingwall palaeoshorelines could be linked to cumulative footwall uplift

caused by the Mirto fault, which uplifts the centre portion of the SCCF hangingwall by greater amounts than the tip areas.

In summary, interpretation of the Coulomb modelling shows that: (i) that the Ptolemy fault may be solely capable of causing the observed uplift along the western section of the research area (Profiles 1–5), but it is also probable that uplift from the Cape Lithino faults makes a minor contribution; a recurrence interval on the Ptolemy fault since 76.5 ka of 546 years is inferred (Section 2.2.4); (ii) that the tilt variation observed along the palaeoshorelines in the hangingwall of the SCCF may partly be explained by uplift along the footwall of the offshore Mirto fault, with the relationship between faulting on the Ptolemy and Mirto faults difficult to disentangle with the modelling approach applied in this chapter – the impact of the Mirto fault may be greater due to a shorter recurrence interval compared to the Ptolemy, but this needs more investigation.

The results presented in this section suggest that the values and patterns of uplift derived from throughout the study area represent total uplift produced by the interaction between footwall uplift from an offshore extensional fault that is imposed on hangingwall subsidence from the SCCF in the case of the eastern section. Importantly, these results show that the upper-plate faults have the capacity to significantly perturb coastal uplift (Fig. 4.21). This is in contrast to the suggestions of Gallen et al. (2014) that regional uplift controls the observed coastal topography (Section 4.3.4) and of Mouslopoulou et al. (2015b) that uplift is controlled by slip on upper-plate reverse faults that splay from the subduction interface (Section 2.3.1).

The discussion above suggests that both the onshore SCCF and the offshore faults are active and contributing to seismic hazard. Specifically, (i) the observed bedrock fault scarps along the SCCF likely record faulting since the Last Glacial Maximum (~12–18 ka) (Gallen et al., 2014), and (ii) the youngest palaeoshorelines on the hangingwall (125 ka) and western footwall (76.5 ka) sections have been successively deformed by faulting since their formation; consequently, suggesting active faulting on the SCCF. For the offshore faults, activity is supported by observations from seismic reflection and bathymetric studies that show that the upper-plate faults offset the seabed and control the basin development in the south of Crete (Alves et al., 2007; Kokinou et al., 2012; Alves et al., 2014) (Section 4.3.2). Based on fault length-scaling relationships (Table 4.9; Wells & Coppersmith, 1994), it is possible to calculate that the SCCF is capable of earthquakes between Mw 6.5-6.9 (where

the lowest value is for a single segment rupture of the SCCF and the upper value is for a full rupture of the 49- km long SCCF), and the offshore normal and Ptolemy faults are capable of earthquakes in the region of Mw 6 and Mw 7.3, respectively.

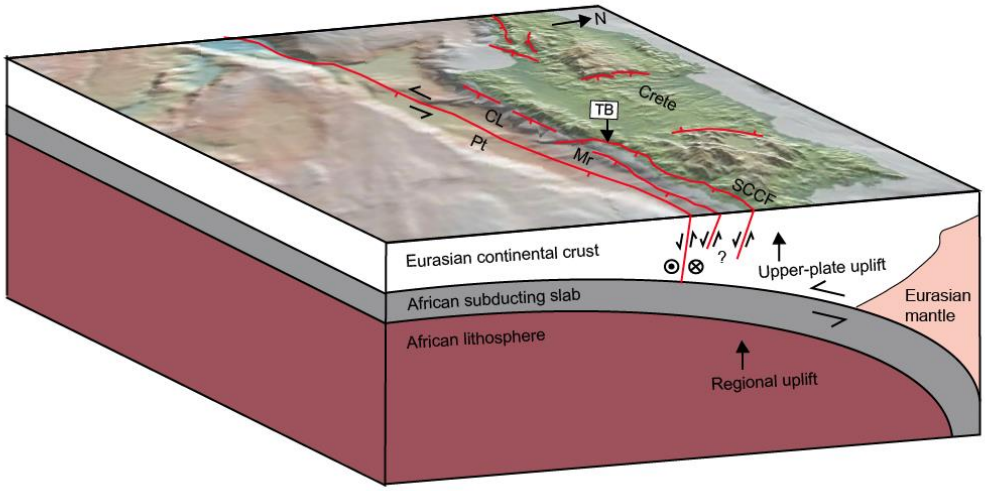

Figure 4.21: 3-D cartoon of the study area illustrating that upper-plate extensional faults in the south central area of Crete may perturb regional uplift and have a controlling effect on the coastal topography. Differential uplift occurs along fault-length scales as a result of footwall and hangingwall deformation. Faults relevant to the study are labelled as follows: SCCF = South Central Crete Fault; Pt = Ptolemy fault; CL = Cape Lithino faults; Mr = Mirto fault; TB = Tsoutsouros Bay. (From Robertson et al., 2019).

The findings presented herein demonstrate the potential role of upper-plate faults in controlling observed coastal uplift. Normal faults that trend parallel to the margins of the western Hellenic subduction zone occur throughout the remainder of southern Crete (e.g. Sfakia fault and Selia/Assomatos faults, Fig. 4.1b), Kythira, the Mani Peninsula (Peloponnese), and western Peloponnese (Mascle et al., 1982; Armijo et al., 1992; Papoulia & Makris, 2004; Tsimi et al., 2007; Papanikolaou et al., 2007; Kokinou & Kamberis, 2009; Gaki-Papanastassiou et al., 2011; Papoulia et al., 2014; Wardell et al., 2014; Kassaras et al., 2018) and are in many places associated with uplifted marine terraces (e.g. Kelletat et al., 1976; Angelier, 1979a; Gaki- Papanastassiou et al., 2011; Athanassas & Fountoulis, 2013). The presence of terraces and onshore/offshore extensional faults throughout the rest of the Hellenic Arc leads to the suggestion that the observed uplift along these coastlines could, in part, also be controlled by upper-plate faults; this is discussed in greater detail in Section 8.3.1.1. Furthermore, similar patterns of upper-plate extension have been described from other subduction zones. For example, differential uplift as a result of forearc extension is observed in Japan (Matsu'ura et al., 2015), Peru (Saillard et al., 2011), Costa Rica (McIntosh et al., 1993; Sak et al., 2009), and along the Calabrian Arc, where sets of normal faults control

the local topography (Michetti et al., 1997; Papanikolaou & Roberts, 2007; Roberts et al., 2013; Meschis et al., 2018); the impact of the findings herein to examine the role of upper-plate extension along other subduction zones is explored in Sections 8.3.1.2 and 8.3.1.3.

4.6 CONCLUSIONS

1. The deformation caused by extensional faulting in the upper plate of the WHSZ, and possibly other upper plates worldwide, may be observed on the length scales of normal faults and are likely to perturb uplift rates that may be assumed to occur from slip on the subduction interface. Uplift contributions made by upper-plate faults should be considered when conclusions about subduction interface slip are made using coastal uplift observations.

2. The south central part of Crete is being uplifted as a consequence of upper-plate faulting probably combined with subduction-related (regional) uplift. Temporally constant uplift rates can successfully be used to explain the observed elevations of palaeoshorelines up to 900 ka in places. The observed spatial variation of uplift rates has been shown to be as a result of slip along upper-plate extensional faults.

3. ^{36}Cl cosmogenic exposure dating of wave-cut platforms, in combination with sea level highstand data, is an acceptable method to derive uplift values over the long term and obtain Late Quaternary ages of palaeoshorelines. The results of this chapter emphasise the importance of sampling in locations with minimal erosion and note the significance of features such as lithophagid borings when carrying out site selection.

4. The SCCF is an active fault capable of a maximum Mw ~6.7 earthquake; it has a throw rate of 0.41 mm/ year, which equates to a slip rate of 0.58 mm/year. Using empirical fault-scaling relationships, a recurrence interval of ~2,700 years can be calculated.

5. Based on the assumption that the Ptolemy fault dominates uplift in the western section of the research area, an inferred mean recurrence interval of 546 years is suggested (this is a minimum value).

5 CHAPTER 5: IMPACT OF DIFFERENT SEA-LEVEL CURVES ON CALCULATIONS OF DEFORMATION RATES FROM DEFORMED PALAEOSHORELINE SEQUENCES.

5.1 SUMMARY

Chapter four showed that investigations of palaeoshorelines can be used to determine which faults may be responsible for observed uplift; specifically employing the following: (i) observations of the spatial variation of along-strike uplift rates, and (ii) calculated recurrence intervals on a fault, using modelled coseismic uplift (obtained via Coulomb modelling) and a dated palaeoshoreline. However, calculation of deformation rates and mean recurrence intervals are reliant on data from sea-level curves and such investigations may be confounded by the presence of multiple sea-level curves that have been derived from different methods. Thus comparing between different uplift studies even in the same area is difficult. The question, therefore, is to what extent the use of different sea-level curves will affect the deformation rates (uplift rates and inferred throw/slip rates) obtained from sequences of palaeoshorelines. The multiple age controls obtained in the previous chapter (4) provide the opportunity to test this.

The findings of this chapter suggest that where different sea-level curves are used, the correlation between sea-level highstands and undated palaeoshorelines varies, but that these result in minor uplift rate differences for each profile in question; importantly, the spatial uplift pattern along strike of the palaeoshorelines observed in Chapter 4 is maintained. The measured variation observed in uplift rates is comparable to values of propagated uplift uncertainties. Inferred recurrence intervals are also shown to vary depending on the sea-level curve employed, in some cases beyond what may be perceived as acceptable values.

The findings of this chapter are in preparation for submission to *Tectonics*.

5.1.1 Introduction

Deformation rates obtained from palaeoshoreline sequences from throughout the world have allowed geologists to explore the potential mechanisms responsible for causing uplift, whether this is related to, for instance, faulting (e.g. Armijo et al., 1996; Roberts et al., 2009, 2013; Robertson et al., 2019), sediment underplating (e.g. Adam and Reuther, 2000; Clift and Hartley, 2007) or isostatic rebound (e.g. Stone et al., 1996). Chapter 1 highlighted that uplift and slip/throw rates and recurrence intervals can be calculated from investigations of palaeoshorelines. Calculation of both these deformation rates and recurrence intervals require knowledge of the elevation and age of a palaeoshoreline, and the age and sea-level elevations of each highstand relative to today (Lajoie, 1986). While studies may adopt differing approaches in order to correlate sequences of palaeoshorelines with highstands (Section 2.1.5), a form of the uplift calculation (Section 3.2) is broadly used by most researchers to derive uplift rates (e.g. Roberts et al., 2009, 2013; Gallen et al., 2014; Jara-Munoz et al., 2017; Pedoja et al., 2018).

Calculating uplift rates and recurrence intervals using palaeoshorelines results in a number of potential factors that contribute to the uncertainties, such as, those from the sea-level curve (highstand ages and relative sea level), measurement of the palaeoshoreline elevations and the ages of the palaeoshoreline, all of which can be propagated to provide possible uplift uncertainty values (Section 3.2). However, given the fact that there are numerous (>20) sea-level curves, each using different methods to calculate historic sea levels (Section 2.1.2), compiled over different timescales and geographical areas (Caputo et al., 2010; Pedoja et al., 2014; 2018; de Gelder et al., 2019), it is possible that the choice of sea-level curve to determine uplift rates may in itself represent variation and potential uncertainty that is 'hidden' from most studies that calculate uplift rates using the data from one sea-level curve (Caputo et al., 2007).

While there are a number of studies that acknowledge the uncertainty associated with the fact that there are many sea-level curves (e.g. Caputo et al., 2007; Pedoja et al., 2014; Sarr et al., 2019; Duffy et al., 2020), there are few studies that quantify how different sea-level curves impact investigations on deformed palaeoshorelines (Caputo et al., 2010; Pedoja et al., 2018; Robertson et al., 2019; de Gelder et al., 2020). The impact of using multiple (12) sea-level curves on the same area in southern Italy was investigated by Caputo et al. (2007) who concluded that the use of individual sea-level curves is subjective; their analyses showed that highstand elevations between curves differed significantly in places (e.g. up to 35 m for the 76 ka and 240 ka highstands) and that using a number of sea-level curves to analyse the

same sequence of palaeoshorelines results in different sea-level highstand to palaeoshoreline correlations and highly variable estimated uplift rates (Caputo et al., 2007). Another study was carried out by de Gelder et al. (2020). These authors analysed multiple topographic profiles obtained from a sequence of palaeoshorelines located within the Gulf of Corinth, Greece, from which averaged palaeoshoreline elevations were calculated and used to create a single topographic profile. de Gelder et al. (2020) used the averaged topographic profile to derive a sea-level curve for the Gulf of Corinth; in doing so they investigated the patterns of palaeoshoreline uplift that would be produced over time by using 14 different sea-level curves. Comparing their results to the observed terrace sequence, they found that: (i) the lowest RMS misfits for the present day to 125 ka and to 240 ka occurred using sea-level curves derived from coral data and ice-sheet data, respectively; (ii) that using high-resolution hydraulic model curves resulted in the most matched terraces, and (iii) that globally-derived sea-level curves result in lower misfits.

What is still unknown, however, is the extent to which deformation rates and recurrence intervals may vary given the chosen sea-level curve and how this variation compares to uncertainties of up to ±~30 m on the relative sea-level elevations (Table 5.1). Knowledge of this topic is important because the deformation rates obtained along palaeoshorelines are used to understand the long-term behaviour within coastal regions where upper-plate and/or subduction-zone faults may have the potential to cause catastrophic earthquakes and tsunamis over recurrence intervals that exceed the instrumental or historic record (Stein et al., 2012), as outlined in Chapter 1.

What is needed in order to explore the variation caused by different sea-level curves is a sequence of palaeoshorelines where there are a number of absolute age controls both at different elevations within a sequence and along the strike of the terraces. The presence of absolute age controls on multiple palaeoshorelines in a sequence is important because it allows the accuracy of the sea-level elevations for the dated highstands to be tested using the Terrace Calculator (Section 3.2). Similarly, multiple age controls along the strike of a fault is beneficial because it removes any ambiguity about the along-strike correlation from a dated palaeoshoreline. However, multiple Late-Quaternary age controls are rare owing to a sparsity of datable materials. One such location is present along the south central area of Crete investigated in Chapter 4 (Robertson et al., 2019).

This chapter aims to carry out an objective analysis of how the implied deformation rates vary with different sea-level curve data by quantifying the potential differences in uplift rates, spatial uplift rate patterns and implied recurrence intervals using sea-level input data from six widely used sea-level curves that have all been derived using different methods (Sections 2.1.2, 5.3.4; Fig. 5.1). Owing to the number of published sea-level curves, this is not intended to be an exhaustive analysis of all sea-level curves, rather a selection of curves that are representative of the different methodologies used to construct sea-level curves over different time periods representing a range of geographical scales (global and regional) (Table 5.1).

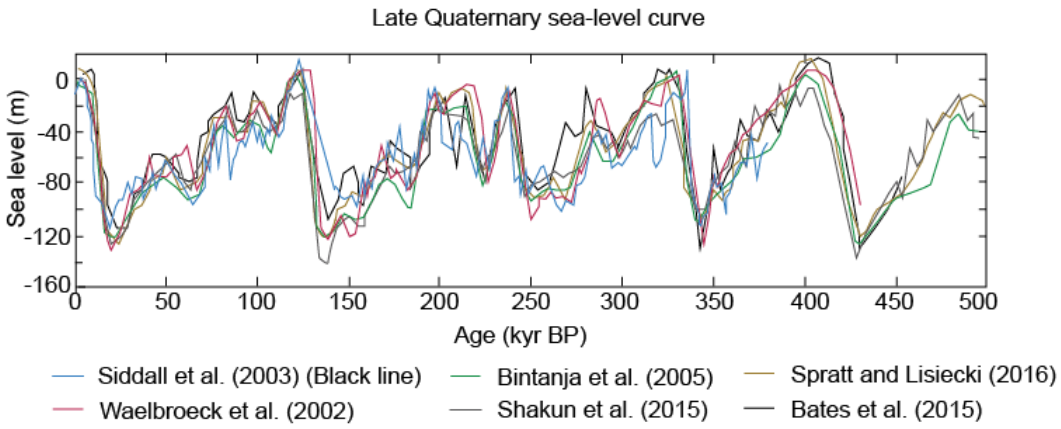

Figure 5.1: Comparison of the six sea level curves in this study

In order to carry out a robust analysis, five topographic profiles from Chapter 4 (Profiles 2, 4, 5, 9 and 10, Fig. 5.2) (Robertson et al., 2019) are employed, each with an age control that constrains at least one palaeoshoreline to a highstand. Following a discussion of the approaches involved in construction of sea-level curves and justification of the selection of curves analysed in this chapter, a number of tests are carried out designed to: (1) examine the differences between the predicted elevations obtained from the six sea-level curves using the uplift rates from each of the profiles in Chapter 4, (2) explore how the palaeoshoreline to highstand allocation varies using each tested sea-level curve in the Terrace Calculator, and (3) using the results from (2), quantify the impact that use of the tested sea-level curves has on the calculated uplift rates and inferred recurrence interval. The results obtained from these tests are discussed in context of the uncertainties of sea-level elevations from each of the sea-level curves.

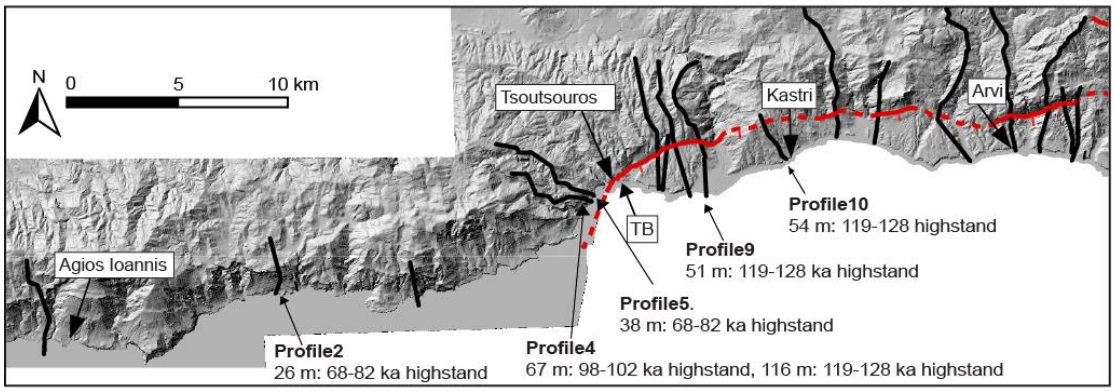

Figure 5.2: Location of the profiles used in this chapter from the south central Crete area in Chapter 4, alongside their absolute ages and dated palaeoshoreline elevations (Modified from Robertson et al., 2019).

5.2 BACKGROUND

Different sea-level curves have been shown to include variations between the timings and sea-level elevations of highstands as well as the number highstand peaks between periods of glaciation and the lengths of the interglacials (Caputo et al., 2007; Dutton and Lambeck, 2012; de Gelder et al., 2020) (e.g. Fig. 5.1). Sea-level curves have been compiled to represent localised, regional and global historic sea-levels (e.g. Table 5.1) and for individual highstands (e.g. Hearty et al., 2007). Variations of the relative sea levels between different curves (e.g. Fig. 5.1) occur as a result of a combination of approach-driven differences, that is the methods used in sea-level construction cause some variation, and also as a result of the natural variation of sea-level behaviour over time linked to Earth's geophysical processes resulting in complex sea-level patterns (e.g. Yokoyama and Esat, 2011; Dutton et al., 2015). For an introduction on each of the approaches in Table 5.1 see Section 2.1.2.)

Study	Location	Duration (ka)	Stated elevation Uncertainty (m)
Oxygen isotope records combined with hydraulic models			
Siddall et al. (2003)	Red sea	400	± 12
Rohling et al. (2009)	Red sea	520	± 12
Grant et al. (2014)	Red sea	500	± 30 (max)
Rohling et al. (2014)	Mediterranean	5300	± 6.3
Oxygen isotope records combined inverse ice-volume models			
Bintanja et al. (2005)	Global stack	1070	± 12
Bintanja and Van de Wal (2008)	Global stack	3000	~ ± 20 (max)
De Boer et al. (2010)	Global stack	35000	~ ± 20 (min)
Oxygen isotope records combined with coral regression			
Waelbroeck et al. (2002)	N Atlantic & Pacific	450	± 13
Siddall et al. (2010)	Pacific	5000	~ ± 15
Bates et al. (2014)	Pacific	5000	± 10
Oxygen isotope records combined with benthic and planktonic proxies			
Shackleton (2000)	Pacific	400	?
Lea et al. (2002)	Eq. Pacific (East)	360	27 (max)
Sosdian and Rosenthal (2009)	North Atlantic	3200	~ ± 20 (max)
Elderfield et al. (2012)	South Pacific	1500	± 20
Shakun et al. (2015)	Global stack	800	± 18

Table 5.1: Selection of the well-known sea-level curves representing large regions or global areas and their sea-level elevation uncertainties for sea-level highstands. Greyed out sea-level curves denote those selected for this study (see section 5.3.4).

5.2.1 Approach-driven variation

In Section 2.1.2, ate Quaternary sea-level curves that were derived using local observations on dated benchmarks (e.g. sand-barrier shorelines, coral reefs, speleothems), the variation of oxygen isotopes in marine sediments, and reconstructions of past ice sheets (Siddall et al., 2007 and *references therein*) were introduced. Sea-level curves derived using some of these methods are further explored in this section with specific attention paid to the approaches employed to derive the sea-level curves highlighted in Table 5.1, as these form the basis for a significant number of investigations into palaeoshoreline uplift (e.g. Roberts et al., 2009; Caputo et al., 2010; Cucci and Tertulliani, 2010; Saillard et al., 2011; Gallen et al., 2014; Jara-Munoz and Melnick, 2015; Binnie et al., 2016; Pedoja et al., 2018; Jara-Munoz et al., 2019; Ott et al., 2019; Robertson et al., 2019).

Sea-level curves in Table 5.1 that are constructed using dated benchmarks rely on ages derived from corals through application of the $^{234}U/^{230}Th$ method (Section 2.1.4.1). The age

resolution obtained using coral benchmarks is excellent, but this method cannot provide a continuous record of sea-level change. Conversely, sea-level curves that involve the use of oxygen isotope proxy records can be used to estimate continuous sea-level elevations over millions of years and determine highstand and lowstand timings, but are subject to sometimes significant assumptions and uncertainties, and limited age and elevation resolution (Dutton et al., 2015).

In more detail, the precision and accuracy of the dating techniques applied to coral benchmarks results in excellent temporal resolution and elevations record of past sea level up to ~140 ka (e.g. Stirling et al., 1998; Dutton and Lambeck, 2012; Dutton et al., 2015). As such, this method has been used to extensively explore sea-level during the Holocene (e.g. Bard et al., 1990; Clark et al., 2009; Lambeck et al., 2014) and up to the Last Interglacial (LIG) (e.g. Stein et al., 1993; Hearty et al., 2007; Stirling et al., 1998; Dutton and Lambeck, 2012; Medina-Elizalde, 2013). Beyond this timing however, there is a lack of data (Hibbert et al., 2016) and corals may be more susceptible to the effects of post-depositional diagenesis, which may result in inaccurate ages (e.g. Stirling et al., 1998; Dutton, 2015). This method is particularly prone to elevation uncertainties associated with a lack of understanding of the palaeodepth at which dated corals grow (Medina-Elizalde, 2013; Dutton et al., 2015; Hibbert et al., 2016). Furthermore, if corals are sampled from uplifted locations, uncertainties are also linked to constraining tectonic or isostatic uplift since their formation. Where there is a lack of understanding of the tectonic setting of the corals used as sea-level benchmarks, sea-level elevations derived from coral benchmarks in non-stationary settings may be circular in their nature (Hibbert et al., 2016).

The conversion of $\delta^{18}O$ from organisms within marine sedimentary cores to derive past sea-level elevations is carried out in combination with independent proxies (e.g. Mg/Ca ratios, inverse ice sheet modelling, $\delta^{18}O$ signals from atmospheric gas in ice cores, and hydraulic models from restricted basins) in order to estimate the temperature component, which is then used to drive ice-volume and sea-water volume calculations (Table 5.1, Section 2.1.2) (e.g. Shackleton et al., 2000; Lea et al., 2002; Waelbroeck et al., 2002; Siddall et al., 2003; Bintanja et al., 2005; Lisiecki and Raymo, 2005; Bintanja and Van de Wal, 2008; Rohling et al., 2009; Siddall et al., 2010; Elderfield et al., 2012; Grant et al., 2012: Bates et al., 2014; Rohling et al., 2014; Shakun et al., 2015). The adoption of different proxies, in combination with sea-level curves influenced by basin-specific variations (i.e. salinity and temperature) as a result of diverse geographical locations (Spratt and Lisiecki, 2016), means that derivation

of past sea levels using oxygen isotopes and their proxies have resulted in significant relative sea-level variation when sea-level curves are compared (Caputo et al., 2007; Yokoyama and Esat, 2011; de Gelder et al., 2020) (e.g. Fig. 2.6).

The intricacies of each approach that employs $\delta^{18}O$ records and temperature proxies are beyond the scope of this chapter, however, there are some points that provide insight into the different approaches, specifically regarding their uncertainties and reported issues (see Section 2.1.2 for an overview). In the application of Mg/Ca ratios, Lea et al. (2002) suggest that estimates of the calcification temperatures of planktonic foraminifera can be obtained using of Mg/Ca ratios because the calcification temperatures are imprinted onto the shells of foraminifera at the same time as the $\delta^{18}O$. Measurement of Mg/Ca ratios allows the temperature signal to be identified and subtracted from the $\delta^{18}O$ signal, which results in derivation of the $\delta^{18}O$ of seawater (e.g. Lea et al., 2002; Shakun et al., 2015) (Section 2.1.2). Where Mg/Ca ratios are used as a proxy (Lea et al., 2002; Elderfield et al., 2012), reported sea-level elevation uncertainties of ±20 m have been suggested to reflect the challenges of this method whereby observations on different species of foraminifera reveal sensitivities to environmental conditions other than temperature that may result in unreliable datasets (Skinner and Shackleton, 2005). Furthermore, the relationship between Mg/Ca and temperature has been shown to vary at the low temperatures experienced during glaciation, thus the reliability of this approach is questioned (Martin et al., 2002). Dutton et al. (2015) suggested that further development of this method is necessary in order to provide precise, reliable estimates of peak sea-level elevations during past warm periods (see also Past Interglacials Working Group (PAGES), 2016). Where a Mg/Ca proxy is used, Lea et al. (2002) acknowledged the possibility of local hydrological differences and suggested that these may be dealt with using a stacked record. Using planktonic data, the stacked records approach was adopted by Shakun et al. (2015) and revealed a common signal interpreted with low standard errors for the last glacial cycle but higher errors over 800 ka owing to fewer records. Criticisms of the use of planktonic records (i.e. Shakun et al., 2015) in comparison to benthic records centre around the fact that planktonic $\delta^{18}O$ represent only the shallow sea-surface temperature (Spratt and Lisiecki, 2016) compared to the deeper water temperature obtained from benthic records, however, Lang and Wolff (2011) showed that planktonic- and benthic-derived records result in similar findings.

Inverse ice-sheet modelling uses a stacked global record of 57 benthic $\delta^{18}O$ datasets to model surface air temperatures in order to derive an ocean-temperature model. This model was applied in Bintanja et al. (2005), Bintanja and Van de Wal (2008) and De Boer et al. (2010). These studies involved assumptions on the deep water temperatures and their relationship to atmospheric temperatures (Bintanja and Van de Wal, 2008) resulting in significant uncertainties; in the work of De Boer et al. (2010) there is a lack of paleoclimate data to constrain the results over the 35 Ma time period. Furthermore, one of the criticisms of this approach is that in the studies by Bintanja et al. (2005) and Bintanja and Van de Wal (2008), these authors did not allow for the fact that deep ocean temperature may not be the same between all ocean basins (Siddall et al., 2010).

Sea-level curves developed using $\delta^{18}O$ records from semi-restricted basins such as the Red Sea (Siddall et al., 2003; Rohling et al., 2008) and Mediterranean basin (Rohling et al., 2014) rely, in part, on the relationship between sea-water elevation, evaporation and knowledge of the sea water exchange above their constraining sills (shallow-water bathymetric features that define the marine basin margin, and hence internal water circulation). Consequently, in addition to the existing uncertainties of using $\delta^{18}O$ records, these sea-level curves derived from hydraulic models may be subject to additional uncertainties related to assumptions based upon the sill depth and regional hydrology (Dutton et al., 2015). However, as their semi-continuous records extend from century to multiple millennial timescales, they are considered to be a particularly innovative approach to deriving sea-level elevations (Dutton et al., 2015).

Making use of the coral benchmark record, and the precision afforded by such a dataset, Waelbroeck at al. (2002) identified robust statistical regressions between relative sea-level and benthic foraminifera up to ~140 ka. These regressions were then used to compile a relative sea-level curve throughout the late Quaternary to ~400 ka using records from the N. Atlantic and Pacific to compile sea-level reconstructions. However, their composite sea-level curve is constructed from the most reliable sections of each of the N. Atlantic and Pacific records rather than a combination of the two, even though their results recognise that reconstructions using the N. Atlantic and Pacific are not wholly in agreement; this is reflected in uncertainties of ±13 m. Similar to this approach, Siddall et al. (2010) estimated a transfer function between temperature and benthic $\delta^{18}O$ and applied this to data from the Pacific in order to identify the deep Pacific temperature signal. Bates et al. (2014) adopted the transfer

function approach of Siddall et al. (2010) but for multiple sites (as per Waelbroeck et al., 2002) throughout the world. Studies that use transfer function/regression methods induce uncertainties during their conversions of sea level to $\delta^{18}O$ ice owing to the fact that the data they use may vary with location (Bates et al., 2014); authors of these studies also acknowledge that while their studies suggest that a temporally constant transfer function can be applied throughout time, it is plausible that differences between the contributions of temperature, ice volumes and hydrography to the benthic $\delta^{18}O$ record may render such an approach unreliable prior to ~700 ka (Waelbroeck et al., 2002; Bates et al., 2014).

The application of principle component analysis, a statistical method designed to identify a common signal from a set of records, was employed by Spratt and Lisiecki (2016). This study used seven sea-level curves derived from $\delta^{18}O$ proxy records to find a common sea-level signal (curve) despite the different underlying assumptions of each of the curves. The sea-level curves employed in the study were representative of a variety of proxies, while the approach identified a strong common signal using the seven sea-level curves to 430 ka, it did not capture brief sea-level highstands <2 ka in length and may have acted to smooth out the sea-level elevation on certain highstands (MIS 5e and 7e) that have higher resolutions compared to other highstands (Spratt and Lisiecki, 2016), possibly resulting in underestimated sea-level elevations.

5.2.2 Natural variation

Natural variations of the timing and magnitudes of sea-level during the same highstand at different locations throughout the world means that different locations across the Earth's surface may experience relative variations of the peak sea-level elevation and the timing of the peak sea level during an interglacial (Farrell and Clark, 1976; Potter and Lambeck, 2004; Dutton and Lambeck, 2012; Lambeck et al., 2012). Such variations are dependent upon the location of ice-sheets and the localised isostatic response to ice and water loading, and gravitational effects (Fig. 5.3). Specifically: (i) the growth and decay of large ice sheets deforms the crust and mantle where bulges occur away from ice sheets as mantle flows away from the ice load, (ii) very large ice sheets (e.g. Laurentide North American ice sheet) are significant enough to shift the Earth's axis of rotation, which distorts sea-level close by; and (iii) ocean basin uplift occurs during glaciations as the load of the water is lower, but when the ice melts water load depresses the basin again (Fig. 5.3) (Yokoyama and Esat, 2011).

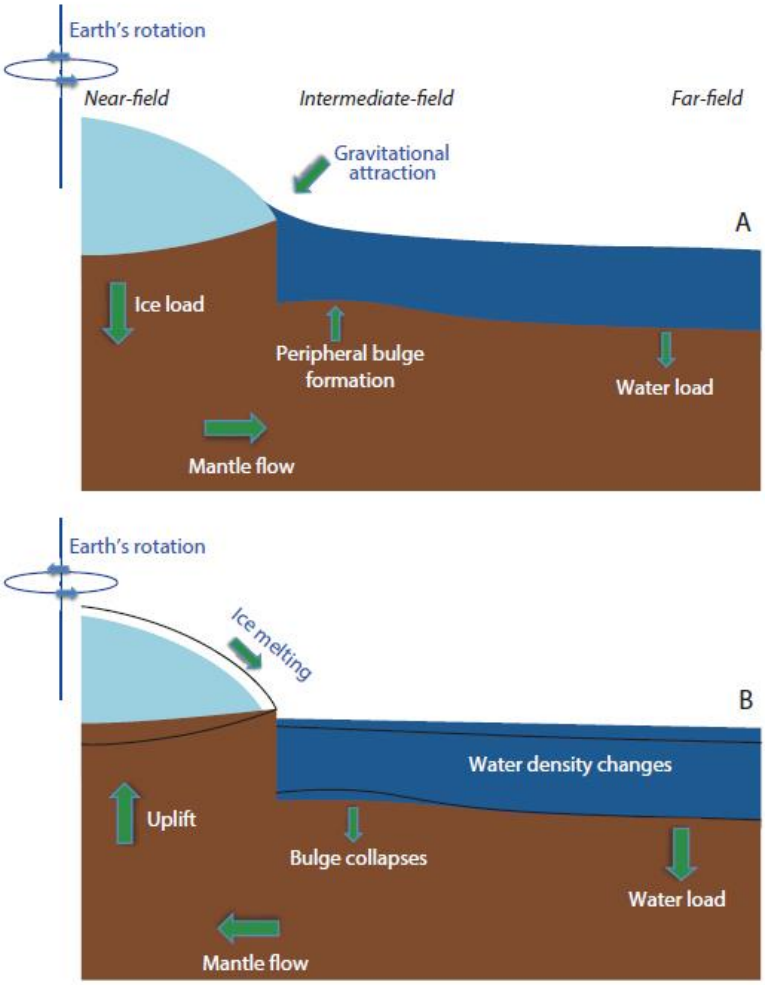

Figure 5.3: Effects of changing the mass of large ice sheets during the growth (A) and melting (B) of large ice sheets. (A) During growth stage, local crustal loading occurs and an intermediate crustal bulge due to mantle flow may form; gravitational attraction of seawater adjacent to and toward the margin occurs due to perturbation of Earth's rotational axis. (B) During melting, local uplift and bulge collapse occurs and rotational disturbances decrease (from Yokoyama and Esat, 2011)

It has been shown that the locations of sites of sea-level investigations relative to large ice sheets has a direct impact on the resultant magnitudes of sea-level elevation in both near- and far-field locations (Nakada and Lambeck, 1988; Dutton and Lambeck, 2012; Lambeck et al., 2012). During an interglacial, near-field locations, that is those that are closely located to a large ice sheet, will be impacted by both eustatic sea-level rise and a slowly rising relative sea level caused by ice sheet unloading dominating the signal (Dutton and Lambeck et al., 2012). Far-field locations may experience a short-term fall in continental coastal sea-levels at the beginning of a highstand because during deglaciation the sea-floor is depressed relative to the continent; this physical process is linked to the change in water load at far-field sites, which dominates the shorter wavelengths of the spatial pattern of sea-level change (Dutton and Lambeck et al., 2012). The wider effect of the complexities of large

volumes of ice melting is captured by Dutton and Lambeck (2012): "…at neither near- nor far-field sites is there a simple relation between observed sea levels and ice volumes during interglacials: the actual relationship requires knowledge of the ice sheets before, during and after the interglacial; of Earth's rheological response to ice-water loads; and of the evolution of the ocean basin shape during the glacial cycles". At first sight, such observations may suggest that the accuracy of all sea-level curves is strongly debatable. However, this chapter makes use of coastal locations within the Mediterranean basin, where past sea-level indicators of numerous Late-Quaternary sea-level highstands have experienced tectonic uplift and are thus well preserved (e.g. Laborel and Laborel-Deguen, 1994; Antonioli et al., 2006), and have shown in Chapter four to result in successful highstand to palaeoshoreline correlations.

In summary, considering the approach- and natural-driven variations identified above, it is clear that measuring past sea-level with a high degree of confidence is complex and that even in the same locations variations between the elevations and timing of past sea levels may occur. Such an array of methodologies leaves the potential user in a position where use of a single sea-level curve to calculate deformation rates may seem like a somewhat arbitrary decision. However, while the absolute uncertainties for each sea-level curve appear large relative to the sea-level elevations, it should be noted that comparison of sea-level curves over similar time periods reveal that the uncertainties are broadly similar to one another (Table 5.1). The question still remains as to the effect of these uncertainties on deformation rates and their associated tectonic interpretations.

5.3 APPROACH AND METHOD

This chapter investigates the extent to which the uplift rates, slip/throw rates and recurrence intervals are sensitive to the use of different sea-level curve data within the Terrace Calculator. This is carried out using five topographic profiles (2, 4, 5, 9 and 10) (Fig. 5.2) from Chapter Four that have absolute age constraints on at least one palaeoshoreline within the profiles. A series of tests was carried out using sea-level elevation data extracted from the sea-level curves of Waelbroeck et al. (2002), Bintanja et al. (2005), Spratt and Lisiecki (2016), Shakun et al. (2015) and Bates et al. (2014) (Section 5.3.4, Table 5.1), in addition to that obtained from Siddall et al. (2003), used in Chapter 4. The tests were designed to investigate the following: (1) the differences in predicted elevations of undated palaeoshorelines given the same uplift rates applied in Chapter 4; (2) how the undated palaeoshoreline to highstand

allocation in each topographic profile differs when different sea-level curve data are used in the Terrace Calculator, (3) what impact the results of test (2) have on uplift rates assigned to individual profiles, the overall pattern of uplift along the strike of the palaeoshorelines, and on the implied recurrence intervals on the fault in question. For all of the tests, the variation of exact highstand ages obtained from the different curves necessitated the need for highstand bins, whereby the highstands from the different studies were grouped with highstands of similar timings within an MIS (Section 2.1.2). These bins and their associated MIS (as per Railsback et al., 2015) are shown in Table 5.2. Details of the approach for each of the tests are outlined below.

Highstand age range (ka)	Marine Isotope Stage (MIS)
50-53	3c
68-82	5a
98-102	5c
119-128	5e
166-186	6d
196-200	7a
210-227	7c
236-240	7e
280-287	9a
305-325	9c
330-340	9e
383	11a
397-410	11c

Table 5.2: Highstand age ranges observed in this study for each MIS.

5.3.1 Test 1: Predicted elevations using different sea-level curves

This test examined the variation of palaeoshoreline elevations using the uplift rates obtained in Chapter 4 and the 6 sea-level curves in question. The sea-level elevations and highstand ages were extracted from each of the six curves (outlined in Section 5.3.4, Fig. 5.1). These sea-level data were, in turn, input into the Terrace Calculator with given uplift rates for each profile obtained from Chapter 4, which results in a set of predicted palaeoshoreline elevations for all highstands within each profile. For each topographic profile, the predicted

elevations obtained from the Terrace Calculator were then plotted against those obtained using the sea-level curve of Siddall et al. (2003). Where the Terrace Calculator predicted that older palaeoshorelines would be destroyed and overprinted during younger highstands, these elevations were not plotted.

5.3.2 Test 2: Palaeoshoreline to highstand allocations of undated terraces

This test examined any differences between the correlation of undated palaeoshorelines to sea-level highstands in each profile using the six different sea-level curves and was designed to mimic studies by different authors on the same geographical area using different sea-level curves. The method mirrors that used in Chapter 4 whereby the elevation of the dated palaeoshoreline is used to obtain an uplift rate (Section 3.2, Fig. 3.12). This uplift rate is applied to the entire topographic profile and highstands are allocated to observed palaeoshoreline elevations if their predicted elevation matches within ±10 m, ensuring that R^2 is minimised. In order to find the exact 'best fit' uplift rate, the uplift rate was iterated by 0.01 mm/yr and the RMSE recorded. Where the RMSE is lowest, this is the uplift rate used (Fig. 3.12d). This analysis was carried out for all 5 profiles using the 5 sea-level curves to allow direct comparison of the results obtained using Siddall et al. (2003) from Chapter 4.

5.3.3 Test 3: Impact of different sea-level curves on along-strike uplift and recurrence intervals

This analysis used the data from Test 2 to examine the uplift rates of each profile and the along-strike pattern of uplift for each of the sea-level curves tested. The impact of the different sea-level curves on the inferred recurrence interval of the Ptolemy fault (Section 4.5) is tested using Profile 2 (Fig. 5.2) as this is the only profile that is likely to be relatively unaffected by slip on the SCCF (Fig. 4.16), it is recognised that this is a rather simplistic approach because Chapter 4 outlined that uplift along this section of Crete also probably involves some background regional value. Analysis of the recurrence interval variations was carried out using the uplifted 68-82 ka palaeoshoreline along Profile 2 measured at 26 m and the sea-level elevation for the 68-82 ka highstand from each sea-level curve in order to calculate the total vertical uplift since 68-82 ka. The recurrence intervals (Section 2.2.4) using each sea-level curve were calculated using knowledge that the modelled coseismic uplift of the Ptolemy during an earthquake is 0.4 m obtained in Section 4.5, which can be used with the total uplift to calculate the number of earthquakes since the 68-82 ka highstand allowing the recurrence interval to be calculated.

5.3.4 Details of the sea-level curves selected for this study

The sea-level curves tested within this chapter are from Siddall et al. (2003), Waelbroeck et al. (2002), Bintanja et al. (2005), Spratt and Lisiecki (2016), Shakun et al. (2015) and Bates et al. (2014); they have been selected from Table 5.1 on the basis of being derived using different approaches, covering varying timescales and representing differing regional or global areas (as opposed to localised). The sea-level curve of Siddall et al. (2003) is selected because it was used in Chapter 4 to derive uplift and recurrence intervals and therefore provides a 'baseline' with which to compare other sea-level curves to. The curve of Bintanja et al. (2005) is selected over the curves of Bintanja and Van de Wal (2008) and De Boer et al. (2010) because it covers a shorter time period that is more fitting to the palaeoshoreline sequences in Chapter 4 (1 Ma compared to 3 Ma and 35 Ma, respectively) and consequently therefore requires fewer assumptions. The curve of Shakun et al. (2015) is selected because it uses a set of stacked records designed to reduce the issues discussed in Section 5.2.1 associated with the paired δ^{18}O-Mg/Ca approach (e.g. Lea et al., 2002; Elderfield et al., 2012) and may therefore be more representative than the other studies using proxies for temperature. While they adopt similar methods, both the curves of Bates et al. (2014) and Waelbroeck et al. (2002) were selected because they represent different geographical areas; in the case of the latter, it was also selected because it makes use of the coral benchmarking data. Finally, the sea-level curve of Spratt and Lisiecki (2016) was selected because it represents a statistical analysis to derive a common signal from a number of sea-level curves, including three from within this selection.

The selected sea-level datasets show differences between their sea-level elevations (relative to today) for highstands and highstand timings within the late Quaternary (Figs. 5.4, 5.5). The extent of the sea-level elevation variance between highstand bins is examined in plots of (i) the calculated mean sea level elevations per highstand bin and their absolute deviations (Fig. 5.6a) and (ii) mean absolute deviation for each highstand bin (Fig 5.6b); where mean absolute deviation is presented because, in comparison to absolute deviation, it minimises the effects of data outliers. These plots reveal differences in the statistical variance between highstand bins; in detail, smaller envelopes of sea-level elevation variations and lower mean absolute deviations (Figs 5.4 and 5.6) are noted for 119-125 ka (MIS 5e), 196-200 ka (MIS 7a), 236-240 ka (MIS 7e) and 398-410 ka (MIS 11c); this observation is broadly in line with those from the Past Interglacials Working Group (2016) who recognised that MIS 1 (present day), 5e, 9e and 11c were the strongest highstands (also known as major highstands) achieving sea-levels

close to or exceeding the present day. Without considering the sea-level curve of Shakun et al. (2015), the 330-340 ka (MIS 9e) highstand in Figs. 5.4 and 5.5 would also exhibit a smaller deviation of sea-level elevation, but as a result of the very low elevation of Shakun et al. (2015) at 330-340 ka compared to other curves it has one of the highest mean absolute deviations of >10 m (Figs. 5.4, 5.6).

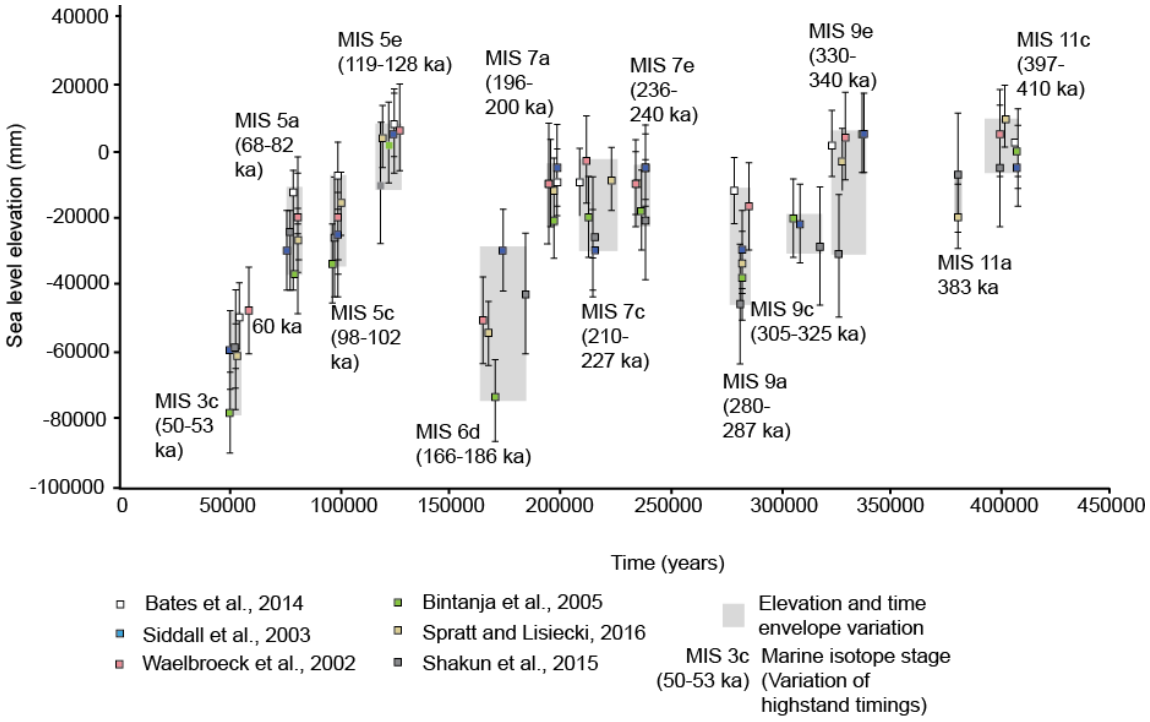

Figure 5.4: Variations in the timing and elevations of past sea-level highstands since ~410 ka shown as plots of the maximum elevations of past sea-level highstands (relative to today) and their timings from the sea-level curves tested in this chapter. Vertical bars represent reported elevation uncertainties. Grey boxes show the envelope of highstand age and elevations obtained from the sea-level curves for all highstands within each MIS (as per Railsback et al. (2015)). Longer and wider grey boxes indicate greater disagreement of sea-level elevation and timing, respectively, in each highstand bin. Detailed plots showing the elevation for each highstand bin in comparison to the mean are in Fig. 5.5.

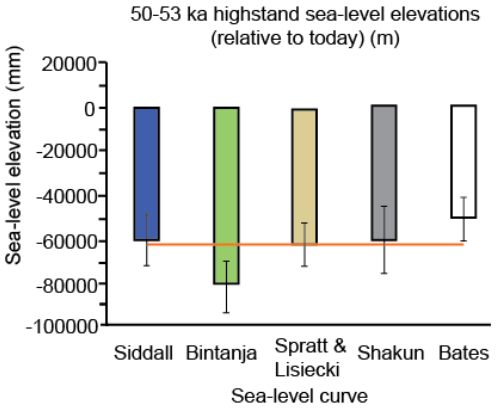
50-53 ka highstand sea-level elevations
(relative to today) (m)
Sea-level elevation (mm)
20000
0
-20000
-40000
-60000
-80000
-100000
Siddall
Bintanja
Spratt & Lisiecki
Shakun
Bates
Sea-level curve

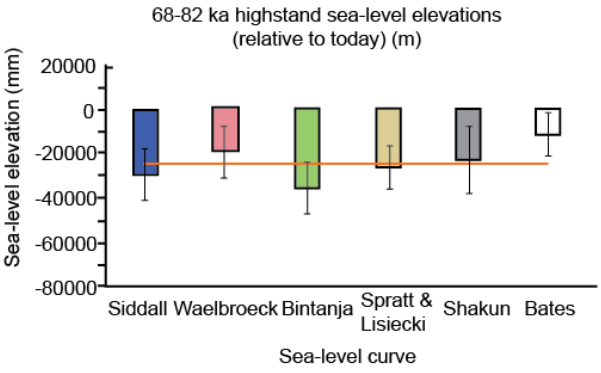
68-82 ka highstand sea-level elevations
(relative to today) (m)
Sea-level elevation (mm)
20000
0
-20000
-40000
-60000
-80000
Siddall
Waelbroeck
Bintanja
Spratt & Lisiecki
Shakun
Bates
Sea-level curve

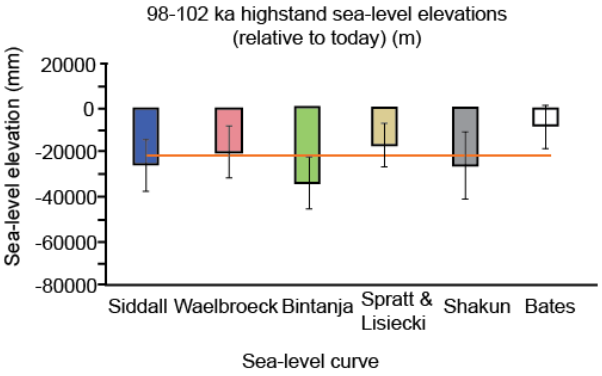
98-102 ka highstand sea-level elevations
(relative to today) (m)
Sea-level elevation (mm)
20000
0
-20000
-40000
-60000
-80000
Siddall
Waelbroeck
Bintanja
Spratt & Lisiecki
Shakun
Bates
Sea-level curve

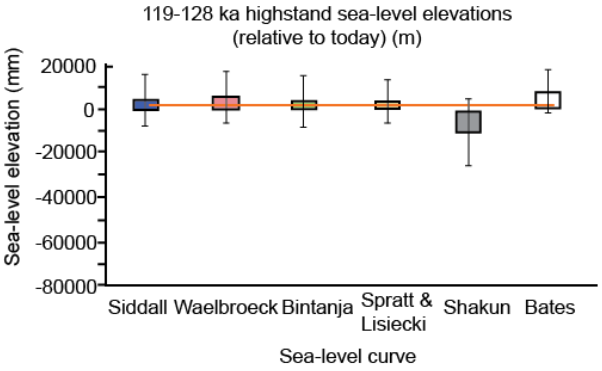
119-128 ka highstand sea-level elevations
(relative to today) (m)
Sea-level elevation (mm)
20000
0
-20000
-40000
-60000
-80000
Siddall
Waelbroeck
Bintanja
Spratt & Lisiecki
Shakun
Bates
Sea-level curve

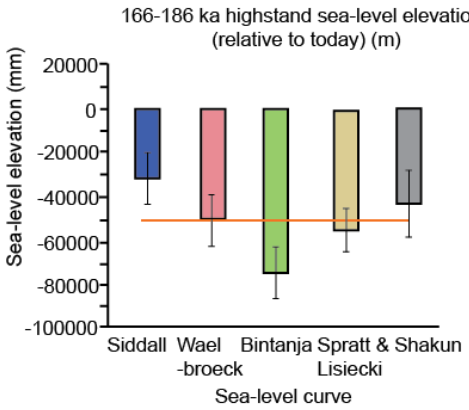
166-186 ka highstand sea-level elevations
(relative to today) (m)
Sea-level elevation (mm)
20000
0
-20000
-40000
-60000
-80000
-100000
Siddall
Wael -broeck
Bintanja
Spratt & Lisiecki
Shakun
Sea-level curve

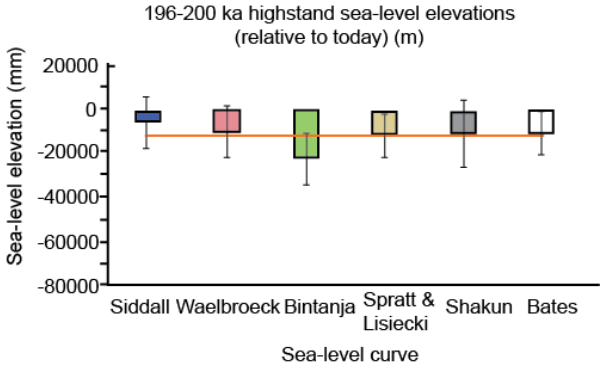
196-200 ka highstand sea-level elevations
(relative to today) (m)
Sea-level elevation (mm)
20000
0
-20000
-40000
-60000
-80000
Siddall
Waelbroeck
Bintanja
Spratt & Lisiecki
Shakun
Bates
Sea-level curve

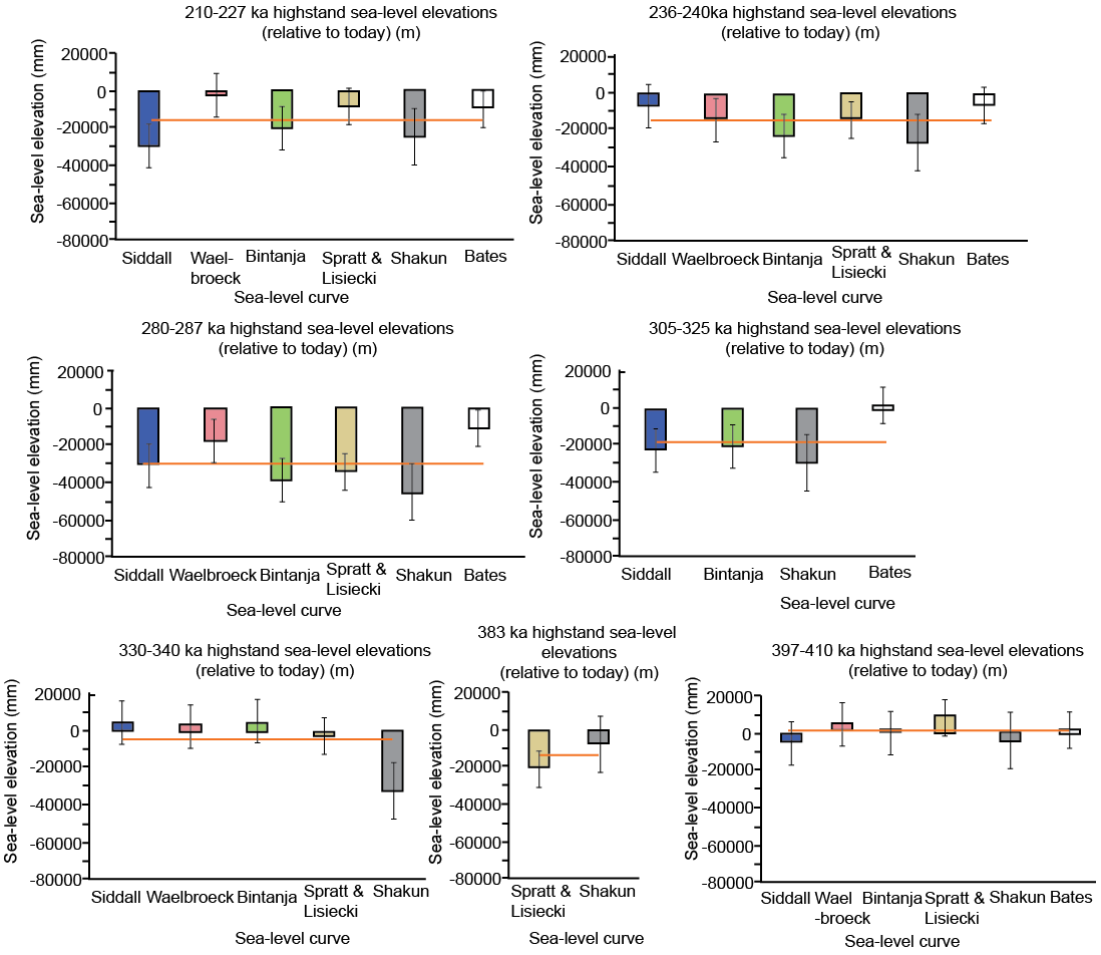

Figure 5.5: Plots of sea-level elevations (thick bars in colour) and uncertainties from the six sea-level curves by highstand bin to show the elevation variations when the sea-level curves are compared. The mean elevation for each highstand bin is shown by the orange line.

In comparison to the 'stronger, major' highstands, the 'weaker' highstands (lower sea-level elevations relative to today, also referred to as 'minor' highstands) of 166-186 ka (MIS 6d), 210-227 ka (MIS 7c), 280-287 ka (MIS 9a) and 305-325 ka (MIS 9c) display higher mean absolute deviations of ~ 10 m (Figs. 5.4, 5.6). More moderate variability is observed for the remaining highstands: 50-53 ka (MIS 3c), 68-82 ka (MIS 5a), 98-102 ka (MIS 5c) and 383 ka (MIS 11a) which have mean absolute deviations of ~6-7 m (Fig. 5.6). It should be noted that two of the older highstands (305-325 ka, MIS 9c, and 383 ka, MIS 11a) are not recognised by all curves.

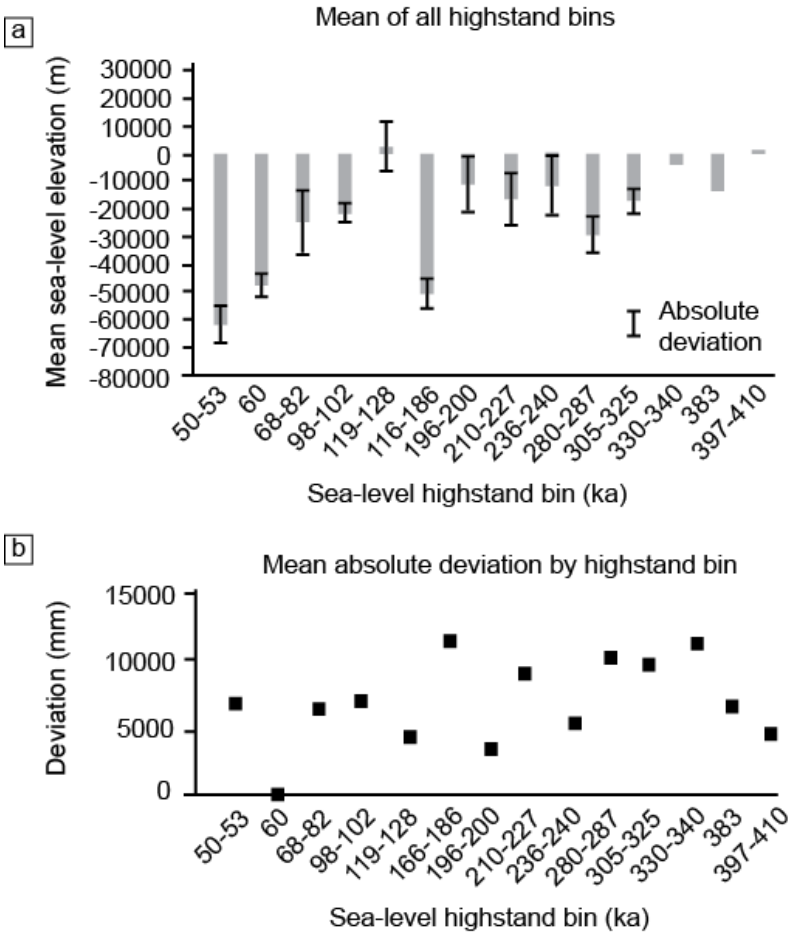

Figure 5.6: Plots of the mean sea-level elevations for each highstand bin. (a) Bar chart to show the mean sea-level elevations for each highstand bin, plots are constructed to show the mean elevation for each sea-level highstand using data from the six sea-level curves featured herein. The absolute deviation associated with each highstand bin are also shown. (b) Plots of the mean absolute deviation for sea-level elevations by highstand bin. Note: mean absolute deviation is a way of reducing the effect of outliers on the value of deviation.

5.4 RESULTS

5.4.1 Test 1: Predicted elevations using different sea-level curves

A comparison of the predicted elevations of sea-level highstands for different sea-level curves using the uplift rates established for Profiles 2, 4, 5, 9 and 10 in Chapter 4 based upon the sea-level curve of Siddall et al. (2003) is shown in Fig. 5.7.

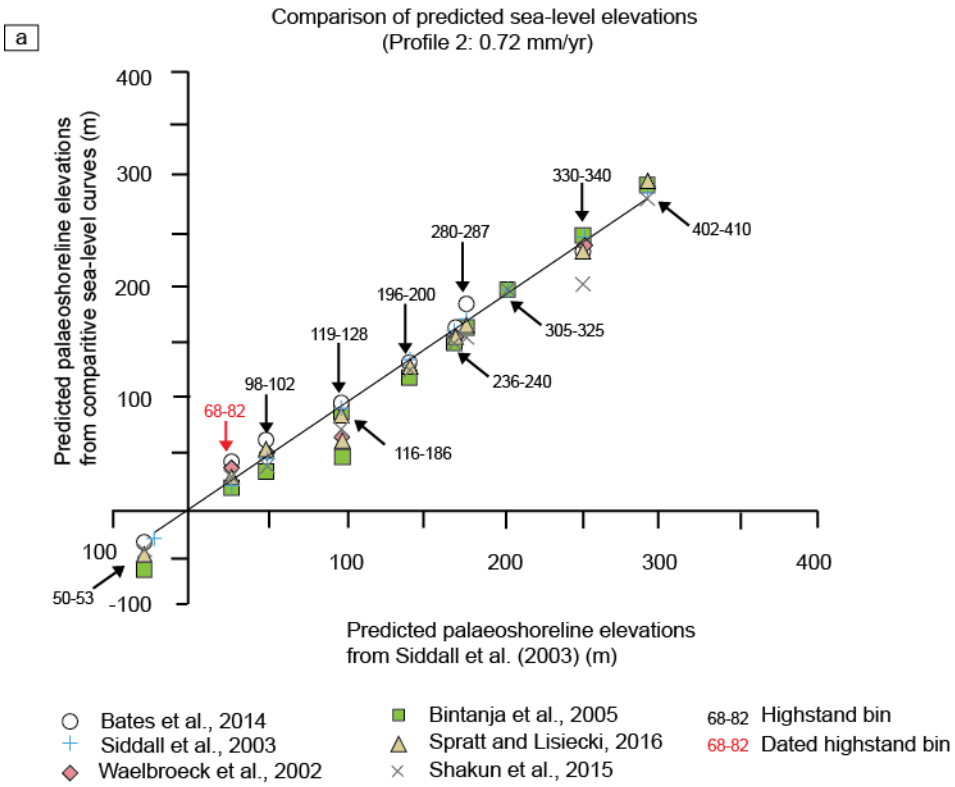
a
Comparison of predicted sea-level elevations
(Profile 2: 0.72 mm/yr)
Predicted palaeoshoreline elevations from comparitive sea-level curves (m)
400
300
200
100
-100
100
200
300
400
330-340
402-410
280-287
196-200
305-325
119-128
236-240
98-102
68-82
116-186
50-53
Predicted palaeoshoreline elevations from Siddall et al. (2003) (m)
Bates et al., 2014
Siddall et al., 2003
Waelbroeck et al., 2002
Bintanja et al., 2005
Spratt and Lisiecki, 2016
Shakun et al., 2015
68-82 Highstand bin
68-82 Dated highstand bin

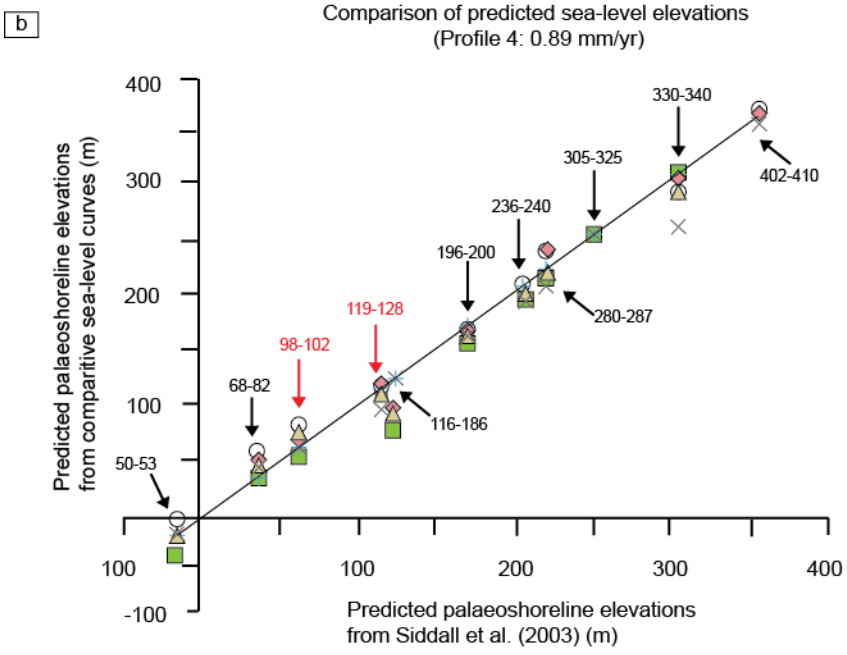
b
Comparison of predicted sea-level elevations
(Profile 4: 0.89 mm/yr)
Predicted palaeoshoreline elevations from comparitive sea-level curves (m)
400
300
200
100
-100
100
200
300
400
330-340
305-325
402-410
236-240
196-200
280-287
119-128
98-102
68-82
116-186
50-53
Predicted palaeoshoreline elevations from Siddall et al. (2003) (m)

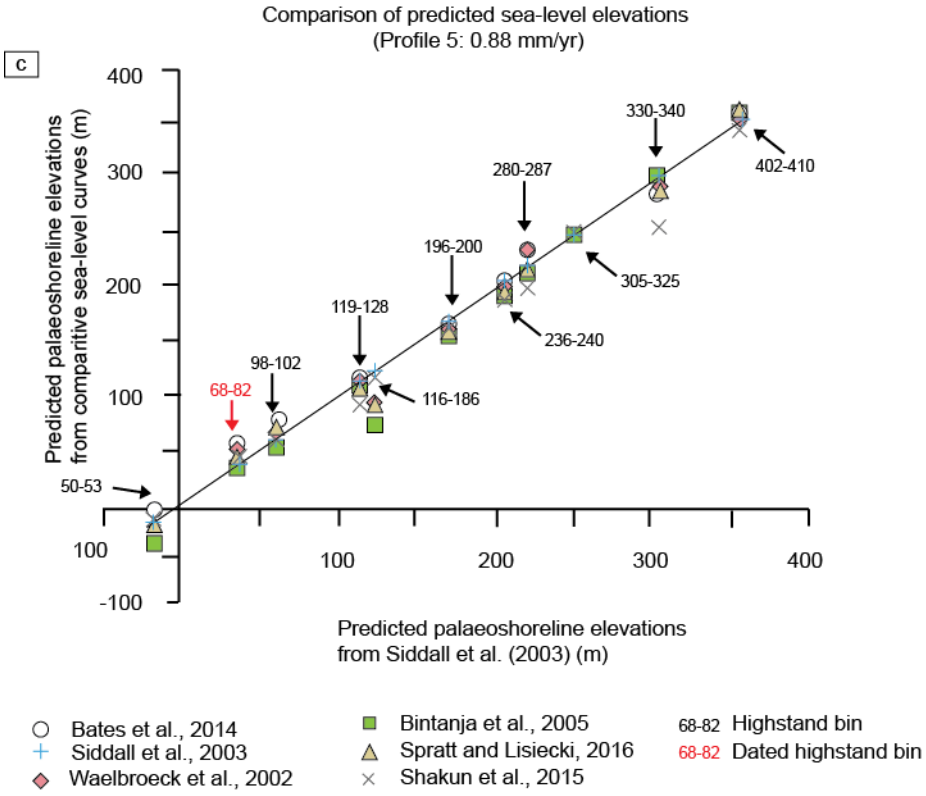
Comparison of predicted sea-level elevations
(Profile 5: 0.88 mm/yr)
c
Predicted palaeoshoreline elevations from comparitive sea-level curves (m)
400
300
200
100
-100
100
200
300
400
330-340
402-410
280-287
196-200
305-325
119-128
236-240
98-102
68-82
116-186
50-53
Predicted palaeoshoreline elevations from Siddall et al. (2003) (m)
Bates et al., 2014
Siddall et al., 2003
Waelbroeck et al., 2002
Bintanja et al., 2005
Spratt and Lisiecki, 2016
Shakun et al., 2015
68-82 Highstand bin
68-82 Dated highstand bin

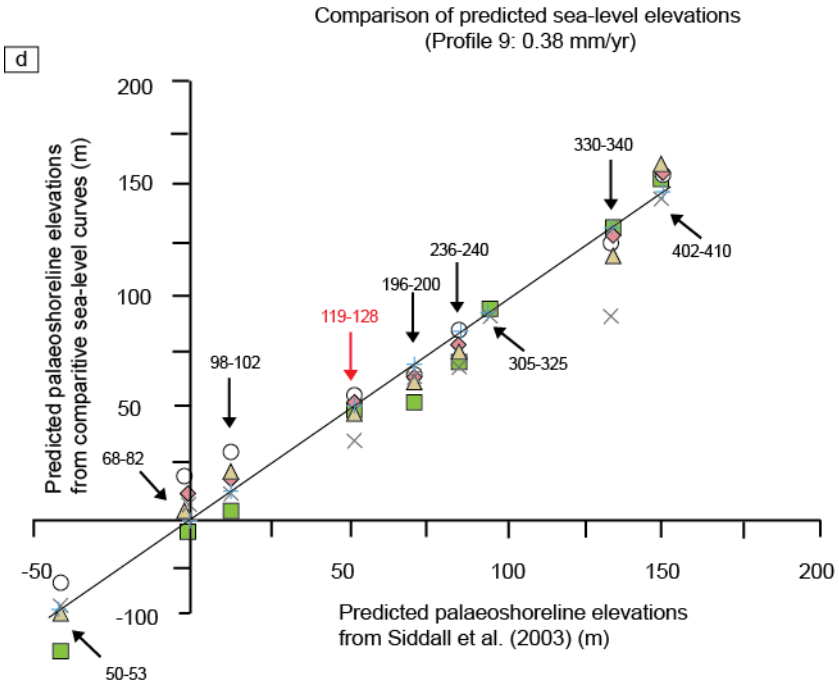
Comparison of predicted sea-level elevations
(Profile 9: 0.38 mm/yr)
d
Predicted palaeoshoreline elevations from comparitive sea-level curves (m)
200
150
100
50
-100
-50
50
100
150
200
330-340
402-410
236-240
196-200
119-128
305-325
98-102
68-82
50-53
Predicted palaeoshoreline elevations from Siddall et al. (2003) (m)

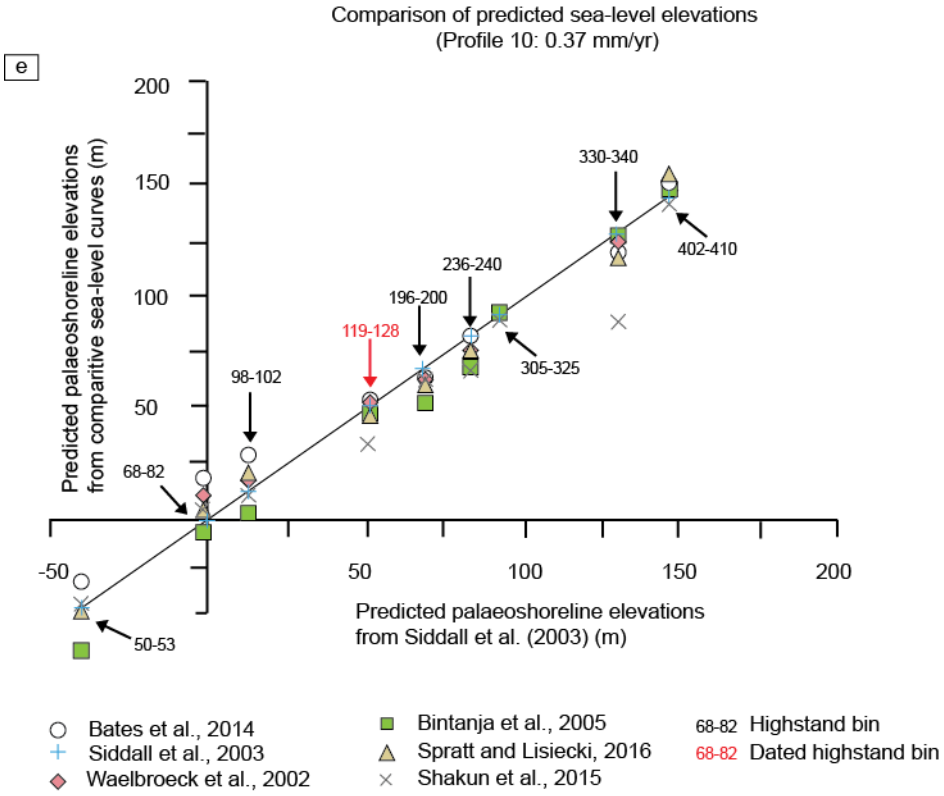

Figure 5.7: Predicted sea-level elevations for Profiles 2 (a), 4 (b), 5 (c), 9 (d) and 10 (e). The predicted elevations are calculated using sea-level highstand elevations from the sea-level curves of Bates et al. (2014), Waelbroeck et al. (2002), Bintanja et al. (2005), Spratt and Lisiecki (2016) and Shakun et al. (2015) plotted against Siddall et al. (2003) and the uplift rates from Chapter 4. The grey line in each profile is the best-fit line of predicted elevations using Siddall et al. (2003).

The broad linearity observed in these plots appears to suggest that given the same uplift rates, the predicted elevations from the tested sea-level curves are similar to those obtained from Siddall et al. (2003). However, variability in the order of up to 46 m is apparent for some highstand bins (Table 5.3) when elevations from all of the sea-level curves are compared. Specifically, comparison of the differences between the highest and lowest predicted elevation values for highstand bins (obtained from: highest predicted elevation minus lowest predicted elevation per bin) in Profiles 2, 4, 5, 9 and 10 show that some highstand bins record larger predicted elevation differences (up to 46 m from: 50-53 ka, 166-186 ka, 280-287 ka and 330-340 ka) compared to other bins (Table 5.3). The remaining highstand bins have lower differences of <28 m (Table 5.3). The highstand bins with larger predicted elevation differences are reflective of highstand bins with high absolute mean deviations for sea-level elevations (Fig. 5.6b).

It is also observed that predicted elevations from the curve of Bates et al. (2014) appear to be higher compared to the other sea-level curves while, conversely, predicted elevations from the sea-level curves of Shakun et al. (2015) and Bintanja et al. (2005) broadly plot at

lower elevations. The elevations obtained using the curves of Waeklbroeck et al. (2002) and Spratt and Lisiecki (2016) are in general agreement with one another and those from Siddall et al. (2003).

Highstand bin (ka)	Maximum difference between the highest and lowest predicted elevations (for Profiles 2, 4 and 5, high uplift)	Maximum difference between the highest and lowest predicted elevations (for Profiles 9 and 10, low uplift)
50-53	33	31
68-82	25	25
98-102	28	27
119-128	23	20
166-186	45	No value, palaeoshoreline overprinted
196-200	13	12
210-227	24	16
236-240	16	16
280-287	33	2
305-325	3	5
330-340	46	41
383	13	7
397-410	17	15

Table 5.3: Comparison of the differences between the highest and lowest predicted elevation values for highstand bins (obtained from: highest predicted elevation minus lowest predicted elevation) for high uplift profiles (2, 4 and 5) and low uplift profiles (9 and 10).

The findings of this section show that comparing the predicted elevations for highstand bins in each profile obtained from different sea-level curves to those from Siddall et al. (2003) (using the uplift rates of Chapter 4) reveal clear differences between the elevations. Highstand bins with the largest difference between the highest and lowest predicted elevations are those that display high mean absolute deviations for sea-level elevations per highstand bin.

5.4.2 Test 2: Palaeoshoreline to highstand allocations of undated terraces

While the results shown in Section 5.4.1 (above) are interesting, they do not provide information about the extent to which the uplift rates for each profile would differ assuming the Terrace Calculator was populated with sea-level elevation data from the curves of

Waelbroeck et al. (2002), Bintanja et al. (2005); Spratt and Lisiecki (2016), Shakun et al. (2015) and Bates et al. (2014); this is the focus of this test. Test 2 also explores how the correlation between undated palaeoshorelines and highstands varies when different sea-level curves are used.

The approach used to carry out this analysis is detailed in Section 5.3. To remind the reader, the uplift rate for each profile was set using the dated palaeoshoreline and respective highstand sea-level elevation from the sea-level curve in question; the Terrace Calculator produced a set of predicted palaeoshoreline elevations and the measured palaeoshoreline elevations were matched to those predicted by the calculator if they were ±10 m in order to correlate undated palaeoshorelines. The palaeoshoreline to highstand correlations made using each sea-level curve on Profiles 2, 4, 5, 9 and 10, were evaluated using R^2. The exact best fit uplift rate for each profile was determined using the lowest RMSE value.

The results of Test 2 are explored below; they are presented based upon the age of the dated palaeoshoreline for each profile because Section 5.3.4. showed differences between the variance (absolute deviation, Fig 5.6a and mean absolute deviation, Fig 5.6b) for the highstand bins, and this variance may impact the results of this analysis. Age controls on the five profiles either constrain the elevation of the 68-82 ka palaeoshoreline (Profiles 2 and 5) or the 119-128 ka palaeoshoreline (Profiles 4, 9 and 10); the absolute variations between the sea-level elevations from the six sea-level curves for the 68-82 ka and 119-128 ka highstands are 25 m and 18 m respectively. The results of Test 2 are presented in Table 5.4, Figs. 5.8, 5.9 for each topographic profile and display the number of sea-level curves that result in the same correlations of palaeoshorelines to highstands and outlined in Section 5.4.2.1.

5.4.2.1 Palaeoshoreline to highstand correlation using different sea-level curves

The results from Profiles 4, 9 and 10 (constrained by the 119-128 ka palaeoshoreline) (Figs 5.8a-c, Table 5.4) show good agreement between the highstand to palaeoshoreline allocations, that is, the results from a number of different sea-level curves allocate the observed palaeoshorelines to the same highstand ages. In detail, along Profile 4 (constrained by the 119-128 ka palaeoshoreline (Fig. 5.8a) four out of the six sea-level curves resulted in predicted elevations that matched the 38 m palaeoshoreline to the 68-82 ka highstand (Waelbroeck et al., 2002; Siddall et al., 2003; Bintanja et al., 2005 and Spratt and Lisiecki).

There were no matches for the 38 m palaeoshoreline to predicted elevations from the curves of Shakun et al., 2015 and Bates et al., 2014. Palaeoshorelines at 67 m and 116 m both have age controls (98-102 and 119-128 ka, respectively), and all sea-level curves predict elevations that can be matched to the measured shoreline elevations. Predicted elevations for the 211 m palaeoshoreline using the curves of Siddall et al. (2003); Bintanja et al. (2005), Spratt and Lisiecki (2016) and Shakun et al. (2015) suggest an allocation of the 236-240 ka highstand bin, whereas the 310 m palaeoshoreline is allocated to the 330-340 ka highstand only using the curve of Siddall et al, (2003).

For Profile 9, (constrained using the 119-128 ka palaeoshoreline (Fig. 5.8b)), the predicted elevations from Spratt and Lisiecki (2016), Waelbroeck et al. (2002), Shakun et al. (2015) and Bates et al. (2014) allocate the 12 m palaeoshoreline to the 98-102 ka highstand, compared to the 98-102 ka highstand allocated using the curves of Siddall et al. (2003) and Bintanja et al. (2005). The 86 m palaeoshoreline is allocated to the 236-240 ka highstand bin by the curves of Siddall et al. (2003); Bintanja et al. (2005), Spratt and Lisiecki (2016) and Shakun et al. (2015) suggest an allocation of the 236-240 ka highstand bin to the 196-200 ka highstand, and Bates et a. (2014) to the 280-287 ka highstand.

Profile 10, (also constrained using the 119-128 ka palaeoshoreline (Fig. 5.8c)) show the lowest palaeoshoreline observed is at 22 m, using the sea-level curves of Spratt and Lisiecki (2016) and Waelbroeck et al. (2002) this is allocated to the 98-102 ka -highstand, while Shakun et al. (2015) and Bates et al. (2014) allocate it to the 68-82 ka highstand. There is no match between the observed elevations and predicted palaeoshoreline elevations using the curves of Siddall et al. (2003) and Bintanja et al. (2005). For the 67 m palaeoshoreline, four of the sea-level curves – Siddall et al. (2003), Bintanja et al. (2005), Spratt and Lisiecki (2016) and Waelbroeck et al. (2002) – result in matching predicted elevations suggestive of the 196-200 ka highstand. With the exception of the predicted elevation using the curve of Spratt and Lisiecki (2016), the same sea-level curves also suggest that the next palaeoshoreline at 83 m belongs to the 234-240 ka highstand. The curve of Spratt and Lisiecki (2016) suggest that the 83 m palaeoshoreline is linked to the 210-227 ka highstand. The highest palaeoshoreline at 99 m has various allocations by the different curves: 305-325 ka using Siddall et al. (2003) and Bintanja et al. (2005), 280-287 ka using the curves of Waelbroeck et al. (2002) and Bates et al. (2014), and 236-240 ka using the curve of Spratt and Lisiecki (2016).

Profiles 2 and 5 are constrained using the 68-82 ka palaeoshoreline (Fig. 5.9a) and show poorer correlation compared to Profiles 4, 9 and 10. Along Profile 2, the palaeoshoreline above the dated shoreline at 54 m is only allocated to a highstand (98-102 ka) using the sea-level data from Waelbroeck et al. (2002), and the 64 m palaeoshoreline is allocated to the 119-128 ka highstand by Shakun et al. (2015) and Bates et al. (2014). Conversely, the sea-level data from Siddall et al. (2003), Bintanja et al. (2005) and Spratt and Lisiecki (2016) suggest that the 97 m palaeoshoreline represents the 119-128 ka highstand, whereas using Waelbroeck et al. (2002) and Bates et al. (2014) the 97 m palaeoshoreline would be allocated to the 196-200 ka and the 210-227 ka highstands, respectively. There is further variability along this profile for the 139 m palaeoshoreline where three sea-level curves result in allocation to the 196-200 ka highstand (Siddall et al., 2003; Bintanja et al., 2005 and Spratt and Lisiecki, 2016), and the same palaeoshoreline is allocated to the 280-287 ka highstand using sea-level data from Waelbroeck et al. (2002) and Shakun et al. (2015). For the 174 ka palaeoshoreline this variability continues with allocations to the following highstands: 236-240 ka using Bintanja et al. (2002), 280-287 ka using Siddall et al. (2003) and Spratt and Lisiecki (2016), 305-325 ka using Shakun et al. (2015) and 330-340 ka using Waelbroeck et al. (2002).

Compared to Profile 2, Profile 5 (also constrained using the 68-82 ka palaeoshoreline (Fig. 5.9b)) has less variability in its allocation of lower palaeoshorelines to highstands, all sea-level curves result in the allocation of the 57 m palaeoshoreline to the 98-102 ka highstand, but the 79 m palaeoshoreline is only allocated to the 119-128 ka highstand using two sea-level curves – Shakun et al. (2015) and Bates et al. (2014). For the allocation of the higher terraces (to older palaeoshorelines) further variability is present, the 201 m palaeoshoreline can be allocated to the 236-240 ka highstand using Siddall et al. (2003) and Bintanja et al. (2005), to the 280-287 ka highstand using Spratt and Lisiecki, 2016 and Waelbroeck et al. (2002), and to the 305-325 ka highstand using Bates et al. (2014). The 258 m palaeoshoreline is allocated to three different highstands; Siddall et al. (2003) and Bintanja et al. (2005) allocate it to the 305-325 ka highstand, Spratt and Lisiecki (2016) and Waelbroeck et al. (2002) allocate it to the 330-340 ka highstand and Bates et al. (2014) allocate it to the 305-325 ka highstand. A similar situation is apparent for the 304 m palaeoshoreline whereby it is allocated to the 305-325 ka highstand by Shakun et al. (2015), the 330-340 ka highstand by Siddall et al. (2003) and Bintanja et al. (2005) and 397-410 ka highstand by Waelbroeck et al. (2002).

Evaluation of all of the highstand to palaeoshoreline correlations made by each of the different sea-level curves in Figs 5.8 and 5.9 are then analysed collectively based upon the total number of matches obtained between predicted and measured sea-level elevations, R^2 and RMSE (Table 5.4, Fig. 5.10).

Profile reference	Measured palaeoshoreline elevations DEM (barometric altimeter) **Dated** (m)	Siddall et al., 2003		Bintanja et al., 2005		Spratt and Lisiecki, 2016		Waelbroeck et al., 2002		Shakun et al., 2015		Bates et al., 2014	
		Predicted palaeoshoreline elevations	Binned Highstand (ka)	Predicted palaeoshoreline elevations	Binned Highstand (ka)	Predicted palaeoshoreline elevations	Binned Highstand (ka)	Predicted palaeoshoreline elevations (m)	Binned Highstand (ka)	Predicted palaeoshoreline elevations	Binned Highstand (ka)	Predicted palaeoshoreline elevations	Binned Highstand (ka)
2	**26**	**25**	**68-82**	**27**	**68-82**	**34**	**68-82**	**23**	**68-82**	**26**	**68-82**	**27**	**68-82**
	54					59	98-102						
	64									66	119-128	69	119-128
	97	95	119-128	100	119-128	93	119-128	97	196-200			93	210-227
	139	139	196-200	137	196-200	135	196-200	135	280-287	135	280-287		
	174	175	280-287	172	236-240	176	280-287	179	330-340	176	305-325		
4	38	38	68-82	40	68-82	48	68-82	48	68-82				
	67	**64**	**98-102**	**60**	**98-102**	**77**	**98-102**	**63**	**98-102**	**71**	**98-102**	**72**	**98-102**
	116	**116**	**119-128**	**120**	**119-128**	**113**	**119-128**	**112**	**119-128**	**107**	**119-128**	**108**	**119-128**
	133												
	211	209	236-240	210	236-240	205	236-240			214	236-240	212	280-287
	310	308	330-340										
	351												
5	**38**	**38**	**68-82**	**35**	**68-82**	**39**	**68-82**	**42**	**68-82**	**39**	**68-82**	**38**	**68-82**
	57	62	98-102	54	98-102	66	98-102	57	98-102	54	98-102	54	98-102
	79									86	119-128	86	119-128
	201	204	236-240	196	236-240	193	280-287	198	280-287			204	305-325
	258	248	305-325	256	305-325	261	330-340	252	330-340			256	397-410
	304	301	330-340	311	330-340			307	397-410	303	305-325		
9	12	12	98-102	8	98-102	7	68-82	13	68-82	14	68-82	18	68-82
	25					26	98-102	20	98-102	23	98-102	29	98-102
	51	**51**	**119-128**	**55**	**119-128**	**53**	**119-128**	**57**	**119-128**	**48**	**119-128**	**54**	**119-128**
	86	84	236-240	84	236-240	87	236-240	84	236-240	86	196-200	92	280-287
	149	147	397-410	151	330-340							154	397-410
10	22					27	98-102	20	98-102	20	68-82	18	68-82
	54	**51**	**119-128**	**52**	**119-128**	**54**	**119-128**	**57**	**119-128**	**58**	**119-128**	**56**	**119-128**
	67	69	196-200	60	196-200	71	196-200	69	196-200	63	166-186	70	210-227
	83	84	236-240	80	236-240	86	210-227	84	236-240			86	236-240
	99	93	305-325	106	305-325	89	236-240	98	280-287	102	196-200	94	280-287

Table 5.4: Allocation of measured versus predicted palaeoshoreline elevations obtained from inputting each sea-level curve into the Terrace Calculator. Measured palaeoshorelines are matched to predicted palaeoshorelines if they agree within ±10 m. Results of this are shown graphically in Figs. 5.7 and 5.8.

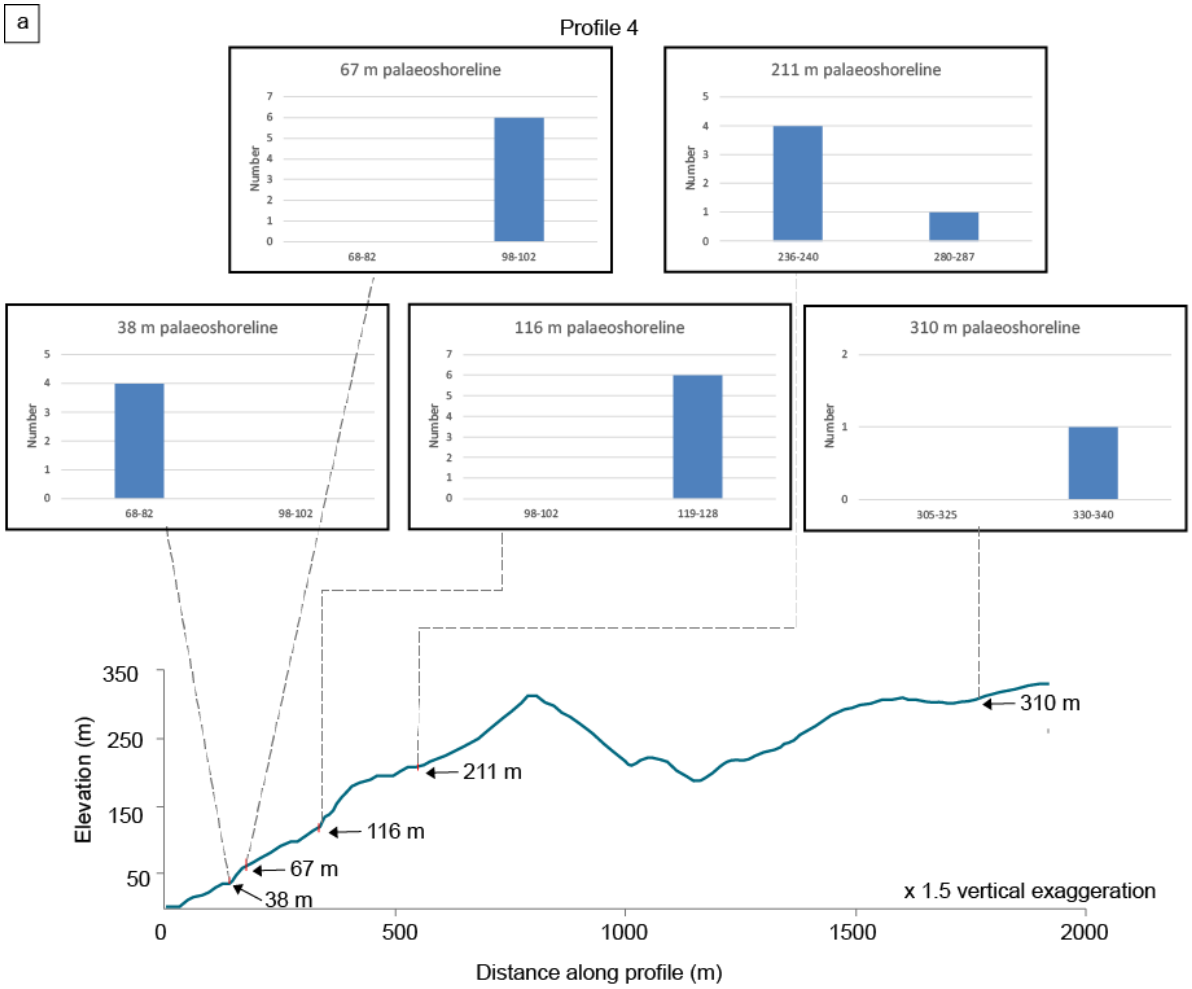

Indicates variation of elevations predicted from other sea-level curves

Measured shoreline elevation (m) **(Dated)**	Highstand with most allocations from all sea-level curves (ka)	No. of sea-level matching selected shoreline to highstand
38	68-82	4
67	**98-102**	**6**
116	**119-128**	**6**
211	236-240	4
310	330-340	1

b

Profile 9

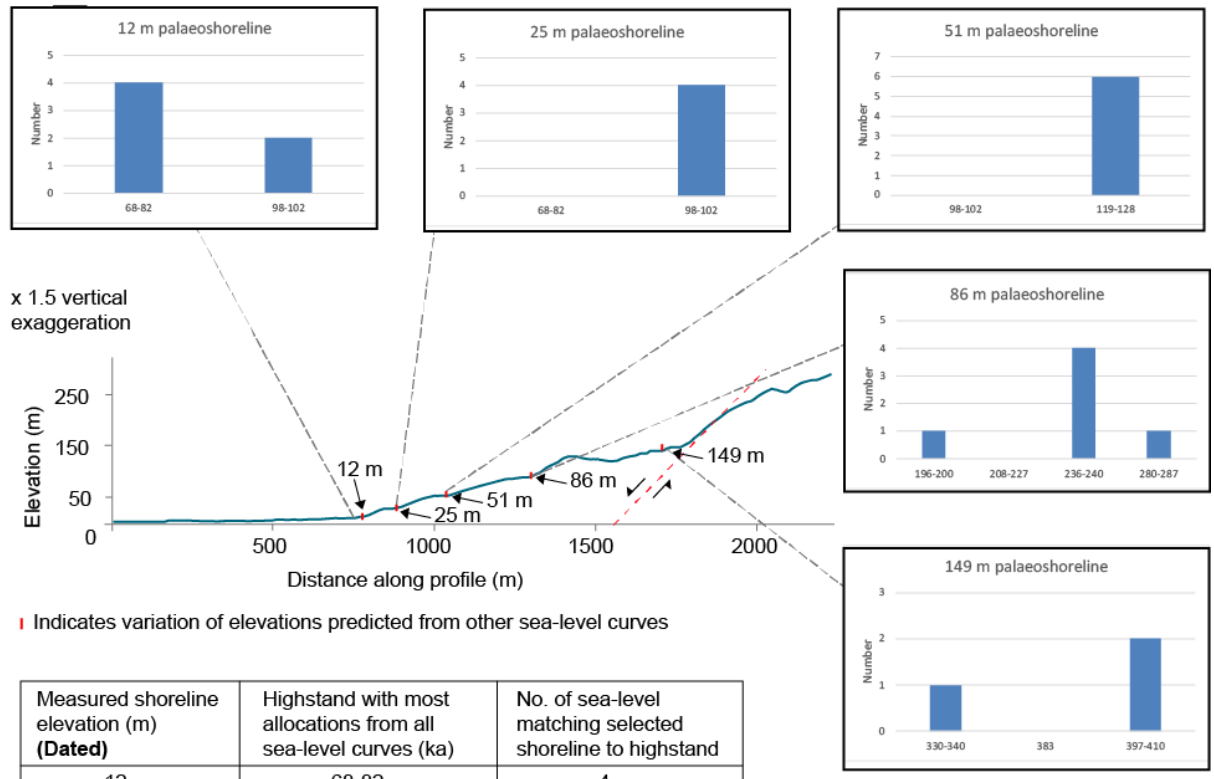

Indicates variation of elevations predicted from other sea-level curves

Measured shoreline elevation (m) **(Dated)**	Highstand with most allocations from all sea-level curves (ka)	No. of sea-level matching selected shoreline to highstand
12	68-82	4
25	98-102	4
51	**119-128**	**6**
86	236-240	4
149	397-410	2

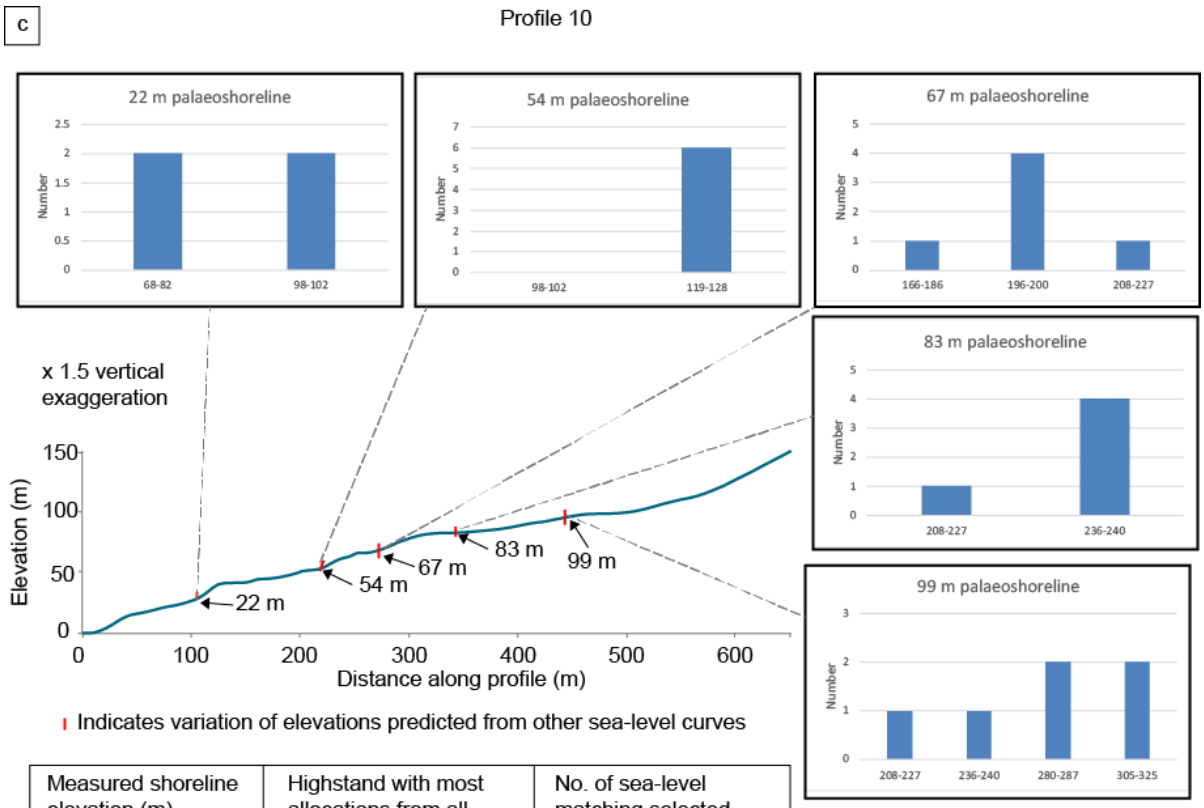

Measured shoreline elevation (m) **(Dated)**	Highstand with most allocations from all sea-level curves (ka)	No. of sea-level matching selected shoreline to highstand
22	68-82	2
	98-102	2
54	**119-128**	**6**
67	196-200	4
83	236-240	4
99	280-287	2
	305-325	2

Figure 5.8: Topographic profiles 4 (a), 9 (b) and 10 (c) constrained by the 119-128 ka palaeoshoreline and the highstand allocations for each palaeoshoreline using different sea-level curves shown via histograms (see also Table 5.4).

For the profiles constrained by the 68-82 ka palaeoshoreline (Profiles 2 and 5), there is less agreement on the palaeoshoreline to highstand allocations between the different sea-level curves (Table 5.4, Fig. 5.9). Profile 2 shows that the 64 m and 97 m palaeoshorelines are allocated to the 119-128 ka and 196-200 ka highstands, respectively, by three sea level curves but such agreement is not apparent for the 54 m and 174 m palaeoshorelines (Fig. 5.9a). On Profile 5, the palaeoshoreline at 57 m, directly above the dated shoreline at 38 m, is matched to the 98-102 ka highstand by all sea-level curves, but for the remaining three palaeoshorelines there is less agreement between the sea-level curves (Fig. 5.9b).

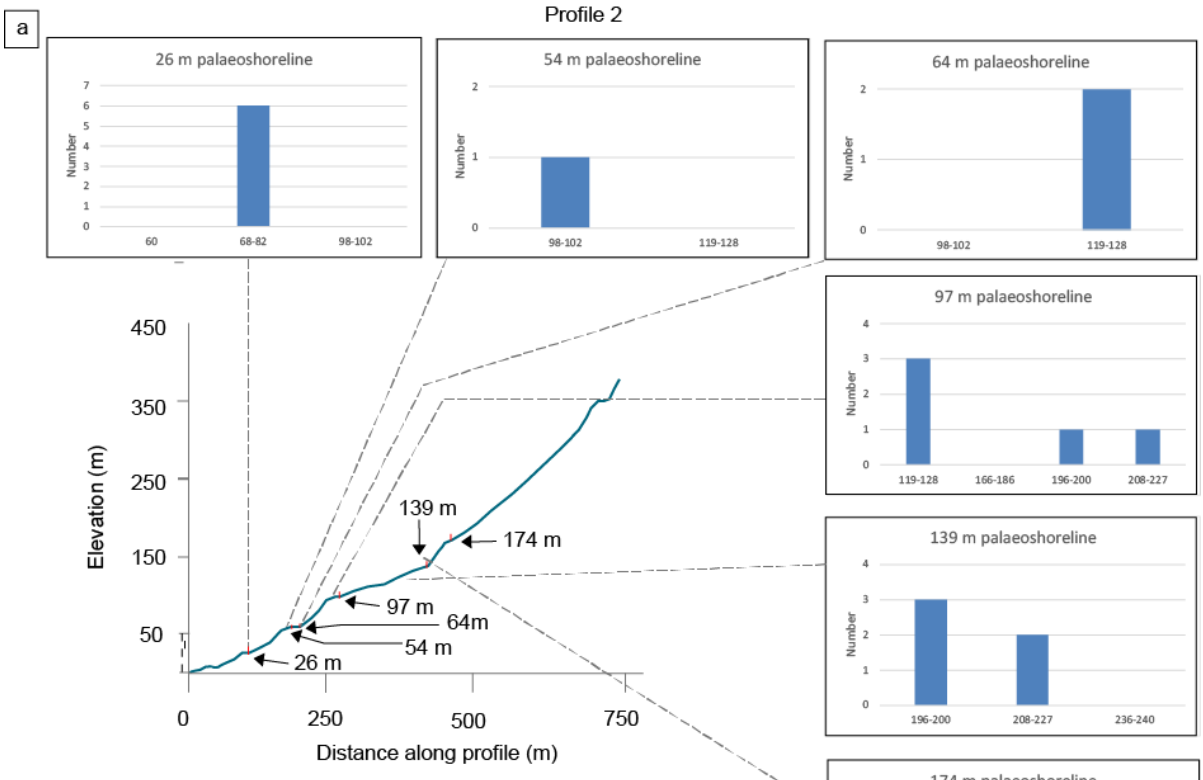

Measured shoreline elevation (m) **(Dated)**	Highstand with most allocations from all sea-level curves (ka)	No. of sea-level matching selected shoreline to highstand
26	**68-82**	**6**
54	98-102	1
64	119-128	2
97	119-128	3
139	196-200	3
174	208-287	2

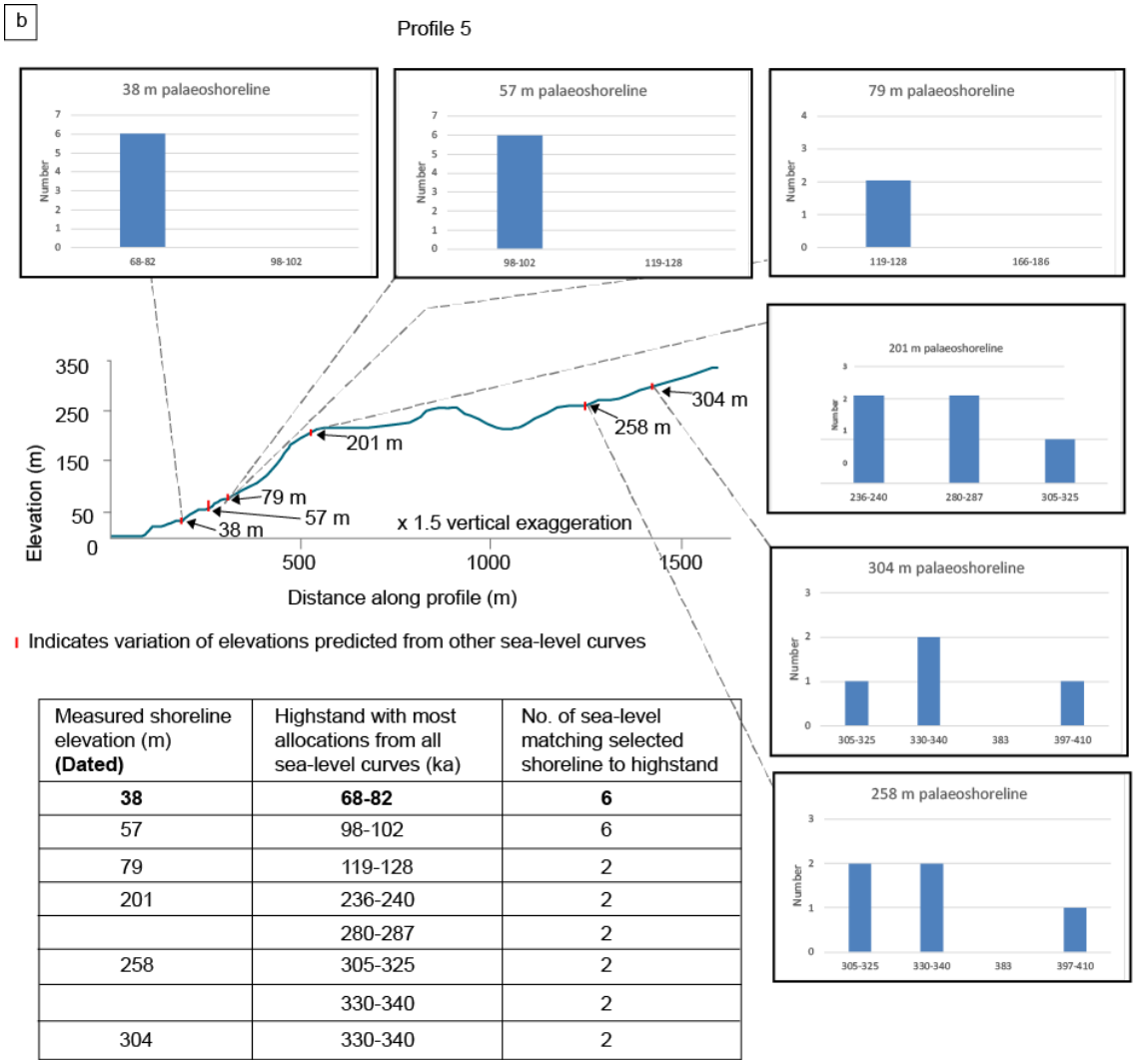

Measured shoreline elevation (m) **(Dated)**	Highstand with most allocations from all sea-level curves (ka)	No. of sea-level matching selected shoreline to highstand
38	**68-82**	**6**
57	98-102	6
79	119-128	2
201	236-240	2
	280-287	2
258	305-325	2
	330-340	2
304	330-340	2

Figure 5.9: Topographic Profiles 2 (a) and 5 (b) constrained by the 68-82 ka palaeoshoreline and the highstand allocations for each palaeoshoreline from different sea-level curves shown via histograms (see also Table 5.4).

While there are clear variations for the highstand to palaeoshoreline allocations when an age control for the 119-128 ka highstand is used (Table 5.4, Fig. 5.8), there is also agreement between the results obtained using a number of sea-level curves, though not consistently agreement between the same combination of sea-level curves (Table 5.4). Commonalities are apparent between the sea-level curves of Siddall et al. (2003), Bintanja et al. (2005) and Spratt and Lisiecki (2016) and to some extent Waelbroeck et al. (2002). In contrast, where the age control is for the 68-82 ka palaeoshoreline, with the exception of the dated palaeoshorelines on Profiles 2 and 5 and the 57 m palaeoshoreline on Profile 5, allocations of palaeoshorelines to highstands on these profiles show less agreement; there are only 3 out of 11 instances where ≥3 sea-level curves achieve the same palaeoshoreline to highstand correlation. Compare this to the undated shorelines on Profiles 4, 9 and 10 (with an age

constraint to the 119-128 ka highstand) where ≥3 sea-level curves result in the same palaeoshoreline to highstand allocation and this occurs for 6 out of 11 instances.

The overall picture from analyses of the five profiles is that where different curves are used to allocate undated palaeoshorelines to highstands with a robust age control for each profile, there is still variation between the allocations made using data from different sea-level curves. However, some agreement is observed between the curves. Where the age control is for the 119-125 ka highstand there is greater agreement compared to where the age control is linked to the 68-82 ka highstand. Moreover, it appears that higher and older palaeoshorelines display greater variation for the palaeoshoreline to highstand allocation than their lower and younger counterparts (see: Profile 2, 97 m (Fig 5.9a), Profile 5, 201 m and 258 m (Fig. 5.9b), Profile 9, 86 m (Fig. 5.8b) and Profile 10, 67 m and 99 m (Fig. 5.8c)).

5.4.2.2 Analysis of correlations by sea-level curve

In this section the total matches and the overall goodness of fit between predicted and measured palaeoshoreline elevations obtained in Section 5.4.2.1 are evaluated for each sea-level curve. Analysis of the total number of palaeoshoreline to highstand matches by each sea-level curve reveals similar values between 22 (Siddall et al., 2003) and 19 (Shakun et al., 2015) (Table 5.5). Overall, the R^2 linear correlation and RMSE values for all profiles per sea-level curve (Table 5.5) show that the predicted versus measured palaeoshoreline elevations using all sea-level curves are well correlated, though there are minor variations of the R^2 and RMSE on a profile-by-profile basis (Fig. 5.10). Using the sea-level curve of Siddall et al. (2003) resulted in the highest R^2 and RMSE for predicted and observed palaeoshorelines. Considering RMSE, Siddall et al. (2003) is closely followed by Shakun et al. (2015), Bintanja et al. (2005), Waelbroeck et al. (2002), Bates et al. (2014) and Spratt and Lisiecki (2016) (Table 5.5.

	Siddall et al. (2003)	Bintanja et al. (2005)	Spratt & Lisiecki (2016)	Waelbroeck et al. (2002)	Shakun et al. (2015)	Bates et al. (2014)
Total no. of matches	22	21	22	21	19	21
R^2 (all predicted vs all measured elevations)	0.9989	0.9976	0.9922	0.9973	0.9974	0.9956
RMSE (all predicted vs all measured	3.19	3.99	5.66	4.01	3.64	4.3

Table 5.5: Total matches, R2 and RMSE for measured versus predicted palaeoshoreline elevations all profiles by sea-level curve

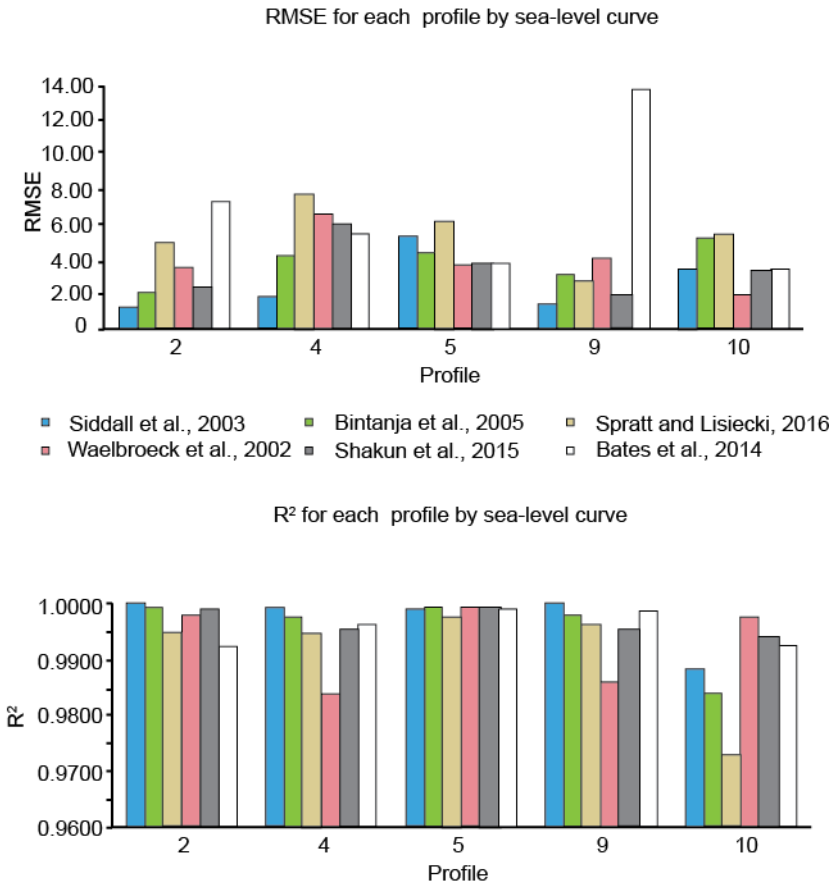

Figure 5.10: RMSE and R^2 for measured versus predicted palaeoshoreline elevations by profile, by sea-level curve.

The result of this test perhaps highlights one of the major challenges of the use of different sea-level curves to interrogate a sequence of palaeoshorelines – that the application of any one of the curves used in this test would result in an acceptable number of palaeoshoreline to highstand matches, reinforced by R^2 and RMSE values suggestive of excellent correlation, despite the observed variation between undated palaeoshoreline to highstand correlations.

5.4.3 Test 3: Impact of different sea-level curves on uplift rates, on along-strike uplift and on earthquake recurrence intervals.

When comparing the results obtained using the six different sea-level curves to allocate undated palaeoshorelines to highstands, observations of the variations prompt consideration as to what affect they would have on the deformation rates associated with the sequences of terraces. For each profile, the difference between the minimum and maximum uplift rates obtained using the six sea-level curves range between 0.1-0.3 mm/yr (Fig. 5.11a, Table 5.6, final column). To put this into context within palaeoshoreline elevations, analysis of the along-strike elevation variation for the 119-128 ka palaeoshoreline (Fig. 5.11b, Table 5.6) shows that the minimum and maximum elevation differences are <13

m (with the exception of Profile 2). However, despite this variation, comparison of the along-strike uplift rates obtained for each profile using the six sea-level curves (Fig 5.11) reveals that there is broad agreement in the pattern of uplift for all sea-level curves, that is, they all suggest the same pattern of deformation along the strike of the fault(s) discussed in Chapter 4.

Profile number	Profile mean uplift rate (mm/yr)	Siddall et al. (2003)		Bintanja et al. (2005)		Spratt & Lisiecki (2016)		Waelbroeck et al. (2002)		Shakun et al. (2015)		Bates et al. (2014)		Difference between min and max (mm/yr)
		Uplift rate (mm/yr)	± (mm/yr)	Uplift rate (mm/yr)	± (mm/yr)	Uplift rate (mm/yr)	± (mm/yr)	Uplift rate (mm/yr)	± (mm/yr)	Uplift rate (mm/yr)	± (mm/yr)	Uplift rate (mm/yr)	± (mm/yr)	
2	0.65	0.72	0.13	0.80	0.13	0.74	0.12	0.53	0.10	0.64	0.15	0.49	0.12	0.31
4	0.90	0.89	0.12	0.96	0.14	0.91	0.13	0.83	0.17	0.98	0.17	0.80	0.10	0.18
5	0.79	0.88	0.10	0.90	0.12	0.80	0.10	0.75	0.11	0.81	0.17	0.62	0.10	0.28
9	0.41	0.38	0.11	0.43	0.11	0.41	0.11	0.40	0.14	0.49	0.20	0.35	0.11	0.14
10	0.43	0.37	0.09	0.41	0.09	0.42	0.09	0.40	0.10	0.57	0.18	0.38	0.09	0.20

Table 5.6: Uplift rates by profile and sea-level curve obtained from Test 2. 'Profile mean' is the mean of uplift rates for each profile, the uncertainties are propagated as per the equation for standard error based upon uncertainties associated with measured palaeoshoreline elevation, sea-level elevation and age of the palaeoshoreline (Section 3.2).

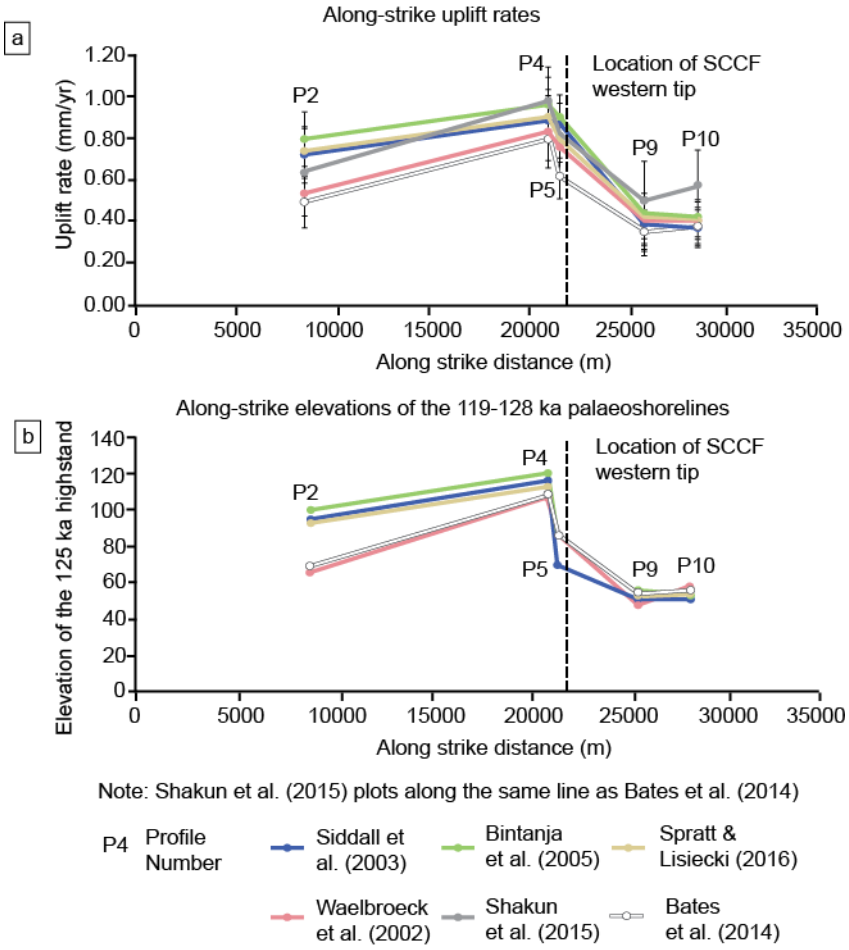

Figure 5.11: (a) Uplift rates by profile for each sea-level curve. (b) Along-strike elevations of the 119-128 ka palaeoshoreline to show the relative elevation differences.

Examining the uplift rates of each profile using the tested sea-level curves (Fig. 5.12) reveals that profiles constrained by the 119-128 ka palaeoshorelines (Fig. 5.12 a-c) show minor variation from the mean. Specifically, uplift rates derived from the curve of Bates et al. (2014) consistently have values less than the mean values of each profile. Those derived from the curve of Bintanja et al. (2005) consistently plot above the mean values on each profile and those derived from the curves of Siddall et al. (2003), Bintanja et al. (2005), Spratt and Lisiecki (2016) and Waelbroeck et al. (2002) plot closer to the mean values on each profile. These observations may be interpreted to indicate that where the 119-128 ka palaeoshoreline is used as an age constraint, the application of the sea-level curves of Siddall et al. (2003), Bintanja et al. (2005), Spratt and Lisiecki (2016) and Waelbroeck et al. (2002) would result in similar calculated uplift rates. In comparison, greater variation about the mean is visible on Profiles 2 and 5 constrained by the 68-82 ka palaeoshorelines (Fig. 5.12d, e), specifically where uplift is higher on Profile 2. Consequently, it appears that where the 68-82 ka palaeoshoreline is used as an age control, the resultant uplift rates obtained using different sea-level curves will vary to a greater extent.

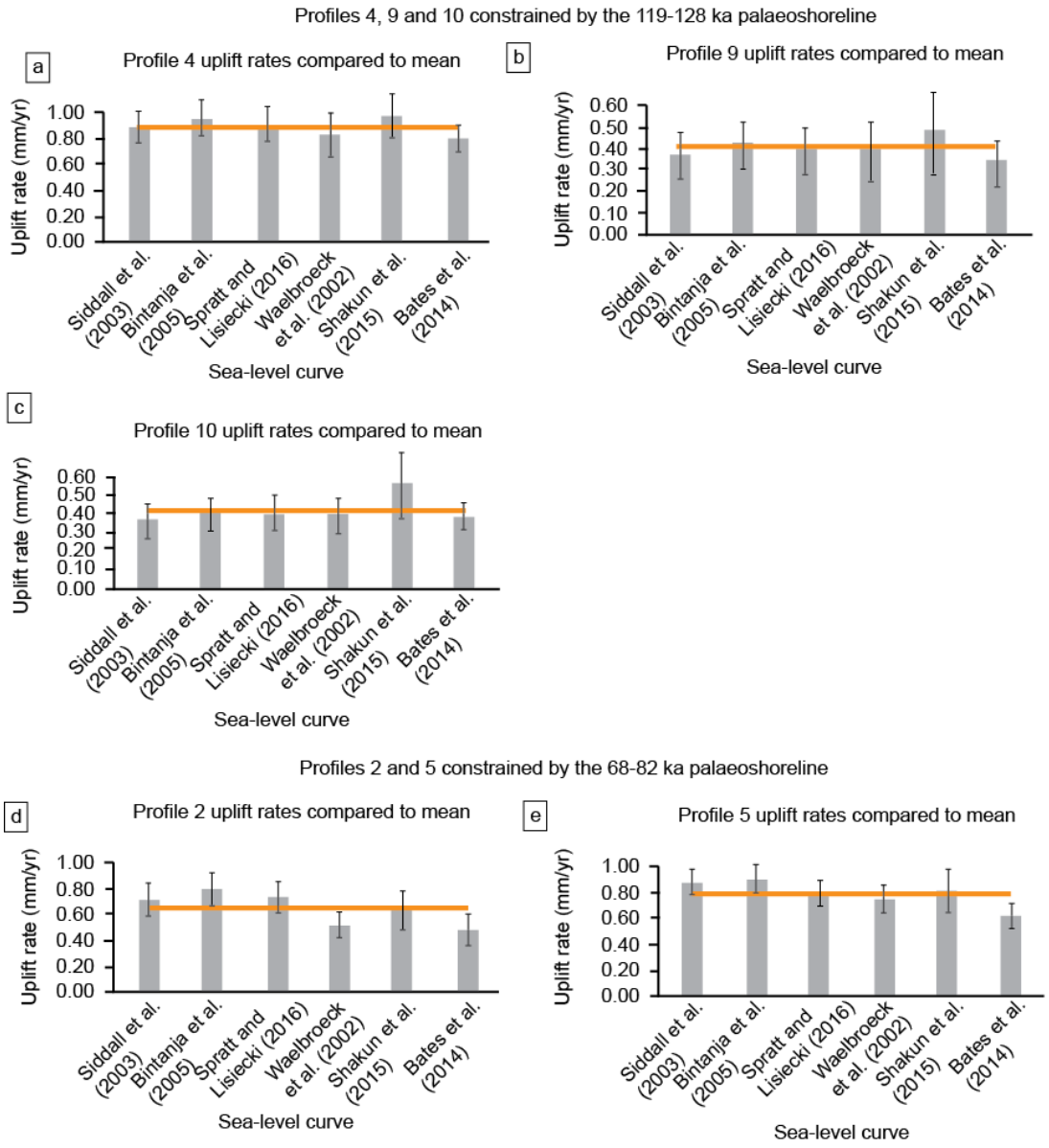

Figure 5.12: Uplift rates per profile, for each sea-level curve with mean uplift rates (orange line) shown. (a-c) are constrained by the 119-128 ka palaeoshoreline. (d, e) are constrained by the 68-82 ka palaeoshoreline.

5.4.3.1 The effect of different sea-level curves on earthquake recurrence intervals

In this thesis, implied earthquake recurrence intervals associated with offshore faults are calculated based upon the total uplift of a dated palaeoshoreline (Section 2.2.4). The application of this approach is useful where faults are located offshore and the slip/throw rate of the fault is unknown and thus cannot be used to determine the recurrence interval. Where this method to calculate recurrence intervals is applied, the total uplift is obtained using knowledge of the sea-level elevation at the time of palaeoshoreline formation (relative to today) and is, therefore, reliant on data from sea-level curves. This section investigates the extent to which using sea-level elevation data from the six sea-level curves within this

chapter may affect implied recurrence intervals. The impact of using different sea-level curves to calculate recurrence intervals is analysed using the dated 68-82 ka palaeoshoreline along Profile 2 (26 m) in Chapter 4 (Figs. 4.4a, 4.18). For the sake of simplicity, in the analysis of earthquake recurrence intervals undertaken in this section, it is assumed that all of the uplift recorded at this location is as a result of motion on the offshore Ptolemy fault (Fig. 4.18a). The actual highstand ages and sea-level elevations (relative to today) from the 68-82 ka highstand from each sea-level curve (Table 5.7) are used alongside modelled coseismic uplift following an earthquake along the entire offshore Ptolemy fault at Profile 2 of 0.4 m (Section 4.5).

Sea-level curve	Sea-level highstand age (ka)	Sea-level elevation (relative to present day) (m)
Siddall et al. (2003)	76.5	-30
Bintanja et al. (2005)	80	-37
Spratt and Lisiecki (2016)	82	-27
Waelbroeck et al. (2002)	82	-20
Shakun et al. (2015)	78	-24
Bates et al. (2014)	80	-12

Table 5.7: Sea-level elevation and age data for the 68-82 ka highstands from each sea-level curve.

Calculated inferred recurrence intervals (Fig. 5.13) along the Ptolemy fault show some variation when data from the different sea-level curves (Table 5.7) is used. Recurrence intervals are calculated between 508-842 years (mean: 642 years) (Fig. 5.13, Table 5.8). Inferred recurrence intervals using the sea-level curves of Siddall et al. (2003), Spratt and Lisiecki (2016), Waelbroeck et al. (2002) and Shakun et al. (2015) vary by <15% from the mean, while those calculated using the curves of Bintanja et al. (2005) and Bates et al. (2014) vary by 20-30% from the mean (Table 5.8). In the case of the recurrence intervals from Bintanja et al. (2005) and Bates et al. (2014), the variation from the mean (134 years and 200 years, respectively) is higher than the calculated standard deviation (120 years) associated with the mean recurrence interval, which suggests that recurrence intervals calculated using these sea-level curves may more likely to be under- or over-estimated. However, it is important to note that the calculated recurrence interval variation is likely to represent maximum values owing to the differences between sea-level elevations from the different sea-level curves (-37 to – 12 m) (Fig. 5.4).

Recurrence intervals	(a) Measured elevation of 68-82 ka highstand (m) (P2)	Sea level elevation at 76500 (m)	Total uplift (m) since 76500	(b) Highstand age (yrs)	No. of earthquakes since time in (b)	Recurrence interval (b/c)	Variation from the mean recurrence int of 642 years	Variation from the mean recurrence int of 642 years as	Uncertainty ± (m)
Siddall et al., 2003	26	-30	56	76500	140	546	-96	-14.9	12.0
Bintanja et al., 2005	26	-37	63	80000	157.5	508	-134	-20.9	12.0
Spratt and Lisiecki, 2016	26	-27	53	82000	132.5	619	-23	-3.6	9.4
Waelbroeck et al., 2002	26	-20	46	82000	115	713	71	11.1	13.0
Shakun et al., 2015	26	-24	50	78000	125	624	-18	-2.8	18.0
Bates et al., 2014	26	-12	38	80000	95	842	200	31.2	10.0

Table 5.8: Calculation of the mean recurrence intervals inferred from the 26 m palaeoshoreline on Profile 2 dated to the 68-82 ka palaeoshoreline. Recurrence interval is calculated assuming an earthquake along the Ptolemy fault (Chapter 4) which based on fault length scaling relationships (Wells and Coppersmith, 1994) produces 0.4 m uplift at Profile 2 (based on the Coulomb modelling, section 4.5.1). Recurrence interval = highstand age/number of earthquakes; number of earthquakes = Total uplift since age of palaeoshoreline/0.4 m.

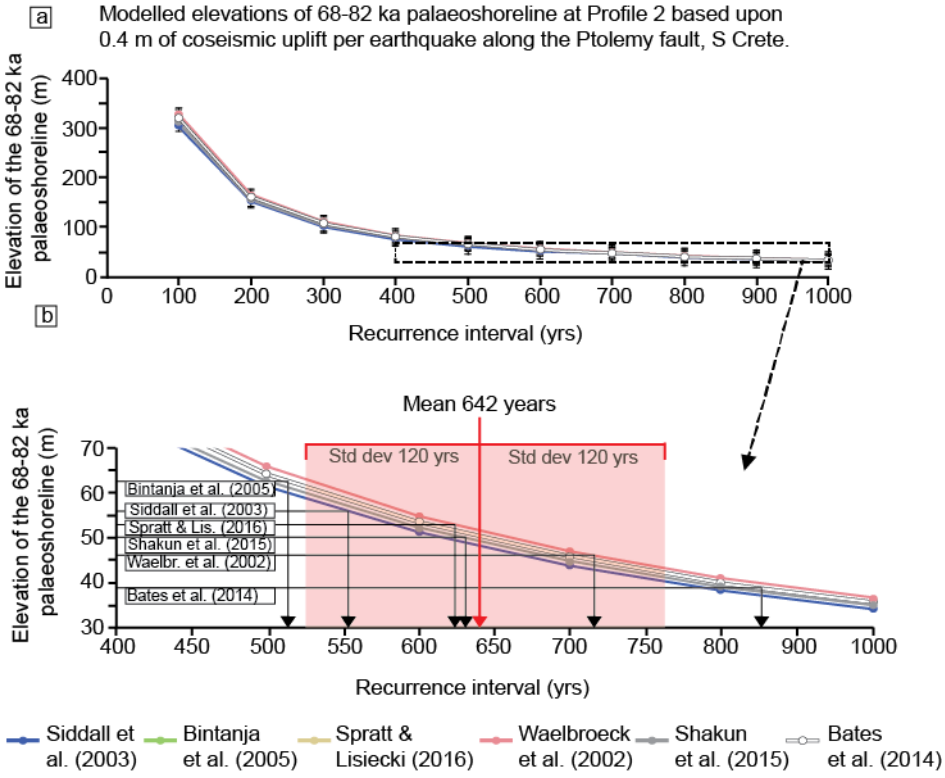

Figure 5.13: Tests to obtain the recurrence interval assuming 0.4 m coseismic uplift on the Ptolemy fault (see Section 4.5) using the six sea-level curves shown in overview (a) and detail (b). Note that the plots of Bintanja et al. (2005) and Bates et al. (2014) plot along the same line, as do the plots of Waelbroeck et al. (2002) and Spratt and Lisiecki (2016). Standard deviation for the mean of the recurrence intervals is shown in order to examine whether the difference sea-level curves result in acceptable earthquake recurrence intervals (see text). See Table 5.8 for calculations.

To summarise the results of Test 3, derived uplift rates show variation as a result of the use of the six different sea-level curves (the extent of the variation is discussed in Section 5.5), but the pattern of the uplift along strike is in agreement with that obtained using Siddall et al. (2003) in Chapter 4. When the recurrence interval of the Ptolemy fault at Profile 2 was calculated using data from each of the sea-level curves on the 68-82 ka highstand, results showed that recurrence intervals varied by 18-200 years (between 3-30%) about the mean value (642 years). Consideration as to whether these variations are acceptable can be made

by comparing them to the standard deviation calculated on the recurrence intervals (120 years) (Fig. 5.13). The recurrence intervals calculated using Bintanja et al. (2005) and Bates et al. (2014) result in values that are further from the mean than the value of standard deviation, which may be used to tentatively suggest that recurrence intervals calculated using these sea-level curves should be used with caution, in comparison to their tested counterparts.

5.5 DISCUSSION

The results of this chapter show that even where at least one palaeoshoreline on each topographic profile has an age constraint, variation between the highstand ages allocated to undated palaeoshorelines when using different sea-level curves is observed. While similar observations have been made in previous studies (e.g. Caputo et al., 2007), the consequence of such allocations between palaeoshorelines and highstands has not been thoroughly explored. This observed variations between undated palaeoshorelines and highstands translates to relatively small differences (0.1-0.3 mm/yr) in uplift rates when results from the six different sea-level curves are compared (Fig. 5.12, Table 5.6), and where plotted along strike, the spatial patterns of uplift are similar (Fig. 5.11). The results also show that a tentative link between the age of a dated palaeoshoreline used within a topographical profile and the absolute variation between the relative sea-level elevations for the highstand in question (Figs. 5.4, 5.5 and 5.6) can be made. For example, where allocating undated palaeoshorelines to highstands, greater agreement between different sea-level curves is apparent when the 119-128 ka palaeoshoreline is used as an age constraint, as opposed to the 68-82 ka palaeoshoreline. This is to be expected, given that the 119-125 ka (MIS 5e) is one of the most well constrained highstands (Fig. 5.6) (e.g. Stirling et al., 1998; Hearty et al., 2007; Dutton and Lambeck, 2012) owing to the fact that its elevation is above the present-day sea level allowing for excellent preservation of shoreline markers and absolute dating of preserved coral benchmarks.

Given the findings presented herein, specifically that differences in uplift rates and inferred recurrence intervals occur when different sea-level curves are used, the extent to which using different sea-level curves can impact the deformation rates obtained from studies of marine terraces and palaeoshorelines should be considered within the context of the propagated uplift uncertainty from the individual sea-level curves (Table 5.6). These propagated uncertainties (Section 3.2) consider all of the uncertainty values linked to calculating the uplift, the most significant of which is that linked to the palaeo sea-level elevation, relative to today (Table 5.1). The results of Test 3 (Section 5.4.3) show that uplift rate variations using different sea-level curves for Profiles 2, 4, 5, 9 and 10 differ between a minimum and maximum of ~0.1-0.3 mm/yr (last column, Table 5.6); these values are comparable to the propagated errors on the uplift rates calculated using all sea-level curves on all profiles of 0.09-0.2 mm/yr (Table 5.6). In other words, the uplift rate uncertainty that is calculated by propagating errors associated with palaeoshoreline elevation measurements

and palaeo sea-level data results in uncertainty values that are very similar to the uplift-rate variation obtained from using the six different sea-level curves that are calculated herein.

Test 3 also showed that obtaining recurrence intervals using data from different sea-level curves leads to a difference of up to 334 years between the highest and lowest values. Considering that the reported sea-level elevation uncertainties for each sea-level curve vary between ±9.4 to 18 m (Table 5.1), it would be of use to explore how the recurrence intervals would vary if the maximum and minimum sea-level elevations were used based upon the uncertainty values. For instance, the 76.5 ka palaeoshoreline on Profile 2 has uplifted by 56 m using the sea-level curve of Siddall et al. (2003). This is based upon the sea level at 76.5 ka being -30 m (this is the measured value from the sea-level curve). But the stated uncertainty of sea-level highstands in the Siddall et al. (2003) sea-level curve is ±12 m, thus the sea-level could be between -18 and -42 m. When these minimum and maximum values are used to calculate the inferred recurrence interval, they result in values of 695 (+21%) and 450 (-18%) years, respectively, compared to the 546-year recurrence interval calculated with the measured value. This analysis was completed for all of the sea-level curves (Fig. 5.14) and shows that total absolute differences of recurrence intervals using minimum and maximum sea-level elevations can vary between 201-516 years (Fig. 5.14) depending on the sea-level curve being discussed. These variations equate to plus/minus values of to 15 to 26.5% and -22 to -56% when compared to the recurrence intervals obtained using the measured sea-level elevations (Fig. 5.13). The higher variations seen in Fig. 5.14 between minimum and maximum recurrence intervals calculated using Waelbroeck et al. (2002), Shakun et al. (2015) and Bates et al. (2014) are reflective of sea-level elevations for the 68-82 ka highstands that are relatively high in comparison to the other sea-level curves (Table 5.7).

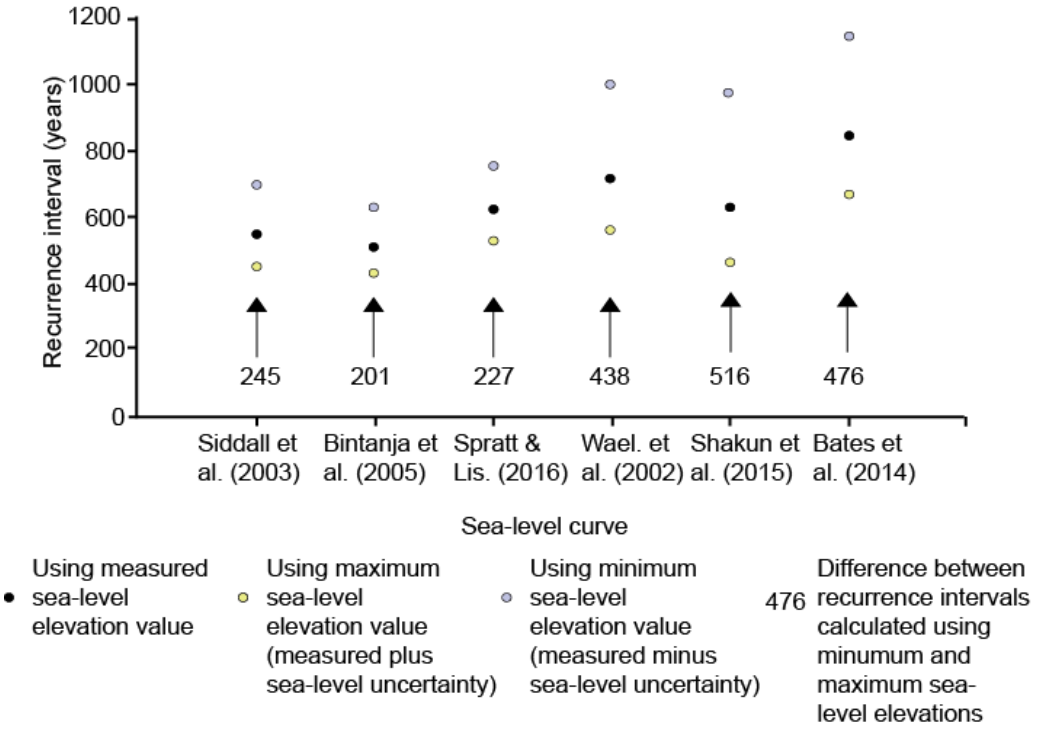

Figure 5.14: Comparison of the inferred recurrence intervals obtained for each sea-level curve using the sea-level elevations measured from the curves (measured) and their published sea-level elevation uncertainties to derive maximum and minimum sea-level values. Analysis is carried out using data from profile 2 on the 26 m palaeoshoreline dated to 68-82 ka.

5.5.1 Possible impacts on seismic hazard modelling

While the recurrence interval has been used as a test to explore the impact of using different sea-level curves, the reality is that this value is mostly used to provide geologists with an understanding of faults in situations where recurrence intervals calculated from previous (typically Holocene) earthquakes are not available (see Chapter 1). In PSHA models (i.e. *FiSH* and SHERIFS) recurrence intervals are calculated from slip/throw rate measurements, fault geometry and knowledge of historic slip events (e.g. Pace et al., 2016; Chartier et al., 2019). With the exception of a fault that offsets marine terraces in its hangingwall and footwall (e.g. Chapters 4 and 6; Roberts et al., 2013; Meschis et al., 2018; Robertson et al., 2019), obtaining the long-term ($10^{4\text{-}5}$ yrs) slip rate of coastal faults is particularly challenging and relies on the application of each or all of the following: uplift to subsidence ratios (U:S) (e.g. Bianca et al., 1999; Meschis et al., 2018), elastic dislocation modelling (e.g. Armijo et al., 1996; Di Martini et al., 2004) and seismic sections to correlate footwall and offshore hangingwall terraces (Bianca et al., 1999; Jara-Munoz et al., 2017; de Gelder et al., 2019). Where such techniques rely on the highstand age of one palaeoshoreline, unless the palaeoshoreline in question has an absolute age constraint, it is possible that the use of different sea-level curves may result

in differing correlations of highstand age to undated palaeoshorelines, which will have a direct impact on the calculated slip rate on the fault. In such studies it may be prudent to apply correlations using multiple sea-level curves and examine the resultant recurrence intervals.

To summarise, the analysis herein shows that undated palaeoshorelines along topographic profiles may be allocated to different sea-level highstands depending on the sea-level curve used, and to some extent, to the age of the dated palaeoshoreline. This will lead to uplift rates that may differ by values that appear to be similar to the propagated error on the uplift rate if only one sea-level curve is used. Where many profiles (e.g. Meschis et al., 2018; Robertson et al., 2019) are used to calculate uplift rates along the strike of a set of deformed palaeoshorelines in order to examine the pattern of uplift, based on analysis herein, the relative pattern of uplift is likely to be representative regardless of the absolute uplift differences, though this may vary with other sea-level curves not tested herein. The picture is less clear with regard to the recurrence intervals calculated using different sea-level curves, as they are shown to differ between 3-30% about the mean calculated value, which in the case of some sea-level curves exceeds the standard deviation. These results suggest that the calculation of inferred recurrence intervals using a single sea-level curve should be undertaken with caution.

5.6 CONCLUSIONS

1. The use of different sea-level curves from Siddall et al. (2003), Waelbroeck et al. (2002), Bintanja et al. (2005), Spratt and Lisiecki (2016), Shakun et al. (2015) and Bates et al. (2014) to examine a sequence of late Quaternary palaeoshorelines results in variation between the correlation of undated palaeoshorelines to highstands and the resultant uplift rates that are calculated using the sea-level curves.
2. The spatial pattern of uplift along a number of topographic profiles is shown to be maintained regardless of the sea-level curve tested. This observation suggests that where palaeoshorelines are used to examine the cause of fault-related uplift, the use of any of the sea-level curves investigated herein would result in interpretations regarding the overall tectonic uplift that are similar.
3. The measured variation of uplift rates that occur as a result using the six tested sea-level curves are comparable to the uncertainties obtained when the sea-level

elevation uncertainties from a single sea-level curve are considered; this was tested for uplift rates between 0.37-0.98 mm/yr.

4. When considering the impact of the use of different sea-level curves on calculated recurrence intervals, this chapter shows that the use of single sea-level curves should be carried out with caution because large differences of up to 30% of the recurrence intervals have been observed.

6 CHAPTER 6: DISTRIBUTED NORMAL FAULTING IN THE TIP ZONE OF THE SOUTH ALKYONIDES FAULT SYSTEM, GULF OF CORINTH, CONSTRAINED USING ^{36}CL EXPOSURE DATING OF LATE-QUATERNARY WAVE-CUT PLATFORMS.

6.1 SUMMARY

In Chapter four, the deformation of a sequence of palaeoshorelines parallel to the strike of faults was explored, using spatial and temporal variation of uplift rates alongside elastic half-space modelling to determine the possible fault mechanisms responsible and quantify the long-term deformation rates. In addition, ^{36}Cl exposure dating of wave-cut platforms composed of limestone bedrock was shown to be a reliable method to obtain age constraints. In this chapter, ^{36}Cl exposure dating on wave-cut platforms of differing carbonate lithologies is further tested at a location where wave-cut platforms exist at elevations between 7-62 m, but the values and causes of uplift have been disputed over the last ~20 years. The wave-cut platforms along Cape Heraion, Gulf of Corinth, Greece, lie in the tip zone of the South Alkyonides Fault System (SAFS), an active normal fault that ruptured in the 1981 Gulf of Corinth earthquake sequence (Mw 6.9, Mw 6.4,) and their variable elevations have been explained via competing hypotheses of multiple active faults offsetting a single wave-cut platform or representing an age sequence of Late-Quaternary palaeoshorelines recording a low value of background regional uplift. Neither hypothesis can be proven or disproven using the existing coral age constraints; this is problematic because the presence of multiple faults will have implications on the seismic hazard of the area and on the scientific community's understanding of the nature of distributed faulting and rates of deformation near to the tip of an active normal fault.

Within this chapter, the geometry, rates and kinematics of active faulting in the region close to the SAFS are investigated using detailed fault mapping and new absolute dating. Wave-cut platforms are dated using a combination of ^{234}U/^{230}Th coral dates and ^{36}Cl cosmogenic exposure dating, which provide complementary age controls, and show that deposits and landforms associated with the Late-Quaternary 125 ka (MIS 5e) marine terrace have been deformed by faulting distributed across as many as eight faults arranged within ~700 m across strike. Summed throw-rates across strike achieve values as high as 0.3-1.6 mm/yr,

values that are comparable to those at the centre of the crustal-scale fault (2-3 mm/yr from Holocene palaeoseismology and 3-4 mm/yr from GPS geodesy) and exceed previous estimates. The relatively high deformation rate and distributed deformation in the tip zone are discussed in terms of stress enhancement from rupture of neighbouring crustal-scale faults and in terms of how this should be considered during fault-based seismic hazard assessment.

6.1.1 Introduction

Understanding the deformation that occurs at the tips of normal faults is important because (a) it contributes to knowledge on fault growth and linkage (e.g. Peacock and Sanderson, 1991; Cowie and Shipton, 1998; McLeod et al., 2000; Peacock, 2002), (b) has the potential to inform fault-based seismic hazard analysis about fault connectivity and maximum rupture extent (Scholz and Gupta, 2000), and (c) influences the scientific community's understanding of fluid connectivity or otherwise of faulted hydrocarbon reservoirs (Yielding et al., 1996). One of the key observations from studies on tip-zone deformation is that the shape of the displacement gradients differs between isolated and interacting faults as a result of perturbation to the surrounding stress field (Peacock and Sanderson, 1991; Willemse et al., 1996; Cartright and Mansfield, 1998; Cowie and Shipton, 1998; Scholz and Lawler, 2004). In particular, steeper displacement gradients occur close to fault tips where adjacent faults are in close proximity (Gupta and Scholz, 2000) (Section 2.2.3). However, it is not known how these steep displacement gradients develop through time, whether displacement is always localised on a single fault or spread across several fault strands, and how tip deformation should be incorporated into studies of seismic hazard. To address these questions, this chapter provides measurements of deformation rates across all faults within a tip zone over timescales that allow one to recognise how many individual faults are active simultaneously.

Interest in this topic was raised because at the tips of some crustal-scale faults, distributed faulting dominates as networks of splay faults that form at acute angles to the main fault (McGrath and Davison, 1995; Perrin et al., 2016) (Fig. 6.1). It is unclear whether these fault patterns and the resultant deformation can be more complex where the tips of two crustal-scale faults overlap along strike and interaction occurs between neighbouring faults (Gupta and Scholz, 2000). Moreover, although typically fault displacement decreases to minimal values toward the tip (Cowie and Roberts, 2001), a shared tip zone can host high displacement gradients relative to the main fault (Peacock and Sanderson, 1991; 1994;

Schlische et al., 1996) and it is unclear if this is accommodated by deformation spread across multiple faults or localised on a single fault.

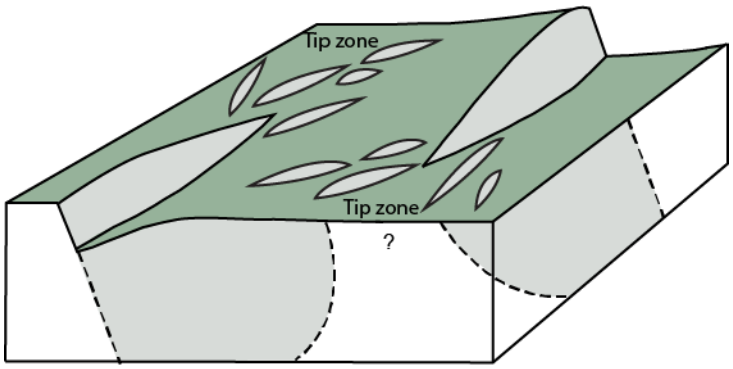

Figure 6.1: Schematic diagram of a possible tip zone deformation and splay faults where the tips of two along-strike faults overlap. (From Robertson et al., 2020)

A detailed analysis of the deformation within a fault tip zone has the capacity to contribute to fault-based seismic hazard assessment (e.g. Pace et al., 2016). If tip zones contain relatively-high displacements, distributed across multiple faults, or localised on a single fault, this may influence whether ruptures can cross the tip zone onto other neighbouring faults (e.g. Field et al. 2014), influencing estimates of maximum earthquake magnitude (Wells and Coppersmith, 1994) (Section 2.2.4). However, the lack of measured displacement data within tip zones means that historic fault-based seismic hazard approaches typically rely on throw/slip rate data from along the main fault and the assumption that displacement gradients decrease toward the tips according to pre-ordained fault shapes (Faure Walker et al., 2019). The above assumptions produce significant uncertainty in Probabilistic Seismic Hazard Assessment (PSHA) (Pace et al., 2016), and have been shown to result in large differences between calculations of recurrence intervals and ground-shaking exceedance probabilities for different fault geometries (Faure Walker et al., 2019). Constraining the rates of deformation at multiple locations along a fault, including within the tip-zone, is therefore a vital component of reducing the uncertainty in PSHA. Furthermore, this may be particularly important if this analysis is carried out in an area where overlapping tip zones occur; higher displacement gradients, and consequently slip/throw rates, may mean that cumulative slip rates may be relatively high, even when compared to slip rates obtained from the main localised fault.

One of the main challenges when gaining insights of how tip-zone deformation accumulates through time, over timescales relevant to earthquake rupture, is to derive knowledge of the timescales over which faulting occurs. Existing approaches use measurements of vertical displacement, coupled with the ages of offset strata/landforms (e.g. Sieh et al. 1989; Armijo et al. 1991; Roberts and Michetti, 2004; Galli et al., 2008; Schlagenhauf et al., 2010, Mozafari et al. 2019; Robertson et al., 2019) (Chapter 1). In tip zones where distributed faulting dominates and slip-rate along individual faults may be (a) relatively low, and (b) difficult to detect, it may be advantageous to concentrate on techniques that average the slip over relatively long time periods. This chapter provides an example of how investigations using deformed Quaternary marine terraces and their associated wave-cut platforms (e.g. Armijo et al., 1996; Roberts et al., 2009, Roberts et al., 2013; Binnie et al., 2016; Jara-Munoz et al., 2017; Meschis et al., 2018; Robertson et al., 2019) allow deformation rates to be measured over 10^{4-5} years, and can be used to resolve the displacement associated with the very low slip rates of individual faults.

The western tip area of the north dipping South Alkyonides Fault System (SAFS) (Morewood and Roberts, 1997), located on the Perachora Peninsula (eastern Gulf of Corinth, Greece) (Section 2.3.2) provides an opportunity to further test the application of ^{36}Cl exposure dating to carbonate wave-cut platforms, and derive the throw rate, 'off-fault' deformation (in other words, faulting that has taken place off the main localised fault) and possible interaction with neighbouring faults. A set of distributed faults at Cape Heraion, in the far west of the Perachora Peninsula, represents the western tip zone of the SAFS (Morewood and Roberts, 1997) (Fig. 6.2). While this area has been studied before (Morewood and Roberts, 1997), this study lacked the detailed mapping of displacement gradients along individual faults, and the age constraints needed to be able to fully examine the rates and spatial variation of deformation. Morewood and Roberts (1997) identified faulted offsets of what they claim is a single marine terrace. Others have made an alternative interpretation where marine terraces at different elevations are not faulted, but instead date from different sea-level highstands (Leeder et al., 2003; Leeder et al., 2005). This disagreement could not be resolved, because although some age constraints were available from $^{234}U/^{230}Th$ dating of corals (Vita-Finzi et al., 1993, Leeder et al., 2003; Leeder et al., 2005; Roberts et al., 2009; Burnside, 2010; Houghton, 2010), ages were not available for marine terrace deposits at different elevations.

The breakthrough reported herein, is that detailed mapping revealed that the coral-bearing strata can be mapped along strike into wave-cut platforms, and wave-cut platforms can be

dated using ^{36}Cl cosmogenic exposure studies (Chapter 4; Robertson et al. 2019). Here, the hypothesis of Morewood and Roberts (1997), that of a single, faulted palaeoshoreline is tested by (i) constraining the ages of marine terrace deposits and landforms at different elevations, (ii) calculating individual and cumulative fault throw values and, (iii) exploring how these vary spatially within the tip zone and how they compare to other normal fault tip zones. The results of these analyses are combined with those from Coulomb stress change modelling to explore the interaction between the tip of the SAFS and neighbouring along-strike faults (see Section 2.2.2 for an overview). These findings are then discussed in the context of fault-based probabilistic seismic hazard assessment.

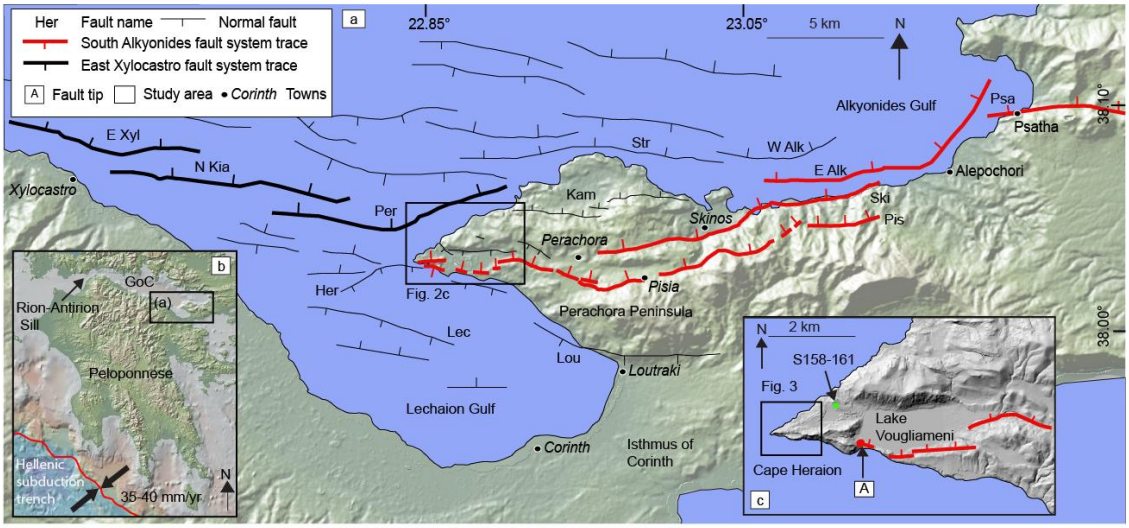

Figure 6.2: (a) Map of the eastern Gulf of Corinth and the Perachora Peninsula, surface trace of the South Alkyonides Fault system (SAFS) (red) (Morewood and Roberts, 2002), East Xylocastro Fault System (EXFS) trace (bold) as per Nixon et al. (2016), all other faults as per Nixon et al. (2016). (b) Location of the Gulf of Corinth relative to the Hellenic subduction zone. Western Hellenic Subuction Zone location taken from Kreemer and Chamot-Rooke (2004), GPS data from Nocquet (2012). (c) 5 m Digital Elevation Model showing the western surface trace of the SAFS as per Morewood and Roberts (2002) and Cape Heraion. 'A' marks the location of the 'on-fault' tip of the SAFS (Morewood and Roberts, 1999), S158-161 is the location of coral samples (Sections 3.2, 6.4.2) (modified from Robertson et al., 2020).

6.2 GEOLOGICAL BACKGROUND

6.2.1 Tectonic setting

The Perachora Peninsula is located between the Alkyonides Gulf to the north and the Lechaion Gulf to the south (Fig. 6.2a). The Perachora Peninsula is dominated by two crustal-scale, north-dipping, active fault systems, the East Xylocastro Fault System (EXFS) (so named in this study) and the South Alkyonides Fault System (SAFS) (Fig. 6.2a). The EAFS is formed

by the East Xylocastro, North Kiato and Perachora faults, located offshore and arranged en-echelon. The linkage of these three faults is unclear (Bell et al., 2009) with some authors suggesting fault connections at depth (Armijo et al., 1996; Nixon et al., 2016) and others suggesting that they are isolated faults (Stefatos et al., 2002; Moretti et al., 2003; Sakellariou et al., 2007). The presence of a set of coherent terraces in the footwall of the East Xylocastro, North Kiato and Perachora faults (Armijo et al., 1996) combined with the formation of a single depocentre bounding the north-dipping faults on the south side of the gulf (Nixon et al., 2016) has been cited as evidence to support a through-going fault that is connected at depth.

The predominantly onshore, ~40 km long SAFS is comprised of the Pisia, Skinos, East Alkyonides and Psatha faults (Fig. 6.2) (Roberts, 1996a; Morewood and Roberts, 1997; 1999; 2001; 2002; Leeder et al., 2005; Roberts et al., 2009). Analysis of the fault system shows that slip vectors converge toward its centre (Roberts, 1996a; 1996b) where a maximum cumulative throw of 2500 m is recorded (Morewood and Roberts, 2002), which decreases toward both tips (Roberts, 1996a; Morewood and Roberts, 1999; Roberts et al., 2009). In the western section of the SAFS, decreasing offset is reflected in deformed Late Quaternary palaeoshorelines and Holocene notches in the footwall (Cooper et al., 2007; Roberts et al., 2009), where uplift rates decrease from 0.52 mm/yr to 0.25 mm/yr from east to west in the most western 5 km of the fault. Roberts et al. (2009) identified that the SAFS experienced an increase in slip rate since ~175 ka by a factor of ~3, suggested to be linked to the cessation of faulting on neighbouring across-strike faults.

Evidence from recent earthquakes combined with Holocene throw and slip rate data provide insight into the activity of faults within the SAFS over decadal to 10^3 year timescales. Specifically, analysis of post-LGM slip on the Pisia fault revealed maximum slip rates of 2.3 mm/yr during the Holocene (Mechernich et al., 2018). Palaeoseismic trenching along the Skinos fault yielded throw rates of 1.2-2.5 mm/yr over ~1500 years (Collier et al., 1998). Two >Ms 6 earthquakes on the 24th and 25th February 1981 are reported to have partially ruptured faults within the SAFS (Jackson et al., 1982; Roberts, 1996a; Collier et al., 1998). Ruptures in bedrock and alluvium that extend for 15-20 km (Jackson et al., 1982; Bornovas et al., 1984; Roberts, 1996a) were observed following the February 1981 earthquakes, with maximum coseismic throw values of 150 cm and 100 cm identified on the Pisia and Skinos faults respectively (Jackson et al., 1982).

The February 1981 earthquake ruptures were mapped to a throw minima along the south of Lake Vouliagmeni (Fig 6.2c) (Bornovas, 1984; Roberts, 1996a; Morewood and Roberts, 1999) where the "throw and geomorphic expression across [the SAFS] tend to zero" (Morewood and Roberts, 1999) and were used to conclude that the SAFS does not extend beyond the western end of the lake. Consequently, this location was identified as the western fault tip of the SAFS (Morewood and Roberts, 1999, Figure 4a) ('A' on Fig. 6.2c). The area to the west of this location, Cape Heraion, appears to be deformed by numerous normal faults, providing an excellent opportunity to explore deformation close to the tip of a normal fault.

6.2.2 Cape Heraion, Perachora Peninsula

The extreme west of the Perachora Peninsula, Cape Heraion, is located beyond the western tip of the SAFS (as defined by Morewood and Roberts, 1999, Fig. 6.2c). It is bounded to the north by the Perachora fault segment, the most eastern fault within the EXFS, and to the south by the south dipping, active Heraion fault (Taylor et al., 2011; Charalampakis et al., 2014; Nixon et al., 2016) (Fig. 6.2a). The geology of Cape Heraion is comprised of a succession of deposits from the Mesozoic to the Late Quaternary (in particular marine terrace deposits), with more recent Late Quaternary-Holocene geomorphic features imprinted such as wave-cut platforms and Holocene sea-level notches.

The stratigraphic succession of the Cape comprises Mesozoic basement limestones unconformably overlain by Plio-Pleistocene marls and sandstones that are, in turn, overlain by algal mound bioherms (also known as cyanobacterial mounds) above which a bioclastic shallow-marine coral-bearing sediment occurs (Bornovas, 1984; see Portman et al., 2005 for descriptions of each lithology). The bioherms are dominated by freshwater branched cyanobacterium *Rivularia haematites*, suggested to have formed when the Gulf of Corinth was a lake (Kershaw and Guo, 2001, 2003, 2006) during MIS 6a. Domal-topped bioherms in the hangingwall and flat-topped bioherms in the footwall along the northern shoreline of Cape Heraion suggest they grew up to water level, possibly during faulting, with restricted vertical growth in the footwall (Kershaw and Guo, 2006). Subsequent relative sea-level rise resulted in the presence of a marine bioclastic layer above the bioherms (Portman et al., 2005; Roberts et al., 2009). Caves are observed within the bioherms, the cave-fill stratigraphy was investigated by Kershaw and Guo (2006) and revealed that cave fills formed after the growth of the bioherms and contain coralline algae and marine biota. Taken together, the above evidence suggests that faults were active during initial freshwater conditions, that

were subsequently changed to marine by a relative sea-level rise. However, these lines of evidence are debated by other authors (Leeder et al., 2005; Portman et al., 2005; Andrews et al., 2007a; Andrews et al., 2007b), who suggest that the coralline algae cave fill in the bioherms grew contemporaneously with the growth of the bioherms, which they suggest is evidence to support that the bioherms grew in a marine environment during MIS 5e. Previous studies have reported a wave-cut platform below the bioherms that was initially suggested to have formed during MIS 5e (see Kersaw and Guo (2006) for a full discussion); however, this assumption does not fit with the suggestion that the bioherms initially formed during the lowstand of MIS 6a. Furthermore, it will be shown later in this chapter that the wave-cut surfaces mapped above the bioherms is constrained to MIS 5e and therefore that it is assumed that the wave-cut surface below the bioherms is older than MIS 5e.

The observed geomorphology on Cape Heraion resembles that of a 'stepped' profile with horizontal to sub-horizontal surfaces (terraces) separated by steep slopes. The sub-horizontal surfaces are interpreted as marine terraces because they are associated with coralliferous sediments, marine shoreface deposits with Quaternary marine fossils, and wave-cut platforms that are commonly bored by marine lithophagid borings (Morewood and Roberts, 1997, 1999; Leeder et al., 2003; Leeder et al., 2005; Roberts et al., 2009). Although the marine terraces and intertidal palaeoshoreline indicators are widely accepted, the explanation for the steep slopes separating marine terraces is debated on Cape Heraion. The slopes are interpreted in two ways by different authors: (1) as palaeo- sea-cliffs, cut by wave-action by three successive Quaternary glacio-eustatic sea-level highstands (Leeder et al., 2003; Leeder et al., 2005) (Fig. 6.3a); (2) the locations of faults offsetting a single terrace surface, where the up-dip termination of a terrace surface at a slope is the hangingwall cut-off of the marine terrace along the fault (Fig. 6.3b; Morewood and Roberts, 1997). In this latter interpretation, the age of the marine terrace is suggested to be ~125 ka, associated with MIS 5e (Morewood and Roberts, 1997; Roberts et al., 2009) (Fig. 6.3b), with the presence of complex faulting representing a Segment Boundary Zone between the EXFS and SAFS (Fig. 6.2). Both of these explanations rely on age constraints that link a wave-cut platform at ~29 m to MIS 5e (125 ka highstand) dated using U-series coral ages (Vita-Finzi et al., 1993, Leeder et al., 2003; Leeder et al., 2005; Houghton, 2010) (Locality F, Fig. 6.4a), but no age constraints have been available for higher elevation surfaces, and this is needed to differentiate between the competing hypotheses.

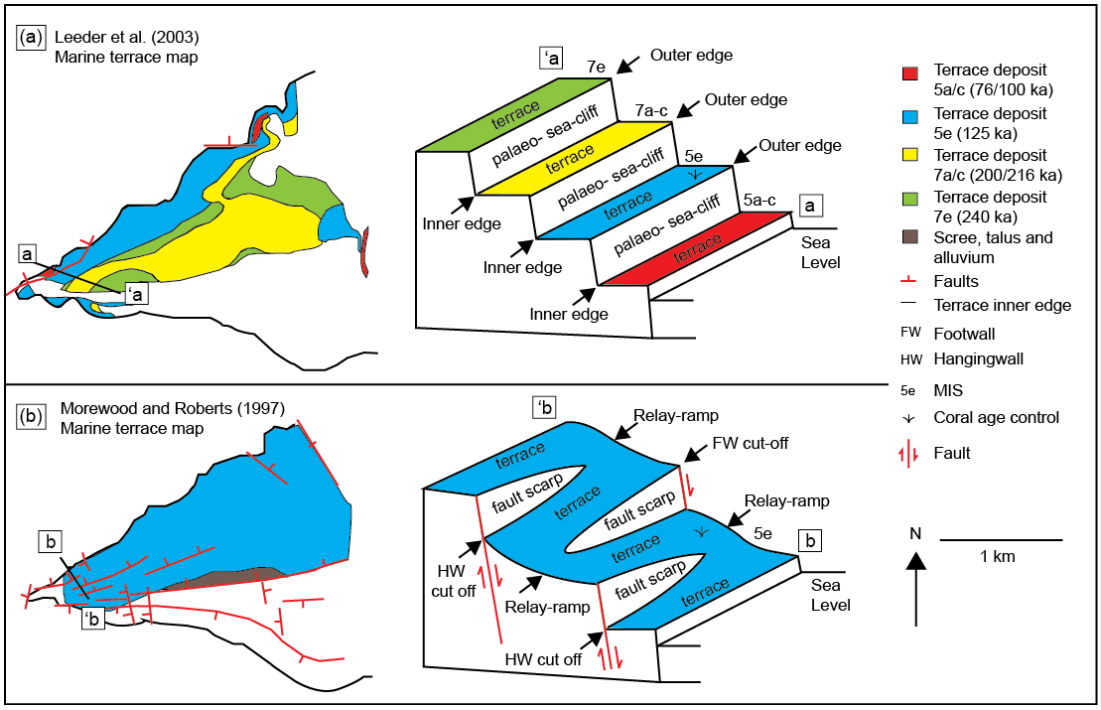

Figure 6.3: Comparison of two explanations for the observed geomorphology on Cape Heraion. (a) Geological map redrawn from Leeder et al. (2003) and interpreted schematic 3D diagram, Leeder et al. (2003) suggest a sequence of palaeoshorelines from MIS 5a/c (76.5 ka/100 ka) to 7e (240 ka). (b) Geological map redrawn from Morewood and Roberts (1997) and interpreted schematic 3D diagram, Morewood and Roberts (1997) suggest Cape Heraion is linked to the MIS 5e 125 ka highstand and has been latterly faulted. (From Robertson et al., 2020)

Detailed mapping and dating was carried out to attempt to resolve the debate of successive palaeoshorelines versus faults. In particular, identifying whether the slopes between terrace locations were continuous along strike, consistent with the suggestion that they represent a succession of palaeoshorelines, or whether the offset of the slopes varied along strike and displayed tip zones and relay ramps, suggestive of faulting (Section 2.2.1). Later the results of field mapping and dating are presented that supports the hypothesis of Morewood and Roberts (1997) that the observed variation in terrace elevation is as a result of faulting.

The significance of Holocene wave-cut notches cut into the cliffs along the most western point of Cape Heraion has also been the subject of debate (Pirazzoli et al., 1994; Stiros and Pirazzoli, 1998; Kershaw and Guo, 2001; Cooper et al., 2007; Boulton and Stewart, 2015; Schneiderwind et al., 2017a; Schneiderwind et al., 2017b). It is clear that these notches form as a result of the chemical, biological and physical wave action eroding the cliffs in the intertidal zone along palaeoshorelines (Pirazzoli, 1986). The ages of four notches observed on Cape Heraion were dated to between 190-440 A.D. and 4440-4320 B.C. from marine shells and used to infer coseismic footwall uplift increments of ~0.8 m from earthquakes with recurrence intervals of ~1600 years (Pirazzoli et al., 1994). However, 0.8 m has been

suggested to be a relatively high value for coseismic footwall uplift (Cooper et al., 2007; Boulton and Stewart, 2015; Schneiderwind et al.,2017b; Meschis et al., 2019). Whatever their mode of formation, deformation of the notches by active faulting is evidenced in this chapter (Section 6.4.4) and used, in part, to explain the geological history of Cape Heraion.

6.2.3 Marine terraces and age constraints on Cape Heraion

Existing coral ages exist on Cape Heraion at localities C, F and H (Fig. 6.4a), dated using $^{234}U/^{230}Th$ dating, reveal ages that agree to coral growth during MIS 5e (125 ka highstand) from platforms at 7 m (Roberts et al., 2009), 29 m (Collier et al., 1992; Vita-Finzi et al., 1993; Leeder et al., 2003; Leeder et al., 2005; Dia et al., 2007; Houghton, 2010) and 15 m (Burnside, 2010). The exact timing of MIS 5e is debated but there is general agreement that it occurred between 138-116 ka (Muhs and Szabo, 1994; Stirling et al., 1998; Hearty et al., 2007; O'Leary et al., 2013; Dutton et al., 2015; Polyak et al., 2018), with the majority (80%) of sea-level rise suggested to have occurred prior to 135 ka (Muchs and Szabo, 1994; Gallup et al., 2002). Knowledge of the elevations and timings of past sea levels will be used below to provide an additional check against the ages obtained from ^{36}Cl exposure dating, which should fall within known highstand time periods. To augment the existing ages, this study provides new coral ages, and ^{36}Cl cosmogenic exposure ages for wave-cut platforms, that can be mapped along strike to correlate with palaeoshoreface sediments consisting of coral–bearing marine terrace sediments. The ^{36}Cl cosmogenic exposure ages are cross checked against new and existing coral ages.

6.3 METHODS

6.3.1 Field mapping and fault analysis

Detailed field mapping and sampling for $^{234}U/^{230}Th$ and ^{36}Cl exposure dating was carried out during field campaigns throughout 2015 and 2017. For the field mapping the key criteria that would differentiate between the palaeo-sea-cliff versus fault interpretations for the steep slopes between terrace locations were focused upon. In particular, if the steep slopes are palaeo- sea-cliffs they ought to be continuous along strike (Fig. 6.3a). In contrast, if the steep slopes are fault scarps, they may display relay-zone geometries where it would be possible to walk continuously on a single surface, along strike, around fault tips, up relay ramps onto the higher parts of the same terrace surface (Fig. 6.3b) (Section 2.2.1).

In order to constrain the geometries and continuity of the marine terraces (Fig. 6.3), 58 spot-height elevations were measured throughout the field area using a handheld barometric altimeter (±3 m vertical error, though repeated elevation measurements suggest the value is closer to ±1 m) that was regularly calibrated at sea level. These measurements were supplemented by 40 additional elevation values obtained from spot heights from a 5 m digital elevation model (DEM) (±4 m vertical error) in ArcGIS (Section 3.1.2.2). Both sets of spot heights were taken along the strike of each fault in both the footwall and hangingwall cut offs (Fig. 6.3b) as well as at their tip locations, which were recognised where the vertical difference of zero occurred between the hangingwall and footwall cut offs. The combination of spot heights, outer edges (the eroded footwall cut-off) and fault trace maps allowed displacement gradients, fault tips to individual faults and relay zones separating individual faults to be identified (Section 2.2.1). These data also allowed the construction of throw profiles for each fault and cumulative throw profiles for all faults; where throw profiles are 2D representations of the vertical offset along the strike of a fault and vertical offsets were obtained by subtracting the hangingwall cut off elevation from the footwall cut off elevation at the same location at multiple points for each fault (Section 3.1.3). Individual throw profiles were constructed by plotting the vertical offset against the UTM location of the measured vertical offset so that along strike differences in displacement are visible. Cumulative throw profiles were obtained by drawing 58 serial profile lines perpendicular to the strike of all faults and adding together the vertical offsets for faults along each profile lines; the total offset was then plotted against UTM.

Rupture traces from recent (possibly 1981) faulting were mapped along faults (as per the approach in Iezzi et al., 2018). Where an exposed lichen free stripe was clear on the limestone bedrock of the fault the vertical offset in the direction of slip was measured using rulers, see Fig, 6.7f for an example. Similarly, offset colluvial deposits in the hangingwall were obtained by measuring vertical offset between matching piercing points using rulers, see Fig. 6.7e for an example. These measurements were taken at multiple locations where bedrock or colluvial offset occurred using a barometric altimeter/GPS to measure the elevation and location of the measurement.

6.3.2 Sampling for corallites and exposure dating

Coral samples were removed from three locations on Cape Heraion, these are outlined as follows. (1) Samples S6U/Th and S7U/Th were removed from a 0.5-1 m thick coral-bearing,

bioclastic layer overlying the bioherms at 44 m at Locality B (Fig 6.4a). The bioclastic deposits were composed of coarse carbonate sands and contained whole corallites of *Cladocora caespitosa*. (2) Four whole corallite samples S158U/Th–S161U/Th were removed from the wall of a cave at 46 m located to the north west of Lake Vouliagmeni (Fig. 6.2c) (UTM: 663744/4211167), outside of the mapping area. (3) Samples S44U/Th-S48U/Th were removed from the vicinity of Locality G (Fig. 6.4a); these corals are the subject of Chapter 7 and are discussed fully within that chapter. For samples S6U/Th, S7U/Th and S158U/Th-S161U/Th, whole corallite samples were removed and prepared, with age determinations made as per the approach outlined in Section 3.4, with all samples analysed for Uranium concentration where values should be ~2-3.5 ppm (Shen and Dunbar, 1985) and $^{230}Th/^{232}Th$ values >100 (van Calsteren and Thomas, 2006).

For ^{36}Cl dating, attention was focused on wave-cut platforms that could be mapped along and across strike into the coral-bearing, bioclastic layers, suggesting they would be close in age, presumably with the sediments deposited and lithified on wave-cut platforms when they were below wave base; as revealed by a few rare exposures of this contact. An overview of ^{36}Cl exposure dating was given in Chapter 2 and the methods involved in sampling and age derivation in Chapter 3, however it is important to note that obtaining the absolute ages of wave-cut platforms using cosmogenic ^{36}Cl exposure dating relies on (i) sampling from a surface composed of a calcium-rich lithology that has (ii) experienced minimal erosion and negligible burial, under soil for example, since exposure. Consequently, the approach to sampling outlined in Chapter 3 is applied, which is reliant on identifying surfaces that have experienced minimal erosion based on the presence of preserved lithophagid borings and millholes and away from sediment pathways, such as where the geomorphology suggests former rocky coastlines or low elevation sea stacks. Wave-cut platforms composed of differing lithologies were sampled for exposure dating from a range of elevations: 62 m, 60 m, 46 m, 42 m and 29 m, including one location where there is an existing age control from $^{234}U/^{230}Th$ coral ages (in the vicinity of Locality F, Fig. 6.4a) from sediments formed quasi-contemporaneously with the wave-cut platform (Vita-Finzi et al., 1993; Leeder et al., 2003; Leeder et al., 2005; Houghton, 2010). It is important to note that wave-cut platform samples removed from 7 m (Locality C, Fig. 6.4) for ^{36}Cl exposure dating were discounted owing to unacceptably high Cl concentrations (Section 3.3.3), possibly as a result of natural Cl contamination by sea splash, water or the presence of minute coral fragments in the matrix.

6.4 RESULTS

This section explores the results of detailed geological mapping of Cape Heraion and the absolute ages obtained from ^{36}Cl cosmogenic exposure dating and $^{234}U/^{230}Th$ dating. Alongside existing published ages, these new absolute ages are used to constrain the ages of surfaces at different elevations on Cape Heraion in order to show that faulting is responsible for offsetting a marine terrace linked to the 125 ka highstand within MIS 5e. The results of the dating are used to drive throw rate analyses in order to calculate cumulative throw within the tip zone since 125 ka.

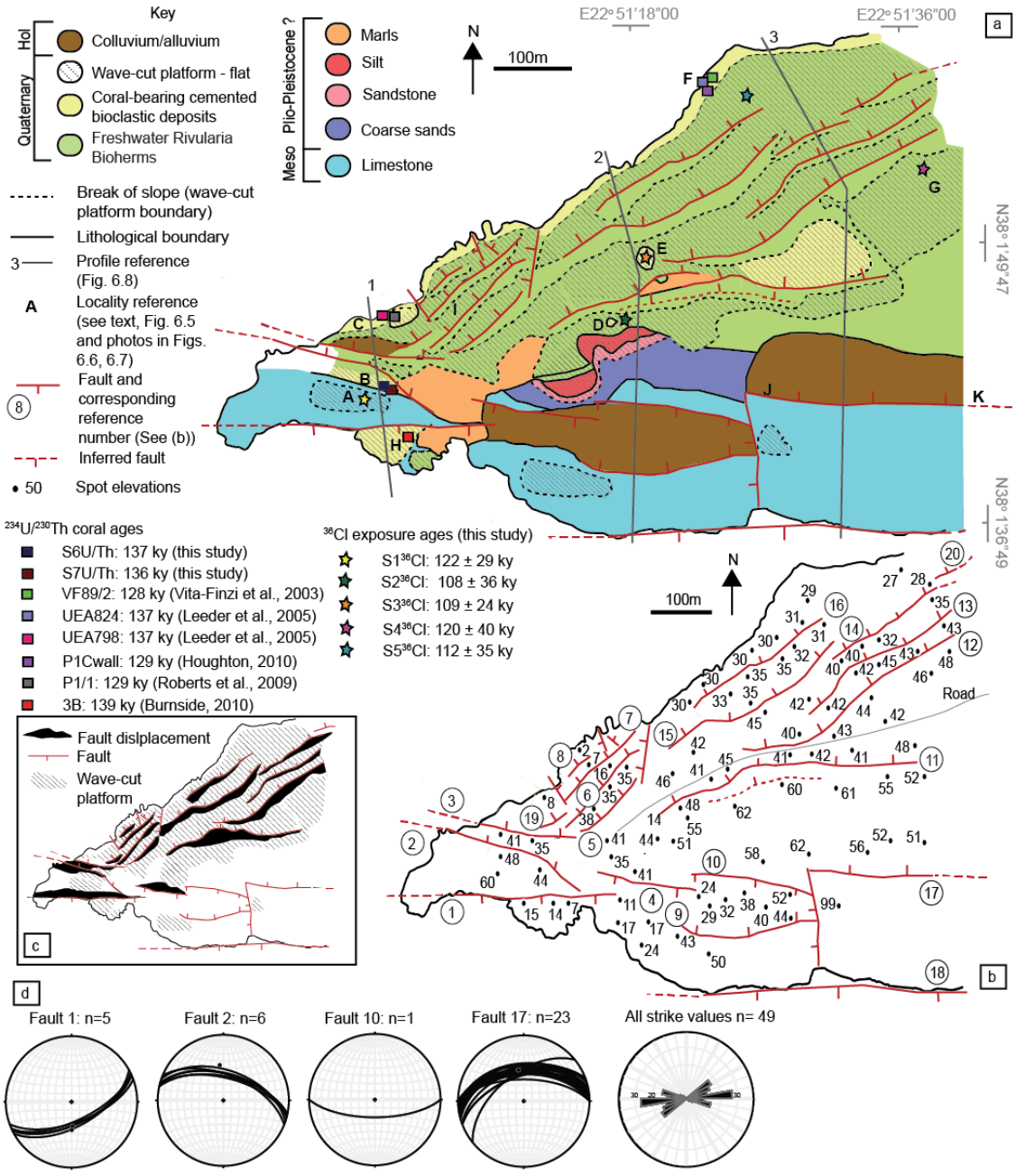

Figure 6.4: (a) Geological and geomorphological map of Cape Heraion, age controls from this study and other coral studies (Vita-Finzi et al., 1993; Leeder et al., 2005; Roberts et al., 2009; Burnside, 2010; Houghton, 2010). (b) Fault map of Cape Heraion and spot height elevations used to plot the fault displacement in (c). (d) Stereonet plots for faults 1, 2, 10 and 17, rose diagram representing all measured strike values. (From Robertson et al., 2020)

6.4.1 Field mapping

Detailed field mapping reveals complicated, but linked spatial relationships between lithologies, the stratigraphy and geomorphic features on Cape Heraion (Fig. 6.4, 6.5). At the base of the stratigraphic column is Mesozoic limestone (Figs. 6.4a, 6.5, Locality A).

Unconformably above the limestone is a sedimentary succession, only observed in the centre of the cape, that fines up from coarse sands to silts (Locality D, Figs. 6.4a and 6.5). Plio-Pleistocene marls are inferred to occur stratigraphically above the sands and silts although the contact between them has not been observed, and they may be lateral equivalents. The marls form large cliff outcrops along the north of the cape (e.g. Locality F in Figs. 6.4 and 6.5) and are overlain by a coarse boulder conglomerate that displays an erosive base cut into the underlying marls (Locality F). Algal carbonate bioherms formed of *Rivularia haematities* have grown on the basal conglomerate (Localities E, F and G, Fig. 6.5) and directly on the basement limestone (Localities B, C and D, Fig. 6.5). In turn, the bioherms are overlain by fossiliferous, coral-bearing, marine bioclastic sands preserved as a continuous 0.6-1.0 m thick layer (Localities B, C, E, F and H, Figs. 6.4a, 6.5) or as patches infilling cavities between or within the bioherms (Locality C and D Figs. 6.4a, 6.5). These bioclastic deposits have rich fossil assemblages with colonies of the branching coral *Cladocora caespitosa* in life position, frameworks of serpulid worm tubes, and bivalves, pectin, turritella, bryozoa, and elsewhere broken fragments of *Cladocora caespitosa* within the sediment that form death assemblages. In places, the inside of the bioherms has been eroded and small caves have formed, which have been bored by lithophagids. The caves contain marine deposits such as *Cladocora caespitosa* (e.g. Locality C), suggesting the cave-filling deposits are the age-equivalents of the coral-bearing bioclastic sands that lie on top of the bioherms.

Wave-cut platform features have been cut into the stratigraphy (Fig. 6.4a) and are widespread throughout the cape at elevations from 6 m to 99 m (Fig. 6.4, 6.5 and 6.6). These horizontal to sub-horizontal surfaces exhibit millholes and lithophagid borings, which are particularly well preserved on the platforms composed of bioclastic packstone (Fig. 6.4a, 6.6f). Associated with the wave-cut platforms, several localities display coastal notches where the wave-cut platforms impinge on steep outcrops. The notches are marked with lithophagid borings, for example close to location B at ~41 m, with another notch observed at ~92 m (Locality J, Fig. 6. 4a).

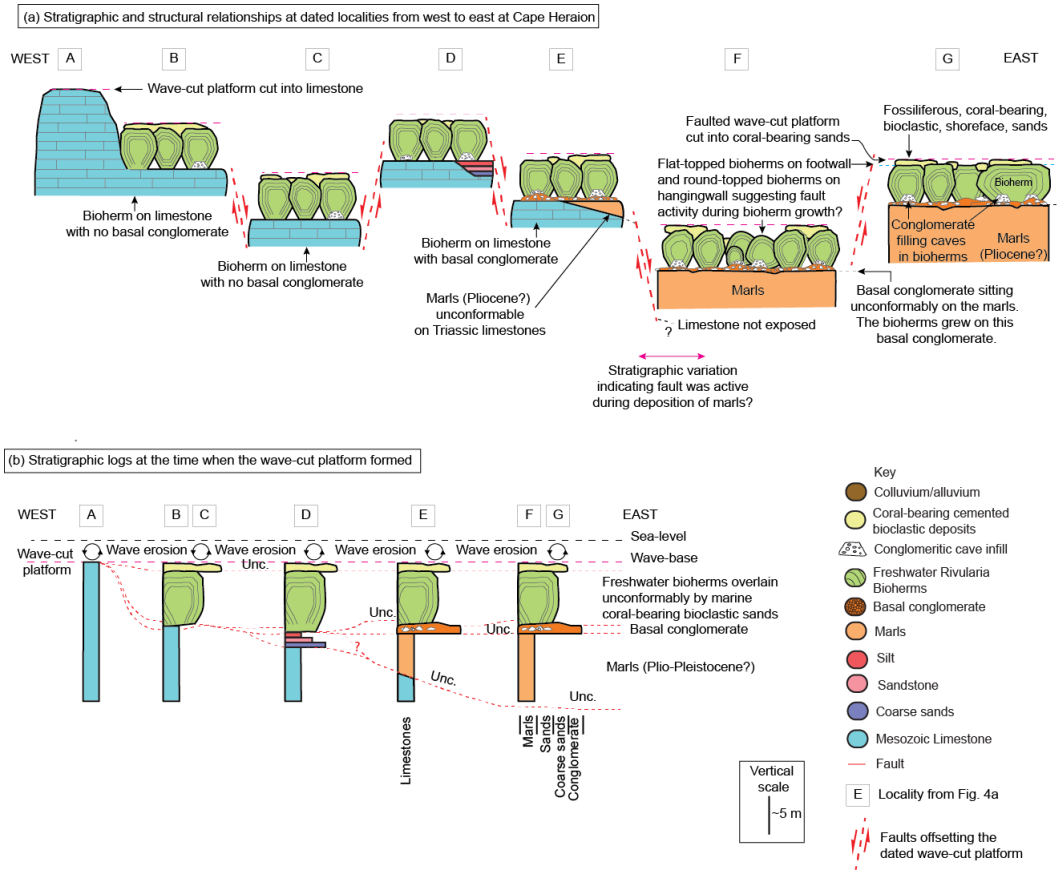

Figure 6.5: (a) Stratigraphic and structural relationships and (b) stratigraphic logs for dated localities from West to East, see Fig. 6.4a for localities. (From Robertson et al., 2020)

Results from the mapping suggests that the lithologic, stratigraphic and geomorphic features can be interpreted as due to the effect of wave-erosion, at the time of wave-cut platform formation, impinging on palaeo- Cape Heraion, characterised at that time by Quaternary sediments onlapping onto an upstanding inlier of Mesozoic limestone (Fig. 6.5b). The lateral stratigraphic variations were denuded by the wave erosion so that the wave cut-platform formed on different stratigraphic units across the mapped area. The stratigraphy, and the wave-cut platform, have been subsequently offset by faulting that may have been contemporaneous with some sedimentation, but continued through time and therefore mostly post-dates the wave-cut platform, the Cladocora-bearing bioclastic sands and the Rivularia-bioherms (Fig. 6.7).

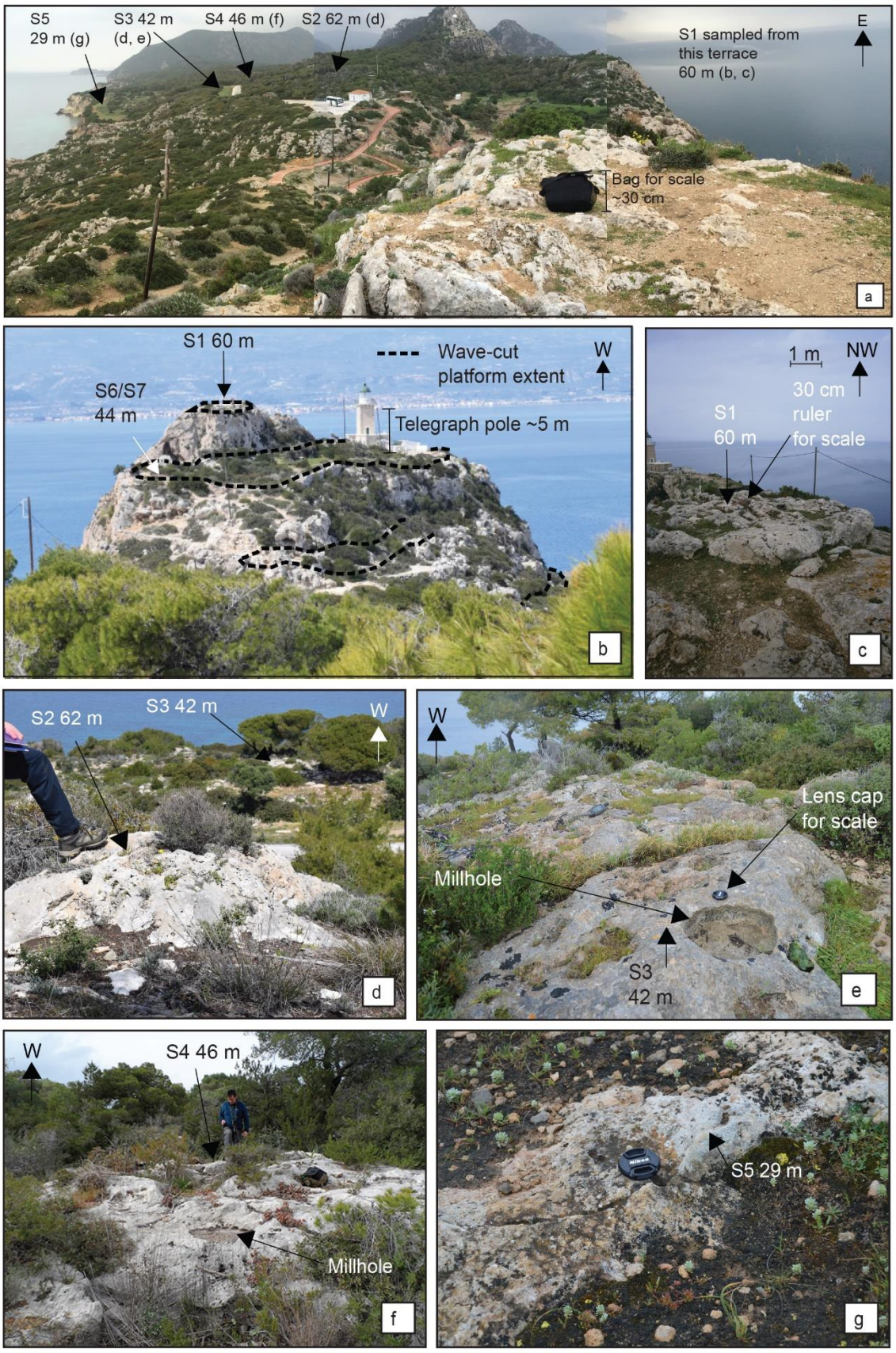

Figure 6.6: (a) overview of ^{36}Cl sample locations. (b–h) Photographs of ^{36}Cl and $^{234}U/^{230}Th$ sample locations. See Fig. 6.4a for locations of samples. (From Robertson et al., 2020)

To gain further insights into the faulting, the steep slopes that occur along the faults, and in particular the breaks of slope, were studied (Fig. 6.4a, c). The map pattern produced by the breaks of slopes reveals patterns that resemble displacement variations along the faults, with slip maximum close to the centres of the map traces, and the positions of relay-ramps at fault tips that allow one to walk in the hangingwall along the strike of one fault, up a relay ramp and into the footwall of an adjacent fault (Figs. 6.3b, 6.4c). Hence, the breaks of slope between the relay zones were interpreted to represent hangingwall and footwall cut offs. Cross-checks on the fault interpretation are further discussed in Section 6.4.3 using absolute ages and cross-sections across the faults and Section 6.4.5 where the fault segmentation in Fig. 6.4c is analysed using the elevation data shown in Fig 6.4b to measure the vertical offsets across the faults, checking that relay-ramps and fault tips identified on Fig. 6.4c are marked by decreased vertical offsets. These cross-checks confirm that locations where the hangingwall and footwall cut-offs converge in map view (e.g. the relay-ramps and fault tips in Fig. 6.9b) have low or zero vertical offsets, consistent with the fault segmentation model presented herein.

As a final check on the geometries of the faults, their displacement (*d*) to length (*L*) ratios (Section 2.2.1) are compared to those in a global database (Schlische et al. 1996), because $d = \gamma L$, where γ= 0.01-0.1 with a preferred value of 0.03. Analysis of the *d/L* ratio is carried out on faults where both fault tips are observed, with the maximum measured throw along the fault taken to represent the throw maximum. Values of γ are between 0.01-0.1 (Table 6.1), suggesting that the vertical extents of the steep slopes separating terrace locations are consistent with the interpretation that they are fault scarps.

Fault number	Length (m)	Throw (m)	d/L ratio
5	139	6	0.04
6	175	9	0.05
7	148	9	0.06
8	63	5	0.08
9	220	10	0.05
11	445	19	0.04
12	413	5	0.01
13	311	7	0.02
14	163	9	0.06
15	332	10	0.03
16	335	10	0.03

Table 6.1: Displacement length (d/L) ratios for mapped faults on Cape Heraion, with the exception of Fault 19 due to a lack of elevation data and Faults 1, 2, 3, 4, 10, 17, 18, 20 as both tips could not be mapped, note that the combined throw pattern of faults 1, 4 and 10 (Fig. 6.9) suggest that they are linked at depth, hence they are treated as one fault – the d/L of which cannot be calculated because Fault 1 continues offshore (Fig. 6.4a, b) (modified from Robertson et al., 2020).

Details of the faulting are described below. With the exception of three faults that strike approximately N-S not considered in this study, all of the faults strike parallel-sub parallel to the average 260˚ of the SAFS between 230˚ and 300˚ (Fig. 6.2, 6.4). The faults in the north of the cape are all north dipping and exhibit short fault lengths (100-400 m) and offsets of 2-20 m. South of Fault 11 the presence of a north dipping fault is inferred owing to the 20 m offset of bioherms observed along the scarp of Fault 11 (Fig. 6.4a, b). Faults along the south of the cape are longer, and extend outside of the mapping area to the east and offshore to the west (Faults 1, 17 and 18) (Fig. 6.4a-c, 6.7a-c). Along the south of the cape, there are four south-dipping faults (1, 4, 10 and 18) (Fig. 6.4b, 6.7a-c, e, f). The scarp of Fault 18 is not accessible and the offset of this fault is a minimum value as its hangingwall is offshore, however, this fault has been mapped by Morewood and Roberts (1999) farther to the east for ~2 km. South dipping Faults 1, 4 and 10 appear to be en-echelon to one another and exhibit limestone fault scarps that decrease in offset from west to east.

Strike and dip values, and, where visible, fault striations were measured along the limestone fault scarps of Faults 1, 2, 10 and 17 (Fig. 6.4d). The fault dip for these faults range between 43-66˚. In places faults display evidence of activity in a marine setting, specifically Faults 1 and 4 display post-slip marine cementation of submarine screes coating the faults (Scott, 1995).

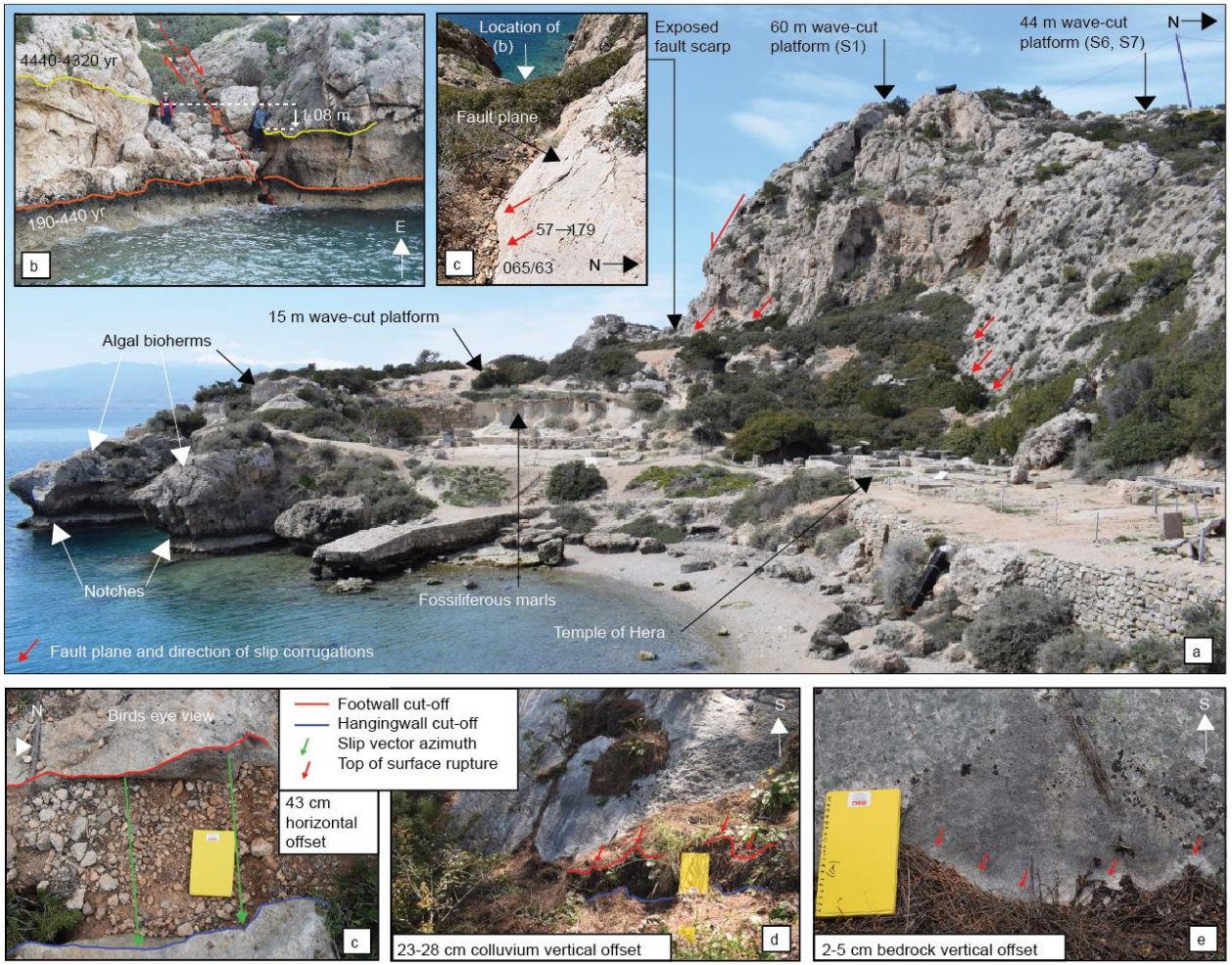

Figure 6.7 (a) View of Fault 1 offsetting a wave-cut platform at 60 m and 15 m (Locality H). (b) Annotated photograph of offset wave-cut notches on Fault 1. (c) Fault plane and annotated direction of fault slip for Fault 1. (d) North-south horizontal offset of 43 cm on a bioherm on the north side of Cape Heraion at Locality I, Fig. 6.4. Offset colluvium (e) and bedrock (f) along fault 17 between localities J and K, Fig. 6.4, UTM location: 663350/4210630. (From Robertson et al., 2020)

In summary, geomorphological observations and elevation measurements suggest that a pattern of distributed faulting is visible on Cape Heraion. In the context of the north-dipping SAFS and its approximate E-W strike, the faulting on Cape Heraion displays a set of synthetic and antithetic faults that display a relatively small 70^{o} variation in strike. While north-dipping faults are more numerous, they appear to have smaller lengths and offsets compared to the four south dipping faults.

6.4.2 $^{234}U/^{230}Th$ coral dating

Cladocora caespitosa corallite dating results for Samples S6U/Th, S7U/Th and S158U/Th-S161U/Th are discussed below. The coral age determinations from S158-161U/Th (Fig. 6.2c, Table 6.2) yielded three ages, sample S160U/Th lost its Th fraction so no age determinations were possible from this sample. Ages for samples S158U/Th, S159U/Th and S161U/Th are 217.4 ky, 288.9 ky and 413.5 ky, respectively. All of these samples have uranium concentration values lower than 2 ppm and sample S161U/Th has an unacceptably low ($^{230}Th/ ^{232}Th$) of 73. Low uranium concentrations and $^{230}Th/ ^{232}Th$ ratios may indicate that the coral samples have been subject to open system conditions, potentially experiencing uranium loss since their formation. In light of this, samples S158-161 were rejected. Furthermore, the ages and $\delta^{234}U_i$ of the samples are not in agreement with one another so their reliability is in doubt, consequently, age determinations from these samples are disregarded.

S6U/Th and S7U/Th (Fig. 6.4a) were removed from within a death assemblage on the 44 m wave-cut platform predominantly composed of friable sediments located on the limestone inlier/horst (Locality B, Fig 6.4; Figs. 6.6c, 6.7a). Multiple analyses using different fragments from corallite samples S6U/Th and S7U/Th were undertaken, an approach suggested by Esat and Yokoyama (2010) and Dutton (2015) (Section 2.1.4.1), in order to examine the reliability of the coral age samples without solely relying on the $\delta^{234}U_i$. $^{234}U/^{230}Th$ coral age dating of corallite S6U/Th (Table 6.2) reveals growth ages of 133.5 ky, 135.4 ky, 142 ky and 173.7 ky; the latter age is excluded because the age of 173.7 ky suggests that it is an outlier and not representative of the age of the corallite. The age determinations of corallite S7U/Th are 140.8 ky, 139.1 ky, 135.2ky, 134.5 ky, 134.7 ky, and 132.3 ky (Table 6.2). The $^{234}U/^{230}Th$ coral ages of corallites S6U/Th and S7U/Th support growth during early MIS 5e and are similar to

existing coral growth ages from Cape Heraion (Fig. 6.8a; Vita-Finzi et al., 1993; Leeder et al., 2005; Roberts et al., 2009; Burnside, 2010; Houghton, 2010).

Note that all samples have relatively high values of $\delta^{234}U_i$ of 191-214‰ (a common way to represent the initial activity ratios of $^{234}U/^{238}U$) compared to modern seawater in the Gulf of Corinth (value of 151‰; Roberts et al., 2009). It is expected that the samples should have $\delta^{234}U_i$ values similar to modern sea-water. However, previous studies of coral ages in the Gulf of Corinth, which successfully produced ages of independently-known glacio-eustatic sea-level highstands, have tended to show elevated values (e.g. Collier et al., 1992; Vita-Finzi et al., 1993; McNeill and Collier, 2004; Dia et al., 1997; Leeder et al., 2005; Roberts et al., 2009; Burnside, 2010; Houghton, 2010; Turner et al., 2010), probably due to the fact that it is a restricted basin with freshwater input, this is explored further in Chapter 7.

The analyses herein also suggest an age similar to the well-known glacio-eustatic sea-level highstand at ~125 ka (e.g. Siddall et al., 2003). Thus, like previous studies, the implied age is used in the later analysis, despite the relatively high initial activity ratio for the samples dated in this study. Importantly, the coral age determinations from samples S6U/Th and S7U/Th, suggestive of growth during MIS 5e are located in the footwall of Faults 1 and 2 (Fig. 6.4a). The hangingwalls of both of these faults have coral ages from previous studies (Roberts et al., 2009 and Burnside, 2010, Fig. 6.4a Localities C and H, respectively) that also constrain their ages to MIS 5e, which demonstrates that the surfaces from which the corals were sampled can be linked to the same palaeoshoreline and allow slip rates since ~125 ka to be calculated.

Sample name	Lab ID	UTM		Sampling elevation (m)	Age (ky)	±2s (abs) (ky)	U (ppm)	^{232}Th (ppb)	(^{230}Th/ ^{232}Th)	(^{232}Th/ ^{238}U)	±2s (%)	(^{230}Th/ ^{238}U)	±2s (%)	(^{234}U/ ^{238}U)	±2s (%)	δ^{234}_{i} (‰)	±2s (%)
		Easting	Northing														
S6U/Th (1)	138-34	662540	4210594	44	133.5	0.7	2.42	0.005	1210.7	0.00068	0.04	0.81787	0.25	1.1354	0.14	197	±2
S6U/Th (2)	141-29	662540	4210594	44	135.4	1.2	2.44	0.006	1073.3	0.00076	0.12	0.82081	0.35	1.1315	0.28	193	±4
S6U/Th (3)	141-30	662540	4210594	44	142.7	1.3	2.57	0.006	1074.0	0.00079	0.10	0.85306	0.34	1.1429	0.25	214	±4
S6U/Th (4)	145-12	662540	4210594	44	173.7	2.0	2.13	0.009	674.9	0.00136	0.17	0.92101	0.34	1.1287	0.29	210	±5
S7U/Th (1)	138-35	662540	4210594	44	140.8	0.8	2.26	0.008	736.1	0.00114	0.04	0.83619	0.22	1.1298	0.13	193	±2
S7U/Th (2)	145-13	662540	4210594	44	139.1	0.9	2.28	0.012	467.2	0.00179	0.08	0.83630	0.25	1.1359	0.18	201	±3
S7U/Th (3)	145-14	662540	4210594	44	135.2	1.0	2.24	0.009	599.5	0.00137	0.10	0.81931	0.29	1.1301	0.21	191	±3
S7U/Th (4)	145-15	662540	4210594	44	134.5	1.0	2.34	0.014	426.6	0.00192	0.11	0.81943	0.29	1.1328	0.22	194	±3
S7U/Th (5)	145-16	662540	4210594	44	134.7	0.9	2.13	0.008	658.4	0.00125	0.09	0.82413	0.26	1.1380	0.19	202	±3
S7U/Th (6)	145-17	662540	4210594	44	132.3	0.9	2.39	0.016	364.2	0.00223	0.08	0.81141	0.29	1.1315	0.21	191	±3
S158U/Th	138-30	663744	4211167	46	217.4	1.8	1.8	0.006	961.3	0.00103	0.05	0.98642	0.23	1.1134	0.14	209	±2
S159U/Th	138-31	663744	4211167	46	288.72	5.5	1.7	0.013	455.6	0.00238	0.18	1.08642	0.38	1.1297	0.15	292	±5
S160U/Th	138-32	663744	4211167	46	Th fraction lost – no data												
S161U/Th	138-33	663744	4211167	46	413.5	13.1	1.73	0.080	74.3	0.01522	0.04	1.13188	0.25	1.1165	0.25	341	±13

Table 6.2: ^{234}U/ ^{230}Th coral age dating analytical results for samples S6U/Th and S7U/Th (see Fig. 6.4a for sample location) and S158-161U/Th (Fig. 6.2c, see text for location description). Activity ratios calculated using the ^{234}U and ^{230}Th decay constants of Cheng et al., (2013). Activity ratios corrected for ^{230}Th, ^{234}U and ^{238}U contribution from the synthetic ^{236}U–^{229}Th tracer, instrument baselines, mass bias, hydride formation and tailing. ^{230}Th blanks amounting to 0.15 ± 0.03 fg were subtracted from each sample. ^{238}U blanks were on the order of 10 pg, and were negligible relative to sample size. Age and $\delta^{234}U_i$ data were corrected for the presence of initial ^{230}Th assuming an initial isotope composition of (^{232}Th/ ^{238}U) = 1.2 ± 0.6, (^{230}Th/ ^{238}U) = 1 ± 0.5 and (^{234}U/ ^{238}U) = 1 ± 0.5 (all uncertainties quoted at the 2σ level). (From Robertson et al., 2020).

6.4.3 ^{36}Cl exposure dating of wave-cut platforms

Cosmogenic ^{36}Cl exposure dating is employed to calculate the time period that sampled surfaces have been subaerially exposed and thus accumulating significantly higher values of ^{36}Cl compared to pre-exposure. Five samples were removed from limestone, bioclastic packstone and algal bioherm wave-cut platforms at different elevations on Cape Heraion (Figs. 6.4a, 6.6). Sample sites were also chosen to see if the terrace surfaces in the footwalls of the interpreted faults have the same age (Morewood and Roberts, 1997) or successively-older ages moving up the overall slope of the coast (Leeder et al., 2005). Field observations are used to inform the erosion rate used as an input parameter into CRONUScalc, which is used to calculate the exposure age of the samples (see Appendix 1 for CRONUScalc input data). The preservation of lithophagid borings and millholes on bioclastic packstone and limestone surfaces (Samples 1 and 3) (Fig. 6.6b, f) indicate total erosion values of less than 0.02-0.03 m, whilst samples from the tops of bioherms (Samples 2, 4 and 5) are expected to have experienced total erosional values similar with the removed depth of bioclastic packstone/grainstone eroded from the surface of ~0.6 m. These limestone/packstone and bioherm values equate to erosion rates of 0.1 and ~6.0 mm/ky, respectively. Note that the 0.1 mm/ky value is the same as that used on limestone wave-cut platforms dated using ^{36}Cl exposure dating in south Crete discussed in Chapter 4 (Robertson et al., 2019).

Assuming the erosion rates stated above are correct, the ^{36}Cl exposure ages of five samples (Fig. 6.8a, Table 6.3) are: S1 (limestone, sampled at 60 m) 122 ± 29 ka; S2 (bioherm, sampled at 62m) 108 ± 36 ka; S3 (bioclastic packstone, sampled at 42 m) 109 ± 24 ka; S4 (bioherm, sampled at 46 m) 120 ± 40 ka; S5 (bioherm, sampled at 29 m) 112 ± 35 ka. These results agree with the new and existing U-series ages presented above (Section 6.4.2), in that they indicate a formation age of the wave-cut platforms during MIS 5e (125 ka highstand). The error bars on the ages appear relatively-large, but are comprised of internal (analytical) and external (total) uncertainties that are associated with measured input parameters into CRONUScalc (e.g. H_2O content, elevation, shielding, erosion rates and the production rate; Marrero et al., 2016) (Section 3.3.3). Where samples are removed from the same geographical location using the same method, the error values of the input parameters used to calculate the external uncertainty will be very similar (i.e. shielding) or even the same (i.e. production rate, elevation values). Consequently, Marrero et al. (2016a) suggests that the external uncertainty value linked to the exposure age may be overestimated when comparing results

from the same geographical area, sampled using the same method (see Dunai, 2010). This possible overestimate of uncertainties should be borne in mind when considering the relatively-large error bars associated with the exposure ages. It is important to note that internal uncertainty values underestimate the uncertainty, so Marrero et al. (2016a) explicitly advise that external uncertainties should be reported for all ages obtained.

Sample name	Lithology and geomorphology	Latitude	Longitude	Elevation (m)	Lithology	Total erosion (cm)	Erosion rate (mm/ky)	Cl (ppm)	±	^{36}Cl (atoms/g)	±	CaO (wt%)	±	Age (kyr)	Internal uncertainty (kyr)	External uncertainty (kyr)
1	Limestone: flat WCP with lithophagid borings. Sample removed from the the area displaying lithophagid borings (Fig. 6.6b)	38.0288	22.85106	60	Limestone	1.2	0.1	17.0503	0.2856	2327699	63421	57.41	1.38	122	3.7	29
2	Bioherm top, bioclastic sands infill spaces between adjacent bioherms. Sample removed from the top of the bioherm (Fig. 6.6e)	38.0292	22.85297	62	Bioherm	64.8	6	22.5328	0.4739	1195064	34923	43.85	1.53	108	8.4	36
3	Bioclastic packstone, excellent millholes preserved. Sample removed from immediately adjacent to the millhole (Fig. 6.6f)	38.0304	22.85522	42	Packstone	1.1	0.1	38.7794	0.8003	1887336	54970	49.02	1.52	109	3.5	24
4	Bioherm top, millholes, abundant lithophagid borings preserved on the adjacent backwall (Fig. 6.6g)	38.032	22.8596	46	Bioherm	72.0	6	33.3263	0.6646	1616569	47009	53.80	1.47	120	8.8	40
5	Bioherm top, visible above surrounding alluvium (Fig. 6.6h)	38.0305	22.85516	29	Bioherm	67.2	6	60.5561	1.6227	1684932	46140	54.01	1.44	112	9.3	35

Table 6.3: ^{36}Cl exposure dating analytical results and sample descriptions (see Fig. 6.4a for the sample locations). ^{36}Cl concentrations are based on 1.2 × 10 −12 ^{36}Cl/Cl ratio for Z93-0005 (PRIME Lab, Purdue). This standard agrees with standards prepared by Nishiizumi (2002), which were used as secondary standards. Cl concentrations were determined by AMS isotope dilution (Stuart and Dunai, 2009). ^{36}Cl/Cl processed blank ratios ranged between 2.4 and 6.03% of the samples ^{36}Cl/Cl ratios. (From Robertson et al., 2020). See Appendix one for all AMS and ICP-OES elemental data used to derive the ages in this table.

While the erosion rates used to calculate exposure ages are based upon field observations, it is recognised that they form an uncertainty in the ages obtained. Therefore, the sensitivity of the exposure age results to uncertainties in the estimated erosion rates is examined. For Samples 1 (limestone) and 3 (packstone), erosion rates between 0.1-1 mm/ky were tested and for Samples 2, 4 and 5 (bioherms) erosion rates between 5.5-6.5 mm/ky (± 0.5 mm/ky of estimated erosion rates) were tested. The results of these analysis (Fig. 6.8) reveal that the exposure ages may all be allocated to the 125 ka highstand even if the proposed erosion rate is adjusted within the range of ± 0.5 mm/ky. Values for erosion rates larger than this would not be consistent with the field observations of features such as preserved millholes and lithophagid borings. Based upon this analysis maximum and minimum values for rates of erosion for Samples 1 and 3 of 0.1-1 mm/ky and for Samples 2, 4 and 5 of 5.5-6.5 mm/ky are suggested. These results support the contention that the erosion rate estimates employed (Samples 1, 3: 0.1 mm/ky and samples 2, 4 and 5: 6 mm/ky) are acceptable.

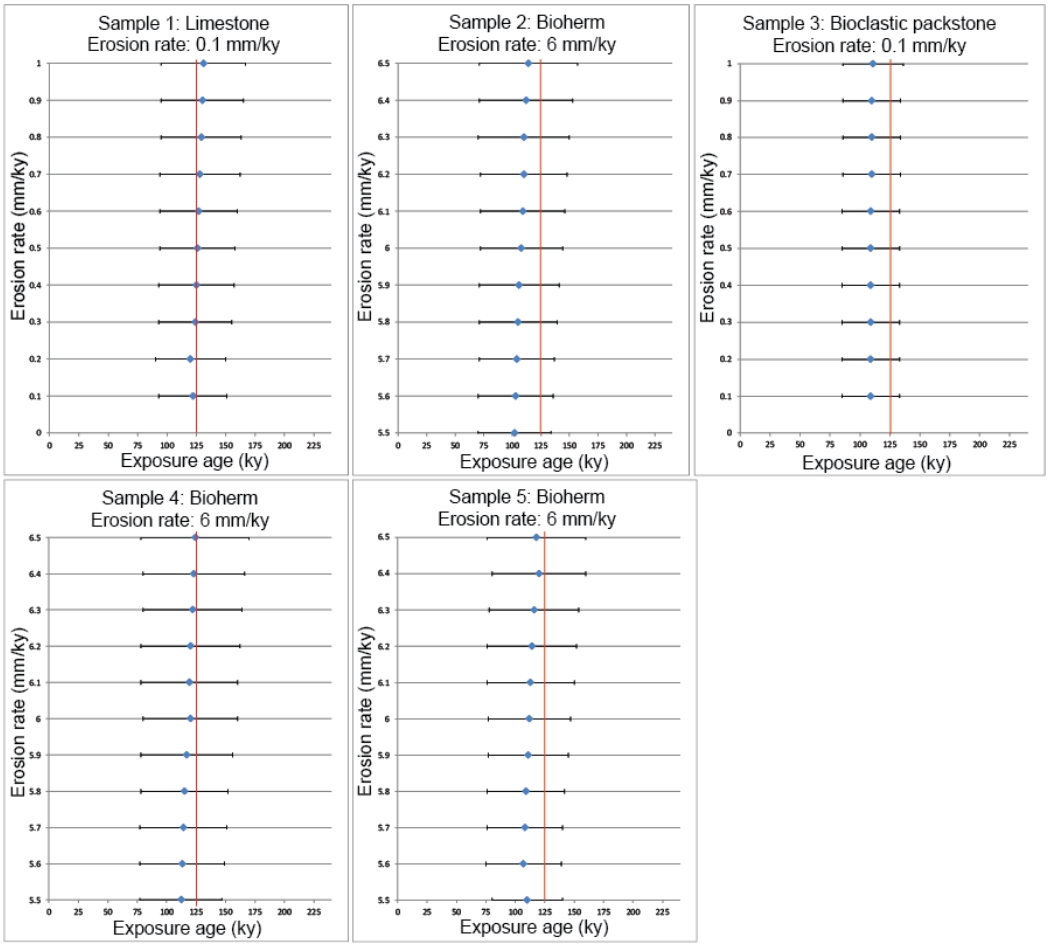

Figure 6.8: Sensitivity tests for the rates of erosion used in ^{36}Cl exposure dating for samples S1-S5 on Cape Heraion. Samples S1 and S3 are tested for 0.1-1 mm/ky, Samples S2, S4 and S5 are tested for 5.5-6.5 mm/ky.

All of the exposure ages for the wave-cut platform are interpreted to be associated with MIS 5e, and this is discussed below. Exposure age results link S1 and S4 and their associated wave-cut platforms to MIS 5e, but the wave-cut platforms that S2, S3 and S5 were removed from, might, at first sight, be linked to either MIS 5c (100 ka highstand) or MIS 5e (125 ka highstand) (Fig. 6.9a). However, using the exposure ages obtained from S1 (60 m, Locality A, Fig. 6.4a) and S4 (46 m, Locality G, Fig. 6.4a), new $^{234}U/^{230}Th$ ages from S6 and S7 (44 m, Locality B Fig. 6.4a) and existing U-series dating of corals on platforms at 7 m (Locality C, Fig. 6.4a) (Roberts et al., 2009), 15 m (Locality H, Fig. 6.4a) (Burnside, 2010) and 29 m (Locality F, Fig. 6.4a) (Vita-Finzi et al., 1993; Leeder et al., 2003; Leeder et al., 2005; Houghton, 2010) alongside sea-level curve data, it is more likely that S2 (62 m, Locality D, Fig. 6.4a), S3 (42 m, Locality E, Fig. 6.4a) and S5 (29 m, Locality F, Fig. 6.4a) are associated with MIS 5e (Fig. 6.9c). The reasoning for this is that it is difficult to reconcile that platforms at 60 m, 46 m, 44 m, 29 m, 15 m and 7 m were formed by the MIS 5e 125 ka highstand and then offset by faulting, yet platforms at similar elevations (62 m, 46 m and 29 m) were formed by the MIS 5c 100 ka highstand. This is especially unlikely, given that the maximum sea level during the 100 ka highstand in MIS 5c was -25 m relative to today, and this is 30 m lower than the 5 m relative sea level during the 125 ka highstand of MIS 5e (Siddall et al., 2003) (Fig. 6.9a).

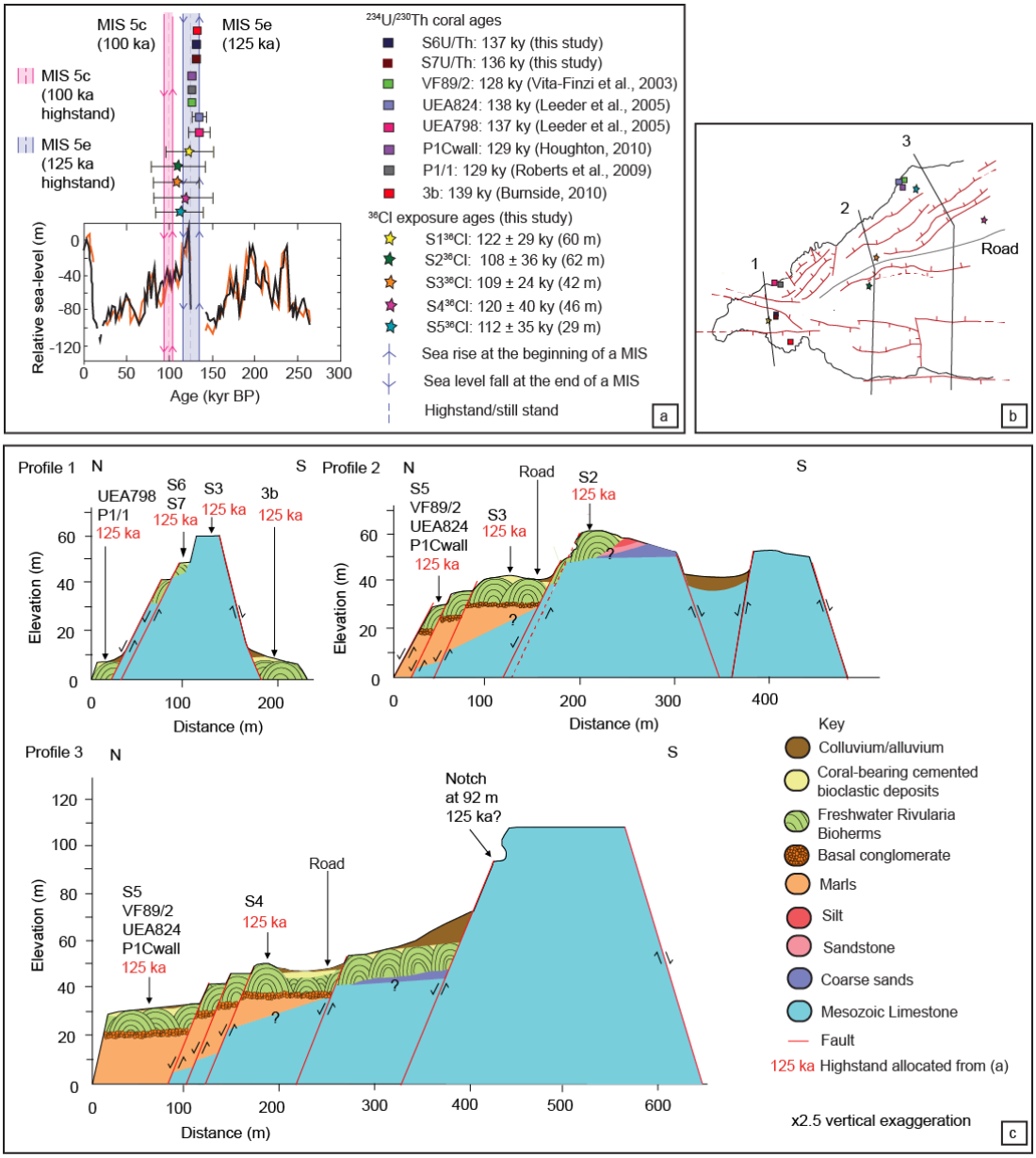

Figure 6.9: (a) ^{36}Cl exposure ages and ^{234}U/^{230}Th coral ages (where error bars are not visible, the value of error is smaller than the plot marker). Ages are plotted against the sea level curve from Siddall et al. (2003), orange and black lines represent different cores used to construct the sea-level curve. (b) Fault map and the location of profile lines from Fig. 6.4a and b that are shown as schematic cross sections in (c). (From Robertson et al., 2020)

The results of the dating in this chapter, combined with existing age controls and detailed geological mapping strongly supports that the observed wave-cut platforms on Cape Heraion were all formed during the 125 ka highstand of MIS 5e and have been subsequently faulted since this time (Fig. 6.9c).

6.4.4 Holocene displacements

Offset Holocene notches and surface faulting that may be associated with the 1981 earthquake suggest occurrence of Holocene faulting on Cape Heraion (Fig. 6.7). An offset

notch exists along the base of a cliff at the south west of the cape of as a result of slip on Fault 1 (Fig. 6.4b, 6.7b). The highest notch is offset by 1.08 m between the footwall and the hangingwall, but it does not appear that a lower notch is also offset (Fig. 6.7b). A possible explanation for these observations is that faulting occurred on Fault 1 following the formation of the upper notch between 4440-4320 B.C. (Pirazzoli et al., 1994) prior to the formation of the lowest notch (at ~1.4 m) between 440-190 A.D.; this may be interpreted as evidence of Holocene faulting on this part of the cape.

Evidence of recent surface faulting may also be present on the north of the cape as a several metre-deep fracture offsetting the bioherms. The fracture (Locality I Fig. 6.4a, and Fig. 6.7d) has a strike of 245^{o}, a horizontal offset of 43 cm defined by the jigsaw-match of the opposite sides of the fracture, and a direction of opening of 332^{o}, as measured by matching piercing points on both hangingwall and footwall. On Fault 17 between Localities J and K (Fig. 6.4a), the occurrence of surface faulting is suggested by a fresh, lichen-free stripe at the base of a carbonate fault plane. These possible surface ruptures, if extrapolated along-strike, cover a distance of ~300 m along the fault. Between Localities J and K seven locations that display fresh lichen-free stripes on bedrock fault planes were observed (Fig. 6.7e and f). Bedrock offsets (measured as vertical throw) appear as a light grey stripe at the base of a free face, preserving what appears to be the relative coseismic movement of the colluvium along the fault rupture, ranging from 3-12 cm of throw. In places, the surface rupture has also stepped forward into the hangingwall, located a few centimetres to decimetres away from the carbonate fault plane, to offset the hangingwall colluvial deposits (Fig. 6.7e); vertical offset in the colluvium ranges between 7-28 cm, measured at eight locations between localities J and K (Fig. 6.4a).

As the 1981 earthquakes are the most recent to result in surface ruptures on the Pisia fault (Jackson et al. 1982; Taymaz et al., 1991; Hubert et al., 1996; Roberts, 1996a), and ruptures were reported as close by as along the shore of Lake Vouliagmeni (Bornavas et al. 1984; Fig. 6.2c), it is plausible that the ruptures on Cape Heraion may have also occurred coseismically during the 24th and/or 25th February 1981 earthquakes although systematic mapping of this area was not conducted at the time of the earthquake (Prof. Geoff King, Pers. Comms); thus uncertainty exists for assigning this surface faulting to 1981.

6.4.5 Throw rates and uplift rates

The absolute ages of wave-cut platforms gained in this paper constrain their formation to the 125 ka highstand within MIS 5e. This means that throw-rate (vertical offset) of faults and uplift-rates since 125 ka (Fig. 6.10) to the present day can be quantified. To constrain the fault geometries, elevation data for the footwall and hangingwall cut-offs along the strike of fault traces are obtained from the geological and geomorphological map (Fig. 6.4) to construct throw profiles across each fault. Plots of the individual throws for all faults show that faults have maximum offset values of <40 m with two faults exceeding this value (17 and 18) (Fig. 6.10a). When all of the fault throw values and rates are summed across strike they show a pattern of decreasing displacement from east to west (Fig. 6.10c). The data in the grey area on Fig. 6.10c should be interpreted with more caution due to the lack of absolute age control obtained for the wave-cut platform located in the footwall of Fault 17 (Fig. 6.4a, 6.10a), but here it is assumed that if the notch and small wave-cut platform at ~92-99 m (Locality J, Fig. 6.4a) cut into the footwall of Fault 17 represents the 125 ka palaeoshoreline (Fig. 6.9c, Profile 3), hence the throw rate can be determined; this is included in the summed values.

When fault throw and throw rates are plotted separately for the north- and south-dipping faults they mirror the pattern of summed values decreasing from east to west (Fig. 6.10c). It is interesting to note that four south-dipping faults accommodate more throw compared to 14 north-dipping faults with the exception between 1900-1800 m to the west of the 'on fault' throw minima (Fig. 6.10c). It can be postulated that this may be a reflection of the broader faulting pattern within the Gulf of Corinth where the polarity of faulting switched from south-dipping faults to north-dipping faults during the late Quaternary (Roberts et al., 2009; Nixon et al., 2016). Specifically, Roberts et al. (2009) suggested that the north-dipping SAFS experienced an increase in slip at ~175 ka. The short fault lengths and small displacements of the north dipping faults on Cape Heraion may indicate that they may be less mature compared to their south-dipping counterparts. As the summed throw values do not decrease to zero in the mapped area, the point of zero vertical offset may lie offshore to the west of Cape Heraion, unless the faulting is actually hard-linked to offshore EXFS.

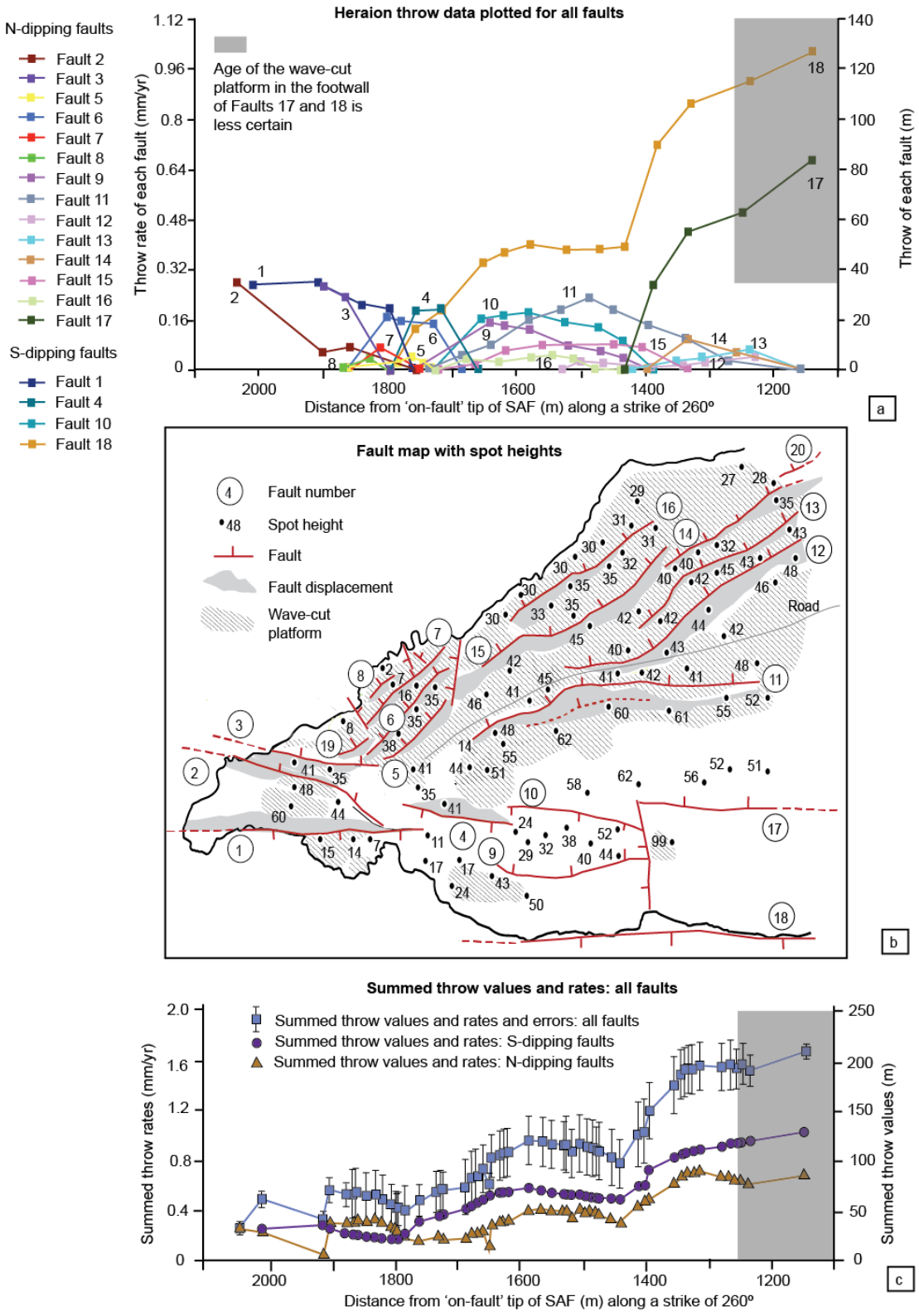

Figure 6.10: (a) Throw profiles for individual faults constructed using elevation data (shown in (b)). Throw values for Fault 19 are not plotted owing to a lack of elevation data. (c) Summed throw values and rates for all faults with uncertainties, summed throw values for north- and south-dipping faults. For (a) and (c) throw for each fault is plotted against the distance from the 'on-fault' tip (A) shown in Fig. 6.2c modified from Morewood and Roberts (1999) (from Robertson et al., 2020).

Another way to consider the results is to explore how throw across active faults has produced spatial variation in uplift relative to present-day sea-level. In other words, the absolute ages of wave-cut platforms, and knowledge of their elevations, allows calculation of spatial variation in uplift rates since 125 ka. Uplift rates since 125 ka from the highest and lowest dated wave-cut platforms are calculated as 0.46 mm/yr (S2, 62 m) and 0.02 mm/yr (Sample P1CWall, 7 m, Roberts et al., 2009) respectively (Fig. 6.4a). If the assertion that the observed notch at 92 m (Locality J, Fig. 6.4a) marks the palaeoshoreline of the 125 ka is correct then a maximum uplift rate of 0.7 mm/yr on Cape Heraion is derived using the 92 m elevation (N.B. these calculations take into account that the sea-level elevation of the MIS 5e highstand was +5 m relative to today's sea-level). The extreme variability in uplift rate over distances of tens of metres or less precludes simple interpretations of regional tectonic signals, as the local uplift is clearly dominated by local faulting (c.f. Leeder et al. 2005).

While the ages obtained in this study and the existing coral U-series link the formation of the wave-cut platforms to the MIS 5e highstand, field observations suggest that some faults were already active prior to MIS 5e. Evidence for this is in the form of (a) marine cementation within submarine screes coating the fault planes on Faults 1 and 4, (b) stratigraphic variations across faults in and below the bioherms, and (c) flat-topped bioherms in the footwall versus domed-topped bioherms in the hangingwall that are suggested to have grown up toward water surface levels during formation (Fig. 6.5) (observed by Kershaw and Guo, 2006). This evidence suggests that faulting on Cape Heraion was active prior to the MIS 5e highstand (~125 ka) and continued throughout the marine stage and beyond. It is possible that along the faults with smaller offsets (such as those in the north) any coseismic offset prior to 125 ka may have either been consequently covered by syn-wave-cut platform sediments or eroded prior to or during the formation of the 125 ka platform; this is particularly plausible given that between the start of MIS 5e at ~138 ka and the highstand at 125 ka any fault offset on the peninsula over this time would have been subject to the erosive forces of rising sea level. Furthermore, coseismic offsets on the faults on the peninsula are expected to be relatively small (a few cm) and therefore easier to erode or obscure with sediment.

6.5 DISCUSSION

Detailed fault mapping and absolute dating on Cape Heraion reveals that the western tip zone of the SAFS accommodates deformation via distributed faulting along synthetic and antithetic faults. Importantly, the findings presented in this chapter provide evidence of

faulting during the Late Quaternary, specifically over decadal, 10^3 and 10^5 year timescales that is ongoing into the Holocene and perhaps even as recently as 1981. Offset marine terraces and their wave-cut platforms throughout the entire mapped area can be linked to the 125 ka highstand within MIS 5e. The findings presented in this study, therefore, provide evidence of significant Late-Quaternary faulting on Cape Heraion. This outcome is in direct contrast to the findings of Leeder et al. (2003) and Leeder et al. (2005) who refute the notion of displacement of Holocene and late Quaternary shoreline deposits within the study area, and conclude that the Perachora Peninsula is uplifting at a constant, low, uniform rate of 0.2-0.3 mm/yr possibly linked to angle of dip of the subducting African plate beneath the eastern Gulf of Corinth (Leeder et al., 2005) and representing a 'background' uplift rate for the region.

Analyses of the fault throws show that summed throw rates in the tip area appear to be relatively high, up to ~1.6 mm/yr (Fig. 6.10), compared to throw and slip rates near the centre of the Pisia and Skinos faults of up to 2.3 mm/yr (Mechernich et al., 2018) and 0.7-2.5 mm/yr (Collier et al., 1998) over the Holocene and 1.2-2.3 mm/yr over the longer term (Collier et al., 1998). From the findings presented here, it is possible to conclude that detailed across strike mapping within the tip zone of a fault is imperative in order to constrain accurate rates of long-term faulting that could otherwise be underestimated. Importantly, the tips of faults should be considered as zones of deformation, rather than localised surface features where a fault stops as they contain multiple active faults.

6.5.1 High throw rates on Cape Heraion

The findings presented herein prompt the question of why the throw values obtained in the western tip zone over 125 ka are anomalously high compared to those observed along the localised fault (Fig. 6.11a). Studies of tip displacement gradients (Section 2.2.2) commonly suggest high gradients occur where the tips of two faults overlap, as a consequence of the interaction between the stress fields of the faults (Section 2.2.3, Fig. 2.24) (e.g. Peacock and Sanderson, 1991; Huggins et al., 1995; Willemse et al., 1996; Cartwright and Mansfield, 1998; Cowie and Shipton, 1998; Gupta and Scholz, 2000; Ferrill and Morris, 2001; Scholz and Lawler, 2004; Fossen and Rotevatn, 2016). Analysis of an isolated fault tip by Cowie and Shipton (1998) revealed an average tip displacement gradient of 0.018, whereas Cartwright and Mansfield (1998) obtained gradients between 0.0164 to 0.25, in their study of 20 normal faults comprised of a mixture of isolated and interacting faults. In comparison, the tip

displacement gradient for the investigated western tip zone of the SAFS is 0.233 (Fig. 6.11b), at the upper range of those observed above.

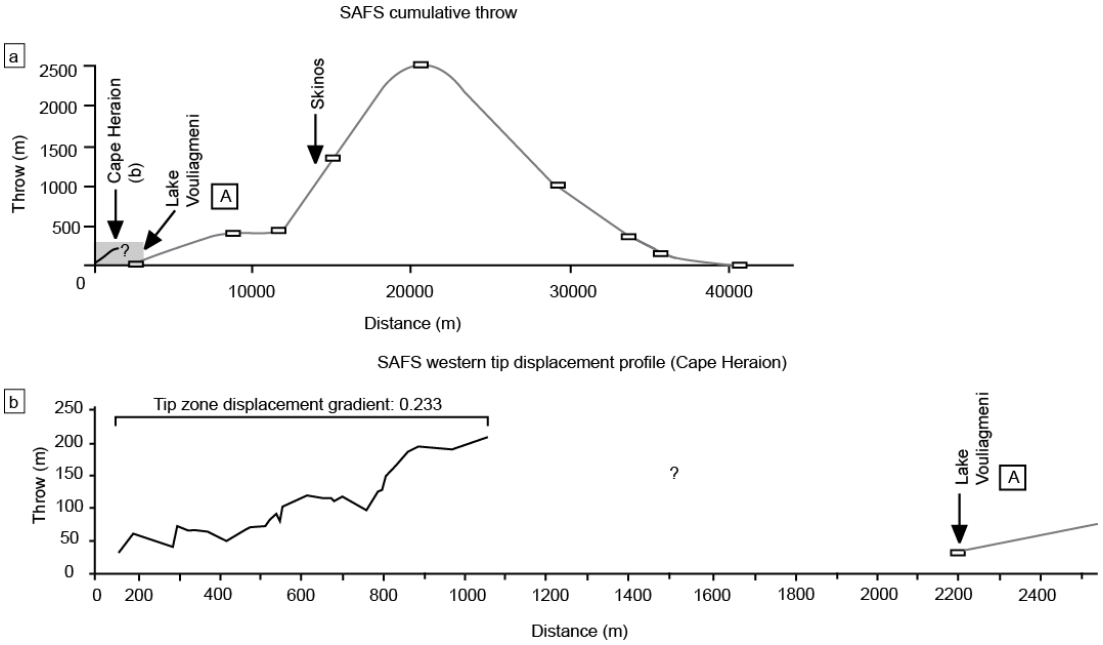

Figure 6.11: (a) Summed throw of Cape Heraion faults plotted alongside cumulative throw of the SAFS (modified from Morewood and Roberts (1999)). (b) Tip zone throw and displacement gradient from Cape Heraion. See Fig. 6.2c for the location of A ('on-fault' tip of the SAFS) (from Robertson et al., 2020).

Thus, analysis of the fault displacement gradient may point to an explanation that the relatively high summed throw rates on Cape Heraion may be due to fault interaction between the stress fields of the EXFS and the SAFS located along strike to one another and whose eastern and western fault tips overlap (Fig. 6.2a). While this suggestion has been proposed by Morewood and Roberts, (1997), it has not been quantitatively investigated. One way of exploring fault interaction between overlapping faults relies on modelling the calculated Coulomb stress transfer from rupturing a source fault onto a receiver fault (Section 2.2.3). Studies of Coulomb stress transfer (King et al., 1994; Toda et al., 2005) show that following an earthquake, changes in the stress around the slipping patch on the source fault occur that may influence seismicity on neighbouring receiver faults, with positive Coulomb stress transfer bringing a receiver fault closer to failure and negative Coulomb stress transfer resulting in stress shadows. The presence of a stress shadow on the tip zone of a receiver fault may result in deceleration of the propagation of the tip of the receiver fault, which consequently results in displacement accumulating near its interacting tips, causing steeper displacement gradients (Fig 2.25) (Gupta and Scholz, 2000). The deceleration occurs because the fault at the interacting tip must overcome the rupture resistance and

stress drop imposed by the adjacent fault (Walsh and Watterson, 1991; Scholz and Lawler, 2004).

The question of whether the location of the eastern EXFS tip zone (Fig. 6.2a) could perturb the stress field of the western tip zone of the SAFS is explored by modelling the Coulomb stress changes following an earthquake on the EXFS (source fault) onto the SAFS (receiver fault) using Coulomb 3.4 software (Section 2.2.3). An accurate fault trace drawn using Google Earth™ and geometries (dip, strike, rake) of the source (EXFS) and receiver (SAFS) faults (Table 6.4) were input into the code from Mildon et al. (2016) (Section 3.5.2). The source fault was then ruptured to produce an earthquake, the Mw of which was determined using fault-scaling relationships linked to the length of the fault rupture (Wells and Coppersmith, 1994) (Section 2.2.4). Three source fault rupture scenarios are modelled: (1) the rupture of the SAFS with the exception of the western 5 km of the SAFS; (2) the rupture of the entire EXFS; (3) a partial rupture of the EXFS, which involves only the most eastern segment (the Perachora fault) (Fig. 6.2a). Scenario (1) was modelled in order to establish the Coulomb stress transfer imparted from a partial rupture of a fault onto its own tip area (e.g. Roberts 1996). Note that within the Coulomb stress transfer scenarios, the western tip area of the SAFS is defined as the western 5 km section of the SAFS (Fig. 6.2a).

The results of Coulomb stress transfer modelling show stress enhancement on the shallow portions of faults in the region of Cape Heraion, or stress enhancement to greater depths, depending on the exact source to receiver geometry. Rupturing the entire SAFS with the exception of the western 5 km section (Scenario 1), results in a significant positive Coulomb stress change of 2 bars onto the entire fault plane of the SAFS western 5 km section (Fig. 6.12b). Rupturing the entire EXFS (Scenario (2)) results in the upper and lower 2 km of the SAFS western 5 km section experiencing positive stress transfer of 2 bars, while the majority of the western 5 km section of the fault plane displays negative stress transfer of up to -2 bars (Fig. 6.12c). Similarly, in Scenario (3), rupturing only the Perachora fault segment of the EXFS also results in negative stress transfer of -2 bars over almost all of the western 5 km section of the fault with the exception of the lower 1 km, which experiences positive stress transfer values of 1-2 bars (Fig. 6.12d), suggesting that Scenario 3 does not enhance the possibility of slip on the SAFS. These results are complex when considered with the tip zone displacement gradient in Fig. 6.11, it is possible that the observed tip zone gradient shows that Scenario 3 is not typical and Scenarios 1 and 2 are more typical; these observations may be used to inform seismic hazard assessment of future rupture scenarios. Overall, the high

values of displacement observed on Cape Heraion over 125 ka may be explained by fault interaction between the overlapping tips of the EXFS and the SAFS given the dominance of Scenarios 1 and 2 over Scenario 3.

Fault name	Fault information (fault trace, kinematics)	Length (km)	Depth of seismogenic zone (km)	Dip °	Facing direction °	Rake °	Sub-surface maximum slip value (m)	Max. Mw	Figure
East Xylocastro Faut System (EAFS)	Whole fault length is used combining fault traces of the East Xylocastro Fault, North Kiato Fault and Perachora Fault as per Nixon et al., 2016.	29	15	55	010	-90	1.6	6.53	11b
Perachora Fault (EXFS)	Fault trace from Nixon et al., 2016	11	15	55	350	-90	1.4	6.21	11c
South Alkyonnides Fault System (SAFS)	Whole fault length is used as per Roberts et al., 2009 (rupturing the Pisia, East Alkyonides and Psatha faults), with the exception of western 5 km tip zone. Dip data averaged from Jackson et al., 1982 (45˚) and Mechernich et al., 2016 (60˚)	38.7	15	55	345	-90	2.4	6.74	11a

Table 6.4: Inputs for Coulomb stress change modelling. Slip at the surface is set at 0.1 (10%) of the slip value at depth. This value is based upon the relationship between surface slip (Vittori et al., 2011) and maximum slip values at depth (Wilkinson et al., 2015) for the Mw 6.3 2009 L'Aquila Earthquake, Italy (from Robertson et al., 2020).

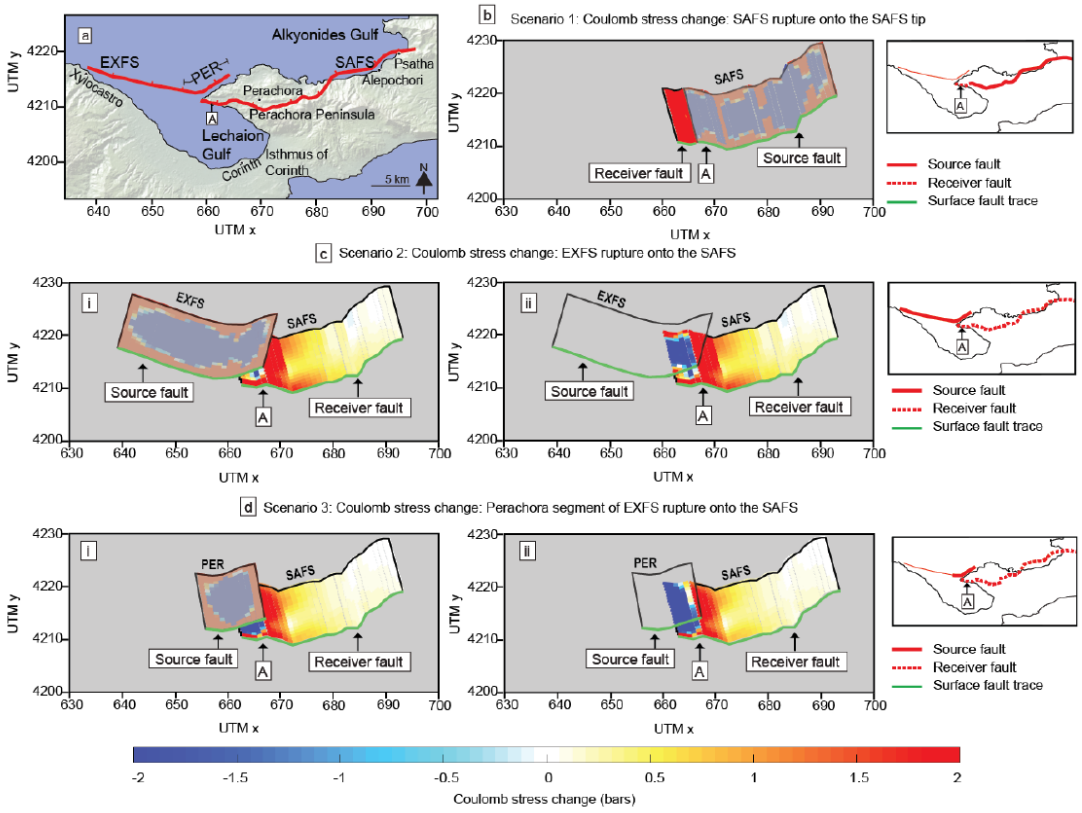

Figure 6.12: (a) Map of eastern Gulf of Corinth showing the fault traces modelled in Coulomb stress change (b–d) for the South Alkyonides Fault System (SAFS) and East Xylocastro Fault System (EXFS) (adapted from Fig. 6.2a). See Table 6.4 for inputs into Coulomb modelling. (b) Coulomb stress change from rupturing the source fault (entire SAFS with the exception of the western 5 km) onto the receiver fault (western 5 km section of the SAFS). (c) Coulomb stress change from rupturing the source fault (entire EXFS) onto the receiver fault (SAFS), (i) shows the source fault rupture, (ii) shows the source fault outline only. (d) Coulomb stress change from rupturing the source fault (Perachora segment of the EXFS) onto the receiver fault (SAFS), (i) shows the source fault rupture, (ii) shows the source fault outline only. (From Robertson et al., 2020)

6.5.2 Impacts on seismic hazard

The findings presented in this chapter have implications for fault-based probabilistic seismic hazard assessment (PSHA). It has been shown that the tip zone of a crustal-scale normal fault can accommodate significant displacement 'off the localised fault', possibly linked to interaction with a neighbouring fault. If these patterns of deformation are assumed to be typical for other normal crustal-scale faults within fault systems that overlap along strike, such as those in the Central and Southern Italian Apennines (Roberts and Michetti, 2004; Papanikolaou et al., 2005; Papanikolaou and Roberts, 2007; Iezzi et al., 2019) and Basin and Range Province, Western USA (e.g. Machette et al., 1991; Anders and Schlische, 1994; Schlische and Anders, 1996, *and references therein*) then the findings of this chapter may help shed light on how to incorporate slip/throw values into regional datasets, and whether displacements can jump from one major fault to another.

It is known that measurements of slip rate are key inputs into PSHA calculations to gain recurrence intervals and probability of shaking events (e.g. Boncio et al., 2004; Pace et al., 2010; 2016; Valentini et al., 2017). However, due to a sparsity of data, it is common to extrapolate slip rate data from measurements collected on a single location along a fault. This is predominantly done by assuming that displacement decreases towards fault tips (Faure walker et al., 2019) (Chapter one). The present study shows that this approach can be problematic, because the interaction between overlapping and interacting fault tips of neighbouring faults might result in anomalously-high displacement in the tip zone, so that throw and slip rates do not simply decrease along strike. Thus, calculation of recurrence rates and the probabilities of given shaking intensities may be in error in such situations.

If the suggestion that high values of displacement in the overlapping tip zones between the EXFS and the SAFS are as a result of fault interaction is correct, then the possibility that earthquake ruptures may jump between the EXFS and SAFS should also be explored. Fault interaction has the capacity to affect rupture sequences whereby seismic events may 'jump' across interacting faults, causing multi-fault earthquakes (e.g. Gupta and Scholz, 2000; Iezzi et al., 2019). For instance, from analysis of the source parameters of the 1981 earthquake sequence, Abercrombie et al. (1995) suggested that the 1981 earthquake sequence might represent a multi-fault rupture between the SAFS and EXFS (or a segment of the EXFS), during which the rupture might have originated offshore and propagated eastward onshore. However, this analysis was carried out without consideration of the distributed faulting reported herein. It is beyond the scope of this chapter to confirm or deny whether the presence of distributed faulting may make jumps between co-located faults more or less likely. However, this topic is important because the recent UCERF 3 model (an earthquake forecast model for California that provides estimates of the magnitude, location, and likelihood of earthquake fault rupture throughout the state) (Field et al., 2017) recognises the potential of ruptures to jump between faults that are co-located along strike separated by small distances (<5 km), a value similar to those identified by empirical studies of normal faulting earthquakes between <5-7 km (e.g. de Polo et al., 1991; Wesnousky, 2008). The maximum step between the SAFS and EXFS is ~4 km (Fig. 6.2), within the values reported above. Moreover, the observation that anomalously high displacement has accumulated in the Cape Heraion tip zone may be evidence that earthquake ruptures do cross the tip zones, but their presence is only detected if detailed mapping is conducted, and excellent age constraints are available to gain rates of deformation. This observation increases the possible rupture length to ~60 km and maximum magnitude to ~Mw 7.1 according to Wells and

Coppersmith (1994), assuming a multi-fault rupture between the EXFS and the Pisia fault within the SAFS (Fig. 6.2a). It is worthy of note, however, that in 1981 a multi-fault rupture did not happen, as there was a few hours' delay between the 24th and 25th February earthquakes; thus it is clearly complicated, but a multi-fault rupture should not be ruled out.

It is possible to contrast the wealth of observations provided from the Cape Heraion tip zone with the more typical situation away from sea-level, where transverse bedrock ridges tend to occupy tip zones, and these ridges are made of uniform pre-rift lithologies. In these locations, sparse Quaternary or Holocene sediments may make it difficult to study and gain evidence for active faulting and rates of deformation (e.g. Roberts and Koukovelas, 1996, elsewhere in central Greece; Roberts and Michetti, 2004, Italian Apennines; Zhang et al., 1991; Crone and Haller, 1991; Wu and Bruhn, 1994 western USA, for examples of such transverse bedrock ridges). It may be that smaller distributed displacements remain undiscovered in tip zones between major active faults, and this warrants more investigation, because their study may be one of the few ways to observe whether ruptures cross tip zones to produce hazardous, multi-fault earthquakes.

6.6 CONCLUSIONS

1. Cape Heraion, in the western tip zone of the South Alkyonides Fault System, deforms via a set of distributed faults that are synthetic and antithetic to the 'main fault' and have been active over decadal, 10^3 yr and 10^5 yr timescales. New age constraints using ^{36}Cl cosmogenic exposure dating and ^{234}U/^{230}Th age dating of corals reinforce that the marine terraces and associated wave-cut platforms on Cape Heraion are linked to the 125 ka highstand within MIS 5e rather than a set of terraces from three successive MIS phases.

2. On Cape Heraion, summed throw values (211 – 35 m), throw rates (1.68 – 0.25 mm/yr) and uplift rates (maximum 0.7 mm/yr) appear to exceed those reported on the main fault and previously estimated. These deformation rates are reflected in an anomalously high displacement gradient of 0.233. Coulomb stress change modelling suggests that this is a consequence of the fault interaction between the overlapping tips of the EXFS and the SAFS.

3. These findings have implications for probabilistic seismic hazard calculations as they show that the tip zones of crustal-scale faults may host high deformation rates caused by distributed faulting and as such should be mapped in detail across strike. This is particularly

important for fault systems worldwide where crustal-scale faults may over lap and where the slip rates are typically propagated along strike from one or two measurements assuming a fault that linearly decreases to zero at the tips.

4. ^{36}Cl exposure dating on carbonate wave-cut platforms composed of limestone, algal bioherms and packstone yield reliable ages that are in agreement with existing and new ^{234}U/^{230}Th coral ages and the timing of a well-known sea-level highstand. Evidence suggests that sampling for ^{36}Cl exposure dating from locations where the erosion values can be constrained from observations is of particular importance.

7 CHAPTER 7: $^{234}U/^{230}TH$ CORAL GROWTH DATING YIELDS RELIABLE AGES IN RESTRICTED BASINS DESPITE ANOMALOUS ^{234}U VALUES

7.1 SUMMARY

Previous chapters have applied ^{36}Cl exposure dating and $^{234}U/^{230}Th$ coral age dating to examine uplift on wave-cut platforms and determine long term (10^{4-5} year) deformation rates associated with crustal-scale faults; thus both dating techniques have been instrumental to reaching the findings presented so far. Specifically, in Chapter 6, agreement between the age constraints obtained from exposure dating of wave-cut platforms and their along-strike coralliferous marine sediments were in agreement that the surfaces represented those from MIS 5e, however, it was noted that the measured $\delta^{234}U_i$ values of dated corals exceed what are widely claimed to be acceptable levels. In particular, the $\delta^{234}U_i$, also known as the initial activity ratio $^{234}U/^{238}U$, is widely thought to be a measure of whether a coral sample is pristine or alternatively degraded by diagenetic alteration (in addition to analysis to quantify whether the sample is composed of calcite or aragonite (Section 3.4.2)). If the $\delta^{234}U_i$ value of a coral is the same as that for modern sea-water (~147‰) then the sample is thought to be pristine, so "ages" from samples with values outside of 147 ± 10‰ are suggested to be treated with caution. However, this approach assumes that all corals grow in normal sea-water, which may or may not be the case for restricted basins like the Mediterranean. This chapter considers the reliability of one of the most common methods of dating palaeoshorelines in studies of long-term coastal deformation.

Late Quaternary coral growth ages from uplifted coastal regions, such as palaeoshorelines, are an essential tool used to derive fault-related uplift and deformation rates, and thus contribute to seismic hazard and constrain past global sea levels. In detail, fossil coral growth ages are assessed for reliability based upon whether the $\delta^{234}U_i$ matches the present-day oceanic value of ~147‰. However, $\delta^{234}U_i$ values outside of this range have been measured at locations throughout the world (e.g. Greece, Italy, western USA; Iran) where the coral ages obtained are typically consistent with glacio-eustatic sea-level highstand timing, their stratigraphic/tectonic settings and other age constraints. In other words, there is evidence that dated corals with $\delta^{234}U_i$ values that exceed the 'acceptable' range provide late Quaternary ages for palaeoshorelines that are interpreted as representative and used to constrain tectonic uplift rates. This controversy is explored via a detailed analysis of coral

growth ages from within the semi-restricted Gulf of Corinth, where only 4% of 155 dated corals display $\delta^{234}U_i$ within the range of 137-157‰ but appear to have growth ages that agree with highstand timing, stratigraphy and ages from ^{36}Cl exposure dating of wave-cut platforms. Multiple new $^{234}U/^{230}Th$ analyses on corallites alongside analysis of existing coral growth age data and $^{87}Sr/^{86}Sr$ values suggest that $\delta^{234}U_i$ within the Gulf of Corinth was elevated throughout highstands between Marine Isotope Stages 5a-7e (~76-200 ka), as a consequence of growth within a basin subject to limited seawater entry during marine highstands and freshwater input from rivers and groundwater combined with episodic fault uplift. Within the Gulf of Corinth, the findings presented herein are used to explore the late Quaternary pattern of gulf-wide fault-related uplift, and are more broadly inferred to suggest that where corals from marginal coastal/restricted basins are dated, the results should not be limited by the $\delta^{234}U_i$.

7.2 INTRODUCTION

U-series coral growth ages provide the foundation for the study of global sea level (e.g. Bard, 1990; Muhs et al., 1994; Gallup et al., 1994; Muhs et al., 2011) and are used to derive uplift rates along tectonically-active coastal margins (e.g. Poole et al., 1990; Muhs et al., 1994; Pirazzoli et al., 1991; Bard et al., 1996; Houghton et al., 2003; Roberts et al., 2009; Roberts et al., 2013) as they provide absolute ages for palaeoshorelines. This latter body of work explores sequences of palaeoshorelines and shallow water coral reefs that have been uplifted as a result of both large and moderate upper-plate and tsunamigenic subduction zone earthquakes and thus contributes to seismic hazard analysis (e.g. Armijo et al., 1996; Grant et al., 1999; McNeill and Collier, 2004; Sieh et al., 2008; Roberts et al., 2009; Roberts et al., 2013). However, as discussed in Section 2.1.4.1, the reliability of fossil coral growth ages is suggested to be dependent upon values of $\delta^{234}U_i$, that should be reflective of present-day homogenous open ocean values (~147 ± 10‰) (e.g. Stirling and Anderson, 2009; Medina-Elizalde et al., 2013). Acceptance of this $\delta^{234}U_i$ value is based upon investigations that show that seawater $\delta^{234}U_i$ has not significantly deviated throughout the late Quaternary (e.g. Hamelin et al., 1991; Henderson et al., 1993) with any observed variation of $\delta^{234}U_i$ attributed to post-depositional diagenetic alteration reflective of open system behaviour since the coral formed (Bard et al., 1992; Gallup et al., 1994; Dutton, 2015).

The problem is that samples of shallow fossil corals used to infer uplift rates are typically obtained from coastal margins and restricted basins, and have been shown to display $\delta^{234}U_i$

outside of the 137-157‰ range of Medina-Elizalde et al. (2013), which some authors suggest limits their utility to provide absolute age constraints (e.g. Bard et al., 1991; Hamelin et al., 1991; Gallup et al., 1994). Typically, whilst corals from these settings display anomalous $\delta^{234}U_i$, in many cases their growth ages are in agreement with other local coral ages and age constraints, eustatic sea-level highstands and expected stratigraphical settings consistent with the local tectonics (e.g. Poole et al., 1990; Muhs et al., 1994; Bard et al., 1996; Roberts et al., 2009; Roberts et al., 2013). While it has been recognised that corals from coastal margins and restricted basins may have $\delta^{234}U_i$ that differs from homogenous oceanic values and that systematic variation of $\delta^{234}U_i$ in corals may be as a result of spatial and temporal differences in water chemistry (Andersen et al., 2008; Esat and Yokoyama, 2010), actual examples and detailed investigations are few.

This chapter investigates new and existing $^{234}U/^{230}Th$ coral growth ages from within the Gulf of Corinth, Greece, (Fig. 7.1) a semi-restricted marine basin (Perissoratis et al., 2000) directly affected by tectonics (e.g. Roberts et al., 2009; Nixon et al., 2016), glacio-eustatic sea-level changes (Collier et al., 2000; Perissoratis et al., 2000; Roberts et al., 2009) and influxes of freshwater from rivers and springs (Perissoratis et al., 2000; Houghton, 2010). Coral growth ages from within the gulf have elevated $\delta^{234}U_i$, but cluster on known glacio-eustatic highstands, agree with other absolute age constraints and can be explained relative to their stratigraphic position. Furthermore, analyses on multiple corals from the same sedimentary layers, and multiple analyses on the same coral corallites reveals age and $\delta^{234}U_i$ clustering, suggestive of unaltered corals. The results show that $^{234}U/^{230}Th$ coral dating is not limited by $^{234}U_i$ that differs from present day open ocean values and that the Late-Quaternary $\delta^{234}U_i$ of the Gulf of Corinth may have been elevated with respect to the open ocean global $\delta^{234}U_i$ due to a combination of the tectonics of the gulf, freshwater influx and eustatic variations of sea level. This outcome is used to explore patterns of gulf-wide fault-displacement throughout the late Quaternary and to infer that age reliability for coral growth ages from other restricted basins and coastal margins should not solely be based upon $\delta^{234}U_i$.

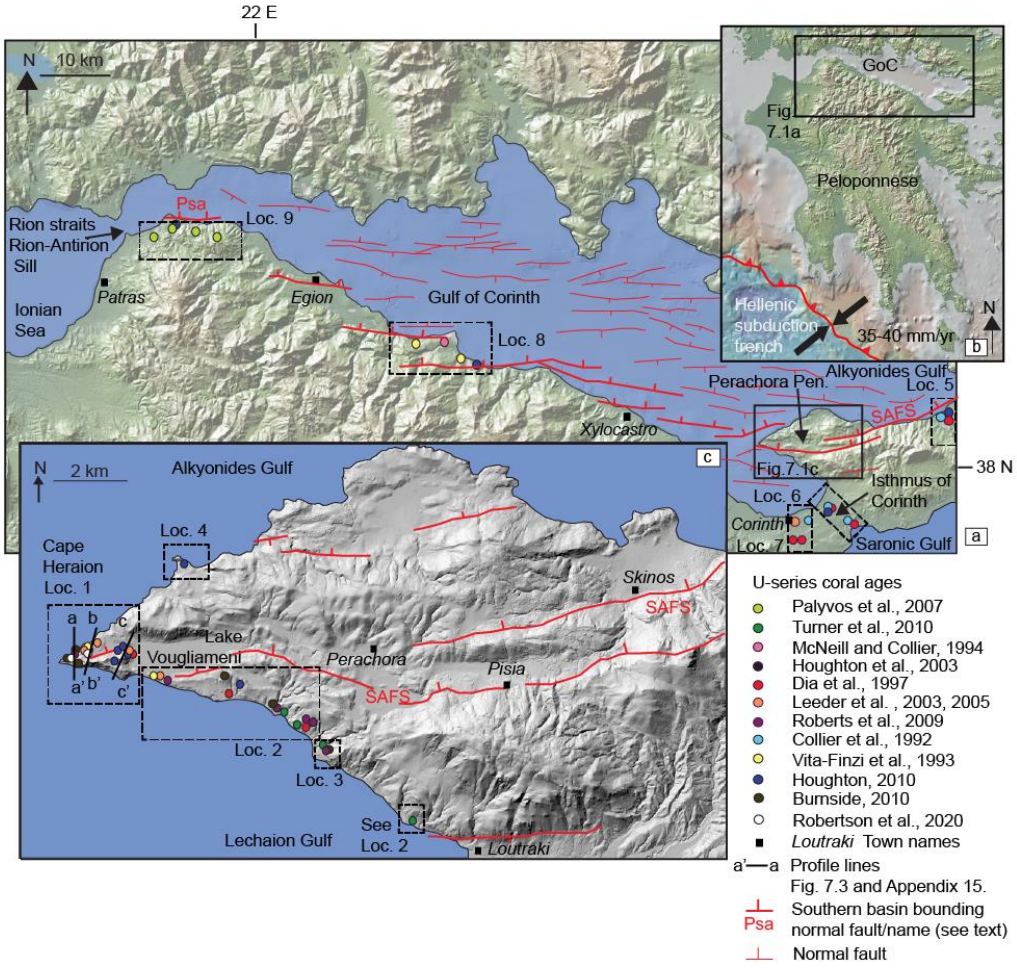

Figure 7.1: (a) Map of the Gulf of Corinth showing normal faults as per Nixon et al. (2016) and the locations of coral growth ages colour coded by study. (b) Location of the Gulf of Corinth within Greece, GPS velocities from Nocquet et al., 2012. (c) Detailed map and coral growth locations on the Perachora Peninsula at the eastern end of the Gulf of Corinth. Profile lines relate to cross sections in Figs. 7.4 and 7.5. Locality references in (a) and (c) relate to Figs. 7.4 and 7.5and discussions in the text.

7.3 BACKGROUND

7.3.1 The Gulf of Corinth

The Gulf of Corinth formed as a result of normal faulting in response to high extensional strain rates across central Greece. The observed north-south extension continues to be active to the present day, seen in geodetic extension rates of ~5-15 mm/yr (Clarke et al., 1998; Briole et al., 2000) and is predominantly accommodated along north-dipping faults that bound the southern margin of the gulf (Sakellariou et al., 2007; Bell et al., 2009; Roberts

et al., 2009; Nixon et al., 2016) (Fig. 7.1a). The gulf is a bathymetrically-restricted marine embayment (Poulos et al., 1996) currently linked to the Ionian Sea at its western point via the Rion Straits and at its eastern point via the human-made Corinth Canal, which cuts through the Isthmus of Corinth (Fig. 7.1a). The present day hydrochemistry of the gulf is marine and influenced by a combination of freshwater run-off from the surrounding mountains, local climate, and the exchange of waters with the Ionian Sea above the Rion-Anterion sill along the Rion Strait, which is 2 km wide and ~65 m deep (Poulos et al., 1996; Soter et al., 1999).

Analyses of multiple seismic reflection studies, boreholes and recent cores from within the Gulf of Corinth provide evidence of alternating lowstand (lake) and highstand (marine) deposits throughout the late Quaternary (e.g. Heezen et al., 1966; Perissoratis et al., 2000; Sakellariou et al., 2007; Bell et al., 2008; 2009; Papanikolaou et al., 2015; McNeill et al., 2019). Recent results from IODP mission 381 (site M0079) in the centre of the Gulf of Corinth shows that over the past ~750 ka the gulf has experienced changing environmental conditions driven by climatic and eustatic changes whereby a range of basin environments between the simple marine and freshwater end-members occurred (McNeill et al., 2019). During sea level lowstands the gulf is dominated by freshwater influx due to precipitation and run off (Collier et al., 2000; Perissoratis et al., 2000; Roberts et al., 2009). The history of seawater ingress into the gulf during highstands is more complex, however, and has changed throughout the late Quaternary as result of the relative motion of uplift and subsidence on normal faults at the eastern and western ends of the gulf (Fig. 7.2) (Roberts et al., 2009; McNeill et al., 2019).

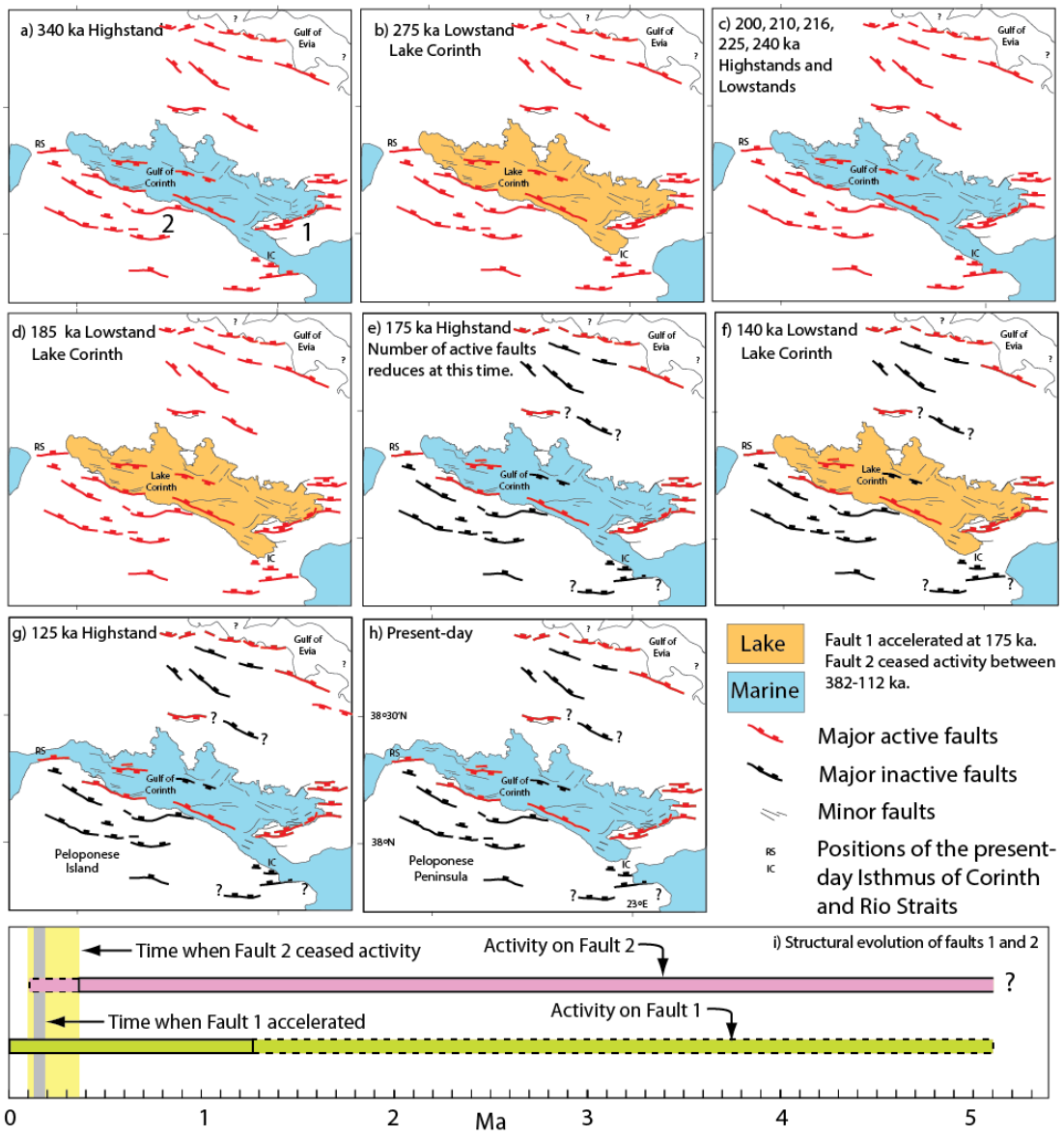

Figure 7.2: (a–h) Speculative paleogeographic and structural evolution of the Gulf of Corinth and locations of active faults. Shoreline geometries are shown schematically to illustrate opening and closure of the eastern and western ends of the gulf to the Mediterranean Sea. Some faults accelerate by cessation of activity on other faults. (i) Activity on faults 1 (SAFS) and shown in (a), with dashed lines indicating uncertainty in timing. The faults were active synchronously, but fault 1 accelerated when fault 2 ceased or slowed in activity. (From Roberts et al., 2009, their Fig. 9).

In particular, knowledge of highstand ages from sea-level curves combined with observations from uplifted preserved marine terraces and palaeoshorelines throughout the gulf have been used to explore the pattern of water ingress throughout the late Quaternary (Roberts et al., 2009). Roberts et al. (2009) (Fig. 7.2) suggest that between 340 ka and ~150 ka the Rion-Anterion sill (western gulf, Fig. 7.1a) was above relative sea levels and that the Rion Strait became an inlet for seawater sometime during MIS 5e (125 ka highstand) due to hangingwall subsidence along the Psathopyrgos fault (Psa, Fig. 7.1a) (Houghton et al., 2003;

Roberts et al., 2009), resulting in a narrow and shallow channel (Perissoratis et al., 2000). During this time seawater from the Saronic Gulf entered the Gulf of Corinth via the Isthmus of Corinth (Roberts et al., 2009) (Figs. 7.1a, 7.2), evidenced by subaqueous dunes of oolitic limestones (Collier and Thompson, 1991), late Quaternary corals (Collier et al., 1990; Collier et al., 1992; Dia et al., 1997) and borehole analysis (Papanikolaou et al., 2015). Evidence suggests that during MIS 5e, a narrow, structural low along the Isthmus of Corinth allowed seawater to enter into the Gulf of Corinth. However, at this time the western Saronic Gulf was a structural high, so direct exchange between the Gulf of Corinth and the Saronic Gulf may have been limited (Collier, 1988). The evolution of the Isthmus of Corinth from a marine inlet to sub-aerial setting occurred sometime after MIS 5e (125 ka) as a result of sustained footwall uplift of ~0.3-0.6 mm/yr due faulting along the South Alkyonides Fault System (SAFS) (Roberts et al., 2009; Papanikolaou et al., 2015) (Fig. 7.1a).

7.3.2 Gulf of Corinth corals

Coral growth ages sampled from the uplifted footwalls along the southern margin of the gulf (Fig. 7.1a, c) typically have elevated $\delta^{234}U_i$ (Fig. 7.3a, b) (Collier et al., 1990; Collier et al., 1992; Vita-Finzi et al., 1993; Dia et al., 1997; Houghton et al., 2003: Leeder et al., 2003; McNeill and Collier, 2004; Leeder et al., 2005; Palyvos et al., 2007; Palyvos et al., 2010; Roberts et al., 2009; Burnside, 2010; Houghton, 2010; Turner et al., 2010; Robertson et al., 2020). Previous studies have calculated fault-related uplift rates using coral ages to inform studies on gulf-wide horizontal deformation over long term (10^4 years) timescales and to analyse the behaviour of normal faulting within an active rift system (e.g. Houghton et al., 2003; Armijo et al., 1996; McNeill and Collier, 2004; Roberts et al., 2009; Bell et al., 2009; Roberts et al., 2009). Within these studies, coral growth age reliability has been based upon growth ages that fit known eustatic sea-level highstands (e.g. Houghton et al., 2003; Leeder et al., 2005; Roberts et al., 2009; Robertson et al., 2020) (Fig. 7.3a, c), are stratigraphically consistent with observed and modelled palaeoshorelines along sequences of terraces (Fig. 7.4a) and palaeoshoreface sections (Fig. 7.4b) (Roberts et al., 2009), and have additional age controls that support coral growth ages, for example ^{36}Cl cosmogenic exposure dating of wave-cut platforms associated with coral growth (Robertson et al., 2020) (Fig. 7.4c).

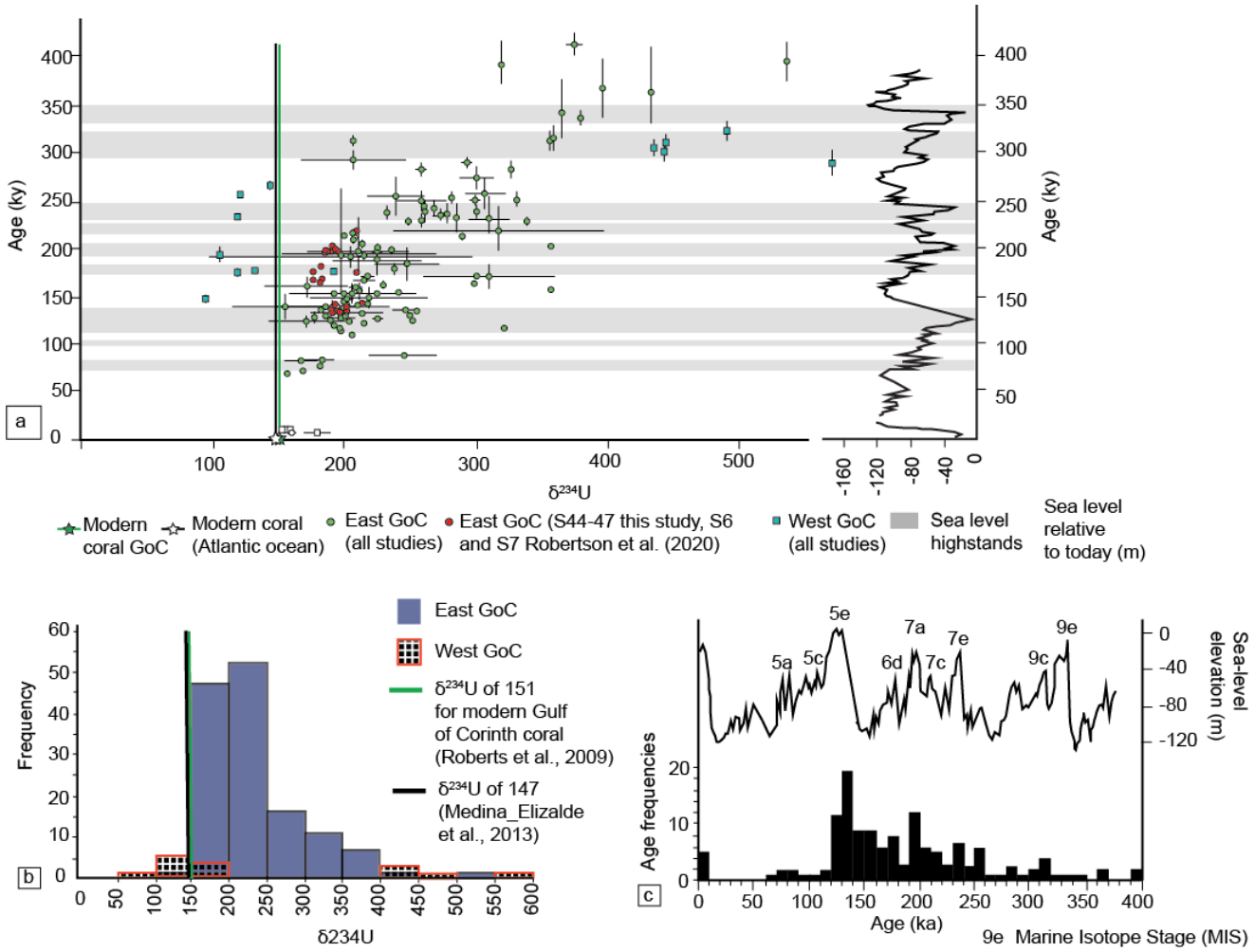

Figure 7.3: (a) Coral growth ages and $\delta^{234}U_i$ values for the Gulf of Corinth (Collier et al., 1990; Collier et al., 1992; Dia et al 1997; McNeill and Collier, 2004; Leeder et al., 2005; Roberts et al., 2009; Burnside, 2010; Houghton, 2010; Turner et al., 2010; Robertson et al., 2020) including this study. All ages and $\delta^{234}U_i$ values have been recalculated according to the decay constants of Cheng et al., 2013 (section 7.4). Sea level curve in (c) adapted from Siddall et al., 2003. See Table 7.2 for MIS and sea-level highstand timing sources. Where uncertainties are not shown, values are within symbol size or not provided from older studies. (b) Histogram of the $\delta^{234}U_i$ values for coral ages from the east and west Gulf of Corinth. (c) Histogram of frequencies of Gulf of Corinth coral growth ages compared to the sea-level curve of Siddall et al., 2003.

Corals from within the Gulf of Corinth are located in three tectonic/stratigraphic settings where different age relationships between growth ages and elevation are observed: (i) sequences of uplifted marine terraces and palaeoshorelines that form during glacio-eustatic highstands and are preserved as a result of the interplay between sea-level change and fault-related uplift (Lajoie, 1986); here corals located on sequences of terraces and palaeoshorelines, and have growth ages that increase with elevation (Fig. 7.4a), (ii) stratigraphical shoreface sections from shallow marine environments where vertically stacked coral colonies are separated by lowstand exposure surfaces; these sections record the transition through late Quaternary highstands and have coral ages that decrease upward through the stratigraphy (Fig. 7.4b), and (iii) marine terraces that have experienced faulting since they were formed; here corals from the same highstand are now located at different elevations having experienced relative subsidence or uplift as a result of normal faulting (Fig. 7.4c). Taken together, these examples highlight the problem explored in this chapter. Why is that coral growth ages that make sense with their stratigraphic setting and coincide with known glacio-eustatic sea-level highstands, are associated with elevated $\delta^{234}U_i$ values?

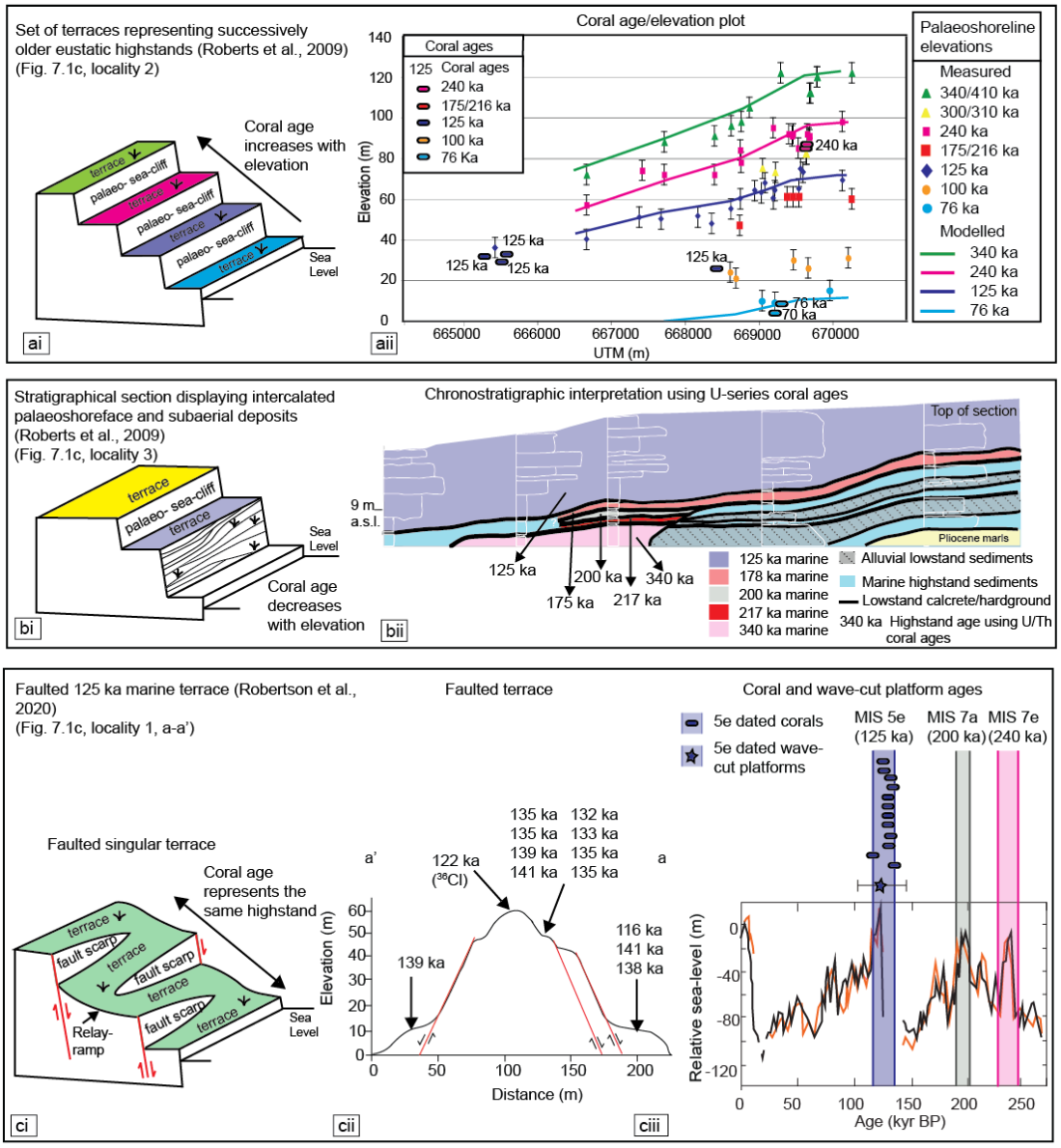

Figure 7.4: Examples of coral growth ages from within the Gulf of Corinth that have multiple ages in agreement and are in the correct stratigraphic order given their setting (see Fig 7.1a for localities): (a) Locality 2 (i) Cartoon of the geomorphological setting of a sequence of marine terraces. (ii) Coral ages that increase with age representing successively older terraces as elevation increases. The coral ages agree with observed and modelled palaeoshoreline elevations (using synchronous correlation), modified from Roberts et al. (2009). (b) Locality 3 (i) Cartoon of the geomorphological setting of stratigraphical section. (ii) Coral ages in a stratigraphic section recording the transitions between highstand and lowstands, coral growth ages become younger as elevation increases, modified from Roberts et al., 2009. (c) Locality 1, profile a'-a. (i) Cartoon of a faulted marine terrace with multiple corals at different elevations on Cape Heraion. (ii) Coral and ^{36}Cl wave cut platform ages that represent MIS 5e (125 ka highstand) and have been faulted from their original position, modified from Robertson et al., 2020. (iii) Coral and ^{36}Cl wave-cut platform ages plotted on the sea-level curve of Siddall et al., 2003 (note that orange and black lines represent curves obtained using different core data).

Previous work to explore the anomalously high $\delta^{234}U_i$ observed in Gulf of Corinth corals used analysis of $^{87}Sr/^{86}Sr$ measured from the dated corals to explore whether the water chemistry of the gulf may have differed during highstands (Dia et al., 1997; Houghton, 2010). Consistently low measurements of $^{87}Sr/^{86}Sr$, relative to the present day, were observed.

Possible explanations for low $^{87}Sr/^{86}Sr$ were cited as diagenetic processes (Dia et al., 1997) or freshwater influx from a carbonate catchment area with low $^{87}Sr/^{86}Sr$ that altered the chemistry of the gulf (Burnside, 2010; Houghton, 2010).

With the exception of corals studied by Collier et al. (1990) and Collier et al. (1992) that used *Acropora sp*, all of the coral growth ages from within the Gulf of Corinth are obtained from *Cladocora caespitosa*. *C. caespitosa* in the Gulf of Corinth grew as isolated colonies rather than extensive reefs (Dia et al., 1997) and differ from many other corals in that they thrive in coastal and brackish/fresh water environments because they are able to tolerate alluvial inputs and higher turbidity (Peirano et al., 2004; 2009). Modern day *C. caespitosa* occur in shallow water between 4-10 m in depth, but have been known to live down to depths of 40 m (Peirano et al., 2004; Montagna et al., 2007).

7.4 APPROACH AND METHODS

The accuracy of coral ages is dependent on: (i) knowledge of the decay constants of U-series nuclides, (ii) that ^{230}Th was not initially present at the time of coral growth and, (iii) that closed system conditions prevailed whereby no further isotopic exchange occurred between the coral and its surrounding environment (Dutton, 2015) (Section 2.1.4.1). While the first two points can be can be satisfied (see below), open system corals (involving the possible addition or loss or uranium as a result of diagenetic alteration) are suggested to form a significant quantity (~90%) of published worldwide data (Thompson and Goldstein, 2005). Corals in the Gulf of Corinth commonly display elevated $\delta^{234}U_i$, which at first sight suggest open system conditions (Collier et al., 1990; Collier et al., 1992; Vita-Finzi et al., 1993; McNeill and Collier, 2004; Dia et al., 1997; Houghton et al., 2003: Leeder et al., 2003; Leeder et al., 2005; Palyvos et al., 2007; Palyvos et al., 2010; Roberts et al., 2009; Burnside, 2010; Houghton, 2010; Turner et al., 2010; Robertson et al., 2020). Open system conditions in corals may give rise to variability in $\delta^{234}U_i$ as a result of diagenetic addition and/or replacement of uranium, specifically the addition of a high $^{234}U/^{238}U$ contaminant, uranium loss or addition of ^{230}Th (e.g. Bard et al., 1991; Hamelin et al., 1991; Gallup et al., 1994). This chapter investigates the suggestion that $\delta^{234}U_i$ may vary spatially and temporally in coastal locations (Esat and Yokoyama, 2010) by adopting techniques that check between the consistency of ages and $\delta^{234}U_i$ of corals that grew adjacent in coastal waters and are now uplifted on marine terraces on Cape Heraion, in the eastern Gulf of Corinth. To explore this, $^{234}U/^{230}Th$ analysis on corals from the same sedimentary layer on Cape Heraion were

undertaken, with multiple $^{234}U/^{230}Th$ analyses on each corallite. These new $^{234}U/^{230}Th$ coral ages were used in addition to data from multiple analyses on two corallites from Chapter 6 (Robertson et al., 2020). The approach adopted herein allows the robustness of the age data to be investigated, which can be established if clustering of ages and $\delta^{234}U_i$ is observed from different corallites and multiple analyses of the same corallite (as per Esat and Yokoyama, 2010 and Dutton, 2015). Such clustering may be indicative of corals displaying closed system behaviour, where measured $\delta^{234}U_i$ are representative of the water chemistry at the time of growth that is different from that of homogenised open ocean. The $\delta^{234}U_i$ of the samples dated herein and in Chapter 6 (Robertson et al., 2020) are then used as the basis to investigate $\delta^{234}U_i$ on all corals dated within the Gulf of Corinth.

7.4.1 Recalculation of all coral ages and $\delta^{234}U_i$ values to the same decay constants

U-series ages of corals from all known studies from within the Gulf of Corinth were compiled (Collier et al., 1990; Collier et al., 1992; Vita-Finzi et al., 1993; McNeill and Collier, 2004; Dia et al., 1997; Houghton et al., 2003: Leeder et al., 2003; Leeder et al., 2005; Palyvos et al., 2007; Palyvos et al., 2010; Roberts et al., 2009; Burnside, 2010; Houghton, 2010; Turner et al., 2010; Robertson et al., 2020) (n=155) (Table 7.1). As these studies have occurred over three decades, different decay constants of ^{230}Th, ^{234}U and ^{238}U have been used to calculate the activity ratios, and thus the age and $\delta^{234}U_i$ of the coral samples. In order to compare the coral ages and $\delta^{234}U_i$ values from different studies, coral ages and $\delta^{234}U_i$ have been recalculated using the same decay constants (Dutton, 2015). Recalculation was carried out using the decay constants of Cheng et al. (2013), the original decay constants, activity ratios and/or isotope data published in the original articles, and has resulted in changes of ~<1% to most coral growth ages (Fig. 7.1a, c; Table 7.1). While the original decay constants were not published in McNeill and Collier (2004), the ages and $\delta^{234}U_i$ values have been recalculated assuming that the decay constants of Edwards et al. (1987) were originally employed. However, a lack of reported measurement data for Palyvos et al., 2007, Palyvos et al., 2010 and samples 89/1 and 89/4 from Vita-Finzi et al., 1993 mean that these coral age data (n=10) cannot be recalculated and are therefore excluded from this study.

Study	Locality number (see Fig. 7.1)	Coral material dated	Original sample name *lab ID	Original $\delta^{234}U$	+/-	Original age (ka)	+/-	Recalc. $\delta^{234}U$	Recalc. age (ka)	$^{87}Sr/^{86}Sr$	Reason for exclusion
Roberts et al., 2009	1	*C. caespitosa*	25 (P1/1w)	323	NR	116	1	321	116		
Vita-Finzi et al., 1993	1	*C. caespitosa*	89/2	201	10	128	3	199	129		
Houghton, 2010	1	*C. caespitosa*	51	202	NR	129	2	201	129	0.709099	
Robertson et al., 2020	1	*C. caespitosa*	S7 (6) *145-17	191	3	132	1	191	132		
Robertson et al., 2020	1	*C. caespitosa*	S6 (1) *138-34	197	2	133	1	197	133	0.7091	
Robertson et al., 2020	1	*C. caespitosa*	S7 (4) *145-15	194	3	135	1	194	135		
Robertson et al., 2020	1	*C. caespitosa*	S7 (5) *145-16	202	3	135	1	202	135		
Robertson et al., 2020	1	*C. caespitosa*	S7 (3) *145-14	191	3	135	1	191	135		
Robertson et al., 2020	1	*C. caespitosa*	S6 (2) *141-29	193	4	135	1	193	135		
Leeder et al., 2003 and 2005	1	*C. caespitosa*	UEA798	157	42	137	+14/-12	156	138		
Leeder et al., 2003 and 2005	1	*C. caespitosa*	UEA824	196	41	138	8	195	139		
Robertson et al., 2020	1	*C. caespitosa*	S7 (2) *145-13	201	3	139	1	201	139		
Burnside, 2010	1	*C. caespitosa*	3B	188	4	138	1	186	139	0.709124	
Robertson et al., 2020	1	*C. caespitosa*	S7 (1) *138-35	193	2	141	1	193	141	0.70916	
Roberts et al., 2009	1	*C. caespitosa*	26 (P1/1s)	221	NR	141	2	218	141	No data	
Robertson et al., 2020	1	*C. caespitosa*	S6 (3) *141-30	214	4	143	1	214	143		
Burnside, 2010	1	*C. caespitosa*	1A	202	4	147	1	200	143	0.709104	
This study	1	*C. caespitosa*	S45(2) *156-18	182	1	165	2	182	165		
This study	1	*C. caespitosa*	S45(3) *156-27	176	1	168	1	176	168		
This study	1	*C. caespitosa*	S45(1) *138-27	176	1	175	1	176	175	0.70908	
This study	1	*C. caespitosa*	S47(1) *138-29	183	1	181	2	183	181		
Leeder et al., 2003 and 2005	1	*C. caespitosa*	UEA834	226	35	186	+16/-14	225	188		
Leeder et al., 2003 and 2005	1	*C. caespitosa*	CTP2(2)	207	4	190	1	206	191		
Houghton, 2010	1	*C. caespitosa*	58	217	NR	191	4	215	192	0.709079	
This study	1	*C. caespitosa*	S44(2) *156-15	186	1	195	3	186	195		
This study	1	*C. caespitosa*	S46(3) *156-30	190	1	196	5	190	196		
This study	1	*C. caespitosa*	S44(3) *156-16	187	1	196	3	187	196		
This study	1	*C. caespitosa*	S44(4) *156-17	196	1	197	3	196	197		
This study	1	*C. caespitosa*	S44(1) *138-26	187	1	198	2	187	198		
Houghton, 2010	1	*C. caespitosa*	60	238	NR	197	4	236	198	0.709077	
This study	1	*C. caespitosa*	S46(1) *138-28	193	1	200	2	193	200		
Houghton, 2010	1	*C. caespitosa*	59	228	NR	200	4	226	201	0.709121	
Houghton, 2010	1	*C. caespitosa*	62	260	NR	228	6	259	229	0.70912	
Houghton, 2010	1	*C. caespitosa*	67	287	NR	230	+16/-13	285	232	0.709103	
Houghton, 2010	1	*C. caespitosa*	68	279	NR	235	+11/-9	278	237	0.709099	
Houghton, 2010	1	*C. caespitosa*	75	235	NR	236	6	233	237	0.709097	

Houghton, 2010	1	*C. caespitosa*	65	303	NR	237	6	301	239	0.709094	
Houghton, 2010	1	*C. caespitosa*	74	261	NR	246	7	259	248	0.709091	
Turner et al., 2010	2	*C. caespitosa*	JS34	160	6	6	0	159	6		
Roberts et al., 2009	2	*C. caespitosa*	1	184	NR	76	1	182	76	0.709121	
Turner et al., 2010	2	*C. caespitosa*	JS5	171	12	82	2	168	82		
Leeder et al., 2003 and 2005	2	*C. caespitosa*	V35-4a	195	3	118	1	192	119		
Roberts et al., 2009	2	*C. caespitosa*	19	206	NR	122	1	204	123	0.70909	
Roberts et al., 2009	2	*C. caespitosa*	2	191	NR	125	4	189	125	0.709129	
Leeder et al., 2003 and 2005	2	*C. caespitosa*	V35-1b	228	4	125	1	226	126		
Leeder et al., 2003 and 2005	2	*C. caespitosa*	V35-1a	203	3	126	1	198	126		
Leeder et al., 2003 and 2005	2	*C. caespitosa*	V35-2b	252	3	129	1	250	130		
Roberts et al., 2009	2	*C. caespitosa*	24	216	NR	131	2	214	132	0.70909	
Leeder et al., 2003 and 2005	2	*C. caespitosa*	V35-2a	257	2	133	1	255	134		
Vita-Finzi et al., 1993	2	*C. caespitosa*	89/3	248	10	134	3	247	135		
Turner et al., 2010	2	*C. caespitosa*	JS2	202	3	137	5	200	138		
Roberts et al., 2009	2	*C. caespitosa*	20	213	NR	139	2	211	140	0.70909	
Roberts et al., 2009	2	*C. caespitosa*	22	220	NR	141	2	218	141	0.70909	
Burnside, 2010	2	*C. caespitosa*	10A	220	5	169	2	218	171	0.709089	
Roberts et al., 2009	2	*C. caespitosa*	3	270	NR	240	6	268	241	0.709054	
Roberts et al., 2009	3	*C. caespitosa*	12	193	NR	138	2	191	138	No data	
Roberts et al., 2009	3	*C. caespitosa*	6	240	NR	178	6	238	178	0.709137	
Roberts et al., 2009	3	*C. caespitosa*	7	359	NR	200	3	357	202	No data	
Roberts et al., 2009	3	*C. caespitosa*	8	291	NR	211	4	290	212	0.709112	
Roberts et al., 2009	3	*C. caespitosa*	9	363	NR	337	+37/-26	365	342	0.709121	
Roberts et al., 2009	4	*C. caespitosa*	27 (modern)	151	NR	1	0	149	1	0.709172	
Houghton, 2010	4	*C. caespitosa*	45	185	NR	135	1	182	135	0.709154	
Houghton, 2010	4	*C. caespitosa*	46	189	NR	138	2	187	138	0.709158	
Houghton, 2010	4	*C. caespitosa*	47	204	NR	140	4	203	140	0.709153	
Houghton, 2010	5	*C. caespitosa*	44	180	NR	128	1	177	128	0.709133	
Houghton, 2010	5	*C. caespitosa*	43	189	NR	129	2	186	129	0.709128	
Collier et al., 1992	6	Acropora sp	UEA316	190	40	205	+33/-26	211	197		
Collier et al., 1992	6	Acropora sp	UEA318	190	40	311	+11/-10	207	292		
Collier et al., 1992	7	Acropora sp	UEA369	290	50	177	+13/-12	310	170		
Collier et al., 1992	7	Acropora sp	UEA368	310	80	232	+24/-20	317	218		
Houghton, 2010	8	*C. caespitosa*	38	159	NR	8	2	157	8	0.709158	
Houghton, 2010	8	*C. caespitosa*	39	156	NR	9	0	154	9	0.709143	
Houghton, 2010	8	*C. caespitosa*	37	154	NR	9	0	152	9	0.70916	
McNeill and Collier, 2004	8	*C. caespitosa*	00.11.7.1	129	NR	230	2	120	233		
McNeill and Collier, 2004	8	*C. caespitosa*	99.8.4.1.8c1	579	NR	284	13	571	288		
McNeill and Collier, 2004	8	*C. caespitosa*	99.8.4.1.8c2	451	NR	296	5	444	301		

McNeill and Collier, 2004	8	*C. caespitosa*	99.8.4.1.8c2	442	NR	300	7	436	305		
McNeill and Collier, 2004	8	*C. caespitosa*	99.8.4.1.8c1	454	NR	307	6	445	311		
Houghton, 2010	9	*C. caespitosa*	30	197	NR	175	3	195	175	0.709065	
Houghton, 2010	9	*C. caespitosa*	28	121	NR	175	3	119	176	0.709078	
Houghton, 2010	9	*C. caespitosa*	29	135	NR	176	5	133	176	0.709073	
Houghton, 2010	9	*C. caespitosa*	31	108	NR	191	6	106	192	0.709071	
Houghton, 2011	10	*C. caespitosa*	31	108	NR	191	6	106	192	0.709071	
Excluded growth ages											
Leeder et al., 2003 and 2005	1	*C. caespitosa*	UEA825	210	48	151	10	200	152		Exact location unknown/Uranium concentration too low
Leeder et al., 2003 and 2005	1	*C. caespitosa*	UEA826	174	36	159	10	172	160		Lowstand age (altered?)
Robertson et al., 2020	1	*C. caespitosa*	S6 (4) *145-12	210	5	174	2	210	174		Outlier in multiple analyses
This study	1	*C. caespitosa*	S46(2) *156-29	183	1	179	4	183	179		Outlier in multiple analyses
Leeder et al., 2003 and 2005	1	*C. caespitosa*	UEA842	248	26	182	17/-14	248	184		Lowstand age (altered?)
Dia et al., 1997	1	*C. caespitosa*	CTP2	233	1	195	2	225	196	0.709105	Excessively high Th values
Houghton, 2010	1	*C. caespitosa*	78	216	NR	202	4	214	203		Original author suggests results are inaccurate
This study	1	*C. caespitosa*	S45(4) *156-28	191	1	203	3	191	203		Outlier in multiple analyses
Houghton, 2010	1	*C. caespitosa*	76	216	NR	203	4	214	204		Original author suggests results are inaccurate
Houghton, 2010	1	*C. caespitosa*	61	210	NR	207	5	208	209		Uranium concentration too low
Houghton, 2010	1	*C. caespitosa*	77	210	NR	210	4	208	211		Original author suggests results are inaccurate
Hougton et al., 2010	1	*C. caespitosa*	79	209	NR	214	4	207	216		Original author suggests results are inaccurate
Houghton, 2010	1	*C. caespitosa*	72	251	NR	226	4	249	228	0.70909	Uranium concentration too low
Houghton, 2010	1	*C. caespitosa*	73	262	NR	241	+12/-10	260	243	0.70909	Uranium concentration too low
Burnside, 2010	1	*C. caespitosa*	2A	260	6	277	8	259	282		Uranium concentration too high
Leeder et al., 2003 and 2005	1	*C. caespitosa*	UEA823	275	101	304	+70/-41				Cannot recalculate (lack of data)
Dia et al., 1997	2	*C. caespitosa*	J-3-3 (2)	163	1	69	1	156	69		Excessively high Th values
Dia et al., 1997	2	*C. caespitosa*	J-3-3	175	1	70	1	169	70	0.709115	Excessively high Th values
Leeder et al., 2003 and 2005	2	*C. caespitosa*	V35-4b	208	2	109	1	206	109		Lowstand age (altered?)
Dia et al., 1997	2	*C. caespitosa*	25a	221	1	120	1	215	121	0.7091	Excessively high Th values
Dia et al., 1997	2	*C. caespitosa*	J-3-1	259	1	123	1	252	124	0.709134	Excessively high Th values
Roberts et al., 2009	2	*C. caespitosa*	23	227	NR	152	3	225	152	0.70909	Lowstand age (altered?)
Roberts et al., 2009	2	*C. caespitosa*	21	243	NR	154	2	242	154	0.70909	Lowstand age (altered?)
Burnside, 2010	2	*C. caespitosa*	8Ar	213	5	154	2	211	155	0.709146	Lowstand age (altered?)
Roberts et al., 2009	2	*C. caespitosa*	18	358	NR	156	2	357	156	No data	Lowstand age (altered?)
Burnside, 2010	2	*C. caespitosa*	8A	211	5	158	3	209	159	0.709146	Lowstand age (altered?)
Dia et al., 1997	2	*C. caespitosa*	J-3-6	308	1	169	2	300	170	0.709105	Excessively high Th values
Dia et al., 1997	2	*C. caespitosa*	25c	269	1	236	3	261	239	0.709037	Excessively high Th values
Roberts et al., 2009	2	*C. caespitosa*	4	333	NR	248	7	332	250	0.709054	Lowstand age (altered?)
Dia et al., 1997	2	*C. caespitosa*	J-3-2	290	1	250	6	281	253	0.709069	Excessively high Th values
Turner et al., 2010	2	*C. caespitosa*	JS11	259	20	252	19	239	254		Lowstand age (altered?)

Turner et al., 2010	2	*C. caespitosa*	JS6	308	16	254	15	307	257		Lowstand age (altered?)
Burnside, 2010	2	*C. caespitosa*	11A	301	12	270	13	301	274		Lowstand age (altered?)
Turner et al., 2010	3	*C. caespitosa*	JS7	186	10	83	2	184	83		Exact location unknown
Burnside, 2010	3	*C. caespitosa*	4C	221	46	147	11	219	148	0.709123	$^{230}Th/^{232}Th$ too low
Burnside, 2010	3	*C. caespitosa*	4B	208	4	152	2	206	153	0.709151	Exact location unknown/Uranium concentration too high
Roberts et al., 2009	3	*C. caespitosa*	11	232	NR	161	4	230	161	0.709114	Lowstand age (altered?)
Roberts et al., 2009	3	*C. caespitosa*	10	301	NR	162	2	299	162	0.709119	Lowstand age (altered?)
Burnside, 2010	3	*C. caespitosa*	4A	217	4	166	2	215	167	0.709128	Exact location unknown
Roberts et al., 2009	3	*C. caespitosa*	13	340	NR	227	5	339	229	0.709119	Original author suggests results are inaccurate
Burnside, 2010	3	*C. caespitosa*	5A	274	6	233	6	273	235	0.07091	Exact location unknown
Burnside, 2010	3	*C. caespitosa*	6A	300	5	247	5	299	250	0.709083	Exact location unknown
Roberts et al., 2009	3	*C. caespitosa*	16	327	NR	279	9	327	282	0.709121	Original author suggests results are inaccurate
Roberts et al., 2009	3	*C. caespitosa*	15	355	NR	308	10	356	311	0.709121	Original author suggests results are inaccurate
Roberts et al., 2009	3	*C. caespitosa*	14	358	NR	312	12	359	315	0.709121	Original author suggests results are inaccurate
Roberts et al., 2009	3	*C. caespitosa*	17	429	NR	356	+50/-32	434	362	0.709119	Original author suggests results are inaccurate
Collier et al., 1992	5	Acropora sp	UEA444	230	30	90	+/-4	245	87		$^{230}Th/^{232}Th$ too low
Collier et al., 1992	5	Acropora sp	UEA459	170	30	127	+6/-6	171	123		$^{230}Th/^{232}Th$ too low
Dia et al., 1997	5	*C. caespitosa*	Meg (2)	200	1	152	2	193	153		Excessively high Th values
Dia et al., 1997	5	*C. caespitosa*	Meg	220	1	154	8	212	155	0.709113	Excessively high Th values
Dia et al., 1997	6	*C. caespitosa*	J-1-3	220	66	193	3	212	194	0.709134	Excessively high Th values
Dia et al., 1997	6	*C. caespitosa*	J-1-2	209	1	211	5	200	213	0.709133	Excessively high Th values
Dia et al., 1997	6	*C. caespitosa*	J-5-1	216	1	306	6	207	312	0.709097	Excessively high Th values
Houghton, 2010	6	*C. caespitosa*	40	316	NR	383	+25/-20	320	392	0.709071	Uranium concentration too low
Leeder et al., 2003 and 2005	7	*C. caespitosa*	2906013	203	32	132	8	202	133		$^{230}Th/^{232}Th$ too low
Dia et al., 1997	7	*C. caespitosa*	J-5-4	387	1	330	7	380	336	0.709099	Excessively high Th values
Dia et al., 1997	7	*C. caespitosa*	3	402	1	359	24	396	368	0.709062	Excessively high Th values
Dia et al., 1997	7	*C. caespitosa*	18	538	2	386	21	536	396	0.70909	Excessively high Th values
McNeill and Collier, 2004	8	*C. caespitosa*	00.11.7.1	131	NR	252	2	122	255		Lowstand age (altered?)
McNeill and Collier, 2004	8	*C. caespitosa*	00.11.7.1	154	NR	262	4	144	265		Lowstand age (altered?)
McNeill and Collier, 2004	8	*C. caespitosa*	99.8.4.1.8c2	508	NR	317	6	491	323		$^{230}Th/^{232}Th$ too low
Vita-Finzi et al., 1993	8	*C. caespitosa*	89/4		10	6	0				Cannot recalculate (lack of data)
Vita-Finzi et al., 1993	8	*C. caespitosa*	89/1		9	386	+56/-38				Cannot recalculate (lack of data)
Houghton, 2010	9	*C. caespitosa*	32	97	NR	147	+3/-4	94	147	0.709075	Lowstand age (altered?)
Palyvos et al 2007	9	*C. caespitosa*	506	130	20	275	+38/-29				Cannot recalculate (lack of data)
Palyvos et al 2007	9	*C. caespitosa*	1003	110	10	350	none				Cannot recalculate (lack of data)
Palyvos et al 2007	9	*C. caespitosa*	1103	100	10	350	none				Cannot recalculate (lack of data)
Palyvos et al 2007	9	*C. caespitosa*	3406	10	10	166	8				Cannot recalculate (lack of data)
Palyvos et al 2010	9	*C. caespitosa*	4607	30	NR	161.8					Cannot recalculate (lack of data)
Palyvos et al 2010	9	*C. caespitosa*	5007	-20	NR	177.9					Cannot recalculate (lack of data)
Palyvos et al 2010	9	*C. caespitosa*	4507	20	NR	197.3					Cannot recalculate (lack of data)
Palyvos et al 2010	9	*C. caespitosa*	4907	30	NR	200.9					Cannot recalculate (lack of data)

Table 7.1 : Coral growth ages, $\delta^{234}U_i$ and $^{86}Sr/^{87}Sr$ ratio values for the Gulf of Corinth (Collier et al., 1990; Collier et al., 1992; McNeill and Collier, 1994; Dia et al 1997; Leeder et al., 2005; Roberts et al., 2009 (note that $^{86}Sr/^{87}Sr$ ratios for coral samples dated in Roberts et al., 2009 are published in Houghton, 2010) ; Burnside, 2010; Houghton, 2010; Turner et al., 2010; Robertson et al., 2020) including this study. See Section 7.4.3 for the methodology of $^{86}Sr/^{87}Sr$ ratios for new samples. All ages and $\delta^{234}U_i$ values have been recalculated according to the decay constants of Cheng et al. (2013).$^{234}U/^{230}Th$ coral age dating from this study included (Table 7.3). Samples are excluded as a result of: $^{230}Th/^{232}Th$ values that are too low (n=6), excessively high Th concentrations (n=16), uranium concentrations that are too low/high (n=4), outlier sample ages from this study (n=3), unreliable growth ages identified by authors of the published coral studies (i.e. due to the presence of calcite) (n=9), a lack of location information from published studies preventing evaluation of the geographical position of corals (n=7) and lowstand ages suggestive that the corals may be altered (n=16). NR: Not reported.

7.4.2 $^{234}U/^{230}Th$ dating

The results of new $^{234}U/^{230}Th$ analyses on *C. caespitosa* coral samples from Cape Heraion (samples 44 (4), 45 (4), 46 (3), 47 (1), where the numbers in brackets are the number of analyses on each corallite) are provided herein and are used alongside recent $^{234}U/^{230}Th$ analyses on coral samples also from Cape Heraion (Samples S6 and S7) (Chapter 6; Robertson et al., 2020). Samples S6 and S7 (Fig. 7.1c, Profile line a-a'; Fig. 7.5a, b, c,) were removed from the same sandy layer on a wave-cut platform (44 m elevation) constrained to MIS 5e (125 ka highstand) using ^{36}Cl exposure dating (Chapter 6; Robertson et al., 2020). Samples 44-47 were removed from the same layer in a sedimentary succession (41 m elevation) accessed via an ancient cistern (Fig. 7.1c Profile line b-b'; Fig. 7.5c, d, e). The sandy layer from which samples 44-47 were removed occurs beneath a reported 125 ka wave-cut surface (Robertson et al., 2020) and is comprised of whole and disarticulated fossils and coarse sand to pebble grain sizes, suggestive of a high-energy environment.

Coral preparation and cleaning was carried out as per the method outlined in Section 3.4. Standard methods for screening for anomalous ^{238}U and the presence of ^{230}Th were applied to coral samples, as set out by Dutton (2015) (Section 2.1.4.1). Specifically, modern corals typically have uranium values ~2–3.5 ppm (Shen and Dunbar, 1985); samples with significantly different values may be indicative of diagenetic processes and are rejected (Section 7.4). The $^{230}Th/^{232}Th$ ratio was checked to ensure that ^{230}Th was not present during initial coral growth (Dutton, 2015), rejecting the sample if the value is too low (<100) (van Calsteren and Thomas, 2006). These methods of screening were applied to corals dated in this study and all existing coral data assessed (Table 7.1).

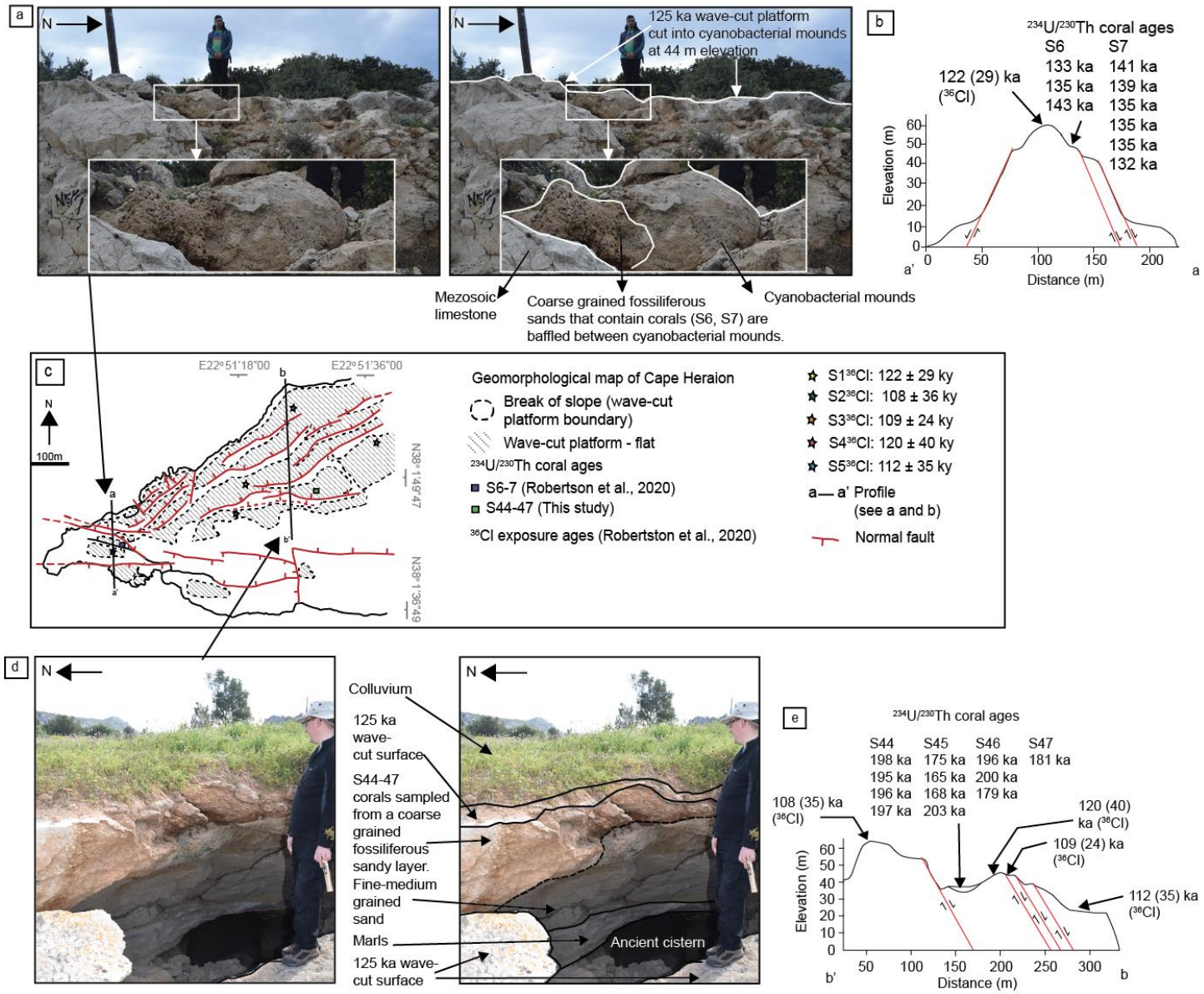

Figure 7.5: Details of the geological setting of coral samples 44-47 (c, d, e) dated within chapter 7 and S6, S7 from Robertson et al. (2020) located on Cape Heraion (a, b, c) (see Fig 7.1c).

7.4.3 $^{86}Sr/^{87}Sr$ ratios

$^{86}Sr/^{87}Sr$ ratios of a number of coral samples were obtained in order to assess how they vary compared to $^{86}Sr/^{87}Sr$ ratios from other reported Late-Quaternary corals from within the Gulf of Corinth and also seawater $^{86}Sr/^{87}Sr$ ratios. These analyses were carried out on coral samples S6U/Th, S7U/Th and S45U/Th (Table 7.1). Strontium ratio analyses were carried out at the British Geological Survey, Keyworth, as per the approach in Birck (1986). In detail, each sample was transferred to a clean (class 100, laminar flow) working area for preparation. In a clean laboratory, the sample was first cleaned ultrasonically in high purity water to remove dust, rinsed twice, and then soaked for an hour at 60° C, rinsed twice, then dried and weighed into pre-cleaned Teflon beakers. The sample was dissolved in (high purity 105 acetic acid) and converted to chloride form using 6M HCl. Strontium was collected using Eichrom AG50 X8 resin columns. Strontium was loaded onto a single Re Filament following the method of Birck (1986) and the isotope composition and strontium concentrations were determined by Thermal Ionisation Mass spectroscopy (TIMS) using a Thermo Triton multi-collector mass spectrometer. The international standard for $^{87}Sr/^{86}Sr$, NBS987, gave a value of 0.710273 ± 0.000016 (n=21, 2σ) during the analysis of these samples; data were corrected to the accepted value for this standard of 0.710250.

7.4.4 MIS and sea-level highstands

Coral ages in this chapter are referred to in reference to their MIS and respective glacio-eustatic highstands (Section 2.1.2). Herein, the highstand ages suggested by Siddall et al. (2003) are used and the lengths of MIS obtained from a number of studies (Table 7.2). The focus was on analysing coral growth ages from eustatic highstands between MIS 5a (76.5 ka) and MIS 7a (200 ka), which occurred between 70-202 ka (Table 7.2). The sea-level curve of de Gelder et al. (2020) for the Gulf of Corinth was not used in this chapter because the coral ages investigated herein are used as one of the constraints in their modelling.

MIS (highstand)	MIS time period (ka)	References
5a (76 ka)	70-82	N/A (used highstand age from Siddall et al., 2003, ± 6 ka error)
5c (100 ka)	94-106	N/A (used highstand age from Siddall et al., 2003, ± 6 ka error)
5e (125 ka)	116-138	Grant et al., 2014
6d (175 ka)	169-181	N/A (used highstand age from Siddall et al., 2003, ± 6 ka error)
7a (200 ka)	188-202	Dutton et al., 2009
7c (217 ka)	206-217	Dutton et al., 2009
7e (240 ka)	231-249	Dutton et al., 2009
9c (310 ka)	282-312	Rohling et al., 1998
9e (340 ka)	322-340	Rohling et al., 1998
11c (400 ka)	384-412	Rohling et al., 1998

Table 7.2: References used to inform the highstand time period within this chapter, where such data was not available, the highstand age ±6 ka uncertainty from Siddall et al. (2003) was applied.

It should be noted that the relative timing of sea-level rise in response to the transition from glacial to interglacial periods carries uncertainties as a result of the spatial and temporal variability of sea-level rise on intermediate and far-field regions relative to major ice sheets (Section 5.2.2) (see Dutton et al., 2015 for detailed discussion). The timing of 138-116 ka for MIS 5e may be considered as a broad time range. While Muhs and Szabo (1994) suggest 138 ka as an acceptable constraint on the start of the MIS 5e highstand there is a general lack of agreement as to the timing of MIS 5e (Hamelin et al., 1991; Stirling et al., 1998; Esat et al., 1999; Hearty et al., 2007; O'Leary et al., 2013; Dutton et al., 2015). Certainly the variation in timing differences may occur as a consequence of the approach-driven and natural variations discussed in Section 5.2, however, defining interglacial timing is complex and prone to differing interpretations and semantic differences; for instance, the timing used by Dutton et al. (2015) for MIS 5e is 129-116 ka, which they suggest marks the time that global mean sea level would be above the present-day sea level. Variation of the timings of interglacial periods has been recognised by the Past Interglacials Working Group (PAGES project, 2016) who note that: "…no single, continuous, integrative, and absolutely dated indicator exists for past interglacial intervals. Instead, a wide range of evidence exists for many climatic components and processes at local, regional, and global scales". What is important within this study is the point at which the sea-level rose following glaciation at ~150 ka (MIS 6a) (Fig. 2.4) to a level allowing it to enter into the Gulf of Corinth. Unfortunately, this exact timing is not yet known. However, it is well accepted that sea-level rise at the beginning of interglacial periods occurs quickly, shown by Gallup et al. (2002) who suggest that 80% of sea-level rise following the glacial period of MIS 6a (~150 ka) would have occurred by 135 ka. Furthermore, Grant et al. (2014) identified that maximum sea-level rise rates occurred within ~2 kyrs of the onset of deglaciation (~150 ka). Analysis of the rates of sea-level rise from Grant et al.

(2014) suggests that from ~150 ka to ~138 ka sea level rise was 5-8 m/ky. An average rate of 6.5 m/ky is used alongside the relative sea-level at 150 ka of -90 m (Grant et al., 2014), to suggest that by 138 ka sea-level within the gulf may have been ~-12 m (±10 m) relative to the present day. Given these suggested sea-level elevations, it is plausible that coral growth at this time could have occurred so 138 ka is used as an approximate age within this study to indicate the beginning of MIS 5e in relation to the gulf.

7.5 RESULTS AND DISCUSSION

The coral growth ages and $\delta^{234}U_i$ from the analysis of 22 coral samples (12 new coral ages from this chapter and 10 from Chapter 6, Robertson et al., 2020) are presented and discussed below and used to suggest tentative $\delta^{234}U_i$ values for the Gulf of Corinth from MIS 5e (125 ka) to MIS 7a (200 ka highstand). Existing coral ages are then investigated using (i) the tentative $\delta^{234}U_i$ values, (ii) the tectonic/stratigraphic settings from which the corals were sampled and, (iii) their spatial relationship relative to other coral ages or age constraints. The outcome of this analysis suggests that the growth ages of corals are consistent with ages expected given their stratigraphic position and, therefore, elevated $\delta^{234}U_i$ is representative of late Quaternary hydrochemistry of the gulf. These findings are discussed in the context of the gulf-wide uplift rates and broader use of coral growth ages to derive uplift rates in coastal margins and restricted basins.

7.5.1 Using $^{234}U/^{230}Th$ analysis of samples 44-47 to explore $\delta^{234}U_i$ for MIS 6d (175 ka) and 7a (200 ka)

The results of coral age dating on samples 44-47 (Fig. 7.1c, Locality 1, Profile line b-b'; Figs. 7.5c, d,e; 7.7B,) reveal ages and $\delta^{234}U_i$ values of multiple analyses on 4 corallites (Fig. 7.6a, Table 7.3). Corallite S44 has 4 ages of 198 ky, 195 ky, 196 ky and 197 ky, suggesting formation during the 200 ka highstand; corallite S45 has 4 ages of 175 ky, 165 ky, 168 ky and 203 ky, suggesting formation during the 175 ka highstand where the 203 ky age is likely to be an outlier and the 165- ky dated sample may be questionable owing to a low uranium concentration of 1.82 ppm. Corallite S46 has 3 ages of 200 ky, 179 ky and 196 ky, suggesting formation during the 200 ka highstand where the 179 ky sample has a low Uranium value of 1.56 ppm and should be disregarded, and corallite 47 has 1 age of 181 ky. Samples 44-47 display acceptable $^{230}Th/^{232}Th$ values >100 indicating negligible detrital thorium contamination (Table 7.3).

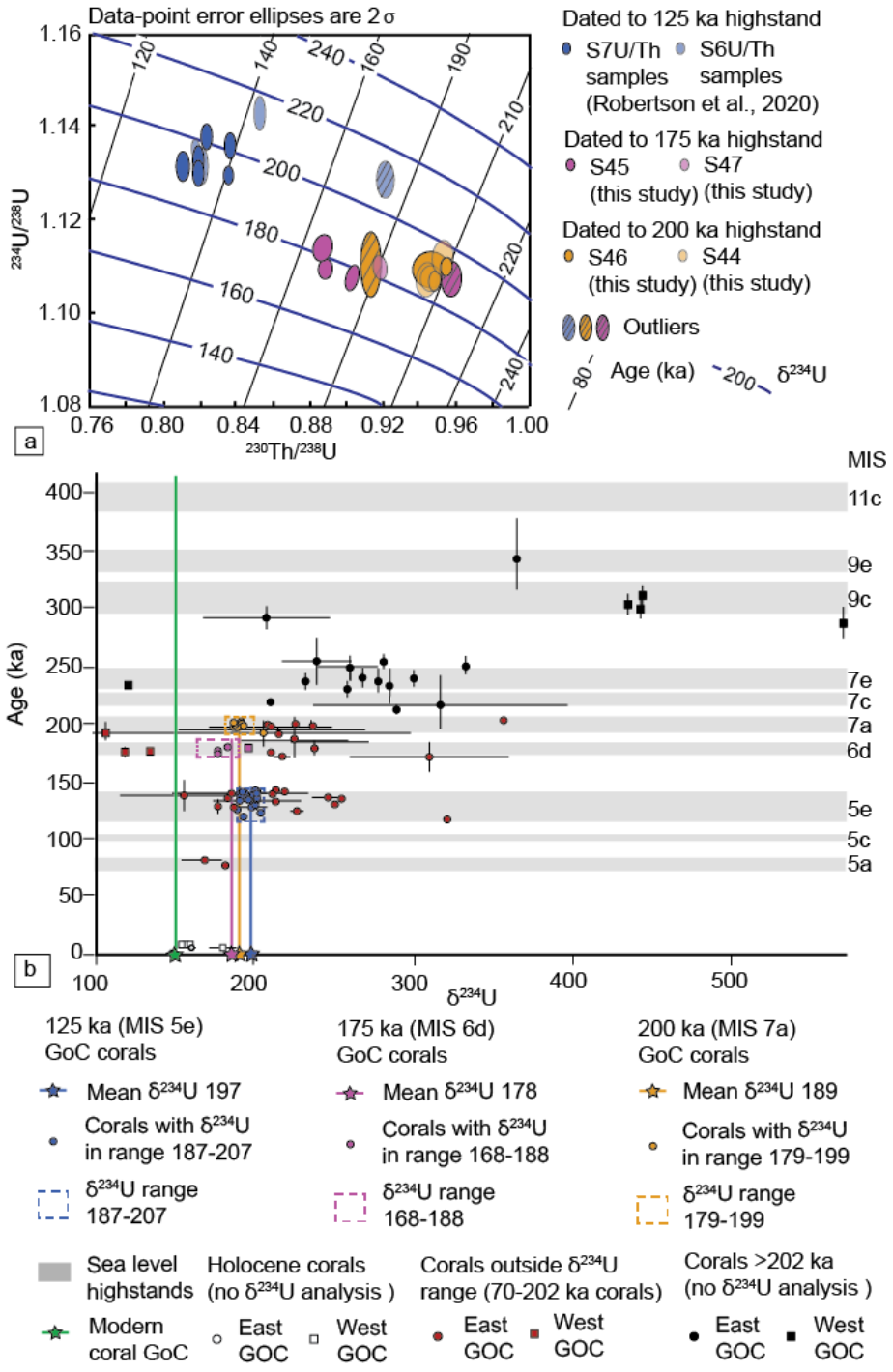

Figure 7.6: (a) U-Th evolution diagram with the results of dating on samples 44-47 (this study) and S6 and S7 (Robertson et al., 2020). (b) Plot of all acceptable (see text for detail), highstand coral growth ages from within the Gulf of Corinth. For samples 116-202 ka, colour coding is according to whether the sample has $\delta^{234}U_i$ within the range identified in this study. Holocene corals and corals ≥203 ka are not evaluated on the basis of their $\delta^{234}U_i$. See Table 7.2 for detail of the sea-level highstand periods and Fig. 7.5 for analysis for each locality.

Corallite sample	Lab ID	UTM		Sampling elevation (m)	Age (ky)	±2s (abs) (ky)	U (ppm)	$^{230}Th/^{232}Th$ (ppb)	$^{232}Th/^{238}U$	±2s (%)	$^{230}Th/^{238}U$	±2s (%)	$^{234}U/^{238}U$ Activity ratio	±2s (%)	Initial $^{234}U/^{238}U$ Activity ratio	±2s (%)	Converted to δ234U (*T*)
		Easting	Northing														
S44(1)	138-26	663124	4210776	41	197.8	1.7	1.91	488.1	0.0019	0.06	0.948	0.25	1.107	0.16	1.187	±0.003	187
S44(2)	156-15	663124	4210776	41	195.3	3.0	2.05	379.7	0.0025	0.35	0.943	0.49	1.107	0.27	1.186	±0.005	186
S44(3)	156-16	663124	4210776	41	196.1	2.8	2.02	354.2	0.0027	0.36	0.945	0.48	1.108	0.21	1.187	±0.004	187
S44(4)	156-17	663124	4210776	41	196.9	2.9	1.91	274.4	0.0035	0.35	0.951	0.47	1.112	0.25	1.196	±0.004	196
S45(1)	138-27	663124	4210776	41	174.7	1.3	2.08	159.3	0.0057	0.05	0.903	0.31	1.108	0.20	1.176	±0.003	176
S45(2)	156-18	663124	4210776	41	165.0	1.9	1.82	281.8	0.0031	0.34	0.887	0.47	1.114	0.21	1.182	±0.004	182
S45(3)	156-27	663124	4210776	41	167.6	1.5	2.06	549.9	0.0016	0.45	0.889	0.35	1.110	0.16	1.176	±0.003	176
S45(4)	156-28	663124	4210776	41	203.1	2.8	2.64	213.4	0.0045	0.29	0.957	0.41	1.107	0.27	1.191	±0.005	191
S46(1)	138-28	663124	4210776	41	199.5	1.6	1.93	288.9	0.0033	0.05	0.954	0.26	1.110	0.15	1.193	±0.003	193
S46(2)	156-29	663124	4210776	41	178.5	3.6	1.56	385.9	0.0024	0.68	0.914	0.58	1.110	0.50	1.183	±0.008	183
S46(3)	156-30	663124	4210776	41	195.7	4.9	1.98	235.4	0.0040	0.82	0.946	0.87	1.110	0.30	1.190	±0.005	190
S47(1)	138-29	663124	4210776	41	181.2	1.6	1.92	526.4	0.0017	0.06	0.918	0.29	1.110	0.18	1.183	±0.003	183

Table 7.3: $^{234}U/^{230}Th$ coral age dating analytical results for all samples 44-47 (this study) - activity ratios calculated using the ^{234}U and ^{230}Th decay constants of Cheng et al. 2013. Activity ratios corrected for ^{230}Th, ^{234}U and ^{238}U contribution from the synthetic ^{236}U-^{229}Th tracer, instrument baselines, mass bias, hydride formation and tailing. ^{230}Th blanks amounting to 0.15 ± 0.03 fg were subtracted from each sample. ^{238}U blanks were on the order of 10 pg, and were negligible relative to sample size. Age and $\delta^{234}U_i$ data were corrected for the presence of initial ^{230}Th assuming an initial isotope composition of ($^{232}Th/^{238}U$) = 1.2 ± 0.6, ($^{230}Th/^{238}U$) = 1 ± 0.5 and ($^{234}U/^{238}U$) = 1 ± 0.5 (all uncertainties quoted at the 2σ level).

Assuming the ages obtained are accurate, samples 44 and 46 place coral growth during MIS 7a (200 ka highstand – 188-202 ka, Dutton et al., 2009) (Table 7.3), while samples 45 and 47 represent growth during MIS 6d (175 ka highstand – 169-181 ka, using the 6 ka error margin of the highstand, Siddall et al., 2003; Rohling et al., 2009, Table 7.2), the 165 ±2 ka age from sample S45(2) is included here even though it is marginally lower than the 169-181 ka age range.

The ages obtained for samples 44-47 are plausible if their tectonic setting is interrogated; sampled from the same bioclastic-rich layer, the corals are located stratigraphically below a 125 ka (MIS 5e) ^{36}Cl exposure dated wave-cut surface (see Sample G, Fig. 6.4 in Chapter 6; Robertson et al., 2020) (Fig. 7.5c, d, e). The presence of 175 ka and 200 ka corals in this location can be explained by the following event, invoking erosion and isolation of whole corallites followed by re-sedimentation, using the sea level curve of Siddall et al. (2003) (sea-level elevations are relative to sea level today): (i) coral samples 44 and 46 grew during MIS 7a (200 ka highstand) below the -5 m (± 12 m) maximum sea level at this time, sea-level fell during lowstand MIS 6e to beyond ~-60 m; (ii) sea-level rose to a maximum of ~-30 m (± 12 m) within MIS 6d (175 ka highstand), during which the growth of samples 45 and 47 occurred, and was followed by a fall in sea level to between ~-60 m to -80 m during MIS 6c-6a; (iii) the subsequent 125 ka highstand (MIS 5e) resulted in sea level rise to ~5 m (± 12 m). This substantial sea-level rise could have eroded the coral colonies of 200 ka and 175 ka from their growth positions and deposited the corallites in their present day location within possible MIS 5e-aged sediments, following which the wave-cut platform formed. Preservation of the wave-cut platform and associated coral samples are as a consequence of sustained fault-controlled uplift since ~125 ka (Morewood and Roberts, 1997; Robertson et al., 2020). The above scenario suggests an uplift rate of 0.41 mm/yr, a value that is similar to those proposed for this location (Robertson et al. 2020), and is hence not unreasonable.

Given what is suggested here to be an acceptable tectonic explanation for the deposition of the corals in their setting and coral ages that fall into sea-level highstand periods, it is tentatively suggested that these ages may be reliable. The $\delta^{234}U_i$ values of samples from each highstand can be evaluated using the coral dating results from this study and from Chapter 6 (Robertson et al., 2020). They show that for the 6 samples allocated to the 200 ka highstand (MIS 7a) (S44 and S46), $\delta^{234}U_i$ values range between 186-196‰. For the 4 samples allocated to the 175 ka highstand (MIS 6d) (S45 and S47), $\delta^{234}U_i$ values range between 176-183‰. All

of these values are higher than that of the present day oceans (~147‰), but similar to the values reported in other Gulf of Corinth corals (Fig. 7.3a; Table 7.1). A $\delta^{234}U_i$ for the 175 ka and 200 ka highstands within the Gulf of Corinth can be tentatively suggested using the mean of values from the new coral ages herein. These values and their ± 10‰ range (Fig. 7.6b) are 189‰ (179-199‰) for the 200 ka highstand (MIS 7a) and 178‰ (168-188‰) for the 175 ka highstand (MIS 6d).

7.5.2 Constraining $\delta^{234}U_i$ values of the Gulf of Corinth during MIS 5e (125 ka highstand)

The coral ages of samples S6 and S7 sampled from an elevation of 44 m on Cape Heraion (Fig. 7.1c, Profile a-a'; Table 7.1; Fig. 7.5a, b, c; Fig. 7.6a) suggest growth during MIS 5e (125 ka highstand) (Robertson et al., 2020). These results are in agreement with Cape Heraion coral growth ages from other studies (e.g. Fig. 7.4c) (Vita Finzi et al., 1993; Leeder et al., 2003; Leeder et al., 2005; Roberts et al., 2009; Burnside, 2010; Houghton, 2010), all of which can be mapped into wave-cut platforms dated to the 125 ka highstand (MIS 5e) (Robertson et al., 2020). In detail, examination of the multiple analyses of samples S6 and S7 (4 and 6, respectively) reveal seven growth ages reflective of MIS 5e (125 ka highstand) (Fig 7.5a, Table 7.1) within the range 132-138 ka, two growth ages just outside the MIS 5e range of 141 ka and 143 ka that are included in the analysis and an age of 174 ka (S6(4)) that appears to be an outlier from analysis of corallite S6 and is herein excluded (see Table 6.2). The nine ages within the range of 132-143 ka all have acceptable uranium concentration levels between 2-3.5 ppm and $^{230}Th/^{232}Th$ significantly in excess of 100. $\delta^{234}U_i$ values of samples 6 and 7 cluster between 191-214‰ (Fig. 7.6a) with a mean of 197‰ (± 10‰ range of 187-207‰). If the growth ages just outside of 138 ka are excluded, then corals with growth ages between 132-138 ka have similar $\delta^{234}U_i$ values that cluster between 191-202‰ with a mean of 196‰.

In summary, comparing the measured $\delta^{234}U_i$ values of multiple analyses on individual corallites reveals elevated values for MIS 5e (125 ka), MIS 6d (175 ka) and MIS 7a (200 ka) of 197‰, 178‰ and 189‰, respectively, but growth ages that make sense with their stratigraphic and structural positions (Fig. 7.5). This observed clustering of samples within and between corallites (Fig. 7.6a) is taken as evidence that the measured $\delta^{234}U_i$ values may be representative of corals that formed during MIS 5e, 6d and 7a. Alternatively, if the elevated $\delta^{234}U_i$ were caused by diagenesis then it may be expected that sub-samples of the same corallite might have different isotopic compositions (Scholz and Mangini, 2007), hence clustered values would be unlikely. The similarity of both age and $\delta^{234}U_i$ values allows for a

tentative suggestion that the $\delta^{234}U_i$ of the Gulf of Corinth during late Quaternary highstands was higher than that of present values and within the range of 160-217‰.

7.5.3 Coral ages and $^{234}U_i$ values within their tectonic setting

Assuming that the late Quaternary $\delta^{234}U_i$ values highlighted above are correct, they are applied to the recalculated coral age dataset (n=155) from within the Gulf of Corinth (Fig. 7.6b; Table 7.1). However, prior to further analysis a number of samples (n=72) are excluded, detailed in Table 7.1. Plotting the age versus $\delta^{234}U_i$ of the remaining acceptable samples (n=83) shows a mixture of growth ages that cluster within glacio-eustatic highstand periods and have $\delta^{234}U_i$ both within and outside of the $\delta^{234}U_i$ range identified herein (for ages 69-202 ka) (Fig. 7.6b). Detailed analysis on the acceptable samples (n=83) reveals five samples that have Holocene ages, 63 samples that have highstand ages between 69-202 ka (76-200 ka highstands, Fig. 7.6b, Table 7.1) with the remaining 15 samples ≥203 ka (Fig. 7.6b).

Exploring the 63 samples with highstand growth ages between 69-202 ka, the $\delta^{234}U_i$ range for each highstand can be applied. This shows that for the corals with 200 ka highstand (MIS 7a) ages (n=16), 38% have $\delta^{234}U_i$ within the range of 179-189‰. For the corals with 175 ka highstand (MIS 6d) ages (n=10), 40% have $\delta^{234}U_i$ within the range of 168-188‰. For the corals with 125 ka highstand (MIS 5e) ages (n=35), 63% have $\delta^{234}U_i$ within the range of 187-207‰. However, the remaining corals with $\delta^{234}U_i$ outside of these ranges have growth ages and sample locations that that fit with the stratigraphical and tectonic relationships in addition to agreeing with other coral ages sampled from the same location (Fig. 7.7). Coral growth ages ≥203 ka (n=15) predominantly exhibit higher $\delta^{234}U_i$ that could be due to diagenetic processes or may be an indication of different hydrochemistry within the gulf at the time of growth. A lack of further analyses on these corals precludes further explanation for ≥203 ka corals. Overall, these results suggest that $\delta^{234}U_i$ may have been elevated during coral growth between 116-202 ka, but they also indicate that within the Gulf of Corinth there appears to have been some spatial and temporal variability of $\delta^{234}U_i$.

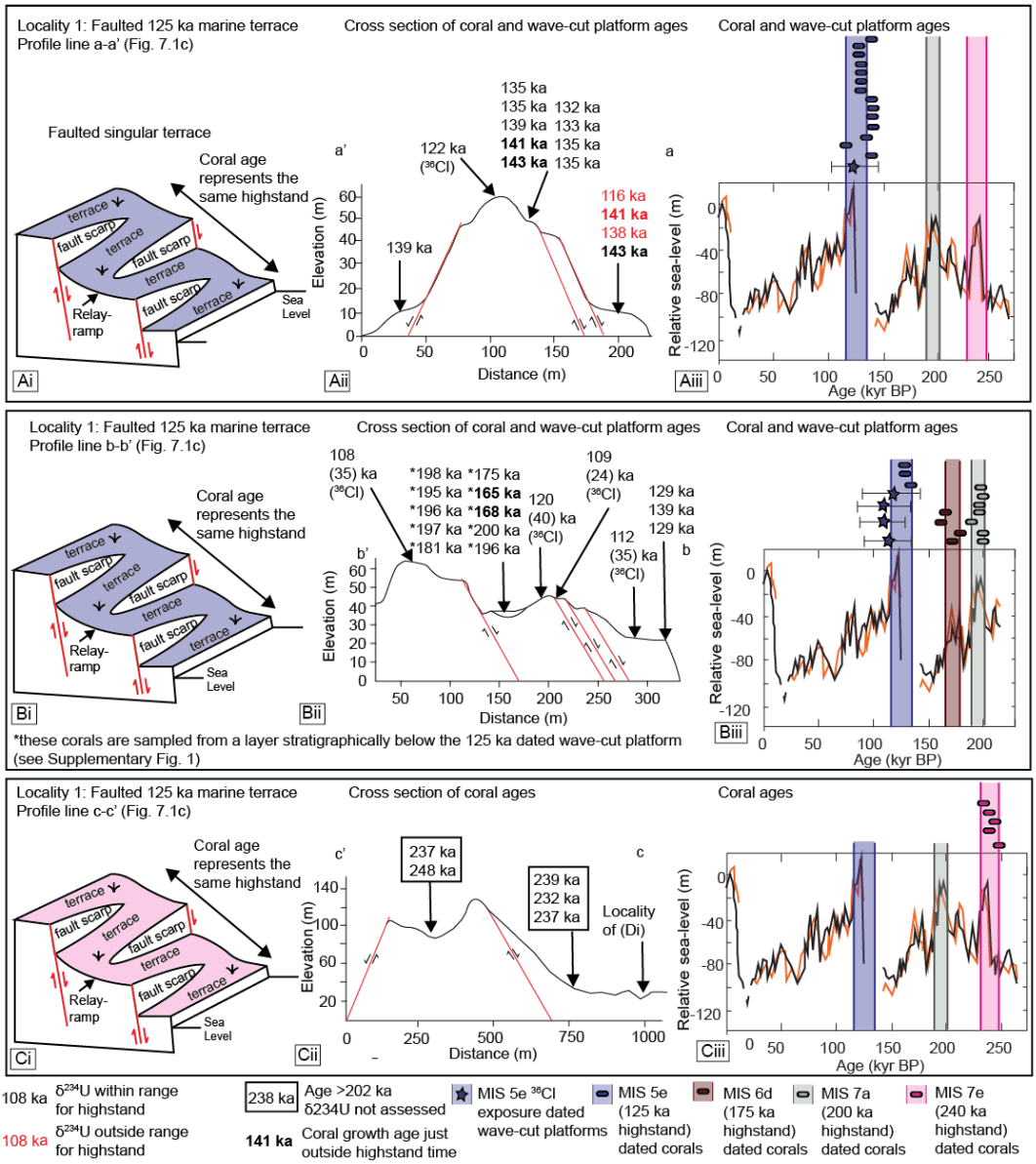
Locality 1: Faulted 125 ka marine terrace
Profile line a-a' (Fig. 7.1c)
Cross section of coral and wave-cut platform ages
Coral and wave-cut platform ages
Faulted singular terrace
Coral age represents the same highstand
terrace
fault scarp
Relay-ramp
Sea Level
Ai
a'
a
122 ka (36Cl)
139 ka
135 ka
135 ka 132 ka
139 ka 133 ka
141 ka 135 ka
143 ka 135 ka
116 ka
141 ka
138 ka
143 ka
Elevation (m)
Distance (m)
Relative sea-level (m)
Age (kyr BP)
Aii
Aiii
Locality 1: Faulted 125 ka marine terrace
Profile line b-b' (Fig. 7.1c)
Cross section of coral and wave-cut platform ages
Coral and wave-cut platform ages
Coral age represents the same highstand
Bi
b'
b
108 (35) ka (36Cl)
*198 ka *175 ka
*195 ka *165 ka
*196 ka *168 ka
*197 ka *200 ka
*181 ka *196 ka
120 (40) ka (36Cl)
109 (24) ka (36Cl)
112 (35) ka (36Cl)
129 ka
139 ka
129 ka
Bii
Biii
*these corals are sampled from a layer stratigraphically below the 125 ka dated wave-cut platform (see Supplementary Fig. 1)
Locality 1: Faulted 125 ka marine terrace
Profile line c-c' (Fig. 7.1c)
Cross section of coral ages
Coral ages
Coral age represents the same highstand
Ci
c'
c
237 ka
248 ka
239 ka
232 ka
237 ka
Locality of (Di)
Cii
Ciii
108 ka δ234U within range for highstand
108 ka δ234U outside range for highstand
238 ka Age >202 ka δ234U not assessed
141 ka Coral growth age just outside highstand time
MIS 5e 36Cl exposure dated wave-cut platforms
MIS 5e (125 ka highstand) dated corals
MIS 6d (175 ka highstand) dated corals
MIS 7a (200 ka highstand) dated corals
MIS 7e (240 ka highstand) dated corals

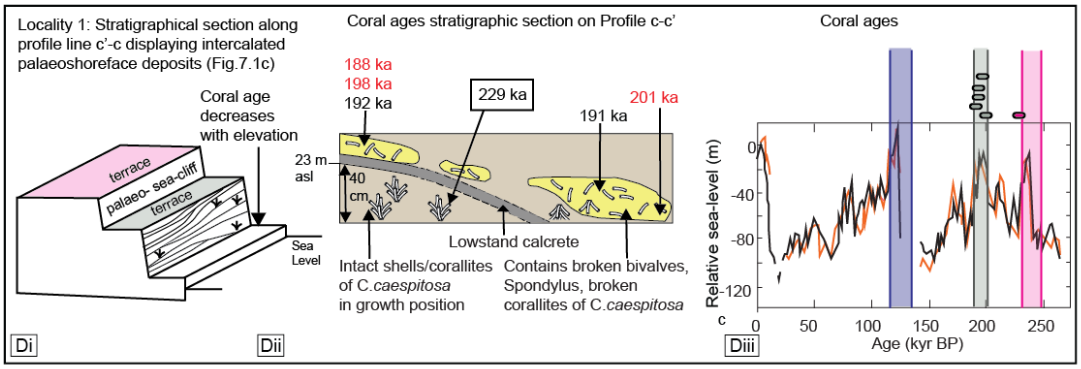

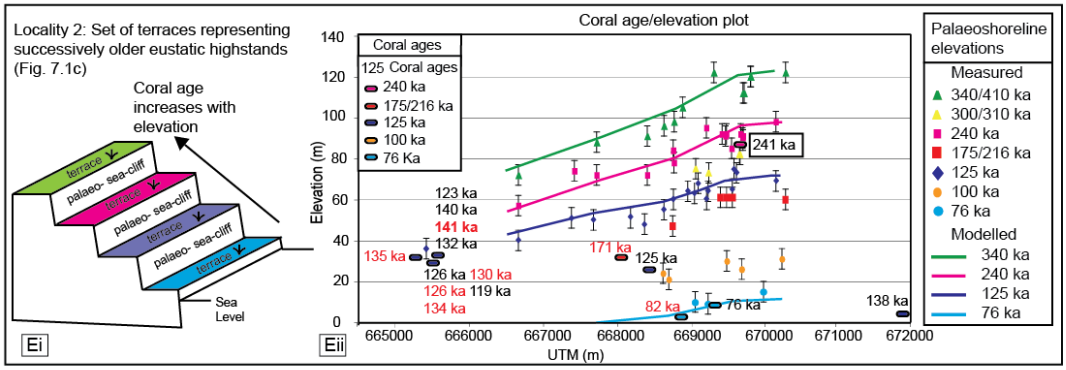

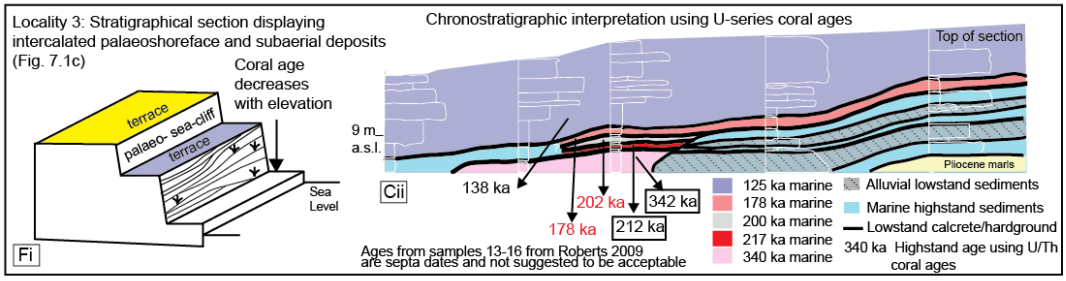

108 ka δ²³⁴U within range for highstand

108 ka δ²³⁴U outside range for highstand

238 ka Age >202 ka δ234U not assessed

141 ka Coral growth age just outside highstand time

MIS 5e ³⁶Cl exposure dated wave-cut platforms

MIS 5e (125 ka highstand) dated corals

MIS 6d (175 ka highstand) dated corals

MIS 7a (200 ka highstand) dated corals

MIS 7e (240 ka highstand) dated corals

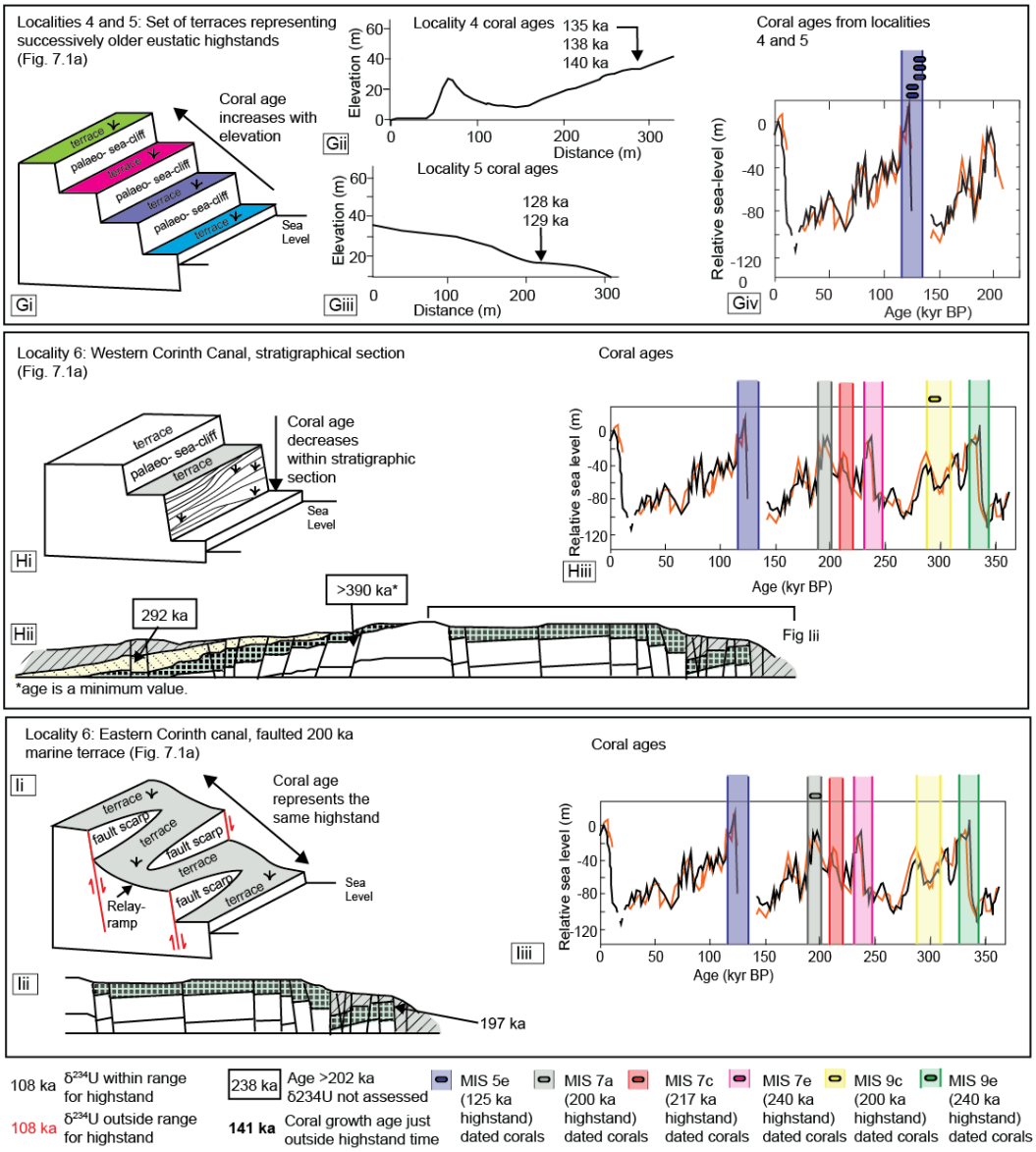
Localities 4 and 5: Set of terraces representing successively older eustatic highstands (Fig. 7.1a)
Coral age increases with elevation
terrace
palaeo- sea-cliff
Sea Level
Gi
Locality 4 coral ages
135 ka
138 ka
140 ka
Elevation (m)
Distance (m)
Gii
Locality 5 coral ages
128 ka
129 ka
Giii
Coral ages from localities 4 and 5
Relative sea-level (m)
Age (kyr BP)
Giv
Locality 6: Western Corinth Canal, stratigraphical section (Fig. 7.1a)
Coral age decreases within stratigraphic section
Hi
Coral ages
Relative sea level (m)
Age (kyr BP)
Hiii
292 ka
>390 ka*
Fig Ii
Hii
*age is a minimum value.
Locality 6: Eastern Corinth canal, faulted 200 ka marine terrace (Fig. 7.1a)
Coral age represents the same highstand
fault scarp
Relay-ramp
Ii
Iii
197 ka
Coral ages
Relative sea level (m)
Age (kyr BP)
Iiii
108 ka δ234U within range for highstand
108 ka δ234U outside range for highstand
238 ka Age >202 ka δ234U not assessed
141 ka Coral growth age just outside highstand time
MIS 5e (125 ka highstand) dated corals
MIS 7a (200 ka highstand) dated corals
MIS 7c (217 ka highstand) dated corals
MIS 7e (240 ka highstand) dated corals
MIS 9c (200 ka highstand) dated corals
MIS 9e (240 ka highstand) dated corals

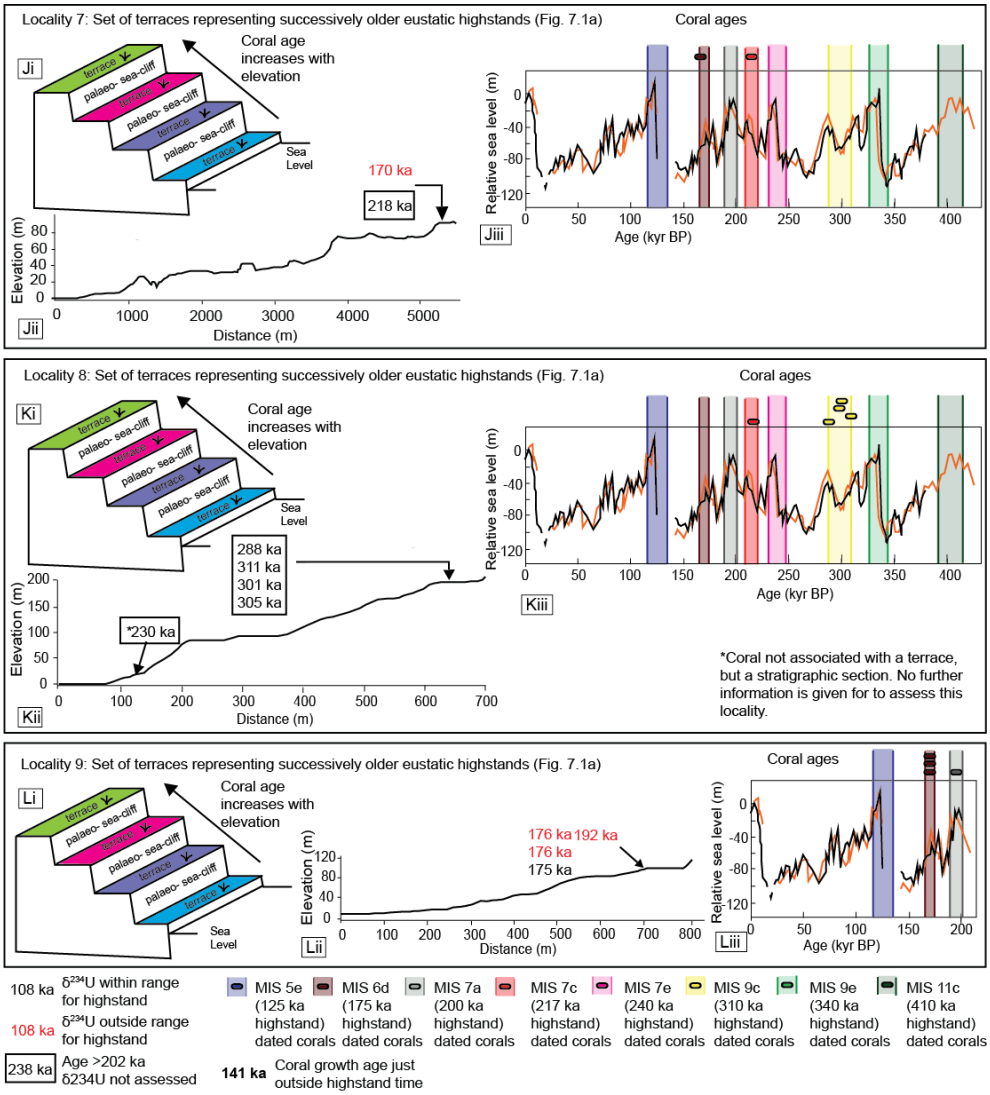

Figure 7.7: : (A-L) (i) Cartoons of the setting of each locality (see Fig. 7.1a, c) – sequence of marine terraces/stratigraphic section/faulted marine terrace (ii) Coral ages plotted on a 2D cross section with colour coding to show whether the δ234Ui exceeds the range (178-217) identified in this study. (iii) Coral growth ages plotted on highstands of the sea level curve of Siddall et al. (2003)

It is observed that 84% coral growth ages come from the eastern Gulf of Corinth compared to the west (Figs. 7.1a, c, 7.3b, 7.5b, Table 7.1), and that all of the MIS 5e (125 ka highstand) dated corals are located in the eastern Gulf of Corinth (Fig. 7.6b). One possible explanation for this is that coral growth is reflective of the dominant seawater entry point during the highstands, but it is not discounted that this could simply be related to sampling and/or preservation bias. If the interpretation of seawater entry via the Rion Straits and Isthmus of Corinth during MIS 5e proposed by Roberts et al. (2009) is accepted (Fig. 7.2), restricted seawater entry via the Rion Straits did not occur until sea level was near its maximum elevation (stillstand) around 125 ka (MIS 5e). Prior to the MIS 5e stillstand, seawater entry would be predominantly via the shallow Isthmus of Corinth into the eastern part of the gulf

~110 km to the east, and coincidental to the location of all of the MIS 5e corals within this study. Further analysis shows that 75% of MIS 5e corals (with $\delta^{234}U_i$ within the acceptable range determined herein) were dated to the earlier part of the highstand from 138 ka to 125 ka (Table 7.1) which could be used to support the notion that water conditions during the early highstand favoured coral growth (Hearty et al., 2007). The coral growth ages herein can be inferred to suggest that sea-level rise during ~143-138 ka was high enough to enter through the Isthmus of Corinth and begin the transition from lake to semi-restricted lagoon and marine conditions.

7.5.4 Variable chemistry of the Gulf of Corinth throughout the Late Quaternary

The interpretation that the $\delta^{234}U_i$ value in the Gulf of Corinth during the late Quaternary was elevated with respect to that of sea water is consistent with suggestions of other authors (Collier et al., 1992; Roberts et al., 2009; Burnside, 2010; Houghton, 2010). The hypotheses of elevated $\delta^{234}U_i$ centres around transitions between a lake and semi-restricted marine basin throughout the Late Quaternary as a result of the interplay between eustatic sea-level variation, freshwater influx and fault-related subsidence/uplift along the Rion-Anterion sill and Isthmus of Corinth, respectively (Figs. 7.1a, 7.2) (Roberts et al., 2009; Burnside, 2010; Houghton, 2010). Restricted/silled basins, partially isolated from an adjacent sea, have been shown to have distinctive hydrochemistry compared to that of the open ocean (Middelburg et al., 1991; Andersson et al., 1995; Esat and Yokoyama, 2010). However, temporal and spatial variations of the hydrochemistry within the faulted basin of the Gulf of Corinth are poorly understood. It is known that marine conditions prevail at highstands (Roberts et al., 2009; McNeill et al., 2019) and that during the transition from lowstand to highstand the gulf is likely to become marine with a significant freshwater content (Perissoratis et al., 2000), evidenced by highly variable microfossil assemblages that reveal complex basin environmental variation between highstand and lowstand intervals (Roberts et al.,2009; McNeill et al. 2019). In more detail, Roberts et al. (2009) showed that *C. caespitosa* coral colonies were accompanied by marine ostracod assemblages, and the interpreted lowstand crusts (visible in Fig. 7.4bii) that separated highstand deposits were dominated by nearshore and non-marine ostracod species. Furthermore, recent findings by McNeill et al. (2019) show that microfossil assemblages within and between highstand intervals indicates salinity changes suggestive of significant variability. Little else is known about the water chemistry, which is expected to be spatially and temporally variable considering that: (i) the seawater inlets were narrow, shallow and changing over time (Collier, 1988; Collier and Thompson,

1991; Perissoratis et al., 2000), (ii) sea level rises are spatially complex (Dutton et al., 2015) and may be non-linear through time (Stanley and Warne, 1994), (iii) late Quaternary cyanobacterial mounds that dominate Cape Heraion at Locality 1 (Fig 7.1. c) may provide evidence of rising groundwater altering the water chemistry (Houghton, 2010), and (iv) coral growth occurs in the footwalls along coastal margins (localities 2-9, Fig. 7.1a) that are subject to episodic fault-related uplift and freshwater influx from rivers and groundwater (Luijendijk et al., 2020). A study of the Holocene marginal marine environment along the southern margin of the western Gulf of Corinth (Soter et al., 2001) provides an analogue to coastal margin conditions during previous highstands. Spatial and temporal variations were evidenced by complex sedimentology and stratigraphy suggestive of repeated transitions between freshwater and brackish to marine conditions over periods of 1-3 ka due to a combination of tectonic uplift, river drainage and the variation between rapid and decelerated sea-level rise (Soter et al., 2001).

In summary, it is proposed that along the fault-controlled southern coastal margins of the Gulf of Corinth, the dominant factor controlling the $\delta^{234}U_i$ of corals during previous highstands may be restricted seawater entry into the gulf combined with freshwater influx from groundwater (Locality 1) and rivers (localities 2-9) (Fig. 7.1). The $\delta^{234}U_i$ of both groundwater and riverine input is dependent on the lithology of the host rocks in the catchment or circulation area (Palmer and Edmond, 1993), which are predominantly comprised of Mesozoic limestone and carbonate lithologies in the Gulf of Corinth (IGME, 1993). In the eastern Gulf of Corinth, at Cape Heraion (Fig. 7.1c, Locality 1) the presence of high Mg/Sr cyanobacterial mounds has been interpreted as evidence that groundwater from submarine springs percolating along normal faults was partially equilibrated with Mesozoic limestones, which have relatively high $\delta^{234}U_i$ (Houghton, 2010). This is particularly relevant given that 18 of the coral samples from within Locality 1 are located on or directly adjacent to these cyanobacterial mounds. In terms of the riverine input (localities 2-9, Fig. 7.1) there are presently ~13 major rivers that drain into the southern gulf (McNeill et al., 2019), and it is suggested that many of these also drained into the Gulf of Corinth throughout the late Quaternary (Seger and Alexander, 1993). Lithological, climatic and seasonal differences mean that riverine $\delta^{234}U_i$ has been shown to be highly variable (Grzymko et al., 2007) in comparison to seawater, with values >200‰ (Chabaux et al., 2003), though studies into individual rivers worldwide report significantly higher values beyond 400-500‰ (e.g. Plater et al., 1992; Andersson et al., 1995; Andersen et al., 2007; Grzymko et al., 2007). While no such data exists for the Gulf of Corinth rivers, spatial and seasonal temporal variation of$\delta^{234}U_i$

as a result of riverine input and restricted circulation has been observed in other restricted basins such as the Baltic Sea (Andersson et al., 1995). Furthermore, a recent study by Luijendijk et al. (2020) suggested that coastal groundwater discharge (a combination of submarine and nearshore terrestrial groundwater discharge) takes place in a zone that extends 400 m from the shore, and that due to spatial variability, this groundwater discharge can significantly impact coastal hydrology.

7.5.5 Analysis of $^{87}Sr/^{86}Sr$ ratios throughout the Late Quaternary

A test of the reliability of elevated $\delta^{234}U_i$ of Gulf of Corinth corals as a direct consequence of freshwater input can be carried out by investigating $^{87}Sr/^{86}Sr$ ratios. Corals and other marine carbonate organisms record the $^{87}Sr/^{86}Sr$ ratios of the water in which they formed. Marine $^{87}Sr/^{86}Sr$ ratios have been shown to be increasing quasi-linearly over the past 2.5 Ma (Hodell et al., 1990), but exhibit less variation on timescales over hundreds of thousands of years (Henderson et al., 1994), with the present day oceanic (Palmer and Edmond, 1992; Allegre et al., 2010) and Gulf of Corinth (Houghton, 2010) values ~0.70917. If freshwater influx dominated conditions along coastal margins, then one may assume that this would be reflected in the $^{87}Sr/^{86}Sr$ chemistry of the corals. However, this assumption has been challenged because of the significant difference between strontium (Sr) concentrations of riverine and oceanic waters, which are 1.0-4.0 µM and 90 µM respectively. This means that even significant riverine input into marginal seas may be unlikely to alter the Sr concentrations (Flecker et al., 2002; Krabbenhoft et al., 2010). The exception is in carbonate organisms grown in brackish/low salinity environments, where the $^{87}Sr/^{86}Sr$ chemistry of the water may be significantly affected by the freshwater $^{87}Sr/^{86}Sr$ (Andersson et al., 1992; Bryant et al., 1995). Brackish/oligohaline conditions are evident from boreholes from the Holocene and late Quaternary (Soter et al., 2001; Papanikolaou et al., 2015), from the presence of cyanobacterial mounds (Houghton, 2010) in the eastern gulf and from analysis of microfossils reported in Roberts et al. (2009) where variable salinity ostracods were shown to be present in sediments alongside *C. Caespitosa* corals that formed during highstand periods. Consequently, it is suggested that the $^{87}Sr/^{86}Sr$ of corals from the Gulf of Corinth corals may be a reliable proxy to investigate the observed elevated $\delta^{234}U_i$.

The $^{87}Sr/^{86}Sr$ ratio of freshwater is directly influenced by the dominant lithology of their circulation/catchment areas (Palmer and Edmond, 1989; Hodell et al., 1990). In the Gulf of Corinth, limestones and other carbonate lithologies dominate. These have the particularly

low observed $^{87}Sr/^{86}Sr$ (Pearce et al., 2015), with worldwide values of 0.707-0.709 (Burke et al., 1982) and Triassic limestones of the Perachora Peninsula (Fig. 7.1a) were measured as 0.70771 (Houghton, 2010). Comparison of the $^{87}Sr/^{86}Sr$ ratios for corals from the Gulf of Corinth to those from the Pacific and Atlantic throughout the late Quaternary reveals that the Gulf of Corinth corals exhibit a range of $^{87}Sr/^{86}Sr$ ratios, that are moderately to significantly lower than Atlantic and Pacific levels from ~75 ka to ~350 ka (Fig. 7.8). Low $^{87}Sr/^{86}Sr$ on Gulf of Corinth corals was also observed by Dia et al. (2007) who considered that sample impurities and/or diagenetic processes may be the cause, however, Houghton, (2010) carried out detailed chemical analysis on meticulously cleaned corals and dismissed this explanation. Therefore, it is tentatively suggested that the observed elevated $\delta^{234}U_i$ in corals is accompanied by low $^{87}Sr/^{86}Sr$, indicative of hydrochemistry influenced by freshwater.

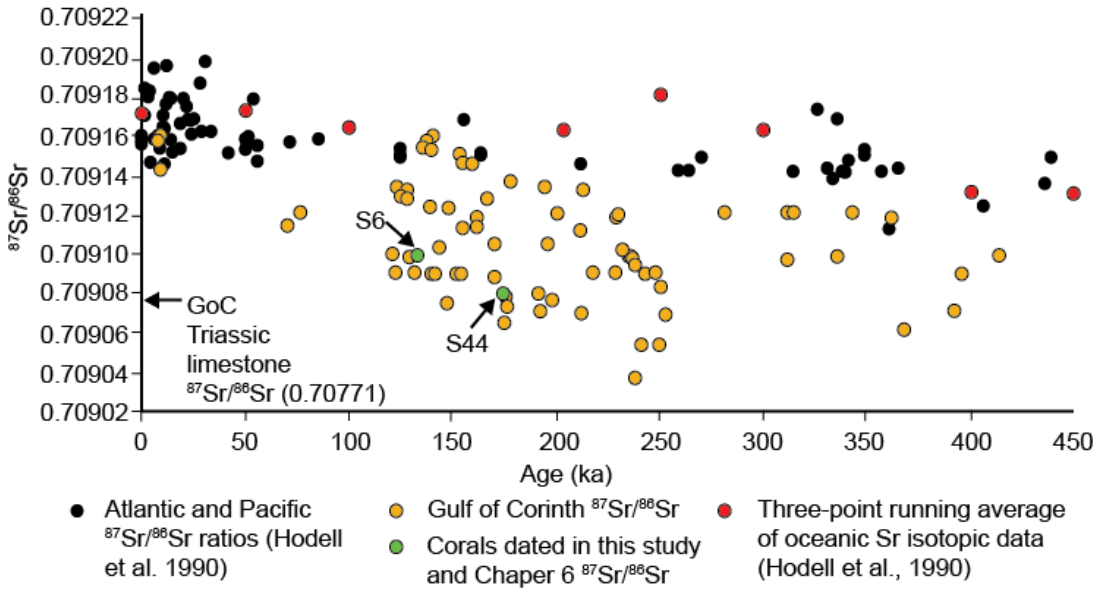

Figure 7.8: $^{87}Sr/^{86}Sr$ and age plot for the Gulf of Corinth from corals assessed within this study (Table 7.1) against those from Hodell et al. (1990) from the Atlantic and Pacific, in addition to a worldwide Sr curve obtained from a three-point running average (Hodell et al., 1990). The Triassic limestone $^{87}Sr/^{86}Sr$ is from Houghton (2010).

7.5.6 Summary of coral age and $\delta^{234}U_i$ findings

In summary, these findings suggest that corals from within the Gulf of Corinth with MIS highstand ages have elevated $\delta^{234}U_i$ reflective of their growth environment, where the hydrochemistry of the gulf deviated from that of the present day. A combination of restricted marine input into the gulf during the highstands and coral growth along fault-controlled margins, where water chemistry was influenced by freshwater, is inferred as the likely cause of elevated $\delta^{234}U_i$. Whilst tentative values of $\delta^{234}U_i$ for three Late-Quaternary highstands are suggested, there is likely to be spatial and temporal variation of this value as a result of seasonal and catchment area differences from riverine input. For this reason, coral growth ages are not excluded from this study solely on the basis of the $\delta^{234}U_i$. The results presented herein are strengthened by the observed stratigraphical and tectonic relationships of Gulf of Corinth corals and other age controls (Fig. 7.7). These findings suggest that where late Quaternary coral ages are obtained from coastal margins or restricted/silled marine basins, age reliability determinations based solely upon $\delta^{234}U_i$ should be avoided. Coral age reliability should be assessed based upon whether multiple analyses on corallites from the same locations reveal clustered ages and $\delta^{234}U_i$, in combination with the location of other coral growth ages/age controls relative to the localised tectonic/stratigraphic setting.

7.5.7 Late Quaternary uplift patterns using coral ages

Uplift rates on the footwalls of active normal faults that bound the south of the Gulf of Corinth (Fig. 7.1a), calculated using the coral ages discussed herein, can be used to explore gulf-wide fault-related deformation over the late Quaternary. Plotted from east to west along the Gulf of Corinth (Fig. 7.9), these data show that uplift maxima occur within the central section of the gulf clearly decreasing to the east and appearing to decrease toward the west, though a lack of data prohibits certainty with latter observation (Fig. 7.9b). These results are consistent with summed late Quaternary fault displacement profiles from Bell et al. (2011) (Fig. 7.9c) who identified a “bell-shaped displacement profile with greatest levels of extension in the central part of the rift”. Long-term uplift and fault displacement data (Fig. 7.9b and c) are not in agreement with short-term geodetic rates of extension (Clarke et al., 1998; Briole et al., 2000; Bell et al., 2011) (Fig. 7.9d), which suggest increasing extension from east to west. Detailed investigations by Bell et al. (2011) led them to hypothesise that this discrepancy may be as a consequence of variation in the location of maximum extension due to fault growth and linkage. While the discrepancy between short-term geodetic and long-

term fault uplift/displacement rates is unresolved, it is clear that the age constraints obtained from uplifted corals make a significant contribution to establishing long-term rates of deformation throughout the Gulf of Corinth.

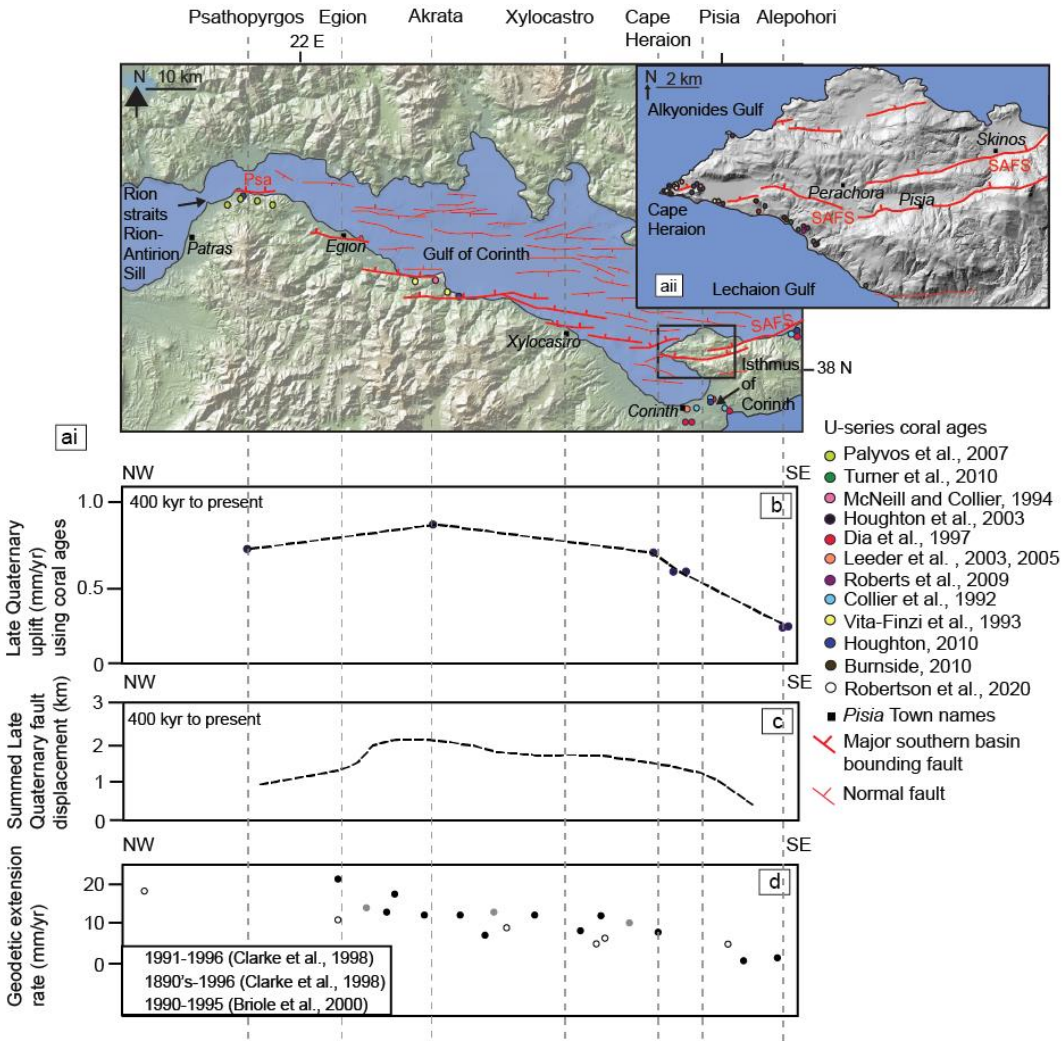

Figure 7.9: (a) Map of the Gulf of Corinth and major faults based upon those used in Nixon et al 2016. (aii) Fault map of Perachora Peninsula (b) Late Quaternary uplift in the footwall of major north dipping faults that bound the south of the Gulf of Corinth derived from ages of corals from the following studies (west to east): McNeill and Collier, 2004; Houghton et al., 2003; Robertson et al., 2020; Roberts et al., 2009; Houghton, 2010; Collier et al., 1992. Uplift values from corals located on the Isthmus of Corinth and eastern Corinth terraces are not plotted as they occur in the back tilted section of the footwall of the South Alkyonides Fault (SAF) and eastern tip of the Xylocastro faults respectively and therefore record minimum uplift values. (c) Summed late Quaternary fault displacement for the Gulf of Corinth, adapted from Bell et al. (2011). (d) Geodetic extension of Clarke et al. (1998) and Briole et al. (2000), adapted from Bell et al. (2011).

7.6 CONCLUSIONS

1. Analysis of new and existing coral growth ages suggest that the $\delta^{234}U_i$ of the Gulf of Corinth during the late Quaternary may been elevated and subject to spatial and

temporal variation as a result of the interplay between eustatic sea-level changes, fault controlled uplift/subsidence that limited the marine water ingress into the gulf and freshwater influx from rivers and groundwater.

2. The age reliability of corals that have grown along coastal margins and in restricted/semi-restricted marine environments should not be solely evaluated on the basis of the $\delta^{234}U_i$ relative to current seawater values. Rather, it is suggested that corallites from the same layer are analysed and that multiple analyses on the same corallites may be useful to determine age and $\delta^{234}U_i$ reliability, in combination with consideration of the stratigraphic and tectonic setting of the corals and their relative position to other age constraints.
3. Coral ages along the southern margin of the Gulf of Corinth provide a reliable means to explore long-term uplift patterns and are in agreement with other geological measurements such as late Quaternary fault displacement profiles.

8 CHAPTER 8: DISCUSSION

This chapter provides a brief overview of the findings from Chapters 4-7, and then explores the implications of the results presented within the context of future studies that are now possible. In particular, the success of ^{36}Cl exposure dating on Quaternary wave-cut platforms is explored compared to previous studies. The reliability of ^{36}Cl exposure dating, ^{234}U/^{230}Th coral age dating and synchronous correlation facilitates the investigation of the tectonics of other complex subduction zones; this is emphasised using examples from the broader WHSZ, Japan and the Peru-Chile subduction zones. The importance of knowledge of the potential causal faults on seismic hazard analysis is then discussed. This is explored by constraining the maximum magnitude of potential earthquakes in the WHSZ. Following this the impact of temporally variable slip rates on expected earthquake rates and probabilities is investigated using PSHA modelling. Throughout this chapter, potential areas for future work that may now be possible given the findings of this thesis are also highlighted. The final section of the chapter summarises the thesis, outlining the implications of the findings presented herein in relation to the scientific problem presented in Chapter 1.

8.1 OVERVIEW OF THE FINDINGS FROM THE PREVIOUS CHAPTERS AND ARISING QUESTIONS

Chapter 1 of this thesis introduced the importance of knowledge of the long-term slip/throw rates on active upper-plate faults to aid scientists with our understanding of fault behaviour and as a contribution to PSHA. There is a clear emphasis in the literature on deriving slip/throw rates from within the Holocene, but evidence has shown that elastic fault interaction may result in (i) clusters and anticlusters of earthquakes over multiple millennia, within the Holocene (e.g. Cowie et al., 2017), or (ii) anomalous slip displacements between overlapping fault tips (Robertson et al., 2020). The effect of fault clusters and anticlusters means that it is unclear as to whether measured Holocene slip/throw rates are representative of the longer-term rates of deformation, and variations in slip/throw rates at the tips of faults may pose an unidentified hazard if it is assumed that rates of deformation close to the tips of potentially interacting faults are near to zero (Faure Walker et al., 2019). Furthermore, where faults are not observable or have relatively low slip rates, there may be a lack of any deformation data and, consequently, little understanding of a fault's seismic

potential and whether it is capable of rupturing. One of the ways in which long term slip/throw rates are obtained is via deformed palaeoshorelines where the effect of faulting is imprinted onto the landscape. Without knowledge of these long-term rates of deformation, the significance of Holocene and geodetic slip/throw rates are not known; this issue is independent of the tectonic setting.

In the results presented in earlier chapters, this thesis has demonstrated improvements to understanding two important techniques applicable to dating palaeoshorelines: (i) the application of ^{36}Cl exposure dating across multiple carbonate lithologies, which was successful based upon low erosion rates proved by lithophagid borings and millholes – an approach lacking in other studies, and (ii) that ^{234}U/^{230}Th coral age dating from coastal settings may yield elevated $\delta^{234}U_i$ values, but produce reliable ages. The ^{36}Cl exposure age results from southern Crete and the Perachora Peninsula yielded ages that were in agreement with existing independent age controls and were some of the first published examples whereby ^{36}Cl exposure dating on Quaternary wave-cut platforms successfully constrained the ages of a sequence of palaeoshorelines (Robertson et al., 2019) and a faulted palaeoshoreline (Robertson et al., 2020). The potential reasons for the success of ^{36}Cl exposure dating herein and the implications associated with this are discussed below (Section 8.2).

One of the most widely applied methods to date palaeoshorelines is through ^{234}U/^{230}Th coral age dating. However, there is evidence that coral samples have yielded acceptable ages but display elevated $\delta^{234}U_i$ values that are suggestive of potentially unreliable age determinations. The corals dated in these types of studies have commonly grown in coastal environments and/or semi-restricted marine basins and have been uplifted along deforming palaeoshorelines. A systematic study of the coral ages and their $\delta^{234}U_i$ from within the Gulf of Corinth (Chapter 7) suggests that in locations where corals grow and are latterly uplifted on palaeoshorelines, such as restricted basins and coastal marine settings, they may have grown in hydrogeochemical environments that are not representative of the homogenous open ocean due to fresh-water influx and natural springs. In such instances, the age reliability of the coral should not solely be assessed based upon the $\delta^{234}U_i$ value of homogenous open ocean but should also consider the tectonics and stratigraphic setting. The approach adopted herein emphasises the power of undertaking ^{234}U/^{230}Th coral age dating on multiple corallites from the same sedimentary layer and carrying out multiple analyses on each corallite. These

findings are applicable to past and future studies that rely on $^{234}U/^{230}Th$ coral dating to constrain the age of palaeoshorelines in any tectonic setting.

This thesis also provides a worked example that allows direct comparison between the application of the sequential and synchronous correlation methods to derive uplift rates. Chapter 4 showed that differing allocations between undated palaeoshorelines and highstands occur when the two methods are employed resulting in opposing uplift scenarios of temporally variable versus constant uplift. Other comparisons between the two correlation methods reveal similar findings of temporally constant uplift when the synchronous method is applied (Roberts et al., 2013; Meschis et al., 2018) in comparison to variable uplift when the sequential method is used. This is important because temporally variable uplift needs a relatively large-scale tectonic explanation, such as fault interaction or a migrating crustal orogenic wave linked to slab retreat (e.g. Tortorici et al., 2003; Gallen et al., 2014). In view of the fact that uplift patterns obtained from the study of palaeoshorelines may be directly used to derive slip/throw rates, this thesis demonstrates that it is of particular importance that correlation between undated palaeoshorelines and highstands is accurate. This is the strength of the synchronous correlation method, particularly at low uplift rates where overprinting of older palaeoshorelines by younger highstands is common. Furthermore, knowledge of sea-level elevations for Late-Quaternary highstands is essential in the derivation of palaeoshoreline uplift rates, and the slip/throw rates and recurrence intervals of the faults that may cause the tectonic uplift. This thesis explores the extent to which the use of different sea-level curve data impacts the calculated deformation rates and recurrence intervals obtained (Chapter 5). The findings of this analysis showed that whilst some variation of uplift rates occurs when different sea-level curves are used, that the magnitude of this variation is comparable to the propagated uncertainties of using a single sea-level curve.

Deformation rates, recurrence intervals and tectonic explanations are proposed in relation to the faults that effect the palaeoshorelines along the south of Crete (Chapter 4) and Cape Heraion on the Perachora Peninsula (Chapter 6). These settings display palaeoshorelines that are deformed over length scales comparable with crustal-scale normal faulting and provide evidence that such faults have the capacity to strongly influence the observed coastal deformation over hundreds of thousands of years. In both of the locations examined, regional subduction-related processes have been suggested to cause the palaeoshoreline deformation (Leeder et al., 2003, 2005; Gallen et al., 2014). This thesis shows, however, that

upper-plate normal faulting appears to be the dominant process. Furthermore, the settings herein also provide geomorphological evidence of across- and along-strike fault interaction that have become apparent following analysis of the deformation of the palaeoshorelines. In south central Crete, evidence of across-strike interaction between faults appears to be visible where the deformation gradient in the hangingwall of the SCCF has been shallowed by uplift from the footwall of another upper-plate extensional fault. In the western tip of the SAFS on Cape Heraion identification of anomalously high slip rates, and thus steep fault displacement gradients, are attributed to stress interaction between two crustal faults whose tips overlap. Observations from other extensional fault systems reveal that along-strike overlapping tip zones are common place (e.g. central and southern Apennines – Italy and Basin and Range – western USA). In such locations away from sea level, transverse bedrock ridges occupy tip zones. These bedrock ridges are typically comprised of uniform pre-rift lithologies and have been suggested to act as fault zone segment boundaries (Crone and Haller, 1991). The absence of Quaternary sediments associated with transverse bedrock ridges means that identifying distributed, small-scale active faulting may be particularly difficult. As such, tip zone observations as detailed as those herein over Late-Quaternary timescales are particularly lacking and represent a gap in the literature that requires further investigations. The outcome from this study (Chapter 6) suggests that where faults are co-located along-strike, interaction may only be apparent when distributed faulting is taken into account over long timescales. Such findings have implications on the data used in PSHA, this is further explored in Section 8.4.

The findings of the research from this thesis open up new avenues of research that are the subject of this chapter, specifically, (i) application of ^{36}Cl exposure dating to wave-cut platforms, (ii) the tectonics of subduction zones and (iii) seismic hazard assessment related to the maximum magnitude of possible earthquakes along the south coast of Crete, and the relationship between slip rates and expected earthquake rates and probabilities; these are explored below.

8.2 Application of ^{36}Cl exposure dating to Late-Quaternary wave-cut platforms

The success of ^{36}Cl exposure dating on wave-cut platforms outlined in this thesis provides greater opportunities to constrain the ages of wave-cut platforms that may, hitherto, have been difficult to date using other methods. Prior to this study, the application of ^{36}Cl

exposure dating to Quaternary wave-cut platforms had yielded mixed results. Some of these previous ^{36}Cl studies (Wegmann, 2008; Spampinato, 2011; de Gelder, 2017) documented limited explanations as to the rationale for sampling locations, with no specific attempts to identify potential sites for ^{36}Cl sampling with low erosion rates based upon wave-cut features. The exception was Meschis (2019) who sampled from close to millholes but unfortunately obtained erroneously young ages. In contrast, the ^{36}Cl exposure ages obtained herein are suggestive of Late-Quaternary palaeoshorelines ages specifically because samples sites have low erosion rates indicated by lithophagid and millhole preservation. It is recognised that the age uncertainties are larger relative to, for instance, ^{234}U/^{230}Th dating, but the ages obtained agree with existing and new age controls and with the expected ages of palaeoshorelines obtained from synchronous modelling using sea-level curve data.

The approach applied in Chapters 4 and 6 (Section 3.3.1) detailed a sampling strategy whereby samples were removed from wave-cut platforms that displayed evidence of low erosion based upon observations of millholes and lithophagid borings, were away from potential contamination from sea spray and with consideration given to wave-cut platform sedimentary cover. As the preservation potential across an entire wave-cut platform may vary, it is advised that sampling occurs as near to the observed low erosion features as possible. Knowledge of the original depths of lithophagid borings and of millholes measured beneath the overall wave-cut platform surface allows the erosion since their formation to be estimated, specifically establishing that values of erosion that approach or exceed the point at which spallation is no longer the dominant production pathway (~2 m of total erosion) will likely yield erroneous ages (Section 2.1.4.2).

The oldest palaeoshoreline dated herein is the 125 ka palaeoshoreline, where total erosion values of 12.5-812.5 mm exist (0.1 mm/ky on basement limestone/packstone from Crete and Perachora to 6.5 mm/ky on algal bioherms on Perachora, Chapters 4, 6). This evidence suggests that wave-cut platforms cut into basement limestone, packstones and algal bioherms that formed during or after the 125 ka highstand may provide acceptable ages using ^{36}Cl exposure dating, provided that erosion rates can be constrained and maximum uplift rates are comparable or less to those identified herein of 0.9 mm/yr (Profile 4, Chapter 4). Significantly higher uplift rates would result in palaeoshorelines at higher elevations, where they may be exposed to increased rates of erosion – such as freeze-thaw processes during the LGM – which may make ^{36}Cl exposure dating of the same age (76.5-125 ka) palaeoshorelines difficult. Evidence of the effect of palaeoshorelines at higher elevations,

specifically older palaeoshorelines, was outlined in Section 3.3.3 following analysis of ^{36}Cl exposure ages obtained from the footwall of the SCCF (>336 m). The apparently 'young' and erroneous ages obtained from the footwall samples (33-65 ka, Table 3.2) provide evidence of the effect of erosion on palaeoshorelines at relatively high elevations.

In order to explore the application of ^{36}Cl exposure dating to older palaeoshorelines, an analysis of the total potential erosion for limestone/packstone wave-cut surfaces is undertaken based upon the rates of erosion identified herein (Fig. 8.1). The results show that the capacity of higher and older wave-cut platforms to yield acceptable ages is dependent on (a) the erosion rates and (b) the age of palaeoshoreline in question. For example, Fig. 8.1 shows that a palaeoshoreline and associated 10 cm deep lithophagid boring exposed to erosion rates of 0.8 mm/ky would be fully eroded after ~130 ky. In comparison, if the erosion rates were lower – 0.4 and 0.2 mm/ky – it is possible that lithophagid borings may be preserved on older palaeoshorelines up to ~ 240 ka and beyond 400 ka, respectively. This analysis assumes erosion rates derived from the 125 ka sample reported herein. These results suggest that where rates of erosion are equal to 0.8 mm/ky, only palaeoshorelines that formed during 125 ka (or younger) have the capacity to host some evidence of lithophagid borings, and thus may be amenable to ^{36}Cl exposure dating. At lower rates of erosion (0.4 and 0.2 mm/ky) older palaeoshorelines may also host evidence indicative of low erosion. The reality, however, is that rates of erosion are unlikely to be linear throughout time, owing to increased rates during glacial periods. Thus, wave-cut platforms with ages in the region of 200 ky, 240 ky, 340 ka and beyond, that experience similar or higher uplift rates to those used in Fig. 8.1, may be subject to higher rates of erosion because they will have been subject to (a) more total uplift and be at higher elevations (Tucker et al., 2011) and (b) multiple glaciation and warming periods.

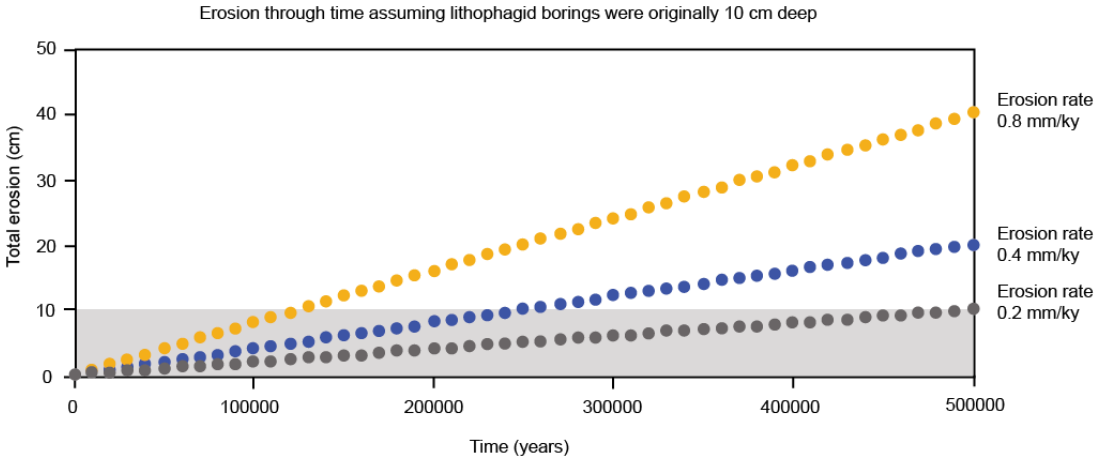

Figure 8.1: Values of total erosion through time based on the erosion rates identified herein, assuming the erosion rates remain constant over time. Grey band is the maximum depth of lithophagid borings at formation.

At erosion rates higher than those tested in Figure 8.1 (>0.8 mm/ky) the potential for older palaeoshorelines to host any low erosion indicators is particularly low. A lack of such indicators means that erosion rates cannot be estimated and that the ages derived may be significantly in error. The success of ^{36}Cl exposure dating on wave-cut platforms presented in this thesis is considered in the context of the study of de Gelder (2017) who obtained 22 ^{36}Cl exposure ages from eastern Crete from five different palaeoshorelines (Table 2.2). When a sequence of palaeoshorelines are being dated, it is expected that the age and ^{36}Cl concentration increase with elevation because higher and older palaeoshorelines have been exposed to bombardment of high-energy neutrons for more time (as per the results from Profile 4, Chapter 4; Fig. 8.2).

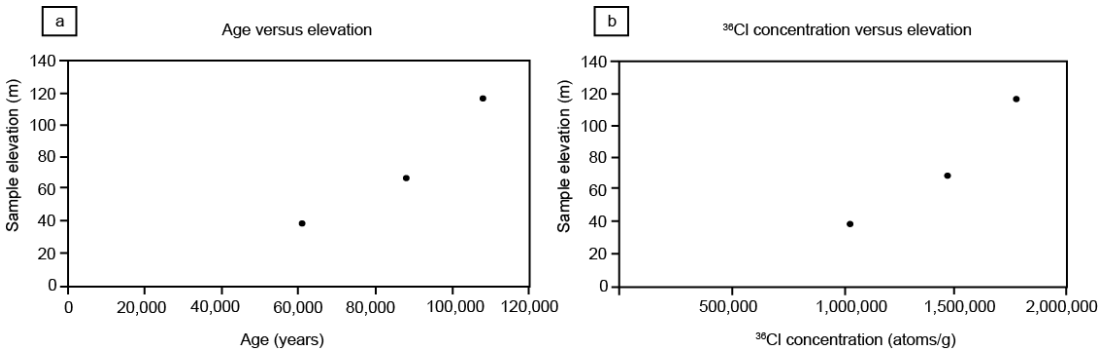

Figure 8.2: Plots of (a) ^{36}Cl exposure age vs elevation and (b) ^{36}Cl concentration vs elevation for samples S3, S4 and S5 from (Profile 4, Fig. 4.4a, Chapter 4) removed from successive palaeoshorelines in the footwall of the Ptolemy fault.

Analysis of ^{36}Cl exposure data from de Gelder (2017) shows that plots of ^{36}Cl exposure ages versus elevation and concentration of ^{36}Cl versus elevation (Fig. 8.3) do not reveal the relationships shown in Fig 8.2 (the data were analysed for each individual lithology sampled).

Rather, there is no observed relationship between age/^{36}Cl concentration and elevation. It could be speculated that one of the reasons for this may be that the higher and older palaeoshorelines have experienced significant enough erosion such that the samples were removed from a depth relative to the original surface that approaches or exceeds 2 m, whereby the ^{36}Cl production rates are significantly lower and spallation is no longer the dominant production pathway. In other words, sample sites were not selected based upon direct observations that support low erosion rates.

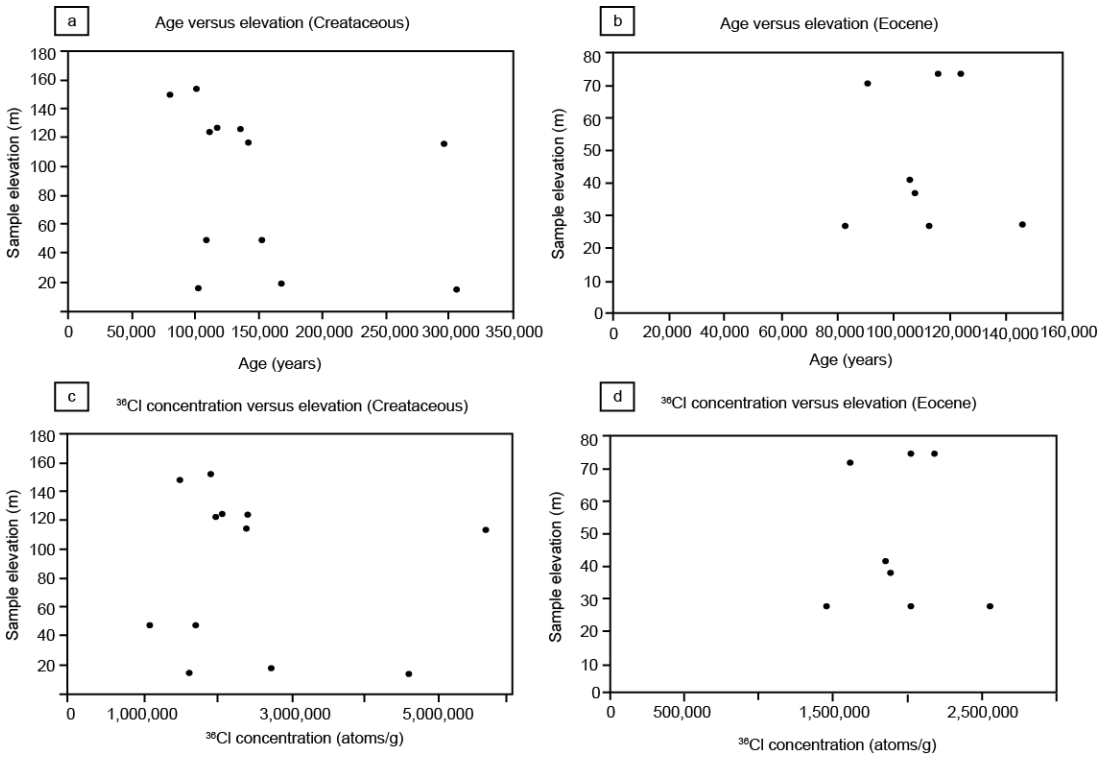

Figure 8.3: Plots of ^{36}Cl exposure age vs elevation from de Gelder (2017) for the (a) Cretaceous bedrock and (b) Eocene bedrock samples and ^{36}Cl atoms/g vs age for the (c) Cretaceous bedrock and (d) Eocene bedrock samples.

The application of this method to constrain the ages of Late-Quaternary platforms is still in its relative infancy. I suggest that the success of ^{36}Cl exposure dating in this thesis, observed because age controls from other independent methods agree with those from ^{36}Cl exposure dating, is as a direct result of the outlined sampling protocol, whereby preserved lithophagid borings and millholes are used as indicators of low erosion, and thus satisfactory sampling sites. The successful application of ^{36}Cl exposure dating to three types of carbonate lithology – bedrock limestone, bioclastic packstone and algal bioherms is suggestive that this method has the potential to be widely applied throughout the Mediterranean where carbonate platforms are prevalent along palaeoshorelines, with consideration given to sampling from lower palaeoshorelines and, where possible, those with a 125 ka age or younger. Presently,

research to examine the reliability of ^{36}Cl exposure ages on higher and older palaeoshorelines is being undertaken using ^{36}Cl exposure dating on other palaeoshorelines that parallel the WHSZ (the author is awaiting the results of 37 ^{36}Cl exposure samples from SUERC).

8.3 TECTONICS OF SUBDUCTION ZONES

Subduction zones in many places throughout the world display uplift along the coastlines that run parallel to the subduction interface. Rates of convergence may be high such that slip on the subduction interface is suggested to be the dominant cause of coastal uplift (e.g. Mouslopolou et al., 2016), though high slip rates have also been attributed to subducting sea mounts and slab bending (e.g. Abercrombie et al., 2001: Yang et al., 2012; Nishikawa and Ide, 2015). The findings of this thesis show that subduction zones and the coastal uplift observed along their leading edges are complex. Extensive investigations on the field sites herein (south Crete and Cape Heraion, Greece) link observations of the structural geology related to upper-plate extensional faulting with those on deformed palaeoshorelines and the results of modelling elastic fault interaction. This thesis emphasises that palaeoshoreline uplift rates change along strike in accordance with footwall uplift and hangingwall subsidence on upper-plate extensional faults. Similar tectonic complexities to those identified in this thesis have been observed at other subduction zones, for example palaeoshoreline deformation caused by normal faults has been observed in southern Italy (Roberts et al., 2013; Meschis et al., 2018), S. America (Saillard et al., 2011; Binnie et al., 2016; Jara-Munoz et al., 2017), Japan (e.g. Matsu'ura et al., 2014, 2015) and New Zealand (Litchfield et al., 2020). Furthermore, there is evidence to suggest that upper-plate normal faults have ruptured in response to large subduction earthquakes; a study by McKenzie and Jackson (2012) highlight such examples from the Tohoku 2011, Nicaragua 1992, Java 1994 and Mentawi 2010 earthquakes. The findings presented in this thesis therefore have implications on investigations and understanding of deformation along subduction zones, particularly where uplift rates derived from palaeoshoreline deformation are directly linked to slip on the subduction interface; this is explored below for the broader WHSZ, the Japan and the south Peru-Chile subduction zones.

8.3.1 Western Hellenic subduction zone

The WHSZ hosts convoluted subduction (Fig. 2.29) where shallow-dipping subduction occurs under the Mediterranean ridge at distances that vary between ~220 and ~400 km from the

coastline of Greece (Kreemer and Chamot Rooke, 2004). The WHSZ has been shown to host normal, reverse and strike-slip faulting in the upper plate in addition to earthquakes on the subduction interface (e.g. Wyss and Baer, 1981; Papazachos, 1990; Ten Veen & Kleinspehn, 2003; Alves et al., 2007; Papanikolaou et al., 2007; Shaw et al., 2008; Ganas and Parsons, 2009; Kokinou et al., 2012; Papoulia et al., 2014; Konstantinou et al., 2016; Sachpazi et al., 2016; Howell et al., 2017). Analysis of fault plane solutions throughout Greece between 1976-2015 at depths of less than 40 km show that principal crustal stresses along the coast of the WHSZ are heterogeneous, whereby strike-slip faulting dominates the north western coastline, which migrates to normal faulting along the coastlines of the western Peloponnese and southern Crete, whilst thrust faulting is evident offshore (Konstantinou et al., 2016) (Fig. 8.4).

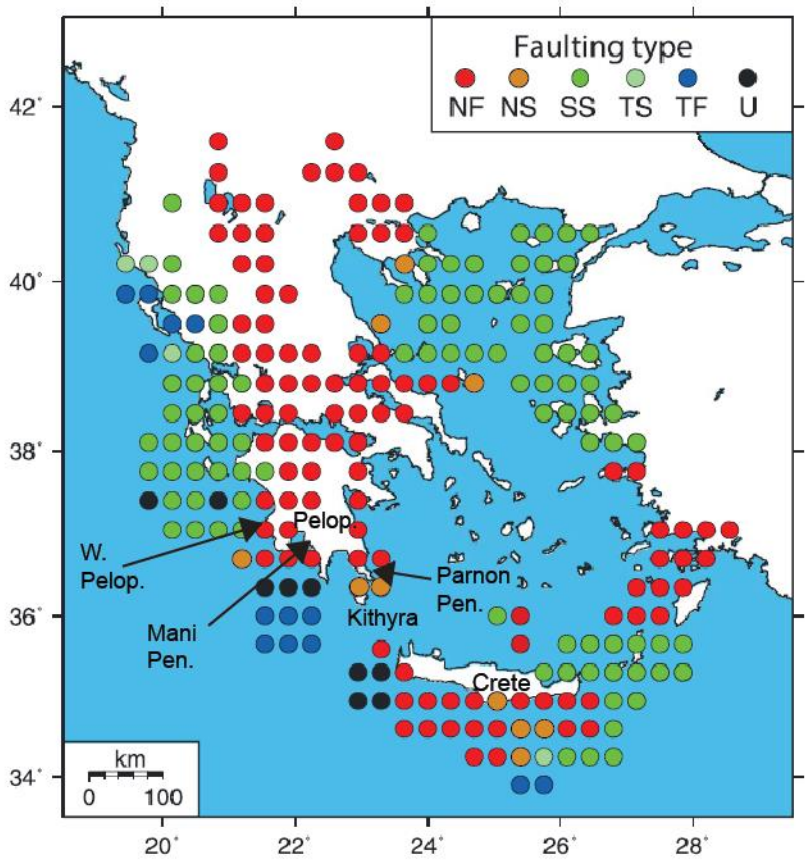

Figure 8.4: Map showing the faulting regime for parts of Greece based on analysis of the crustal fault plane solutions, NF = normal faulting, NS = normal and strike slip faulting, SS = strike slip faulting, TS = thrust and strike slip faulting, TF = thrust faulting and U = unclear (modified from Konstantinou et al., 2016). Location names are referred to in the text, W. Pelop: Western Peloponnese; Mani Pen: Mani peninsula, Parnon Pen: Parnon peninsula.

Chapter 4 showed that the observed upper-plate faulting in southern Crete results in uplift changes indicated by deformed palaeoshorelines occurring over the length scale of upper

crustal extensional faults (20-50 km and ~90 km in the case of the Ptolemy fault) rather than the length scale of the subduction interface (100s of km). If normal faults are a controlling factor on uplift along the coast parallel to the WHSZ in a similar way to those along southern Crete, then (i) the locations of known normal faults should coincide with sequences of palaeoshorelines, and (ii) palaeoshorelines would be expected to show deformation patterns representative of the displacement patterns associated with normal faulting; this is briefly explored below.

Normal faults have been shown to result in footwall uplift up to half the length of the fault away from the footwall cut off (Section 2.2.1, Fig. 2.17a) (Stein and Barrientos, 1985); therefore, knowledge of the kinematics, fault length and their location relative to the Greek coastline may be used to infer whether a fault is capable of causing coastal uplift. The traces of upper-plate faults located close to the Greek coastline (that runs parallel to the WHSZ) have been obtained from the NOA FAULTS version 3 database (Ganas et al., 2013), a database for active Greek faults. The faults, their uplift areas and the locations of known palaeoshorelines from the literature (Kelletat et al., 1976; Angelier, 1979a; Papanikolaou et al., 2007; Tsimi et al., 2007; Caputo et al., 2010; Gaki-Papanastassiou et al., 2011; Athanassas & Fountoulis, 2013; Gallen et al., 2014; Ott et al., 2019; Robertson et al., 2019) are shown on Fig. 8.5. Palaeoshorelines appear to be co-located with mapped normal faults whose footwalls are capable of perturbing the coastline and reveal length scales that are similar to the faults. The location of the faults also coincides with the extensional areas identified in Fig. 8.4, namely, south and south western Crete, Kythira, the Mani Peninsula and the western coast of the Peloponnese (Fig. 8.5).

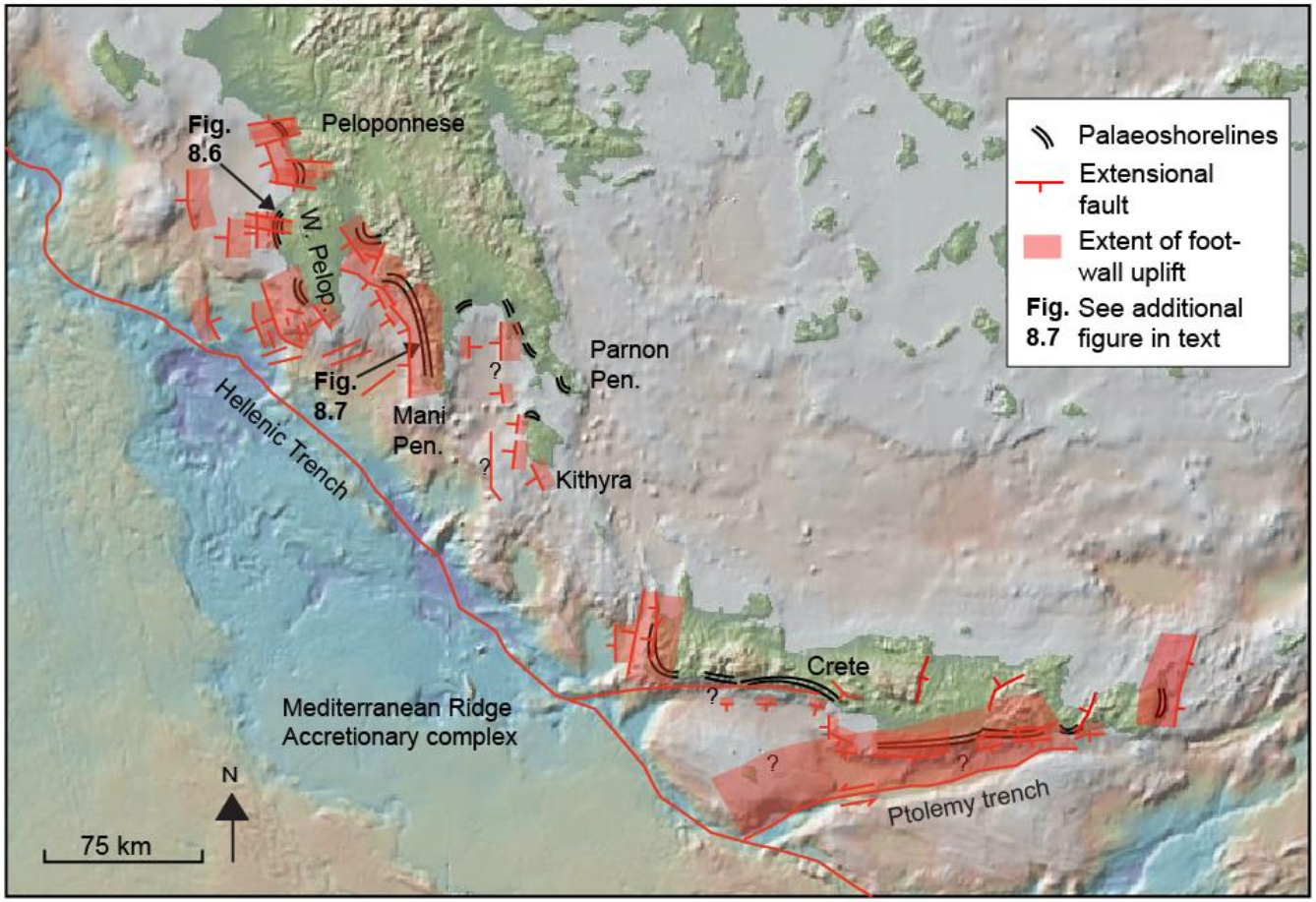

Figure 8.5: Reported locations of palaeoshorelines and faults along the coastlines of southern Crete, Kythira, the Mani Peninsula, Parnon Peninsula and the western Peloponnese. Faults from NOA fault database, version 3 (Ganas et al., 2013), palaeoshorelines from Kelletat et al. (1976); Papanikolaou et al. (2007); Tsimi et al. (2007); Gaki-Papanastassiou et al. (2011); Papanikolaou et al. (2011); Athanassas & Fountoulis (2013); Gallen et al. (2014); Robertson et al. (2019). W. Pelop: western Peloponnese, Mani Pen: Mani peninsula, Parnon Pen: Parnon peninsula. Arrows and figure references refer to subsequent figures in this chapter. Faults and their footwall uplift extent are shown assuming that footwall uplift perpendicular to the strike of the fault is ~0.5 x length (Stein and Barrientos, 1985). The extent of the 'footwall' uplift in the Ptolemy transtensional fault is less understood, the location of uplift influence is tentatively based upon the coseismic model of uplift from a rupture along the Ptolemy fault in Chapter (Fig. 4.16a).

Investigating each of these extensional areas further, it can be shown that at least some of these examples have palaeoshoreline geometries reminiscent of those expected from the influence of normal faulting rather than subduction interface slip. A study along the western Peloponnese coastline (Athanassas and Fountoulis, 2013) (Fig. 8.5, 'W.Pelop') showed that five palaeoshorelines are present, which are associated with MIS 5 (125 ka), 7 (200/217/240 ka) and 9 (310/340 ka) (Fig. 8.6a). A 35 m-along-strike topographic profile along the MIS 7 palaeoshoreline displays higher topography in the centre of the palaeoshorelines decreasing to low topography at the northern and southern limits of the palaeoshoreline sequences (Fig. 8.6b) (Athanassas and Fountoulis, 2013). Assuming the topographic profile is representative of uplift rates that are higher in the centre and lower at the northern and southern limits of the palaeoshorelines then this uplift pattern may represent footwall uplift from an offshore fault identified by Papanikolaou, D. et al. (2007). The offshore fault trends parallel to this coastline (Fig. 8.5) and has been suggested be a normal fault that displaces Holocene shelf deposits and dips to the west (Papanikolaou, D. et al., 2007).

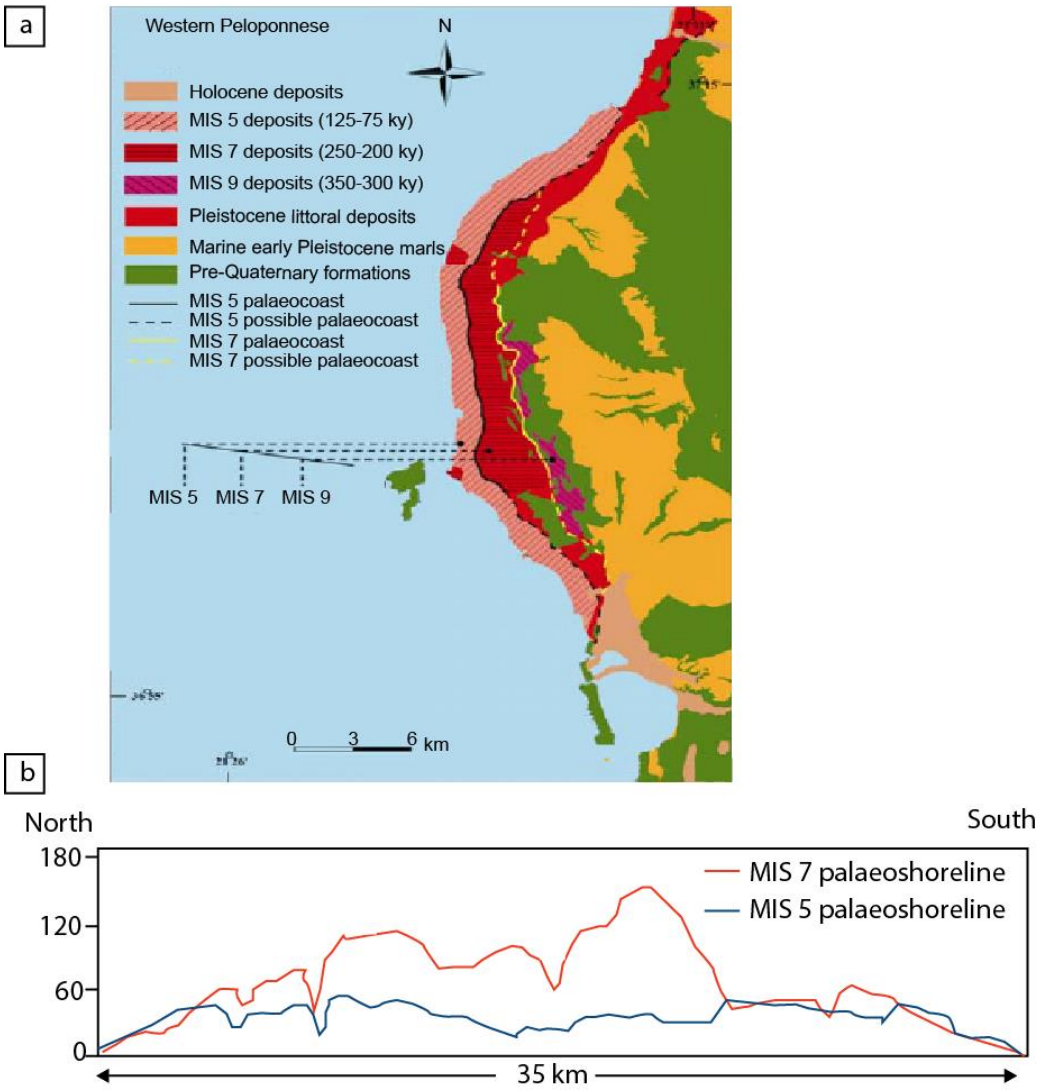

Figure 8.6: (a) Palaeoshorelines on the western Peloponnese. (b) North-south topographic profiles of the MIS 7 and 5 palaeoshorelines taken along the palaeoshoreline MIS 7 deposits (250-200 ky) (Modified from Athanassas and Fountoulis, 2013). Location of this is shown in in Fig. 8.5.

In some of the extensional areas in Fig. 8.5, knowledge of the deformation patterns on sequences of palaeoshorelines is limited, for instance, while palaeoshorelines have been documented along the Parnon and Mani Peninsulas (Fig. 8.5) (Kelletat et al., 1976; Sabatakakis et al., 2016), spatial patterns of palaeoshoreline uplift in these areas are not yet known. Along the Mani Peninsula (Fig. 8.5, 'Mani Pen'), brief interrogation of the onshore topography (using a 5 m DEM) parallel to the strike of the offshore normal fault reveals that topography appears to increase toward the centre of the peninsula and decrease in the northern and southern areas over a length of ~55 km, possibly representative of a footwall uplift pattern (Fig 8.7). A segmented west-dipping offshore normal fault is suggested to parallel this coastline (Fig. 8.5). If the topographic profile represents a pattern of uplift, then this would be in agreement with the expected footwall displacement from the offshore fault.

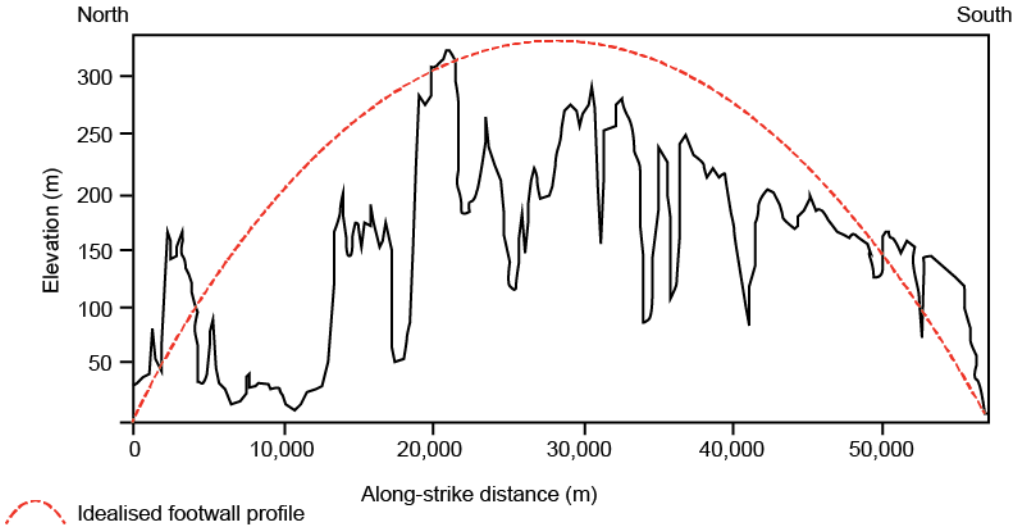

Figure 8.7: North-south topographic profile of the Mani Peninsula (Fig. 8.5). The topographic profile is taken parallel to the strike of the palaeoshorelines identified in Fig. 8.5 and broad similarity compared to the idealised footwall topography of highest uplift in the centre of the fault (Section 2.2.1).

Along south western Crete (Fig. 8.5), palaeoshorelines occur in the hangingwalls of onshore normal faults (Tsimi et al., 2007; Ott et al., 2019) (Fig. 2.29c, Faults: Sf and Sa/A). However, the source of their uplift is less clear because this location is subject to the effects of an offshore fault whose mechanism is debated (Ott et al., 2019), in combination with a possible upper-plate reverse fault that is suggested to be the source of the 365 C.E. Mw 8.2 megathrust earthquake (Shaw et al., 2008), the presence of which is also debated (Ganas and Parsons, 2009). So while it is clear that the hangingwalls of the active faults are being uplifted and deformed, it is not apparent what the cause of the uplift is because knowledge of the along-strike deformation pattern associated with the palaeoshorelines is lacking.

Based upon the observations in this section, it is plausible that the some of the deformation of the WHSZ palaeoshorelines (Fig. 8.5) may be linked to onshore and offshore normal faulting, but further research is necessary especially regarding south western Crete, western Crete the Mani and Parnon Peninsulas. The WHSZ would benefit from the application of the approach detailed in this thesis in order to firstly determine the patterns of palaeoshoreline deformation and then explore the cause of the deformation using elastic half-space modelling. Furthermore, these locations suffer from a lack of age controls but have been shown to host carbonate surfaces that occur coevally with the locations of palaeoshorelines (e.g. IGME 1:50,000 Koroni-Pylos-Skhiza sheet; IGME 1:50,000 Mavrovoynion-Areopolis-Yerolimin sheet; Athanassas and Fountoulis, 2013; Gallen et al., 2014; Sabatakakis et al., 2015; Ott et al., 2019) making them potential candidates for ^{36}Cl exposure dating.

8.3.2 Subduction zones bounding the south of Japan

Late Quaternary palaeoshorelines are documented along the eastern and southern coasts of Japan (Ota and Omura, 1992 *and references therein*), parallel to the Japan trench (which hosted the 2011 Tohoku earthquake) and the Nankai trough (which hosted Mw 8.1 and 8.4 earthquakes in 1944 and 1946, respectively) (Matsu'ura et al., 2014, 2015) (Fig. 8.8). Plate convergence along the Japan trench and Nankai trough is accommodated via large subduction zone earthquakes and forearc reverse faulting suggesting that the dominant tectonic regime is compressional (e.g. Umeda et al., 2015; Lin et al., 2016; Matsu'ura et al., 2019). However, one month after the 2011 Mw 9.0 Tohoku earthquake, a shallow normal-faulting earthquake sequence (Mw 6.6, 11 April 2011 Iwaki earthquake) in the forearc of the Japan trench resulted in two 15 km long surface ruptures (Imanishi et al., 2012; Toda and Tsutsumi, 2013) (Fig 8.8). Investigations into the normal faulting sequence suggest that while stress transfer from the Tohoku megathrust contributed to the rupturing of the upper-plate normal faults, the stress regime in existence in this area prior to the megathrust was extensional and not compressional (Imanishi et al., 2012; Toda and Tsutsumi, 2013; Lin et al., 2016). Furthermore, normal faults have also been shown to occur in part of the forearc basin adjacent to the Nankai trough (Moore et al., 2013), where an extensional stress regime has been identified (Lin et al., 2016) (Fig. 8.8). 3D seismic analyses of parts of the forearc adjacent to both the Nankai trough and Japan trench reveal that horizontal compression dominates at deeper levels but at shallow levels (<8 km), an extensional regime is apparent (Umeda et al., 2015; Lin et al., 2016); it is interesting that this tectonic regime bears some similarities to those seen along the south of Crete (e.g. Kokinou et al., 2012).

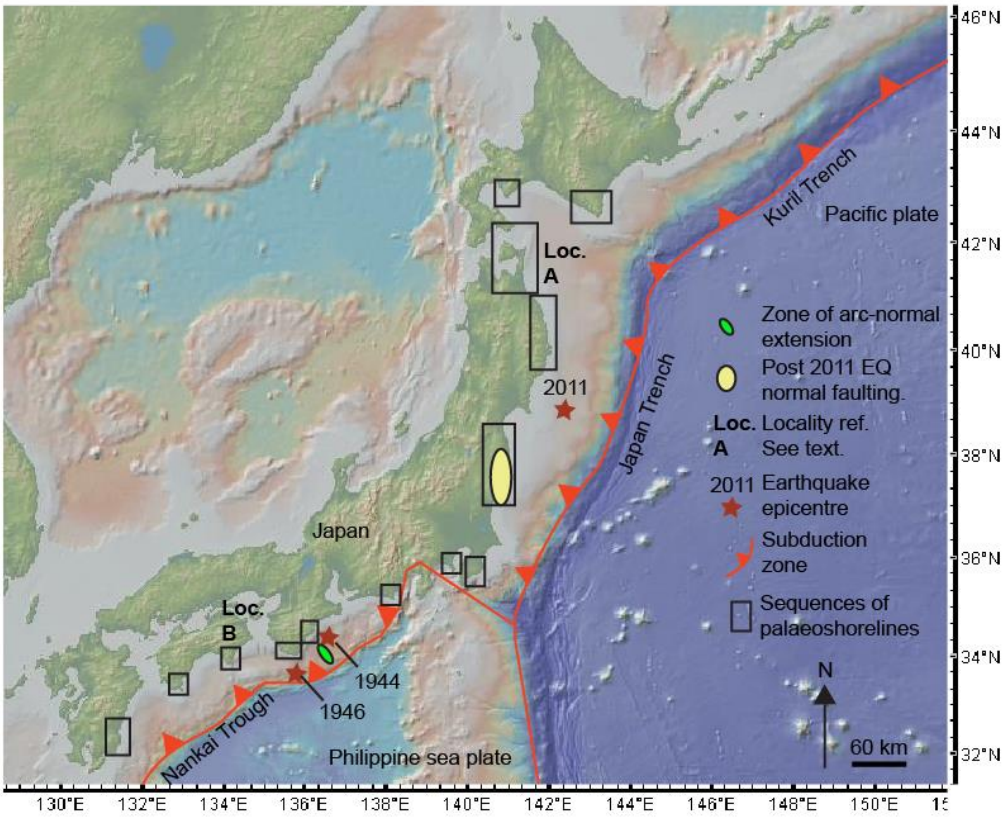

Figure 8.8: Map of Japan (from GeomapApp: http://www.geomapapp.org) showing the subduction zone (Matsu'ura et al., 2014), megathrust earthquake epicentres (Matsu'ura et al., 2014; 2015), locations of palaeoshorelines (Miyoshi, 1983; Kumaki, 1985; Matsu'ura et al., 2014; 2015; 2019) and zones of known extension (Lin et al., 2016) and upper plate normal faulting following the 2011 Tohoku earthquake (Imanish et al., 2012). Localities A and B are discussed in the text.

The evidence presented above suggests that in the forearc of the Japan subduction zone, normal faulting occurs in addition to subduction interface earthquakes and reverse faulting; implying a complex tectonic regime. Studies on palaeoshorelines adjacent to the Japan subduction zone (Fig. 8.8, Loc. A and B) (Matsu'ura et al., 2014; 2015; 2019) provide insight to palaeoshoreline deformation that displays along-strike differential uplift which occurs on relatively short length scales (<25 km). The studies of Matsu'ura et al., (2014) and Matsu'ura (2015) propose that upper-plate reverse faults have a controlling relationship on the deformation of these coastal palaeoshorelines. Both of the aforementioned studies calculated uplift rates for each palaeoshoreline, as per the sequential method; the authors of the studies were unable to assign palaeoshorelines to specific sea-level highstands and instead relied upon correlating a palaeoshoreline to a broader MIS.

Based on the conclusions made by Lin et al., (2016) and Imanishi et al. (2012) that parts of the upper forearc of the Nankai trough and Japan trench are dominated by extensional stress fields, it would be interesting to explore whether the palaeoshorelines adjacent to areas of extension display any

evidence of deformation from normal faults using the approaches applied in this thesis. Namely the application of synchronous correlation, dating and half-space elastic modelling to further investigate along-strike changes of palaeoshoreline uplift rates within the context of upper-plate faulting and subduction.

8.3.3 Peru-Chile Subduction zone

Along the Peru-Chile trench (Fig. 8.9a), adjacent to the Nazca ridge (an aseismic ridge that is elevated above the surrounding sea floor), sequences of palaeoshorelines are being uplifted as a result of regional subduction related processes in combination with multiple onshore normal faults that displace the palaeoshorelines (Saillard et al., 2017, *and references therein*). This section examines the approach used by Saillard et al. (2011) to investigate the deformation of the southern Peru palaeoshorelines. Palaeoshorelines in the hangingwall and footwall of the normal faults have been dated using absolute ages obtained from ^{10}Be exposure dating on wave-cut platforms. In much the same way as the ^{36}Cl exposure dating carried out herein, the ^{10}Be ages obtained by Saillard et al. (2011) have relatively large error values and thus the ages may be allocated to more than one sea-level highstand. For instance, one of the ages they obtained was 228 ± 28 ka for a palaeoshoreline at ~150 m. Thus the 150 m palaeoshoreline could belong to a sea-level highstand between the ages of 200 and 256 ka (namely the 200, 217 and 240 ka highstands of Siddall et al. (2003)). In much the same way, the palaeoshoreline at +190 m was dated at 318 ± 37 ka, which could belong to the 285, 310 or 340 ka highstands of Siddall et al. (2003). In their study, Saillard et al. (2011) allocated the dated palaeoshorelines to the highstands with the age that is closest to the absolute age obtained.

Once the authors had allocated the dated palaeoshorelines to highstands, the remaining undated palaeoshorelines were correlated on the basis of the sequential method (Section 2.1.5). This was carried out for two profiles located ~15 km from one another (Fig 8.9a). The correlation between the palaeoshorelines and the highstands on both topographic profiles revealed uplift values that varied throughout time for each palaeoshoreline (Fig. 8.9b), in much the same way as those from Gallen et al. (2014) varied through time along the southern Cretan coastline.

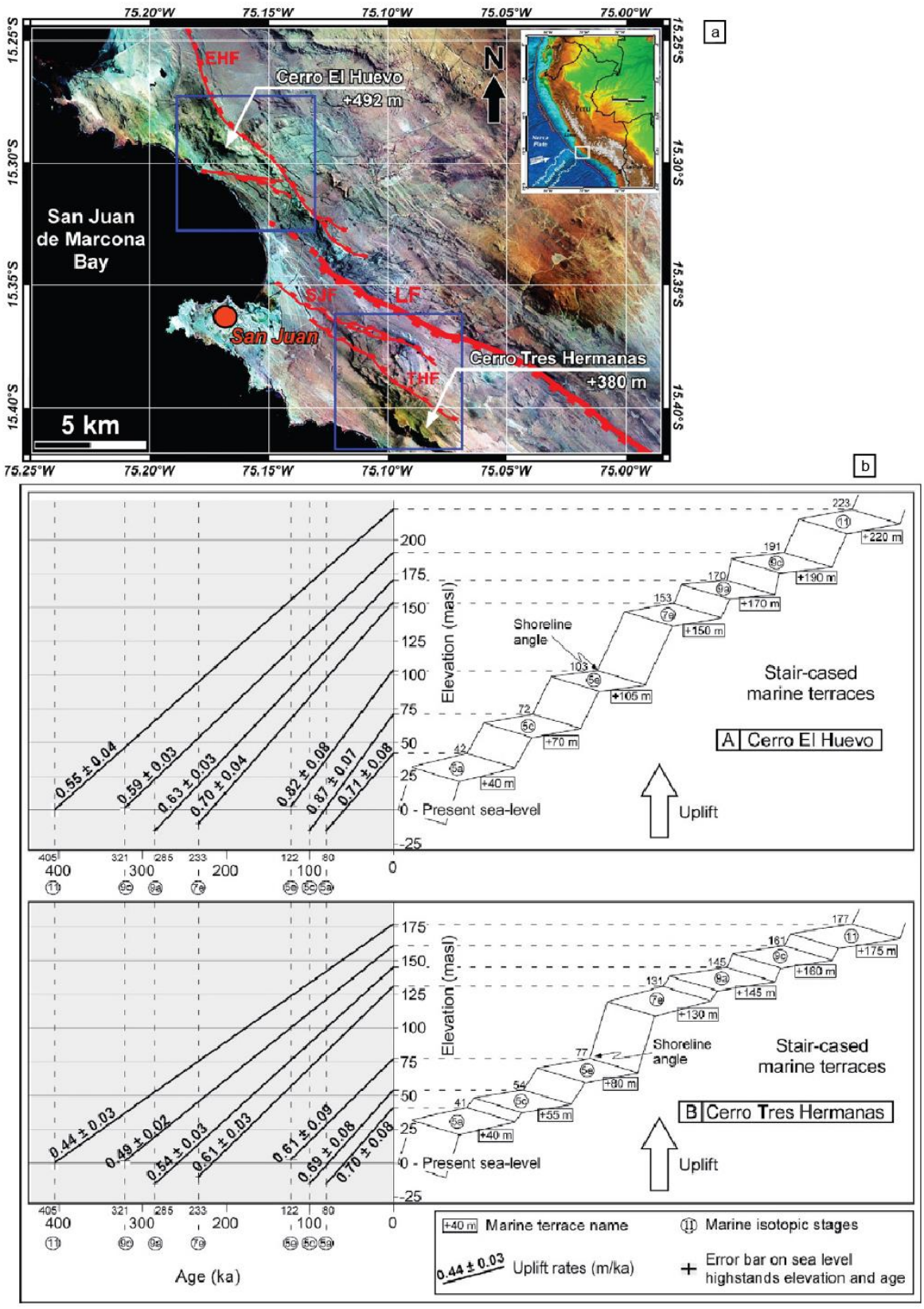

Figure 8.9: (a) Map of the area and faults investigated by Saillard et al. (2011). (b) Palaeoshoreline correlation for the El Huevo and Tres Hermanas palaeoshorelines, ages and magnitudes of sea-level highstands used to calculate uplift rates are from Siddall et al. (2006), locations of these palaeoshorelines are in (a).

It is clear that uplift in this area is complex, especially as there are multiple faults that cut the palaeoshorelines within a ~20 km along-strike area (Fig. 8.9a). But it is not clear as to what extent the uplift rates observed at this location are as a result of temporal variability of the slip/throw rates on the normal faults and subduction-related uplift or a function of correlation using the sequential method. In light of the fact that Saillard et al. (2011) use the findings of their study to suggest that the palaeoshoreline offsets from normal faults are directly associated with seismic events linked to subduction zone activity, further investigation using the methods applied in Chapter 4 would be of benefit to this area; specifically the analysis of palaeoshoreline elevations from multiple serial topographic profiles along the strike of the faulted palaeoshorelines and employment of the synchronous method to correlate both dated and undated palaeoshorelines to highstands.

To summarise this section, the multi-disciplinary approach employed herein to date and correlate palaeoshorelines and determine causes of tectonic uplift could be applied to other areas of the WHSZ, where carbonate palaeoshorelines are known to dominate, to the palaeoshorelines of eastern and southern Japan and the southern coast of Peru. Future work on these subduction zones would allow greater understanding into the potential seismic hazard associated with upper-plate faulting and provide deformation rates that can be used in PSHA.

8.4 UNDERSTANDING THE SEISMIC HAZARD

8.4.1 Maximum magnitude earthquakes in the WHSZ

Along the south of Crete, the WHSZ hosts complex tectonics as evidenced from fault plane solutions (Fig. 2.19) whereby earthquakes occur along the subduction interface and in the upper plate attributed to compressional, transtensional and extensional tectonics (Wyss and Baer, 1981; Mercier et al., 1987; Papazachos, 1990; Ten Veen & Kleinspehn, 2003; Alves et al., 2007; Shaw et al., 2008; Caputo et al., 2010; Kokinou et al., 2012; Yolsal-Cevikbilen and Taymaz, 2012; Konstantinou et al., 2016; Zygouri et al., 2016; Ganas et al., 2017). Debates on the cause of uplift along the coastline of southern Crete continue from the 1980s to the present day (Angelier et al., 1982; Taymaz et al., 1990; Meier et al., 2007; Shaw et al., 2008; Ganas & Parsons, 2009; Caputo et al., 2010; Gallen et al., 2014; Strobl et al., 2014; Tiberti et al., 2014; Mouslopoulou et al., 2015b; Robertson et al., 2019; Ott et al., 2019). A significant number of these aforementioned studies are associated with observations on deformed palaeoshorelines from south western Crete, the location of the Mw 8.2 365 C.E. earthquake. Palaeoshorelines in this area have been suggested to be associated with slip on the subduction interface, an upper-plate reverse fault that splays from the subducting plate, or from a combination

of normal faulting and steady-state regional uplift (e.g. Shaw et al., 2008; Ganas and Parsons, 2009; Ott et al., 2019). These opposing opinions have led to questions associated with the broader tectonics of southern Crete related to the role of upper-plate normal faulting and whether the WHSZ deforms seismically or aseismically and is therefore capable or incapable of hosting large magnitude (> Mw 7.5) subduction interface earthquakes (e.g. Jackson and McKenzie, 1988; Laigle et al., 2002; Papadimitriou and Karakostas, 2008; Ganas and Parsons, 2009; Vernant et al., 2014; Ott et al., 2019). Such debate confounds scientists' ability to accurately constrain the potential seismic hazard of the region.

An aseismic WHSZ (e.g. Jackson and McKenzie, 1988; Vernant et al., 2014) assumes that convergence-based deformation is accommodated aseismically along a subduction zone with low coupling (where coupling is the fraction of motion across the plate boundary accommodated by elastic strain accumulation, Vernant et al. (2014)). In such a scenario, large magnitude historical earthquakes (i.e. Mw 8.2, 365 A.D earthquake) are accommodated on upper-plate reverse faults that splay from the subduction interface and would not be expected along the subduction interface; however, this hypothesis is contested (e.g. Ganas and Parsons, 2009). Contrary to the hypotheses of an aseismic WHSZ there is evidence that earthquakes with magnitudes from Mw 5.5 to ~8.0 have been associated with ruptures on the subduction interface in the WHSZ adjacent to the western Peloponnese, Kythira and Crete (e.g. Wyss and Baer, 1981; Konstantinou et al., 2006; Yolsal-Cevikbilen and Taymaz, 2012; Howell et al., 2017). Furthermore, there is evidence, throughout the world, of uncharacteristic subduction interface ruptures, such that very large megathrust earthquakes occur along subduction zones where they have not been expected, for example the Tohoku 2011 and Sumatra 2004 megathrust earthquakes (Stein and Okal, 2011). This is suggested to be as a result of the fact that large earthquakes occur over timescales that significantly exceed human observations (McCaffrey, 2009). So, where individual segments along, for instance, the Peru-Chile, Sumatran and Japan trenches have been known to rupture, through-going trench-length ruptures were not expected yet occurred in 1960, 2004 and 2011, respectively (Stein and Okal, 2011). McCaffrey (2009) notes that present evidence cannot rule out that any subduction zone may produce a Mw 9 or larger earthquake, and that slow convergence may act to increase the recurrence time on subduction zones such that in a finite time period, slow subduction zones are simply less likely to have a great earthquake. The observations from Stein and Okal, (2011) and McCaffrey (2009) outlined above, in addition to knowledge of previous earthquakes and the Mw 8.2 earthquake that potentially occurred on the WHSZ in 365 A.D. (e.g. Stiros and Papageorgiou, 2001; Konstantinou et al., 2006) prompt consideration that it would be dangerous to accept an aseismic WHSZ scenario and therefore not to consider the potential hazards posed by subduction interface earthquakes along the WHSZ in addition to those from normal faulting.

This section explores the seismic potential of active faults in the region of southern Crete by making use of the empirical fault-scaling relationship that exists between the fault length and the maximum magnitude where log-linear regression between earthquake magnitude and sub-surface rupture length is well correlated (Wells and Coppersmith, 1994) (Section 2.2.4). This relationship allows estimation of the potential maximum magnitude of an earthquake given knowledge of its fault length. Given that evidence suggests that subduction interface earthquakes along the WHSZ have occurred in historical times and that this thesis demonstrates that the presence of active extensional faults along south central Crete appear to control the deformation of palaeoshorelines, it is appropriate to consider the maximum earthquake magnitudes from both subduction interface and upper plate extensional faults. A number of earthquake scenarios are tested (Fig. 8.10, Table 8.1): (i) a full WHSZ 1,221 km rupture, a length that is similar to the 1960 Chilean (Barrientos and Ward, 1990) and 2004 Sumatran (Stein and Okal, 2005) megathrusts; (ii) partial rupture of the WHSZ along the entire southern coastline of Crete (329 km); (iii) partial rupture of the WHSZ from the south central to the south eastern area of Crete (155 km); (iv) rupture of the upper plate Ptolemy transtensional fault which has a length of 94 km; (v) full rupture of the SCCF (49 km), this value is the combined length of all fault segments within the SCCF because the kinematics from this fault suggests it is linked at depth (Gallen et al., 2014); (vi) single segment (western) of the SCCF, 29 km; (vii) Cape Lithino offshore fault (37 km); and (viii) Mirto offshore fault (32 km).

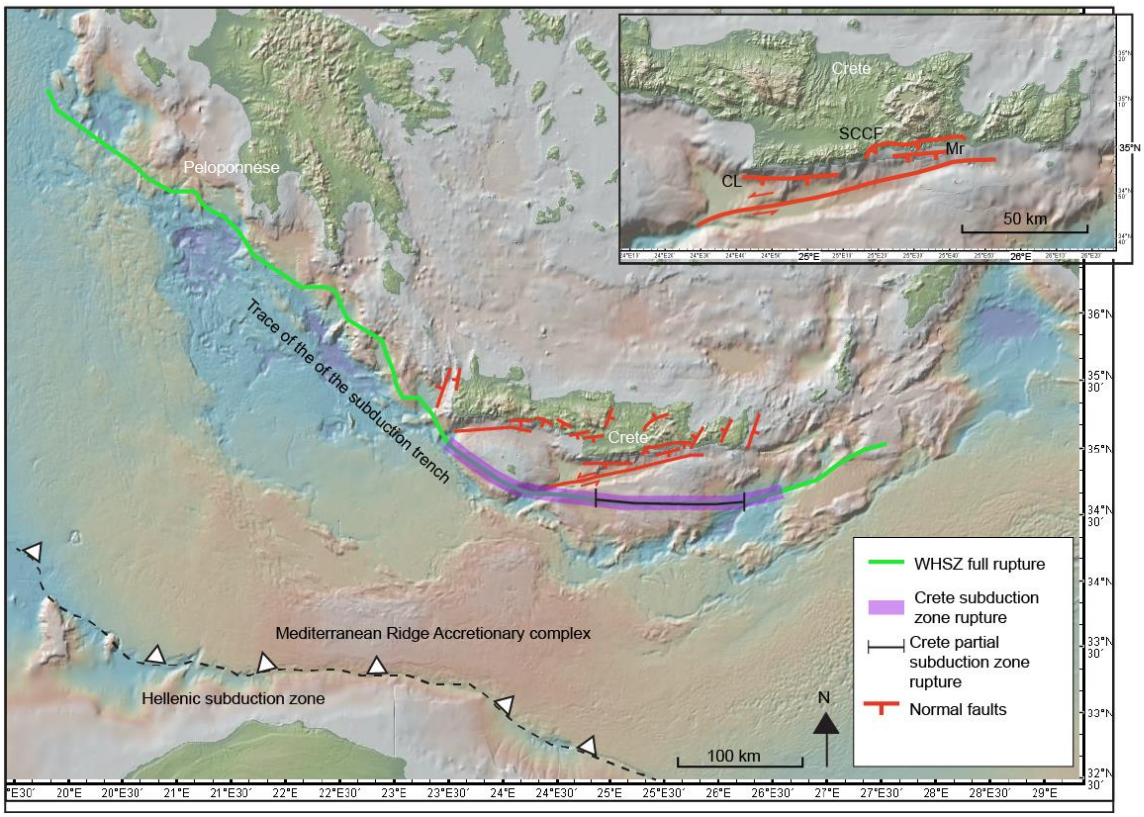

Figure 8.10: Earthquake rupture scenarios for the WHSZ: full subduction zone rupture, Crete subduction zone rupture and eastern Crete subduction zone rupture. Inset: Upper-plate rupture scenarios investigated in Chapter 4.

Rupture area	Fault mechanism	Length (km)	Max. Mw
Whole length of subduction zone	Reverse	1221	9.0
Subduction zone all of Crete	Reverse	329	8.1
Subduction zone S.E. Crete	Reverse	155	7.6
Ptolemy fault	Transtensional	94	7.3
SCCF full	Normal	49	6.9
SCCF single segment	Normal	29	6.6
Lithino*	Normal	32	6.6
Mirto*	Normal	37	6.7

Table 8.1: Maximum magnitudes of earthquake scenarios shown in Fig. 8.10. Fault lengths were from measurements in Chapter 4 and those measured on Google Earth using the subduction trace of Kreemer and & Chamot-Rooke (2004). Max. Mw is calculated using the Wells and Coppersmith (1994) calculation in Section 2.2.4. *It is unclear in the literature whether the Cape Lithino and Mirto faults are each comprised of one fault or two faults; the fault lengths used herein assume they are comprised of one fault linked at depth.

Based on the length of the WHSZ, a whole trench rupture has the capacity to produce a Mw 9.0 earthquake similar to those observed during the Mw 9.0 2011 Tohoku and Mw 8.8 2010 Chile earthquakes. Partial ruptures on the subduction interface south of Crete could result in earthquakes in the region of Mw 7.6-8.1, similar to the reported Mw 8.2 for the C.E 365 earthquake in western Crete (Stiros and Papageorgiou, 2001) (Fig 8.11, Table 8.1). The length of the Ptolemy upper-plate transtensional fault suggests a maximum Mw of 7.3, while the normal faults have the capacity to produce maximum magnitudes between Mw 6-6.9, depending on their measured lengths (Fig 8.11, Table 8.1).

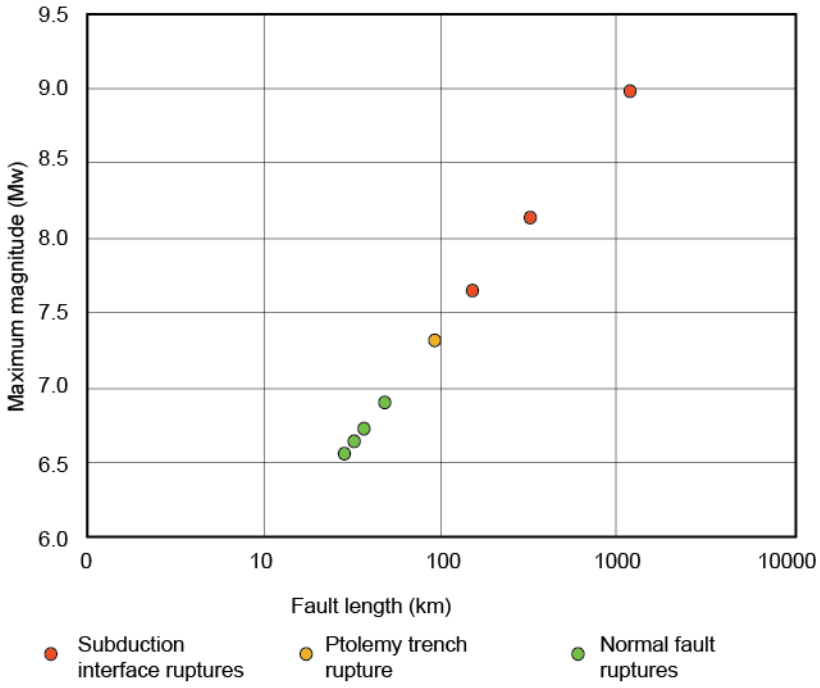

Figure 8.11: Semi-log plot of the seismic potential of active faults along the WHSZ in the region of south Crete based upon the faults in Table 8.1 calculated using fault-scaling relationships from Wells and Coppersmith (1994).

Comparing the range of maximum magnitudes in Table 8.1 and Fig 8.11 shows that there is a significant difference between the magnitudes of whole and partial WHSZ ruptures versus those from upper-plate extensional faults. The very high potential earthquake magnitudes from subduction interface ruptures (Table 8.1, Fig 8.11) show that they pose a severe hazard, if it is accepted that the WHSZ is capable of such events (cf. Jackson and McKenzie, 1988; Vernant et al., 2014). Specifically, subduction interface earthquake events between Mw 7.6-9.0 elsewhere throughout the world have been shown to be linked to catastrophic tsunamis (e.g. Cascadia 1700, Chile 1960, Nicaragua 1992, Sumatra 2004, Tohoku 2011), landslides (e.g. Costa Rica 1950, Chile 2010, Tohoku 2011) and liquefaction (Satake, 1994; Marshall and Anderson, 1995; Satake and Atwater, 2007; Mori et al., 2011; Wartman et al., 2013). In light of the fact that this thesis shows that upper-plate extensional faults in south central Crete exert a controlling influence on the length scale of the deformation of

palaeoshorelines, it may be appropriate to tentatively suggest that earthquakes on upper-plate faults in this region (Mw ≤7.3, Table 8.1) may be more prevalent in comparison to large subduction events. Extensional upper-plate earthquakes with equivalent and lower magnitudes to those identified along south central Crete have been shown to be highly destructive (e.g. Tsapanos, 2003). Analysis of the ground shaking probabilities for moderate versus large earthquakes (Minson et al., 2020) shows that small to moderate earthquakes (up to ~M 5.5-6.5) have the capacity to produce larger than expected ground motion, which significantly contributes to seismic hazard. This finding is linked to the mathematical relationship between the frequency distribution of large magnitude earthquakes compared to smaller magnitude earthquakes; Minson et al. (2018) point out that the chances of a M 5.5 earthquake generating strong shaking (>10%g Peak Ground Acceleration (PGA)) is only 1%, but show that M 5.5 earthquakes occur frequently.

In summary, this section makes use of fault-scaling relationships to investigate the seismic potential along southern Crete, it shows that there are a range of earthquake magnitudes that could impact the southern part of Crete and the wider WHZS and emphasises that while the maximum magnitudes of earthquakes on normal faults are lower than those on subduction interface faults, they may still pose a significant hazard. This finding places importance on constraining the long-term deformation rates associated with the upper-plate extensional faults that not only bound south central Crete but are also found elsewhere along the southern, western and eastern coasts. In order to do this, it is necessary to investigate the relative impacts of slip on the subduction interface versus upper-plate faults. The approach using palaeoshorelines outlined in this thesis may be one way to do this.

8.4.2 The relationship between slip rates and expected earthquake rates and probabilities

In PSHA modelling, computer programmes are used to turn fault data into seismic-hazard models, for example *FiSH* (Pace et al., 2016) and SHERIFS (Chartier et al., 2019). These programmes allow the quantification of earthquake rates and probabilities given known seismic sources. In this section *FiSH* is used to explore the impact of temporal slip rate variability on calculated recurrence intervals (*Tmean*) and expected earthquake rates. This is important because slip/throw rates on faults have been shown to vary spatially and temporally as a result of fault interaction linked to earthquake clustering, partial ruptures owing to stress heterogeneities and in interacting overlapping tip zones (e.g. Bull et al., 2006; Dolan et al., 2007; Luo and Liu, 2012, Cowie et al., 2013, 2017; Mildon et al., 2017; Iezzi et al., 2020; Robertson et al., 2020). Knowledge of temporal slip rate variation may lead to confusion as to which slip rate to apply in PSHA; therefore, it is of benefit to explore how differing temporal slip rates on the same fault affect calculated *Tmean* and expected earthquake rates.

The seismic hazard modelling software *FiSH* (Pace et al., 2016) is a package of MATLAB tools that is based on the assumption that the geometry and kinematic measurements from a fault are directly linked to its seismogenic potential (Pace et al., 2016). Thus, if the fault length, timing of previous ruptures and slip rate of a fault is known, *FiSH* can provide insight into factors such as the long-term recurrence interval (*Tmean*), maximum earthquake magnitude (Mmax), and the expected earthquake rates and probabilities over a set time period (Fig 8.12). *FiSH* software is comprised of a number of work packages – MB (moment budget), RP (recurrence parameters) and AR (activity rates) (Fig. 8.12). The MB tool calculates the seismic moment released in a given time frame. Fault data is input into the MB tool alongside the crustal properties of shear modulus and strain drop (this is defined as the displacement to length ratio of the fault) – these latter two values are pre-set in the MB tool as they have been shown to be constant in a seismotectonic region (Pace et al., 2016 *and references therein*); the user must also select the fault-scaling relationship code, which is set as WC94-N in this analysis representative of Wells and Coppersmith (1994) for normal faults (Section 2.2.4). Output values from the MB tool are used as inputs into the AR tool. In addition, the AR tool requires selection of a magnitude frequency distribution (MFD) model, these are models that describe the likelihood of different magnitudes of earthquakes on a fault, in these tests a Brownian Passage Time model is applied (Matthews et al., 2002). The AR tool derives the annual cumulative rates over a set time period, selected as 50 years, of an earthquake of a given magnitude.

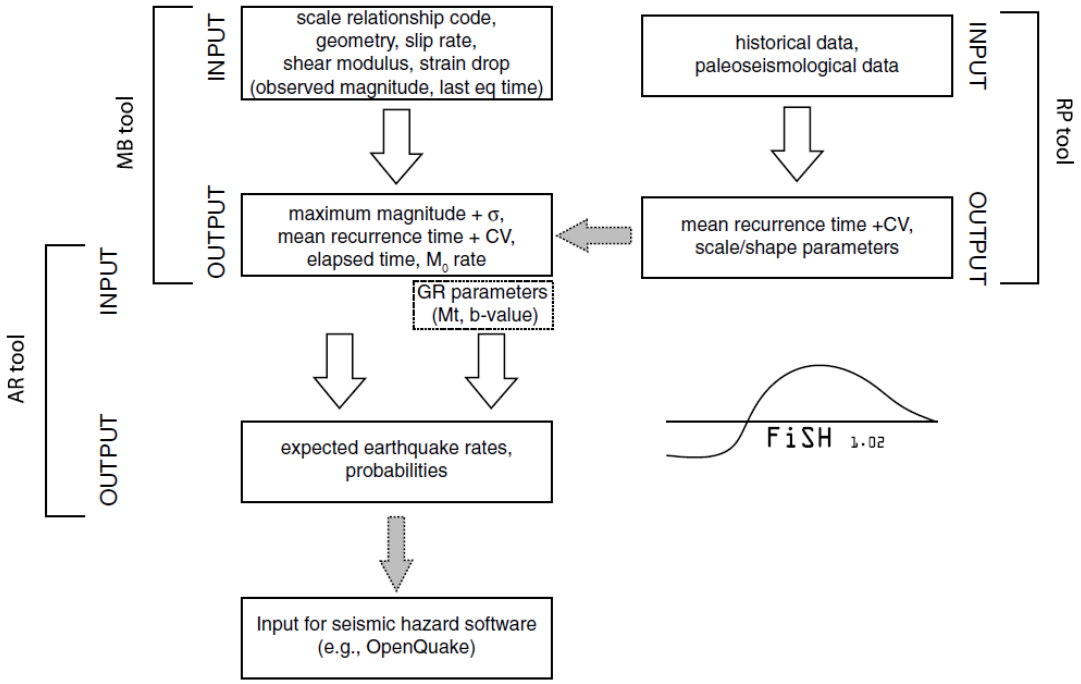

Figure 8.12: Workflow packages for the MB, RP and AR tools within FiSH seismic hazard modelling software used in this section, dotted box indicates optional inputs. σ refers to the standard deviation, M0 is the seismic moment (modified from Pace et al., 2016).

In order to test how varying slip rates impact *Tmean* and earthquake rates, slip rates are obtained from Fault 17, located in the western tip of the SAFS, Cape Heraion (Figs. 6.2) and used within *FiSH.* Fault 17 (Figs. 6.4, 8.13a, b) is north dipping, forms the 'spine' of Cape Heraion and is believed to have ruptured in the 1981 Gulf of Corinth earthquakes. It is 1.71 km long and has an average dip of 51˚ (obtained from dip measurements on the fault) (Fig 8.13a, b). Slip rates over three timescales are available from fault 17 (Fig. 8.13, Table 8.2), this illustrates a typical problem in seismic hazard assessment of deciding which slip-rate value to use if several are proposed for different time periods; below, the effect of using these different slip rates in *FiSH* are demonstrated.

(i) Along its eastern section there are age controls for coral colonies that date the 240 ka marine terrace in the hangingwall and in the footwall (Fig. 8.13e) (ages obtained from Houghton, 2010). The hangingwall coral colonies are in-life position and found in a sedimentary layer at 21 m, sampled from a road cutting. The footwall corallites are part of a death assemblage found in a modern soil forming within a poorly preserved marl at ~80 m, they were located down-dip from a limestone notch, with an elevation difference of ~2-3 m between the coral sampling elevation and the notch elevation. The footwall and hangingwall corals were sampled and dated by Houghton (2010) using $^{234}U/^{230}Th$ dating and resulted in footwall ages of 241 ka, 226 ka, 246 ka, 235 ka and hangingwall ages 237 ka, 230 ka and 235 ka, which are all suggestive of formation during the 240 ka highstand. Based on their present day locations, it may be interpreted that the 240 ka corals formed and some colonies were eroded at the point of the 240 ka highstand and deposited close to the notch. This evidence can be used to tentatively suggest that the 80 m footwall surface and the hangingwall elevation of the corals (21 m) have been displaced by Fault 17 since 240 ka. The present elevations of these samples can be used to identify an offset of 59 m since 240 ka and a calculated slip rate of 0.32 mm/yr (Table 8.2). There is an uncertainty associated with this value because the palaeo-depth of the coral formation is unknown; observations suggest typical values of up to -10 m (Peirano et al., 2004; Montanga et al., 2007). Thus, the actual offset elevation of the 240 ka may be less than that measured. This uncertainty is accounted for by calculating the offset and slip rates assuming that the corals grew in palaeodepths of -10 m and -20 m. Thus the offsets and slip rates would be 49 m (0.26 mm/yr) and 39 m (0.21 mm/yr), respectively (Table 8.2).

(ii) The western section of Fault 17 was explored in Chapter 6 (Fig 6.8c) (Robertson et al., 2020). In this location the wave-cut platform in the hangingwall of the fault has been dated to the 125 ka highstand using ^{36}Cl exposure dating (Fig 8.13f). Chapter 6 suggested that the 92 m-notch present in the footwall of Fault 17 directly above the 125 ka terrace

belongs to the 125 ka. If the suggested age of the notch is accepted, then the offset of 40 m of Fault 17 over 125 ka can be used to calculate a slip rate of 0.41 mm/yr (Table 8.2).

(iii) Also within the western section of the fault, a semi-continuous post-glacial bedrock scarp is preserved at multiple locations within a 300 m distance. These scarps are comprised of an upper slope, fault scarp, and a lower slope (Fig. 8.13c, d). The shallower upper and lower slopes may be representative of a pre-LGM eroded scarp and post-LGM fault slip is apparent from a steeper fault scarp, which is typically observed as a free face. The point at which the upper slope meets the top of the fault scarp is the footwall cut off, and where the lower slope meets the base of the fault scarp is the hangingwall cut off. Assuming this fault scarp represents offset since the LGM, identification of the throw is carried out using these cut offs, measured on fault scarp profiles (see Papanikolaou et al., 2005 for further detail) (Fig. 8.13c, d). These scarp profiles are made in the field by measuring the dip values at regularly-spaced intervals (i.e. 1 m) perpendicular to the strike of the fault along a continuous section from the upper slope, down the fault scarp and the lower slope. Presented in 2D sections, the scarp profiles display the change in dip along the upper and lower slopes and fault scarp and allow the elevations of footwall and hangingwall cut offs to be identified; these values are then used to derive the vertical offset (fault throw) that has occurred, possibly since the LGM (given as 15 ka). Two scarp profiles measure total slip since the LGM of 6.7 m (Holocene Profile 1) and 7.6 m (Holocene Profile 2) (Fig. 8.6c, d), which equate to slip rates of 0.57 mm/yr and 0.65 mm/yr respectively (Table 8.2).

Time period (ka)	Assumed slope age (ky)	FW cut off (m)	HW cut off (m)	Fault dip (˚)	UTM FW	UTM HW	Offset (m)	Throw rate (mm/yr)	Slip rate (mm/yr)	Tmean (yrs)	FISH ref
Late Quaternary	240	80	21	51	663899/ 4210470	664325/ 4210911	59	0.25	0.32	177	F17_1c
Late Quaternary	240	80	31	51	663899/ 4210470	664325/ 4210911	49	0.20	0.26	218	F17_1b
Late Quaternary	240	80	41	51	663899/ 4210470	664325/ 4210911	39	0.16	0.21	270	F17_1a
Late Quaternary	125	92	52	51	663090/ 4210576	663080/ 4210648	40	0.32	0.41	139	F17_2
Holocene P1	15	71	64.3	51	663189/ 4210579	663191/ 4210611	6.7	0.45	0.57	100	F17_3
Holocene P2	15	77.8	70.2	51	663349/ 4210617	663350/ 4210640	7.6	0.51	0.65	87	F17_4

Table 8.2: Calculated throw/slip rates for each timescale. HW and FW refer to hangingwall and footwall elevations a.s.l. Slip-rate calculations used the average dip measured on fault 17 of 51˚. Note that for the calculation of the 240 ka deformation rates the HW and FW cut off elevations are the elevation of the offset sedimentary layers containing the 240 ka dated corals; for the 125 ka deformation rates HW and FW cut off elevations are the elevation of the HW marine terrace and the elevation of the FW notch.

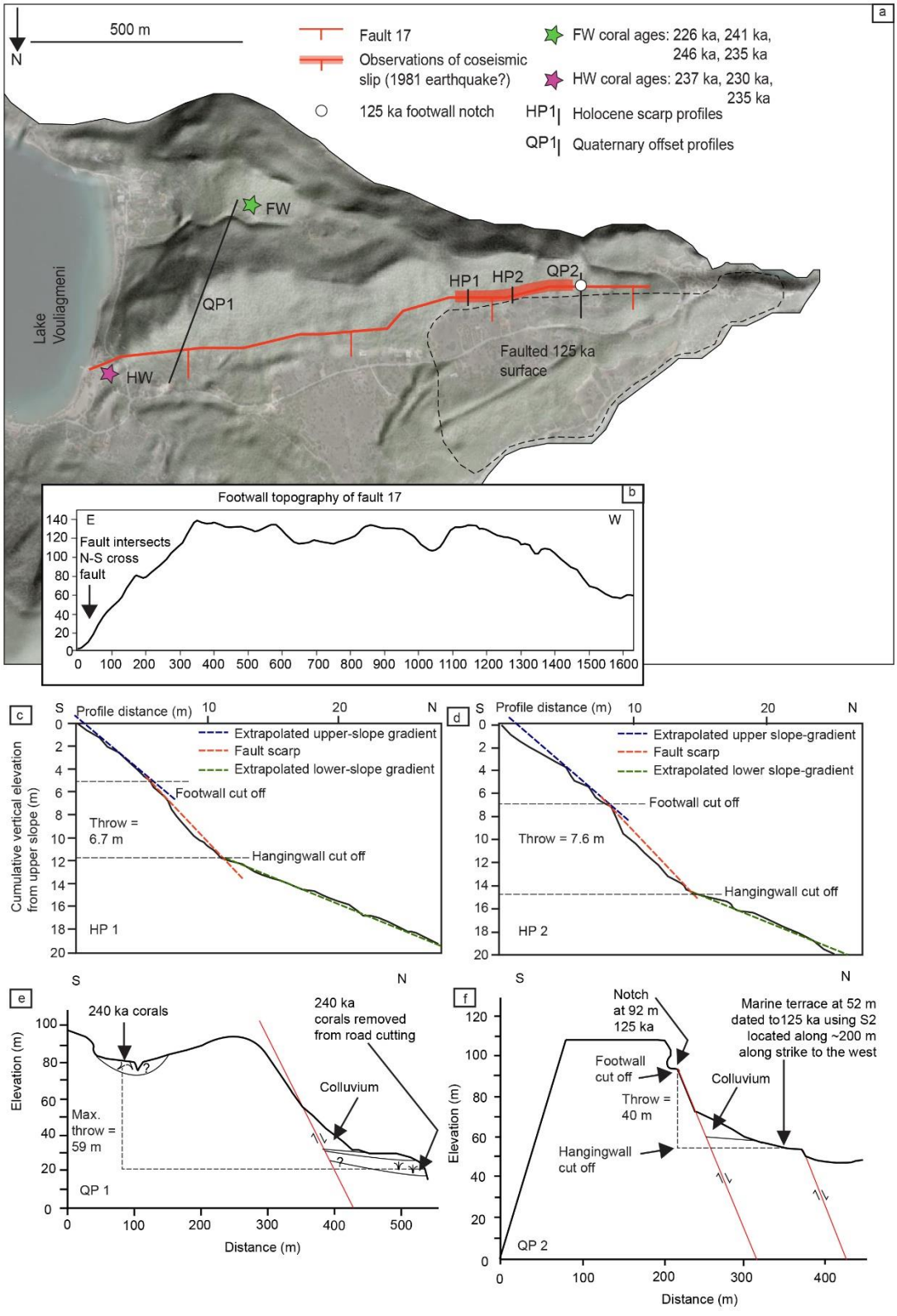

Figure 8.13: (a) view of fault 17 using a 5 m DEM: fault trace, location of fault scarp profiles and coseismic mapped offsets, likely associated with the 1981 earthquake, are also shown. (b) Footwall topographic profile of Fault 17. (c and d) Scarp profiles displaying throw values, assumed to have formed since the LGM (15 ka) for Holocene profile (HP) 1 (c) and 2 (d). (e) Offset of the 240 ka corals along the east of Fault 17. (f) Note that the elevation of the hangingwall cut off for (e and f) is taken as the measured value on the offset sampled corals (in e) and wave-cut platform (in f) because a colluvial wedge obscures the actual location of the hangingwall cut off.

Slip rates calculated over 240 ka, 125 ka and 15 ka timescales reveal variation of between 0.21-0.65 mm/yr (Table 8.2). The uncertainty associated with the palaeodepth of the corals means that the 240 ka slip rates may range between 0.21-0.32 mm/yr; values that are lower when compared to the 0.41 mm/yr slip obtained over 125 ka. If the observations that the offset scarps (Figs. 8.14 e and f) represent Holocene offset are accepted, then higher slip rates are calculated for the last 15 ka, where values of 0.57 mm/yr and 0.65 mm/yr belong to Holocene fault scarp profiles 1 and 2, respectively. The Late-Quaternary measurements are taken from different parts of the fault (Fig. 8.13a), note that slip rate variation is expected along the length of a fault owing to different displacement gradients between the centre and the tips of the fault (e.g. Schlische et al., 1996), but in this instance the measurements of both the 240 ka and 125 ka slip rates are located away from the centre of the fault and close to opposing tips. I tentatively suggest that these data may represent temporal variations in slip rates.

Assuming calculations of the slip rates are accurate, direct comparison of the rates from the late Quaternary to those that represent the Holocene may initially indicate that Holocene slip rates are higher than late Quaternary slip rates (Table 8.2) by a factor of ~3 (lowest 240 ka slip rate versus Holocene profile 2). If the variation between the Late-Quaternary slip rate and the Holocene rate is accepted as representative, then one explanation could be linked to the observation made by Roberts et al. (2009) that the broader SAFS increased in slip at ~175 ka by a factor of 3.2.

8.4.3 Comparison of *Tmean*

Slip-rate tests were carried out in *FiSH* using input values obtained from Fault 17 (Table 8.3) using the MB tool (Fig. 8.12) to derive the *Tmean*, maximum magnitude, CV, elapsed time and seismic moment (Table 8.4). As a result of the uncertainty in the 240 ka offset, the three potential slip values from the 240 ka offsets (Fig. 8.14e) are calculated (F17_1a, 1b and 1c).

Name	ScR	Length (km)	Dip˚	Seismo thickness (km)	Srmin (mm/yr)	Srmax (mm/yr)	Mobs	sdMobs	Last EQ
F17_1a	WC94-N	1.71	51	15	0.21	0.21	NaN	NaN	1981
F17_1b	WC94-N	1.71	51	15	0.26	0.26	NaN	NaN	1981
F17_1c	WC94-N	1.71	51	15	0.32	0.32	NaN	NaN	1981
F17_2	WC94-N	1.71	51	15	0.41	0.41	NaN	NaN	1981
F17_3	WC94-N	1.71	51	15	0.57	0.57	NaN	NaN	1981
F17_4	WC94-N	1.71	51	15	0.65	0.65	NaN	NaN	1981
F17_5	WC94-N	1.71	51	15	0.21	0.65	NaN	NaN	1981

Table 8.3: Input values into FiSH (Pace et al., 2016), ScR is the fault-scaling relationship used in the calculations (WC94-N represents Wells and Coppersmith (1994) normal fault), Sr refers to the slip rate measured in this section, Mobs is the maximum known magnitude, sdMobs is the standard deviation of the maximum known magnitude (NaN is the entry used where this is unknown) and Last EQ is the time of the last earthquake.

Time period (ka)	Assumed slope age (ky)	Slip rate (mm/yr)	Mmax	sdMmax	Tmean (yrs)	CV	Telap (yrs)	Mo-rate (N x M x yr^{-1})	*Fish* ref.
Late Quaternary	240	0.21	5.1	0.4	270	1.38	39	2.08E+14	F17_1a
Late Quaternary	240	0.26	5.1	0.4	218	1.38	39	2.58E+14	F17_1b
Late Quaternary	240	0.32	5.1	0.4	177	1.38	39	3.18E+14	F17_1c
Late Quaternary	125	0.41	5.1	0.4	139	1.38	39	4.05+14	F17_2
Holocene P1	15	0.57	5.1	0.4	100	1.38	39	5.62+14	F17_3
Holocene P2	15	0.65	5.1	0.4	87	1.38	39	6.46+14	F17_4

Table 8.4: Output values from the MB tool for each of the slip rates tests. Mmax: maximum magnitude, sdMmax: standard deviation of Mmax, Tmean: mean recurrence interval, CV: coefficient of variation, Telap: time elapsed since last assigned earthquake, Mo_rate: seismic moment. Note that the CV is not expected to be representative of Fault 17 because it has not been calculated with known historic earthquake data, which does not exist for this part of the fault.

Output values obtained from the MB tool reveal the same Mmax values, which is expected given this analysis is for the same fault, but values of *Tmean* that vary between 87-270 years; the *Tmean* obtained using the 240 ka slip rate (minimum offset) is nearly double that obtained using the 125 ka slip rate. The two Holocene *Tmean* values are similar and close to the *Tmean* obtained for the 125 ka. What this shows is that lower slip rates from a fault have a direct impact on the *Tmean* derived in PSHA modelling; if only knowledge of the 240 ka slip rate was known for this fault, it may result in *Tmean* values that may be misleading.

The output values from the MB tool were used in the AR tool to model the probability of occurrence of earthquakes using a Brownian Passage Time model (referred to as the 'Characteristic Gaussian model (BPT)', Pace et al. (2016)) of earthquake magnitude-frequency for a 50-year period (Fig. 8.14). A BPT model is an earthquake recurrence model that has an asymmetrical probability density function; it has been shown to take into account that earthquakes may be in clusters and anti-clusters (e.g. Cowie et al., 2012).

The higher slip rate values associated with the Holocene and 125 ka timeframes (and shorter *Tmean* values) result in higher rates of annual earthquakes in comparison to those calculated using the 240 ka slip rates. In more detail, using the potential slip rates and associated data over 240 ka, a Mw 4.7 earthquake will have annual rates of earthquakes of 0.02-0.04 over a 50-year period, compared to annual rates of earthquakes of 0.08 using the slip rate and associated data from Holocene Profile 2 given the same magnitude of earthquake and 50-year time period. These tests show that variations in slip rates obtained over different timescale give rise to differing *Tmean* values and annual earthquake rates.

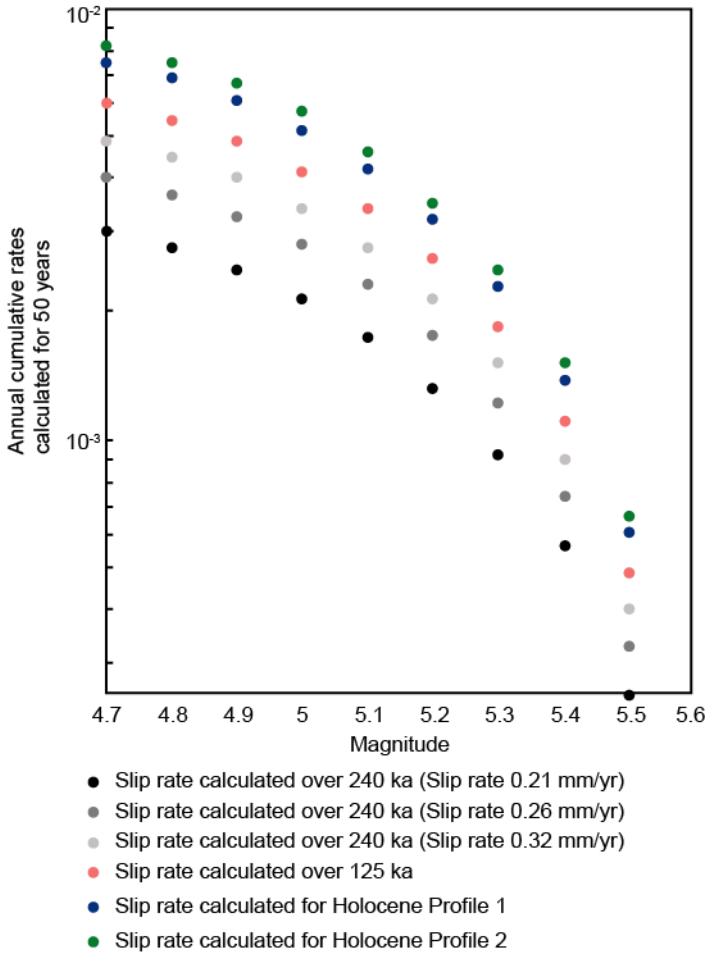

Figure 8.14: Earthquake magnitude frequency using a characteristic Gaussian model (BPT) calculated over 50 years for slip rates obtained over 240 ka, 125 ka and Holocene time periods.

If it is accepted that the variation of slip on Fault 17 is as a consequence of slip-rate changes on the fault at ~175 ka, then this raises the issue that if the only fault measurement available for PSHA was using 240 ka slip rates, the calculated *Tmean* would represent an unrecognised underestimate of the potential seismic hazard. Future work on Fault 17 to undertake additional ^{36}Cl exposure dating of wave-cut platforms observed in the footwall of the fault would allow greater investigation into the Late-Quaternary activity on the fault. Similarly, ^{36}Cl exposure dating on the Holocene fault scarp would provide high resolution recurrence intervals and slip rates throughout the Holocene and a more accurate calculation of the CV value. Furthermore, this work has the potential to provide insights into the influence of earthquake clustering. The findings of this section are in agreement with those from Faure Walker et al. (2019) and Sgambato et al. (2020) who identify the importance of obtaining slip/throw rates at multiple locations on a fault in order to carry out PSHA. While the work of Faure Walker et al. (2019) and Sgambato et al. (2020) is applied to data collected from faults in the Holocene, the results herein suggest that the same is true for the collection of slip/throw rates from faults over

the long term. This finding has broader implications for PSHA in general as to the importance of establishing slip/throw rates on faults over multiple time scales.

8.5 SUMMARY

This thesis set out to apply a new approach to study deformed palaeoshorelines in order to provide insights into the long term deformation of upper-plate faults, which is necessary to further our understanding of fault deformation over multiple seismic cycles and to derive deformation rates to be used within PSHA. Given the context of the aims and objectives outlined in Section 1.4 of this thesis, the findings herein reveal that ^{36}Cl exposure dating is a new, innovative and acceptable method to derive age controls for late Quaternary carbonate wave-cut platforms, provided that sampling is carried out on low-erosion sites. This was shown at two localities (Crete and Perachora, Chapters 4 and 6, respectively), where nine exposure ages were obtained, which were in agreement with existing age controls. The studies in Crete and Perachora facilitated detailed investigations into active faulting in the upper-plate of the WHSZ and revealed that this upper-plate extensional faulting was predominantly responsible for the deformation of palaeoshorelines and their associated wave-cut platforms. Both of these studies provide important insights into the causal faults and the effects of fault interaction throughout the long term. A systematic analysis of the validity of Late-Quaternary $^{234}U/^{230}Th$ coral growth ages, given their elevated $\delta^{234}U_i$ values, reinforces that within the Gulf of Corinth, it is highly likely that the hydrogeochemistry of the gulf margins has significantly varied through time. Such findings have the capacity to encourage future studies that date deformed palaeoshorelines to examine uplifted corals using the multiple analyses method applied herein. Finally, investigation of the impact of differing sea-level curves to calculate deformation rates using palaeoshorelines reinforces the strength of the synchronous correlation method and the importance of using this method on areas where uplift rates less than 1 mm/yr may prevail. While caution should be applied when deriving earthquake recurrence intervals using palaeoshoreline measurements and data from a single sea-level curve, the differences in individual uplift rates from different curves are comparable with propagated uncertainties; furthermore, the pattern of uplift is maintained regardless of the sea-level curve used.

This thesis began by highlighting that earthquake behaviour has been shown to be episodic, where faults may rupture in clusters and experience anticlusters that result in periods of quiescence (e.g. Sieh et al., 1989; Dolan et al., 2007; Benedetti et al., 2013; Cowie et al., 2017; Mildon et al., 2019). Earthquake clustering and anticlustering are suggested to be linked to elastic stress interaction between faults (e.g. Cowie, 1998). The timescale between individual clusters and periods of clustered

and anticlustered activity varies between hundreds and thousands of years (e.g. de Polo and Slemmons, 1997; Benedetti et al., 2013) and introduces uncertainty about whether a fault is active. The consequence of such behaviour is that it is unknown to what extent deformation rates obtained over short-term timescales are representative of long-term fault rates and this impacts scientists' ability to appropriately plan for the building and maintenance of critical facilities undertake PSHA, which is vital for local population centres.

The successful application of ^{36}Cl exposure dating, $^{234}U/^{230}Th$ coral growth dating and synchronous correlation allows long term deformation rates to be obtained from deformed palaeoshorelines, importantly, this approach can provide insight into the activity of faults that are located offshore (but close to the shoreline) and where faults intersect and offset the coastline. The success of the approach adopted and applied herein is that it can be applied elsewhere, where deformed palaeoshorelines exist, in order to derive long-term deformation rates that can act as a baseline from which short term rates deviate. Insights of this nature are necessary to establish fault CV values that do not solely represent clustered behaviour. This approach herein is particularly powerful because it allows investigation into the extent to which upper-plate or subduction-related uplift dominates the deformation observed above subduction zones. Moreover, long-term deformation rates are also beneficial for studies of tectonic crustal processes. One such example is in studies that explore the relationship between strain rates and mechanical properties of the deforming continental crust, whereby long-term rates of crustal deformation can be used as baseline to constrain long-term strain rates and the extent to which they are perturbed by short-term rates. To conclude, it is hoped that this thesis provides a framework to investigate deformed carbonate palaeoshorelines such that they may afford reliable fault-related deformation rates in order to provide insight into the long-term behaviour of faults and contribute to effective PSHA.

9 CHAPTER 9: CONCLUSIONS

This chapter details the conclusions that result from the research undertaken within this thesis. They are outlined in accordance with the aims (i-v) proposed in Chapter 1, with further detailed observations provided.

(i) Establish the reliability of two methods used to investigate deformed palaeoshorelines and their associated wave-cut platforms: cosmogenic ^{36}Cl exposure dating and ^{234}U/^{230}Th coral growth ages.

This thesis has demonstrated that ^{36}Cl exposure dating can reliably be used to provide age controls on Late-Quaternary carbonate wave cut platforms. The age constraints obtained agree with the ages of eustatic sea-level highstands, existing age controls and uplift modelling. The ^{36}Cl exposure approach has been proven as successful on various carbonate lithologies, namely, basement limestone (Mesozoic to Tertiary in age), algal bioherms and packstones.

1) New ^{36}Cl exposure age controls agree with existing age controls in two locations using ^{234}U/^{230}Th coral growth ages from Cape Heraion and OSL-based age controls from south Central Crete.
2) ^{36}Cl exposure dating of wave-cut platforms is reliant on careful site selection where samples that have experienced minimal and, ideally quantifiable, erosion since formation. Preserved lithophagid borings and millholes are shown to be particularly reliable indicators.
3) ^{36}Cl exposure sampling on successive wave-cut platforms is particularly powerful as it allows for checks to be made on the concentration of ^{36}Cl atoms, which should increase with elevation and age.
4) Age results obtained for ^{36}Cl exposure samples with high bulk rock chlorine do not yield reliable ^{36}Cl exposure ages. This point emphasises the need to undertake petrological analysis on samples that are not comprised of bedrock.
5) Wave-cut platforms aged ~125 ka and younger have been shown to yield reliable ^{36}Cl exposure ages for uplift rates up to ~0.8 mm/ky. Where possible future ^{36}Cl exposure samples should be focussed upon wave-cut platforms at lower elevations to avoid higher levels of erosion and older platforms that have been subject to numerous periods of glaciation. Further research into the reliability of ^{36}Cl exposure dating on older and higher palaeoshorelines is necessary.
6) Erosion sensitivity tests reveal that the calculated ^{36}Cl exposure ages for samples do not significantly alter if erosion rates are adjusted by a total of up to 1 mm/ky.

This thesis shows that in locations where *C. Caespitosa* corals have grown in marginal marine settings (restricted basins/coastal areas subject to freshwater influx) and are latterly uplifted as a result of palaeoshoreline formation and deformation, validity of the growth ages should be associated with detailed analysis of coral samples in relation to the local tectonics and stratigraphy, other age controls and multiple $^{234}U/^{230}Th$ analyses on (i) corals from the same sedimentary sample location and (ii) on the same corallites, such that age and $\delta^{234}U_i$ clustering can be analysed.

7) A systematic analysis of late Quaternary coral growth ages in the Gulf of Corinth shows that coral growth ages are associated with elevated $\delta^{234}U_i$ values. The coral ages are in agreement with the tectonic and stratigraphical relationships, age controls obtained using ^{36}Cl exposure dating on associated wave-cut platforms and synchronous correlation modelling, suggesting that they are accurate.
8) Elevated $\delta^{234}U_i$ can be explained by hydrogeochemical history of the gulf associated with freshwater and spring water influx and spatial and temporal variation linked to the interplay between eustatic sea-level change and fault-controlled tectonics that impacted the marine water ingress into the gulf.
9) Measured $\delta^{234}U_i$ values are obtained for three highstands/MIS and show some variation: 125 ka (MIS 5e): 191-214‰; 175 ka (MIS 6d): 176-183‰; 200 ka (MIS 7a): 186-196‰.
10) The dominant sea-water ingress during MIS 5e (125 ka highstand) can be tentatively inferred to be via the Isthmus of Corinth in the eastern gulf, based upon the fact that all of the MIS 5e corals are located in the eastern area.
11) $^{87}Sr/^{86}Sr$ ratios of Gulf of Corinth corals support that variable geochemistry within the Gulf of Corinth existed throughout the late Quaternary. The $^{87}Sr/^{86}Sr$ ratios are interpreted to represent a reliable proxy for elevated $\delta^{234}U_i$.
12) Uplift rates calculated using Gulf of Corinth corals mirror the findings of previous studies into late Quaternary deformation where displacement profiles along the length of the gulf reveal a bell-shaped profile.

(ii) Interrogate the sensitivity of uplift calculations and deformation rates to different sea-level curves.

Analysis of the extent to which different sea-level curves influence the calculated deformation rates and recurrence intervals showed that the variation in propagated uplift uncertainties (0.09-0.2 mm/yr) using a single sea-level curve is very similar to the range of difference between uplift rates calculated using the six different sea-level curves (0.14-0.28 mm/yr). This is reassuring as these results imply that calculated uplift rates should not differ too dramatically given the sea-level curve employed.

13) The application of different sea-level curves (Waelbroeck et al., 2002; Siddall et al., 2003; Bintanja et al., 2005; Bates et al., 2014; Shakun et al., 2016; Spratt and Lisiecki, 2016) results in variation between the correlation of undated palaeoshorelines to sea-level highstands.
14) The variance between predicted sea-level elevations for highstands from different sea-level curves has been shown to differ. Depending on the age control used to determine uplift rates, this may have an impact on the palaeoshoreline to highstand correlations. When the ~125 ka palaeoshoreline is used as an age control, it appears to result in a higher number of palaeoshoreline to highstand correlations and greater agreement between the different sea-level curves.
15) The spatial pattern of along strike uplift for the south central Crete area is maintained when uplift rates are calculated using six different sea-level curves.
16) Earthquake recurrence intervals appear to be more impacted when they are calculated using different sea-level curves – the variation in recurrence intervals using the curves of Bintanja et al. (2005) and Bates et al. (2014) exceed the standard deviation calculated from the mean for all of the sea-level curves. Caution should be applied when calculating recurrence intervals using the sea-level data from a single curve.

(iii) Investigate whether synchronous correlation of palaeoshorelines to sea-level highstands outperforms sequential correlation.

17) The constant uplift rates derived for south central Crete in this thesis contrast with previous application of the sequential method in the same area, which was used to suggest temporally variable uplift rates. This is because the synchronous approach takes into account overprinting of older palaeoshorelines by younger highstands, which is of particular importance because fault displacement gradients that change along strike are reflected in uplift rates in deformed hangingwall and footwall palaeoshorelines that have been shown to vary. Re-examination of sequences of palaeoshorelines previously investigated using sequential correlation is recommended.

(iv) Apply ^{36}Cl exposure dating and $^{234}U/^{230}Th$ on corals to derive the ages of deformed palaeoshorelines, correlate palaeoshorelines to eustatic highstands and apply elastic half-space modelling in order to investigate the tectonic processes and faults responsible for uplift in two field locations, (1) south central Crete and (2) Cape Heraion, Perachora.

Detailed analysis of deformed palaeoshorelines in south central Crete reveals that coastal uplift is dominated by upper-plate faults, a finding that contrasts with the suggestion that regional subduction-related processes are responsible. This is emphasised using the length scale of palaeoshoreline

deformation, fault analysis and elastic half-space modelling. Overall, it has been shown that in order to attempt to suggest values of uplift related to regional processes, it is first necessary to derive the deformation related to upper-plate faults.

18) Elastic half-space modelling of the Ptolemy transtensional fault reveals an uplift profile that is broadly in agreement with the observed palaeoshoreline deformation in the high uplift area adjacent to the SCCF. This suggests that the Ptolemy fault is capable of causing coastal uplift and that is has been active since 76.5 ka (as this is the youngest deformed palaeoshoreline). Uplift on the 76.5 ka palaeoshoreline in the footwall of the Ptolemy fault can be used to calculate an inferred recurrence interval of ~546 years.
19) The SCCF is an active fault that deforms palaeoshorelines in its hangingwall and footwall and has a calculated slip rate of 0.41 mm/yr since 478 ka.
20) Palaeoshorelines in south central Crete are shown to have been uplifting at temporally constant rates since between 600-900 ka.
21) Across strike interaction between upper-plate faults has been shown to influence the tilt angles of palaeoshorelines. Analysis of tilt angles alongside elastic half-space modelling is a powerful method to examine elastic interaction between faults.

This thesis has demonstrated that wave-cut platforms on Cape Heraion (Perachora) were formed during the 125 ka highstand and have been latterly faulted within the western tip zone of the SAFS. This finding contrasts with historical interpretations that Cape Heraion is comprised of a sequence of palaeoshorelines that increase in age with elevation and were formed as a result regional-related processes.

22) There is evidence of Late Quaternary to Holocene faulting throughout Cape Heraion, with some observations implying deformation during the 1981 Gulf of Corinth earthquakes, suggesting the area continues to deform since 125 ka.
23) Deformation in the western tip of the SAFS is accommodated via distributed faulting where the strike of the faults varies from the main SAFS by 70˚, this finding is in accordance with observations from other tip zones accommodate deformation in faults that splay from the main fault.
24) South dipping faults on Cape Heraion are longer and have larger throw offsets in comparison to north dipping faults, implying that the south dipping faults are more mature compared to their north dipping counterparts. The dip of the faults on Cape Heraion may reflect the

broader faulting pattern in the Gulf of Corinth where the polarity of faulting switched from south-dipping faults to north-dipping faults in the late Quaternary.

25) Summed throw rates on Cape Heraion reveal values between 1.6 mm/yr and 0.3 mm/yr; uplift rates associated with wave-cut platforms vary between 0.02 mm/yr and 0.7 mm/yr.
26) The summed throw rates in Cape Heraion are anomalously high compared to the SAFS and results in a high displacement gradient in the tip zone. This is postulated to be as a result of fault interaction between two crustal-scale faults whose tips overlap (western tip of the South Alkyonides Fault System and eastern tip of the East Xylocastro Fault System).

(v) Derive deformation rates that are essential to contribute to probabilistic seismic hazard assessment (PSHA) and our understanding of fault deformation over multiple seismic cycles.

27) Potential seismic hazard from active faults in south Crete may be from the subduction interface, Ptolemy trench fault and normal faults, which have the capacity to host earthquakes that range in magnitudes of Mw 9.0, Mw 7.3 and Mw 6.6-6.9, respectively.
28) Shared tip zones have the capacity to host higher than expected rates of deformation, this has seismic hazard implications because they are commonly considered to host minimal throw. This finding should be borne in mind for other shared fault tip zones within normal fault systems throughout the world, especially in areas of high population density or where critical facilities are located. Detailed across-strike mapping is necessary in order to adequately investigate tip zone deformation.
29) Slip rates in the tip zone (Fault 17) of the SAFS are tentatively inferred to have been temporally variable. Modelling of the variable slip rates using a probabilistic seismic hazard approach result in differing *Tmean* values between 87 and 270 years and illustrates the challenge faced when using geological data over different timescales to calculate recurrence intervals and earthquake rates.

10 LIST OF REFERENCES

Abercrombie, R.E., Antolik, M., Felzer, K. and Ekström, G., 2001. The 1994 Java tsunami earthquake: Slip over a subducting seamount. *Journal of Geophysical Research: Solid Earth*, *106*(B4), pp.6595-6607.

Abercrombie, R. E., Main, I. G., Douglas, A., and Burton, P. W, 1995. The nucleation and rupture process of the 1981 Gulf of Corinth earthquakes from deconvolved broad-band data. *Geophysical Journal International*, *120*(2), pp.393-405.

Adam, J. and Reuther, C.D., 2000. Crustal dynamics and active fault mechanics during subduction erosion. Application of frictional wedge analysis on to the North Chilean Forearc. *Tectonophysics*, *321*(3), pp.297-325.

Adey, W.H., 1986. Coralline algae as indicators of sea-level. In *Sea-Level Research* (pp. 229-280). Springer, Dordrecht.

Anders, M. H., and Schlische, R. W, 1994. Overlapping faults, intrabasin highs, and the growth of normal faults. *The Journal of Geology*, *102*(2), pp.165-179.

Andersen, M.B., Stirling, C.H., Porcelli, D., Halliday, A.N., Andersson, P.S. and Baskaran, M., 2007. The tracing of riverine U in Arctic seawater with very precise 234U/238U measurements. *Earth and Planetary Science Letters*, *259*(1-2), pp.171-185.

Andersson, P.S., Wasserburg, G.J., Chen, J.H., Papanastassiou, D.A. and Ingri, J., 1995. 238U234U and232Th230Th in the Baltic Sea and in river water. *Earth and Planetary Science Letters*, *130*(1-4), pp.217-234.

Andersson, P.S., Wasserburg, G.J. and Ingri, J., 1992. The sources and transport of Sr and Nd isotopes in the Baltic Sea. *Earth and Planetary Science Letters*, *113*(4), pp.459-472.

Andrews, J.E., Portman, C., Rowe, P.J., Leeder, M.R. and Kramers, J.D., 2007a. Sub-orbital sea-level change in early MIS 5e: new evidence from the Gulf of Corinth, Greece. *Earth and Planetary Science Letters*, *259*(3-4), pp.457-468.

Andrews, J.E., Leeder, M.R., Portman, C., Rowe, P.J., Smith, J., Kershaw, S. and Guo, L., 2007b. Discussion on Pleistocene calcified cyanobacterial mounds, Perachora peninsula, central Greece: a controversy of growth and historyGeological Society, London, Special Publications, Vol. 255, 2006, 53–69. *Journal of the Geological Society*, *164*(5), pp.1065-1072.

Allègre, C.J., Louvat, P., Gaillardet, J., Meynadier, L., Rad, S. and Capmas, F., 2010. The fundamental role of island arc weathering in the oceanic Sr isotope budget. *Earth and Planetary Science Letters*, *292*(1-2), pp.51-56.

Alves, T.M., Kokinou, E. and Zodiatis, G., 2014. A three-step model to assess shoreline and offshore susceptibility to oil spills: The South Aegean (Crete) as an analogue for confined marine basins. *Marine pollution bulletin*, *86*(1-2), pp.443-457.

Alves, T.M., Lykousis, V., Sakellariou, D., Alexandri, S. and Nomikou, P., 2007. Constraining the origin and evolution of confined turbidite systems: southern Cretan margin, Eastern Mediterranean Sea (34 30–36 N). *Geo-Marine Letters*, *27*(1), p.41.

Alexander, C.S., 1953. *The marine and stream terraces of the Capitola-Watsonville area* (Vol. 10, No. 1-4). University of California Press.

Ambraseys, N., 2009. *Earthquakes in the Mediterranean and Middle East: a multidisciplinary study of seismicity up to 1900*. Cambridge University Press.

Andrews, J. E., Leeder, M. R., Portman, C., Rowe, P. J., Smith, J., Kershaw, S., and Guo, L, 2007. Discussion on Pleistocene calcified cyanobacterial mounds, Perachora peninsula, central Greece: a controversy of growth and historyGeological Society, London, Special Publications, Vol. 255, 2006, 53–69. *Journal of the Geological Society*, *164*(5), pp.1065-1072.

Angelier, J., 1979a. Recent Quaternary tectonics in the Hellenic arc: examples of geological observations on land. *Tectonophysics*, *52*(1-4), pp.267-275.

Angelier, J., 1979b. *Néotectonique de l'arc égéen.* These d'etat: University de Paris Vi, 405.

Angelier, J., Lyberis, N., Le Pichon, X., Barrier, E. and Huchon, P., 1982. The tectonic development of the Hellenic arc and the Sea of Crete: a synthesis. *Tectonophysics*, *86*(1-3), pp.159-196.

Anderson, R.S., Densmore, A.L. and Ellis, M.A., 1999. The generation and degradation of marine terraces. *Basin Research*, *11*(1), pp.7-20.

Anderson, R.S. and Menking, K.M., 1994. The Quaternary marine terraces of Santa Cruz, California: Evidence for coseismic uplift on two faults. *Geological Society of America Bulletin*, *106*(5), pp.649-664.

Antonioli, F., Ferranti, L., Lambeck, K., Kershaw, S., Verrubbi, V. and Dai Pra, G., 2006. Late Pleistocene to Holocene record of changing uplift rates in southern Calabria and northeastern Sicily (southern Italy, Central Mediterranean Sea). *Tectonophysics*, *422*(1-4), pp.23-40.

Antonioli, F., Presti, V.L., Rovere, A., Ferranti, L., Anzidei, M., Furlani, S., Mastronuzzi, G., Orru, P.E., Scicchitano, G., Sannino, G. and Spampinato, C.R., 2015. Tidal notches in Mediterranean Sea: a comprehensive analysis. *Quaternary Science Reviews*, *119*, pp.66-84.

Armijo, R., Lyon-Caen, H., and Papanastassiou, D, 1991. A possible normal-fault rupture for the 464 BC Sparta earthquake. *Nature*, 351(6322), p.137.

Armijo, R., Lyon-Caen, H. and Papanastassiou, D., 1992. East-west extension and Holocene normal-fault scarps in the Hellenic arc. *Geology*, *20*(6), pp.491-494.

Armijo, R., Meyer, B.G.C.P., King, G.C.P., Rigo, A. and Papanastassiou, D., 1996. Quaternary evolution of the Corinth Rift and its implications for the Late Cenozoic evolution of the Aegean. *Geophysical Journal International*, *126*(1), pp.11-53.

Athanassas, C. and Fountoulis, I., 2013. Quaternary neotectonic configuration of the southwestern Peloponnese, Greece, based on luminescence ages of marine terraces. *Journal of Earth Science*, *24*(3), pp.410-427.

Atzori, S., Manunta, M., Fornaro, G., Ganas, A. and Salvi, S., 2008. Postseismic displacement of the 1999 Athens earthquake retrieved by the Differential Interferometry by Synthetic Aperture Radar time series. *Journal of Geophysical Research: Solid Earth*, *113*(B9).

Azougagh, M., Choukri, A., Lferde, M., El Moursli, R.C., Chouak, A. and Abrkan, M., 2001. Mollusc shell dating by uranium series method on quaternary material at Moroccan sea level. *Radiation Physics and Chemistry*, *61*(3-6), pp.713-715.

Balco, G., Stone, J.O., Lifton, N.A. and Dunai, T.J., 2008. A complete and easily accessible means of calculating surface exposure ages or erosion rates from 10Be and 26Al measurements. *Quaternary geochronology*, *3*(3), pp.174-195.

Bard, E., Fairbanks, R.G., Arnold, M. and Hamelin, B., 1992. 230Th/234U and 14C ages obtained by mass spectrometry on corals from Barbados (West Indies), Isabela (Galapagos) and Mururoa (French Polynesia). In *NATO advanced research workshop on the last deglaciation: Absolute and radiocarbon chronologies* (pp. 103-110).

Bard, E., Fairbanks, R.G., Hamelin, B., Zindler, A. and Hoang, C.T., 1991. Uranium-234 anomalies in corals older than 150,000 years. *Geochimica et Cosmochimica Acta*, *55*(8), pp.2385-2390.

Bard, E., Hamelin, B. and Fairbanks, R.G., 1990. U-Th ages obtained by mass spectrometry in corals from Barbados: sea level during the past 130,000 years. *Nature*, *346*(6283), pp.456-458.

Bard, E., Jouannic, C., Hamelin, B., Pirazzoli, P., Arnold, M., Faure, G. and Sumosusastro, P., 1996. Pleistocene sea levels and tectonic uplift based on dating of corals from Sumba Island, Indonesia. *Geophysical Research Letters*, *23*(12), pp.1473-1476.

Barreto, A.M.F., Bezerra, F.H.R., Suguio, K., Tatumi, S.H., Yee, M., Paiva, R.P. and Munita, C.S., 2002. Late Pleistocene marine terrace deposits in northeastern Brazil: sea-level change and tectonic implications. *Palaeogeography, palaeoclimatology, palaeoecology*, *179*(1-2), pp.57-69.

Barrientos, S.E., Plafker, G. and Lorca, E., 1992. Postseismic coastal uplift in southern Chile. *Geophysical Research Letters*, *19*(7), pp.701-704.

Barrientos, S.E. and Ward, S.N., 1990. The 1960 Chile earthquake: inversion for slip distribution from surface deformation. *Geophysical Journal International*, *103*(3), pp.589-598.

Bates, S.L., Siddall, M. and Waelbroeck, C., 2014. Hydrographic variations in deep ocean temperature over the mid-Pleistocene transition. *Quaternary science reviews*, *88*, pp.147-158.

Becker, D. and Meier, T., 2010. Seismic Slip Deficit in the Southwestern Forearc of the Hellenic Subduction ZoneSeismic Slip Deficit in the Southwestern Forearc of the Hellenic Subduction Zone. *Bulletin of the Seismological Society of America*, *100*(1), pp.325-342.

Becker, D., Meier, T., Bohnhoff, M. and Harjes, H.P., 2010. Seismicity at the convergent plate boundary offshore Crete, Greece, observed by an amphibian network. *Journal of seismology*, *14*(2), pp.369-392.

Becker, D., Meier, T., Rische, M., Bohnhoff, M. and Harjes, H.P., 2006. Spatio-temporal microseismicity clustering in the Cretan region. *Tectonophysics*, *423*(1-4), pp.3-16.

Bell, R.E., McNeill, L.C., Bull, J.M. and Henstock, T.J., 2008. Evolution of the offshore western Gulf of Corinth. *Geological Society of America Bulletin*, *120*(1-2), pp.156-178.

Bell, R.E., McNeill, L.C., Henstock, T.J. and Bull, J.M., 2011. Comparing extension on multiple time and depth scales in the Corinth Rift, Central Greece. *Geophysical Journal International*, *186*(2), pp.463-470.

Bell, R.E., McNeill, L.C., Bull, J.M., Henstock, T.J., Collier, R.L. and Leeder, M.R., 2009. Fault architecture, basin structure and evolution of the Gulf of Corinth Rift, central Greece. *Basin Research*, *21*(6), pp.824-855.

Benedetti, L., Manighetti, I., Gaudemer, Y., Finkel, R., Malavieille, J., Pou, K., Arnold, M., Aumaître, G., Bourlès, D. and Keddadouche, K., 2013. Earthquake synchrony and clustering on Fucino faults (Central Italy) as revealed from in situ ^{36}Cl exposure dating. *Journal of Geophysical Research: Solid Earth*, *118*(9), pp.4948-4974.

Berger, A., 1988. Milankovitch theory and climate. *Reviews of geophysics*, *26*(4), pp.624-657.

Berger, A., 2013. *Milankovitch and climate: understanding the response to astronomical forcing* (Vol. 126). Springer Science & Business Media.

Berryman, K.R., 1993. Distribution, age, and deformation of late Pleistocene marine terraces at Mahia Peninsula, Hikurangi subduction margin, New Zealand. *Tectonics*, *12*(6), pp.1365-1379.

Berryman, K. and Hull, A., 2003. Tectonic controls on Late Quaternary shorelines: a review and prospects for future research. *The New Zealand Coast*, pp.9-24.

Bianca, M., Catalano, S., De Guidi, G., Gueli, A.M., Monaco, C., Ristuccia, G.M., Stella, G., Tortorici, G., Tortorici, L. and Troja, S.O., 2011. Luminescence chronology of Pleistocene marine terraces of Capo Vaticano peninsula (Calabria, southern Italy). *Quaternary International*, *232*(1-2), pp.114-121.

Bianca, M., Monaco, C., Tortorici, L. and Cernobori, L., 1999. Quaternary normal faulting in southeastern Sicily (Italy): a seismic source for the 1693 large earthquake. *Geophysical Journal International*, *139*(2), pp.370-394.

Binnie, A., Dunai, T.J., Binnie, S.A., Victor, P., González, G. and Bolten, A., 2016. Accelerated late quaternary uplift revealed by 10Be exposure dating of marine terraces, Mejillones Peninsula, northern Chile. *Quaternary Geochronology*, *36*, pp.12-27.

Bintanja, R. and Van de Wal, R.S.W., 2008. North American ice-sheet dynamics and the onset of 100,000-year glacial cycles. *Nature*, *454*(7206), pp.869-872.

Bintanja, R., Van De Wal, R.S. and Oerlemans, J., 2005. Modelled atmospheric temperatures and global sea levels over the past million years. *Nature*, *437*(7055), pp.125-128.

Birck, J.L., 1986. Precision K Rb Sr isotopic analysis: application to Rb Sr chronology. *Chemical geology*, *56*(1-2), pp.73-83.

Bird, E. C. (2011). *Coastal geomorphology: an introduction*. John Wiley & Sons.

Bohnhoff, M., Harjes, H.P. and Meier, T., 2005. Deformation and stress regimes in the Hellenic subduction zone from focal mechanisms. *Journal of Seismology*, *9*(3), pp.341-366.

Bohnhoff, M., Makris, J., Papanikolaou, D. and Stavrakakis, G., 2001. Crustal investigation of the Hellenic subduction zone using wide aperture seismic data. *Tectonophysics*, *343*(3-4), pp.239-262.

Bonaduce, A., Pinardi, N., Oddo, P., Spada, G. and Larnicol, G., 2016. Sea-level variability in the Mediterranean Sea from altimetry and tide gauges. *Climate Dynamics*, *47*(9-10), pp.2851-2866.

Boncio, P., Lavecchia, G., and Pace, B, 2004. Defining a model of 3D seismogenic sources for Seismic Hazard Assessment applications: the case of central Apennines (Italy). *Journal of Seismology*, *8*(3), pp.407-425.

Bordoni, P. and Valensise, G., 1999. Deformation of the 125 ka marine terrace in Italy: tectonic implications. *Geological Society, London, Special Publications*, *146*(1), pp.71-110.

Bornovas, J., Gaitanakis, P., and Spiridopoulos, A. (1984). *Geological map of Greece, 1:50,000, Perachora Sheet.* Athens: IGME.

Böttner, C., Gross, F., Geersen, J., Crutchley, G.J., Mountjoy, J.J. and Krastel, S., 2018. Marine forearc extension in the Hikurangi margin: New insights from high-resolution 3-D seismic data. *Tectonics*, *37*(5), pp.1472-1491.

Boulton, S.J. and Stewart, I.S., 2015. Holocene coastal notches in the Mediterranean region: Indicators of palaeoseismic clustering?. *Geomorphology*, *237*, pp.29-37.

Braga, J.C. and Bassi, D., 2011. Facies and coralline algae from Oligocene limestones in the Malaguide Complex (SE Spain). *Annalen des Naturhistorischen Museums in Wien. Serie A für Mineralogie und Petrographie, Geologie und Paläontologie, Anthropologie und Prähistorie*, pp.291-308.

Briole, P., Rigo, A., Lyon-Caen, H., Ruegg, J.C., Papazissi, K., Mitsakaki, C., Balodimou, A., Veis, G., Hatzfeld, D. and Deschamps, A., 2000. Active deformation of the Corinth rift, Greece: results from repeated Global Positioning System surveys between 1990 and 1995. *Journal of Geophysical Research: Solid Earth*, *105*(B11), pp.25605-25625.

Brozzetti, F., Boncio, P., Cirillo, D., Ferrarini, F., De Nardis, R., Testa, A., Liberi, F. and Lavecchia, G., 2019. High-resolution field mapping and analysis of the August–October 2016 coseismic surface faulting (Central Italy earthquakes): Slip distribution, parameterization, and comparison with global earthquakes. *Tectonics*, *38*(2), pp.417-439.

Bradley, W.C. and Griggs, G.B., 1976. Form, genesis, and deformation of central California wave-cut platforms. *Geological Society of America Bulletin*, *87*(3), pp.433-449.

Bryant, J.D., Jones, D.S. and Mueller, P.A., 1995. Influence of freshwater flux on 87 Sr/86 Sr chronostratigraphy in marginal marine environments and dating of vertebrate and invertebrate faunas. *Journal of Paleontology*, pp.1-6.

Bull, J.M., Barnes, P.M., Lamarche, G., Sanderson, D.J., Cowie, P.A., Taylor, S.K. and Dix, J.K., 2006. High-resolution record of displacement accumulation on an active normal fault: implications for models of slip accumulation during repeated earthquakes. *Journal of Structural Geology*, *28*(7), pp.1146-1166.

Burbank, D.W. and Anderson, R.S., 2013. Tectonic geomorphology.

Burke, W.H., Denison, R.E., Hetherington, E.A., Koepnick, R.B., Nelson, H.F. and Otto, J.B., 1982. Variation of seawater 87Sr/86Sr throughout Phanerozoic time. *Geology*, *10*(10), pp.516-519.

Burnett, W.C. and Veeh, H.H., 1992. Uranium-series studies of marine phosphates and carbonates. In *Uranium-series disequilibrium: applications to earth, marine, and environmental sciences. 2. ed*.

Burnside, 2010. Unpublished thesis. U-Th dating of travertine on the Colorado Plateau: Implications for the leakage of geologically stored CO2. University of Glasgow.

Busschers, F.S., Wesselingh, F., Kars, R.H., Versluijs-Helder, M., Wallinga, J., Bosch, J.H.A., Timmner, J., Nierop, K.G.J., Meijer, T., Bunnik, F.P.M. and De Wolf, H., 2014. Radiocarbon dating of Late Pleistocene marine shells from the Southern North Sea. *Radiocarbon*, *56*(3), pp.1151-1166.

Byrne, D.E., Sykes, L.R. and Davis, D.M., 1992. Great thrust earthquakes and aseismic slip along the plate boundary of the Makran subduction zone. *Journal of Geophysical Research: Solid Earth*, *97*(B1), pp.449-478.

Caputo, R., 2007. Sea-level curves: perplexities of an end-user in morphotectonic applications. *Global and Planetary Change*, *57*(3-4), pp.417-423.

Caputo, R., Catalano, S., Monaco, C., Romagnoli, G., Tortorici, G. and Tortorici, L., 2010. Active faulting on the island of Crete (Greece). *Geophysical Journal International*, *183*(1), pp.111-126.

Caputo, R., Monaco, C. and Tortorici, L., 2006. Multiseismic cycle deformation rates from Holocene normal fault scarps on Crete (Greece). *Terra Nova*, *18*(3), pp.181-190.

Carobene, L., 2015. Marine notches and sea-cave bioerosional grooves in microtidal areas: examples from the Tyrrhenian and Ligurian coasts—Italy. *Journal of Coastal Research*, *31*(3), pp.536-556.

Cartwright, J.A. and Mansfield, C.S., 1998. Lateral displacement variation and lateral tip geometry of normal faults in the Canyonlands National Park, Utah. *Journal of Structural Geology*, *20*(1), pp.3-19.

Cashman, S.M. and Kelsey, H.M., 1990. Forearc uplift and extension, southern Hawke's Bay, New Zealand: Mid-Pleistocene to present. *Tectonics*, *9*(1), pp.23-44.

Chabaux, F., Dequincey, O., Lévèque, J.J., Leprun, J.C., Clauer, N., Riotte, J. and Paquet, H., 2003. Tracing and dating recent chemical transfers in weathering profiles by trace-element geochemistry and 238U□ 234U□ 230Th disequilibria: the example of the Kaya lateritic toposequence (Burkina-Faso). *Comptes Rendus Geoscience*, *335*(16), pp.1219-1231.

Chappell, J., 1974. Geology of coral terraces, Huon Peninsula, New Guinea: a study of Quaternary tectonic movements and sea-level changes. *Geological Society of America Bulletin*, *85*(4), pp.553-570.

Chappell, J. and Shackleton, N., 1986. Oxygen isotopes and sea level. *Nature*, *324*(6093), pp.137-140.

Chapman, N., Berryman, K., Villamor, P., Epstein, W., Cluff, L. and Kawamura, H., 2014. Active faults and nuclear power plants. *Eos, Transactions American Geophysical Union*, *95*(4), pp.33-34.

Charalampakis, M., Lykousis, V., Sakellariou, D., Papatheodorou, G. and Ferentinos, G., 2014. The tectono-sedimentary evolution of the Lechaion Gulf, the south eastern branch of the Corinth graben, Greece. *Marine Geology*, *351*, pp.58-75.

Chaumillon, E. and Mascle, J., 1997. From foreland to forearc domains: new multichannel seismic reflection survey of the Mediterranean Ridge accretionary complex (Eastern Mediterranean). *Marine Geology*, *138*(3-4), pp.237-259.

Cheloni, D., De Novellis, V., Albano, M., Antonioli, A., Anzidei, M., Atzori, S., Avallone, A., Bignami, C., Bonano, M., Calcaterra, S. and Castaldo, R., 2017. Geodetic model of the 2016 Central Italy earthquake sequence inferred from InSAR and GPS data. *Geophysical Research Letters*, *44*(13), pp.6778-6787.

Chartier, T., Scotti, O. and Lyon-Caen, H., 2019. SHERIFS: Open-Source Code for Computing Earthquake Rates in Fault Systems and Constructing Hazard Models. *Seismological Research Letters*, *90*(4), pp.1678-1688.

Cheng, H., Edwards, R.L., Shen, C.C., Polyak, V.J., Asmerom, Y., Woodhead, J., Hellstrom, J., Wang, Y., Kong, X., Spötl, C. and Wang, X., 2013. Improvements in 230Th dating, 230Th and 234U half-life values, and U–Th isotopic measurements by multi-collector inductively coupled plasma mass spectrometry. *Earth and Planetary Science Letters*, *371*, pp.82-91.

Choi, J.H., Kim, J.W., Murray, A.S., Hong, D.G., Chang, H.W. and Cheong, C.S., 2009. OSL dating of marine terrace sediments on the southeastern coast of Korea with implications for Quaternary tectonics. *Quaternary International*, *199*(1-2), pp.3-14.

Chousianitis, K., Ganas, A. and Evangelidis, C.P., 2015. Strain and rotation rate patterns of mainland Greece from continuous GPS data and comparison between seismic and geodetic moment release. *Journal of Geophysical Research: Solid Earth*, *120*(5), pp.3909-3931.

Chutcharavan, P.M., Dutton, A. and Ellwood, M.J., 2018. Seawater 234U/238U recorded by modern and fossil corals. *Geochimica et Cosmochimica Acta*, *224*, pp.1-17.

Clark, P.U. and Huybers, P., 2009. Interglacial and future sea level. *Nature*, *462*(7275), pp.856-857.

Clarke, P.J., Davies, R.R., England, P.C., Parsons, B., Billiris, H., Paradissis, D., Veis, G., Cross, P.A., Denys, P.H., Ashkenazi, V. and Bingley, R., 1998. Crustal strain in central Greece from repeated GPS measurements in the interval 1989–1997. *Geophysical Journal International*, *135*(1), pp.195-214.

Clift, P.D. and Hartley, A.J., 2007. Slow rates of subduction erosion and coastal underplating along the Andean margin of Chile and Peru. *Geology*, *35*(6), pp.503-506.

Cockburn, H.A. and Summerfield, M.A., 2004. Geomorphological applications of cosmogenic isotope analysis. *Progress in physical Geography*, *28*(1), pp.1-42.

Collier, R.E.L., 1988. *Sedimentary facies evolution in continental fault-bounded basins formed by crustal extension: the Corinth basin, Greece* (Doctoral dissertation, University of Leeds).

Collier, R.L., 1990. Eustatic and tectonic controls upon Quaternary coastal sedimentation in the Corinth Basin, Greece. *Journal of the Geological Society*, *147*(2), pp.301-314.

Collier, R.L., Leeder, M.R., Rowe, P.J. and Atkinson, T.C., 1992. Rates of tectonic uplift in the Corinth and Megara basins, central Greece. *Tectonics*, *11*(6), pp.1159-1167.

Collier, R.E., Leeder, M.R., Trout, M., Ferentinos, G., Lyberis, E. and Papatheodorou, G., 2000. High sediment yields and cool, wet winters: Test of last glacial paleoclimates in the northern Mediterranean. *Geology*, *28*(11), pp.999-1002.

Collier, R. E., Pantosti, D., D'addezio, G., De Martini, P. M., Masana, E., and Sakellariou, D., 1998. Paleoseismicity of the 1981 Corinth earthquake fault: Seismic contribution to extensional strain in central Greece and implications for seismic hazard. *Journal of Geophysical Research: Solid Earth*, *103*(B12), pp.30001-30019.

Collier, R.E.L. and Thompson, J., 1991. Transverse and linear dunes in an Upper Pleistocene marine sequence, Corinth Basin, Greece. *Sedimentology*, *38*(6), pp.1021-1040.

Cooper, F.J., Roberts, G.P. and Underwood, C.J., 2007. A comparison of 103–105 year uplift rates on the South Alkyonides Fault, central Greece: Holocene climate stability and the formation of coastal notches. *Geophysical Research Letters*, *34*(14).

Cowgill, E., Gold, R.D., Xuanhua, C., Xiao-Feng, W., Arrowsmith, J.R. and Southon, J., 2009. Low Quaternary slip rate reconciles geodetic and geologic rates along the Altyn Tagh fault, northwestern Tibet. *Geology*, *37*(7), pp.647-650.

Cowie, P.A., 1998. A healing–reloading feedback control on the growth rate of seismogenic faults. *Journal of Structural Geology*, *20*(8), pp.1075-1087.

Cowie, P.A., Phillips, R.J., Roberts, G.P., McCaffrey, K., Zijerveld, L.J.J., Gregory, L.C., Walker, J.F., Wedmore, L.N.J., Dunai, T.J., Binnie, S.A. and Freeman, S.P.H.T., 2017. Orogen-scale uplift in the central Italian Apennines drives episodic behaviour of earthquake faults. *Scientific reports*, *7*, p.44858.

Cowie, P. A., and Roberts, G. P., 2001. Constraining slip rates and spacings for active normal faults. *Journal of Structural Geology*, *23*(12), pp.1901-1915.

Cowie, P.A., Roberts, G.P., Bull, J.M. and Visini, F., 2012. Relationships between fault geometry, slip rate variability and earthquake recurrence in extensional settings. *Geophysical Journal International*, *189*(1), pp.143-160.

Cowie, P.A. and Scholz, C.H., 1992a. Growth of faults by accumulation of seismic slip. *Journal of Geophysical Research: Solid Earth*, *97*(B7), pp.11085-11095.

Cowie, P.A. and Scholz, C.H., 1992b. Physical explanation for displacement-length relationship of faults using a post-yield fracture mechanics model. *Journal of Structural Geology*, *14*, pp.1133-1133.

Cowie, P.A., Scholz, C.H., Roberts, G.P., Walker, J.F. and Steer, P., 2013. Viscous roots of active seismogenic faults revealed by geologic slip rate variations. *Nature Geoscience*, *6*(12), pp.1036-1040.

Cowie, P. A., and Shipton, Z. K., 1998. Fault tip displacement gradients and process zone dimensions. *Journal of Structural Geology*, *20*(8), pp.983-997.

Crémière, A., Lepland, A., Chand, S., Sahy, D., Condon, D.J., Noble, S.R., Martma, T., Thorsnes, T., Sauer, S. and Brunstad, H., 2016. Timescales of methane seepage on the Norwegian margin following collapse of the Scandinavian Ice Sheet. *Nature communications*, *7*(1), pp.1-10.

Crone, A. J., and Haller, K. M., 1991. Segmentation and the coseismic behavior of Basin and Range normal faults: examples from east-central Idaho and southwestern Montana, USA. *Journal of Structural Geology*, 13(2), pp.151-164.

Cronin, T.M., 1981. Rates and possible causes of neotectonic vertical crustal movements of the emerged southeastern United States Atlantic Coastal Plain. *Geological Society of America Bulletin*, *92*(11), pp.812-833.

Cucci, L., 2004. Raised marine terraces in the Northern Calabrian Arc (Southern Italy): a~ 600 kyr-long geological record of regional uplift. *Annals of Geophysics*, *47*(4).

Cucci, L. and Cinti, F.R., 1998. Regional uplift and local tectonic deformation recorded by the Quaternary marine terraces on the Ionian coast of northern Calabria (southern Italy). *Tectonophysics*, *292*(1-2), pp.67-83.

Cucci, L. and Tertulliani, A., 2010. The Capo Vaticano (Calabria) coastal terraces and the 1905 M7 earthquake: the geomorphological signature of regional uplift and coseismic slip in southern Italy. *Terra Nova*, *22*(5), pp.378-389.

D'agostino, N., Cheloni, D., Fornaro, G., Giuliani, R. and Reale, D., 2012. Space-time distribution of afterslip following the 2009 L'Aquila earthquake. *Journal of Geophysical Research: Solid Earth*, *117*(B2).

Darvill, C.M., 2013. Cosmogenic nuclide analysis. *Geomorphological techniques*, pp.1-25.

Davies, R., England, P.C., Parsons, B., Billiris, H., Paradissis, D. and Veis, G., 1997. Geodetic strain of Greece in the interval 1892–1992. *Journal of Geophysical Research: Solid Earth*, *102*(B11), pp.24571-24588.

De Boer, B., Van de Wal, R.S.W., Bintanja, R., Lourens, L.J. and Tuenter, E., 2010. Cenozoic global ice-volume and temperature simulations with 1-D ice-sheet models forced by benthic δ 18 O records. *Annals of glaciology*, *51*(55), pp.23-33.

de Gelder, G., 2017. Unpublished Thesis *Plio-Quaternary tectonic changes along the Hellenic Arc (Greece) induced by a propagating plate boundary*. l'Institut De Physique Du Globe De Paris.

de Gelder, G., Fernández-Blanco, D., Melnick, D., Duclaux, G., Bell, R.E., Jara-Muñoz, J., Armijo, R. and Lacassin, R., 2019 Lithospheric flexure and rheology determined by climate cycle markers in the Corinth Rift. *Scientific reports*, *9*(1), pp.1-12.

de Gelder, G., Jara-Munoz, J., Melnick, D., Fernández-Blanco, D., Rouby, H., Pedoja, K., Husson, L., Armijo, R. and Lacassin, R., 2020. How do sea-level curves influence modeled marine terrace sequences?. *Quaternary Science Reviews*, *229*, p.106132.

De Guidi, G., Catalano, S., Monaco, C. and Tortorici, L., 2003. Morphological evidence of Holocene coseismic deformation in the Taormina region (NE Sicily). *Journal of Geodynamics*, *36*(1-2), pp.193-211.

De Martini, P.M., Pantosti, D., Palyvos, N., Lemeille, F., McNeill, L. and Collier, R., 2004. Slip rates of the Aigion and Eliki faults from uplifted marine terraces, Corinth Gulf, Greece. *Comptes Rendus Geoscience*, *336*(4-5), pp.325-334.

de Polo, C.M. and Anderson, J.G., 2000. Estimating the slip rates of normal faults in the Great Basin, USA. *Basin Research*, *12*(3-4), pp.227-240.

de Polo, C. M., Clark, D. G., Slemmons, D. B., and Ramelli, A. R., 1991. Historical surface faulting in the Basin and Range province, western North America: implications for fault segmentation. *Journal of structural Geology*, *13*(2), pp.123-136.

de Polo, C.M., Slemmons, D.B., 1997. Age criteria for active faults in the Basin and Range Province. In: Lund, W.R. , Western States Seismic Policy Council Proceeding Volume, Basin and Range Province Seismic-Hazards Summit, pp. 7483

Devescovi, M. and Iveša, L., 2008. Colonization patterns of the date mussel Lithophaga lithophaga (L., 1758) on limestone breakwater boulders of a marina. *Periodicum biologorum*, *110*(4), pp.339-345.

Dia, A. N., Cohen, A. S., O'nions, R. K., and Jackson, J. A., 1997. Rates of uplift investigated through 230Th dating in the Gulf of Corinth (Greece). *Chemical Geology*, *138*(3-4), pp.171-184.

Diehl, R., Halloin, H., Kretschmer, K., Lichti, G.G., Schönfelder, V., Strong, A.W., Von Kienlin, A., Wang, W., Jean, P., Knödlseder, J. and Roques, J.P., 2006. Radioactive 26 Al from massive stars in the Galaxy. *Nature*, *439*(7072), pp.45-47.

Dolan, J.F., Bowman, D.D. and Sammis, C.G., 2007. Long-range and long-term fault interactions in Southern California. *Geology*, *35*(9), pp.855-858.Cucci, L., D'Addezio, G., Valensise, G. and Burrato, P., 1996. Investigating seismogenic faults in Central and Southern Apennines (Italy): modeling of fault-related landscape features. *Annals of Geophysics*, *39*(3).

Doutsos, T. and Kokkalas, S., 2001. Stress and deformation patterns in the Aegean region. *Journal of Structural Geology*, *23*(2-3), pp.455-472.

Doutsos, T. and Piper, D.J., 1990. Listric faulting, sedimentation, and morphological evolution of the Quaternary eastern Corinth rift, Greece: First stages of continental rifting. *Geological Society of America Bulletin*, *102*(6), pp.812-829.

Duffy, B., 2020. A geometric model to estimate slip rates from terrace rotation above an offshore, listric thrust fault, Kaikōura, New Zealand. *Tectonophysics*, p.228460.

Dunai, T.J., 2010. *Cosmogenic Nuclides: Principles, concepts and applications in the Earth surface sciences*. Cambridge University Press.

Dutton, A., 2015. Uranium-thorium dating. *Handbook of sea-level research. Chichester: John Wiley & Sons, Ltd*, pp.386-403

Dutton, A., Bard, E., Antonioli, F., Esat, T.M., Lambeck, K. and McCulloch, M.T., 2009. Phasing and amplitude of sea-level and climate change during the penultimate interglacial. *Nature Geoscience*, *2*(5), pp.355-359.

Dutton, A. and Lambeck, K., 2012. Ice volume and sea level during the last interglacial. *science*, *337*(6091), pp.216-219.

Dutton, A., Webster, J.M., Zwartz, D., Lambeck, K. and Wohlfarth, B., 2015. Tropical tales of polar ice: evidence of Last Interglacial polar ice sheet retreat recorded by fossil reefs of the granitic Seychelles islands. *Quaternary Science Reviews*, *107*, pp.182-196.

Dwyer, G.S., Cronin, T.M., Baker, P.A., Raymo, M.E., Buzas, J.S. and Corrège, T., 1995. North Atlantic deepwater temperature change during late Pliocene and late Quaternary climatic cycles. *Science*, *270*(5240), pp.1347-1351.

Dziewonski, A.M., Chou, T.A. and Woodhouse, J.H., 1981. Determination of earthquake source parameters from waveform data for studies of global and regional seismicity. *Journal of Geophysical Research: Solid Earth*, *86*(B4), pp.2825-2852.

Edwards, R.L., Chen, J.H. and Wasserburg, G.J., 1987. 238U234U230Th232Th systematics and the precise measurement of time over the past 500,000 years. *Earth and Planetary Science Letters*, *81*(2-3), pp.175-192.

Elderfield, H., Ferretti, P., Greaves, M., Crowhurst, S., McCave, I.N., Hodell, D. and Piotrowski, A.M., 2012. Evolution of ocean temperature and ice volume through the mid-Pleistocene climate transition. *science*, *337*(6095), pp.704-709.

Ekström, G., Nettles, M. and Dziewoński, A.M., 2012. The global CMT project 2004–2010: Centroid-moment tensors for 13,017 earthquakes. *Physics of the Earth and Planetary Interiors*, *200*, pp.1-9.

Emiliani, C. (1955). Pleistocene temperatures. *The Journal of geology*, *63*(6), 538-578.

Esat, T.M., McCulloch, M.T., Chappell, J., Pillans, B. and Omura, A., 1999. Rapid fluctuations in sea level recorded at Huon Peninsula during the penultimate deglaciation. *Science*, *283*(5399), pp.197-201.

Esat, T.M. and Yokoyama, Y., 2006. Variability in the uranium isotopic composition of the oceans over glacial–interglacial timescales. *Geochimica et Cosmochimica Acta*, *70*(16), pp.4140-4150.

Esat, T.M. and Yokoyama, Y., 2010. Coupled uranium isotope and sea-level variations in the oceans. *Geochimica et Cosmochimica Acta*, *74*(24), pp.7008-7020.

Evelpidou, N., Vassilopoulos, A. and Pirazzoli, P.A., 2012. Submerged notches on the coast of Skyros Island (Greece) as evidence for Holocene subsidence. *Geomorphology*, *141*, pp.81-87.

Falkenroth, M., Adolphs, S., Cahnbley, M., Bagci, H., Kázmér, M., Mechernich, S. and Hoffmann, G., 2020. Biological Indicators Reveal Small-Scale Sea-Level Variability During MIS 5e (Sur, Sultanate of Oman). *Open Quaternary*, *6*(1).

Farrell, W.E. and Clark, J.A., 1976. On postglacial sea level. *Geophysical Journal International*, *46*(3), pp.647-667.

Farías, M., Vargas, G., Tassara, A., Carretier, S., Baize, S., Melnick, D. and Bataille, K., 2010. Land-level changes produced by the Mw 8.8 2010 Chilean earthquake. *Science*, *329*(5994), pp.916-916.

Fassoulas, C.G., 2000. *Field guide to the geology of Crete*. Natural History Museum of Crete.

Fassoulas, C., 2001. The tectonic development of a Neogene basin at the leading edge of the active European margin: the Heraklion basin, Crete, Greece. *Journal of Geodynamics*, *31*(1), pp.49-70.

Fassoulas, C., Kilias, A. and Mountrakis, D., 1994. Postnappe stacking extension and exhumation of high-pressure/low-temperature rocks in the island of Crete, Greece. *Tectonics*, *13*(1), pp.127-138.

Faure Walker, J.., Roberts, G.P., Cowie, P.A., Papanikolaou, I., Michetti, A.M., Sammonds, P., Wilkinson, M., McCaffrey, K.J.W. and Phillips, R.J., 2012. Relationship between topography, rates of extension and mantle dynamics in the actively-extending Italian Apennines. *Earth and Planetary Science Letters*, *325*, pp.76-84.

Faure Walker, J., Roberts, G.P., Cowie, P.A., Papanikolaou, I.D., Sammonds, P.R., Michetti, A.M. and Phillips, R.J., 2009. Horizontal strain-rates and throw-rates across breached relay zones, central Italy: Implications for the preservation of throw deficits at points of normal fault linkage. *Journal of Structural Geology*, *31*(10), pp.1145-1160.

Faure Walker, J.P., Roberts, G.P., Sammonds, P.R. and Cowie, P., 2010. Comparison of earthquake strains over 102 and 104 year timescales: Insights into variability in the seismic cycle in the central Apennines, Italy. *Journal of Geophysical Research: Solid Earth*, *115*(B10).

Faure Walker, J., Visini, F., Roberts, G., Galasso, C., McCaffrey, K. and Mildon, Z., 2019. Variable Fault Geometry Suggests Detailed Fault-Slip-Rate Profiles and Geometries Are Needed for Fault-Based Probabilistic Seismic Hazard Assessment (PSHA) Variable Fault Geometry Suggests Detailed Fault-Slip-Rate Profiles and Geometries Are Needed. *Bulletin of the Seismological Society of America*, *109*(1), pp.110-123.

Fernández-Blanco, D., de Gelder, G., Lacassin, R. and Armijo, R., 2019. A new crustal fault formed the modern Corinth Rift. *Earth-Science Reviews*, *199*, p.102919.

Ferranti, L., Antonioli, F., Mauz, B., Amorosi, A., Dai Pra, G., Mastronuzzi, G., Monaco, C., Orrù, P., Pappalardo, M., Radtke, U. and Renda, P., 2006. Markers of the last interglacial sea-level high stand along the coast of Italy: tectonic implications. *Quaternary international*, *145*, pp.30-54.

Ferrill, D. A., and Morris, A. P., 2001. Displacement gradient and deformation in normal fault systems. *Journal of Structural Geology*, *23*(4), pp.619-638.

Ferrill, D.A., Stamatakos, J.A. and Sims, D., 1999. Normal fault corrugation: Implications for growth and seismicity of active normal faults. *Journal of Structural Geology*, *21*(8-9), pp.1027-1038.

Field, E.H., Arrowsmith, R.J., Biasi, G.P., Bird, P., Dawson, T.E., Felzer, K.R., Jackson, D.D., Johnson, K.M., Jordan, T.H., Madden, C. and Michael, A.J., 2014. Uniform California earthquake rupture forecast, version 3 (UCERF3)—The time-independent model. *Bulletin of the Seismological Society of America*, *104*(3), pp.1122-1180.

Field, E.H., Milner, K.R., Hardebeck, J.L., Page, M.T., van der Elst, N., Jordan, T.H., Michael, A.J., Shaw, B.E. and Werner, M.J., 2017. A spatiotemporal clustering model for the third Uniform California Earthquake Rupture Forecast (UCERF3-ETAS): Toward an operational earthquake forecast. *Bulletin of the Seismological Society of America*, *107*(3), pp.1049-1081.

Firth, C., Stewart, I., McGuire, W.J., Kershaw, S. and Vita-Finzi, C., 1996. Coastal elevation changes in eastern Sicily: implications for volcano instability at Mount Etna. *Geological Society, London, Special Publications*, *110*(1), pp.153-167.

Flecker, R., De Villiers, S. and Ellam, R.M., 2002. Modelling the effect of evaporation on the salinity–87Sr/86Sr relationship in modern and ancient marginal-marine systems: the Mediterranean Messinian Salinity Crisis. *Earth and Planetary Science Letters*, *203*(1), pp.221-233.

Floyd, M.A., Billiris, H., Paradissis, D., Veis, G., Avallone, A., Briole, P., McClusky, S., Nocquet, J.M., Palamartchouk, K., Parsons, B. and England, P.C., 2010. A new velocity field for Greece: Implications for the kinematics and dynamics of the Aegean. *Journal of Geophysical Research: Solid Earth*, *115*(B10).

Fossen, H. and Rotevatn, A., 2016. Fault linkage and relay structures in extensional settings—A review. *Earth-Science Reviews*, *154*, pp.14-28.

Friedrich, A.M., Wernicke, B.P., Niemi, N.A., Bennett, R.A. and Davis, J.L., 2003. Comparison of geodetic and geologic data from the Wasatch region, Utah, and implications for the spectral character of Earth deformation at periods of 10 to 10 million years. *Journal of Geophysical Research: Solid Earth*, *108*(B4).

Gaki-Papanastassiou, K., Karymbalis, E., Papanastassiou, D. and Maroukian, H., 2009. Quaternary marine terraces as indicators of neotectonic activity of the Ierapetra normal fault SE Crete (Greece). *Geomorphology*, *104*(1-2), pp.38-46.

Gaki-Papanastassiou, K., Maroukian, H. and Kourmpanian, V., 2011. The morphotectonic evolution of southern half of Kythira Island (Ionian sea, Greece) during the Quaternary. *Prace Geograficzne*, (127).

Gallen, S. 2014. Viewed 2020. <https://sites.google.com/site/theseanswebsite/current-research/crete-greece>.

Gallen, S.F. and Wegmann, K.W., 2017. River profile response to normal fault growth and linkage: An example from the Hellenic forearc of south-central Crete, Greece. *Earth Surface Dynamics*, *5*(1), pp.161-186.

Gallen, S.F., Wegmann, K.W., Bohnenstiehl, D.R., Pazzaglia, F.J., Brandon, M.T. and Fassoulas, C., 2014. Active simultaneous uplift and margin-normal extension in a forearc high, Crete, Greece. *Earth and Planetary Science Letters*, *398*, pp.11-24.

Galli, P., Galadini, F. and Pantosti, D., 2008. Twenty years of paleoseismology in Italy. *Earth-Science Reviews*, *88*(1-2), pp.89-117.

Gallup, C. D., Cheng, H., Taylor, F. W., and Edwards, R. L., 2002. Direct determination of the timing of sea level change during Termination II. *Science*, *295*(5553), pp.310-313.

Gallup, C.D., Edwards, R.L. and Johnson, R.G., 1994. The timing of high sea levels over the past 200,000 years. *Science*, *263*(5148), pp.796-800.

Ganas, A., Fassoulas, C., Moshou, A., Bozionelos, G., Papathanassiou, G., Tsimi, C. and Valkaniotis, S., 2017. Geological and seismological evidence for NW-SE crustal extension at the southern margin of Heraklion basin, Crete. *Bulletin of the Geological Society of Greece*, *51*, pp.52-75.

Ganas, A., Oikonomou, I.A. and Tsimi, C., 2013. NOAFAULTS: A Digital Database for Active Faults in Greece in Bulletin of the Geological Society of Greece, v. XLVII. *Proceedings fo the 13th International Cogfress, Chania*.

Ganas, A. and Parsons, T., 2009. Three-dimensional model of Hellenic Arc deformation and origin of the Cretan uplift. *Journal of Geophysical Research: Solid Earth*, *114*(B6).

Giba, M., Walsh, J.J. and Nicol, A., 2012. Segmentation and growth of an obliquely reactivated normal fault. *Journal of Structural Geology*, *39*, pp.253-267.

Gosse, J.C. and Phillips, F.M., 2001. Terrestrial in situ cosmogenic nuclides: theory and application. *Quaternary Science Reviews*, *20*(14), pp.1475-1560.

Grant, L.B., Mueller, K.J., Gath, E.M., Cheng, H., Lawrence Edwards, R., Munro, R. and Kennedy, G.L., 1999. Late Quaternary uplift and earthquake potential of the San Joaquin Hills, southern Los Angeles basin, California. *Geology*, *27*(11), pp.1031-1034.

Grant, K.M., Rohling, E.J., Bar-Matthews, M., Ayalon, A., Medina-Elizalde, M., Ramsey, C.B., Satow, C. and Roberts, A.P., 2012. Rapid coupling between ice volume and polar temperature over the past 150,000 years. *Nature*, *491*(7426), pp.744-747.

Grant, K.M., Rohling, E.J., Ramsey, C.B., Cheng, H., Edwards, R.L., Florindo, F., Heslop, D., Marra, F., Roberts, A.P., Tamisiea, M.E. and Williams, F., 2014. Sea-level variability over five glacial cycles. *Nature communications*, *5*(1), pp.1-9.

Griggs, G.B. and Trenhaile, A.S., 1994. *Coastal cliffs and platforms* (pp. 425-450). Cambridge University Press, Cambridge, UK.

Grzymko, T.J., Marcantonio, F., McKee, B.A. and Stewart, C.M., 2007. Temporal variability of uranium concentrations and 234U/238U activity ratios in the Mississippi river and its tributaries. *Chemical Geology*, *243*(3-4), pp.344-356.

Gupta, A. and Scholz, C.H., 2000. A model of normal fault interaction based on observations and theory. *Journal of Structural Geology*, *22*(7), pp.865-879.

Gutiérrez, F., Carbonel, D., Sevil, J., Moreno, D., Linares, R., Comas, X., Zarroca, M., Roqué, C. and McCalpin, J.P., 2020. Neotectonics and late Holocene paleoseismic evidence in the Plio-Quaternary Daroca Half-graben, Iberian Chain, NE Spain. Implications for fault source characterization. *Journal of Structural Geology*, *131*, p.103933.

Harris, R.A., 1998. Introduction to special section: Stress triggers, stress shadows, and implications for seismic hazard. *Journal of Geophysical Research: Solid Earth*, *103*(B10), pp.24347-24358.

Hamelin, B., Bard, E., Zindler, A. and Fairbanks, R.G., 1991. 234U/238U mass spectrometry of corals: How accurate is the UTh age of the last interglacial period?. *Earth and Planetary Science Letters*, *106*(1-4), pp.169-180.

Hearty, P.J., Bonfiglio, L., Violante, D. and Szabo, B.J., 1986. Age of late Quaternary marine deposits of southern Italy determined by aminostratigraphy, faunal correlation, and uranium-series dating. *Rivista italiana di Paleontologia e Stratigrafia*, *92*(1).

Hearty, P.J., Hollin, J.T., Neumann, A.C., O'Leary, M.J. and McCulloch, M., 2007. Global sea-level fluctuations during the Last Interglaciation (MIS 5e). *Quaternary Science Reviews*, *26*(17-18), pp.2090-2112.

Hearty, P.J., Kindler, P., Cheng, H. and Edwards, R.L., 1999. A+ 20 m middle Pleistocene sea-level highstand (Bermuda and the Bahamas) due to partial collapse of Antarctic ice. *Geology*, *27*(4), pp.375-378.

Heezen, B.C., Ewing, M. and Johnson, G.L., 1966, June. The Gulf of Corinth floor. In *Deep Sea Research and Oceanographic Abstracts* (Vol. 13, No. 3, pp. 381-411). Elsevier.

Heisinger, B., Lal, D., Jull, A.J.T., Kubik, P., Ivy-Ochs, S., Neumaier, S., Knie, K., Lazarev, V. and Nolte, E., 2002a. Production of selected cosmogenic radionuclides by muons: 1. Fast muons. *Earth and Planetary Science Letters*, *200*(3-4), pp.345-355.

Heisinger, B., Lal, D., Jull, A.J.T., Kubik, P., Ivy-Ochs, S., Knie, K. and Nolte, E., 2002b. Production of selected cosmogenic radionuclides by muons: 2. Capture of negative muons. *Earth and Planetary Science Letters*, *200*(3-4), pp.357-369.

Henderson, G.M., Cohen, A.S. and O'nions, R.K., 1993. 234U/238U ratios and230Th ages for Hateruma Atoll corals: implications for coral diagenesis and seawater234U/238U ratios. *Earth and Planetary Science Letters*, *115*(1-4), pp.65-73.

Henderson, G.M., Martel, D.J., O'Nions, R.K. and Shackleton, N.J., 1994. Evolution of seawater 87Sr86Sr over the last 400 ka: the absence of glacial/interglacial cycles. *Earth and Planetary Science Letters*, *128*(3-4), pp.643-651.

Hibbert, Fiona D., Eelco J. Rohling, Andrea Dutton, Felicity H. Williams, Peter M. Chutcharavan, Cheng Zhao, and Mark E. Tamisiea. "Coral indicators of past sea-level change: A global repository of U-series dated benchmarks." *Quaternary Science Reviews* 145 (2016): 1-56.

Hillaire-Marcel, C., Gariépy, C., Ghaleb, B., Goy, J.L., Zazo, C. and Barcelo, J.C., 1996. U-series measurements in Tyrrhenian deposits from Mallorca—further evidence for two last-interglacial high sea levels in the Balearic Islands. *Quaternary Science Reviews*, *15*(1), pp.53-62.

Hodell, D.A., Mead, G.A. and Mueller, P.A., 1990. Variation in the strontium isotopic composition of seawater (8 Ma to present): Implications for chemical weathering rates and dissolved fluxes to the oceans. *Chemical Geology: Isotope Geoscience section*, *80*(4), pp.291-307.

Hodgkinson, K.M., Stein, R.S. and King, G.C., 1996. The 1954 Rainbow Mountain-Fairview Peak-Dixie Valley earthquakes: A triggered normal faulting sequence. *Journal of Geophysical Research: Solid Earth*, *101*(B11), pp.25459-25471.

Houghton, 2010. Unpublished Thesis. Localization of Quaternary slip rates in an active rift in 10(5) years: an example from central Greece constrained by U-234-Th-230 coral dates from uplifted paleoshorelines. University of London, Birkbeck College.

Houghton, S.L., Roberts, G.P., Papanikolaou, I.D., McArthur, J.M. and Gilmour, M.A., 2003. New 234U-230Th coral dates from the western Gulf of Corinth: Implications for extensional tectonics. *Geophysical Research Letters*, *30*(19).

Howell, A., Jackson, J., Copley, A., McKenzie, D. and Nissen, E., 2017. Subduction and vertical coastal motions in the eastern Mediterranean. *Geophysical Journal International*, *211*(1), pp.593-620.

Howell, A., Palamartchouk, K., Papanikolaou, X., Paradissis, D., Raptakis, C., Copley, A., England, P. and Jackson, J., 2017. The 2008 Methoni earthquake sequence: the relationship between the

earthquake cycle on the subduction interface and coastal uplift in SW Greece. *Geophysical Journal International*, *208*(3), pp.1592-1610.

Hu, Y., Wang, K., He, J., Klotz, J. and Khazaradze, G., 2004. Three-dimensional viscoelastic finite element model for postseismic deformation of the great 1960 Chile earthquake. *Journal of Geophysical Research: Solid Earth*, *109*(B12).

Hubert, A., King, G., Armijo, R., Meyer, B., and Papanastasiou, D., 1996. Fault re-activation, stress interaction and rupture propagation of the 1981 Corinth earthquake sequence. *Earth and Planetary Science Letters*, *142*(3-4), pp.573-585.

Huggins, P., Watterson, J., Walsh, J. J., and Childs, C., 1995. Relay zone geometry and displacement transfer between normal faults recorded in coal-mine plans. *Journal of Structural Geology*, *17*(12), pp.1741-1755.

Huguen, C., Zitter, T., Mascle, J., Woodside, J., Benkhelil, J., Giresse, P. and Foucher, J.P., 2001, September. Tectonic control of mud volcanoes from the Central Mediterranean Ridge (South of Crete): a multiscale analysis. In *Extended abstracts to the Subsurface Sediment Mobilisation Conference, Ghent*.

Iezzi, F., Mildon, Z., Walker, J.F., Roberts, G., Goodall, H., Wilkinson, M. and Robertson, J., 2018. Coseismic throw variation across along-strike bends on active normal faults: Implications for displacement versus length scaling of earthquake ruptures. *Journal of Geophysical Research: Solid Earth*, *123*(11), pp.9817-9841.

Iezzi, F., Roberts, G. and Walker, J.F., 2020. Throw-rate variations within linkage zones during the growth of normal faults: Case studies from the Western Volcanic Zone, Iceland. *Journal of Structural Geology*, *133*, p.103976.

Iezzi, F., Roberts, G., Walker, J.F. and Papanikolaou, I., 2019. Occurrence of partial and total coseismic ruptures of segmented normal fault systems: Insights from the Central Apennines, Italy. *Journal of Structural Geology*, *126*, pp.83-99.

Institute of Geology and Mineral Exploration of Greece (IGME). 'Akhendhrias sheet, Crete' 1:50,000.

Institute of Geology and Mineral Exploration of Greece (IGME). 'Ano Viannos sheet, Crete' 1:50,000.

Institute of Geology and Mineral Exploration of Greece (IGME). 'Koroni-Pylos-Skhiza sheet, Peloponnese' 1:50,000.

Institute of Geology and Mineral Exploration of Greece (IGME). 'Mavrovoynion-Areopolis-Yerolimin sheet, Mani Peninsula' 1:50,000.

International Seismological Centre, 2016. On-line bulletin, http://www.isc.ac.uk, Internatl. Seismol. Cent., Thatcham, United Kingdom, 2016.

Imanishi, K., Ando, R. and Kuwahara, Y., 2012. Unusual shallow normal-faulting earthquake sequence in compressional northeast Japan activated after the 2011 off the Pacific coast of Tohoku earthquake. *Geophysical Research Letters*, *39*(9).

Imbrie, J., Hays, J.D., Martinson, D.G., McIntyre, A., Mix, A.C., Morley, J.J., Pisias, N.G., Prell, W.L. and Shackleton, N.J., 1984. The orbital theory of Pleistocene climate: support from a revised chronology of the marine d18O record.

International Seismological Centre (2016). On-line bulletin, http://www.isc.ac.uk, Internatl. Seismol. Cent., Thatcham, United Kingdom, 2016.

Ivy-Ochs, S., Kerschner, H., Reuther, A., Maisch, M., Sailer, R., Schaefer, J., Kubik, P.W., Synal, H. and Schluchter, C., 2006. The timing of glacier advances in the northern European Alps based on surface exposure dating with cosmogenic^ 1^ 0Be,^ 2^ 6Al,^ 3^ 6Cl, and^ 2^ 1Ne. *Special Papers-Geological Society of America*, *415*, p.43.

Ivy-Ochs, S. and Kober, F., 2008. Surface exposure dating with cosmogenic nuclides. *Quaternary Science Journal*, *57*(1-2), pp.179-209.

Ivy-Ochs, S., Schäfer, J., Kubik, P.W., Synal, H.A. and Schlüchter, C., 2004. Timing of deglaciation on the northern Alpine foreland (Switzerland). *Eclogae Geologicae Helvetiae*, *97*(1), pp.47-55.

Jackson, J., 1994. Active tectonics of the Aegean region. *Annual Review of Earth and Planetary Sciences*, *22*(1), pp.239-271.

Jackson, J. A., Gagnepain, J., Houseman, G., King, G. C. P., Papadimitriou, P., Soufleris, C., and Virieux, J., 1982. Seismicity, normal faulting, and the geomorphological development of the Gulf of Corinth (Greece): the Corinth earthquakes of February and March 1981. *Earth and Planetary Science Letters*, *57*(2), pp.377-397.

Jackson, J. and McKenzie, D., 1988. The relationship between plate motions and seismic moment tensors, and the rates of active deformation in the Mediterranean and Middle East. *Geophysical Journal International*, *93*(1), pp.45-73.

Jackson, J.A. and White, N.J., 1989. Normal faulting in the upper continental crust: observations from regions of active extension. *Journal of Structural Geology*, *11*(1-2), pp.15-36.

Jacobs, A., Sandwell, D., Fialko, Y. and Sichoix, L., 2002. The 1999 (M w 7.1) Hector Mine, California, earthquake: Near-field postseismic deformation from ERS interferometry. *Bulletin of the Seismological Society of America*, *92*(4), pp.1433-1442.

Jara-Muñoz, J. and Melnick, D., 2015. Unraveling sea-level variations and tectonic uplift in wave-built marine terraces, Santa María Island, Chile. *Quaternary Research*, *83*(1), pp.216-228.

Jara-Muñoz, J., Melnick, D., Pedoja, K. and Strecker, M.R., 2019. Terracem-2: A matlab® interface for mapping and modeling marine and lacustrine terraces. *Frontiers in Earth Science*, *7*, p.255.

Jara-Muñoz, J., Melnick, D. and Strecker, M.R., 2016. TerraceM: A MATLAB® tool to analyze marine and lacustrine terraces using high-resolution topography. *Geosphere*, *12*(1), pp.176-195.

Jara-Muñoz, J., Melnick, D., Zambrano, P., Rietbrock, A., González, J., Argandoña, B. and Strecker, M.R., 2017. Quantifying offshore fore-arc deformation and splay-fault slip using drowned Pleistocene shorelines, Arauco Bay, Chile. *Journal of Geophysical Research: Solid Earth*, *122*(6), pp.4529-4558.

Jolivet, L., Faccenna, C., Huet, B., Labrousse, L., Le Pourhiet, L., Lacombe, O., Lecomte, E., Burov, E., Denèle, Y., Brun, J.P. and Philippon, M., 2013. Aegean tectonics: Strain localisation, slab tearing and trench retreat. *Tectonophysics*, *597*, pp.1-33.

Jónsson, S., Zebker, H., Segall, P. and Amelung, F., 2002. Fault slip distribution of the 1999 M w 7.1 Hector Mine, California, earthquake, estimated from satellite radar and GPS measurements. *Bulletin of the Seismological Society of America*, *92*(4), pp.1377-1389.

Karymbalis, E., Papanastassiou, D., Gaki-Papanastassiou, K., Tsanakas, K. and Maroukian, H., 2013. Geomorphological study of Cephalonia Island, Ionian Sea, Western Greece. *Journal of Maps*, *9*(1), pp.121-134.

Kassaras, I., Kazantzidou-Firtinidou, D., Ganas, A., Kapetanidis, V., Tsimi, C., Valkaniotis, S., Sakellariou, N. and Mourloukos, S., 2018. Seismic risk and loss assessment for Kalamata (SW Peloponnese, Greece) from neighbouring shallow sources. *Bollettino di Geofisica Teorica ed Applicata*, *59*(1).

Kelletat, D., 1991. The 1550 BP tectonic event in the Eastern Mediterranean as a basis for assessing the intensity of shore processes. *Zeitschrift für Geomorphologie, Supplementbande*, *81*, pp.181-194.

Kelletat, D., Kowalczyk, G., Schröder, B. and Winter, K.P., 1976. A synoptic view on the neotectonic development of the Peloponnesian coastal regions. *Zeitschrift der deutschen geologischen Gesellschaft*, pp.447-465.

Kenner, S.J. and Segall, P., 2000. Postseismic deformation following the 1906 San Francisco earthquake. *Journal of Geophysical Research: Solid Earth*, *105*(B6), pp.13195-13209.

Kershaw, S. and Guo, L., 2001. Marine notches in coastal cliffs: indicators of relative sea-level change, Perachora Peninsula, central Greece. *Marine Geology*, *179*(3-4), pp.213-228.

Kershaw, S., and Guo, L., 2003. Pleistocene cyanobacterial mounds in the Perachora Peninsula, Gulf of Corinth, Greece: structure and applications to interpreting sea-level history and terrace sequences in an unstable tectonic setting. *Palaeogeography, Palaeoclimatology, Palaeoecology*, *193*(3-4), pp.503-514.

Kershaw, S., and Guo, L., 2006. Pleistocene calcified cyanobacterial mounds, Perachora Peninsula, central Greece: a controversy of growth and history. *Geological Society, London, Special Publications*, *255*(1), pp.53-69.

Kershaw, S., Guo, L. and Braga, J.C., 2005. A Holocene coral–algal reef at Mavra Litharia, Gulf of Corinth, Greece: structure, history, and applications in relative sea-level change. *Marine geology*, *215*(3-4), pp.171-192.

King, G.C., Stein, R.S. and Lin, J., 1994. Static stress changes and the triggering of earthquakes. *Bulletin of the Seismological Society of America*, *84*(3), pp.935-953.

King, G.C., Stein, R.S. and Rundle, J.B., 1988. The growth of geological structures by repeated earthquakes 1. Conceptual framework. *Journal of Geophysical research: solid Earth*, *93*(B11), pp.13307-13318.

Kokinou, E. and Kamberis, E., 2009. The structure of the Kythira–Antikythira strait, offshore SW Greece (35.7–36.6 N). *Geological Society, London, Special Publications*, *311*(1), pp.343-360.

Kominz, M.A., 2009. Sea Level Variations Over Geological Time. *Elements of Physical Oceanography: A derivative of the Encyclopedia of Ocean Sciences*, p.115.

Konstantinou, K.I., Kalogeras, I.S., Melis, N.S., Kourouzidis, M.C. and Stavrakakis, G.N., 2006. The 8 January 2006 earthquake (Mw 6.7) offshore Kythira Island, Southern Greece: seismological, strong-motion, and macroseismic observations of an intermediate-depth event. *Seismological Research Letters*, *77*(5), pp.544-553.

Konstantinou, K., Mouslopoulou, V., Liang, W.T., Heidbach, O., Oncken, O. and Suppe, J., 2016. Crustal stress field in the Greek region inferred from inversion of moment tensor solutions. *EGUGA*, pp.EPSC2016-3671.

Kopp, R. E., Simons, F. J., Mitrovica, J. X., Maloof, A. C., and Oppenheimer, M., 2009. Probabilistic assessment of sea level during the last interglacial stage. *Nature*, *462*(7275), p.863.

Kouskouna, V. and Makropoulos, K., 2004. Historical earthquake investigations in Greece. *Annals of Geophysics*.

Kokinou, E., Tiago, A. and Evangelos, K., 2012. Structural decoupling in a convergent forearc setting (southern Crete, Eastern Mediterranean). *GSA Bulletin*, *124*(7-8), pp.1352-1364.

Krabbenhöft, A., Eisenhauer, A., Böhm, F., Vollstaedt, H., Fietzke, J., Liebetrau, V., Augustin, N., Peucker-Ehrenbrink, B., Müller, M.N., Horn, C. and Hansen, B.T., 2010. Constraining the marine strontium budget with natural strontium isotope fractionations (87Sr/86Sr∗, δ88/86Sr) of carbonates, hydrothermal solutions and river waters. *Geochimica et Cosmochimica Acta*, *74*(14), pp.4097-4109.

Kreemer, C. and Chamot-Rooke, N., 2004. Contemporary kinematics of the southern Aegean and the Mediterranean Ridge. *Geophysical Journal International*, *157*(3), pp.1377-1392.

Kumaki, Y., 1985. The deformations of Holocene marine terraces in southern Kanto, central Japan. *Geographical review of Japan, Series B.*, *58*(1), pp.49-60.

Labonne, M. and Hillaire–Marcel, C., 2000. Geochemical gradients within modern and fossil shells of Concholepas concholepas from Northern Chile: An insight into U–Th systematics and diagenetic/authigenic isotopic imprints in mollusk shells. *Geochimica et Cosmochimica Acta*, *64*(9), pp.1523-1534.

Laborel, J., 1986. Vermetid gastropods as sea-level indicators. In *Sea-level Research* (pp. 281-310). Springer, Dordrecht.

Laborel, J. and Laborel-Deguen, F., 2005. Sea-level indicators, biologic. *Encyclopedia of Coastal Science*, pp.833-834.

Laigle, M., Hirn, A., Sachpazi, M. and Clément, C., 2002. Seismic coupling and structure of the Hellenic subduction zone in the Ionian Islands region. *Earth and Planetary Science Letters*, *200*(3-4), pp.243-253.

Lajoie, K.R., 1986. Coastal tectonics. *Active tectonics*, pp.95-124.

Lambeck, K. and Chappell, J., 2001. Sea level change through the last glacial cycle. *Science*, *292*(5517), pp.679-686.

Lambeck, K., Esat, T.M. and Potter, E.K., 2002. Links between climate and sea levels for the past three million years. *Nature*, *419*(6903), pp.199-206.

Lambeck, K., Purcell, A. and Dutton, A., 2012. The anatomy of interglacial sea levels: the relationship between sea levels and ice volumes during the Last Interglacial. *Earth and Planetary Science Letters*, *315*, pp.4-11.

Lambeck, K., Rouby, H., Purcell, A., Sun, Y. and Sambridge, M., 2014. Sea level and global ice volumes from the Last Glacial Maximum to the Holocene. *Proceedings of the National Academy of Sciences*, *111*(43), pp.15296-15303.

Lang, N. and Wolff, E.W., 2011. Interglacial and glacial variability from the last 800 ka in marine, ice and terrestrial archives. *Climate of the Past*, *7*(2), pp.361-380.

Lavecchia, G., Castaldo, R., De Nardis, R., De Novellis, V., Ferrarini, F., Pepe, S., Brozzetti, F., Solaro, G., Cirillo, D., Bonano, M. and Boncio, P., 2016. Ground deformation and source geometry of the 24 August 2016 Amatrice earthquake (Central Italy) investigated through analytical and numerical modeling of DInSAR measurements and structural-geological data. *Geophysical Research Letters*, *43*(24), pp.12-389.

Le Pichon, X. and Angelier, J., 1979. The Hellenic arc and trench system: a key to the neotectonic evolution of the eastern Mediterranean area. *Tectonophysics*, *60*(1-2), pp.1-42.

Lea, D.W., Martin, P.A., Pak, D.K. and Spero, H.J., 2002. Reconstructing a 350 ky history of sea level using planktonic Mg/Ca and oxygen isotope records from a Cocos Ridge core. *Quaternary Science Reviews*, *21*(1-3), pp.283-293.

Lee, S.Y., Seong, Y.B., Kang, H.C., Choi, K.H. and Yu, B.Y., 2015. Cosmogenic 10Be and OSL dating of marine terraces along the central-east coast of Korea: spatio-temporal variations in uplift rates. *The Open Geography Journal*, *7*(1).

Leeder, M.R., McNeill, L.C., Ll Collier, R.E., Portman, C., Rowe, P.J., Andrews, J.E. and Gawthorpe, R.L., 2003. Corinth rift margin uplift: New evidence from Late Quaternary marine shorelines. *Geophysical Research Letters*, *30*(12).

Leeder, M. R., C. Portman, J. E. Andrews, RE Ll Collier, E. Finch, Robert L. Gawthorpe, L. C. McNeill, M. Perez-Arlucea, and P. Rowe. "Normal faulting and crustal deformation, Alkyonides Gulf and Perachora peninsula, eastern Gulf of Corinth rift, Greece." *Journal of the Geological Society* 162, no. 3 (2005): 549-561.

Leeder, M. R., Seger, M. J., and Stark, C. P., 1991. Sedimentation and tectonic geomorphology adjacent to major active and inactive normal faults, southern Greece. *Journal of the Geological Society*, *148*(2), pp.331-343.

Lemoine, A., Madariaga, R. and Campos, J., 2001. Evidence for earthquake interaction in Central Chile: the July 1997–September 1998 sequence. *Geophysical Research Letters*, *28*(14), pp.2743-2746.

Leonard, E.M. and Wehmiller, J.F., 1992. Low uplift rates and terrace reoccupation inferred from mollusk aminostratigraphy, Coquimbo Bay area, Chile. *Quaternary Research*, *38*(2), pp.246-259.

Licciardi, J.M., Denoncourt, C.L. and Finkel, R.C., 2008. Cosmogenic 36Cl production rates from Ca spallation in Iceland. *Earth and Planetary Science Letters*, *267*(1-2), pp.365-377.

Lin, W., Byrne, T.B., Kinoshita, M., McNeill, L.C., Chang, C., Lewis, J.C., Yamamoto, Y., Saffer, D.M., Moore, J.C., Wu, H.Y. and Tsuji, T., 2016. Distribution of stress state in the Nankai subduction zone, southwest Japan and a comparison with Japan Trench. *Tectonophysics*, *692*, pp.120-130.

Lin, J. and Stein, R.S., 2004. Stress triggering in thrust and subduction earthquakes and stress interaction between the southern San Andreas and nearby thrust and strike-slip faults. *Journal of Geophysical Research: Solid Earth*, *109*(B2).

Lisiecki, L.E. and Raymo, M.E., 2005. A Pliocene-Pleistocene stack of 57 globally distributed benthic δ18O records. *Paleoceanography*, *20*(1).

Litchfield, N.J., Clark, K.J., Cochran, U.A., Palmer, A.S., Mountjoy, J., Mueller, C., Morgenstern, R., Berryman, K.R., McFadgen, B.G., Steele, R. and Reitman, N., 2020. Marine Terraces Reveal Complex Near-Shore Upper-Plate Faulting in the Northern Hikurangi Margin, New Zealand. *Bulletin of the Seismological Society of America*, *110*(2), pp.825-849.

Loperfido, A., 1909. Livellazione geometrica di precisione eseguita dall'IGM sulla costa orientale della Sicilia, da Messina a Catania, a Gesso ed a Faro Peloro e sulla costa occidentale della Calabria da Gioia Tauro a Melito di Porto Salvo. *Relazione della Commissione Reale incaricata di designare filezone più adatte per la ricostruzione degli abitati colpiti dal terremoto del 28 dicembre 1908 o da altri precedenti*, pp.131-156.

Luijendijk, E., Gleeson, T. and Moosdorf, N., 2020. Fresh groundwater discharge insignificant for the world's oceans but important for coastal ecosystems. *Nature communications*, *11*(1), pp.1-12.

Luo, G. and Liu, M., 2012. Multi-timescale mechanical coupling between the San Jacinto fault and the San Andreas fault, southern California. *Lithosphere*, *4*(3), pp.221-229.

Machette, M.N., 2000. Active, capable, and potentially active faults—a paleoseismic perspective. *Journal of Geodynamics*, *29*(3-5), pp.387-392.

Machette, M. N., Personius, S. F., Nelson, A. R., Schwartz, D. P., and Lund, W. R., 1991. The Wasatch fault zone, Utah—Segmentation and history of Holocene earthquakes. *Journal of Structural Geology*, *13*(2), pp.137-149.

Magnani, G., Bartolomei, P., Cavulli, F., Esposito, M., Marino, E.C., Neri, M., Rizzo, A., Scaruffi, S. and Tosi, M., 2007. U-series and radiocarbon dates on mollusc shells from the uppermost layer of the archaeological site of KHB-1, Ra's al Khabbah, Oman. *Journal of Archaeological Science*, *34*(5), pp.749-755.

Makropoulos, K., Kaviris, G. and Kouskouna, V., 2012. An updated and extended earthquake catalogue for Greece and adjacent areas since 1900. *Natural Hazards & Earth System Sciences*, *12*(5).

Marquardt, C., Lavenu, A., Ortlieb, L., Godoy, E. and Comte, D., 2004. Coastal neotectonics in Southern Central Andes: uplift and deformation of marine terraces in Northern Chile (27 S). *Tectonophysics*, *394*(3-4), pp.193-219.

Marrero, S.M., Phillips, F.M., Borchers, B., Lifton, N., Aumer, R. and Balco, G., 2016a. Cosmogenic nuclide systematics and the CRONUScalc program. *Quaternary Geochronology*, *31*, pp.160-187.

Marrero, S.M., Phillips, F.M., Caffee, M.W. and Gosse, J.C., 2016b. CRONUS-Earth cosmogenic 36Cl calibration. *Quaternary Geochronology*, *31*, pp.199-219.

Marshall, J.S. and Anderson, R.S., 1995. Quaternary uplift and seismic cycle deformation, Peninsula de Nicoya, Costa Rica. *Geological Society of America Bulletin*, *107*(4), pp.463-473.

Marshall, S.J. and Clark, P.U., 2002. Basal temperature evolution of North American ice sheets and implications for the 100-kyr cycle. *Geophysical Research Letters*, *29*(24), pp.67-1.

Martin, P.A., Lea, D.W., Rosenthal, Y., Shackleton, N.J., Sarnthein, M. and Papenfuss, T., 2002. Quaternary deep sea temperature histories derived from benthic foraminiferal Mg/Ca. *Earth and Planetary Science Letters*, *198*(1-2), pp.193-209.

Mascle, J., Le Quellec, P., Leité, O. and Jongsma, D., 1982. Structural sketch of the Hellenic continental margin between the western Peloponnesus and eastern Crete. *Geology*, *10*(2), pp.113-116.

Matsu'ura, T., 2015. Late Quaternary uplift rate inferred from marine terraces, Muroto Peninsula, southwest Japan: Forearc deformation in an oblique subduction zone. *Geomorphology*, *234*, pp.133-150.

Matsu'ura, T., Furusawa, A., Shimogama, K., Goto, N. and Komatsubara, J., 2014. Late Quaternary tephrostratigraphy and cryptotephrostratigraphy of deep-sea sequences (Chikyu C9001C cores) as tools for marine terrace chronology in NE Japan. *Quaternary Geochronology*, *23*, pp.63-79.

Matsu'ura, T., Komatsubara, J. and Wu, C., 2019. Accurate determination of the Pleistocene uplift rate of the NE Japan forearc from the buried MIS 5e marine terrace shoreline angle. *Quaternary Science Reviews*, *212*, pp.45-68.

Matthews, M.V., Ellsworth, W.L. and Reasenberg, P.A., 2002. A Brownian model for recurrent earthquakes. *Bulletin of the Seismological Society of America*, *92*(6), pp.2233-2250.

McCaffrey, R., 2009. The tectonic framework of the Sumatran subduction zone. *Annual Review of Earth and Planetary Sciences*, *37*, pp.345-366.

McCalpin, J.P. and Nelson, A.R., 1996. Introduction to paleoseismology.

McClusky, S., Balassanian, S., Barka, A., Demir, C., Ergintav, S., Georgiev, I., Gurkan, O., Hamburger, M., Hurst, K., Kahle, H. and Kastens, K., 2000. Global Positioning System constraints on plate kinematics and dynamics in the eastern Mediterranean and Caucasus. *Journal of Geophysical Research: Solid Earth*, *105*(B3), pp.5695-5719.

McGrath, A. G., and Davison, I., 1995. Damage zone geometry around fault tips. *Journal of Structural Geology*, *17*(7), pp.1011-1024.

McIntosh, K., Silver, E. and Shipley, T., 1993. Evidence and mechanisms for forearc extension at the accretionary Costa Rica convergent margin. *Tectonics*, *12*(6), pp.1380-1392.

McKenzie, D., 1978. Active tectonics of the Alpine—Himalayan belt: the Aegean Sea and surrounding regions. *Geophysical Journal International*, *55*(1), pp.217-254.

McKenzie, D. and Jackson, J., 2012. Tsunami earthquake generation by the release of gravitational potential energy. *Earth and Planetary Science Letters*, *345*, pp.1-8.

McLaren, S.J. and Rowe, P.J., 1996. The reliability of uranium-series mollusc dates from the western Mediterranean basin. *Quaternary Science Reviews*, *15*(7), pp.709-717.

McLeod, A. E., Dawers, N. H., and Underhill, J. R., 2000. The propagation and linkage of normal faults: insights from the Strathspey–Brent–Statfjord fault array, northern North Sea. *Basin Research*, *12*(3-4), pp.263-284.

McNeill, L.C. and Collier, R.L., 2004. Uplift and slip rates of the eastern Eliki fault segment, Gulf of Corinth, Greece, inferred from Holocene and Pleistocene terraces. *Journal of the Geological Society*, *161*(1), pp.81-92.

McNeill, L.C., Cotterill, C.J., Henstock, T.J., Bull, J.M., Stefatos, A., Collier, R.L., Papatheoderou, G., Ferentinos, G. and Hicks, S.E., 2005. Active faulting within the offshore western Gulf of Corinth, Greece: Implications for models of continental rift deformation. *Geology*, *33*(4), pp.241-244.

McNeill, L.C., Goldfinger, C., Yeats, R.S. and Kulm, L.D., 1999. The effects of upper plate deformation on records of prehistoric Cascadia subduction zone earthquakes. *Geological Society, London, Special Publications*, *146*(1), pp.321-342.

McNeill, L.C., Shillington, D.J., Carter, G.D., Everest, J.D., Gawthorpe, R.L., Miller, C., Phillips, M.P., Collier, R.E.L., Cvetkoska, A., De Gelder, G. and Diz, P., 2019. High-resolution record reveals climate-driven environmental and sedimentary changes in an active rift. *Scientific reports*, *9*(1), pp.1-11.

Medina-Elizalde, M., 2013. A global compilation of coral sea-level benchmarks: implications and new challenges. *Earth and Planetary Science Letters*, *362*, pp.310-318.

Meier, T., Becker, D., Endrun, B., Rische, M., Bohnhoff, M., Stöckhert, B. and Harjes, H.P., 2007. A model for the Hellenic subduction zone in the area of Crete based on seismological investigations. *Geological Society, London, Special Publications*, *291*(1), pp.183-199.

Meier, T., Rische, M., Endrun, B., Vafidis, A. and Harjes, H.P., 2004. Seismicity of the Hellenic subduction zone in the area of western and central Crete observed by temporary local seismic networks. *Tectonophysics*, *383*(3-4), pp.149-169.

Meletti, C., Galadini, F., Valensise, G., Stucchi, M., Basili, R., Barba, S., Vannucci, G. and Boschi, E., 2008. A seismic source zone model for the seismic hazard assessment of the Italian territory. *Tectonophysics*, *450*(1-4), pp.85-108.

Meltzner, A.J., Sieh, K., Abrams, M., Agnew, D.C., Hudnut, K.W., Avouac, J.P. and Natawidjaja, D.H., 2006. Uplift and subsidence associated with the great Aceh-Andaman earthquake of 2004. *Journal of Geophysical Research: Solid Earth*, *111*(B2).

Mercier, J.L., Sorel, D. and Simeakis, K., 1987. Changes in the state of stress in the overriding plate of a subduction zone: the Aegean Arc from the Pliocene to the Present.

Merritts, D. and Bull, W.B., 1989. Interpreting Quaternary uplift rates at the Mendocino triple junction, northern California, from uplifted marine terraces. *Geology*, *17*(11), pp.1020-1024.

Meschis, M., 2019. Unpublished Thesis *Quantifying rates of active extension and seismic hazard in the upper plate of subduction zones.* (Doctoral dissertation, Birkbeck, University of London).

Meschis, M., Roberts, G.P., Mildon, Z.K., Robertson, J., Michetti, A.M. and Walker, J.F., 2019. Slip on a mapped normal fault for the 28 th December 1908 Messina earthquake (Mw 7.1) in Italy. *Scientific reports*, *9*(1), pp.1-8.

Meschis, M., Roberts, G.P., Robertson, J. and Briant, R.M., 2018. The Relationships Between Regional Quaternary Uplift, Deformation Across Active Normal Faults, and Historical Seismicity in the Upper Plate of Subduction Zones: The Capo D'Orlando Fault, NE Sicily. *Tectonics*, *37*(5), pp.1231-1255.

Meulenkamp, J.E., Van der Zwaan, G.J. and Van Wamel, W.A., 1994. On Late Miocene to recent vertical motions in the Cretan segment of the Hellenic arc. *Tectonophysics*, *234*(1-2), pp.53-72.

Michetti, A.M., Ferreli, L., Esposito, E., Porfido, S., Blumetti, A.M., Vittori, E., Serva, L. and Roberts, G.P., 2000. Ground effects during the 9 September 1998, Mw= 5.6 Lauria earthquake and the seismic potential of the "aseismic" Pollino region in southern Italy. *Seismological Research Letters*, *71*(1), pp.31-46.

Michetti, A.M., Ferreli, L., Serva, L. and Vittori, E., 1997. Geological evidence for strong historical earthquakes in an "aseismic" region: The Pollino case (southern Italy). *Journal of Geodynamics*, *24*(1-4), pp.67-86.

Middelburg, J.J., Calvert, S.E. and Karlin, R., 1991. Organic-rich transitional facies in silled basins: Response to sea-level change. *Geology*, *19*(7), pp.679-682.

Mildon, Z., Roberts, G., Faure Walker, J., Beck, J., Papanikolaou, I., Michetti, A., Toda, S., Iezzi, F., Campbell, L., McCaffrey, K. and Shanks, R., 2019. Earthquake clustering controlled by shear zone interaction [Preprint].

Mildon, Z.K., Roberts, G.P., Faure Walker, J.P. and Iezzi, F., 2017. Coulomb stress transfer and fault interaction over millennia on non-planar active normal faults: the M w 6.5–5.0 seismic sequence of 2016–2017, central Italy. *Geophysical Journal International*, *210*(2), pp.1206-1218.

Mildon, Z.K., Toda, S., Faure Walker, J.P. and Roberts, G.P., 2016. Evaluating models of Coulomb stress transfer: Is variable fault geometry important?. *Geophysical Research Letters*, *43*(24), pp.12-407.

Miller, W.R. and Mason, T.R., 1994. Erosional features of coastal beachrock and aeolianite outcrops in Natal and Zululand, South Africa. *Journal of Coastal Research*, pp.374-394.

Minson, S.E., Baltay, A.S., Cochran, E.S., McBride, S.K. and Milner, K.R., 2018. Shaking is Almost Always a Surprise: The Earthquakes That Produce Significant Ground Motion. *Seismological Research Letters*.

Miyoshi, M., 1983. Estimated ages of late Pleistocene marine terraces in Japan, deduced from uplift rate. *Geographical Review of Japan*, *56*(12), pp.819-834.

Moore, G.F., Boston, B.B., Sacks, A.F. and Saffer, D.M., 2013. Analysis of normal fault populations in the Kumano Forearc Basin, Nankai Trough, Japan: 1. Multiple orientations and generations of faults from 3-D coherency mapping. *Geochemistry, Geophysics, Geosystems*, *14*(6), pp.1989-2002.

Monaco, C. and Tortorici, L., 2000. Active faulting in the Calabrian arc and eastern Sicily. *Journal of Geodynamics*, *29*(3-5), pp.407-424.

Monaco, C. and Tortorici, L., 2004. Faulting and effects of earthquakes on Minoan archaeological sites in Crete (Greece). *Tectonophysics*, *382*(1-2), pp.103-116.

Montagna, P., McCulloch, M., Mazzoli, C., Silenzi, S. and Odorico, R., 2007. The non-tropical coral Cladocora caespitosa as the new climate archive for the Mediterranean: high-resolution (~ weekly) trace element systematics. *Quaternary Science Reviews*, *26*(3-4), pp.441-462.

Moretti, I., Sakellariou, D., Lykousis, V. and Micarelli, L., 2003. The Gulf of Corinth: an active half graben?. *Journal of Geodynamics*, *36*(1-2), pp.323-340.

Morewood, N.C. and Roberts, G.P., 1997. Geometry, kinematics and rates of deformation in a normal fault segment boundary, central Greece. *Geophysical Research Letters*, *24*(23), pp.3081-3084.

Morewood, N.C. and Roberts, G.P., 1999. Lateral propagation of the surface trace of the South Alkyonides normal fault segment, central Greece: its impact on models of fault growth and displacement–length relationships. *Journal of Structural Geology*, *21*(6), pp.635-652.

Morewood, N. C., and Roberts, G. P., 2001. Comparison of surface slip and focal mechanism slip data along normal faults: an example from the eastern Gulf of Corinth, Greece. *Journal of Structural Geology*, *23*(2-3), pp.473-487.

Morewood, N. C., and Roberts, G. P., 2002. Surface observations of active normal fault propagation: implications for growth. *Journal of the Geological Society*, *159*(3), pp.263-272.

Mori, N., Takahashi, T., Yasuda, T. and Yanagisawa, H., 2011. Survey of 2011 Tohoku earthquake tsunami inundation and run-up. *Geophysical research letters*, *38*(7).

Moriarty, K.C., McCulloch, M.T., Wells, R.T. and McDowell, M.C., 2000. Mid-Pleistocene cave fills, megafaunal remains and climate change at Naracoorte, South Australia: towards a predictive model using U-Th dating of speleothems. *Palaeogeography, Palaeoclimatology, Palaeoecology*, *159*(1-2), pp.113-143.

Mouslopoulou, V., Begg, J., Nicol, A., Oncken, O. and Prior, C., 2015a. Formation of late quaternary paleoshorelines in Crete, Eastern Mediterranean. *Earth and Planetary Science Letters*, *431*, pp.294-307.

Mouslopoulou, V., Begg, J., Fülling, A., Moraetis, D., Partsinevelos, P. and Oncken, O., 2017. Distinct phases of eustatic and tectonic forcing for late Quaternary landscape evolution in southwest Crete, Greece. *Earth Surface Dynamics*, *5*, pp.511-527.

Mouslopoulou, V., Oncken, O., Hainzl, S. and Nicol, A., 2016. Uplift rate transients at subduction margins due to earthquake clustering. *Tectonics*, *35*(10), pp.2370-2384.

Mouslopoulou, V., Nicol, A., Begg, J., Oncken, O. and Moreno, M., 2015b. Clusters of megaearthquakes on upper plate faults control the Eastern Mediterranean hazard. *Geophysical Research Letters*, *42*(23), pp.10-282.

Mozafari, N., Sümer, Ö., Tikhomirov, D., Ivy-Ochs, S., Alfimov, V., Vockenhuber, C., Inci, U., Sözbilir, H. and Akçar, N., 2019. Holocene seismic activity of the Priene-Sazlı Fault revealed by cosmogenic 36Cl, western Anatolia, Turkey. *Turk. J. Earth Sci*, *28*, pp.410-437.

Muhs, D.R., 2013. Loess and its geomorphic, stratigraphic and paleoclimatic significance in the Quaternary.

Muhs, D.R., Kennedy, G.L. and Rockwell, T.K., 1994. Uranium-series ages of marine terrace corals from the Pacific coast of North America and implications for last-interglacial sea level history. *Quaternary Research*, *42*(1), pp.72-87.

Muhs, D.R., Kelsey, H.M., Miller, G.H., Kennedy, G.L., Whelan, J.F. and McInelly, G.W., 1990. Age estimates and uplift rates for late Pleistocene marine terraces: Southern Oregon portion of the Cascadia forearc. *Journal of Geophysical Research: Solid Earth*, *95*(B5), pp.6685-6698.

Muhs, D.R., Rockwell, T.K. and Kennedy, G.L., 1992. Late Quaternary uplift rates of marine terraces on the Pacific coast of North America, southern Oregon to Baja California Sur. *Quaternary International*, *15*, pp.121-133.

Muhs, D.R., Simmons, K.R., Schumann, R.R. and Halley, R.B., 2011. Sea-level history of the past two interglacial periods: new evidence from U-series dating of reef corals from south Florida. *Quaternary Science Reviews*, *30*(5-6), pp.570-590.

Muhs, D.R. and Szabo, B.J., 1994. New uranium-series ages of the Waimanalo Limestone, Oahu, Hawaii: implications for sea level during the last interglacial period. *Marine Geology*, *118*(3-4), pp.315-326.

Nalbant, S., McCloskey, J., Steacy, S., NicBhloscaidh, M. and Murphy, S., 2013. Interseismic coupling, stress evolution, and earthquake slip on the Sunda megathrust. *Geophysical research letters*, *40*(16), pp.4204-4208.

Nalin, R., Massari, F. and Zecchin, M., 2007. Superimposed cycles of composite marine terraces: the example of Cutro terrace (Calabria, Southern Italy). *Journal of Sedimentary Research*, *77*(4), pp.340-354.

Nakada, M. and Lambeck, K., 1988. The melting history of the late Pleistocene Antarctic ice sheet. *Nature*, *333*(6168), pp.36-40.

National Observatory of Athens, Institute of Geodynamics, Athens, 1997. National observatory of Athens seismic network. International Federation of Digital Seismograph Networks. Other/Seismic Network. http://www.gein.noa.gr/en/seismicity/earthquake-catalogs https://doi.org/10.7914/SN/HL

Nicol, A., Walsh, J., Berryman, K. and Villamor, P., 2006. Interdependence of fault displacement rates and paleoearthquakes in an active rift. *Geology*, *34*(10), pp.865-868.

Nishikawa, T. and Ide, S., 2015. Background seismicity rate at subduction zones linked to slab-bending-related hydration. *Geophysical Research Letters*, *42*(17), pp.7081-7089.

Nishimura, T., 2014. Pre-, co-, and post-seismic deformation of the 2011 Tohoku-oki earthquake and its implication to a paradox in short-term and long-term deformation. *Journal of disaster research*, *9*(3), pp.294-302

Nixon, C.W., McNeill, L.C., Bull, J.M., Bell, R.E., Gawthorpe, R.L., Henstock, T.J., Christodoulou, D., Ford, M., Taylor, B., Sakellariou, D. and Ferentinos, G., 2016. Rapid spatiotemporal variations in rift structure during development of the Corinth Rift, central Greece. *Tectonics*, *35*(5), pp.1225-1248.

Nocquet, J.M., 2012. Present-day kinematics of the Mediterranean: A comprehensive overview of GPS results. *Tectonophysics*, *579*, pp.220-242.

Normand, R., Simpson, G., Herman, F., Biswas, R.H., Bahroudi, A. and Schneider, B., 2019. Dating and morpho-stratigraphy of uplifted marine terraces in the Makran subduction zone (Iran). *Earth Surface Dynamics*, *7*(1), pp.321-344.

Nyst, M. and Thatcher, W., 2004. New constraints on the active tectonic deformation of the Aegean. *Journal of Geophysical Research: Solid Earth*, *109*(B11).

O'Leary, M.J., Hearty, P.J., Thompson, W.G., Raymo, M.E., Mitrovica, J.X. and Webster, J.M., 2013. Ice sheet collapse following a prolonged period of stable sea level during the last interglacial. *Nature Geoscience*, *6*(9), pp.796-800.

Ori, G.G., 1989. Geologic history of the extensional basin of the Gulf of Corinth (? Miocene-Pleistocene), Greece. *Geology*, *17*(10), pp.918-921.

Ortlieb, L., Zazo, C., Goy, J., Hillaire-Marcel, C., Ghaleb, B. and Cournoyer, L., 1996. Coastal deformation and sea-level changes in the northern Chile subduction area (23 S) during the last 330 ky. *Quaternary Science Reviews*, *15*(8-9), pp.819-831.

Oskin, M., Perg, L., Shelef, E., Strane, M., Gurney, E., Singer, B. and Zhang, X., 2008. Elevated shear zone loading rate during an earthquake cluster in eastern California. *Geology*, *36*(6), pp.507-510.

Ota, Y. and Omura, A., 1992. Contrasting styles and rates of tectonic uplift of coral reef terraces in the Ryukyu and Daito Islands, southwestern Japan. *Quaternary International*, *15*, pp.17-29.

Ott, R.F., Gallen, S.F., Wegmann, K.W., Biswas, R.H., Herman, F. and Willett, S.D., 2019. Pleistocene terrace formation, Quaternary rock uplift rates and geodynamics of the Hellenic Subduction Zone revealed from dating of paleoshorelines on Crete, Greece. *Earth and Planetary Science Letters*, *525*, p.115757.

Ozawa, S., Nishimura, T., Suito, H., Kobayashi, T., Tobita, M. and Imakiire, T., 2011. Coseismic and postseismic slip of the 2011 magnitude-9 Tohoku-Oki earthquake. *Nature*, *475*(7356), pp.373-376.

Pace, B., Peruzza, L., Lavecchia, G. and Boncio, P., 2006. Layered seismogenic source model and probabilistic seismic-hazard analyses in central Italy. *Bulletin of the Seismological Society of America*, *96*(1), pp.107-132.

Pace, B., Peruzza, L., and Visini, F., 2010. LASSCI2009. 2: layered earthquake rupture forecast model for central Italy, submitted to the CSEP project. *Annals of Geophysics*.

Pace, B., Visini, F. and Peruzza, L., 2016. FiSH: MATLAB tools to turn fault data into seismic-hazard models. *Seismological Research Letters*, *87*(2A), pp.374-386.

Palamara, D.R., Dickson, M.E. and Kennedy, D.M., 2007. Defining shore platform boundaries using airborne laser scan data: a preliminary investigation. *Earth Surface Processes and Landforms: The Journal of the British Geomorphological Research Group*, *32*(6), pp.945-953.

Palmer, M.R. and Edmond, J.M., 1989. The strontium isotope budget of the modern ocean. *Earth and Planetary Science Letters*, *92*(1), pp.11-26.

Palmer, M.R. and Edmond, J.M., 1992. Controls over the strontium isotope composition of river water. *Geochimica et Cosmochimica Acta*, *56*(5), pp.2099-2111.

Palmer, M.R. and Edmond, J.M., 1993. Uranium in river water. *Geochimica et Cosmochimica Acta*, *57*(20), pp.4947-4955.

Palyvos, N., Mancini, M., Sorel, D., Lemeille, F., Pantosti, D., Julia, R., Triantaphyllou, M. and De Martini, P.M., 2010. Geomorphological, stratigraphic and geochronological evidence of fast Pleistocene coastal uplift in the westernmost part of the Corinth Gulf Rift (Greece). *Geological Journal*, *45*(1), pp.78-104.

Palyvos, N., Sorel, D., Lemeille, F., Mancini, M., Pantosti, D., Julia, R., Triantaphyllou, M. and De Martini, P.M., 2007. Review and new data on uplift rates at the W termination of the Corinth Rift and the NE Rion graben area (Achaia, NW Peloponnesos). *Bulletin of the Geological Society of Greece*, *40*(1), pp.412-424.

Papadimitriou, E.E. and Karakostas, V.G., 2008. Rupture model of the great AD 365 Crete earthquake in the southwestern part of the Hellenic Arc. *Acta Geophysica*, *56*(2), pp.293-312.

Pánek, T., Minár, J., Vitovič, L. and Břežný, M., 2020. Post-LGM faulting in Central Europe: LiDAR detection of the> 50 km-long Sub-Tatra fault, Western Carpathians. *Geomorphology*, p.107248.

Papanikolaou, D., Fountoulis, I. and Metaxas, C., 2007. Active faults, deformation rates and Quaternary paleogeography at Kyparissiakos Gulf (SW Greece) deduced from onshore and offshore data. *Quaternary International*, *171*, pp.14-30.

Papanikolaou, D. and Vassilakis, E., 2010. Thrust faults and extensional detachment faults in Cretan tectono-stratigraphy: implications for Middle Miocene extension. *Tectonophysics*, *488*(1-4), pp.233-247.

Papanikolaou, I.D., Foumelis, M., Parcharidis, I., Lekkas, E.L. and Fountoulis, I.G., 2010. Deformation pattern of the 6 and 7 April 2009, MW= 6.3 and MW= 5.6 earthquakes in L'Aquila (Central Italy) revealed by ground and space based observations. *Natural Hazards and Earth System Sciences*, *10*(1), p.73.

Papanikolaou, I.D. and Roberts, G.P., 2007. Geometry, kinematics and deformation rates along the active normal fault system in the southern Apennines: Implications for fault growth. *Journal of Structural Geology*, *29*(1), pp.166-188.

Papanikolaou, I. D., Roberts, G. P., and Michetti, A. M., 2005. Fault scarps and deformation rates in Lazio–Abruzzo, Central Italy: Comparison between geological fault slip-rate and GPS data. *Tectonophysics*, *408*(1-4), pp.147-176.

Papanikolaou, I.D., Triantaphyllou, M., Pallikarakis, A. and Migiros, G., 2015. Active faulting at the Corinth Canal based on surface observations, borehole data and paleoenvironmental interpretations. Passive rupture during the 1981 earthquake sequence?. *Geomorphology*, *237*, pp.65-78.

Papazachos, B.C., 1990. Seismicity of the Aegean and surrounding area. *Tectonophysics*, *178*(2-4), pp.287-308.

Papazachos, B.C., Papadimitriou, E.E., Kiratzi, A.A., Papazachos, C.B. and Louvari, E.K., 1998. Fault plane solutions in the Aegean Sea and the surrounding area and their tectonic implication. *Boll. Geof. teor. appl*, *39*(3), pp.199-218.

Papoulia, J., Nicolich, R., Makris, J., Slejko, D., Mascle, J., Papadopoulos, G., Anagnostou, C., Camera, L., Daskalaki, E., Fasoulaka, C. and Fokaefs, A., 2014. A new seismogenic model for the Kyparissiakos Gulf and western Peloponnese (SW Hellenic Arc). *Bollettino di Geofisica Teorica ed Applicata*, *55*(2).

Papoulia, J. and Makris, J., 2004. Microseismicity and active deformation of Messinia, SW Greece. *Journal of seismology*, *8*(4), pp.439-451.

Past Interglacials Working Group of PAGES, 2016. Interglacials of the last 800,000 years. *Reviews of Geophysics*, *54*(1), pp.162-219.

Peacock, D. C. P., 2002. Propagation, interaction and linkage in normal fault systems. *Earth-Science Reviews*, *58*(1-2), pp.121-142.

Peacock, D. C. P., and Sanderson, D. J., 1991. Displacements, segment linkage and relay ramps in normal fault zones. *Journal of Structural Geology*, *13*(6), pp.721-733.

Peacock, D. C. P., and Sanderson, D. J., 1994. Geometry and development of relay ramps in normal fault systems. *AAPG bulletin*, *78*(2), pp.147-165.

Pearce, C.R., Parkinson, I.J., Gaillardet, J., Charlier, B.L., Mokadem, F. and Burton, K.W., 2015. Reassessing the stable (δ88/86Sr) and radiogenic (87Sr/86Sr) strontium isotopic composition of marine inputs. *Geochimica et Cosmochimica Acta*, *157*, pp.125-146.

Pedoja, K., Husson, L., Johnson, M.E., Melnick, D., Witt, C., Pochat, S., Nexer, M., Delcaillau, B., Pinegina, T., Poprawski, Y. and Authemayou, C., 2014. Coastal staircase sequences reflecting sea-level oscillations and tectonic uplift during the Quaternary and Neogene. *Earth-Science Reviews*, *132*, pp.13-38.

Pedoja, K., Husson, L., Regard, V., Cobbold, P.R., Ostanciaux, E., Johnson, M.E., Kershaw, S., Saillard, M., Martinod, J., Furgerot, L. and Weill, P., 2011. Relative sea-level fall since the last interglacial stage: are coasts uplifting worldwide?. *Earth-Science Reviews*, *108*(1-2), pp.1-15.

Pedoja, K., Jara-Muñoz, J., De Gelder, G., Robertson, J., Meschis, M., Fernández-Blanco, D., Nexer, M., Poprawski, Y., Dugué, O., Delcaillau, B. and Bessin, P., 2018. Neogene-Quaternary slow coastal uplift of Western Europe through the perspective of sequences of strandlines from the Cotentin Peninsula (Normandy, France). *Geomorphology*, *303*, pp.338-356.

Peharda, M., Puljas, S., Chauvaud, L., Schöne, B.R., Ezgeta-Balić, D. and Thébault, J., 2015. Growth and longevity of Lithophaga lithophaga: what can we learn from shell structure and stable isotope composition?. *Marine biology*, *162*(8), pp.1531-1540.

Peirano, A., Kružić, P. and Mastronuzzi, G., 2009. Growth of Mediterranean reef of Cladocora caespitosa (L.) in the Late Quaternary and climate inferences. *Facies*, *55*(3), p.325.

Peirano, A., Morri, C., Bianchi, C.N., Aguirre, J., Antonioli, F., Calzetta, G., Carobene, L., Mastronuzzi, G. and Orrù, P., 2004. The Mediterranean coral Cladocora caespitosa: a proxy for past climate fluctuations?. *Global and planetary Change*, *40*(1-2), pp.195-200.

Peltier, W.R., 1998. "Implicit ice" in the global theory of glacial isostatic adjustment. *Geophysical Research Letters*, *25*(21), pp.3955-3958.

Peppe, D.J. and Deino, A.L., 2013. Dating rocks and fossils using geologic methods. *Nature Education Knowledge*, *4*(10), p.1.

Perissoratis, C., Piper, D.J.W. and Lykousis, V., 2000. Alternating marine and lacustrine sedimentation during late Quaternary in the Gulf of Corinth rift basin, central Greece. *Marine Geology*, *167*(3-4), pp.391-411.

Perrin, C., Manighetti, I., and Gaudemer, Y., 2016. Off-fault tip splay networks: A genetic and generic property of faults indicative of their long-term propagation. *Comptes Rendus Geoscience*, *348*(1), pp.52-60.

Peterek, A. and Schwarze, J., 2004. Architecture and Late Pliocene to recent evolution of outer-arc basins of the Hellenic subduction zone (south-central Crete, Greece). *Journal of Geodynamics*, *38*(1), pp.19-55.

Phillips, F.M., Stone, W.D. and Fabryka-Martin, J.T., 2001. An improved approach to calculating low-energy cosmic-ray neutron fluxes near the land/atmosphere interface. *Chemical Geology*, *175*(3-4), pp.689-701.

Pillans, B., 1990. Pleistocene marine terraces in New Zealand: a review. *New Zealand journal of geology and geophysics*, *33*(2), pp.219-231.

Pillans, B., 1994. Direct marine-terrestrial correlations, Wanganui Basin, New Zealand: the last 1 million years. *Quaternary science reviews*, *13*(3), pp.189-200.

Pirazzoli, P.A., 1986. Marine notches. In *Sea-Level Research* (pp. 361-400). Springer, Dordrecht.

Pirazzoli, P.A., 2005. A review of possible eustatic, isostatic and tectonic contributions in eight late-Holocene relative sea-level histories from the Mediterranean area. *Quaternary Science Reviews*, *24*(18-19), pp.1989-2001.

Pirazzoli, P.A., 2013. SEA LEVEL STUDIES. Geomorphological Indicators.

Pirazzoli, P.A., Laborel, J. and Stiros, S.C., 1996. Earthquake clustering in the Eastern Mediterranean during historical times. *Journal of Geophysical Research: Solid Earth*, *101*(B3), pp.6083-6097.

Pirazzoli, P.A., Radtke, U., Hantoro, W.S., Jouannic, C., Hoang, C.T., Causse, C. and Best, M.B., 1991. Quaternary raised coral-reef terraces on Sumba Island, Indonesia. *Science*, *252*(5014), pp.1834-1836.

Pirazzoli, P. A., Stiros, S. C., Arnold, M., Laborel, J., Laborel-Deguen, F., and Papageorgiou, S., 1994. Episodic uplift deduced from Holocene shorelines in the Perachora Peninsula, Corinth area, Greece. *Tectonophysics*, *229*(3-4), pp.201-209.

Pirazzoli, P.A., Thommeret, J., Thommeret, Y., Laborel, J. and Montag-Gioni, L.F., 1982. Crustal block movements from Holocene shorelines: Crete and Antikythira (Greece). *Tectonophysics*, *86*(1-3), pp.27-43.

Piccardi, L., Gaudemer, Y., Tapponnier, P. and Boccaletti, M., 1999. Active oblique extension in the central Apennines (Italy): evidence from the Fucino region. *Geophysical Journal International*, *139*(2), pp.499-530.

Plafker, G., Lajoie, K.R. and Rubin, M., 1992. Determining recurrence intervals of great subduction zone earthquakes in southern Alaska by radiocarbon dating. In *Radiocarbon after Four Decades* (pp. 436-453). Springer, New York, NY.

Plater, A.J., Ivanovich, M. and Dugdale, R.E., 1992. Uranium series disequilibrium in river sediments and waters: the significance of anomalous activity ratios. *Applied Geochemistry*, *7*(2), pp.101-110.

Polyak, V.J., Onac, B.P., Fornós, J.J., Hay, C., Asmerom, Y., Dorale, J.A., Ginés, J., Tuccimei, P. and Ginés, A., 2018. A highly resolved record of relative sea level in the western Mediterranean Sea during the last interglacial period. *Nature Geoscience*, *11*(11), pp.860-864.

Poole, A.J., Shimmield, G.B. and Robertson, A.H., 1990. Late Quaternary uplift of the Troodos ophiolite, Cyprus: Uranium-series dating of Pleistocene coral. *Geology*, *18*(9), pp.894-897.

Pope, R.J., Candy, I. and Skourtsos, E., 2016. A chronology of alluvial fan response to Late Quaternary sea level and climate change, Crete. *Quaternary Research*, *86*(2), pp.170-183.

Pope, R., Wilkinson, K., Skourtsos, E., Triantaphyllou, M. and Ferrier, G., 2008. Clarifying stages of alluvial fan evolution along the Sfakian piedmont, southern Crete: New evidence from analysis of post-incisive soils and OSL dating. *Geomorphology*, *94*(1-2), pp.206-225.

Portman, C., Andrews, J.E., Rowe, P.J., Leeder, M.R. and Hoogewerff, J., 2005. Submarine-spring controlled calcification and growth of large Rivularia bioherms, Late Pleistocene (MIS 5e), Gulf of Corinth, Greece. *Sedimentology*, *52*(3), pp.441-465.

Postma, G. and Nemec, W., 1990. Regressive and transgressive sequences in a raised Holocene gravelly beach, southwestern Crete. *Sedimentology*, *37*(5), pp.907-920.

Potter, E.K. and Lambeck, K., 2004. Reconciliation of sea-level observations in the Western North Atlantic during the last glacial cycle. *Earth and Planetary Science Letters*, *217*(1-2), pp.171-181.

Poulos, S.E., Collins, M.B., Pattiaratchi, C., Cramp, A., Gull, W., Tsimplis, M. and Papatheodorou, G., 1996. Oceanography and sedimentation in the semi-enclosed, deep-water Gulf of Corinth (Greece). *Marine Geology*, *134*(3-4), pp.213-235.

Quigley, M.C., Duffy, B., Woodhead, J., Hellstrom, J., Moody, L., Horton, T., Soares, J. and Fernandes, L., 2012. U/Pb dating of a terminal Pliocene coral from the Indonesian Seaway. *Marine Geology*, *311*, pp.57-62.

Railsback, L. Bruce, Philip L. Gibbard, Martin J. Head, Ny Riavo G. Voarintsoa, and Samuel Toucanne. "An optimized scheme of lettered marine isotope substages for the last 1.0 million years, and the climatostratigraphic nature of isotope stages and substages." *Quaternary Science Reviews* 111 (2015): 94-106.

Rasser, M.W. and Piller, W.E., 1999. Application of neontological taxonomic concepts to Late Eocene coralline algae (Rhodophyta) of the Austrian Molasse Zone. *Journal of Micropalaeontology*, *18*(1), pp.67-80.

Richards, D.A., Smart, P.L. and Edwards, R.L., 1994. Maximum sea levels for the last glacial period from U-series ages of submerged speleothems. *Nature*, *367*(6461), pp.357-360.

Richter, D.K. and Sedat, R., 1983. Brackish-water oncoids composed of blue-green and red algae from a Pleistocene terrace near Corinth, Greece. In *Coated grains* (pp. 299-307). Springer, Berlin, Heidelberg.

Roberts, G.P., 1996a. Noncharacteristic normal faulting surface ruptures from the Gulf of Corinth, Greece. *Journal of Geophysical Research: Solid Earth*, *101*(B11), pp.25255-25267.

Roberts, G. P., 1996b. Variation in fault-slip directions along active and segmented normal fault systems. *Journal of Structural Geology*, 18(6), pp.835-845.

Roberts, G.P., 2007. Fault orientation variations along the strike of active normal fault systems in Italy and Greece: Implications for predicting the orientations of subseismic-resolution faults in hydrocarbon reservoirs. *AAPG bulletin*, *91*(1), pp.1-20.

Roberts, G.P. and Ganas, A., 2000. Fault-slip directions in central and southern Greece measured from striated and corrugated fault planes: Comparison with focal mechanism and geodetic data. *Journal of Geophysical Research: Solid Earth*, *105*(B10), pp.23443-23462.

Roberts, G.P., Houghton, S.L., Underwood, C., Papanikolaou, I., Cowie, P.A., van Calsteren, P., Wigley, T., Cooper, F.J. and McArthur, J.M., 2009. Localization of Quaternary slip rates in an active rift in 10^5 years: An example from central Greece constrained by ^{234}U-^{230}Th coral dates from uplifted paleoshorelines. *Journal of Geophysical Research: Solid Earth*, *114*(B10).

Roberts, G.P. and Koukouvelas, I., 1996. Structural and seismological segmentation of the Gulf of Corinth fault system: implications for models of fault growth.

Roberts, G.P., Meschis, M., Houghton, S., Underwood, C. and Briant, R.M., 2013. The implications of revised Quaternary palaeoshoreline chronologies for the rates of active extension and uplift in the upper plate of subduction zones. *Quaternary Science Reviews*, *78*, pp.169-187.

Roberts, G.P. and Michetti, A.M., 2004. Spatial and temporal variations in growth rates along active normal fault systems: an example from The Lazio–Abruzzo Apennines, central Italy. *Journal of Structural Geology*, *26*(2), pp.339-376.

Roberts, G.P., Michetti, A.M., Cowie, P., Morewood, N.C. and Papanikolaou, I., 2002. Fault slip-rate variations during crustal-scale strain localisation, central Italy. *Geophysical Research Letters*, *29*(8), pp.9-1.

Roberts, S., and Jackson, J., 1991. Active normal faulting in central Greece: an overview. *Geological Society, London, Special Publications*, *56*(1), pp.125-142.

Robertson, J., Meschis, M., Roberts, G.P., Ganas, A. and Gheorghiu, D.M., 2019. Temporally constant Quaternary uplift rates and their relationship with extensional upper-plate faults in south Crete (Greece), constrained with ^{36}Cl cosmogenic exposure dating. *Tectonics*, *38*(4), pp.1189-1222.

Robertson, J., Roberts, G.P., Iezzi, F., Meschis, M., Gheorghiu, D.M., Sahy, D., Bristow, C. and Sgambato, C., 2020. Distributed normal faulting in the tip zone of the South Alkyonides Fault System, Gulf of Corinth, constrained using ^{36}Cl exposure dating of Late-Quaternary wave-cut platforms. *Journal of Structural Geology*, p.104063.

Robinson, L.F., Henderson, G.M., Hall, L. and Matthews, I., 2004. Climatic control of riverine and seawater uranium-isotope ratios. *Science*, *305*(5685), pp.851-854.

Rockwell, T.K., Lindvall, S., Dawson, T., Langridge, R., Lettis, W. and Klinger, Y., 2002. Lateral offsets on surveyed cultural features resulting from the 1999 Izmit and Duzce earthquakes, Turkey. *Bulletin of the Seismological Society of America*, *92*(1), pp.79-94.

Rockwell, T.K., Lindvall, S., Herzberg, M., Murbach, D., Dawson, T. and Berger, G., 2000. Paleoseismology of the Johnson Valley, Kickapoo, and Homestead Valley faults: Clustering of earthquakes in the eastern California shear zone. *Bulletin of the Seismological Society of America*, *90*(5), pp.1200-1236.

Rohling, E.J., Fenton, M.J.J.F., Jorissen, F.J., Bertrand, P., Ganssen, G. and Caulet, J.P., 1998. Magnitudes of sea-level lowstands of the past 500,000 years. *Nature*, *394*(6689), pp.162-165.

Rohling, E.J., Foster, G.L., Grant, K.M., Marino, G., Roberts, A.P., Tamisiea, M.E. and Williams, F., 2014. Sea-level and deep-sea-temperature variability over the past 5.3 million years. *Nature*, *508*(7497), pp.477-482.

Rohling, E.J., Grant, K., Bolshaw, M., Roberts, A.P., Siddall, M., Hemleben, C. and Kucera, M., 2009. Antarctic temperature and global sea level closely coupled over the past five glacial cycles. *Nature Geoscience*, *2*(7), pp.500-504.

Rohling, E.J., Grant, K., Hemleben, C.H., Siddall, M., Hoogakker, B.A.A., Bolshaw, M. and Kucera, M., 2008. High rates of sea-level rise during the last interglacial period. *Nature geoscience*, *1*(1), p.38.

Rovere, A., Antonioli, F. and Bianchi, C.N., 2015. Fixed biological indicators. *Handbook of Sea-Level Research*, pp.268-280.

Rovere, A., Raymo, M.E., Vacchi, M., Lorscheid, T., Stocchi, P., Gomez-Pujol, L., Harris, D.L., Casella, E., O'Leary, M.J. and Hearty, P.J., 2016b. The analysis of Last Interglacial (MIS 5e) relative sea-level indicators: Reconstructing sea-level in a warmer world. *Earth-Science Reviews*, *159*, pp.404-427.

Rovere, A., Stocchi, P. and Vacchi, M., 2016a. Eustatic and relative sea level changes. *Current Climate Change Reports*, *2*(4), pp.221-231.

Rowe, P.J., Turner, J.A., Andrews, J.E., Leeder, M.R., van Calsteren, P. and Thomas, L., 2015. Uranium-thorium dating potential of the marine bivalve Lithophaga lithophaga. *Quaternary Geochronology*, *30*, pp.80-89.

Rust, D. and Kershaw, S., 2000. Holocene tectonic uplift patterns in northeastern Sicily: evidence from marine notches in coastal outcrops. *Marine Geology*, *167*(1-2), pp.105-126.

Sabatakakis, N., Nikolakopoulos, K.G., Papatheodorou, G. and Kelasidis, G., 2016. A multisource approach for coastal mapping purposes: Limeni bay, Mani and surrounding area, southern Greece. *Earth Science Informatics*, *9*(2), pp.183-196.

Sachpazi, M., Clément, C., Laigle, M., Hirn, A. and Roussos, N., 2003. Rift structure, evolution, and earthquakes in the Gulf of Corinth, from reflection seismic images. *Earth and Planetary Science Letters*, *216*(3), pp.243-257.

Sachpazi, M., Laigle, M., Charalampakis, M., Diaz, J., Kissling, E., Gesret, A., Becel, A., Flueh, E., Miles, P. and Hirn, A., 2016. Segmented Hellenic slab rollback driving Aegean deformation and seismicity. *Geophysical Research Letters*, *43*(2), pp.651-658.

Saillard, M., Audin, L., Rousset, B., Avouac, J.P., Chlieh, M., Hall, S.R., Husson, L. and Farber, D.L., 2017. From the seismic cycle to long-term deformation: Linking seismic coupling and Quaternary coastal geomorphology along the Andean megathrust. *Tectonics*, *36*(2), pp.241-256.

Saillard, M., Hall, S.R., Audin, L., Farber, D.L., Hérail, G., Martinod, J., Regard, V., Finkel, R.C. and Bondoux, F., 2009. Non-steady long-term uplift rates and Pleistocene marine terrace development along the Andean margin of Chile (31 S) inferred from 10Be dating. *Earth and Planetary Science Letters*, *277*(1-2), pp.50-63.

Saillard, M., Hall, S.R., Audin, L., Farber, D.L., Regard, V. and Hérail, G., 2011. Andean coastal uplift and active tectonics in southern Peru: 10Be surface exposure dating of differentially uplifted marine terrace sequences (San Juan de Marcona,~ 15.4 S). *Geomorphology*, *128*(3-4), pp.178-190.

Sak, P.B., Fisher, D.M., Gardner, T.W., Marshall, J.S. and LaFemina, P.C., 2009. Rough crust subduction, forearc kinematics, and Quaternary uplift rates, Costa Rican segment of the Middle American Trench. *Geological Society of America Bulletin*, *121*(7-8), pp.992-1012.

Sakellariou, D., Lykousis, V., Alexandri, S., Kaberi, H., Rousakis, G., Nomikou, P., Georgiou, P. and Ballas, D., 2007. Faulting, seismic-stratigraphic architecture and Late Quaternary evolution of the Gulf of Alkyonides Basin–East Gulf of Corinth, Central Greece. *Basin Research*, *19*(2), pp.273-295.

Sarr, A.C., Husson, L., Sepulchre, P., Pastier, A.M., Pedoja, K., Elliot, M., Arias-Ruiz, C., Solihuddin, T. and Aribowo, S., 2019. Subsiding sundaland: reply. *Geology*, *47*(7), pp.e470-e470.

Satake, K., 1994. Mechanism of the 1992 Nicaragua tsunami earthquake. *Geophysical Research Letters*, *21*(23), pp.2519-2522.

Satake, K. and Atwater, B.F., 2007. Long-term perspectives on giant earthquakes and tsunamis at subduction zones. *Annu. Rev. Earth Planet. Sci.*, *35*, pp.349-374.

Sato, T., Higuchi, H., Miyauchi, T., Endo, K., Tsumura, N., Ito, T., Noda, A. and Matsu'ura, M., 2016. The source model and recurrence interval of Genroku-type Kanto earthquakes estimated from paleo-shoreline data. *Earth, Planets and Space*, *68*(1), p.17.

Sato, T. and Matsu'Ura, M., 1992. Cyclic crustal movement, steady uplift of marine terraces, and evolution of the island arc-trench system in southwest Japan. *Geophysical Journal International*, *111*(3), pp.617-629.

Schellmann, G. and Radtke, U., 2000. ESR dating stratigraphically well-constrained marine terraces along the Patagonian Atlantic coast (Argentina). *Quaternary International*, *68*, pp.261-273.

Scheffers, A.M., Scheffers, S.R. and Kelletat, D.H., 2012. Destructive coastlines. In *The Coastlines of the World with Google Earth* (pp. 97-124). Springer, Dordrecht.

Schimmelpfennig, I., Benedetti, L., Finkel, R., Pik, R., Blard, P.H., Bourles, D., Burnard, P. and Williams, A., 2009. Sources of in-situ 36Cl in basaltic rocks. Implications for calibration of production rates. *Quaternary Geochronology*, *4*(6), pp.441-461.

Schlagenhauf, A., Manighetti, I., Benedetti, L., Gaudemer, Y., Finkel, R., Malavieille, J. and Pou, K., 2011. Earthquake supercycles in Central Italy, inferred from 36Cl exposure dating. *Earth and Planetary Science Letters*, *307*(3-4), pp.487-500.

Schlagenhauf, A., Manighetti, I., Benedetti, L., Gaudemer, Y., Malavieille, J., Finkel, R.C. and Pou, K., 2010. Three time scales of earthquake clustering inferred from in-situ 36Cl cosmogenic dating on the Velino-Magnola fault (Central Italy). *AGUFM*, *2010*, pp.T43D-05.

Schlische, R. W., and Anders, M. H., 1996. Stratigraphic effects and tectonic implications of the growth of normal faults and extensional basins. *Special Papers-Geological Society of America*, pp.183-203.

Schlische, R.W., Young, S.S., Ackermann, R.V. and Gupta, A., 1996. Geometry and scaling relations of a population of very small rift-related normal faults. *Geology*, *24*(8), pp.683-686.

Scholz, C. H., and Gupta, A., 2000. Fault interactions and seismic hazard. *Journal of Geodynamics*, *29*(3-5), pp.459-467.

Scholz, D. and Hoffmann, D., 2008. 230Th/U-dating of fossil corals and speleothems. *Quaternary Science Journal*, *57*(1-2), pp.52-76.

Scholz, C. H., and Lawler, T. M., 2004. Slip tapers at the tips of faults and earthquake ruptures. *Geophysical research letters*, *31*(21).

Schneiderwind, S., Boulton, S. J., Papanikolaou, I., Kázmér, M., and Reicherter, K., 2017a. Numerical modeling of tidal notch sequences on rocky coasts of the Mediterranean Basin. *Journal of Geophysical Research: Earth Surface*, 122(5), pp.1154-1181.

Schneiderwind, S., Boulton, S. J., Papanikolaou, I., and Reicherter, K., 2017b. Innovative tidal notch detection using TLS and fuzzy logic: Implications for palaeo-shorelines from compressional (Crete) and extensional (Gulf of Corinth) tectonic settings. *Geomorphology*, *283*, pp.189-200.

Schneiderwind, S., Kazmer, M., Boulton, S., Papanikolaou, I. and Reicherter, K., 2016. Geometry of Holocene tidal notches–sea level markers at Perachora peninsula, Gulf of Corinth, Greece. *Bulletin of the Geological Society of Greece*, *50*(1), pp.468-477.

Scott, A., 1995. Unpublished Thesis, University of Manchester.

Seger, M. and Alexander, J., 1993. Distribution of Plio-Pleistocene and Modern coarse-grained deltas south of the Gulf of Corinth, Greece. *Tectonic controls and signatures in sedimentary successions*, *20*, pp.37-48.

Sgambato, C., Faure Walker, J.P. and Roberts, G.P., 2020. Uncertainty in strain-rate from field measurements of the geometry, rates and kinematics of active normal faults: Implications for seismic hazard assessment. *Journal of Structural Geology*, *131*, p.103934.

Shackleton, N.J., 1969. The last interglacial in the marine and terrestrial records. *Proceedings of the Royal Society of London. Series B. Biological Sciences*, *174*(1034), pp.135-154.

Shackleton, N.J., 1987. Oxygen isotopes, ice volume and sea level. *Quaternary Science Reviews*, *6*(3-4), pp.183-190.

Shackleton, N.J., 2000. The 100,000-year ice-age cycle identified and found to lag temperature, carbon dioxide, and orbital eccentricity. *Science*, *289*(5486), pp.1897-1902.

Shakun, J.D., Lea, D.W., Lisiecki, L.E. and Raymo, M.E., 2015. An 800-kyr record of global surface ocean δ18O and implications for ice volume-temperature coupling. *Earth and Planetary Science Letters*, *426*, pp.58-68.

Shaw, B., 2012. *Active tectonics of the Hellenic subduction zone*. Springer Science & Business Media.

Shaw, B., Ambraseys, N.N., England, P.C., Floyd, M.A., Gorman, G.J., Higham, T.F.G., Jackson, J.A., Nocquet, J.M., Pain, C.C. and Piggott, M.D., 2008. Eastern Mediterranean tectonics and tsunami hazard inferred from the AD 365 earthquake. *Nature Geoscience*, *1*(4), pp.268-276.

Shaw, B. and Jackson, J., 2010. Earthquake mechanisms and active tectonics of the Hellenic subduction zone. *Geophysical Journal International*, *181*(2), pp.966-984.

Shaw, B., Jackson, J.A., Higham, T.F.G., England, P.C. and Thomas, A.L., 2010. Radiometric dates of uplifted marine fauna in Greece: Implications for the interpretation of recent earthquake and tectonic histories using lithophagid dates. *Earth and Planetary Science Letters*, *297*(3-4), pp.395-404.

Shen, G.T. and Dunbar, R.B., 1995. Environmental controls on uranium in reef corals. *Geochimica et Cosmochimica Acta*, *59*(10), pp.2009-2024.

Shen, Z.K., Jackson, D.D., Feng, Y., Cline, M., Kim, M., Fang, P. and Bock, Y., 1994. Postseismic deformation following the Landers earthquake, California, 28 June 1992. *Bulletin of the Seismological Society of America*, *84*(3), pp.780-791.

Siddall, M., Chappell, J. and Potter, E.K., 2007. Eustatic sea level during past interglacials. In *Developments in Quaternary Sciences* (Vol. 7, pp. 75-92). Elsevier.

Siddall, M., Hönisch, B., Waelbroeck, C. and Huybers, P., 2010. Changes in deep Pacific temperature during the mid-Pleistocene transition and Quaternary. *Quaternary Science Reviews*, *29*(1-2), pp.170-181.

Siddall, M., Rohling, E.J., Almogi-Labin, A., Hemleben, C., Meischner, D., Schmelzer, I. and Smeed, D.A., 2003. Sea-level fluctuations during the last glacial cycle. *Nature*, *423*(6942), pp.853-858.

Siddall, M., Smeed, D.A., Matthiesen, S. and Rohling, E.J., 2002. Modelling the seasonal cycle of the exchange flow in Bab el Mandab (Red Sea). *Deep Sea Research Part I: Oceanographic Research Papers*, *49*(9), pp.1551-1569.

Sieh, K.E., 1981. *A review of geological evidence for recurrence times of large earthquakes* (No. 4, pp. 181-207). Washington, DC: American Geophysical Union.

Sieh, K., Natawidjaja, D.H., Meltzner, A.J., Shen, C.C., Cheng, H., Li, K.S., Suwargadi, B.W., Galetzka, J., Philibosian, B. and Edwards, R.L., 2008. Earthquake supercycles inferred from sea-level changes recorded in the corals of west Sumatra. *Science*, *322*(5908), pp.1674-1678.

Sieh, K., Stuiver, M. and Brillinger, D., 1989. A more precise chronology of earthquakes produced by the San Andreas fault in southern California. *Journal of Geophysical Research: Solid Earth*, *94*(B1), pp.603-623.

Simms, A.R., DeWitt, R., Kouremenos, P. and Drewry, A.M., 2011. A new approach to reconstructing sea levels in Antarctica using optically stimulated luminescence of cobble surfaces. *Quaternary Geochronology*, *6*(1), pp.50-60.

Sivan, D., Sisma-Ventura, G., Greenbaum, N., Bialik, O.M., Williams, F.H., Tamisiea, M.E., Rohling, E.J., Frumkin, A., Avnaim-Katav, S., Shtienberg, G. and Stein, M., 2016. Eastern Mediterranean sea levels through the last interglacial from a coastal-marine sequence in northern Israel. *Quaternary Science Reviews*, *145*, pp.204-225.

Skinner, L.C. and Shackleton, N.J., 2005. An Atlantic lead over Pacific deep-water change across Termination I: implications for the application of the marine isotope stage stratigraphy. *Quaternary Science Reviews*, *24*(5-6), pp.571-580.

Skourtsos, E., 2007, May. Pope. and Triantaphyllou, MV 2007: Tectono-Sedimentary evolution and rates of tectonic uplift of the Sfakia coastal zone, southwestern Crete. In *11th International Conference of the Geological Society of Greece, Athens* (pp. 24-26).

Snopek, K., Meier, T., Endrun, B., Bohnhoff, M. and Casten, U., 2007. Comparison of gravimetric and seismic constraints on the structure of the Aegean lithosphere in the forearc of the Hellenic subduction zone in the area of Crete. *Journal of Geodynamics*, *44*(3-5), pp.173-185.

Sosdian, S. and Rosenthal, Y., 2009. Deep-sea temperature and ice volume changes across the Pliocene-Pleistocene climate transitions. *Science*, *325*(5938), pp.306-310.

Soter, S., 1999. Holocene uplift and subsidence of the Helike Delta, Gulf of Corinth, Greece. *Geological Society, London, Special Publications*, *146*(1), pp.41-56.

Soter, S., Blackwelder, P., Tziavos, C., Katsonopoulou, D., Hood, T. and Alvarez-Zarikian, C., 2001. Environmental analysis of cores from the Helike Delta, Gulf of Corinth, Greece. *Journal of Coastal Research*, pp.95-106.

Speed, R.C. and Cheng, H., 2004. Evolution of marine terraces and sea level in the last interglacial, Cave Hill, Barbados. *Geological Society of America Bulletin*, *116*(1-2), pp.219-232.

Spratt, R.M. and Lisiecki, L.E., 2016. A Late Pleistocene sea level stack. *Climate of the Past*, *12*(4), pp.1079-1092.

Stanley, D.J. and Warne, A.G., 1994. Worldwide initiation of Holocene marine deltas by deceleration of sea-level rise. *Science*, *265*(5169), pp.228-231.

Stefatos, A., Papatheodorou, G., Ferentinos, G., Leeder, M., and Collier, R., 2002. Seismic reflection imaging of active offshore faults in the Gulf of Corinth: their seismotectonic significance. *Basin Research*, *14*(4), pp.487-502.

Stein, R.S. and Barrientos, S.E., 1985. Planar high-angle faulting in the Basin and Range: Geodetic analysis of the 1983 Borah Peak, Idaho, earthquake. *Journal of Geophysical Research: Solid Earth*, *90*(B13), pp.11355-11366.

Stein, S., Geller, R.J. and Liu, M., 2012. Why earthquake hazard maps often fail and what to do about it. *Tectonophysics*, *562*, pp.1-25.

Stein, S. and Okal, E.A., 2005. Speed and size of the Sumatra earthquake. *Nature*, *434*(7033), pp.581-582.

Stein, S. and Okal, E.A., 2011. The size of the 2011 Tohoku earthquake need not have been a surprise. *Eos, Transactions American Geophysical Union*, *92*(27), pp.227-228.

Stein, M., Wasserburg, G.J., Aharon, P., Chen, J.H., Zhu, Z.R., Bloom, A. and Chappell, J., 1993. TIMS U-series dating and stable isotopes of the last interglacial event in Papua New Guinea. *Geochimica et Cosmochimica Acta*, *57*(11), pp.2541-2554.

Stephenson, T.A. and Stephenson, A., 1949. The universal features of zonation between tide-marks on rocky coasts. *The Journal of Ecology*, pp.289-305.

Stepp, J.C., Wong, I., Whitney, J., Quittmeyer, R., Abrahamson, N., Toro, G., Youngs, R., Coppersmith, K., Savy, J., Sullivan, T. and Yucca Mountain PSHA Project Members, 2001. Probabilistic seismic hazard analyses for ground motions and fault displacement at Yucca Mountain, Nevada. *Earthquake Spectra*, *17*(1), pp.113-151.

Stirling, C.H., Esat, T.M., Lambeck, K. and McCulloch, M.T., 1998. Timing and duration of the Last Interglacial: evidence for a restricted interval of widespread coral reef growth. *Earth and Planetary Science Letters*, *160*(3-4), pp.745-762.

Stirling, C.H. and Andersen, M.B., 2009. Uranium-series dating of fossil coral reefs: extending the sea-level record beyond the last glacial cycle. *Earth and Planetary Science Letters*, *284*(3-4), pp.269-283.

Stiros, S.C., 2001. The AD 365 Crete earthquake and possible seismic clustering during the fourth to sixth centuries AD in the Eastern Mediterranean: a review of historical and archaeological data. *Journal of Structural Geology*, *23*(2-3), pp.545-562.

Stiros, S.C., 2010. The 8.5+ magnitude, AD365 earthquake in Crete: Coastal uplift, topography changes, archaeological and historical signature. *Quaternary International*, *216*(1-2), pp.54-63.

Stiros, S.C. and Papageorgiou, S., 2001. Seismicity of Western Crete and the destruction of the town of Kisamos at AD 365: Archaeological evidence. *Journal of Seismology*, *5*(3), pp.381-397.

Stiros, S. C., and Pirazzoli, P. A., 1995. Palaeoseismic studies in Greece: a review. *Quaternary International*, *25*, pp.57-63.

Stone, J.O.H., Evans, J.M., Fifield, L.K., Allan, G.L. and Cresswell, R.G., 1998. Cosmogenic chlorine-36 production in calcite by muons. *Geochimica et Cosmochimica Acta*, *62*(3), pp.433-454.

Stone, J., Lambeck, K., Fifield, L.K., Evans, J.T. and Cresswell, R.G., 1996. A lateglacial age for the main rock platform, western Scotland. *Geology*, *24*(8), pp.707-710.

Strasser, T.F., Runnels, C., Wegmann, K., Panagopoulou, E., Mccoy, F., Digregorio, C., Karkanas, P. and Thompson, N., 2011. Dating Palaeolithic sites in southwestern Crete, Greece. *Journal of Quaternary Science*, *26*(5), pp.553-560.

Strobl, M., Hetzel, R., Fassoulas, C. and Kubík, P.W., 2014. A long-term rock uplift rate for eastern Crete and geodynamic implications for the Hellenic subduction zone. *Journal of Geodynamics*, *78*, pp.21-31.

Spampinato, C. R. (2011) Unpublished Thesis. Metodi di analisi delle deformazioni verticali lungo aree costiere della Sicilia orientale e Calabrai meridionale. Universita degli studi di Catania.

Stuart, F. M., and Dunai, T. J., 2009. Advances in cosmogenic isotope research from CRONUS-EU. *Quaternary Geochronology*, 4(6), pp.435-436.

Subarya, C., Chlieh, M., Prawirodirdjo, L., Avouac, J.P., Bock, Y., Sieh, K., Meltzner, A.J., Natawidjaja, D.H. and McCaffrey, R., 2006. Plate-boundary deformation associated with the great Sumatra–Andaman earthquake. *Nature*, *440*(7080), pp.46-51.

Taylor, B., Weiss, J.R., Goodliffe, A.M., Sachpazi, M., Laigle, M. and Hirn, A., 2011. The structures, stratigraphy and evolution of the Gulf of Corinth rift, Greece. *Geophysical Journal International*, *185*(3), pp.1189-1219.

Taymaz, T., Jackson, J., and McKenzie, D., 1991. Active tectonics of the north and central Aegean Sea. *Geophysical Journal International*, *106*(2), pp.433-490.

Taymaz, T., Jackson, J. and Westaway, R., 1990. Earthquake mechanisms in the Hellenic Trench near Crete. *Geophysical Journal International*, *102*(3), pp.695-731.

Teichert, B.M.A., Eisenhauer, A., Bohrmann, G., Haase-Schramm, A., Bock, B. and Linke, P., 2003. U/Th systematics and ages of authigenic carbonates from Hydrate Ridge, Cascadia Margin: recorders of fluid flow variations. *Geochimica et Cosmochimica Acta*, *67*(20), pp.3845-3857.

Ten Veen, J.H. and Kleinspehn, K.L., 2003. Incipient continental collision and plate-boundary curvature: Late Pliocene–Holocene transtensional Hellenic forearc, Crete, Greece. *Journal of the Geological Society*, *160*(2), pp.161-181.

Ten Veen, J.H. and Meijer, P.T., 1998. Late Miocene to Recent tectonic evolution of Crete (Greece): geological observations and model analysis. *Tectonophysics*, *298*(1-3), pp.191-208.

Thenhaus, P.C. and Campbell, K.W., 2003. Seismic hazard analysis. *Earthquake engineering handbook*, *8*, pp.1-50.

Thompson, W.G. and Goldstein, S.L., 2005. Open-system coral ages reveal persistent suborbital sea-level cycles. *Science*, *308*(5720), pp.401-404.

Tiberti, M.M., Basili, R. and Vannoli, P., 2014. Ups and downs in western Crete (Hellenic subduction zone). *Scientific reports*, *4*, p.5677.

Toda, S., Stein, R.S., Richards-Dinger, K. and Bozkurt, S.B., 2005. Forecasting the evolution of seismicity in southern California: Animations built on earthquake stress transfer. *Journal of Geophysical Research: Solid Earth*, *110*(B5).

Toda, S., Stein, R.S., Reasenberg, P.A., Dieterich, J.H. and Yoshida, A., 1998. Stress transferred by the 1995 Mw= 6.9 Kobe, Japan, shock: Effect on aftershocks and future earthquake probabilities. *Journal of Geophysical Research: Solid Earth*, *103*(B10), pp.24543-24565.

Toda, S., Stein, R.S., Sevilgen, V. and Lin, J., 2011. Coulomb 3.3 Graphic-rich deformation and stress-change software for earthquake, tectonic, and volcano research and teaching—user guide. *US Geological Survey open-file report*, *1060*(2011), p.63.

Toda, S. and Tsutsumi, H., 2013. Simultaneous reactivation of two, subparallel, inland normal faults during the M w 6.6 11 April 2011 Iwaki earthquake triggered by the M w 9.0 Tohoku-oki, Japan, earthquake. *Bulletin of the Seismological Society of America*, *103*(2B), pp.1584-1602.

Tortorici, G., Bianca, M., de Guidi, G., Monaco, C. and Tortorici, L., 2003. Fault activity and marine terracing in the Capo Vaticano area (southern Calabria) during the Middle-Late Quaternary. *Quaternary International*, *101*, pp.269-278.

Thenhaus, P.C. and Campbell, K.W., 2003. Seismic hazard analysis. *Earthquake engineering handbook*, *8*, pp.1-50.

Trenhaile, A.S., 2000. Modeling the development of wave-cut shore platforms. *Marine Geology*, *166*(1-4), pp.163-178.

Trenhaile, A.S., 2002. Rock coasts, with particular emphasis on shore platforms. *Geomorphology*, *48*(1-3), pp.7-22.

Trenhaile, A.S., 2015. Coastal notches: Their morphology, formation, and function. *Earth-Science Reviews*, *150*, pp.285-304.

Tsapanos, T.M., Papadopoulos, G.A. and Galanis, O.C., 2003. Time independent seismic hazard analysis of Greece deduced from Bayesian statistics.

Tsapanos, T.M., Mäntyniemi, P. and Kijko, A., 2004. A probabilistic seismic hazard assessment for Greece and the surrounding region including site-specific considerations. *Annals of Geophysics*, *47*(6).

Tsimi, C., Ganas, A., Ferrier, G., Drakatos, G., Pope, R.J. and Fassoulas, C., 2007. Morphotectonics of the Sfakia normal fault, southwestern Crete, Greece. In *Proceedings of 8th Pan-Hellenic Geographical Conference* (pp. 4-7).

Tucker, G.E., McCoy, S.W., Whittaker, A.C., Roberts, G.P., Lancaster, S.T. and Phillips, R., 2011. Geomorphic significance of postglacial bedrock scarps on normal-fault footwalls. *Journal of Geophysical Research: Earth Surface*, *116*(F1).

Turner, J.A., Leeder, M.R., Andrews, J.E., Rowe, P.J., Van Calsteren, P. and Thomas, L., 2010. Testing rival tectonic uplift models for the Lechaion Gulf in the Gulf of Corinth rift. *Journal of the Geological Society*, *167*(6), pp.1237-1250.

Umeda, K., 2015. Localized extensional tectonics in an overall reverse-faulting regime, Northeast Japan. *Geoscience Letters*, *2*(1), pp.1-8.

Valensise, G. and Ward, S.N., 1991. Long-term uplift of the Santa Cruz coastline in response to repeated earthquakes along the San Andreas fault. *Bulletin of the Seismological Society of America*, *81*(5), pp.1694-1704.

Valentini, A., Visini, F., and Pace, B., 2017. Integrating faults and past earthquakes into a probabilistic seismic hazard model for peninsular Italy. *Natural Hazards Earth System Sciences*.

van Calsteren, P. and Thomas, L., 2006. Uranium-series dating applications in Natural Environmental Science. *Earth-Science Reviews*, *75*(1-4), pp.155-175.

Vernant, P., Reilinger, R. and McClusky, S., 2014. Geodetic evidence for low coupling on the Hellenic subduction plate interface. *Earth and Planetary Science Letters*, *385*, pp.122-129.

Vigny, C., Socquet, A., Peyrat, S., Ruegg, J.C., Métois, M., Madariaga, R., Morvan, S., Lancieri, M., Lacassin, R., Campos, J. and Carrizo, D., 2011. The 2010 Mw 8.8 Maule megathrust earthquake of central Chile, monitored by GPS. *Science*, *332*(6036), pp.1417-1421.

Vita-Finzi, C., 1993. Evaluating late Quaternary uplift in Greece and Cyprus. *Geological Society, London, Special Publications*, *76*(1), pp.417-424.

Vittori, E., Di Manna, P., Blumetti, A.M., Comerci, V., Guerrieri, L., Esposito, E., Michetti, A.M., Porfido, S., Piccardi, L., Roberts, G.P. and Berlusconi, A., 2011. Surface faulting of the 6 April 2009 M w 6.3 L'Aquila earthquake in central Italy. *Bulletin of the Seismological Society of America*, *101*(4), pp.1507-1530.

Waelbroeck, C., Labeyrie, L., Michel, E., Duplessy, J.C., McManus, J.F., Lambeck, K., Balbon, E. and Labracherie, M., 2002. Sea-level and deep water temperature changes derived from benthic foraminifera isotopic records. *Quaternary Science Reviews*, *21*(1-3), pp.295-305.

Walsh, J.J. and Watterson, J., 1989. Displacement gradients on fault surfaces. *Journal of Structural Geology*, *11*(3), pp.307-316.

Walsh, J.J. and Watterson, J., 1990. New methods of fault projection for coalmine planning. *Proceedings of the Yorkshire Geological Society*, *48*(2), pp.209-219.

Wardell, N., Camera, L., Mascle, J., Nicolich, R., Marchi, M. and Barison, E., 2014. The structural framework of the Peloponnese continental margin from Zakynthos to Pylos from seismic reflection and morpho-bathymetric data. *Bollettino di Geofisica Teorica ed Applicata*, *55*(2).

Wartman, J., Dunham, L., Tiwari, B. and Pradel, D., 2013. Landslides in Eastern Honshu Induced by the 2011 Tohoku EarthquakeLandslides in Eastern Honshu Induced by the 2011 Tohoku Earthquake. *Bulletin of the Seismological Society of America*, *103*(2B), pp.1503-1521.

Wegmann, K.W., 2008. Unpublished Thesis *Tectonic geomorphology above Mediterranean subduction zones: northeastern Apennines of Italy and Crete, Greece*. Lehigh University.

Wells, D.L. and Coppersmith, K.J., 1994. New empirical relationships among magnitude, rupture length, rupture width, rupture area, and surface displacement. *Bulletin of the seismological Society of America*, *84*(4), pp.974-1002.

Wesnousky, S. G., 2008. Displacement and geometrical characteristics of earthquake surface ruptures: Issues and implications for seismic-hazard analysis and the process of earthquake rupture. *Bulletin of the Seismological Society of America*, *98*(4), pp.1609-1632.

Wesnousky, S. G., and Biasi, G. P., 2011. The length to which an earthquake will go to rupture. *Bulletin of the Seismological Society of America*, *101*(4), pp.1948-1950.

Wessel, J.K., Fryer, P., Wessel, P. and Taylor, B., 1994. Extension in the northern Mariana inner forearc. *Journal of Geophysical Research: Solid Earth*, *99*(B8), pp.15181-15203.

Westaway, R., 1993. Quaternary uplift of southern Italy. *Journal of Geophysical Research: Solid Earth*, *98*(B12), pp.21741-21772.

Westaway, R., 2002. The Quaternary evolution of the Gulf of Corinth, central Greece: coupling between surface processes and flow in the lower continental crust. *Tectonophysics*, *348*(4), pp.269-318.

Willemse, E. J., Pollard, D. D., and Aydin, A., 1996. Three-dimensional analyses of slip distributions on normal fault arrays with consequences for fault scaling. *Journal of Structural Geology*, *18*(2-3), pp.295-309.

Wilkinson, M., Roberts, G.P., McCaffrey, K., Cowie, P.A., Walker, J.P.F., Papanikolaou, I., Phillips, R.J., Michetti, A.M., Vittori, E., Gregory, L. and Wedmore, L., 2015. Slip distributions on active normal faults measured from LiDAR and field mapping of geomorphic offsets: an example from L'Aquila, Italy, and implications for modelling seismic moment release. *Geomorphology*, *237*, pp.130-141.

Wu, D., and Bruhn, R. L., 1994. Geometry and kinematics of active normal faults, South Oquirrh Mountains, Utah: implication for fault growth. Journal of Structural Geology, 16(8), pp.1061-1075.

Wyss, M. and Baer, M., 1981. Earthquake hazard in the Hellenic arc. *Earthquake Prediction: An International Review*, *4*, pp.153-172.

Yaltirak, C., Sakinç, M., Aksu, A.E., Hiscott, R.N., Galleb, B. and Ulgen, U.B., 2002. Late Pleistocene uplift history along the southwestern Marmara Sea determined from raised coastal deposits and global sea-level variations. *Marine Geology*, *190*(1-2), pp.283-305.

Yang, G., Li, Y., Santosh, M., Gu, P., Yang, B., Zhang, B., Wang, H., Zhong, X. and Tong, L., 2012. A Neoproterozoic seamount in the Paleoasian Ocean: Evidence from zircon U–Pb geochronology and geochemistry of the Mayile ophiolitic mélange in West Junggar, NW China. *Lithos*, *140*, pp.53-65.

Yielding, G., Needham, T., and Jones, H., 1996. Sampling of fault populations using sub-surface data: a review. *Journal of Structural Geology*, 18(2-3), pp.135-146.

Yokoyama, Y. and Esat, T.M., 2011. Global climate and sea level: Enduring variability and rapid fluctuations over the past 150,000 years. *Oceanography*, *24*(2), pp.54-69.

Yolsal-Çevikbilen, S. and Taymaz, T., 2012. Earthquake source parameters along the Hellenic subduction zone and numerical simulations of historical tsunamis in the Eastern Mediterranean. *Tectonophysics*, *536*, pp.61-100.

Zachos, J., Pagani, M., Sloan, L., Thomas, E. and Billups, K., 2001. Trends, rhythms, and aberrations in global climate 65 Ma to present. *science*, *292*(5517), pp.686-693.

Zelilidis, A., 2000. Drainage evolution in a rifted basin, Corinth graben, Greece. *Geomorphology*, *35*(1-2), pp.69-85.

Zhang, P., Slemmons, D. B., and Mao, F., 1991. Geometric pattern, rupture termination and fault segmentation of the Dixie Valley—Pleasant Valley active normal fault system, Nevada, USA. *Journal of Structural Geology*, 13(2), pp.165-176.

Zygouri, V., Koukouvelas, I. and Ganas, A., 2016. Palaeoseismological analysis of the east Giouchtas Fault, Heraklion Basin, Crete (prelimenary results). *Bulletin of the Geological Society of Greece*, *50*(1), pp.563-571.

APPENDICES

APPENDIX 1: INPUT DATA FOR CRONUSCALC TO DETERMINE THE AGES OF ALL ^{36}CL EXPOSURE SAMPLES FEATURED WITHIN THIS THESIS (NUMBERS 1-81 REFER TO THE INPUT CELLS WITHIN CRONUSCALC)

Location	Chapter discussed in	Sample name	Age accepted or rejected	1: Lab Sample Name	2: Scaling (Select One)	3: Latitude decimal degrees	4: Longitude decimal degrees	5: Elevation meters	6: Pressure hPa	7: Atmospheric Pressure or Elevation (Select One)	8: Sample Thickness cm	9: Bulk Density g/cm 3	10: Shielding Factor unitless	11: Erosion Rate mm/kyr	12: Conc. 36Cl Atoms of 36 Cl/g of sample	13: Attenuation length g/cm 2	14: Depth to Top of Sample g/cm 2	15: Year Collected Year A.D.
Cape Heraion	3	CH6	Rejected*	Her-6	DE	38.02851	22.85106	8		Elevation	2.8	2.233	0.9898	0.2	708221	160	0	2000
Cape Heraion	3	CH7	Rejected*	Her-7	DE	38.02851	22.85106	8		Elevation	3.5	2.233	0.9898	0.2	1255949	160	0	2000
South Crete	3	S9	Rejected**	Cr-Ar-9	DE	35.00268	25.45582	397		Elevation	3	2.649	0.961309	0.2	1430271	160	0	2000
South Crete	3	S11	Rejected**	Cr-Ar-11	DE	35.00592	25.45144	349		Elevation	3.8	2.649	0.988434	0.2	1119629	160	0	2000
South Crete	3	S12	Rejected**	Cr-Ar-12	DE	35.00515	25.45003	328		Elevation	3	2.649	0.94298	0.2	811964	160	0	2000
South Crete	3	S13	Rejected**	Cr-Ar-13	DE	35.00515	25.45003	336		Elevation	3.2	2.649	0.94298	0.2	674158	160	0	2000
South Crete	4	S1	Accepted	Cr-Ka-14	DE	34.98335	25.34718	43		Elevation	6	2.649	0.983948	0.2	2137936	160	0	2000
South Crete	4	S2	Rejected***	Cr-WTS-6	DE	34.98417	25.28201	20		Elevation	4.2	2.649	0.967895	0.2	677147	160	0	2000
South Crete	4	S5	Accepted	Cr-WTS-17	DE	34.98207	25.27847	80		Elevation	4.5	2.649	0.974302	0.2	1770564	160	0	2000
South Crete	4	S4	Accepted	Cr-WTS-18	DE	34.98106	25.27817	65		Elevation	5	2.649	0.974302	0.2	1464291	160	0	2000
South Crete	4	S3	Accepted	Cr-WTS-19	DE	34.98303	25.27876	34		Elevation	4.5	2.649	0.967895	0.2	1027505	160	0	2000
Cape Heraion	6	S3	Accepted	Her-10	DE	38.03036	22.85522	42		Elevation	3.4	2.565	0.9981	0.2	1887336	160	0	2000
Cape Heraion	6	S5	Accepted	Her-12	DE	38.03046	22.85516	29		Elevation	4.1	2.565	0.9995	0.2	1684932	160	0	2000
Cape Heraion	6	S2	Accepted	Her-13a	DE	38.02919	22.85297	62		Elevation	4	2.565	0.9999	0.2	1195064	160	0	2000
Cape Heraion	6	S1	Accepted	Her-14b	DE	38.02877	22.85106	60		Elevation	3.7	2.649	0.9999	0.2	2327699	160	0	2000
Cape Heraion	6	S4	Accepted	Her-15	DE	38.03203	22.8596	46		Elevation	4.5	2.233	0.9999	0.2	1616569	160	0	2000

16: Water Content in Pores volume fraction	17: Mineral Separation (Select One)	18: Bulk Rock SiO2 oxide weight %	19: Bulk Rock TiO2 oxide weight %	20: Bulk Rock Al2O3 oxide weight %	21: Bulk Rock Fe2O3 oxide weight %	22: Bulk Rock MnO oxide weight %	23: Bulk Rock MgO oxide weight %	24: Bulk Rock CaO oxide weight %	25: Bulk Rock Na2O oxide weight %	26: Bulk Rock K2O oxide weight %	27: Bulk Rock P2O5 oxide weight %	28: Analytical Water weight %	29: Bulk Rock CO2 oxide weight %	30: Bulk Rock Cl ppm	31: Bulk Rock B ppm	32: Bulk Rock Sm ppm	33: Bulk Rock Gd ppm	34: Bulk Rock U ppm	35: Bulk Rock Th ppm
0.01	No	0	0	0	0.103983	0	0.00	53.93082	0	0.00000	0	1.00000	45.96520	103.1002	0	0	0	0	0
0.01	No	0	0	0	0.115239	0	0.00	49.76099	0	0.00000	0	1.00000	50.12377	198.4709	0	0	0	0	0
0.01	No	0	0	0	0.18480	0	0.00	50.05671	0	0.00000	0	1.00000	49.75849	18.41055	0	0	0	0	0
0.01	No	0	0	0	0.02952	0	0.00	47.50108	0	0.00000	0	1.00000	52.46940	15.97013	0	0	0	0	0
0.01	No	0	0	0	0.00000	0	0.00	50.29194	0	0.00000	0	1.00000	49.70806	14.40672	0	0	0	0	0
0.01	No	0	0	0	0.04222	0	0.00	50.14535	0	0.00000	0	1.00000	49.81243	5.804851	0	0	0	0	0
0.01	No	0	0	0	0.01222	0	0.00	50.81103	0	0.00000	0	1.00000	49.17675	26.74987	0	0	0	0	0
0.01	No	0	0	0	0.00000	0	0.00	49.45339	0	0.00000	0	1.00000	50.54661	40.54125	0	0	0	0	0
0.01	No	0	0	0	0.09718	0	0.00	48.56664	0	0.00000	0	1.00000	51.33618	33.00228	0	0	0	0	0
0.01	No	0	0	0	0.17975	0	0.00	50.14857	0	0.00000	0	1.00000	49.67168	29.49288	0	0	0	0	0
0.01	No	0	0	0	0.17257	0	0.00	49.58401	0	0.00000	0	1.00000	50.24342	41.04639	0	0	0	0	0
0.01	No	0	0	0	0.061312	0	0.00	48.98905	0	0.00000	0	1.00000	50.94964	38.77938	0	0	0	0	0
0.01	No	0	0	0	0.120106	0	0.00	53.98398	0	0.00000	0	1.00000	45.89592	60.55609	0	0	0	0	0
0.01	No	0	0	0	0.02843	0	0.00	43.82164	0	0.00000	0	1.00000	56.14993	22.5328	0	0	0	0	0
0.01	No	0	0	0	0.05148	0	0.00	57.38099	0	0.00000	0	1.00000	42.56753	17.05027	0	0	0	0	0
0.01	No	0	0	0	0.02793	0	0.00	53.77027	0	0.00000	0	1.00000	46.20180	33.32635	0	0	0	0	0

36: Bulk Rock Cr ppm	37: Bulk Rock Li ppm	38: Target K2O weight %	39: Target CaO weight %	40: Target TiO2 weight %	41: Target Fe2O3 weight %	42: Target Cl ppm	43: Latitude Uncertainty decimal degrees	44: Longitude Uncertainty decimal degrees	45: Elevation Uncertainty meters	46: Pressure Uncertainty hPa	47: Sample Thickness Uncertainty cm	48: Bulk Density Uncertainty g/cm 3	49: Shielding Factor Uncertainty unitless	50: Erosion-Rate Uncertainty mm/kyr	51: Conc. 36 Cl Uncertainty Atoms of 36 Cl/g of sample	52: Attenuation Length Uncertainty g/cm 2	53: Depth to Top of Sample Uncertainty g/cm 2	54: Year Collected Uncertainty Year A.D.
0	0	0.00000	53.96032	0.00000	0.103983	103.10	0	0	10		0.5	0.2	0	0	37385	10	0	10
0	0	0.00000	49.78821	0.00000	0.115239	198.47	0	0	10		0.5	0.2	0	0	75770	10	0	10
0	0	0.00000	50.08409	0.00000	0.18480	18.41	0	0	10		0.5	0.2	0	0	41051	10	0	10
0	0	0.00000	47.52707	0.00000	0.02952	15.97	0	0	10		0.5	0.2	0	0	32694	10	0	10
0	0	0.00000	50.31946	0.00000	0.00000	14.41	0	0	10		0.5	0.2	0	0	23111	10	0	10
0	0	0.00000	50.17278	0.00000	0.04222	5.80	0	0	10		0.5	0.2	0	0	16674	10	0	10
0	0	0.00000	50.83883	0.00000	0.01222	26.75	0	0	10		0.5	0.2	0	0	74973	10	0	10
0	0	0.00000	49.48044	0.00000	0.00000	40.54	0	0	10		0.5	0.2	0	0	21952	10	0	10
0	0	0.00000	48.59321	0.00000	0.09718	33.00	0	0	10		0.5	0.2	0	0	53271	10	0	10
0	0	0.00000	50.17601	0.00000	0.17975	29.49	0	0	10		0.5	0.2	0	0	44509	10	0	10
0	0	0.00000	49.61114	0.00000	0.17257	41.05	0	0	10		0.5	0.2	0	0	33320	10	0	10
0	0	0.00000	49.01585	0.00000	0.061312	38.78	0	0	10		0.5	0.2	0	0	54970	10	0	10
0	0	0.00000	54.01351	0.00000	0.120106	60.56	0	0	10		0.5	0.2	0	0	46140	10	0	10
0	0	0.00000	43.84561	0.00000	0.02843	22.53	0	0	10		0.5	0.2	0	0	34923	10	0	10
0	0	0.00000	57.41238	0.00000	0.05148	17.05	0	0	10		0.5	0.2	0	0	63421	10	0	10
0	0	0.00000	53.79968	0.00000	0.02793	33.33	0	0	10		0.5	0.2	0	0	47009	10	0	10

55: Water Content in Pores Uncertainty Volume %	56: Bulk Rock SiO 2 Uncertainty oxide weight %	57: Bulk Rock TiO 2 Uncertainty oxide weight %	58: Bulk Rock Al 2 O 3 Uncertainty oxide weight %	59: Bulk Rock Fe 2 O 3 Uncertainty oxide weight %	60: Bulk Rock MnO Uncertainty oxide weight %	61: Bulk Rock MgO Uncertainty oxide weight %	62: Bulk Rock CaO Uncertainty oxide weight %	63: Bulk Rock Na 2 O Uncertainty oxide weight %	64: Bulk Rock K 2 O Uncertainty oxide weight %	65: Bulk Rock P 2 O 5 Uncertainty oxide weight %	66: Analytical Water Uncertainty weight %	67: Bulk Rock CO 2 Uncertainty oxide weight %	68: Bulk Rock Cl Uncertainty ppm	69: Bulk Rock B Uncertainty ppm	70: Bulk Rock Sm Uncertainty ppm	71: Bulk Rock Gd Uncertainty ppm
0.01	0	0.0000	0	0.4540071	0	0	1.3428739	0	0.0000	0	1.00000	1.3428739	6.329419	0	0	0
0.01	0	0.0000	0	0.4653392	0	0	1.3763925	0	0.0000	0	1.00000	1.3763925	14.287165	0	0	0
0.01	0	0.0000	0	0.4471901	0	0	1.3227105	0	0.0000	0	1.00000	1.3227105	0.3513534	0	0	0
0.01	0	0.0000	0	0.4214781	0	0	1.2466588	0	0.0000	0	1.00000	1.2466588	0.291954	0	0	0
0.01	0	0.0000	0	0.4123611	0	0	1.2196926	0	0.0000	0	1.00000	1.2196926	0.2589134	0	0	0
0.01	0	0.0000	0	0.4274038	0	0	1.2641861	0	0.0000	0	1.00000	1.2641861	0.0976822	0	0	0
0.01	0	0.0000	0	0.3948666	0	0	1.1679469	0	0.0000	0	1.00000	1.1679469	0.6260466	0	0	0
0.01	0	0.0000	0	0.40899	0	0	1.2097213	0	0.0000	0	1.00000	1.2097213	1.1910384	0	0	0
0.01	0	0.0000	0	0.4102159	0	0	1.2133472	0	0.0000	0	1.00000	1.2133472	0.8683457	0	0	0
0.01	0	0.0000	0	0.3857355	0	0	1.1409387	0	0.0000	0	1.00000	1.1409387	0.720745	0	0	0
0.01	0	0.0000	0	0.4328924	0	0	1.2804204	0	0.0000	0	1.00000	1.2804204	1.2004864	0	0	0
0.01	0	0.0000	0	0.5135604	0	0	1.5190225	0	0.0000	0	1.00000	1.5190225	0.8002648	0	0	0
0.01	0	0.0000	0	0.4855127	0	0	1.436062	0	0.0000	0	1.00000	1.436062	1.6227309	0	0	0
0.01	0	0.0000	0	0.5157272	0	0	1.5254315	0	0.0000	0	1.00000	1.5254315	0.4739153	0	0	0
0.01	0	0.0000	0	0.4667019	0	0	1.3804232	0	0.0000	0	1.00000	1.3804232	0.2856176	0	0	0
0.01	0	0.0000	0	0.4971407	0	0	1.4704558	0	0.0000	0	1.00000	1.4704558	0.6645615	0	0	0

72: Bulk Rock U Uncertainty ppm	73: Bulk Rock Th Uncertainty ppm	74: Bulk Rock Cr Uncertainty ppm	75: Bulk Rock Li Uncertainty ppm	76: Target K2O Uncertainty weight %	77: Target CaO Uncertainty weight %	78: Target TiO2 Uncertainty weight %	79: Target Fe2O3 Uncertainty weight %	80: Target Cl Uncertainty ppm	81: Covariance unitless
0	0	0	0	0.00000	1.3428739	0.00000	0.4540071	6.329419	0
0	0	0	0	0.00000	1.3763925	0.00000	0.4653392	14.287165	0
0	0	0	0	0.00000	1.3227105	0.00000	0.4471901	0.3513534	0
0	0	0	0	0.00000	1.2466588	0.00000	0.4214781	0.291954	0
0	0	0	0	0.00000	1.2196926	0.00000	0.4123611	0.2589134	0
0	0	0	0	0.00000	1.2641861	0.00000	0.4274038	0.0976822	0
0	0	0	0	0.00000	1.1679469	0.00000	0.3948666	0.6260466	0
0	0	0	0	0.00000	1.2097213	0.00000	0.40899	1.1910384	0
0	0	0	0	0.00000	1.2133472	0.00000	0.4102159	0.8683457	0
0	0	0	0	0.00000	1.1409387	0.00000	0.3857355	0.720745	0
0	0	0	0	0.00000	1.2804204	0.00000	0.4328924	1.2004864	0
0	0	0	0	0.00000	1.5190225	0.00000	0.5135604	0.8002648	0
0	0	0	0	0.00000	1.436062	0.00000	0.4855127	1.6227309	0
0	0	0	0	0.00000	1.5254315	0.00000	0.5157272	0.4739153	0
0	0	0	0	0.00000	1.3804232	0.00000	0.4667019	0.2856176	0
0	0	0	0	0.00000	1.4704558	0.00000	0.4971407	0.6645615	0

*Sample rejected because bulk rock Cl >80 ppm (Section 3.3.3) (Marrero et al., 2016b)
** Sample rejected because ages are indicative of significant erosion (Section 3.3.1.4)
***Sample rejected because the age obtained and geomorphic evidence suggests a complex exposure-covering-re-exposure history (Section 4.